

Transactions of the ASME®

HEAT TRANSFER DIVISION
Chair, L. C. WITTE
Vice Chair, J. H. KIM
Past Chair, R. A. NELSON
Secretary, Y. BAYAZITOGU
Treasurer, R. D. SKOCYPEC
Technical Editor, V. DHIR (2005)
Associate Technical Editors,
C. T. AVEDISIAN (2002)
H. H. BAU (2003)
C. BECKERMANN (2001)
A. BEJAN (2003)
V. P. CAREY (2003)
F. B. CHEUNG (2002)
T. Y. CHU (2002)
B. T. F. CHUNG (2001)
M. FAGHRI (2003)
J. G. GEORGIADIS (2003)
J. P. GORE (2002)
M. HUNT (2002)
D. A. KAMINSKI (2001)
R. L. MAHAJAN (2001)
A. MAJUMDAR (2001)
G. P. PETERSON (2003)
D. POULIKAKOS (2002)
S. S. SADHAL (2002)
R. D. SKOCYPEC (2003)
D. A. ZUMBRUNNEN (2001)

BOARD ON COMMUNICATIONS
Chairman and Vice President
R. K. SHAH

OFFICERS OF THE ASME
President, J. R. PARKER
Executive Director,
D. L. BELDEN
Treasurer,
J. A. MASON

PUBLISHING STAFF
Managing Director, Engineering
CHARLES W. BEARDSLEY
Director, Technical Publishing
PHILIP DI VIETRO
Managing Editor, Technical Publishing
CYNTHIA B. CLARK
Managing Editor, Transactions
CORNELIA MONAHAN
Production Coordinator
JUDITH SIERANT
Production Assistant
MARISOL ANDINO

Transactions of the ASME, Journal of Heat Transfer (ISSN 0022-1481) is published quarterly (Feb., May, Aug., Nov.) by The American Society of Mechanical Engineers, Three Park Avenue, New York, NY 10016. Periodicals postage paid at New York, NY and additional mailing offices. POSTMASTER: Send address changes to Transactions of the ASME, Journal of Heat Transfer, c/o THE AMERICAN SOCIETY OF MECHANICAL ENGINEERS, 22 Law Drive, Box 2300, Fairfield, NJ 07007-2300.

CHANGES OF ADDRESS must be received at Society headquarters seven weeks before they are to be effective. Please send old label and new address.

STATEMENT from By-Laws. The Society shall not be responsible for statements or opinions advanced in papers or ... printed in its publications (B7.1, Para. 3). COPYRIGHT © 2000 by The American Society of Mechanical Engineers. For authorization to photocopy material for internal or personal use under those circumstances not falling within the fair use provisions of the Copyright Act, contact the Copyright Clearance Center (CCC), 222 Rosewood Drive, Danvers, MA 01923, tel: 978-750-8400, www.copyright.com. Request for special permission or bulk copying should be addressed to Reprints/Permission Department. INDEXED by Applied Mechanics Reviews and Engineering Information, Inc. Canadian Goods & Services Tax Registration #126148048.

Journal of Heat Transfer

Published Quarterly by The American Society of Mechanical Engineers

VOLUME 122 • NUMBER 3 • AUGUST 2000

HEAT TRANSFER GALLERY

- 421 Introduction
K. D. Kihm
- 422 Photographs and Simulations of Molten Metal Droplets Landing on a Solid Surface
M. Bussmann, S. D. Aziz, S. Chandra, and J. Mostaghimi
- 423 Lagrangian Flow Mapping of Heated Capillary Pore and Thin Film Using Molecular Fluorescence Velocimetry (MFV)
J. S. Park, C. McCarty, K. D. Kihm, and D. M. Pratt
- 424 Plasma Development During Picosecond Laser Processing of Electronic Materials
Samuel S. Mao, Ralph Greif, Xianglei Mao, and Richard E. Russo
- 425 The Differences in the Counter-Rotating Vortex Pair Structures in a Crossflow Jet Subjected to Various Thermal Stratifications
Kyung Chun Kim, Sang Ki Kim, Sang Youl Yoon, and Kyung Hyun Park
- 426 Interaction of Downward and Upward Convection of Water Between Two Cooling Tubes
Ichiro Nakane, Akira Narumi, and Takao Kashiwagi
- 427 Adiabatic Effectiveness and Nusselt Number Distribution on a Flat Surface With an Oblique Impinging Jet
J. W. Baughn, M. Dietzel, and J. E. Mayhew
- 428 Infrared Photographs of a Gas Loaded Flat Heat Pipe
M. Cerza
- 429 Visualization of Solidification in a Simulated Czochralski System
Michele Ferland, Debasish Mishra, and Vishwanath Prasad

TECHNICAL PAPERS

1999 Max Jakob Memorial Award Lecture

- 430 From Heat Transfer Principles to Shape and Structure in Nature: Constructal Theory
Adrian Bejan

Conduction Heat Transfer

- 450 Inverse Determination of Temperature-Dependent Thermal Conductivity Using Steady Surface Data on Arbitrary Objects
T. J. Martin and G. S. Dulikravich

Forced Convection

- 460 Inverse Convection Problem for Determining Wall Heat Flux in Annular Duct Flow
H.-Y. Li and W.-M. Yan
- 465 Heat Transfer and Pressure Drop of Laminar Flow in Horizontal Tubes With/Without Longitudinal Inserts
S.-S. Hsieh and I.-W. Huang

(Contents continued on inside back cover)

This journal is printed on acid-free paper, which exceeds the ANSI Z39.48-1992 specification for permanence of paper and library materials. ©™
♻️ 85% recycled content, including 10% post-consumer fibers.

Natural and Mixed Convection

- 476 Effect of Double Dispersion on Mixed Convection Heat and Mass Transfer in Non-Darcy Porous Medium
P. V. S. N. Murthy
- 485 Laminar Natural Convection in Isosceles Triangular Enclosures Heated From Below and Symmetrically Cooled From Above
G. A. Holtzman, R. W. Hill, and K. S. Ball

Radiative Transfer

- 492 Inverse Design Model for Radiative Heat Transfer
J. R. Howell, O. A. Ezekoye, and J. C. Morales
- 503 Comparison of Monte Carlo Surface Exchange With Radiative Continuum Results in Large Particle Dispersions
E. Nisipeanu and P. D. Jones

Boiling and Condensation

- 509 Pool Boiling Heat Transfer From Plain and Microporous, Square Pin-Finned Surfaces in Saturated FC-72
K. N. Rainey and S. M. You

Combustion

- 517 Optical Properties in the Visible of Overfire Soot in Large Buoyant Turbulent Diffusion Flames
S. S. Krishnan, K.-C. Lin, and G. M. Faeth

Heat Pipes

- 525 An Experimental Investigation of the Transient Characteristics on a Flat-Plate Heat Pipe During Startup and Shutdown Operations
Y. Wang and K. Vafai

Microscale Heat Transfer

- 536 Molecular Dynamics Study of Solid Thin-Film Thermal Conductivity
J. R. Lukes, D. Y. Li, X.-G. Liang, and C.-L. Tien
- 544 An Experimental Study of Molten Microdroplet Surface Deposition and Solidification: Transient Behavior and Wetting Angle Dynamics
D. Attinger, Z. Zhao, and D. Poulikakos

Porous Media, Particles, and Droplets

- 557 Forced Convection in High Porosity Metal Foams
V. V. Calmidi and R. L. Mahajan

Heat Exchangers

- 566 Estimating Number of Shells in Shell and Tube Heat Exchangers: A New Approach Based on Temperature Cross
B. B. Gulyani
- 572 Flow and Heat Transfer Correlations for Porous Fin in a Plate-Fin Heat Exchanger
S. Y. Kim, J. W. Paek, and B. H. Kang
- 579 Optimization of Matrix Heat Exchanger Geometry
K. Pavan Kumar and G. Venkatarathnam

Heat Transfer Enhancement

- 587 Influence of Crossflow-Induced Swirl and Impingement on Heat Transfer in an Internal Coolant Passage of a Turbine Airfoil
S. V. Ekkad, G. Pamula, and S. Acharya

TECHNICAL NOTES

- 598 Transient Double Diffusive Convection in a Vertical Enclosure With Asymmetrical Boundary Conditions
S. Mergui and D. Gobin
- 602 Natural Convection in Low Prandtl Number Fluids With a Vertical Magnetic Field
S. Saravanan and P. Kandaswamy
- 606 Approximate Solution of a Class of Radiative Heat Transfer Problems
H. Qiao, Y. Ren, and B. Zhang
- 613 An Analytical Model to Predict Condensation of R-410A in a Horizontal Rectangular Channel
Z. Guo and N. K. Anand
- 620 Subcooled Flow Boiling in Circumferentially Nonuniform and Uniform Heated Vertical Channels With Downward Flow
Q. Peatiwala and R. D. Boyd, Sr.

- 626 Fusion Zone Shapes in Electron-Beam Welding Dissimilar Metals
P. S. Wei, Y. K. Kuo, and J. S. Ku

DISCUSSION

- 632 Discussion of "Heat Transfer Measurement and Analysis for Sintered Porous Channels," by G. J. Hwang and C. H. Chao—Discussion by S. J. Kim and D. Kim

ANNOUNCEMENTS AND SPECIAL NOTES

- 634 Second ICHMT Symposium on Advances in Computational Heat Transfer—Announcement
636 2000 IMECE Session on Photogallery of Heat Transfer Phenomena—Call for Photographs
637 Turbulent Heat Transfer III—Announcement
638 35th National Heat Transfer Conference—Call for Papers
639 Information for Authors

Heat Transfer Gallery

The fourth "Heat Transfer Photogallery" was held at the 1999 International Mechanical Engineering Congress and Exhibition in Nashville last November. The Heat Transfer Visualization Committee sponsored the session and attracted 13 photo displays, which illustrate phenomena that occur in the presence of a temperature gradient. Eight entries were selected for publication in this special section of the ASME *Journal of Heat Transfer*.

The purpose of publishing these photographs is to draw attention to the innovative features of optical diagnostics and aesthetic qualities of thermal processes. To focus on the visualization, the text is kept at a minimum and further details should be found through the listed references or directly from the authors. The photographs include visualizations of: (1) phenomena of molten droplet breakup on a solid surface, (2) microscale flow velocity mapping using molecular fluorescence velocimetry (MFV), (3) picosecond laser pulse impact on a surface, (4) counter-rotating thermal cross flows, (5) natural convection using interferometry, (6) oblique impinging jet using liquid crystal technique, (7) gas loaded heat pipe using infrared imaging, and (8) solidification of water using liquid crystal thermography. It is now proposed that the journal readers enjoy viewing these collections, acquire knowledge of the state-of-the-art features potentially applicable for their own research, and promote their participation in IMECE Photogallery session presentation (refer to the Call for Photogallery for 2000-IMECE announced in this volume).

The web-based review (<http://www.mengr.tamu.edu/otherlinks/htppr/index.asp>) has been carried out and the review was based on the subjective measure of the merit of individual entries, i.e., their innovative features in visualization techniques, scientific importance on heat and mass transfer phenomena, and the artistic beauty of the presentation. Sincere thanks go to the following who participated in the web-based reviews in ranking the entries: C. Ammerman, J. Baughn, Y. Bayazitoglu, C. Beckermann, M. Bussmann, M. Cerza, S. Chandra, T. Y. Chu, R. Douglass, S. V. Ekkad, D. K. Ezekoye, A. Haji-Sheikh, J. Howell, M. Hung, M. K. Jensen, D. Juric, J. Kim, K. C. Kim, J. Lage, J. H. Lienhard, J. R. Lloyd, S. S. Mao, I. Nakane, J. M. Ochterbeck, C. H. Oh, T. O'Hern, and R. H. Page. Special thanks go to the Technical

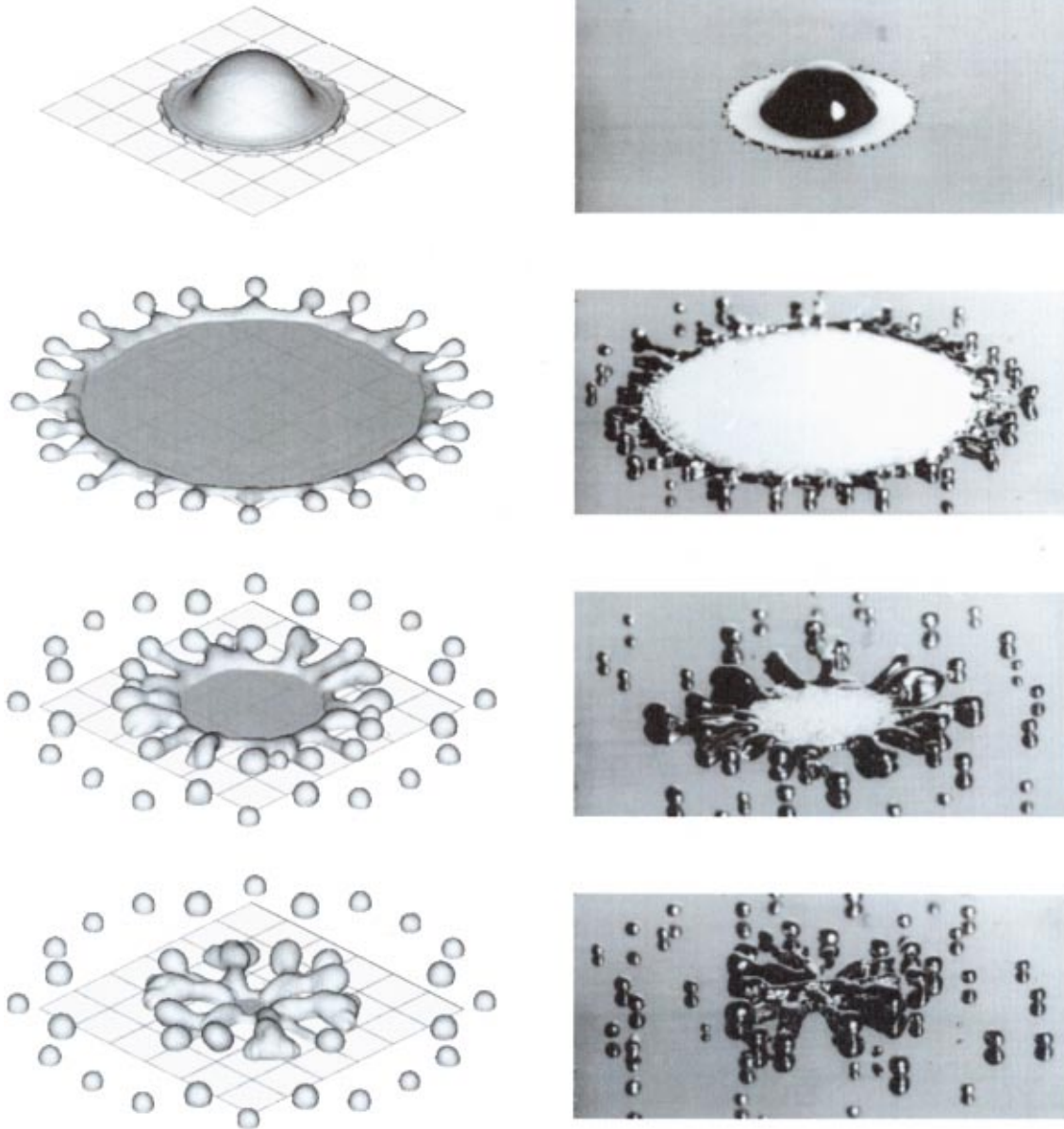
Editor, Jack Howell, for his support and editorial guidance toward the publication of the photogallery entries. The editorial assistance of Ms. Judith Sierant of ASME is appreciated in the production of this photo collection.

References

- Aziz, S. D., and Chandra, S., 2000, "Impact, Recoil and Splashing of Molten Metal Droplets," *Int. J. Heat Mass Transf.*, **43**, pp. 2841–2857.
- Bussmann, M., Mostaghimi, J., and Chandra, S., 1999, "On a Three-Dimensional Volume Tracking Model of Droplet Impact," *Phys. Fluids*, **11**, pp. 1406–1417.
- Cerza, M., Boughey, B., and Lindler, K. W., 2000, "A Flat Heat Pipe for Use as a Cold Side Heat Sink," Session on Heat Pipes, *Proceedings of the 35th Intersociety Energy Conversion Engineering Conference*, AIAA, July 24–28, AIAA, Washington, DC, pp. 1418–1427.
- Kim, Kyung Chun, and Kim, Sang Ki, 1998, "Flow Visualization Study on Plume Behavior in Thermally Stratified Wind," *Int. J. Environ. Conscious Design Manuf.*, **7**, No. 4, pp. 25–35.
- Kihm, K. D., Kim, H. J., and Pratt, D. M., 1999, "Image Corrections for Heated Micro-Scale Capillary Pore Flows," 2nd Pacific Symposium on Flow Visualization and Image Processing (PSFVIP-2), Paper No. OF203, May, Honolulu, HI.
- Kihm, K. D., and Pratt, D. M., 1999, "Contour Mapping of Thin Liquid Film Thickness Using Fizeau Interferometer," Paper No. NHTC99-224, Aug., Albuquerque, NM.
- Mao, S. S., Mao, X. L., Grief, R., and Russo, R. E., 2000, "Dynamics of an Air Breakdown Plasma on a Solid Surface During Picosecond Laser Ablation," *Appl. Phys. Lett.*, **76**, p. 31.
- Mukherjee, D. K., Prasad, V., Dutta, P., and Yuan, T., 1996, "Liquid Crystal Visualization of the Effects of Crucible and Crystal Rotation on the CZ Melt Flows," *J. Cryst. Growth*, **169**, pp. 136–146.
- Narumi, A., Ohishi, S., Nakane, I., and Kashiwagi, T., 1995, "Flow Visualization of Convective Interference of Water Around Two Cooling Tubes by Holographic Interferometry," *Proceedings, 7th International Symposium on Flow Visualization*, J. P. Crowder, ed., Begell House, New York, pp. 314–319.
- Russo, R. E., Mao, X. L., Liu, H. C., Yoo, J. H., and Mao, S. S., 1999, "Time-Resolved Plasma Diagnostics and Mass Removal During Single-Pulse Laser Ablation," *Appl. Phys. A: Mater. Sci. Process.*, **69A**, p. S887.

K. D. Kihm

Department of Mechanical Engineering,
Texas A&M University,
College Station, TX 77843-3123



PHOTOGRAPHS AND SIMULATIONS OF MOLTEN METAL DROPLETS LANDING ON A SOLID SURFACE

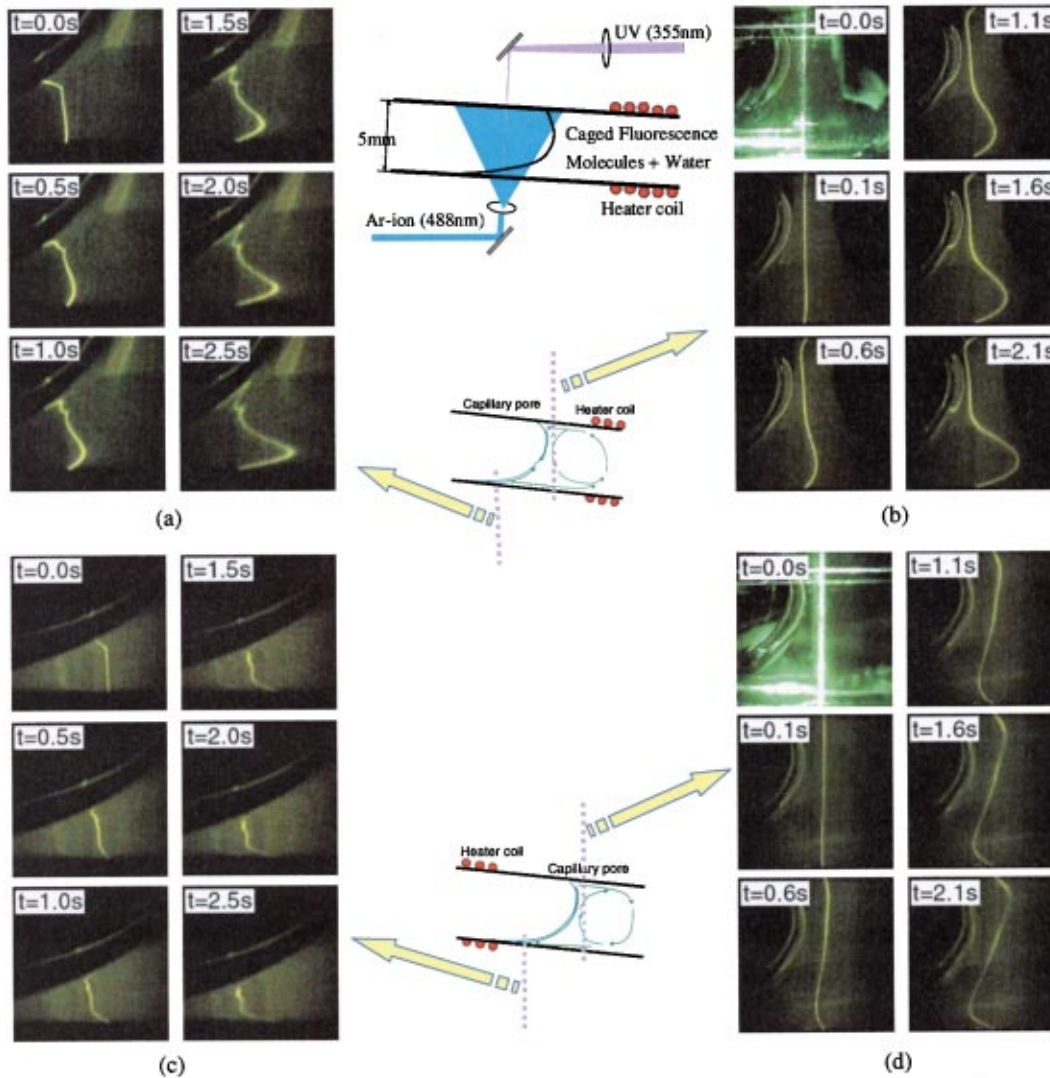
M. Bussmann, S. D. Aziz, S. Chandra, and J. Mostaghimi

Department of Mechanical & Industrial Engineering, University of Toronto, Toronto, Canada

We present photographs and numerical simulations of the impact of molten tin droplets onto a solid stainless steel surface. A single-shot flash photographic technique is used to capture droplet impact. An electronic flash unit takes a single 35-mm photograph of a droplet at one instant after impact. As a droplet falls towards the surface it interrupts the beam of a 0.5 mW He-Ne laser. A photodiode detects this interruption and signals the time delay circuit, which opens the shutter of a 35-mm camera and then after a preset delay triggers the flash unit, producing an 8- μ s duration flash. Impacting droplets are photographed at different stages of deformation by varying the time delay before triggering the flash,

and the entire impact process pieced together from these photographs.

To simulate droplet impact we have developed a three-dimensional free surface flow model. The model combines a fixed-grid finite volume discretization of the Navier-Stokes equations with a volume tracking method to track the free surface location. The model is capable of predicting complex fluid deformation during droplet impact, including spreading and recoil. We simulate the growth of instabilities around the rim of an impacting droplet, which leads to splashing and the detachment of satellite droplets.



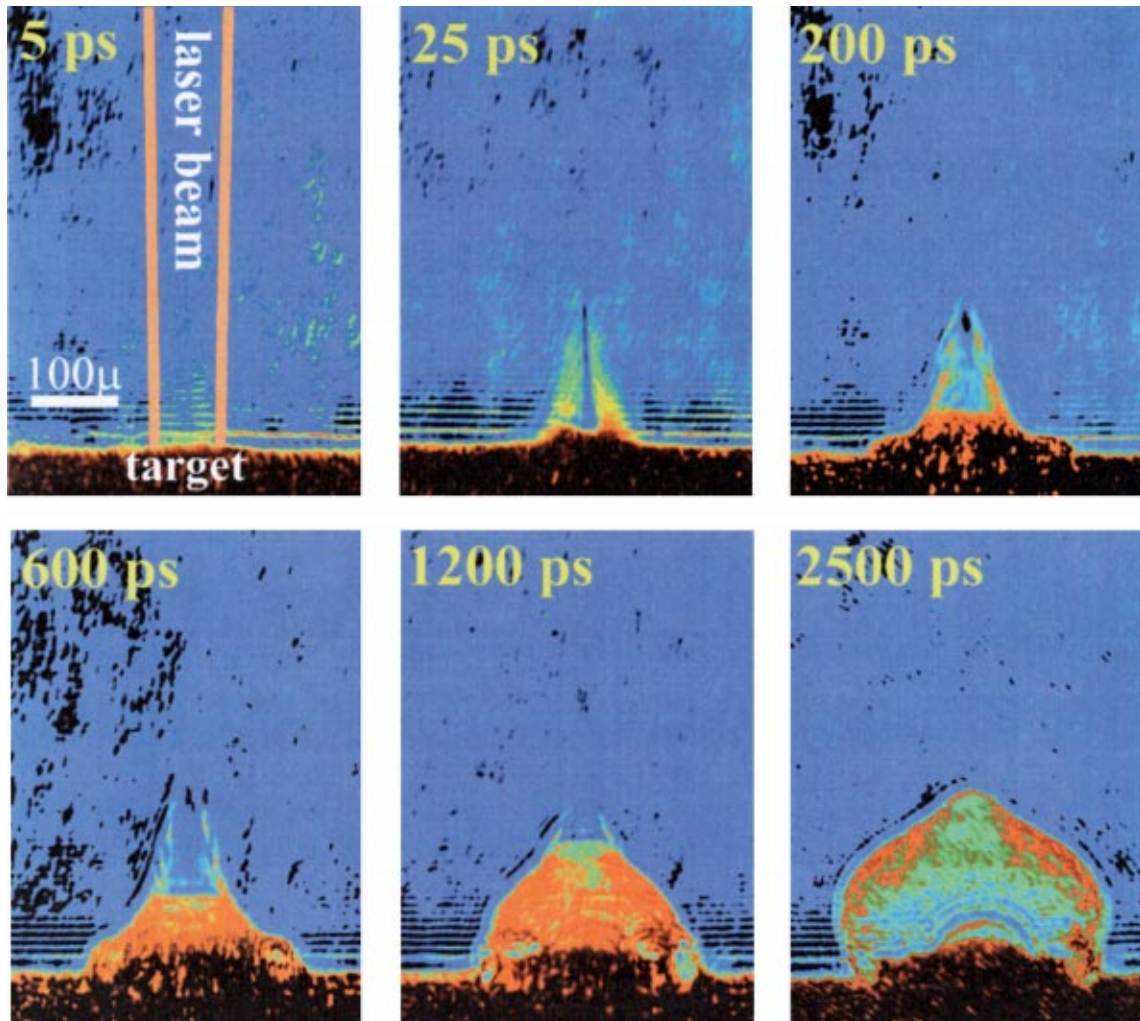
LAGRANGIAN FLOW MAPPING OF HEATED CAPILLARY PORE AND THIN FILM USING MOLECULAR FLUORESCENCE VELOCIMETRY (MFV)

J. S. Park, C. McCarty, and K. D. Kihm
Texas A&M University, College Station, Texas

D. M. Pratt
Wright-Patterson AFRL, Dayton, Ohio

Molecular Fluorescence Velocimetry (MFV) technique has been developed and applied to map the Lagrangian velocity fields for a heated capillary pore and its thin film region. MFV uses caged fluorescence dye molecules (Dextran Photo-Activated Fluorophores of less than 10 nm size) that are uncaged and tagged with the exposure to UV line of 355 nm in wavelength and 15- μ m beam diameter. The tagged molecules are pumped by the blue laser ($\lambda=488$ nm) for fluorescence and sequentially recorded fluorescence images reveal detailed flow history for an extremely small scale flow field such as a microscale thin film region. For the nearly horizontal pore of 5-mm diameter

with five degrees of inclination, (a) and (b) show the flow development for the thin film region and the bulk pore region, respectively, when the heater is located in the liquid side. For the heater located in the vapor side, (c) and (d) show the flow development. The thermally driven flow near the bottom surface is directed to the heater location for both cases and the present study evidences a fully three-dimensional flow exists below the meniscus and inside the thin film region. Note that the distorted, but similar images just below the interface shown in (a) and (c) are formed by the mirror-like reflection of the real fluorescence image from the concave meniscus surface.



PLASMA DEVELOPMENT DURING PICOSECOND LASER PROCESSING OF ELECTRONIC MATERIALS

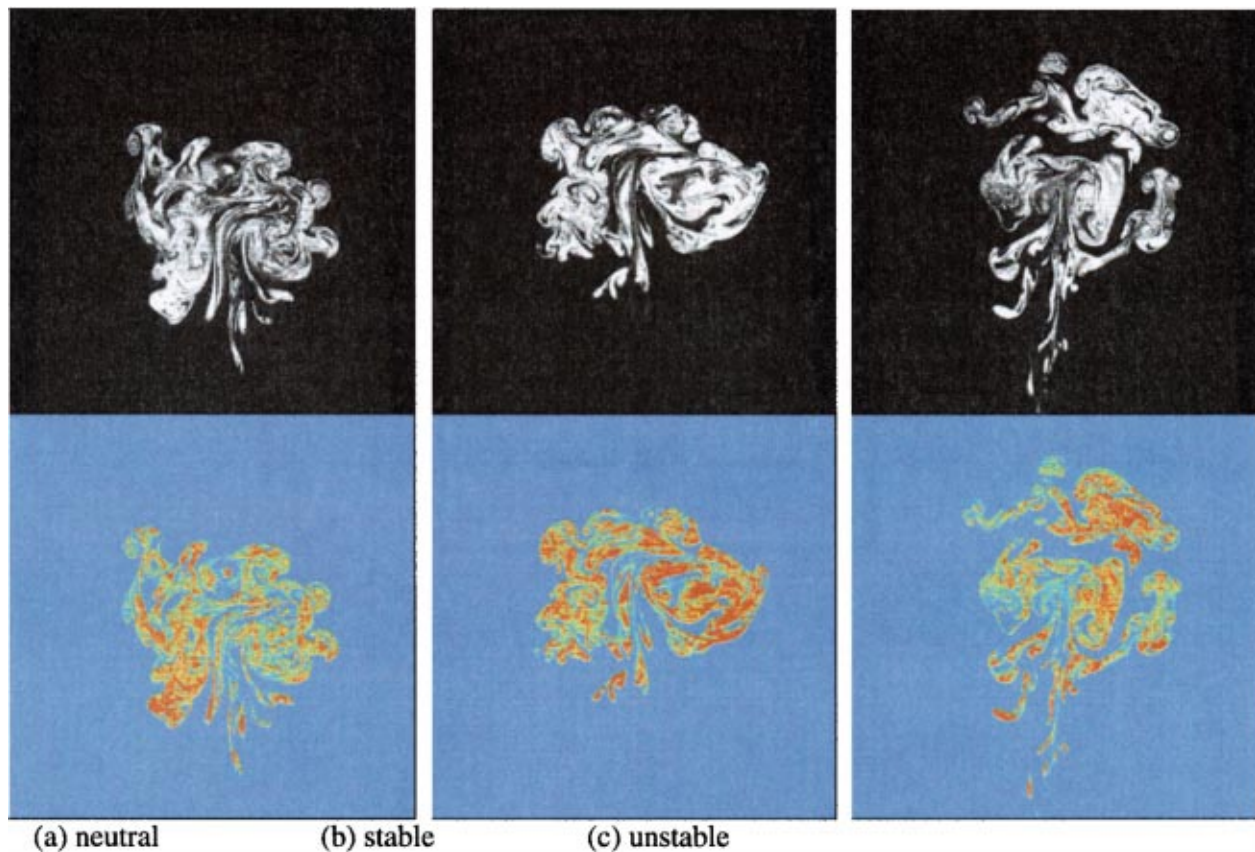
Samuel S. Mao, Ralph Greif, Xianglei Mao, and Richard E. Russo

Department of Mechanical Engineering and Lawrence Berkeley National Laboratory,
University of California, Berkeley, California

Lasers with picosecond and shorter pulse duration are receiving much attention due to their capabilities for direct-write micro-machining on most materials with minimal lateral damage. Deposition of energy from lasers of large power density inevitably creates plasmas that often shield the target and reduce material processing efficiency. Nevertheless, there is little knowledge on the formation and subsequent evolution of plasmas during laser processing of materials at the picosecond time scale. Such information is essential for precise control of laser energy coupling with target materials, particularly for machining at microscale depth.

We have performed experiments by imaging the spatial and temporal development of plasmas during picosecond laser processing of electronic materials. The color plate (1064 nm

laser irradiation of a copper target) shows a series of plasma images at times ranging from 5 to 2500 ps. For the first time, a cone-shaped plasma plume has been observed to grow during the early stage of picosecond laser-material interactions. The plasma front moves away from the target at 10^9 cm/s during the laser pulse (35 ps), but expands primarily in the radial direction after the pulse. The origin of this early-stage plasma has been attributed to gas breakdown assisted by laser-induced electron emission from the target. Beginning at about 200 ps, a second plume emerges from the target surface, which consists of vaporized target material and expands at 10^6 cm/s into the free space above the target. This vapor plume gradually reaches the front of the early-stage plasma at times about 2000 ps.

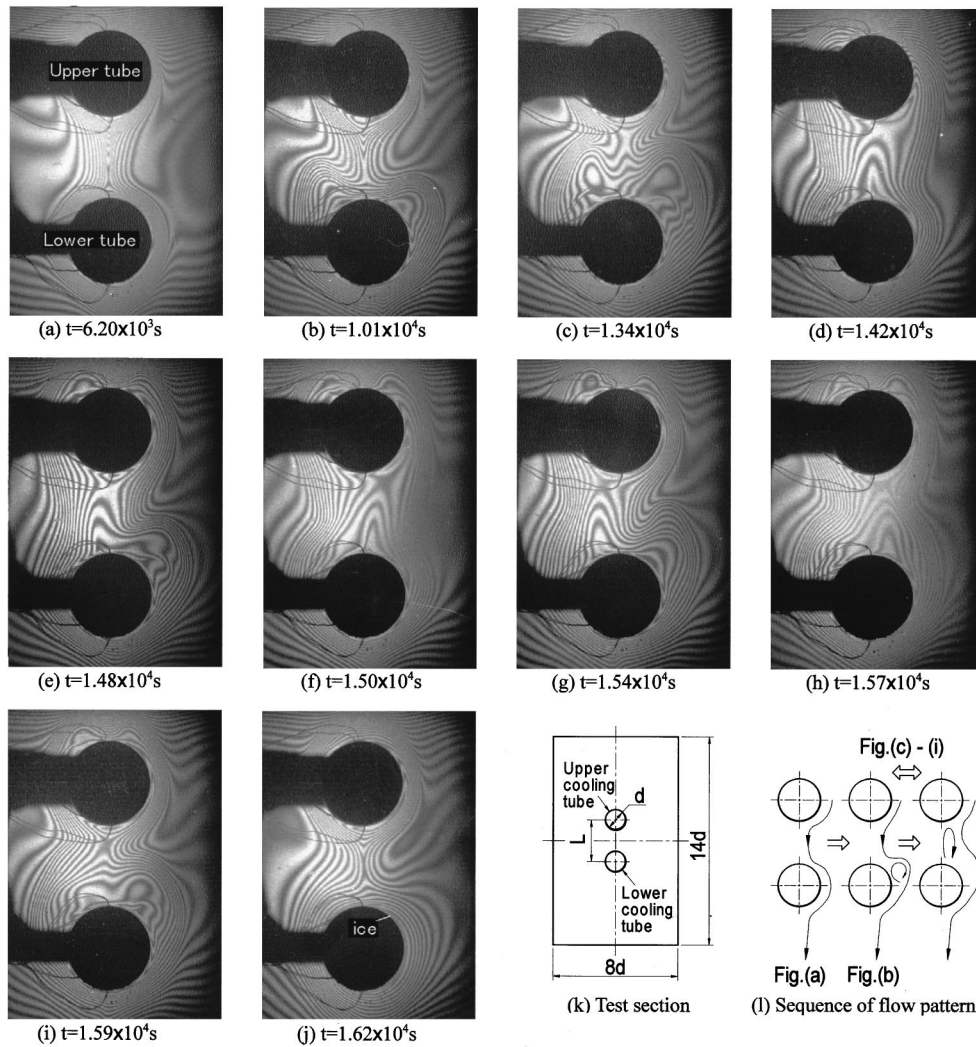


THE DIFFERENCES IN THE COUNTER-ROTATING VORTEX PAIR STRUCTURES IN A CROSSFLOW JET SUBJECTED TO VARIOUS THERMAL STRATIFICATIONS

Kyung Chun Kim, Sang Ki Kim, Sang Youl Yoon, and Kyung Hyun Park
School of Mechanical Engineering, Pusan National University, Pusan 609-735, Korea

The instantaneous cross-cuts of the crossflow jet show the well-known kidney shape structures, but the features change their topology as well as scales according to the stability of the crossflow. Typical images of the counter-rotating structures taken at $x/d=50$ of the round jet issued normally to the uniform crossflow with the neutral, stable ($269\text{ }^{\circ}\text{C/m}$), and unstable ($-65.1\text{ }^{\circ}\text{C/m}$) stratifications are shown in Figs. (a), (b) and (c), respectively. The velocity ratio between the jet and the crossflow is 5.8. The corresponding Reynolds number based on the jet diameter (6 mm) and the jet velocity (5.8 ms/) was 2300. We used the olive oil aerosol having 2 microns of mean diameter as the seeding particles. The particles

were supplied to the jet flow only in order to identify the interactions between the jet and the crossflow. A 200 mJ/pulse Nd:Yag laser with optical devices was used to provide a light sheet less than 1 mm thickness. The illumination time was set to be 4 ns. The instantaneous image was captured by a $1\text{K}\times 1\text{K}$ digital CCD camera and stored in a computer. The pseudo-colored images were obtained from the original black and white images to illustrate the relative concentration fields. The pictures give us physical insights implied in the “conning” and “looping” behaviors of the plumes which are mainly due to the thermal stratifications.



INTERACTION OF DOWNWARD AND UPWARD CONVECTION OF WATER BETWEEN TWO COOLING TUBES

Ichiro Nakane and Akira Narumi

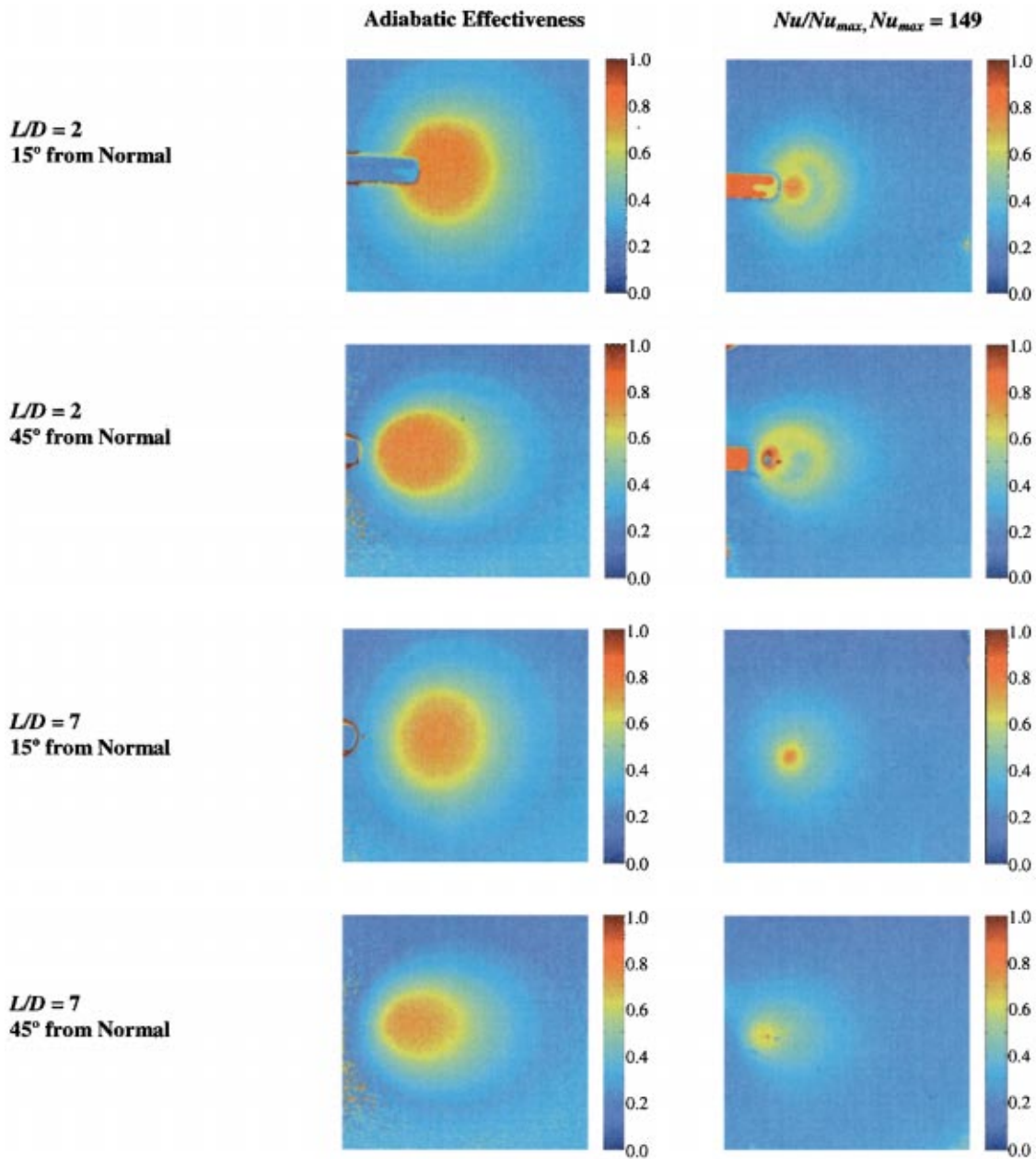
Department of Mechanical Engineering, Kanagawa Institute of Technology

Takao Kashiwagi

Division of Mechanical System Engineering, Faculty of Engineering, Tokyo A&T

When water is cooled through 4°C, downward and upward convection may be produced due to its anomalous relationship between temperature and density. In the case of placing two horizontal cooling tubes vertically in a rectangular enclosure, a downward convection dominates the entire flow field in the early process of cooling. With the progress of cooling, the interaction of downward and upward convection occurs between the two cooling tubes. In most cases, the upward convection develops smoothly and becomes dominant between the two cooling tubes. In a rare case, however, the upward and downward convection keeps the balance making oscillation between the two cooling

tubes like a seesaw. Figures (a)–(j) shows the interferograms of this phenomenon, where $d=30$ mm and $L/d=2.0$ (see Figure (k)). The heart-shaped fringe over the lower tube is formed because the development of the upward convection at the lower tube is prevented by the downward convection from the upper tube. Note that, when the upward convection develops further to reach just before the bottom of the upper tube, it comes back to the point of a heart shaped fringe. This behavior repeats several times. Finally the release of supercooling occurs at the lower tube, and then this behavior is ended. Figure (1) shows a schematic of this phenomenon.



ADIABATIC EFFECTIVENESS AND NUSSULT NUMBER DISTRIBUTION ON A FLAT SURFACE WITH AN OBLIQUE IMPINGING JET

J. W. Baughn, M. Dietzel, and J. E. Mayhew
University of California, Davis, California

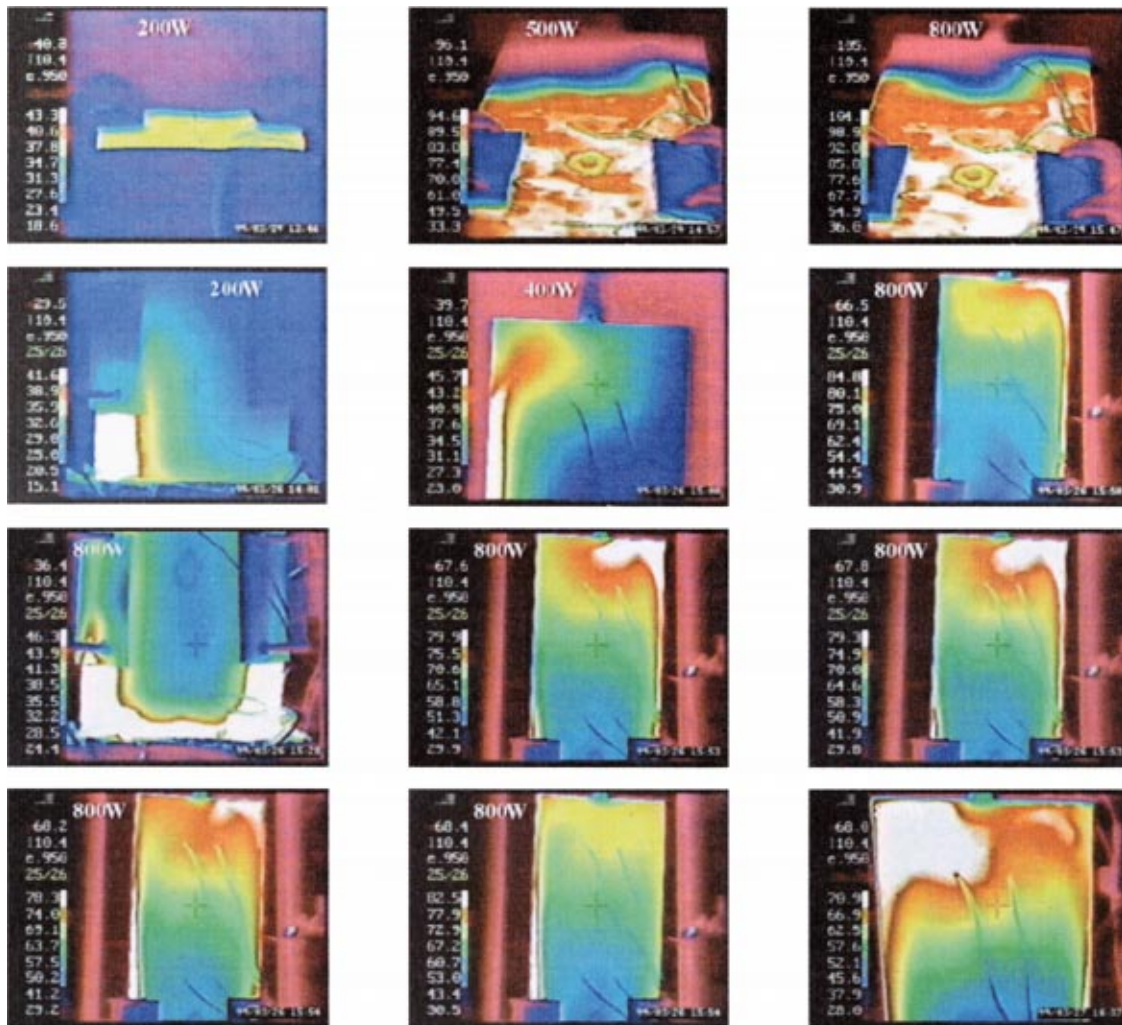
These pictures show the hue values (calibrated against temperature) of thermochromic liquid crystals on a flat surface with an oblique impinging air jet.

The pictures in the left column are obtained on an insulated surface with a heated jet. For these pictures the hue values represent the adiabatic effectiveness distribution and illustrate the region of entrainment effects.

The pictures in the right column are for the same insulated surface. However, in these pictures the jet is unheated; instead a micro-thin gold coating on the surface is electrically heated to

produce a uniform surface heat flux. In this case, the hue values represent the heat transfer coefficient distribution and illustrate the region of enhanced heat transfer.

Comparing the adiabatic effectiveness distribution to the heat transfer coefficient distribution it can be seen that there is a region of strong variation in heat transfer coefficient in which entrainment effects are small (i.e., high effectiveness). Outside this region, both adiabatic effectiveness and heat transfer coefficient are needed to calculate the overall heat transfer.



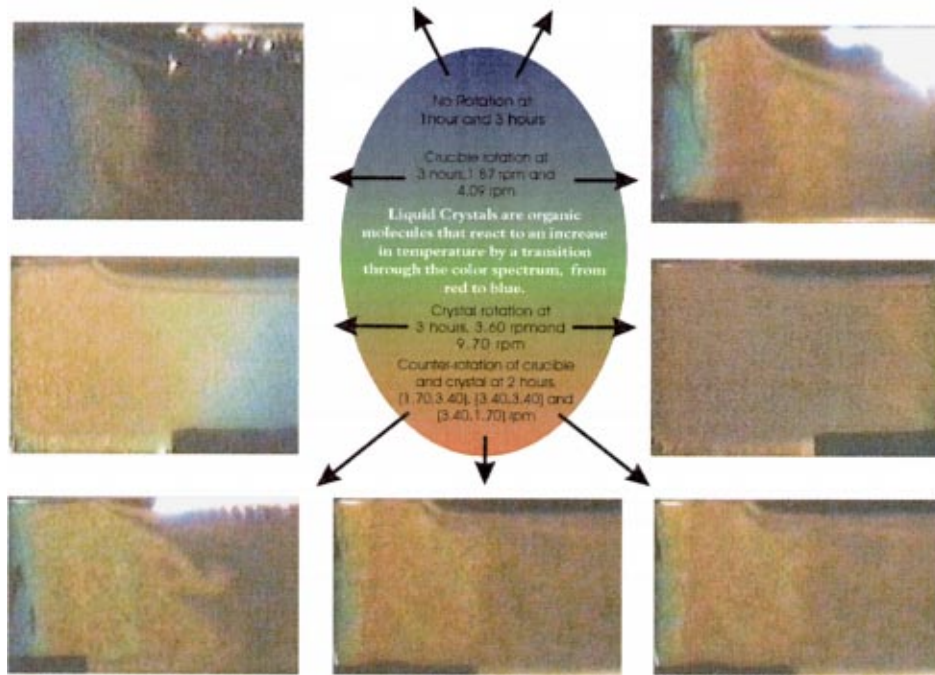
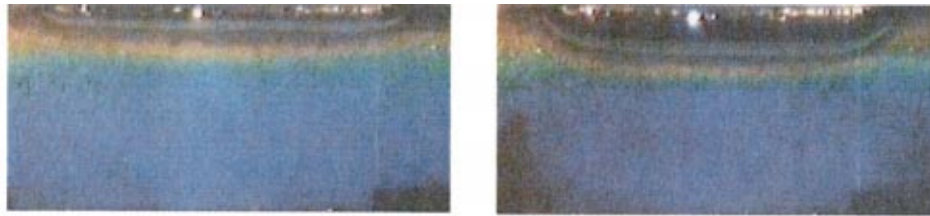
INFRARED PHOTOGRAPHS OF A GAS LOADED FLAT HEAT PIPE

M. Cerza

Mechanical Engineering Department, U.S. Naval Academy, Annapolis, Maryland

A large, gas loaded, flat heat pipe was videographed at horizontal and vertical orientations with an infrared video camera. The heat pipe was fabricated from sheets of Monel R-400 and Monel screen and measured 1.22 m \times 0.30 m \times 0.01127 m. The heat pipe evaporator section consisted of a 0.305 m \times 0.305 m area (one heated side) while the side opposite the heated section was insulated. The remaining area of the heat pipe served as the condenser which was videographed. In the horizontal orientation, the heated section was on the bottom. In the vertical orientation, the evaporator was aligned below the condenser. The first row sequence of photographs (horizontal)

depict the effects of a noncondensable gas at heat inputs between 200 to 800 W. As the heat input is increased, vapor compresses the gas back activating more condenser area. In the vertical orientation (second row), the noncondensable gas is seen to sink down into the central portion of the heat pipe, while water vapor rises up the edges of the heat pipe. The last two rows (vertical orientation) depict a time sequence which shows transient condensation oscillations caused by buoyancy and diffusion effects of the air and water vapor. The condensing vapor front was seen to switch from side to side. Temperature is in Celsius.



VISUALIZATION OF SOLIDIFICATION IN A SIMULATED CZOCHRALSKI SYSTEM

Michele Ferland, Debasish Mishra, and Vishwanath Prasad

Department of Mechanical Engineering, SUNY Stony Brook University, Stony Brook, New York

Solidification of water from a crystal seed in a simulated Czochralski growth system is investigated for various rotation rates of the crystal and crucible. Under the influence of a differentially heating condition imposed by the crystal seed and the surrounding melt, a complex flow and thermal field is visualized. Three convection-driving currents, temperature gradient, surface tension gradient, and centrifugal forces due to rotation, along with the density inversion of water are responsible for the resulting flow and thermal field.

Liquid Crystal Thermography is employed to capture the images of the temperature field and the transport phenomena in the melt. The liquid crystals have a bandwidth of 10°C ; starting with red at $\sim 1.2^{\circ}\text{C}$, green at $\sim 2.1^{\circ}\text{C}$, blue at $\sim 3.6^{\circ}\text{C}$ and clearing at 10°C . These crystals are employed in 0.005 percent by volume to

visualize the solidification process.

Experiments are conducted for a range of Grashof numbers of 400,000. Interesting temperature fields are seen in the shape of simple Benard roll type structures to a formation of complex oscillatory finger like patterns with many different size vertices. A quantitative estimate of the temperature field is obtained via a suitable calibration of the liquid crystals in a pure conduction state.

The first set of images captures the temperature field present with no rotation present in the melt. The next set of images is under crucible rotation rates of 1.87 and 4.09 rpm. Crystal rotation effects at 3.60 and 9.70 rpm can be seen in the next set of images. In the last set of images, counter-rotation effects of the crystal and crucible can be seen for (1.70, 3.40) and (3.40, 1.70) rpm.

From Heat Transfer Principles to Shape and Structure in Nature: Constructal Theory

Adrian Bejan

Fellow ASME,
J. A. Jones Professor of Mechanical
Engineering,
Duke University,
Durham, NC 27708-0300
e-mail: abejan@duke.edu

This lecture reviews a relatively recent body of heat transfer work that bases on a deterministic (constructal) principle the occurrence of geometric form in systems with internal flows. The same principle of global optimization subject to constraints allow us to anticipate the natural (animate and inanimate) flow architectures that surround us. The lecture starts with the example of the optimal spatial distribution of material (e.g., heat exchanger equipment) in power plants. Similarly, void space can be allocated optimally to construct flow channels in the volume occupied by a heat generating system. The lecture continues with the optimization of the path for heat flow between a volume and one point. It shows that when the heat flow can choose between at least two paths, low conductivity versus high conductivity, the optimal flow structure for minimal global resistance in steady flow is a tree. Nearly the same tree is deduced by minimizing the time of discharge in the flow from a volume to one point. Analogous tree-shaped flows are constructed in pure fluid flows, and in flow through a heterogeneous porous medium. The optimization of trees that combine heat transfer and fluid flow is illustrated by means of two-dimensional trees of plate fins. The method is extended to the superposition of two fluid trees in counterflow, as in vascularized tissues under the skin. The two trees in counterflow are one tree of convective heat currents that effect the loss of body heat. It is shown that the optimized geometry of the tree is responsible for the proportionalities between body heat loss and body size raised to the power 3/4, and between breathing time and body size raised to the power 1/4. The optimized structures are robust with respect to changes in some of the externally specified parameters. When more degrees-of-freedom are allowed, the optimized structure looks more natural. The lecture outlines a unique opportunity for engineers to venture beyond their discipline, and to construct an engineering theory on the origin and workings of naturally organized systems. [S0022-1481(00)02403-8]

Keywords: Crystal Growth, Geophysical, Heat Exchangers, Heat Transfer, Natural Convection, Optimization, Second Law, Topology, Constructal

Looking Back

First, I want to thank the Max Jakob Memorial Award Committee for this greatest honor in heat transfer. I consider myself very fortunate, to be honored at this stage in my career, and to have so many friends in heat transfer and thermodynamics all over the world.

Research has a lot to do with luck. I have been very lucky, not only for coming to America young and at MIT, but also for encountering extraordinary role models in my path. My cryogenics theses advisor at MIT, Prof. Joseph L. Smith, Jr., introduced me to the second law and the legitimate role of entropy generation considerations in engineering in general. My postdoctoral advisor in Berkeley, Prof. Chang-Lin Tien, changed my direction toward fundamental research and the mainstream of heat transfer. The early work that he and I contributed to the now developed fields of natural convection in enclosures and convection in porous media was the result of his vision and coaching.

Looking Ahead

Instead of a review of highlights from my research past, in this lecture I propose to discuss an issue that has always been and always will be important. The basic idea is that the constrained

optimizations that we, the engineers, perform routinely in thermo-fluid system design can help all of us make better sense of the natural (animate and inanimate) architectures that surround us.

Better sense means a simpler, easier to understand, and more general summary of explanations of what we see in nature. Such a summary is called principle or law. The thirst for better sense—for rationalizing—has always been the driving force in the historic development of science.

There are three aspects of this idea that I emphasize in this lecture and in a new book ([1]). First, to start from principle and to arrive through a mental viewing in the powerful position of predicting geometric forms that appear in nature is to practice *theory*. The time arrow of theory, from principle to nature, runs against the time arrow of empiricism, which begins with nature—the unexplained observation. Empiricism has been the preferred method in the study of naturally organized systems, from river and lung morphology to turbulent eddies and fractal geometry.

The second aspect is useful to us as engineers. Engineering is the *science* of systems and processes with purpose. It is the science of the useful. By identifying the principle that accounts for geometric form in natural flow we improve our own vision as designers, as creators. For example, nature impresses us with a multitude of tree-shaped flows: Each tree flow connects an infinity of points (volume, area) with a single point (source, sink). Perhaps, we can use similar structures in engineered systems that require similar volume-point connections.

The third aspect has to do with the role of engineering in soci-

Contributed by the Heat Transfer Division for publication in the JOURNAL OF HEAT TRANSFER. Manuscript received and accepted by the Heat Transfer Division, March 20, 2000. Technical Editor: J. R. Howell.

ety. Once a noble and revered occupation (think of Leonardo da Vinci, Sadi Carnot, and the airplane builders during World War II), engineering is now taken for granted. Everywhere we look, from university campus politics to the Nobel prize, engineering ranks either low or not at all on the ladder of respect. The engineering reality is a lot brighter. Scientists of all ages and types have pondered the origin of shape and structure in nature. They have been wondering about our own origins. Zoologists and geophysicists speak quite freely of design, function, necessity, and optimization in their descriptions of natural patterns. Optimization implies an objective, or a purpose. All these are engineering concepts. This is why I believe that engineers are destined to play a role in the quest for a rational basis—a principle—for the generation of geometric form in nature.

Many of our engineering colleagues are already proving this through bioengineering. Their designs blur the supposed demarcations between the natural and the artificial. Engineers, with their language and feel for the concepts of objective (purpose), constraints and optimization, are ideally positioned to define the theoretical agenda for life science in this new century.

What I am describing is a position that I have advocated throughout my work. Our engineering methods are undergoing changes and improvements. In parallel with academic pursuits, it is extremely important that we test the *usefulness* of our methods not only in the real world of engineering but also in the equally real world of *natural* systems. If our methods show promise, we can improve them further in partnerships and disputes with physicists, zoologists, botanists, and medical researchers. In this way even our teaching improves, because it becomes more immediate and reaches a much wider audience. Even better, the value of engineering to society becomes more evident to larger groups.

Distribution of Material in Energy Systems

I begin with the most basic example of how heat transfer principles shed light on why energy systems are imperfect, and why they possess geometric structure—why their hardware is arranged in certain amounts, and in certain ways in space. A heat engine or power plant is a system with *purpose*. Its purpose is to change

heating (Q_H) into working (W), and to do it as well as *possible*. “Well,” or better, means more W from the given input Q_H , which is fixed. “As well as possible” means that the pursuit of “better” is subjected to several constraints, Q_H and other physical (size) and economic constraints.

A power plant owes its irreversibility to many factors, one of which is the transfer of heat across finite temperature differences. This effect has been isolated in Fig. 1 ([2]). The power plant is the vertical segment marked between the high temperature T_H and the ambient temperature T_L . The heat input Q_H and the rejected heat Q_L must be driven by temperature differences: The white temperature gaps $T_H - T_{HC}$ and $T_{LC} - T_L$ account for some of the space occupied by the power plant. Heat transfer surfaces (shown in yellow) reside in these spaces. The rest of the space is reserved for the rest of the power plant: For simplicity, this inner space (green) is assumed to be irreversibility free,

$$S_{\text{gen}} = \frac{Q_L}{T_{LC}} - \frac{Q_H}{T_{HC}} = 0. \quad (1)$$

All the irreversibility of this power plant model is concentrated in the two temperature gaps. The simplest heat transfer model for these is the proportionality between heat current and temperature difference,

$$Q_H = C_H(T_H - T_{HC}) \quad (2)$$

$$Q_L = C_L(T_{LC} - T_L). \quad (3)$$

Each thermal conductance (C_H, C_L) is proportional to its area for heat transfer. This is why the simplest way to account for the finiteness of the heat transfer surface available to the power plant is to recognize the constraint ([3])

$$C_H + C_L = C \quad (4)$$

where C is fixed. This constraint is adequate when the overall heat transfer coefficients of the two surfaces are equal. More general constraints, valid for unequal heat transfer coefficients, can also be used.

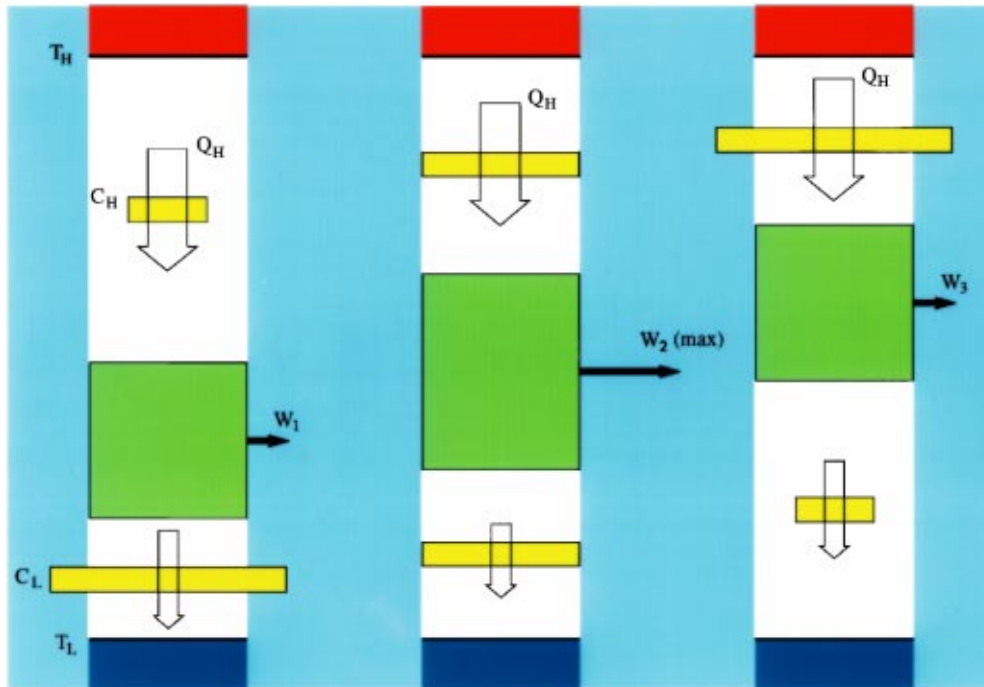


Fig. 1 Model of power plant with two heat transfer surfaces, and the maximization of power output subject to fixed heat input (Q_H) and fixed total heat transfer surface (C)

The analytical model is completed by the first law, written for the power plant as a closed system operating in steady state or in an integral number of cycles, $W = Q_H - Q_L$. Combining this with the preceding relations, we obtain the power output as a function of the conductance allocation fraction $x = C_H/C$,

$$\frac{W}{Q_H} = 1 - \frac{T_L/T_H}{1 - \frac{Q_H}{T_H C} \left(\frac{1}{x} + \frac{1}{1-x} \right)}. \quad (5)$$

This expression can be maximized with respect to x , and the result is $x_{\text{opt}} = 1/2$, or

$$C_{H,\text{opt}} = C_{L,\text{opt}}. \quad (6)$$

In conclusion, there is an optimal way to allocate the constrained hardware (C) to the two ends of the power plant, that is, if the maximization of power output subject to fixed heat input (Q_H) and fixed size (C) is the purpose. Equation (6) also holds for refrigerating machines modeled in the same way ([4]).

The maximization of W is shown graphically in Fig. 1. Small conductances strangle the flow of heat, and demand large temperature differences. The power output is large when the temperature difference across the green (reversible) compartment is large. The first and third frames of Fig. 1 show that when the two conductances are highly dissimilar in size, large temperature gaps are present, and the power output is small. The best irreversible (imperfect) performance is somewhere in the middle, where the conductances are comparable in size.

There is now a large body of literature in which models similar to Fig. 1 are used for the purpose of identifying the existence of basic tradeoffs in the conceptual design of all kinds of energy systems. These models are used for orientation. More refined optimizations, which are based on increasingly more realistic models, come later in the design process ([5]). The defining characteristic of this relatively new sector of heat transfer is the combination of heat transfer with thermodynamics in the pursuit of optimization of global performance subject to global constraints. Reviews of the current activity in this area are given in a new line of books ([6–16]).

Why start with power plants, when the lecture is also about structure in nature? The optimal allocation of conductance means, geometrically, the distribution of hardware in a certain way, in space. Better performance is achieved when the distribution is relatively uniform, or balanced. Thermodynamically this means that the generation of entropy in the system—its irreversibility—is distributed in a relatively balanced way between the parts that operate with losses. The greater system works best when its imperfection is spread around, so that more and more of the internal parts are “stressed” as much as the hardest working points. The more we think of engineered systems in this way, the more they look and function like living systems.

The structure of animals has been a big puzzle in biology for centuries. From the mouse and the salamander, to the crocodile and the whale, animals are correlated by surprisingly precise power laws between body size and other flow and performance parameters ([17–22]). Metabolism, or the rate at which the exergy of food is consumed, is distributed in balanced and tightly correlated proportions among the organs. These proportions are fairly insensitive to animal size.

To predict the distribution of metabolic rate through the body is to predict the structure of the animal—its parts, their relative sizes, and their relative irreversibilities. One way to construct a theory of structure in living systems is to treat them as energy systems with flows, constraints and, above all, *purpose*, just as in Fig. 1. This is the theoretical line that is explored in this lecture.

Distribution of Void Space for Flow Channels

Another familiar story that holds new meaning in biological design is the sizing of internal details for compact heat exchangers

(channels, hydraulic diameters, fins, etc.). The volume of the device is constrained, while the objective is to maximize in a global sense the thermal conductance between the solid parts “compact” into this volume and the fluid stream that bathes all the parts.

The opportunity for optimizing internal geometry becomes evident if we focus on single-stream heat exchangers intended for cooling electronics. The global thermal conductance of the electronics is the ratio between the total rate of heat generation in the package (q) and the maximum excess temperature registered in the hot spots ($T_{\text{max}} - T_{\text{min}}$). The entrance temperature of the coolant is T_{min} . Desirable are designs with more components and circuitry installed in a given volume: Desirable is a larger q . This can be accommodated by increasing the ceiling temperature T_{max} (usually limited by the design of electronics), and by increasing the conductance ratio $q/(T_{\text{max}} - T_{\text{min}})$. The latter sends us on a course of geometry optimization, because the conductance is dictated by the flow geometry.

We can expect an optimal geometry by reasoning based on the comparison shown in Fig. 2. Three competing designs are illustrated. The volume and the heat generation rate (q) are the same in each design. The hot spots are shown in red: to maximize the global thermal conductance means to minimize the areas covered by red. In the first frame the spacings are wide, the heat transfer surface is small, the global conductance is small, and, consequently, each heat-generating part is overheated (engulfed in red).

The competing extreme is shown in the third frame. When the spacings are too tight, the coolant cannot flow through the package. The heat current is removed only by raising the temperature of the entire volume, including the outlet temperature of the coolant that manages to flow through.

An optimal spacing size exists somewhere between the two extremes. In this design the void volume allocated to each channel is used to the maximum: In every channel, the boundary layers merge just as the coolant flows out of the channel. Very compact and successful formulas for determining optimal spacings for cooling heat-generating volumes have been developed based on the tradeoff identified in Fig. 2. Reviews can be found in ([23–26]). For example, if the volume is occupied by a vertical stack of equidistant heat-generating plates of height H , the optimal plate-to-plate spacing for laminar natural convection is ([27–29])

$$\frac{D_{\text{opt}}}{H} \cong 2.3 \text{Ra}_H^{-1/4} \quad (7)$$

where $\text{Ra}_H = g\beta(T_{\text{max}} - T_{\text{min}})H^3/(\alpha\nu)$. Similar results have been found for other internal configurations of volumetrically heated volumes cooled by natural convection. If the heat generation occurs in a bundle of equidistant cylinders with diameter D and narrowest spacing S between adjacent cylinders, the optimal spacing has the scale ([30])

$$\frac{S_{\text{opt}}}{H} \sim \left(\frac{H}{D} \right)^{1/12} \text{Ra}_H^{-1/4} \quad (8)$$

where H is the height of the entire volume. Note that Eq. (8) is nearly the same as Eq. (7). Expressed in terms of the cylinder diameter and $\text{Ra}_D = g\beta(T_{\text{max}} - T_{\text{min}})D^3/(\alpha\nu)$, Eq. (8) becomes

$$\frac{S_{\text{opt}}}{D} \sim \left(\frac{H}{D} \right)^{1/3} \text{Ra}_D^{-1/4}. \quad (9)$$

The validity of this prediction was confirmed numerically and experimentally. The numerical data were fitted within 1.7 percent by a relation suggested by Eq. (9),

$$\frac{S_{\text{opt}}}{D} = 2.72 \left(\frac{H}{D} \right)^{1/3} \text{Ra}_D^{-1/4} + 0.263. \quad (10)$$

Constrained volumes with optimized arrays of horizontal heated cylinders were also considered by Fisher and Torrance [31]. Simi-

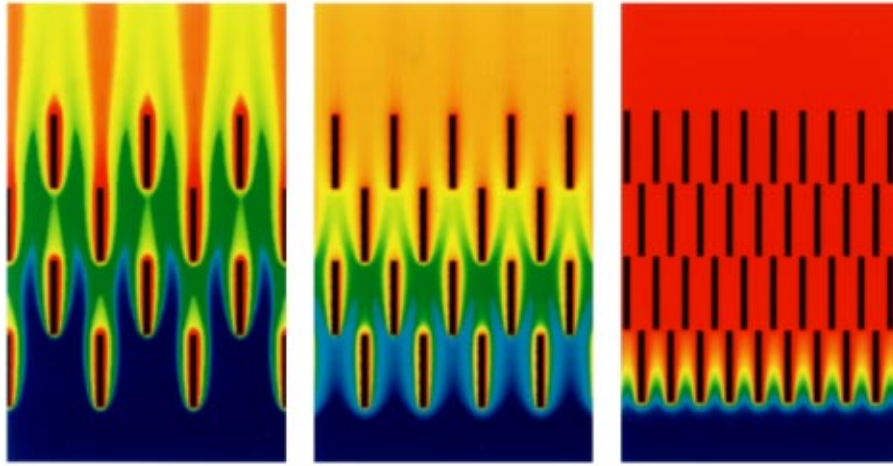


Fig. 2 Three designs for the internal structure of a fixed volume with fixed total heat generating rate and stream of coolant flowing vertically. The objective is to maximize the global thermal conductance between the volume and the stream, which is equivalent to minimizing the area with hot-spot temperatures (red).

lar spacings were optimized for staggered vertical plates assembled in a fixed heat-generating volume ([32]).

If the cooling is by forced convection with fixed pressure difference (ΔP) maintained between the ends of a stack of plates of length L , the optimal spacing is ([33])

$$\frac{D_{\text{opt}}}{L} \cong 2.7\Pi_L^{-1/4} \quad (11)$$

where $\Pi_L = \Delta P \cdot L^2 / (\mu\alpha)$ is a new “pressure drop number.” Petrescu [34] commented on the similarity between Eqs. (7) and (11), and pointed out that the pressure drop number is as important as the Rayleigh number. The pressure drop number does for the optimization of forced convection design what the Rayleigh number does for natural convection. This observation is reinforced by the optimal-spacing formulas developed for other geometries designed for forced convection: staggered plates ([35]), round cylinders in cross-flow ([36,37]), and three-dimensional square pin fins on a heat generating surface cooled by impinging flow ([38]).

From Principle to Internal Structure

We are entitled to disregard for a moment the reasoning that generated the optimal spacings reviewed in the preceding section. We may act as natural scientists, cut open the “animal”—the electronics package, heat exchanger, or electric winding—and marvel at the spatial organization of the diversity that we see. We marvel also at how much alike are the internal structures of contemporary systems (e.g., two competing personal computers), in the same way that a zoologist marvels at the similarity in bronchial tube sizes and numbers in two animals that have nearly the same mass. In this way we *observe* structure, and, just like the natural scientist, we may go on and measure, correlate, and catalogue (classify) the dimensions and patterns that we see.

In contrast with this empirical course, the reasoning exposed in this paper has nothing to do with observations. We invoked consistently a single principle of purpose (global maximization) and constraints, and from this principle we *deduced* the optimal internal structure. We practiced theory. The discovery is that geometric form (internal structuring) emerges as the *mechanism* through which the system achieves its global objective.

We are now at that late moment in time when we look at nature. Natural systems also develop internal spacings. Bees control the hot-spot temperatures in their swarm by opening nearly parallel

vertical channels through which the ambient air cools the swarm. As shown in Fig. 3, the bees construct wider channels when the ambient air is warm and the required air flow rate is larger ([39,40]). Inanimate systems also have optimal internal spacings. Cracks form at surprisingly regular intervals in volumetrically

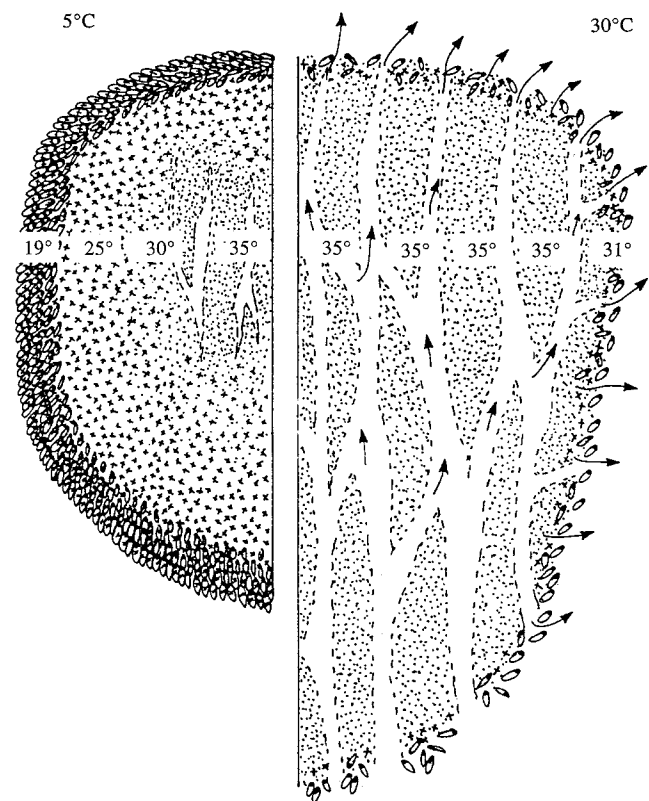


Fig. 3 The regulation of temperature in a swarm of honeybees ([39]). The left side shows the structure of the swarm cluster at a low ambient temperature. The right side is for a high ambient temperature, and shows the construction of almost equidistant ventilation channels with a characteristic spacing. Indicated are also the heat transfer from the swarm (arrows), areas of active metabolism (crosses), areas of resting metabolism (dots), and local approximate temperature.



Fig. 4 Patterns of cracks on the ground

shrinking solids (Fig. 4). The spacing between cracks has been deduced on the same basis of constrained maximization of global conductance ([41]).

Distribution of Channels (Streams) for Volume-Point Flow

In Figs. 2–4 the flow of heat was from a fixed volume to a stream that flows through the volume. In particular, Fig. 2 is relevant to the optimization of the internal structure of electronic assemblies. In such systems the objective is to install a maximum amount of electronics (i.e., heat generation rate) in a given volume such that the maximum temperature does not exceed a certain level. The technological frontier is being pushed toward smaller package dimensions. There comes a point where miniaturization makes convection cooling impractical, because the cooling channels would take too much space. The only option left is to channel the generated heat by conduction, along paths (inserts) of very high thermal conductivity (k_p).

Conduction paths too take space: Designs with fewer and smaller paths are better suited for the miniaturization evolution. The fundamental problem is how to connect an entire volume with one point (the heat sink), cf. the formulation given in ([42]):

“Consider a finite-size volume in which heat is being generated at every point, and which is cooled through a small patch (heat sink) located on its boundary. A finite amount of high-conductivity (k_p) material is available. Determine the optimal distribution of k_p material through the given volume such that the highest temperature is minimized.”

The purpose of any portion of the conducting path k_p is to be “in touch” with the material that generates heat volumetrically. This material fills the volume (V), and its thermal conductivity is low (k_0). The optimal-access problem reduces to the geometric problem of allocating conducting path length to volume of k_0 material, or vice versa. A key observation is this: The allocation

cannot be made at infinitesimally small scales throughout V , because the k_p paths must be of finite length so that they can be interconnected to channel the total heat current (q) to the heat-sink point. There is only one option, namely:

- (i) to optimize the allocation of conductive path to one sub-system (volume element) at a time; and
- (ii) to optimize the manner in which the volume elements are assembled and their k_p paths are connected.

The result developed in ([42]) is purely geometric: Any finite-size portion of the heat generating volume can have its shape optimized such that its overall thermal resistance is minimal. Optimized volume elements are then assembled into a larger volume the shape of which is also optimized. This assembly and geometric optimization sequence is repeated in steps, from the smallest volume element to the largest assembly, until the given volume is covered. One of the features of the structure that emerges—a byproduct of the construction—is a network of k_p paths that is shaped as a tree. All the features of the structure of the (k_0, k_p) composite material that covers the volume, and all the features of the associate tree of k_p paths are the result of a purely theoretical, deterministic process guided by a single principle.

The simplest example of shape optimization is provided by the two-dimensional volume element represented by the rectangle $H_0 \times L_0$ in Fig. 5. The area $H_0 \times L_0$ is fixed but its shape may vary. The amount of k_p material allocated to $H_0 L_0$ is fixed, and is represented by the volume fraction $\phi_0 = D_0 / H_0$, which is a materials or manufacturing constraint. The heat current ($q_0 = q'' H_0 L_0 W$) generated by this volume element is collected by a blade (D_0, L_0) of high-conductivity material, and taken out of the volume through the point M_0 . The rest of the $H_0 \times L_0$ boundary is adiabatic, and W is the dimension perpendicular to the plane $H_0 \times L_0$. The volumetric heat generation rate q'' is uniform. The hot spot occurs at the point P , which is the farthest from the heat sink M_0 . Since the heat current q_0 is fixed, the minimization of the thermal resistance of the volume element is equivalent to the minimization of the peak excess temperature—the temperature drop (ΔT_0) from P to M_0 .

When $k_0/k_p \ll \phi_0 \ll 1$, the conduction through the k_0 material is practically parallel to y , while the conduction through the k_p material is along the x -axis. In this limit, ΔT_0 or the volume-to-point thermal resistance $\Delta T_0 / (q'' H_0 L_0)$, is the sum of two contributions, one for k_0 conduction from the corner $(L_0, H_0/2)$ to $(L_0, 0)$, and the other for k_p conduction from $(L_0, 0)$ to the origin $(0, 0)$ ([42]):

$$\frac{\Delta T_0}{q'' H_0 L_0 / k_0} = \frac{1}{8} \times \frac{H_0}{L_0} + \frac{k_0}{2 \phi_0 k_p} \times \frac{L_0}{H_0}. \quad (12)$$

This quantity can be minimized *geometrically*, that is, by varying the shape of the system. The derivation of shape from principle is illustrated in color in Fig. 6. The optimal shape is

$$\left(\frac{H_0}{L_0} \right)_{\text{opt}} = 2 \left(\frac{k_0/k_p}{\phi_0} \right)^{1/2}. \quad (13)$$

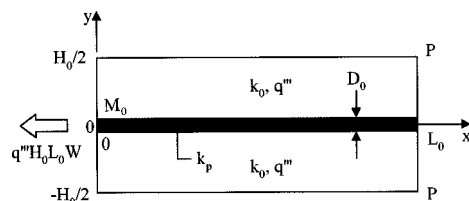


Fig. 5 Elemental volume with uniform volumetric heat generation rate and high-conductivity insert along its axis of symmetry ([42])

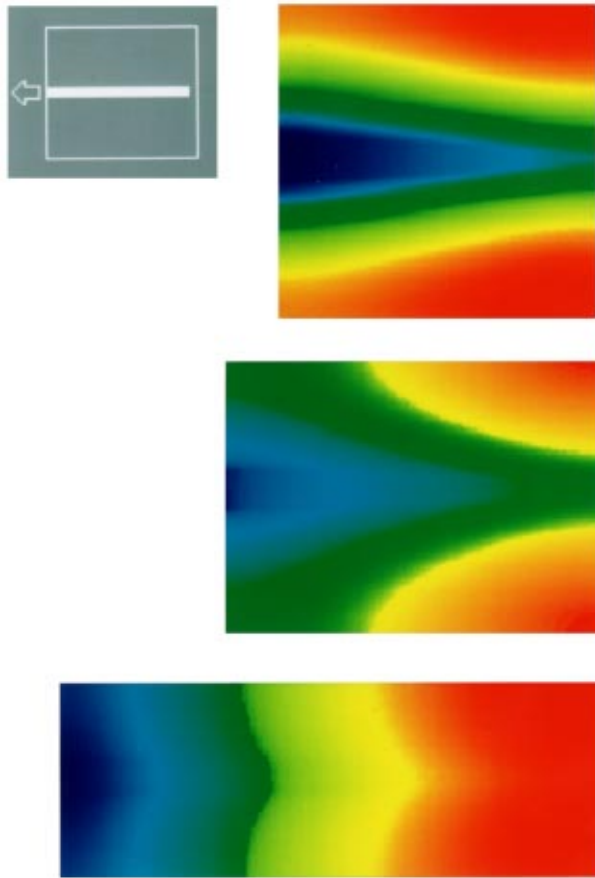


Fig. 6 How optimal shape is derived from the minimization of global resistance between a volume and one point. Three competing designs are shown. The volume and the heat generation rate are fixed. Variable is the aspect ratio of the rectangular domain. The resistance is proportional to the peak temperature difference, which is measured between the hot spots (red) and the heat sink (blue). The middle shape minimizes the areas covered by red, and has the smallest volume-point resistance.

The same geometric optimization principle applies at larger scales. The next larger volume is an assembly—a construct—of optimized elemental volumes. Figure 7 was drawn intentionally to look like Fig. 5, so that we may see at a glance that the optimization of the $H_1 \times L_1$ shape is the same problem as the optimization of the $H_0 \times L_0$ shape. In place of the low conductivity k_0 , this time we have the effective conductivity $k_1 = k_p D_0 / H_0 = k_p \phi_0$. When the total volume of k_p material contained by the first construct is fixed, in addition to an optimal shape (H_1 / L_1) there is an optimal way to allocate the k_p material, i.e., an optimal ratio D_1 / D_0 .

At the second-construct level the optimal external aspect ratio is $H_2 / L_2 = 2$, as in the examples shown in Fig. 8. This figure is discussed in more detail in the section on More Degrees of Freedom. For example, on the left side of Fig. 8 there are only two first constructs assembled into the second construct, and each first construct has eight elemental volumes (see the black & white diagram on top of the color plate). There are also optimal ratios of thicknesses, D_1 / D_0 and D_2 / D_1 , where D_2 is the thickness of the central (thickest) high-conductivity insert.

Numerical optimizations of the elemental system, first construct and second construct are exhibited in ([43]) for the more general case where the assumptions $k_0 / k_p \ll \phi_0 \ll 1$ are not made.

In Fig. 9 we see the optimized fourth construct and its distribution of k_p material. The square shape of this assembly is an “optimization result,” not an arbitrary choice made by the graphic

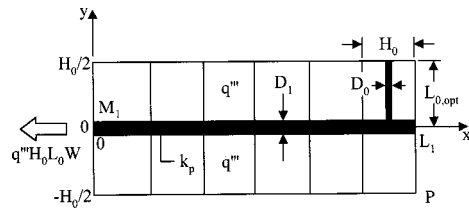


Fig. 7 The first construct: a large number of elemental volumes connected to a central high-conductivity path ([42])

artist. Again, every single geometric feature of the cooling scheme shown in Fig. 9 is the result of analysis. The fact that at higher orders of assembly the optimized high-conductivity paths exhibit the “bifurcated” (dichotomous) structure of natural tree networks is also a result, i.e., not an assumption. At no time did the designer borrow from nature.

The geometrically optimal construction started in Figs. 5–9 can be continued to a higher order of assembly, until the structured composite (k_0, k_p) covers the given space. One interesting feature in this limit is that the construction settles into a recurring pattern of pairing (or bifurcation, from the reverse point of view), in which the integer 2 is a result of geometric optimization. For example, Fig. 10 shows this pairing and size doubling pattern. If the shaded corner of Fig. 10 is one of the optimized fourth constructs of Fig. 9, then the large square domain of Fig. 10 represents the optimized eighth construct. All the fibers that are visible in Fig. 10 have the same conductivity (k_p). The geometric parameters, volume fractions occupied by high-conductivity material (ϕ_i), and the global resistance of each construct, are reported analytically in tabular form in ([2,42]).

From Principle to Tree-Shaped Flow

We saw that the geometric optimization of flow access between a volume and one point takes us to the geometric structure called “tree.” This geometric pattern and method of deduction bring under the same deterministic umbrella a wide variety of natural phenomena, the “tree” structure which so far has been assumed to lie beyond the powers of determinism. The examples are literally everywhere: trees, roots, leaves, river deltas, river basins, lightning, streets, and the pulmonary, nervous and vascular systems.

The method has technological and theoretical implications:

Technologically, it is possible to construct in a few simple geometric steps a near-optimal network for channeling a current that is generated volumetrically. This finding is important in practice: If the designer were to start with the given volume V , he or she would have to guess (postulate) an existing network, and then optimize (numerically and randomly) a prohibitively large number of parameters, as is done currently in the numerical simulations of river drainage basins and vascularized tissues ([44,45]).

Theoretically, it means that at the basis of the tree architecture of many animate and inanimate systems rests one design principle: the volume-constrained minimization of the global resistance to flow between one point and a finite volume (an infinite number of points). Reliance on such a universal design principle makes the tree network structure—its main features—predictable, contrary to the prevailing doctrine.

To appreciate how much is new in this geometric construction, it is important to note that one portion of the network pattern (namely, the portion formed by the higher-order assemblies, Fig. 10) is not new. It was first proposed in physiology as a three-dimensional “heuristic model” for the vascular system ([46]), where it was known empirically that each tube is followed by two smaller tubes, i.e., each tube undergoes bifurcation. It was

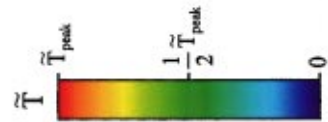
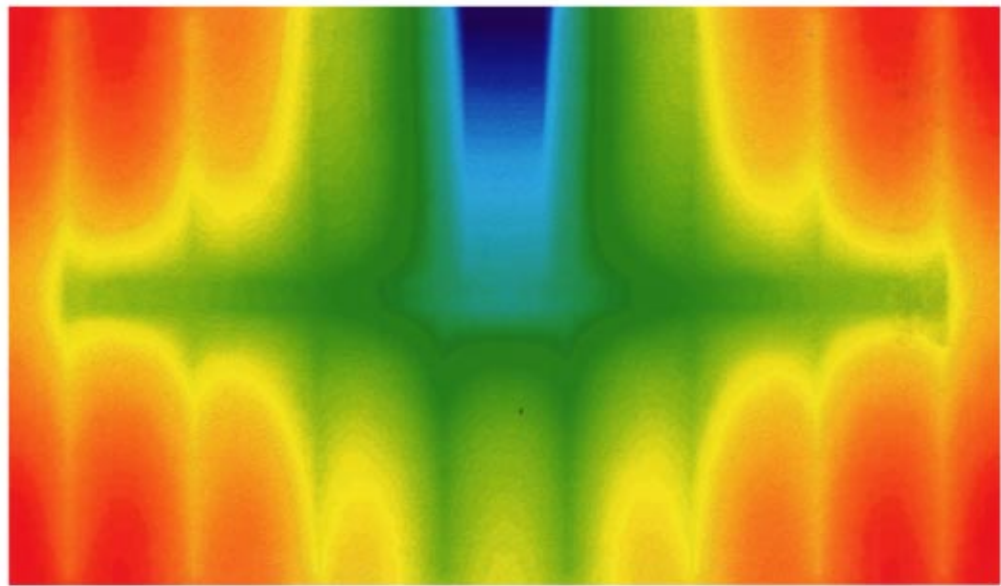
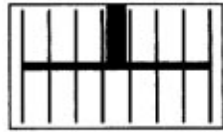
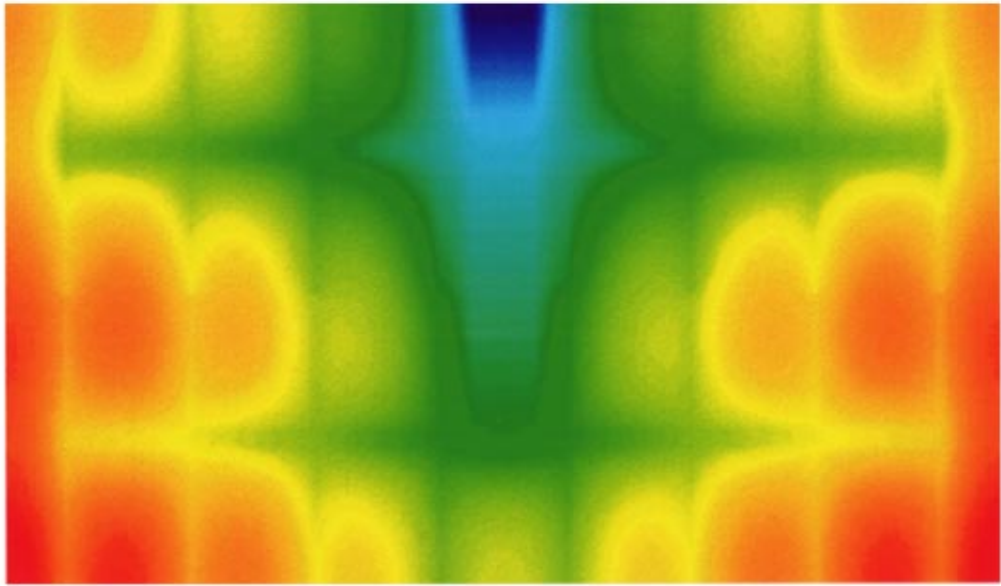


Fig. 8 The internal and external geometry of a second construct optimized numerically ($\phi_2=0.1$, $k_p/k_0=300$, $n_1=8$; left side, $n_2=2$; right side, $n_2=4$) ([49])

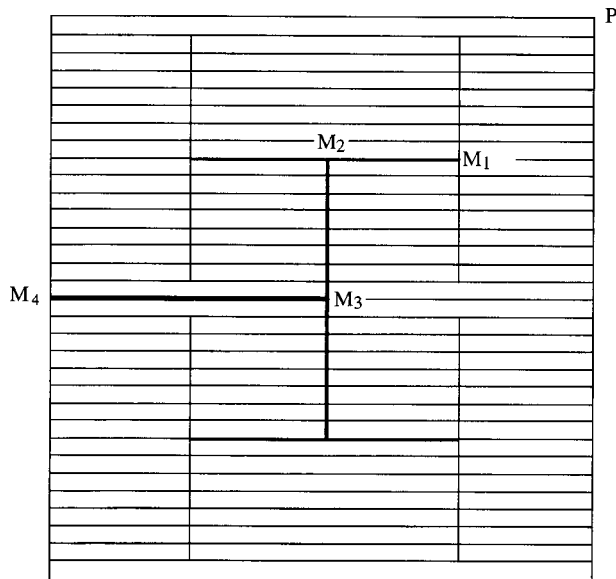


Fig. 9 The optimized fourth construct ([42])

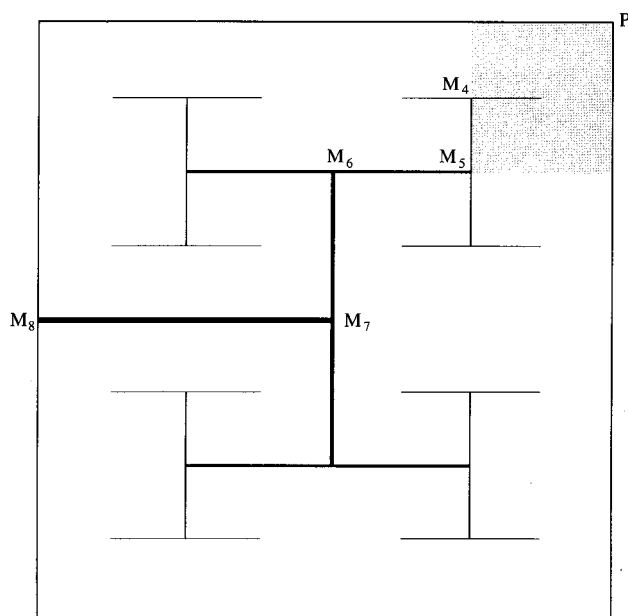


Fig. 10 The optimized eighth construct ([42])

also known that the tube diameter must decrease by a constant factor ($2^{-1/3}$) during each bifurcation: This result had been derived based on flow resistance minimization ([47]) coupled with the assumption that each tube is continued by “two” tubes (see also the section Tree of Convective Heat Currents). The description of these geometric constructions was made popular through the advent of fractal geometry: In fact, a two-dimensional version of Cohn’s [46] branching fluid network was presented without theory in the book of Mandelbrot [48], where it is proposed heuristically as a “model of the lung.”

More Degrees-of-Freedom

The heat trees of Figs. 8–10 do not look entirely “natural.” This is due to the simplifying assumptions on which their derivation was based. For example, the high-conductivity inserts were always drawn with constant thickness and perpendicular to their tributaries. These features served their purpose. They kept the

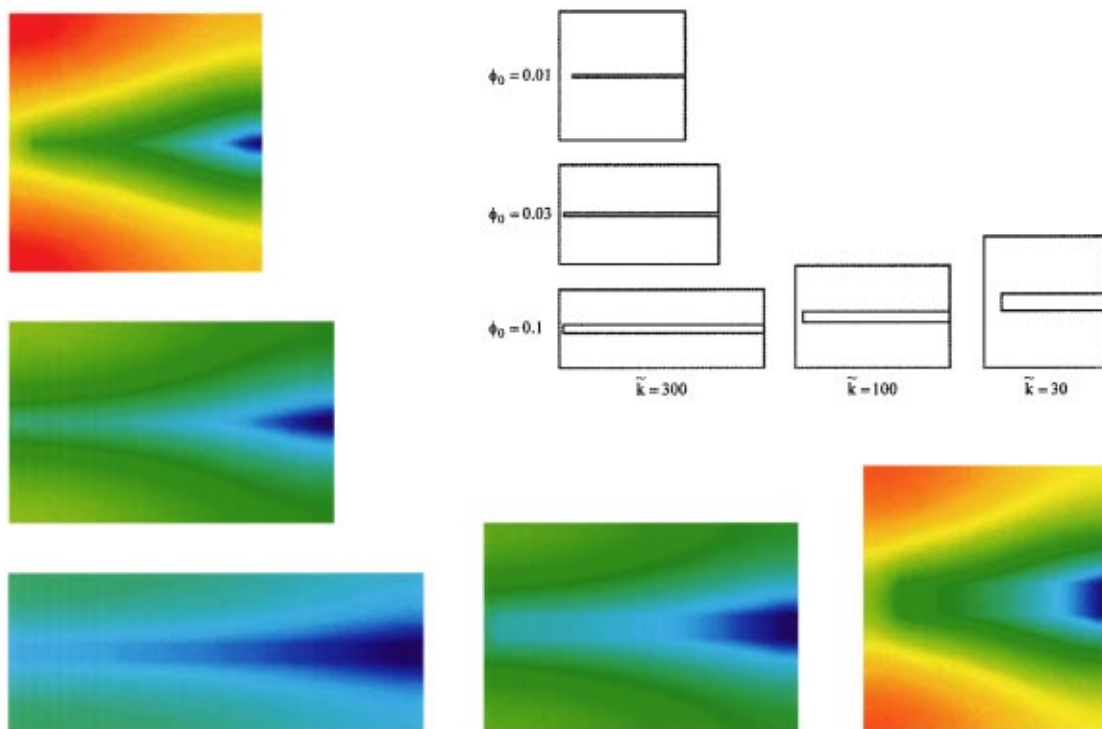


Fig. 11 Optimal shapes of elemental volumes with spacings at the tips of the high-conductivity channels: the effect of varying $\tilde{k} = k_p/k_0$ and $\phi_0 = D_0/H_0$ ([49])

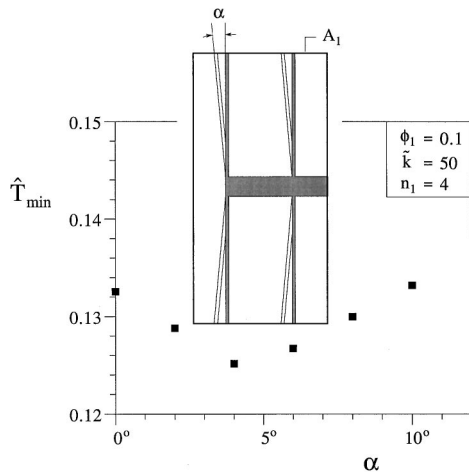


Fig. 12 The optimization of the angle of confluence between tributaries and their common stem in a first construct ($\phi_1 = 0.1$, $\bar{k} = 50$, $n_1 = 4$) ([43])

number of geometric degrees-of-freedom to a minimum, and in this way they made possible the closed-form presentation of the geometric optimization.

Constructal trees look more and more natural if their freedom to provide easier access to their internal currents is expanded. In the elemental system of Fig. 5 it was assumed that the k_p channel stretches all the way across the volume. When this assumption is not made, we find numerically that there is an optimal spacing between the tip of the k_p channel and the adiabatic boundary of the elemental volume ([49]). Figure 11 shows five cases of optimized elemental volumes with spacings at the tips, i.e., with k_0 material all around the tips of the k_p blades. This figure also shows how the optimized elemental volume—the smallest building block of the constructal design—changes as the proportions of the composite material change: The elemental shape becomes more slender as either $\bar{k} (= k_p/k_0)$ or $\phi_0 (= D_0/H_0)$ increases.

When the angle formed between each tributary channel and its central stem is allowed to vary, numerical calculations of the two-dimensional heterogeneous conduction field show that there exists an optimal angle for minimal volume-to-point resistance at the construct level ([43]). This effect is illustrated for a first construct in Figs. 12, where, for simplicity, it was assumed that all the tributaries are tilted at the same (variable) angle. The position of the hot spots moves along the top and bottom sides as the angle

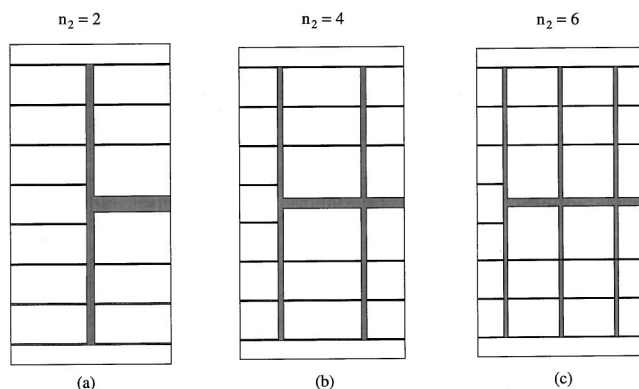


Fig. 13 The second construct optimized for minimum resistance in steady volume-point flow, and the effect of changing the number of first constructs, n_2 ; see also Table 1 ([43])

Table 1 The effect of increasing the number of first constructs (n_2) in the optimized second construct when $\phi_2 = 0.1$ and $\bar{k} = 300$ ([43])

| Figure | n_2 | $(T_{\max} - T_{\min})_{\min} k_0 / (q'' A_2)$ | $(H_2/L_2)^{1/2}_{\text{opt}}$ |
|--------|-------|--|--------------------------------|
| 13(a) | 2 | 0.0379 | 1.412 |
| 13(b) | 4 | 0.0354 | 1.375 |
| 13(c) | 6 | 0.0374 | 1.360 |

changes. The optimal inclination is similar to that of tributaries in nature: Pine needles, rivulets and bronchial ramifications point away from the root of the tree.

Figure 12 also shows that the volume-to-point resistance of the construct, $\hat{T}_{\min} = [(T_{\max} - T_{\min})_{\min} k_0 / (q'' A_1)]_{\min}$, decreases only marginally (by 5.8 percent) as the angle α changes from the perpendicular position ($\alpha = 0$ deg) to the optimal position ($\alpha \approx 4$ deg). The optimized tip spacings of Fig. 11 produce reductions of 20 percent in the global elemental resistance.

These relatively unimportant improvements tell a very important story: The tree design is *robust* with respect to various modifications in its internal structure. This means that the global performance of the system is relatively insensitive to changes in some of the internal geometric details. Trees that are not identical have nearly identical performance, and nearly identical macroscopic features such as the external shape.

The robustness of the tree design sheds light on why natural tree flows are never identical geometrically. They do not have to be, if the maximization of global performance is their guiding principle. The ways in which the details of natural trees may differ from case to case are without number because, unlike in the constructions presented in this paper, the number of degrees-of-freedom of the emerging form is not constrained. Local details differ from case to case because of unknown and unpredictable local features such as the heterogeneity of the natural flow medium, and the history and lack of uniformity of the volumetric flow rate that is distributed over the system. Marvelous illustrations of this element of “chance” are provided by seemingly irregular river drainage basins all over the world. The point is that the global performance and structure (tree) are predictable, and the principle that takes the system to this level of performance is deterministic.

Robustness continues to impress as we increase the number of degrees-of-freedom of the geometric design. In Fig. 13 we see the results of a fully numerical optimization of the second construct with perpendicular and constant-thickness inserts (D_0, D_1, D_2), where all the other geometric parameters were allowed to vary—the aspect ratios of all the rectangles, large and small, the number of elemental volumes in each first construct (n_1), and the number of first constructs in each second construct (n_2). The three designs shown in Fig. 13 have been optimized with respect to all the free parameters except n_2 , and they have been drawn to scale [$n_{1,\text{opt}} = 8$, $(D_1/D_0)_{\text{opt}} = 5$, $(D_2/D_0) = 10$]. The figure shows visually the effect of fine-tuning the number of first constructs incorporated in the second construct (n_2).

The same effect is documented numerically in Table 1. The size of the second construct ($A_2 = H_2 L_2$) is fixed. The cold spot (T_{\min}) is at the root of the tree, and the two hot spots are in the farthest (left-side) corners. The aspect ratio H_2/L_2 refers to the vertical/horizontal external dimensions of the largest rectangle. The best second construct is the one with $n_2 = 4$; however, the neighboring designs ($n_2 = 2, 6$) perform nearly as well. The global resistances of designs (a), (b) and (c) agree within seven percent even though their internal structures are markedly different. Their optimized external shapes are also nearly the same. The case of Fig. 13(a) was optimized further in Fig. 8, by allowing spacings (k_0 material) all around the tips of the elemental (D_0) inserts ([49]). In Fig. 8 the dimensionless temperature is defined as $\tilde{T} = (T - T_{\min}) k_0 / (q'' A_2)$.

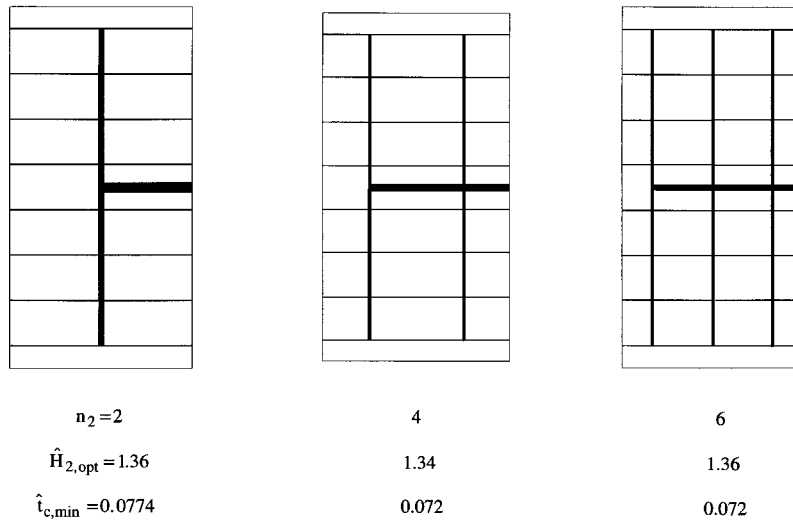


Fig. 14 The second construct optimized for minimum time of discharge from a volume to one point, and the effect of changing the number of first constructs, n_2 ($\phi_2=0.1$, $k=300$, $D_1/D_0=5$, $D_2/D_0=10$) ([50])

Once again, the global optimization principle leads us to very robust (invariant) features such as the global performance level and the external shape of the construct. Surprisingly, we will arrive at the same conclusions via a completely different optimization in Fig. 14. Changes in the internal tree structure, such as overgrowth and surgery (adding or cutting branches) has almost no effect on the globally optimized features.

Time-Dependent Discharge From Volume to Point

In Figs. 5–13 we saw how the tree structure is derived from principle (minimum global resistance, size constraints), when the flow is *steady* from volume to point, or point to volume. Practically the same structure is deduced when the objective is to minimize the time of discharge of a volume to a sink, as in lightning, exhaling, and river basin construction after a sudden downpour. The maximized performance in steady flow is the same as the minimization of the time of approach to equilibrium: The mechanism that allows the system to reach this objective is *the construction of optimal flow shape and structure*.

We demonstrated the construction of the tree for volume-point discharge by minimizing geometrically the cooldown time of an initially isothermal conducting solid (k_0 , without heat generation), which is placed suddenly in contact with a boundary sink point (T_{\min}) [50]. With reference to the elemental volume of Fig. 5 this new problem means that $q'''=0$, and at the time $t=0$ the entire $A_0=H_0L_0$ rectangle is at the temperature T_i . The energy stored in this volume flows out through the origin. All the temperatures decrease, however, the slowest to do so are the instantaneous hot spots [$T_{\max}(t)$] located in the farthest corners ($x=L_0$, $y=\pm H_0/2$). The effective cooldown time t_c is defined as the time when the highest temperature has reached within ten percent its final (equilibrium) level,

$$\frac{T_{\max}(t_c) - T_{\min}}{T_i - T_{\min}} = \varepsilon, \quad (14)$$

where $\varepsilon=0.1$. The cooldown time has a sharp minimum with respect to the rectangle shape H_0/L_0 . Numerical minimization of t_c in the range $0.03 \leq \phi_0 \leq 0.3$ and $3 \leq \bar{k} \leq 300$ showed that the optimal elemental shape is given by the same formula as Eq. (13) in which the factor 2 is replaced by 2.11—not a significant difference.

That the optimized structure in volume-point discharge is the same as in volume-point steady flow is stressed further by Fig. 14.

Compared are three optimized constructs of the second kind, for which we minimized the cooldown time by varying all the geometric features except n_2 . The optimized structures are drawn to scale. Listed under each drawing are the assumed number of first constructs in the structure (n_2), the optimized external shape $\hat{H}_{2,\text{opt}}=(H_2/L_2)_{\text{opt}}^{1/2}$, and the minimized dimensionless cooldown time, $\hat{t}_{c,\text{min}}=t_{c,\text{min}}\alpha_0/A_2$, where α_0 is the thermal diffusivity of the k_0 material. The three designs have practically the same global performance ($\hat{t}_{c,\text{min}}$) and external shape. Their robustness and internal details support in every respect the conclusions reached on the basis of maximizing global performance in steady flow between a volume and one point (Fig. 13).

The volume-point discharge optimization shows clearly why the principle recognized in this work is new on the currently accepted background. The approach to equilibrium, the direction of time, or the difference between before and after, is the domain covered by the second law of thermodynamics. The objective and constraints (constructal) principle invoked in this work accounts for an equally important part of nature, that is, of everything: The mechanism for reaching equilibrium faster is the construction of macroscopic flow architecture, i.e., the generation of geometric form.

More Efficient Structures Look More “Natural”

An interesting trend becomes visible as we continue to relax the geometric optimization, and increase the number of degrees-of-freedom optimized at every volume scale. This work was illustrated in Figs. 11–13. The ultimate move in this direction is to abandon the assumption that the elemental volumes are rectangular ([51,52]). We illustrate this by reviewing chronologically the evolution of the elemental-volume design with volumetric heat generation. This is shown in Fig. 15, where each design is optimal and drawn to scale. The total volume, the volume fraction ($\phi_0=0.04$) occupied by the high-conductivity material (black), and the ratio of thermal conductivities ($k_p/k_0=\bar{k}=575$) are the same in each design.

The earliest design (Fig. 15(a)) was the simplest, and the roughest. The elemental volume was assumed to be rectangular, and the long k_p insert was assumed to have uniform thickness, D_0 . The thermal resistance is minimum when the large rectangle has a certain shape—an optimal slenderness ratio. The hot spots are concentrated in the two corners (T_{\max}) that are situated the farthest relative to the heat sink. See also Figs. 5 and 6.

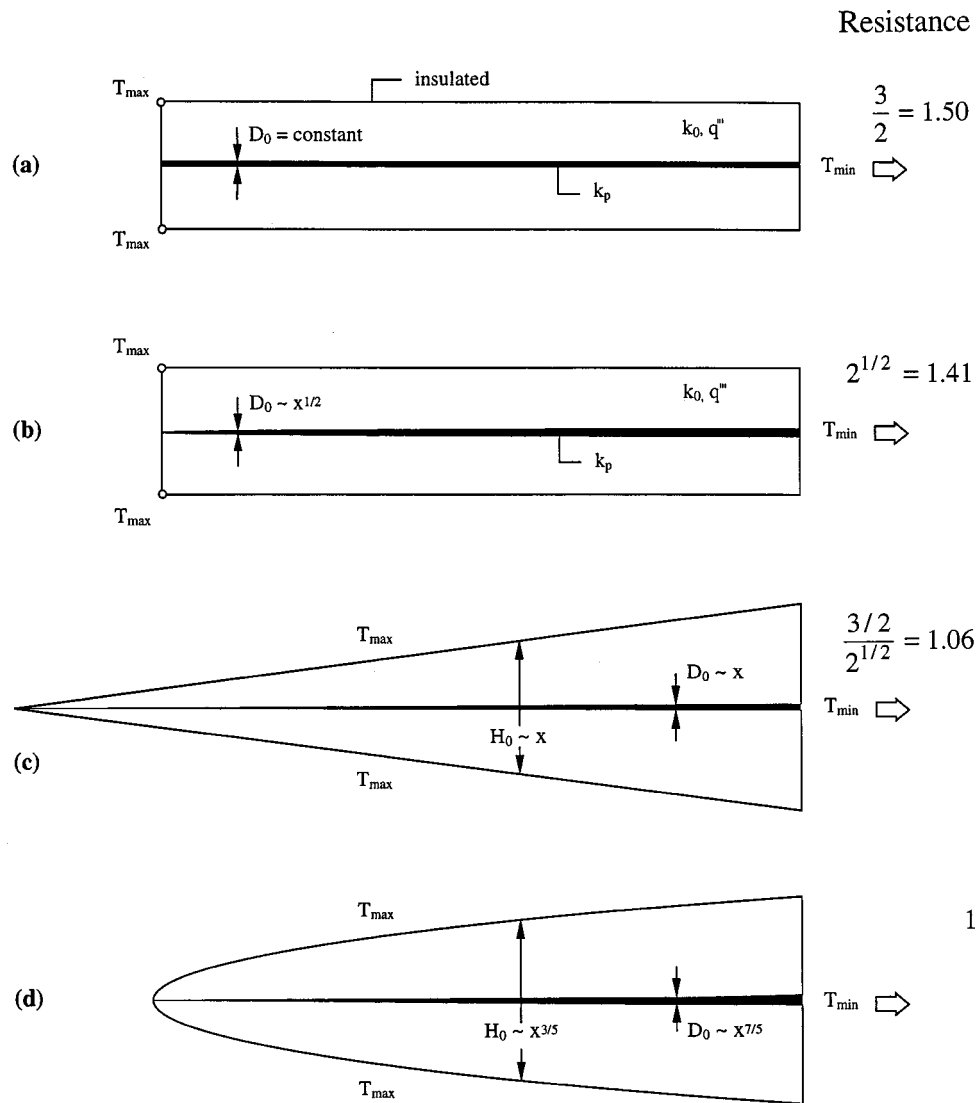


Fig. 15 Evolution of the optimized elemental-volume design for minimum flow resistance between a volume and one point ([52]). The numbers in the right column indicate the global volume-point resistance as a multiple of the resistance of design (d).

The resistance of the optimized elemental rectangle was lowered by six percent after abandoning the constant- D_0 feature, and optimizing the profile of the k_p channel. In the design shown in Fig. 15(b), two degrees-of-freedom were optimized: the slenderness ratio of the rectangle, and the shape function of the high-conductivity blade, $D_0 \sim x^{1/2}$, where x is measured away from the thin end ([43]). The hot spots continue to reside in two points—the two most distant corners (T_{\max}).

A more substantial reduction in volume-point resistance is registered when the hot spots are distributed continuously over an optimally curved portion of the boundary (Fig. 15(d)). The design is said to have “constant resistance” because the temperature difference between each boundary point (T_{\max}) and the common heat sink (T_{\min}) is constant ([51]). Three degrees-of-freedom were optimized: the outer shape ($H_0 \sim x^{3/5}$), the slenderness ratio of the outer shape, and the shape of the k_p insert ($D_0 \sim x^{7/5}$). The global resistance of design (d) is only two thirds of the resistance of design (a), and 71 percent of the resistance of design (b).

Figure 15(c) shows a triangle-in-triangle approximation of the most polished design (d). This approximation is also a constant-resistance design with continuous hot-spot lines (T_{\max}), but the external triangular shape is assumed, not optimized. The two

degrees-of-freedom optimized are the aspect ratio of the outer triangle and the shape of the high conductivity inserts ($D_0 \sim x$). The resistance of design (c) exceeds by only six percent the resistance of design (d).

In the triangle-in-triangle structure, the formation of continuous hot-spot lines has its origin in the optimization of the aspect ratio of the external triangle. When the external triangle is too slender, the hot spot is concentrated in one point: the sharp tip of the triangle. In the opposite extreme, the hot spots are located in the two corners on the side with the heat sink. The optimal slenderness is in between, when the hot spot “jumps” from the tip of the triangle to the two base corners. At that moment the hot spot traces with T_{\max} the two long sides of the triangle, and the design acquires its constant resistance.

Viewed in ensemble, Fig. 15 shows that the performance improves at every step, from (a) to (d), and the improvement ranges from the significant to the marginal. When these elemental designs are assembled into larger constructs, they cover the innermost scales of the tree structure. Designs based on elements (c) and (d) cover their allotted space *incompletely*.

Figure 16 shows the optimized first construct that results from using the best elements (Fig. 15(d)). The optimal shape of the area

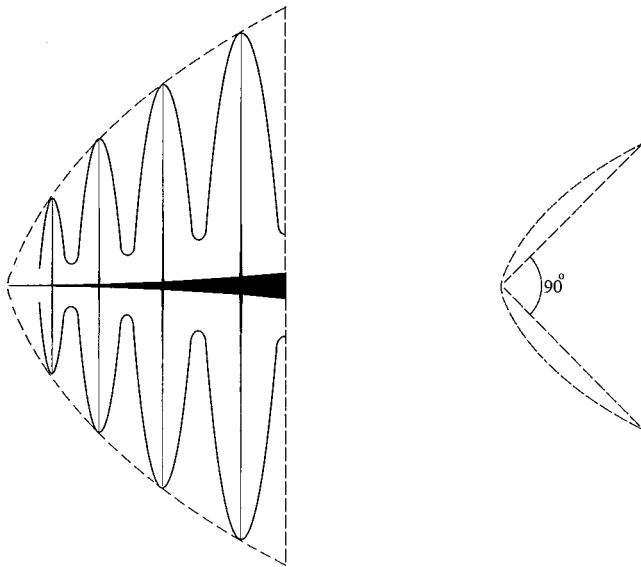


Fig. 16 Optimal external and internal features of the first construct with constant thermal resistance ([51])

allocated to the construct is such that the vertical dimension (H_1) of the structure increases as $x^{3/5}$, where x increases away from the left end. The optimal thickness (D_1) of the central blade (horizontal, black) increases as $x^{7/5}$. In this design the volume fraction of k_p -material in the elemental volumes (ϕ_0) and the volume fraction averaged over the entire first construct (ϕ_1) satisfy the optimized proportion $\phi_0 = (1/2)\phi_1$.

The right side of Fig. 16 shows that the isosceles triangle inscribed in the optimized first construct has a 90 deg tip angle. Unlike the slenderness of the elemental rectangles and triangles (Fig. 15), which decreases with $\bar{k}\phi_0$, this tip angle is an invariant: it is independent of $\bar{k}\phi_1$.

The increased internal complexity of the first construct has the effect of decreasing dramatically the resistance in volume-to-point flow. The global resistances of the optimized elemental volume (Fig. 15(d)) and first construct (Fig. 16) are

$$\frac{T_{\max} - T_{\min}}{q'''A_0/k_0} = \frac{1}{3(\bar{k}\phi_0)^{1/2}} \quad (15)$$

$$\frac{T_{\max} - T_{\min}}{q'''A_1/k_0} = \frac{8}{9\bar{k}\phi_1} \quad (16)$$

where A_0 and A_1 are the actual areas covered by k_0 material and uniform heat generation (q''') in the two figures. Comparing the two resistances on an equal basis, namely, $A_0 = A_1$ and $\phi_0 = \phi_1 = \phi$, we see that the first-construct resistance is smaller as soon as the product $\bar{k}\phi$ exceeds 64/9. This marks the transition from one configuration (elemental) to a more complex one (first construct) in the pursuit of better access for the volume-point current. As the product $\bar{k}\phi$ increases above 64/9, the first-construct configuration becomes a considerably more effective path for the current, while its elemental volumes become more slender and numerous.

Other transition phenomena, all the laminar-turbulent transitions, Rayleigh-Bénard convection, and dendrites in solidification have been predicted based on the same principle of flow access maximization ([1]). In particular, the optimization of access for heat currents in Rayleigh-Bénard convection ([53]) leads analytically to predicting the onset of transition and the entire $Nu \sim Ra^n$ curve, with the exponent n decreasing as Ra increases. This theoretical progress is made not only for convection in fluids but also for convection in porous media. These developments should re-

new interest in a piece of classical work that, from today's point of view, looks even more important. The maximization of heat transfer rate (or Nusselt number) in Bénard convection was a hypothesis introduced by Malkus [54] and used in several studies of convection in pure fluids and fluid-saturated porous media. It was related by Glansdorff and Prigogine [55] to a principle of entropy generation minimization subject to imposed boundary conditions. Constructal theory ([53]) develops the connection between conductance maximization and the optimization of geometric shape of a single finite-size flow element. In this way Malkus' hypothesis becomes part of a more direct and transparent theory of geometrical shape and pattern formation in nature. Constructal theory brings many of the advances made by others in the past under the same deterministic umbrella ([1]).

Second constructs can be perfected in a similar way, for optimal external shape of the occupied territory, and for optimal shape of the new central k_p blade of thickness D_2 ([51]). Similar progress can be made in three dimensions ([52]). At the elemental volume level, we begin with a body of revolution with unknown diameter variation, $H_0(x)$, and unknown diameter function $D_0(x)$ for the high-conductivity fiber. The total volume (V_0) and the volume of high-conductivity material ($\phi_0 V_0$) are constrained. The optimal shapes compatible with the presence of hot spots (T_{\max}) all over the external surface of revolution are $H_0 \sim x$ and $D_0 \sim x$. This cone-in-cone design emerges as the configuration for constant resistance at the elemental level. The cones become more slender as the product $\bar{k}\phi_0$ increases. The optimized first construct exhibits $H_1 \sim x^{1/2}$ and $D_1 \sim x$, which means that the central D_1 fiber is a cone. The shape of the volume inhabited by the first construct is relatively robust (invariant), almost hemispherical.

The flow structures reviewed in this section break new ground on several fronts. First, their performance is superior to that of previously optimized paths for minimum resistance to flow between a volume and one point. By allowing the external shape of the fixed-size domain to serve as a degree-of-freedom, in addition to the internal structure of the high-conductivity path, it is possible to optimize both the shape and structure to generate designs that maintain a constant resistance between every peripheral point (T_{\max}) and the heat sink (T_{\min}). The architectures that emerge are more efficient, and look more like the tree structures found in nature (leaves, branches, snowflakes, pine cones).

The second new aspect is that the theoretical constant-resistance structures are fractals. They do not fill their allotted space completely because the addition of geometrically similar elemental volumes can, in principle, be continued indefinitely toward the tips of the first constructs (e.g., Fig. 16). These structures represent a theoretical limit. They are not real because they cannot be built or seen. Only the approximate, Euclidian structures generated using a finite number of elements (with a finite-size smallest element) can be built and seen ([2,56]).

Furthermore, the continuous hot-spot surfaces of the constant-resistance constructs must be both isothermal (T_{\max}) and adiabatic. The interstitial spaces that are left uncovered by the structure would have to be completely inactive. Then, the uncovered spaces would be filled with useless material—zero heat generation rate and zero conductivity. It just does not make sense to work so hard on maximizing the use of the volume fraction occupied by the dendritic heat-generating structure, when the uncovered volume is not used at all.

The constant-resistance structure—the fact that this geometric form represents the ultimate with respect to minimizing volume-point resistance—lends credence to the thesis that as natural structures evolve toward better performance in time, they also acquire shapes that look closer to fractal ones. The classical fractal approach postulates a priori self-similarity, that is, scale invariance of the geometry of the objects, of “invariance in the zoom direction.” Constructal theory establishes instead relations between successive scales (“scale covariance,” not invariance) as a “de-

terministic result'' of constrained optimization ([57]). The quotes indicate concepts introduced by Nottale [58], who wrote:

''One of the possible ways to understand fractals would be to look at the fractal behavior as the result of an optimization process . . . Such a combination . . . may come from a process of optimization under constraint, or more generally of optimization of several quantities sometimes apparently contradictory (for example) maximizing surface while minimizing volume . . .''

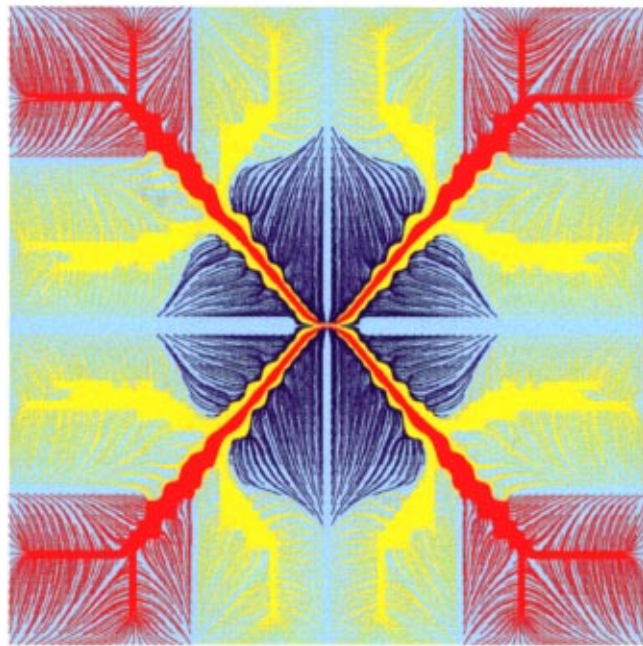
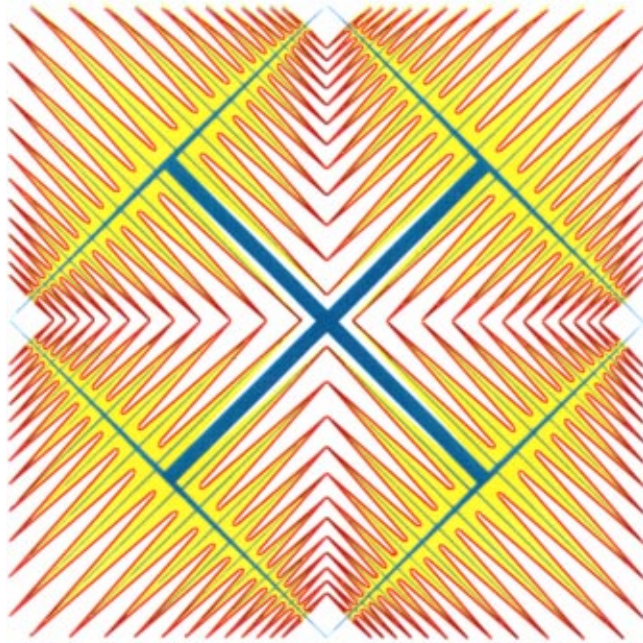


Fig. 17 The top drawing shows the third construct containing four constant-resistance second constructs or eight first constructs, cf. Fig. 16 ([51]). The bottom figure is the river drainage basin generated by a deterministic erosion model based on global flow resistance minimization ([59]).

Constructal theory is about the geometry-generating principle envisioned by Nottale.

Physicists, biologists, and engineers have a joint interest in the constructal-theory and constant-resistance concepts. These methods provide (i) direct routes to resistance minimization by design, (ii) rational explanations for the occurrence of flow structures in nature, and (iii) a deterministic basis for the repeatability, regularity, and beauty of all such structures, natural and man made.

It is fitting that we end this section on point (iii), which is also made in the upper part of Fig. 17. This figure shows the design that the engineer would produce by covering a larger volume with four second-construct structures of the type optimized in the sequence represented by Figs. 15(d) and 16. The heat current integrated over the four quadrants of the large square domain is led by the diagonal D_2 channels to the center of the cross, which is cooled by a sufficiently strong stream that flows perpendicularly to Fig. 17. The lower part of the figure shows the streaklines and the pattern of high-permeability channels developed numerically, in time, based on a fully deterministic erosion model of a river drainage basin ([59]). Rain falls on every point of the square low-permeability domain, and is driven by pressure differences toward the central sink. The domain is made of 51×51 square grains. At every time step, certain grains were selected and removed (washed downstream) based on the same constructal principle: the minimization of the global volume-point resistance subject to constraints. The river basin grows and marbleizes itself into nearly square territories that are served by central main streams.

The similarities (origin and image) between this unexpected structure (Fig. 17, bottom) and the designed version (Fig. 17, top) are worth contemplating. They reinforce a familiar view, which is new when seen from the reverse. Familiar is the empirical view that the more we look at natural systems the more we find that they operate most efficiently. The reverse is the theoretical direction of this work: The more we invoke the constructal law the more we discover that the deduced designs—our own drawings—look more and more “natural.” The constructal principle works, in the inanimate, the animate, and the engineered.

Trees of Fins

In this section we turn our attention to the more complex configurations where the flow of heat between a finite volume and one point is aided by the flow of a fluid. The resulting structures are trees in which convection plays an important role, but not the complete role. In every elemental volume convection is intimately coupled with pure conduction, in a phenomenon of conjugate heat transfer. The key to developing the optimal flow architecture, from the smallest elemental volumes to larger and larger constructs, is to find this optimal coupling, or optimal balance between convection and conduction.

Convective flow architectures are of two types, depending on which portions of the structure are reserved for convection. In the first type the interstices are occupied by solid that generates heat at every point, and conducts the heat by diffusion in the manner of the k_0 material analyzed in Fig. 5. Convection is located in the branches of a tree formed by ducts filled with flowing fluid. The ramifications of two trees of this type visit each elemental volume. One tree delivers cold fluid to each element. The other tree collects the fluid heated by the element, and reconstitutes it into a single stream that eventually leaves the volume ([60]).

The circulatory system performs its mass transfer function and secondary heat transfer function by using a convective double-tree structure of the first type (see the section on Trees for Convective Heat Currents). In the respiratory system the two flow trees are superimposed, as they rely on the same network of bronchial tubes, one tree during inhaling, and the other during exhaling. Engineering applications of trees of convective channels abound in the cooling of virtually every enclosed electrical heat-generating system, e.g., windings of electrical machines, comput-

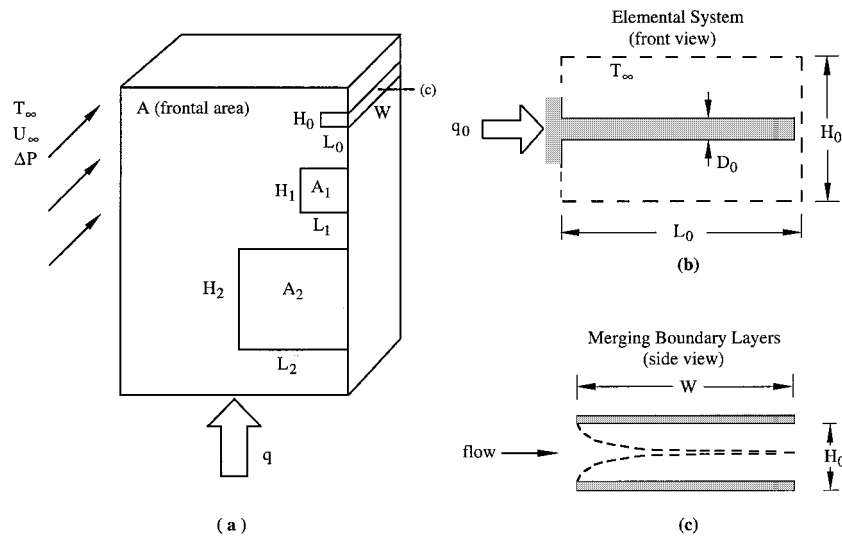


Fig. 18 (a) The volume AW that serves as convective heat sink for the concentrated heat current q , and (b) the smallest volume element defined by a single plate fin ([64])

ers, and electrical and electronic packages of many types and sizes. All must be cooled at every point, using forced or natural convection.

In the convective tree of the second type the spaces occupied by conduction and convection are reversed. Convection is in the interstices, and is coupled with pure conduction in solid parts, which form trees. Every interstitial space serves as sink or source for the current that passes through the root of the tree. Numerous applications for this flow structure are found in the design of heat transfer-enhanced surfaces for heat exchangers, and for cooling small scale electronics. In the latter, the tree structures are better known as fin trees and fin bushes ([61,62]).

Let us review the constructal fin-tree problem statement, this time with reference to the general geometry sketched in Fig. 18. We consider the two-dimensional volume of frontal area A and fixed length W , where W is aligned with the free stream (U_∞, T_∞). The problem consists of distributing optimally through this volume a fixed amount of high-conductivity (k_p) material, which takes heat from one spot on the boundary and discharges it throughout the volume. We may think of the boundary spot (root) as the external surface of an electronic module that must be cooled. In this case the volume AW is the space that is allocated for the purpose of cooling the module by forced convection. This volume constitutes a global constraint.

As in the pure-conduction applications of the constructal method (Fig. 5), we start the space filling optimization sequence from the smallest finite-size scale. The smallest system (the “elemental system” in constructal terminology) consists of a two-dimensional volume $H_0 L_0 W$, in which there is only one blade of k_p material (Fig. 18(b)). The thickness of this blade is D_0 . Heat is transferred from one boundary spot (T_0 , at the root of the fin) to the entire elemental volume. If we neglect the heat transfer through the fin tip, and use the unidirectional fin conduction model ([63]) the elemental heat current is

$$\frac{q_0}{(T_0 - T_\infty)W} = (2k_p D_0 h_0)^{1/2} \tanh\left[\left(\frac{2h_0}{k_p D_0}\right)^{1/2} L_0\right]. \quad (17)$$

Unlike in Fig. 5, where it was possible to optimize the shape of the elemental volume, in the present problem the thickness of the elemental volume (H_0) is fixed because it is the same as the optimal spacing between two successive D_0 -thick plate fins. The spacing is optimal when the laminar boundary layers that develop over the swept length W became thick enough to touch at the

trailing edge of each plate fin (see the section on Distribution of Void Space for Flow Channels). Conversely, the spacing is optimal when the time of fluid travel along W matches the thermal diffusion time across the D_0 channel. This feature is illustrated in Fig. 18(c). The optimal spacing ($H_0 - D_0 \sim H_0$) is determined uniquely by the length W and the pressure difference ΔP maintained across the swept volume, cf. Eq. (11),

$$\frac{H_0}{W} \cong 2.7 \Pi_w^{-1/4} = 2.7 \left(\frac{\mu \alpha}{W^2 \Delta P} \right)^{1/4}. \quad (18)$$

It can be shown that the minimized thermal resistance that corresponds to this spacing is also characterized by an average heat transfer coefficient that is given approximately by ([33])

$$h_0 \cong 0.55 \frac{k}{W} \left(\frac{W^2 \Delta P}{\mu \alpha} \right)^{1/4}. \quad (19)$$

Here k is the thermal conductivity of the fluid. The factor ΔP that appears in Eq. (19) refers to the pressure difference that is maintained in the W direction (e.g., by a fan), where $H_0 \times L_0$ is the cross section of one duct. If the H_0 -wide channel is open to one side (the side that would connect the tips of two successive fins), and if the entire assembly is immersed in a stream of velocity U_∞ , then Eqs. (18) and (19) are adequate if ΔP is replaced by the dynamic pressure associated with the free stream, $\Delta P \cong \rho U_\infty^2 / 2$.

We now proceed toward larger scales by recognizing that at the elemental level the h_0 and H_0 values are two known constants. The next volume is the first assembly of constant frontal area $H_1 L_1 = A_1$, which is shown in Fig. 19. The shape of this volume (H_1 / L_1) is free to vary. The assembly is defined by a central blade of thickness D_1 , which is connected to all the elemental volumes that are needed to fill the $A_1 W$ volume. The D_1 blade connects the roots of all the D_0 fins. When the number of elemental volumes in this assembly is large, the cooling effect provided by the D_0 fins is distributed almost uniformly along the D_1 stem. In this limit the D_1 stem performs as a fin immersed in a convective medium with constant heat transfer coefficient. The effective heat transfer coefficient of this medium (h_1) can be deduced from Eq. (17) by noting that each q_0 current flows out of the D_1 blade through an area of size $H_0 W$. In other words, we combine $h_1 = q_0 / [H_0 W (T_0 - T_\infty)]$ with Eq. (17) and $L_0 = H_1 / 2$, and obtain

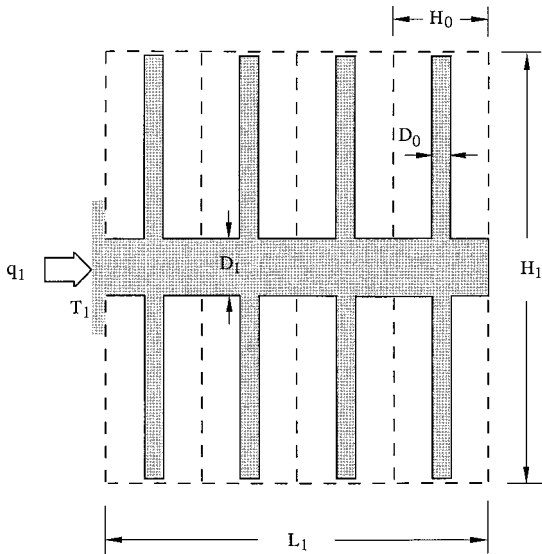


Fig. 19 First construct consisting of a large number of elemental one-fin volumes ([64])

$$h_1 = \frac{1}{H_0} (2k_p D_0 h_0)^{1/2} \tanh \left[\left(\frac{2h_0}{k_p D_0} \right)^{1/2} \frac{H_1}{2} \right]. \quad (20)$$

The D_1 blade functions as a fin with insulated tip, therefore we write cf. Eq. (17)

$$\frac{q_1}{(T_1 - T_\infty)W} = (2k_p D_1 h_1)^{1/2} \tanh \left[\left(\frac{2h_1}{k_p D_1} \right)^{1/2} L_1 \right]. \quad (21)$$

Two constraints must be satisfied, the total volume, or frontal area ($A_1 = H_1 L_1$), and the frontal area of all the solid ($A_{p,1} = D_1 L_1 + n_1 D_0 L_0$), or the volume fraction $\phi_1 = A_{p,1} / A_1$. Alternatively, the constraints are represented by the dimensionless numbers $\tilde{A}_1 = A_1 / H_0^2$ and $\Phi_1 = \phi_1 k_p / (h_0 H_0)$.

The geometry of the construct has two degrees-of-freedom. In the numerical work detailed in ([64]) the two optimized features were the external shape H_1 / L_1 and the internal ratio D_1 / D_0 .

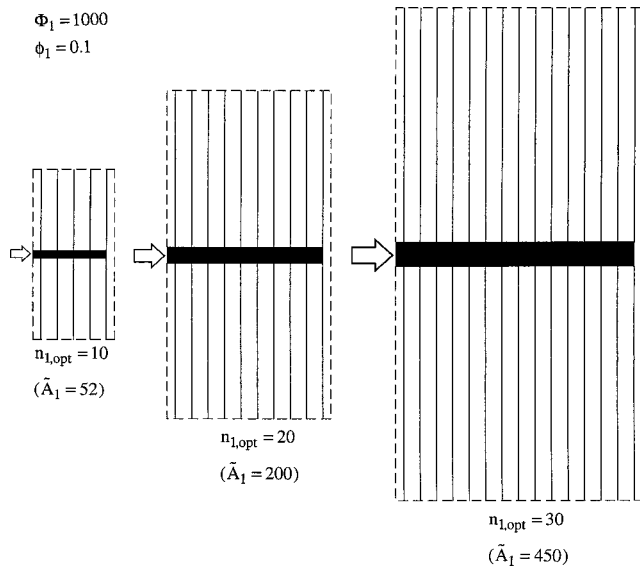


Fig. 20 The evolution of the optimized first construct of plate fins as the total volume increases ([64])

These were developed by maximizing the global conductance (21). Associated results are the number of elemental fins (n_1) and the twice-maximized conductance.

In Fig. 20 we see the evolution of the twice-optimized geometry of the first assembly, while the size parameter \tilde{A}_1 increases at constant volume fraction of fin material ($\Phi_1 = 1000$). In other words, the amount of fin material increases in proportion to the volume occupied by the fin tree. The drawing was made by assuming that $\phi_1 = 0.1$, or $\Phi_1 = 10^4 \phi_1$. Each frame was drawn to scale, to show the growth of the volume occupied by the assembly. The role of unit length is played by the thickness of the elemental volume (H_0), which is constant. The exhibited structures were selected to correspond to even values of n_1 . The corresponding values of the assembly size \tilde{A}_1 are also listed.

Two invariant features of the fin trees of Fig. 20 are worth noting. The overall shape of the volume occupied by the assembly does not change much as the volume size increases. Another feature is the thickness of the elemental fin, $D_{0,opt}$, which in Fig. 20 does not vary from frame to frame.

Future work may address various improvements and refinements of the classical fin conduction model that was used in setting up the present analysis and optimization. For example, the effects of temperature-dependent thermal conductivity, radiative heat transfer, and spatially varying heat transfer coefficient can be incorporated at the elemental level, while paying a penalty through the increased complexity of the analysis, and the need for numerical work even at the elemental level. Equation (18) will most definitely be replaced by a numerical procedure in the re-fined model. The performance of the second construct is described further in ([64]), which also reports a fully numerical simulation and optimization of the first-construct configuration.

Trees of fins may also be pursued in simpler configurations. When there are only two elemental plate fins in the first construct, the assembly has the shape of a T or, when the elemental tips are bent downward, the shape of ‘‘tau’’ ([62,65]).

Constructal trees of fins can also be developed in cylindrical geometries. The first construct consists of a number of elemental circular plate fins mounted on a cylindrical stem ([66]). Fluid is forced to flow through the spaces between adjacent fins. Again, there are two geometric features that can be optimized, the external aspect ratio of the cylindrical construct (diameter/length), and the ratio between the elemental plate-fin thickness and the stem diameter.

Trees of fins will continue to attract interest as heat transfer augmentation techniques in heat exchangers, e.g., the cooling of electronics. More recently, similar structures have generated interest in chemical engineering ([67]) and entropy generation minimization ([68,69]), where the analyses relied on concepts of fractal geometry.

Trees for Fluid Flow

Analogous tree-shaped paths can be deduced for fluid flow between a volume and a point, or an area and a point. For brevity, we omit the details because they are available in the literature ([2,59,70–72]). These constructs come on an impressive background of older descriptive work that covers several decades. Of all the tree flows studied in the past, the trees for fluid flow have been studied the most. Their features have been described quantitatively in surprisingly sharp (reproducible) terms, notably in the study of lungs, vascularized tissues, botanical trees, and rivers ([46,73–80]). In recent years, these natural phenomena have been visualized on the computer by means of repetitive fracturing algorithms, which had to be postulated. The origin of the phenomena was left to the ‘‘explanation’’ that the broken pieces (or building blocks from the reverse point of view of constructal theory) are the fruits of a nondeterministic process of *self*-optimization and *self*-organization.

The analogy with the heat-current trees described in the preceding sections is based on the fact that a fluid flow may exist in more

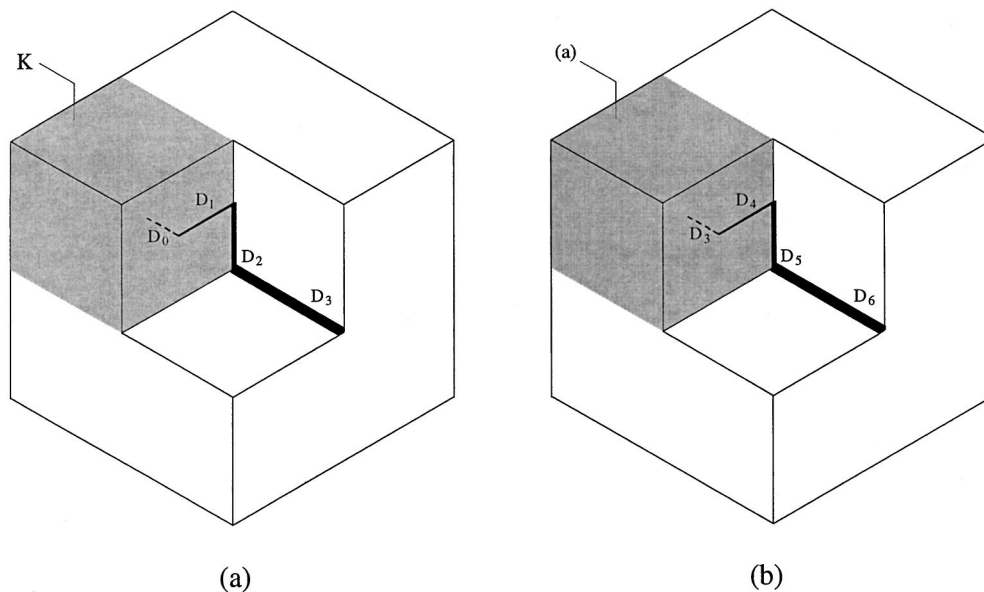


Fig. 21 Three-dimensional constructs for flow between a volume and one point: the doubling of the outer dimension in going from the optimized third construct (a) to the optimized sixth construct (b) ([2,70])

than one flow regime. In the heat flow example of Fig. 5 the two regimes were high-resistance conduction through most of the material (k_0), and low-resistance conduction through the inserts (k_p). The analogous regimes for pure fluid flow are viscous diffusion and, respectively, streams. In flow through heterogeneous porous media the two regimes are Darcy flow and, respectively, channel flow through fissures.

The existence, structure, and transport capability of turbulent flows can be reasoned from the same theoretical viewpoint. See the first eddy and growth rate of turbulent shear layers ([1,24]), and the onset of Rayleigh-Bénard convection and the entire Nu-Ra curve in fluids and fluid-saturated porous media ([53]).

What we recognize as macroscopic structure is none other than the geometric arrangement of the spatial domain of one flow regime relative to (or through) the territory occupied by the other. The structure is not visible—it is not even an issue—when only one flow regime is present. In such cases the lone regime is the one with the highest resistance. Note that the volume-to-point flows of Figs. 5–16 could also be effected by molecular diffusion alone, namely, thermal diffusion through a single material (k_0), or Darcy flow through a single porous medium with low permeability. Such flows are disorganized microscopically, and *shapeless* macroscopically. They become visible, as background, only when a second flow regime emerges (streams, channels). The latter represents organized motion, or *flow with shape*.

Figure 21 is a summary of the volume-to-point flow structure in three dimensions, which is obtained by optimizing each volume element according to the constructal sequence. This figure may be viewed as a three-dimensional counterpart of Figs. 9 and 10. The volume is filled mostly with Darcy flow through a porous medium of low permeability K . The flow is collected into streams guided by round tubes with Hagen-Poiseuille flow. The tube diameters (D_0, D_1, \dots), tube lengths (not shown in Fig. 21), and dimensions of each volume scale (elemental, first construct, ...) are results of the optimization principle, and are reported in ([2,70]). The elemental volume is the dark cube highlighted in Fig. 21(a).

An important feature of this theoretical structure is that the changes in dimensions settle into a pattern, but only after the order of the volume construct becomes high enough. For example, the optimized diameter factor settles at $D_{i+1}/D_i = 2^{1/3}$ after the second construct. The factor for tube lengths L_{i+1}/L_i exhibits a cy-

clical pattern for each sequence of three construct sizes, provided that $i \geq 2$. We return to this cyclical pattern in the closing paragraph of this section.

Another feature of this architecture is that the outer linear dimension of the construct of order $(i+3)$ is the double of the outer dimension of the construct of order (i) . This factor of 2 increase also applies to the diameters of the largest (collecting) ducts of the two constructs. Figure 21 illustrates the doubling of the size, from the third construct (a) to the sixth construct (b).

The internal details do not double their sizes in going from construct (i) to construct $(i+3)$. In other words, construct $(i+3)$ is not the same as magnifying by a factor of 2 every feature of construct (i) . The reason is that the fluid network constructed theoretically in this line of work has a definite (finite, known) beginning: the smallest scale (K , or D_0) and the optimized first construct. The geometry and finite size of this beginning distinguish the present theoretical construction from the algorithms used in fractal geometry. In the latter, the algorithm (from large to small) is repeated conceptually *ad infinitum* ([48]), all the way down to the scale of size zero. Because of the infinite series of steps, the fractals-generated image of a certain size could be obtained in principle by magnifying an image of a smaller size. That does not happen in any of the constructs derived from principle. The inner cutoff, and the breakdown of the algorithm at small enough scales are as important as any other geometric feature. The visible tree (channels) is not more important than the invisible flow through the interstitial spaces. The interstices, cutoffs and smallest (finite) size scales are as much a part of natural structures as the tree-connected channels. This is why the geometry of nature is not fractal.

In the spring of 1999, while teaching the interdisciplinary course based on this material ([1]), we found that some of the features of the structure of Fig. 21 can be deduced much more succinctly by optimizing a plane construct consisting of a T-shaped junction (Fig. 22(a)). For simplicity, assume right angles and Hagen-Poiseuille flow with constant properties. Extensive numerical optimization work on constructal trees for conduction heat transfer ([43]) has shown that the optimization of the angle of confluence plays only a minor role in the overall resistance of the construct.

The stream m_i encounters the flow resistance of two L_{i+1} tubes

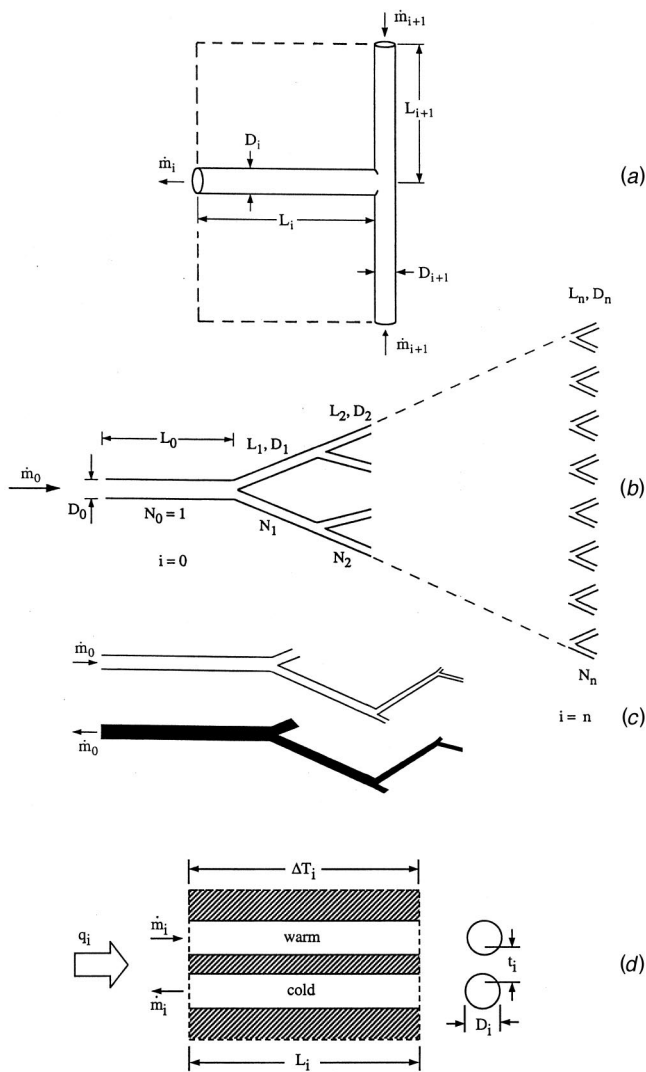


Fig. 22 The construction of the tree of convective heat currents: (a) the constrained optimization of the geometry of a T-shaped construct; (b) the stretched tree of optimized constructs; (c) the superposition of two identical trees oriented in counterflow; and (d) the convective heat flow along a pair of tubes in counterflow ([81])

in parallel, which are connected in series with one L_i tube. When the resistance is minimized by fixing the total tube volume we find the optimal diameter ratio $D_{i+1}/D_i = 2^{-1/3}$, just as in the optimization of the construction of Fig. 21. This old result is known as Murray's law ([47]). It is an extremely robust result, because it is independent of the lengths (L_i, L_{i+1}) and the relative position of the three tubes.

New is the optimization of the lengths when the space allocated to the construct is fixed. Now geometry and relative positions are taken into account. In the configuration of Fig. 22(a) the space constraint is

$$2L_{i+1}L_i = \text{constant}. \quad (22)$$

This second minimization of the flow resistance yields the optimal length ratio

$$\frac{L_{i+1}}{L_i} = f = 2^{-1/3} \quad (23)$$

which happens to match the optimal ratio of diameters. The optimized diameter and length ratios are drawn to scale in Fig. 22(a).

In the tree that was optimized step by step into three-dimensional parallelepipedic constructs (Fig. 21), the tube lengths increase by factors in the cyclical sequence 2, 1, 1, 2, 1, 1, The average of this factor for one step is $2^{1/3}$; therefore, the optimization of the plane construct of Fig. 22(a) is a condensed summary of the optimized three-dimensional construct averaged over each three-step cycle. The averaged tree is laid out (stretched) in Fig. 22(b) so that we may see all the tubes and levels (i) of construction. The number of tubes at level i is $N_i = 2^i$ and the total number of levels is n . Note that unlike in Fig. 21, in Fig. 22(b) the index i proceeds from the largest to the smallest tube, where L_n and D_n are the fixed dimensions of the elemental tube.

Trees of Convective Heat Currents: Heat Loss Versus Body Size

Consider next the flow of heat from the roots to the edges of the canopies of fluid trees such as Fig. 22(b). This proposal is new ([1,81]). Of interest is the heat lost by an animal through the body volume situated under its skin.

The trees of blood vessels are one geometric feature under the skin, but not the only one. The other is the *superposition* of the arterial and venous trees, so closely and regularly that tube i of one tree is in counterflow with tube i of the other (Fig. 22(c)). The existence of counterflows of blood and other fluids is widely recognized in physiology ([19]). It is also recognized in bioengineering where it serves as basis for a successful model of heat transfer through living tissues ([82,83]).

The counterflow formed by two tubes of level i is shown in the detailed drawing of Fig. 22(d). The arterial stream is warmer than the venous stream: heat flows transversally, from stream to stream. Consider now the adiabatic control surface drawn with dashed line around the counterflow. Since the enthalpy of the warmer stream is greater than that of the colder stream, the counterflow convects longitudinally the energy current $q_i = \dot{m}_i c_p \Delta T_{i,i}$, where c_p is the blood specific heat, and $\Delta T_{i,i}$ is the stream-to-stream temperature difference at level i . It was known even earlier in cryogenic engineering ([7,84]) that such a counterflow sustains a longitudinal temperature gradient, $\Delta T_i/L_i$, and that the convective energy current is proportional to this gradient:

$$q_i = \frac{(\dot{m}_i c_p)^2 \Delta T_i}{h_i p_i L_i}. \quad (24)$$

In this expression h_i and p_i are the overall stream-to-stream heat transfer coefficient and the perimeter of contact between the two streams. In the case of blood counterflow, the stream-to-stream thermal resistance h_i^{-1} is the sum of two resistances: the resistance through the fluid in the duct ($\sim D_i/k_f$, where k_f is the fluid thermal conductivity), plus the resistance through the solid tissue that separates two tubes ($\sim t_i/k$, where k is the tissue thermal conductivity). Even when the tubes touch, t_i is of the same order as D_i . In addition, since $k_f \sim k$, we conclude that $h_i \sim k/D_i$, and Eq. (24) becomes

$$\Delta T_i \sim \frac{q_i L_i k}{\dot{m}_i^2 c_p^2}. \quad (25)$$

The double tree structure of fluid streams is a single tree of convective heat streams with zero net mass flow. The convective tree stretches from the core temperature of the animal (at $i=0$) to the skin temperature. The latter is registered in many of the elemental volumes ($i=n$) that happen to be near the skin. The many counterflows of the double tree sustain the overall temperature difference ΔT (constant),

$$\Delta T = \sum_{i=0}^n \Delta T_i \sim \frac{q_0 k}{\dot{m}_0^2 c_p^2} \sum_{i=0}^n N_i L_i. \quad (26)$$

In going from Eq. (25) to Eq. (26), we used the continuity relations for fluid flow ($N_i \dot{m}_i = \dot{m}_0$, constant) and heat flow ($N_i q_i = q_0$, constant). Recalling Eq. (23), we substitute $L_i = L_0 f^i$, $L_n = L_0 f^n$ and $N_i = 2^i$ into Eq. (26), and after rearranging we obtain

$$q_0 \sim \left(\frac{q_0}{\dot{m}_0} \right)^2 \frac{k L_n f^{-n} [(2f)^{n+1} - 1]}{c_p^2 \Delta T (2f - 1)}. \quad (27)$$

Separated on the right-hand side are the quantities that are constant, and the quantities that depend on n (the number of construction steps). Note that the ratio q_0/\dot{m}_0 is independent of body size (n) because both q_0 and \dot{m}_0 are proportional to the metabolic rate.

The volume scale is estimated by regarding the stretched tree as a cone in Fig. 22(b). The base of the cone (at $i = n$) has an area of size $N_n L_n^2 \sim 2^n L_n^2$. The height of the cone is of the same order as the sum of all the tube lengths, $L_0 + L_1 + \dots + L_n = L_0(1 - f^{n+1})/(1 - f)$. In conclusion, the volume scale is

$$V \sim L_n^3 \left(\frac{2}{f} \right)^n \frac{1 - f^{n+1}}{1 - f}. \quad (28)$$

The relation between metabolic rate and total volume is obtained by eliminating n between Eqs. (27) and (28). The result is visible in closed form if we assume that n is sufficiently large so that $(2f)^{n+1} \gg 1$ in Eq. (27) and $f^{n+1} \ll 1$ in Eq. (28). In this limit q_0 is proportional to 2^n , and V is proportional to $(2/f)^n$. From this follows the nakedly simple result

$$\frac{\log q_0}{\log V} = \frac{3}{4} \quad (29)$$

which means that q_0 must be proportional to $V^{3/4}$. The proportionality between metabolic rate and body size raised to the power 3/4 has just been predicted, from pure theory. It can be verified numerically that Eq. (29) is accurate even for small n .

The 3/4 exponent that has been so puzzling over the years is a reflection of the optimized ratio of successive tube lengths, in a fixed space, $L_{i+1}/L_i = f = 2^{-1/3}$. Specifically, if we use $f = 2^{-a}$ in the derivation of Eq. (29), instead of 3/4 we obtain $(1+a)^{-1}$, where $a = 1/3$. The 3/4 exponent is intimately tied to the optimization that generated the tube lengths ratio subject to the total volume constraint, after the ratio of tube diameters had been optimized subject to the tube volume constraint. This double geometric optimization, the two constrains, and the pairing of tubes into constructs larger than the fixed elemental volume, is the essence of the constructal method ([1,2]).

In conclusion, what had been missing was the combination of (i) the tree architecture optimized for minimum pumping power, and (ii) the convective heat transfer (or, better, thermal insulation) characteristics of two identical fluid trees superimposed in counterflow. Putting (i) and (ii) together into a body heat-loss theory of animal design is the contribution of constructal theory.

Breathing and Heartbeating Times Versus Body Size

The proportionality between heat loss and body size raised to the power 3/4 is just one of the many allometric laws that can be predicted based on geometric optimization subject to constraints ([1]). Another famous example is the proportionality between breathing (or heartbeating) time and body size raised to the power 1/4.

It was shown in Bejan [2,85] that when the pumping power is minimized subject to a specified (global) mass transfer rate constraint, optimal breathing and heartbeating times exist, and are proportional to $(A/\dot{m})^2$,

$$t_{\text{opt}} \sim \left(\frac{A}{\dot{m}} D^{1/2} \Delta C \right)^2 \quad (30)$$

where A , \dot{m} , D , and ΔC are, in order, the total internal surface of all the tubes, the total mass flow rate of the tree, the mass diffusivity, and the driving concentration difference. To predict the

relation between t_{opt} and body size (mass M , or volume V) we need to substitute into Eq. (30) two additional relations:

- (i) the relation between metabolic rate (\dot{m}) and body size (M), and
- (ii) the relation between the mass-transfer contact area (A) and body size.

Relation (i) is $\dot{m} \sim M^{3/4}$, cf. Eq. (29). For relation (ii) we have the geometric argument outlined in ([2]), pp. 786–787. The thickness of the tissue penetrated by mass diffusion during the time t_{opt} is proportional to $t_{\text{opt}}^{1/2}$. The body volume (or mass) of the tissue penetrated by mass diffusion during this time obeys the proportionality $M \sim A t_{\text{opt}}^{1/2}$. Eliminating t_{opt} between $M \sim A t_{\text{opt}}^{1/2}$ and $t_{\text{opt}} \sim (A/\dot{m})^2$ (see Eq. (30)), and using $\dot{m} \sim M^{3/4}$, we conclude that the contact area should be almost proportional to the body mass, $A \sim M^{7/8}$. Finally, by substituting $\dot{m} \sim M^{3/4}$ and $A \sim M^{7/8}$ into $t_{\text{opt}} \sim (A/\dot{m})^2$, we conclude that the time intervals must vary as

$$t_{\text{opt}} \sim M^{1/4}. \quad (31)$$

This allometric law is supported convincingly by a very large volume of observations accumulated in the physiology literature ([19–22]).

Optimal Geometric Form: A Prevalent Natural Phenomenon

The flow of this lecture has been from engineering to nature. Along the way we reviewed a theory of how geometric form is generated in nature. Now the theory returns the favor to engineering: The same principle can be used to perfect the structure of engineering systems and to develop concepts for entirely new systems.

The progress of tree designs toward the constant-resistance limit (Fig. 15) exemplifies the work that can be done in engineering. Better global performance is achieved when more of the internal points are forced to work as hard as the few hardest working points. The system is destined to remain imperfect. The resistances to the internal flows cannot be eliminated because of the reality of design: Amounts and types of materials are given, volumes and matching (neighboring) systems are specified, and the time to contemplate changes is limited. In spite of these constraints, we can spread the imperfection around in optimal or nearly optimal ways. The highs and the lows must be balanced. The optimal spreading of slopes and differences takes us to the architecture that serves the global purpose. Geometric structure springs out of principle.

In the engineering of flow systems, the search for geometric configurations that offer better global performance subject to present-day constraints is known as thermodynamic optimization, irreversibility minimization, or entropy generation minimization. In this lecture I focused on the mechanism through which optimization is accomplished: the deterministic relationship between the improvement of performance (objective, constraints) and the generation of flow geometry (shape and structure) in the system. Most of this work was done first in heat transfer.

Performance improvement, or optimization is an old idea and a much older natural phenomenon. It has been with us throughout the history of engineering. Its reach, however, is much broader and more permanent: *Everything* exhibits it. We can be sure that the performance of power plants—our own performance, really—will continue to improve in time, in the same way that, in time, rainfall will always generate a more effective dendritic flow structure.

If this phenomenon is so old and prevalent, then what is new? New is the streamlining of its study into a single principle, a new principle distinct from the second law. Most of this work could have been done one or two centuries ago, before thermodynamics. The geometric minimization of resistances to heat and fluid flow could have been accomplished based on Fourier's heat transmis-

sion and the hydraulics of Bernoulli, Poiseuille, and Darcy. It is a mystery that this was not done then, because that period was still influenced by Maupertuis', Leibnitz' and Castigliano's intuition that of all possible processes the only ones that actually occur are those that involve minimum expenditure of "action." Instead, as Hildebrandt and Tromba [86] have noted, modern physics embarked on a course tailored to the principle of infinitesimal local effects. The constructal principle is a jolt the other way, a means to rationalize *macroscopic* features, objective, and behavior.

Acknowledgment

This research was supported by a grant from the National Science Foundation.

Nomenclature

| | |
|------------|---|
| A | = area, m^2 |
| c_p | = specific heat at constant pressure, $J/kg \cdot K$ |
| C | = thermal conductance, W/K |
| D | = thickness, diameter, m |
| D | = mass diffusivity, m^2/s |
| f | = ratio of successive tube length sizes |
| H | = height, transversal dimension, m |
| i | = level of assembly |
| K | = permeability, m^2 |
| k | = thermal conductivity, $W/m \cdot K$ |
| k_f | = fluid thermal conductivity, $W/m \cdot K$ |
| k_p | = high thermal conductivity, $W/m \cdot K$ |
| k_0 | = low thermal conductivity, $W/m \cdot K$ |
| k_1 | = effective thermal conductivity, $W/m \cdot K$ |
| \bar{k} | = ratio of conductivities, k_p/k_0 |
| L | = length, m |
| \dot{m} | = mass flow rate, kg/s |
| M | = mass, kg |
| n | = number of constituents in a construct; number of levels of assembly |
| N | = number of tubes |
| p | = perimeter of contact, m |
| q, Q | = heat transfer rate, W |
| q''' | = heat generation rate, W/m^3 |
| Ra | = Rayleigh number |
| S | = spacing, m |
| S_{gen} | = entropy generation rate, W/K |
| t | = time, s |
| t_c | = cooldown time, s |
| T | = temperature, K |
| V | = volume, m^3 |
| W | = power, W |
| W | = width, m |
| x | = conductance allocation fraction |
| x, y | = cartesian coordinates, m |
| α | = angle, rad |
| α | = thermal diffusivity, m^2/s |
| β | = coefficient of thermal expansion, K^{-1} |
| ΔC | = concentration difference, kg/m^3 |
| ΔP | = pressure difference, N/m^2 |
| ΔT | = peak excess temperature, K |

Greek Symbols

| | |
|---------------|--|
| ε | = small number, Eq. (14) |
| μ | = viscosity, $kg/s \cdot m$ |
| ν | = kinematic viscosity, m^2/s |
| Π | = pressure drop number |
| ϕ, Φ | = parameters indicating the relative amount of high-conductivity (or fin) material |

Subscripts

| | |
|-----|----------------------|
| C | = reversible, Carnot |
| H | = high |
| L | = low |

| | |
|-----|-----------|
| max | = maximum |
| min | = minimum |
| opt | = optimum |

Superscripts

(\wedge), (\sim) = dimensionless variables

References

- [1] Bejan, A., 2000, *Shape and Structure, From Engineering to Nature*, Cambridge University Press, Cambridge, UK.
- [2] Bejan, A., 1997, *Advanced Engineering Thermodynamics*, Second Ed., John Wiley and Sons, New York.
- [3] Bejan, A., 1988, "Theory of Heat Transfer-Irreversible Power Plants," *Int. J. Heat Mass Transf.*, **31**, pp. 1211–1219.
- [4] Bejan, A., 1989, "Theory of Heat Transfer-Irreversible Refrigeration Plants," *Int. J. Heat Mass Transf.*, **32**, pp. 1631–1639.
- [5] Bejan, A., Tsatsaronis, G., and Moran, M., 1996, *Thermal Design and Optimization*, John Wiley and Sons, New York.
- [6] Moran, M. J., 1982, *Availability Analysis: A Guide to Efficient Energy Use*, Prentice-Hall, Englewood Cliffs, NJ.
- [7] Bejan, A., 1982, *Entropy Generation Through Heat and Fluid Flow*, John Wiley and Sons, New York.
- [8] Bejan, A., 1988, *Advanced Engineering Thermodynamics*, John Wiley and Sons, New York.
- [9] Bejan, A., 1996, *Entropy Generation Minimization*, CRC Press, Boca Raton, FL.
- [10] Bejan, A., 1996, "Entropy Generation Minimization: The New Thermodynamics of Finite-Size Devices and Finite-Time Processes," *J. Appl. Phys.*, **79**, pp. 1191–1218.
- [11] Feidt, M., 1987, *Thermodynamique et Optimisation Énergétique des Systèmes et Procédés*, Technique et Documentation, Lavoisier, Paris.
- [12] Sieniutycz, S., and Salamon, P., eds., 1990, *Finite-Time Thermodynamics and Thermoeconomics*, Taylor and Francis, New York.
- [13] De Vos, A., 1992, *Endoreversible Thermodynamics of Solar Energy Conversion*, Oxford University Press, Oxford, UK.
- [14] Radcenco, V., 1994, *Generalized Thermodynamics*, Editura Tehnica, Bucharest.
- [15] Bejan, A., and Mamut, E., eds., 1999, *Thermodynamic Optimization of Complex Energy Systems*, Kluwer Academic Publishers, Dordrecht, The Netherlands.
- [16] Bejan, A., Vadász, P., and Kröger, D. G., 1999, *Energy and the Environment*, Kluwer Academic Publishers, Dordrecht, The Netherlands.
- [17] Schmidt-Nielsen, K., 1964, *Desert Animals: Physiological Problems of Heat and Water*, Oxford University Press, Oxford, UK.
- [18] Schmidt-Nielsen, K., 1972, *How Animals Work*, Cambridge University Press, Cambridge, UK.
- [19] Schmidt-Nielsen, K., 1984, *Scaling: Why Is Animal Size So Important?*, Cambridge University Press, Cambridge, UK.
- [20] Peters, R. H., 1983, *The Ecological Implications of Body Size*, Cambridge University Press, Cambridge, UK.
- [21] Calder, W. A., III, 1984, *Size, Function, and Life History*, Harvard University Press, Cambridge, MA.
- [22] Vogel, S., 1988, *Life's Devices*, Princeton University Press, Princeton, NJ.
- [23] Kraus, A. D., and Bar-Cohen, A., 1995, *Design and Analysis of Heat Sinks*, John Wiley and Sons, New York.
- [24] Bejan, A., 1995, *Convection Heat Transfer*, 2nd Ed., John Wiley and Sons, New York.
- [25] Kim, S. J., and Lee, S. W., eds., 1996, *Air Cooling Technology for Electronic Equipment*, CRC Press, Boca Raton, FL.
- [26] Sathe, S., and Sammakia, B., 1998, "A Review of Recent Developments in Some Practical Aspects of Air-Cooled Electronic Packages," *ASME J. Heat Transfer*, **120**, pp. 830–839.
- [27] Bejan, A., 1984, *Convection Heat Transfer*, John Wiley and Sons, New York, Chapter 4, Problem 11, p. 157.
- [28] Bar-Cohen, A., and Rohsenow, W. M., 1984, "Thermally Optimum Spacing of Vertical, Natural Convection Cooled, Parallel Plates," *ASME J. Heat Transfer*, **106**, pp. 116–123.
- [29] Anand, N. K., Kim, S. H., and Fletcher, L. S., 1992, "The Effect of Plate Spacing on Free Convection between Heated Parallel Plates," *ASME J. Heat Transfer*, **114**, pp. 515–518.
- [30] Bejan, A., Fowler, A. J., and Stanescu, G., 1995, "The Optimal Spacing Between Horizontal Cylinders in a Fixed Volume Cooled by Natural Convection," *Int. J. Heat Mass Transf.*, **38**, pp. 2047–2055.
- [31] Fisher, T. S., and Torrance, K. E., 1998, "Free Convection Limits for Pin-Fin Cooling," *ASME J. Heat Transfer*, **120**, pp. 633–640.
- [32] Ledezma, G. A., and Bejan, A., 1997, "Optimal Geometric Arrangement of Staggered Vertical Plates in Natural Convection," *ASME J. Heat Transfer*, **119**, pp. 700–708.
- [33] Bejan, A., and Sciubba, E., 1992, "The Optimal Spacing for Parallel Plates Cooled by Forced Convection," *Int. J. Heat Mass Transf.*, **35**, pp. 3259–3264.
- [34] Petrescu, S., 1994, "Comments on the Optimal Spacing of Parallel Plates Cooled by Forced Convection," *Int. J. Heat Mass Transf.*, **37**, pp. 1283.
- [35] Fowler, A. J., Ledezma, G. A., and Bejan, A., 1997, "Optimal Geometric

- Arrangement of Staggered Plates in Forced Convection," *Int. J. Heat Mass Transf.*, **40**, pp. 1795–1805.
- [36] Bejan, A., 1995, "The Optimal Spacings for Cylinders in Crossflow Forced Convection," *ASME J. Heat Transfer*, **117**, pp. 767–770.
- [37] Stanescu, G., Fowler, A. J., and Bejan, A., 1996, "The Optimal Spacing of Cylinders in Free-Stream Cross-Flow Forced Convection," *Int. J. Heat Mass Transf.*, **39**, pp. 311–317.
- [38] Ledezma, G. A., Morega, A. M., and Bejan, A., 1996, "Optimal Spacing Between Fins With Impinging Flow," *ASME J. Heat Transfer*, **118**, pp. 570–577.
- [39] Heinrich, B., 1981, "The Mechanism and Energetics of Honeybee Swarm Temperature Regulation," *J. Exp. Biol.*, **91**, pp. 25–55.
- [40] Basak, T., Rao, K. K., and Bejan, A., 1996, "A Model for Heat Transfer in a Honey Bee Swarm," *Chem. Eng. Sci.*, **51**, pp. 387–400.
- [41] Bejan, A., Ikegami, Y., and Ledezma, G. A., 1998, "Constructal Theory of Natural Crack Pattern Formation for Fastest Cooling," *Int. J. Heat Mass Transf.*, **41**, pp. 1945–1954.
- [42] Bejan, A., 1997, "Constructal-Theory Network of Conducting Paths for Cooling a Heat Generating Volume," *Int. J. Heat Mass Transf.*, **40**, pp. 799–816.
- [43] Ledezma, G., Bejan, A., and Errera, M. R., 1997, "Constructal Tree Networks for Heat Transfer," *J. Appl. Phys.*, **82**, pp. 89–100.
- [44] Rodriguez-Iturbe, I., and Rinaldo, A., 1997, *Fractal River Basins*, Cambridge University Press, Cambridge, UK.
- [45] Meakin, P., 1998, *Fractals, Scaling and Growth Far From Equilibrium*, Cambridge University Press, Cambridge, UK.
- [46] Cohn, D. L., 1954, "Optimal Systems: I. The Vascular System," *Bull. Math. Biophys.*, **16**, pp. 59–74.
- [47] Thompson, D'A., 1942, *On Growth and Form*, Cambridge University Press, Cambridge, UK.
- [48] Mandelbrot, B. B., 1982, *The Fractal Geometry of Nature*, Freeman, New York.
- [49] Almgöbel, M., and Bejan, A., 1999, "Conduction Trees With Spacings at the Tips," *Int. J. Heat Mass Transf.*, **42**, pp. 3739–3756.
- [50] Dan, N., and Bejan, A., 1998, "Constructal Tree Networks for the Time-Dependent Discharge of a Finite-Size Volume to One Point," *J. Appl. Phys.*, **84**, pp. 3042–3050.
- [51] Neagu, M., and Bejan, A., 1999, "Constructal-Theory Tree Networks of 'Constant' Thermal Resistance," *J. Appl. Phys.*, **86**, pp. 1136–1144.
- [52] Neagu, M., and Bejan, A., 1999, "Three-Dimensional Tree Constructs of 'Constant' Thermal Resistance," *J. Appl. Phys.*, **86**, pp. 7107–7115.
- [53] Nelson, R. A., and Bejan, A., 1998, "Constructal Optimization of Internal Flow Geometry in Convection," *ASME J. Heat Transfer*, **120**, pp. 357–364.
- [54] Malkus, W. V. R., 1954, "The Heat Transport and Spectrum of Thermal Turbulence," *Proc. R. Soc. London, Ser. A*, **225**, pp. 196–212.
- [55] Glansdorff, P., and Prigogine, L., 1971, *Thermodynamic Theory of Structure, Stability and Fluctuations*, John Wiley and Sons, London.
- [56] Avnir, D., Biham, O., Lidar, D., and Malcai, O., 1998, "Is the Geometry of Nature Fractal?," *Science*, **279**, pp. 39–40.
- [57] Bejan, A., and Tondeur, D., 1998, "Equipartition, Optimal Allocation, and the Constructal Approach to Predicting Organization in Nature," *Rev. Gen. Therm.*, **37**, pp. 165–180.
- [58] Nottale, L., 1993, *Fractal Space-Time and Microphysics*, World Scientific, Singapore.
- [59] Errera, M. R., and Bejan, A., 1998, "Deterministic Tree Networks for River Drainage Basins," *Fractals*, **6**, pp. 245–261.
- [60] Bejan, A., and Errera, M. R., 2000, "Convective Trees of Fluid Channels for Volumetric Cooling," *Int. J. Heat Mass Transf.*, **43**, pp. 3105–3118.
- [61] Hamburg, W. R., 1986, "Optimal Finned Heat Sinks," WRL Research Report 86/4, Digital, Western Research Laboratory, Palo Alto, CA.
- [62] Kraus, A. D., 1999, "Developments in the Analysis of Finned Arrays," *Int. J. Transp. Phenom.*, **1**, pp. 141–164.
- [63] Gardner, K. A., 1945, "Efficiency of Extended Surfaces," *Trans. ASME*, **67**, pp. 621–631.
- [64] Bejan, A., and Dan, N., 1999, "Constructal Trees of Convective Fins," *ASME J. Heat Transfer*, **121**, pp. 675–682.
- [65] Bejan, A., and Almgöbel, M., 2000, "Constructal T-Shaped Fins," *Int. J. Heat Mass Transf.*, **43**, pp. 2101–2115.
- [66] Alebrahim, A., and Bejan, A., 1999, "Constructal Trees of Circular Fins for Conductive and Convective Heat Transfer," *Int. J. Heat Mass Transf.*, **42**, pp. 3585–3597.
- [67] Lin, W. W., and Lee, D. J., 1997, "Diffusion-Convection Process in a Branching Fin," *Chem. Eng. Commun.*, **158**, pp. 59–70.
- [68] Lee, D. J., and Lin, W. W., 1995, "Second-Law Analysis on a Fractal-Like Fin Under Crossflow," *AIChE J.*, **41**, pp. 2314–2317.
- [69] Lin, W. W., and Lee, D. J., 1997, "Second-Law Analysis on a Pin-Fin Array Under Cross-Flow," *Int. J. Heat Mass Transf.*, **40**, pp. 1937–1945.
- [70] Bejan, A., 1997, "Constructal Tree Network for Fluid Flow Between a Finite-Size Volume and One Source or Sink," *Rev. Gen. Therm.*, **36**, pp. 592–604.
- [71] Bejan, A., and Errera, M. R., 1997, "Deterministic Tree Networks for Fluid Flow: Geometry for Minimal Flow Resistance between a Volume and One Point," *Fractals*, **5**, pp. 685–695.
- [72] Errera, M. R., and Bejan, A., 1999, "Tree Networks for Flows in Porous Media," *J. Porous Media*, **2**, pp. 1–18.
- [73] Weibel, E. R., 1963, *Morphometry of the Human Lung*, Academic Press, New York.
- [74] Nonnenmacher, T. F., Losa, G. A., and Weibel, E. R., eds., 1994, *Fractals in Biology and Medicine*, Birkhäuser Verlag, Basel, Switzerland.
- [75] MacDonald, N., 1983, *Trees and Networks in Biological Models*, Wiley, Chichester, UK.
- [76] Bloom, A. L., 1978, *Geomorphology*, Prentice-Hall, Englewood Cliffs, NJ.
- [77] Leopold, L. B., Wolman, M. G., and Miller, J. P., 1964, *Fluvial Processes in Geomorphology*, W. H. Freeman, San Francisco, CA.
- [78] Scheiddeger, A. E., 1970, *Theoretical Geomorphology*, 2nd Ed., Springer-Verlag, Berlin.
- [79] Chorley, R. J., Schumm, S. A., and Sugden, D. E., 1984, *Geomorphology*, Methuen, London.
- [80] Morisawa, M., 1985, *Rivers: Form and Process*, Longman, London.
- [81] Bejan, A., 2000, "The Tree of Convective Heat Streams: Its Thermal Insulation Function and the Predicted 3/4-Power Relation between Body Heat Loss and Body Size," *Int. J. Heat Mass Transf.*, **43**, to appear.
- [82] Weinbaum, S., and Jiji, L. M., 1985, "A New Simplified Bioheat Equation for the Effect of Blood Flow on Local Average Tissue Temperature," *ASME J. Biomech. Eng.*, **107**, pp. 131–139.
- [83] Huang, H. W., Chen, Z. P., and Roemer, R. B., 1996, "A Counter Current Vascular Network Model of Heat Transfer in Tissues," *ASME J. Biomech. Eng.*, **118**, pp. 120–129.
- [84] Bejan, A., 1979, "A General Variational Principle for Thermal Insulation System Design," *Int. J. Heat Mass Transf.*, **22**, pp. 219–228.
- [85] Bejan, A., 1997, "Theory of Organization in Nature: Pulsating Physiological Processes," *Int. J. Heat Mass Transf.*, **40**, pp. 2097–2104.
- [86] Hildebrandt, S., and Tromba, A., 1985, *Mathematics and Optimal Form*, Scientific American Books, New York.

Inverse Determination of Temperature-Dependent Thermal Conductivity Using Steady Surface Data on Arbitrary Objects

T. J. Martin

Mem. ASME,
Systems Engineer,
Turbine System & Optimization,
M/S 201-20,
Pratt & Whitney Aircraft Company,
400 Main Street,
East Hartford, CT 06108
e-mail: martinj@pweh.com

G. S. Dulikravich

Fellow ASME,
Professor,
Department of Mechanical and
Aerospace Engineering,
Box 19018,
The University of Texas at Arlington,
Arlington, TX 76019
e-mail: dulikra@mae.uta.edu

An inverse computational method has been developed for the nonintrusive and nondestructive evaluation of the temperature-dependence of thermal conductivity. The methodology is based on an inverse computational procedure that can be used in conjunction with an experiment. Given steady-state heat flux measurements or convection heat transfer coefficients on the surface of the specimen, in addition to a finite number of steady-state surface temperature measurements, the algorithm can predict the variation of thermal conductivity over the entire range of measured temperatures. Thus, this method requires only one temperature probe and one heat flux probe. The thermal conductivity dependence on temperature (k - T curve) can be completely arbitrary, although a priori knowledge of the general form of the k - T curve substantially improves the accuracy of the algorithm. The influence of errors of measured surface temperatures and heat fluxes on the predicted thermal conductivity has been evaluated. It was found that measurement errors of temperature up to five percent standard deviation were not magnified by this inverse procedure, while the effect of errors in measured heat fluxes were even lower. The method is applicable to two-dimensional and three-dimensional solids of arbitrary shape and size. [S0022-1481(00)01703-5]

Keywords: Conduction, Heat Transfer, Inverse, Nonintrusive Diagnostics, Properties

1 Introduction

The ASTM standard for the measurement of heat flux and thermal properties ([1]) mandates the use of a guarded-hot-plate apparatus. This apparatus limits the size and shape of the test specimen to a flat rectangular slab or a rod having circular cross section. Therefore, it cannot be considered to be a nondestructive experimental procedure. The test method may be operated only with one-dimensional heat flow and the specimen conductance is limited to less than $16 \text{ W m}^{-2} \text{ K}$. Errors in the measurements may be caused by deviations from the idealized assembly configuration, heat radiation, temperature gradients in the test specimen, specimen thickness, material inhomogeneity, and material phase change. Compliance with this experimental testing method requires the establishment of a steady-state condition.

These limitations exclude the measurement of thermal conductivity, k , under a variety of circumstances. For example, it may be impractical or even impossible to extract a properly sized and shaped laboratory test specimen out of the given object. In cryogenic materials, it is quite difficult to measure the variation of thermal conductivity particularly because the thermal conductivity versus temperature, $k(T)$, curve is very steep or has inflections in the range of low temperatures. Similarly, thermal conductivity and specific heat are extremely difficult to measure directly within the thin mushy region of a solidifying or melting medium.

It is therefore very desirable to develop a nondestructive evaluation (NDE) technique that can provide information about the temperature-dependence of thermal conductivity. Thermal tomography and inverse thermal design techniques using the boundary element method offer attractive possibilities for these types of problems. Iterative solution procedures with finite differencing or finite element methods are the most often used when solving in-

verse parameter identification problems ([2–5]). They are often classified as inverse heat conduction problems. Orlande and Ozisik [6] have noted that most work on parameter identification problems has involved the use of finite dimensional minimization techniques. That is, a finite number of interior temperature measurements are taken and the $k(T)$ curve is iteratively modified until the difference between the measured and computed temperatures is minimized in a least-squares fashion. This means that such numerical procedures require intrusive instrumentation.

Algorithms involving an adjoint form of the heat conduction equation have also been used to obtain fairly accurate predictions of thermal conductivities using temperature histories at a single measurement point ([7]). The approach of using unsteady temperature measurements means that there is no need for fairly expensive heat flux probes. On the other hand, the typical inverse methods for determination of $k(T)$ via utilization of the unsteady temperature measurements have not been demonstrated to work on arbitrarily shaped multidimensional objects ([8–11]) and for arbitrary $k(T)$ distributions ([11]).

In this work, we are presenting an inverse numerical procedure that differs substantially from the iterative approaches and from the formulations based on the unsteady temperature measurements. We start by assuming that measured values of steady heat fluxes (or convection heat transfer coefficients) are available everywhere on the surface of an arbitrarily shaped solid. Kirchhoff's transformation ([12]) is then used to convert the governing heat conduction equation into a linear boundary value problem that can be solved for the unknown Kirchhoff's heat functions on the boundary using the boundary element method. Given several boundary temperature measurements, these heat functions are then inverted using numerical differentiation ([13]) to obtain thermal conductivity at the points where the overspecified temperature measurements were taken.

The experimental part of this inverse method requires one thermocouple and one heat flux probe placed sequentially only on the surface of an arbitrarily shaped and sized specimen. Thus, this

Contributed by the Heat Transfer Division for publication in the JOURNAL OF HEAT TRANSFER. Manuscript received by the Heat Transfer Division, April 12, 1999; revision received, February 14, 2000. Associate Technical Editor: A. Majumdar.

method is nonintrusive and directly applicable to field testing since special test specimens do not need to be manufactured. This method could still use steady temperature measurements at isolated interior points if additional accuracy is desired ([14]).

Our inverse method addresses many of the limitations of the guarded-hot-plate experimental test method and offers the ability to overcome most of them. The method is inherently multidimensional and allows for multidirectional temperature gradients in the test specimen. The computer algorithm for the steady-state inverse determination of the temperature variation of thermal conductivity is noniterative (when steady-state boundary heat fluxes and temperatures are provided) and robust, requiring only several seconds on a personal computer.

It should be pointed out that this paper offers a method which is significantly more versatile than our original method ([15]). The present method does not require that experimentally measured surface temperatures must be in equal temperature intervals. The present method also allows that heat transfer coefficients can be used instead of heat flux boundary conditions. The new algorithm also accepts experimentally measured temperatures having same value, but measured at different boundary points.

2 Numerical Formulation

The governing equation for steady-state heat conduction in an isotropic medium with temperature-dependent thermal conductivity is an elliptic quasi-linear partial differential equation,

$$\nabla \cdot [k(T)\nabla T] = 0 \quad (1)$$

This equation can be linearized by the application of Kirchhoff's transformation where the temperature variable, T , can be transformed uniquely to the heat function, $u(T)$,

$$u = \int_0^T \frac{k(T)}{k_0} dT$$

$$\nabla u = \frac{k(T)}{k_0} \nabla T. \quad (2)$$

Kirchhoff's transform converts the governing steady-state heat conduction equation into Laplace's equation, $\nabla^2 u = 0$. Dirichlet boundary conditions can also be transformed by applying Kirchhoff's transformation directly to the boundary temperatures. Neumann boundary conditions can easily be related to the heat flux, Q , in the direction, n , normal to the boundary.

$$Q = -k \frac{\partial T}{\partial n} = k_0 \frac{\partial u}{\partial n} \quad (3)$$

The specification of convective heat transfer coefficients on the boundaries falls into the category of a Robin-type boundary condition. It is a special case of the more general nonlinear heat flux boundary condition, where the heat flux is a function of temperature.

$$Q(T) = -k \frac{\partial T}{\partial n} = h(T - T_\infty) \quad (4)$$

Here, the boundary temperature is a function of the Kirchhoff function, $T = T(u)$. This condition does not pose any difficulties whenever the temperature is overspecified over the entire convective boundary. But, in general, an iterative solution procedure, such as the Newton-Raphson method, will be required. The Robin condition can be made linear by the use of the Jacobian, $\partial Q / \partial u$, of the Kirchhoff transformation.

$$\left(\frac{\partial u}{\partial n} \right)^n = \left(\frac{\partial u}{\partial n} \right)^{n-1} + \frac{1}{k_0} \left(\frac{\partial Q}{\partial u} \right)^{n-1} (u^n - u^{n-1}) \quad (5)$$

Since the thermal conductivity variation is unknown, the iteration must also include the inverse procedure, which will be explained in greater detail in the next section.

To summarize, in the case of Robin boundary conditions, an initial guess to the boundary values of temperature, T , leads to an initial thermal conductivity function, $k(T)$. Given this information, the Jacobian of the transformed nonlinear heat flux boundary condition, $\partial Q / \partial u$, allows for the solution of the field of Kirchhoff functions, $u(T)$.

The inverse procedure uses knowledge of the discrete boundary heat function values, u_i , at the same physical locations where the boundary temperature, T_i , were measured, in order to yield the unknown thermal conductivity curve, $k(T)$. In the case of Robin boundary conditions, this new $k(T)$ curve will produce a heat flux Jacobian that is, in general, different from the initial guess. Therefore, in the case of Robin boundary conditions the aforementioned procedure must be solved iteratively until the heat flux, $Q(T)$, converges to a user-specified tolerance. In most instances, the system of equations is only weakly nonlinear, and the initial thermal conductivity can be a guessed constant. The use of such an iterative procedure allows for the temperature-dependence of the convective heat transfer coefficient, $h(T)$, as well as for any arbitrary temperature-dependent heat flux boundary condition, such as heat radiation. The numerical implementation of this nonlinear methodology for well-posed problems does not produce any serious difficulties ([16]). The implementation of this procedure for the inverse determination of thermal conductivity has yet to be fully investigated.

2.1 Solution to the Direct Problem Using the Boundary Element Method. The boundary element method ([17]) is a powerful computational tool for solving linear and quasi-linear boundary value problems. Its effectiveness in solving inverse problems, such as ill-posed boundary conditions, unknown heat sources, or when temperature measurements are enforced at isolated interior points, has been demonstrated ([18,14]).

In this work, the boundary element method system for steady-state nonlinear heat conduction was written as a system of boundary integral equations ([19]), valid for arbitrary two and three-dimensional geometries. A well-posed (direct or analysis) problem was created when Neumann (or Robin) conditions were provided on all boundaries except for a single boundary point where Dirichlet condition was specified. Integral of all heat fluxes over the entire boundary had to amount to zero. The boundary of the test specimen was discretized with N_{BE} elements connected at their end points with N_{BN} boundary nodes. The variation of u and $\partial u / \partial n$ over each boundary element (line segment) was assumed to be linear. The integration over each boundary element was accomplished using Gaussian quadrature. In the case where a singularity existed at one of the end points of a boundary element, analytic integration was performed. This discretization procedure allowed the nodal quantities of u and $\partial u / \partial n$ to be factored into matrix form, $[\mathbf{H}]\{\mathbf{U}\} = [\mathbf{G}]\{\mathbf{Q}\}$. Thus, the $[\mathbf{H}]$ and $[\mathbf{G}]$ matrices are known because they are strictly dependent upon the Green's function and the geometry.

3 Inverse Method for Determining $k(T)$ Variation

When heat fluxes are known over the entire boundary via steady-state measurements taken on the entire surface of the object, the boundary element method can be used to solve for the transform of the Kirchhoff heat functions on the boundary.

$$[\mathbf{H}]\{\mathbf{U}\} = [\mathbf{G}]\{\mathbf{Q}\} = \{\mathbf{F}\} \quad (6)$$

The matrix $[\mathbf{G}]$ can be multiplied by the vector $\{\mathbf{Q}\}$ to form a vector of known quantities $\{\mathbf{F}\}$ so that the matrix $[\mathbf{H}]$ can be inverted to obtain the values of $\{\mathbf{U}\}$ at each boundary node. The matrix $[\mathbf{H}]$ appears to be well conditioned so that regularization methods are not required. A caution should be exercised since the level of ill-conditioning exhibited by the matrix $[\mathbf{H}]$ could be reduced artificially due to coarse discretization. Since the inversion is nonunique when only Neumann-type (heat flux) boundary conditions are provided everywhere on the boundary, the arbitrary

constant can be determined by specifying at least one Dirichlet boundary condition. Therefore, a modified Kirchhoff transform is required.

$$u = u_1 + \int_{T_1}^T \frac{k(T)}{k_0} dT \quad (7)$$

Here, k_0 is a reference conductivity value and T_1 is the minimum value of the measured boundary temperature. The minimum value of Kirchhoff function, u_{\min} , occurs at the minimum temperature, T_{\min} . Thus, $u_1 = T_1 = T_{\min}$ makes one Dirichlet boundary condition. Then, the boundary element method can be used to obtain the values of the heat function $\{U\}$ on the entire boundary except at the location of the minimum temperature reading. At this point, the normal derivative $q_1 = (\partial u / \partial n)_1$ will be computed since T_{\min} is specified there.

Now that the nodal boundary values of $\{U\}$ are known, the entire field of heat functions is known. At any interior point, the values of the Kirchhoff heat function can be obtained in a post-processing fashion. Since the boundary value problem is over-specified, a number of steady temperature measurements, taken either nonintrusively on the boundary, or intrusively, at isolated interior points, can be used to convert the heat functions, $u(T)$, into the corresponding values of thermal conductivity, $k(T)$, at the same physical locations where the measuring instruments were placed. Thus, knowing both vectors $\{U\}$ and $\{T\}$, the vector $\{K\}$ can be determined by performing numerical differentiation of $\{U\}$. A book by Hansen [13] represents an authoritative text on the general aspects of ill-conditioning and numerical differentiation. For the benefit of general engineering audience we will provide a detailed set of various numerical differentiation procedures that were tested with the objective of finding the most appropriate algorithm for the determination of $k(T)$.

In order to evaluate the sensitivity of the algorithm to errors in the measurement data, random errors based on the Gaussian probability density distribution were added intentionally to the temperature and heat flux measurements. A random number $0 < R < 1$ with a uniform distribution was generated using a standard utility subroutine. The desired variance σ^2 was specified and error was added to the analytic temperature data points, T_{analyt} .

$$T_n = T_{\text{analyt}} \pm \sqrt{-2\sigma^2 \ln R} \quad (8)$$

3.1 Trapezoid Rule for Inverting $u(T)$ Function. Given the value of the computed heat function and the measured temperature at the same point on the boundary, the thermal conductivity can be determined at that point via the inverse Kirchhoff's transform. The integral can be evaluated numerically using the trapezoid rule.

$$u_n = u_1 + \int_{T_1}^T \frac{k(T)}{k_0} dT = T_1 + \sum_{n=2}^N (T_n - T_{n-1}) \left(\frac{k_n + k_{n-1}}{2k_0} \right) \quad (9)$$

The values of temperature, T_n , are known at a finite number of boundary locations. At these points, the values of the computed heat function, u_n , are also known. Therefore, the values of thermal conductivity, k_n , at these points can be determined using the Kirchhoff's transformation. The inverse of the Kirchhoff's transformation can be expressed as a system of algebraic equations represented in the following matrix form:

$$[C]\{K/k_0\} = \{U - T_{\min}\} \quad (10)$$

where the elements of the lower-triangular matrix, $[C]$, have been determined as follows:

$$C_{i1} = \frac{T_2 - T_1}{2} \quad \text{when } j=1 \quad (11a)$$

$$C_{ii} = \frac{T_j - T_{j-1}}{2} \quad \text{when } i=j \quad (11b)$$

$$C_{ij} = \frac{T_{j+1} - T_{j-1}}{2} \quad \text{when } j < i_{\max}. \quad (11c)$$

By inverting the $[C]$ matrix, the values of the thermal conductivity can be obtained at the same locations where the temperature measurements were taken. The values of the temperature must be sorted in ascending order $\{T_1, T_2, \dots, T_N\}$ and identical temperature readings must be discarded. This system represents $N-1$ equations for N unknowns. The additional equation arises from the knowledge of the conductivity at the minimum temperature point. At this point both the heat flux, $Q|_{T_{\min}}$, and the normal derivative of the heat function, $k_0(\partial u / \partial n)|_{u_{\min}} = k(\partial T / \partial n)|_{T_{\min}}$ are known from the boundary element method solution.

The trapezoid rule provided good results, but the predicted values of the thermal conductivity were often oscillatory. Simpson's rule was attempted to remove this oscillatory behavior and it was successful at doing this, but the $k(T)$ curve that it predicted was often incorrect at the endpoints of the measured temperature range. Instead, very good results were obtained by simply averaging the results predicted by the trapezoid rule.

Regularization was required to properly invert the $[C]$ matrix whenever random error was introduced into the temperature measurements. Tikhonov's regularization ([20]) is a single-parameter minimization where the solution vector $\{K/k_0\}$ minimizes the weighted sum of the norm of the error vector. A minimum error norm was found by differentiating Eq. (10) with respect to each component of the unknown vector $\{K/k_0\}$ and setting the result equal to zero. Substituting the singular value decomposition where $[C] = [E][W][D]$ ([21-22]) and solving for the unknown vector $\{K\}$ resulted in

$$\frac{1}{k_0} \{K\} = [E]([W]^T[W] + \lambda[I])^{-1}[W]^T[D](1 - T_{\min})\{U\} \quad (12)$$

where $[I]$ is the identity matrix. Tikhonov's regularization is a generalization of least-squares truncation, but instead of simply eliminating terms associated with small singular values, they are weighted by a factor $(1 + \lambda/w^2)$, where w are the eigenvalues of matrix $[C]$. Larger regularization parameters, λ , had the effect of increased smoothing of the $k(T)$ curve without adding error into the solution of the heat conduction equation ([18]).

A similar regularization procedure ([23,13]) provided even greater smoothing of the predicted $k(T)$ function with the addition of a smoothing matrix $[S]$.

$$\frac{1}{k_0} \{K\} = [[C]^T[C] + \gamma[S]]^{-1}[C]^T(1 - T_{\min})\{U\} \quad (13)$$

The smoothing parameter, γ , was increased with the increased amount of error in the temperature and/or heat flux boundary conditions. The optimal magnitude of γ was proportional to the square of the error in temperature.

3.2 Finite Differentiation for Inverting $u(T)$ Function.

As an alternative method, the nodal quantities of $\{U\}$ and $\{T\}$ were easily converted into values of thermal conductivity $\{K\}$ using finite difference formulas. Second and third-order accurate finite difference formulas for thermal conductivity, $k_{i,2}$ and $k_{i,3}$, respectively, were used with irregular temperature intervals. Thus,

$$k_{i,2} = \frac{\delta_{u1}}{\delta T_1} \quad (14)$$

$$k_{i,3} = \frac{\delta_{u1} \delta_{T_2}^2 - \delta_{u2} \delta_{T_1}^2}{\delta T_2 \delta T_3} \quad (15)$$

where

$$\delta_{u1} = u_{i+1}(T_i - T_{i-1})^2 - u_i[(T_i - T_{i-1})^2 - (T_{i+1} - T_i)^2] - u_{i-1}(T_{i+1} - T_i)^2 \quad (16a)$$

$$\delta_{u2} = u_{i+2}(T_i - T_{i-2})^2 - u_i[(T_i - T_{i-2})^2 - (T_{i+2} - T_i)^2] - u_{i-1}(T_{i+2} - T_i)^2 \quad (16b)$$

$$\delta_{T1} = (T_{i+1} - T_i)(T_i - T_{i-1})(T_{i+1} - T_{i-1}) \quad (16c)$$

$$\delta_{T2} = \delta_{T1}(T_{i+2} - T_i)(T_i - T_{i-2})(T_{i+2} - T_{i-2}) \quad (16d)$$

$$\delta_{T3} = [(T_{i+2} - T_i)(T_i - T_{i-2}) - (T_{i+1} - T_i)(T_i - T_{i-1})] \quad (16e)$$

$$\delta_{T1}^2 = (T_{i+1} - T_i)^2(T_i - T_{i-1})^2(T_{i+1} - T_{i-1}) \quad (16f)$$

$$\delta_{T2}^2 = (T_{i+2} - T_i)^2(T_i - T_{i-2})^2(T_{i+2} - T_{i-2}) \quad (16g)$$

Here, $k_{i,2}$ and $k_{i,3}$ are the thermal conductivities obtained at the i th boundary node with the second and third-order differencing formulas, respectively. These finite difference formulas gave satisfactory results for $k(T)$ whenever the errors in the temperature measurements were small. The use of finite differencing method required the discarding of temperature readings that were within the error bounds of the temperature readings.

3.3 Linear Least Squares for Inverting $u(T)$ Function.

In an effort to improve the inverse procedure, as well as to utilize an a priori knowledge about the general shape of thermal conductivity function, $k(T)$, a general linear least-squares algorithm ([21,22]) was employed. The objective of this approach was to fit the set of N data points $[T_n, u_n]$ to a selected mathematical model. The general linear least-squares model used a linear combination of M basis functions.

$$u(T) = \sum_{m=1}^M c_m P_m(T) \quad (17)$$

where $P_1(T), P_2(T), \dots, P_M(T)$ are arbitrary fixed nonlinear functions of temperature, called the basis functions. The merit function, called chi-squared, χ^2 , is a measure of how well the models fit the data. It assumes that the measurement errors are supplied as standard deviations, σ_n , of the temperature. Then,

$$\chi^2 = \sum_{n=1}^N \left[\frac{u_i - \sum_{m=1}^M c_m P_m(T_n)}{\sigma_n} \right]^2 \quad (18)$$

The minimum of this function occurs where the derivative of χ^2 with respect to all M basis function coefficients, c_m , vanishes. The resulting system of equations was cast into the following covariance matrix formulation:

$$\left[\sum_{n=1}^N \frac{P_i(T_n)P_j(T_n)}{\sigma_n^2} \right] \{c_j\} = \left\{ \sum_{n=1}^N \frac{u_n P_i(T_n)}{\sigma_n^2} \right\} \quad (19)$$

Here, $\{c\}$ is the vector of unknown basis function coefficients. The inversion of the covariance matrix with Gaussian elimination or the SVD algorithm ([21,22]) yielded the basis function coefficients. Knowing these coefficients, the basis functions were differentiated with respect to temperature in order to obtain the values of thermal conductivity, k_n , at the N data points.

The challenge here was to select an appropriate set of the basis functions that best modeled the integral of the thermal conductivity function. In this paper, several basis functions were attempted; standard polynomials, Chebyshev polynomials, and third-order beta-splines ([24]), in addition to nonarbitrary basis functions in which a priori knowledge of the $k(T)$ curve was assumed. In the latter case, for example, arctangent integral basis functions were used to estimate a step-like $k(T)$ variation. These basis functions were integrated either analytically or numerically. We also tried

using Fourier sine and cosine series basis functions, but the results were less than satisfactory, with large oscillations increasing with increasing input error.

3.3.1 Polynomial Basis Functions. The thermal conductivity was represented by a standard series of polynomial basis functions.

$$k(T) = c_1 + c_2 T + c_3 T^2 + \dots + c_M T^{M-1} \quad (20)$$

The Kirchhoff function, $u(T)$, was obtained by analytical indefinite integration of these polynomials with respect to temperature, thereby yielding an additional basis function coefficient, c_0 . The general linear least-squares algorithm then determined the unknown coefficients, c_0, c_1, \dots, c_M .

3.3.2 Chebyshev Basis Functions. The thermal conductivity variation was represented by the series of orthogonal Chebyshev functions,

$$k(T) = \sum_{m=0}^M c_m \cos(m \arccos(\theta)), \quad (21)$$

where the temperature was affected by a change of variable.

$$\theta = \frac{T - (T_{\min} + T_{\max})/2}{(T_{\max} - T_{\min})/2} \quad (22)$$

In order to use these functions to approximate the $u(T)$ data, the Chebyshev basis functions were integrated numerically. When the explicit polynomial expressions were used instead of the trigonometric functions, the basis functions were integrated analytically. The general linear least-squares algorithm then determined the coefficients of the integrated Chebyshev basis functions.

3.3.3 Beta-Spline Basis Functions. The Kirchhoff function was represented by a piecewise beta-spline of cubic polynomial segments, $b_k(s)$.

$$u(T) = \sum_{i=1}^{N_{\text{vert}}} \left[\sum_{k=-1}^3 b_k(\beta_1, \beta_2, s) V_{i+k} \right] \quad (23)$$

Each segment was regarded as a weighted average of its four local vertices, so that each segment was a function of the parameter $s(T)$ in a nondimensional curve-following coordinate system that varied from 0 at the beginning of the segment to 1 at the end of that segment.

$$s(T) = 1 + \frac{T - T_{\min}}{T_{\max} - T_{\min}} (N_{\text{vert}} - 1) - \text{int} \left\{ 1 + \frac{T - T_{\min}}{T_{\max} - T_{\min}} (N_{\text{vert}} - 1) \right\} \quad (24)$$

Here, the $\text{int}\{\}$ function also defines the truncated integer value of its argument. V_{i+k} are the control vertex coordinates and $b_k(\beta_1, \beta_2, s)$ are the basis functions. Given a temperature T , the local beta-spline was controlled by the $i-1$ to $i+2$ vertices, where the index i was determined from the above integer truncation. Each basis function was itself described as a cubic polynomial.

$$b_k(\beta_1, \beta_2, s) = \sum_{j=0}^3 c_{j,k}(\beta_1, \beta_2) s^j \quad (25)$$

The unknown constants $c_{j,k}(\beta_1, \beta_2)$ were fixed quantities, provided β_1 and β_2 were fixed. They were found by imposing the three connectivity boundary conditions on any two neighboring segments ([24]). The shape parameter β_1 is referred to as the bias parameter. It could produce clustering towards the end vertices. The second parameter, β_2 , is called the tension parameter, and it was always positive. For high values of β_2 , the curve is strongly pulled toward the control vertices and, in the limit as $\beta_2 \rightarrow \infty$, the

beta-spline is identical to the control polygon. The least-squares fitting algorithm ([22]) determined the beta-spline control vertices as basis function coefficients. The thermal conductivity function was then determined by numerically differentiating the piecewise spline with respect to the temperature.

In an alternative approach, the $k(T)$ curve was modeled with the beta-spline, while the Kirchhoff function, $u(T)$, was evaluated as the integral of it.

$$u(T) = \frac{1}{k_0} \int_0^T \sum_{i=1}^{N_{\text{vert}}} \left[\sum_{k=-1}^3 b_k(\beta_1, \beta_2, s) V_{i+k} \right] dT + c_0 \quad (26)$$

In both cases, the beta-spline curve was either numerically differentiated or numerically integrated. When using the differentiated beta-spline, the basis function coefficients influenced only a local portion of the $k(T)$ curve between the $i-1$ to $i+2$ control vertices. When the integrated beta-spline was used, each basis

function coefficient affected the $u(T)$ curve from the beginning of the curve ($T=T_{\text{min}}$) up to the local temperature, T .

4 Numerical Results

All of the above-mentioned methods have been programmed and tested on a simple two-dimensional specimen and an unconventionally shaped two-dimensional specimen. The general formulation of this inverse methodology is also applicable to arbitrary three-dimensional objects.

4.1 Results for a Rectangular Plate. Although the inverse boundary element method approach with the Kirchhoff's transform is directly applicable to arbitrary three-dimensional problems, for the sake of simplicity it will be demonstrated on a two-dimensional geometry. A rectangular plate test specimen 10-cm wide by 1-cm long was used. The opposite ends of the plate were

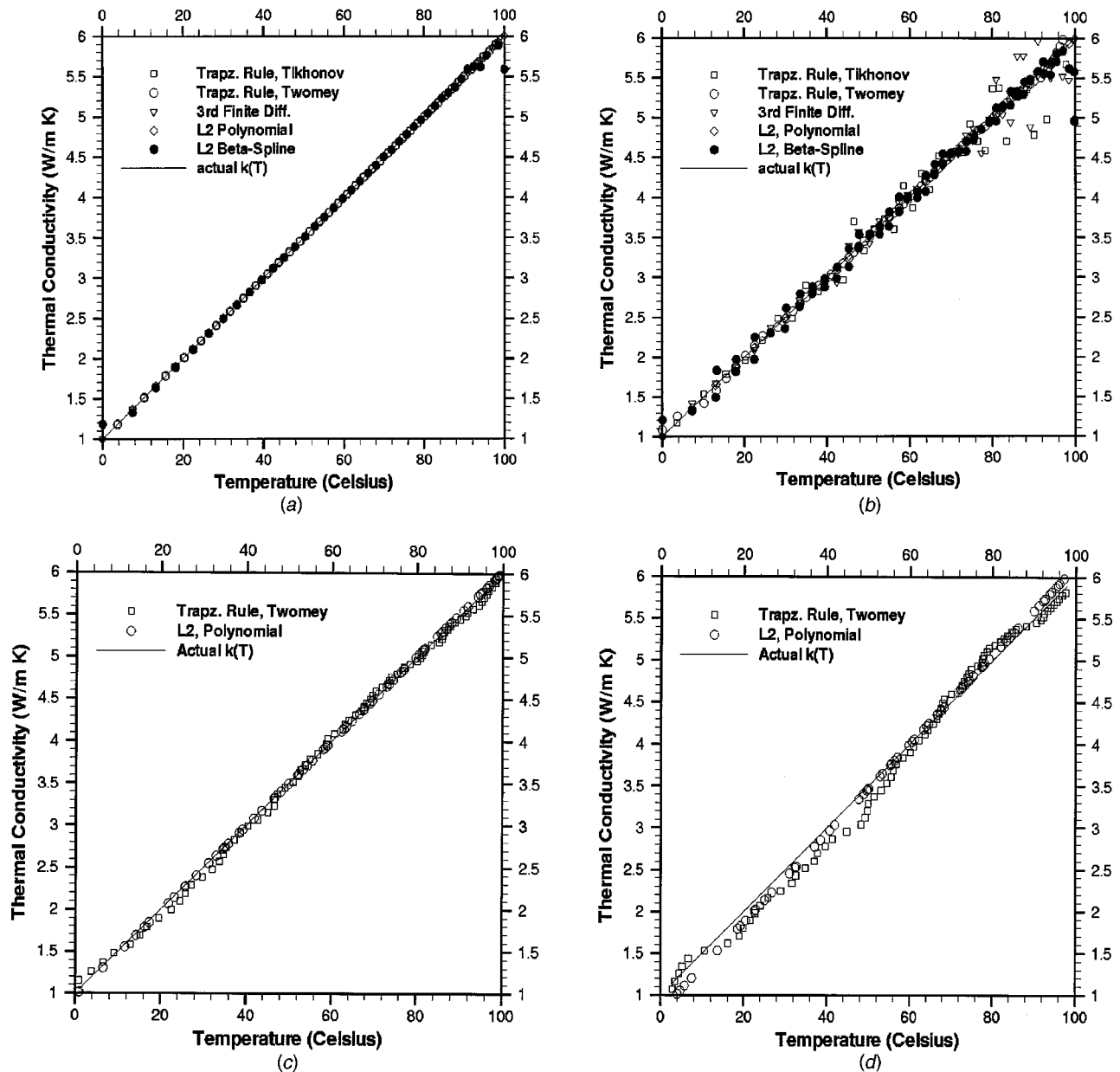


Fig. 1 Variation of the actual thermal conductivity versus temperature for various amounts of input error in temperature (a) $\sigma = 0.0^\circ\text{C}$, (b) $\sigma = 0.1^\circ\text{C}$, (c) $\sigma = 1.0^\circ\text{C}$, and (d) $\sigma = 5.0^\circ\text{C}$. The inverse boundary element method results are compared to the actual linear conductivity versus temperature function, where $\beta = 0.05^\circ\text{C}^{-1}$, $T_0 = 0.0^\circ\text{C}$, and $k_0 = 1.0 \text{ W m}^{-1}\text{ }^\circ\text{C}$.

kept at constant temperatures of 100.0°C and 0.0°C, respectively. The long side walls were considered to be adiabatic.

When the conductivity versus temperature was a linear function,

$$k(T) = k_0(1 + \beta(T - T_0)), \quad (27)$$

the temperatures and heat fluxes can be found from an analytic solution ([25]),

$$\frac{\beta}{2}T^2 + T = \left(T_{\text{hot}} + \frac{\beta}{2}T_{\text{hot}}^2\right) - \left(1 + \frac{\beta}{2}(T_{\text{hot}} + T_{\text{cold}})\right) \times \frac{(z_{\text{hot}} - z_{\text{cold}})}{(z_{\text{cold}} - z_{\text{hot}})}(T_{\text{hot}} - T_{\text{cold}}). \quad (28)$$

For the computational analysis, each of the long sides of the specimen was discretized with 40 equal-length linear isoparametric boundary elements. Only four such elements were used on each of the two short sides. In the case of an actual experimental evaluation of the surface heat fluxes this means that a single heat flux probe was applied at a total of 88 locations corresponding to the midpoints of the 88 boundary elements. The forward boundary element method solution compared very well with the analytic solution, averaging an error of less than 0.1 percent for a wide range of the parameter β ([14]).

4.1.1 Linear Variation of Thermal Conductivity. The actual variation of thermal conductivity versus temperature was linear between the values of $k(T=0^\circ\text{C})=1.0\text{ Wm}^{-1}\text{C}$ and $k(T=100.0^\circ\text{C})=6.0\text{ Wm}^{-1}\text{C}$. The top and bottom walls of the rectangular plate were specified to be adiabatic. The right and left end walls were specified with the heat flux taken from the analytic solution ($Q = \pm 35.0\text{ Wm}^{-2}$), except for the center of the right side at which a single temperature measurement was specified, T_{min} .

The boundary element method computed the Kirchhoff's heat functions at each of the boundary nodes. These heat functions were inverted into values of thermal conductivity at the nodes where the overspecified temperature measurements were provided. These temperatures existed at discrete locations along the adiabatic long sides of the specimen.

Figure 1 shows the predicted values of thermal conductivity versus temperature using various procedures for inverting the $u(T)$ function. Errors in the temperature measurements were simulated by adding standard deviations of 0.1°C up to 5.0°C (0.1 percent to 5.0 percent). All of the inverse methods had very good accuracy whenever the errors were less than 1.0 percent. For errors above 1.0 percent, only the Twomey regularization procedure and the linear least squares with polynomial basis functions were accurate enough. The beta-spline basis functions were not used on this example. The magnitude of the optimum Twomey regularization parameter, γ , was proportional to the square of the average temperature. The Chebyshev polynomial and beta-spline methods had problems at the endpoints due to their oscillatory nature. The linear least-squares with polynomial basis functions were the most accurate because the actual conductivity and Kirchhoff functions were represented by polynomials.

4.1.2 Errors in the Heat Flux Boundary Conditions. The inverse procedure was also evaluated given errors in the measured heat fluxes. The behavior of the inverse algorithm on the same rectangular test specimen with linear temperature-dependence of thermal conductivity was observed with intentionally introduced errors in the measured heat fluxes of 1.0 percent, 5.0 percent, and 10.0 percent. It is remarkable that the inverse algorithm is less sensitive to errors in the measured heat fluxes (Fig. 2) than in the measured temperatures. This was because heat fluxes were applied as boundary conditions to the boundary element method, and the Laplacian operator smoothed errors in these heat fluxes. On the other hand, errors in the measured temperatures directly affect the results of the inverse procedure.

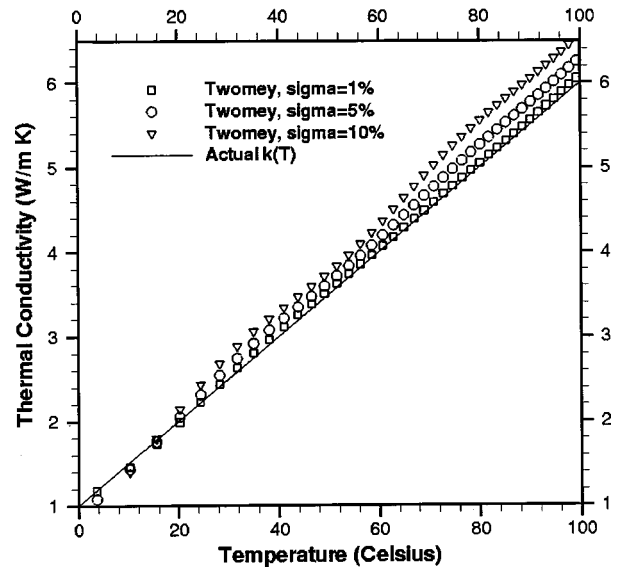


Fig. 2 Predicted temperature-dependence of thermal conductivity when errors were added to the heat fluxes compared to the actual linear variation of $k(T)$

It is noticeable that the predicted thermal conductivity values are somewhat biased towards the hot end of the test specimen (Fig. 2). This was most likely due to the fact that the only Dirichlet (temperature) boundary condition was specified on the cold end. This confirms our earlier observations ([18]) that the farthest point from the overspecified temperature boundary condition has the greatest amount of bias in the predicted temperature and, subsequently, thermal conductivity.

4.1.3 Steep Jump Variation of Thermal Conductivity. Next, the actual variation of thermal conductivity versus temperature was described by the arctangent function.

$$k(T) = \frac{1}{2}(1 - \xi)k_{\text{min}} + \frac{1}{2}(1 + \xi)k_{\text{max}}$$

$$\xi = \frac{k_{\text{max}} - k_{\text{min}}}{2\pi} \arctan\left(\alpha \frac{(T_{\text{max}} + T_{\text{min}})}{2}\right) \quad (29)$$

Here, α is a parameter that sets the slope of the jump in the $k-T$ curve. The top and bottom walls of the rectangular plate were specified to be adiabatic and the right and left walls were specified with the heat flux taken from the well-posed boundary element method solution ($Q = \pm 15.0\text{ Wm}^{-2}$). The boundary temperatures were taken from the well-posed boundary element method solution and prescribed to the inverse program with varying degrees of error ($\sigma = 0.0, 0.1^\circ\text{C}, 1.0^\circ\text{C},$ and 5.0°C). Figure 3 shows the computed $k-T$ curves when the Tikhonov, Twomey, and finite differencing inverse methods were used. Again with these methods, the results were good when the input temperature measurements have errors with a standard deviation of less than 0.5°C.

Figure 4 shows the results of the linear least-squares algorithm whenever polynomial, arctangent, and Chebyshev basis functions were used. Notice that the use of arctangent basis functions produced very accurate results, indicative of the advantage of having at least some a priori knowledge of the $k(T)$ function shape. The oscillatory behavior of the polynomial and Chebyshev basis functions is evident in these figures, but the general nature of the $k(T)$ curve was captured.

Beta splines were also used with the least squares in an attempt to reduce the severity of these oscillations. Figure 5 presents the results when using the beta-spline basis functions. Here, the beta-spline was used to approximate the $u(T)$ curve so that the thermal

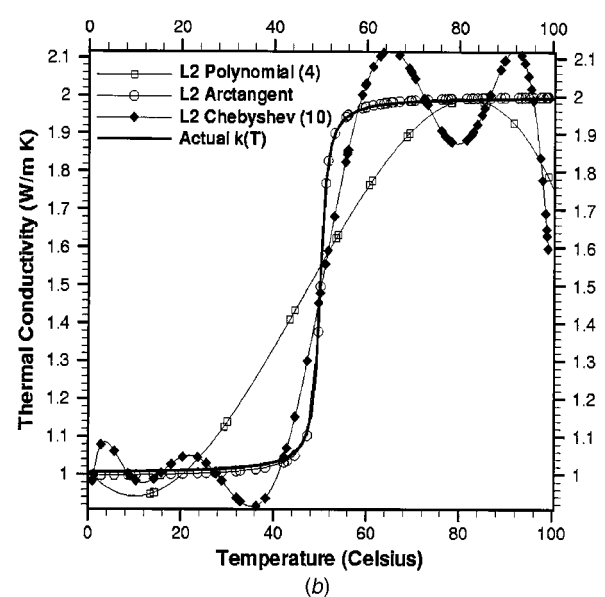
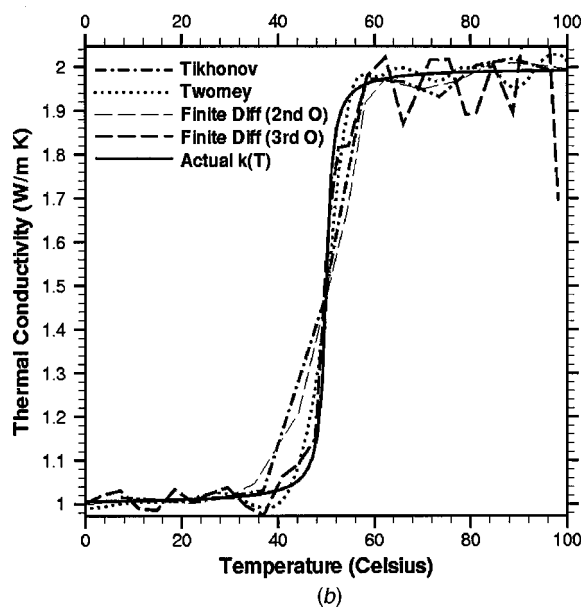
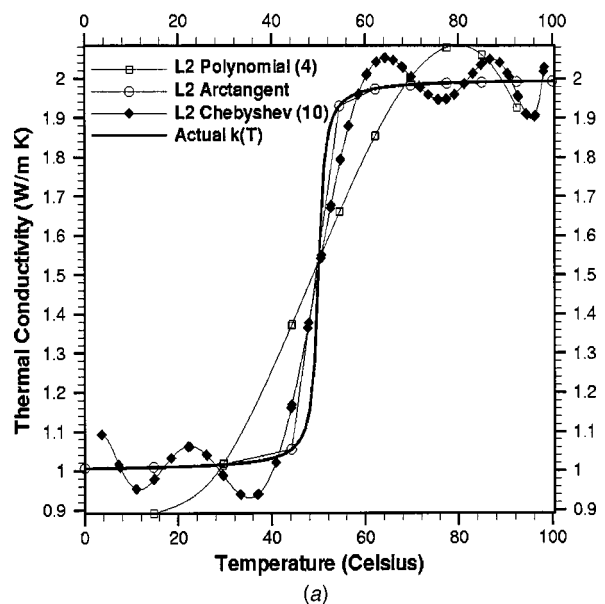
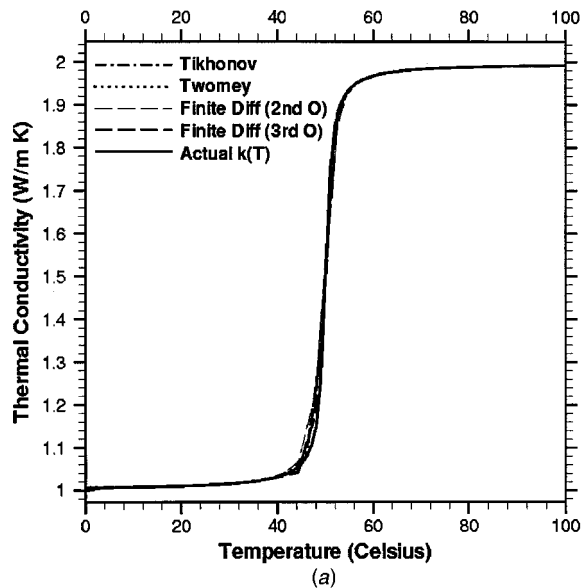


Fig. 3 Variation of the thermal conductivity versus temperature for various levels of input error in temperature, (a): $\sigma = 0.0^\circ\text{C}$, and (b): $\sigma = 0.5^\circ\text{C}$. The boundary element method results are compared to the actual arctangent conductivity versus temperature function when $\delta = 1.0^\circ\text{C}^{-1}$.

Fig. 4 Variation of the thermal conductivity versus temperature for various levels of input error in temperature, (a): $\sigma = 1.0^\circ\text{C}$, and (b): $\sigma = 5.0^\circ\text{C}$. The inverse boundary element method results are compared to the actual arctangent conductivity versus temperature function when $\delta = 1.0^\circ\text{C}^{-1}$.

conductivity was numerically differentiated. The oscillations were somewhat suppressed at low input errors, but they became worse with input errors above 1.0 percent. Although more beta-spline vertices produced more accurate representations of the $k(T)$ curve at low input error, the reduction in the number of beta-spline vertices was needed at higher input errors because the oscillatory behavior of the beta-splines needed to be reduced. Consequently, the number of beta-spline vertices had to be reduced from 48 with no input error, down to six vertices for the cases with 5.0 percent input error.

As an alternative, the option of fitting the integrated beta-spline slightly improved the results. This improvement was probably due to the fact that the coefficients of the integrated beta-spline had a more global impact on the least squares objective. Figure 6 demonstrates the ability of the inverse formulation to capture a steep jump in thermal conductivity with the integrated beta splines.

4.2 Inverse Determination of Thermal Conductivity of Copper at Low Temperatures.

Thermal Conductivity at Very Low Values at Very Low Temperatures. Thermal conductivity reaches very high values at very low temperatures because the lattice waves are harmonic and can be superimposed without mutual interference. There, the lattice thermal conductivity of crystals depends upon the grain size. As the temperature increases, the lattice vibrations become nonharmonic, scattering is increased, and the thermal conductivity decreases sharply. In metals, heat is predominantly transported by valence electrons rather than by the lattice vibrations, but the effect is the same. The electronic component of thermal conductivity is dependent upon the scale of the impurities rather than upon the crystal grain size and, in pure metals, is one to two orders of magnitude larger than the lattice conductivity. The thermal conductivity decreases sharply beyond 10.0 K primarily because electrons are scattered by thermal vibrations in the lattice.

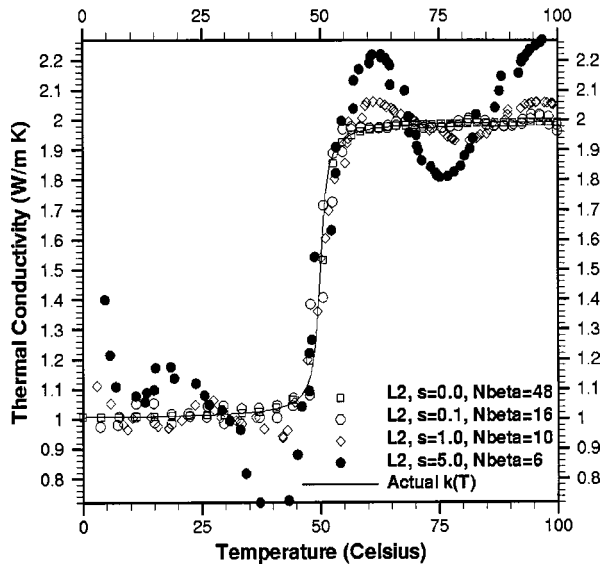


Fig. 5 Variation of thermal conductivity versus temperature predicted with the beta-spline basis functions. The inverse boundary element method results are compared to the actual arctangent conductivity versus temperature function when $\delta = 1.0^\circ\text{C}^{-1}$.

Our inverse boundary element method algorithm was attempted on a real material, copper, in the range of very low temperatures to see if the temperature-dependency of thermal conductivity can be determined where there are steep gradients in the $k(T)$ function. The actual temperature-dependency was taken from the *Journal of Physical and Chemical Reference Data* ([26]). The test specimen had the same geometry and grid specifications as in the previous examples.

When there was no error intentionally added to the temperature measurements, the results of the inverse procedure were very accurate for the methodologies used (Fig. 7(a)). The finite differencing and the least squares algorithm with beta-spline basis func-

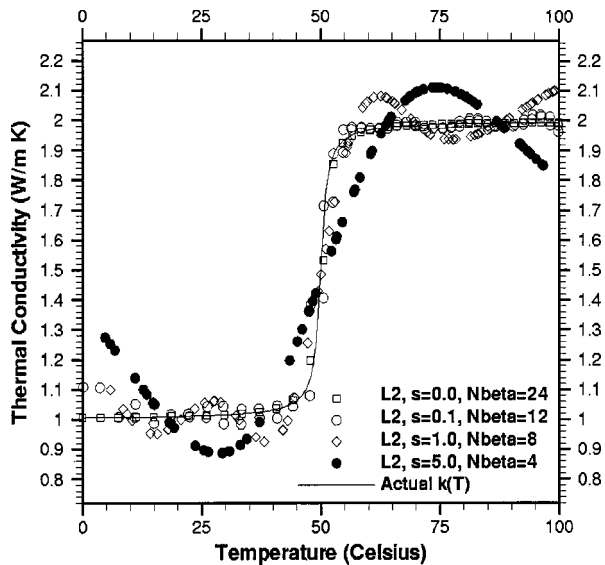


Fig. 6 Variation of thermal conductivity versus temperature predicted with the integrated beta-spline basis functions. The inverse boundary element method results are compared to the actual arctangent conductivity versus temperature function when $\delta = 1.0^\circ\text{C}^{-1}$.

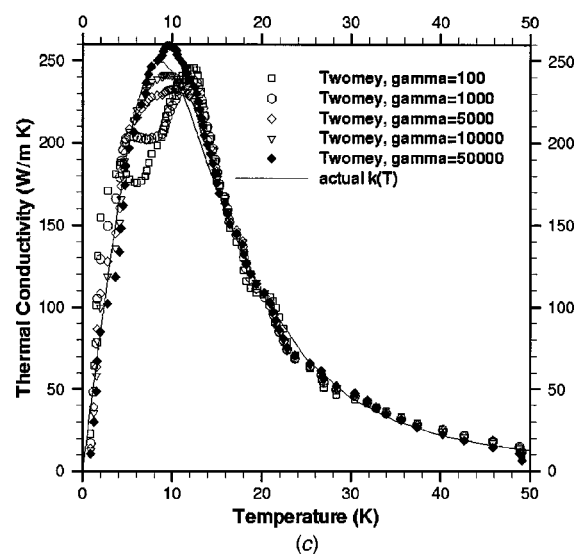
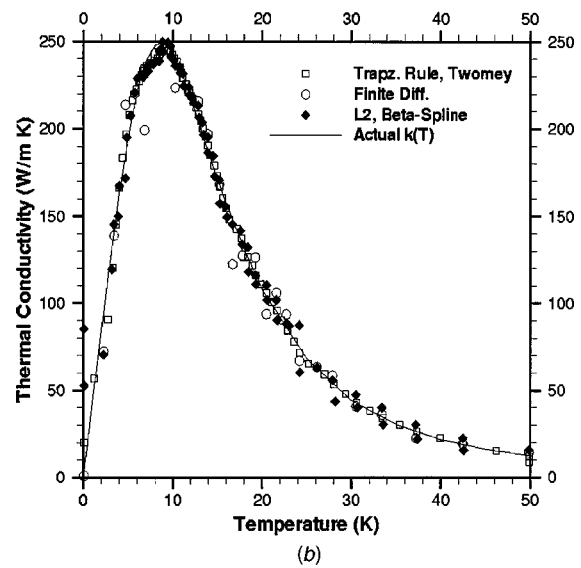
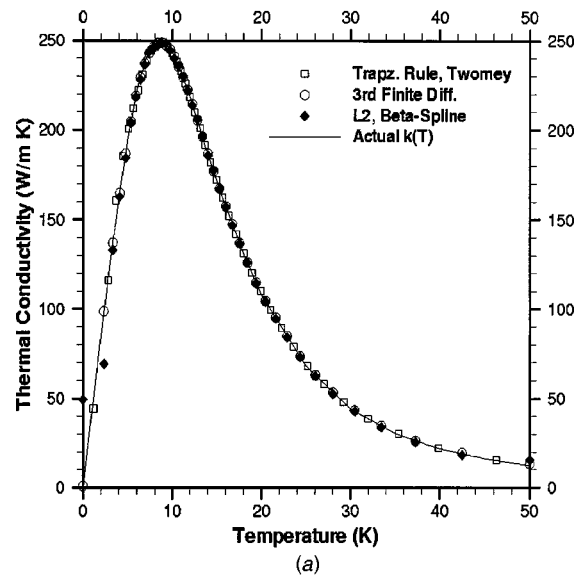


Fig. 7 Inverse determination of the thermal conductivity of copper in the cryogenic range. The best inverse results are shown with various levels of input error: (a) $\sigma = 0.0$ K, (b) $\sigma = 0.1$ K, and (c) $\sigma = 1.0$ K.

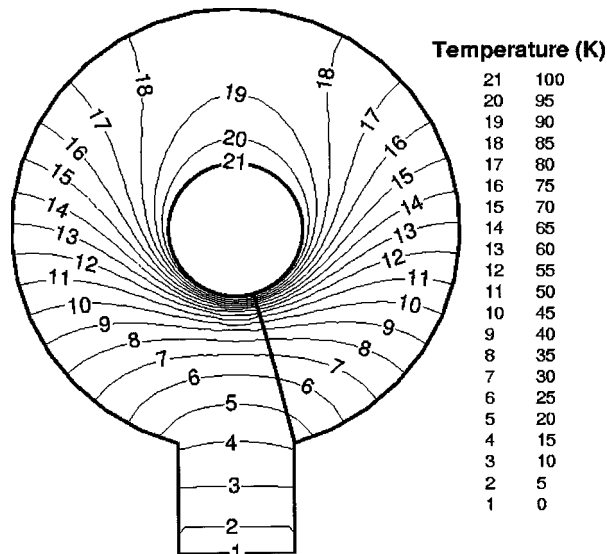


Fig. 8 Temperature contours predicted by nonlinear boundary element method within an arbitrarily shape specimen that was internally heated and made of copper (b)

tions had greater difficulty in capturing the curve once the errors were increased much beyond 0.1 K. The Twomey regularization procedure stayed effective beyond errors of 1.0 K. Figure 7(c) demonstrates that the accuracy of the solution is affected by the magnitude of the regularization parameter. The best result existed at very high values of γ , and also where the k - T curve was the smoothest, that is, where the integrated function, dk/dT , was at the first local minimum.

4.3 Applicability to Arbitrary Shapes. To demonstrate the applicability of the general inverse methodology to specimens of arbitrary shapes, we developed the geometry shown in Fig. 8. This object was assumed to be made of a homogenous material with an internally heated cylindrical core and an attachment (bottom surface) kept at a very cold temperature. The forward (direct) boundary element method heat conduction algorithm solved for the temperature field in the object such that the internal circular boundary was held at a constant temperature of 100.0 K and the bottom of the cold attachment was held at a constant temperature of 0.0 K. All other boundaries were assumed to be adiabatic. Figure 8 shows the predicted isotherms in the object made of copper.

Next, the material of the object was assumed to be unknown. The temperatures predicted on the outer (adiabatic) circular boundary by the forward boundary element method were applied as the overspecified boundary conditions for the inverse thermal conductivity problem. Only temperatures were assumed known on the inner circular boundary and the bottom of the attachment. Twomey smoothing was used to invert the coefficient matrix arising from the trapezoid rule. The β -spline was used as the alternative method with 16 vertices computed as the unknown coefficients of the least-squares method. The inversely predicted thermal conductivity variations with temperature are shown in Fig. 9. This figure shows results with and without intentionally introduced errors in the boundary temperature data. Notice that the inverse prediction of the $k(T)$ is very good over the entire range of measured temperatures for this doubly connected two-dimensional object.

5 Conclusions

An inverse computational procedure has been developed to predict the unknown temperature variation of thermal conductivity for arbitrarily shaped test specimens. The procedure is entirely nonintrusive and nondestructive, relying only upon boundary

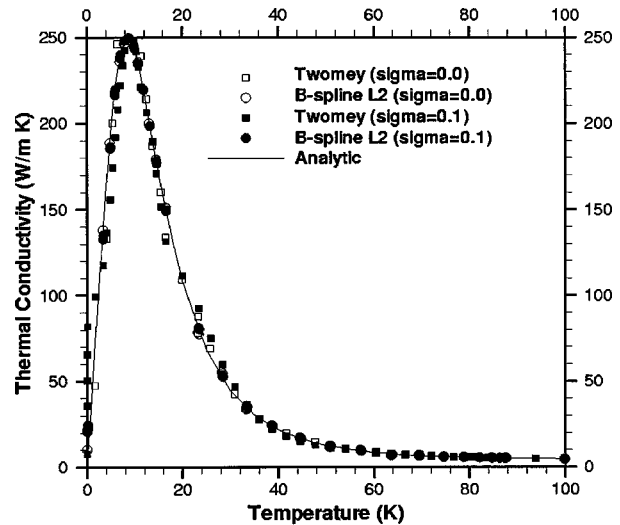


Fig. 9 Inverse prediction of thermal conductivity variation of an arbitrarily shaped specimen made of copper

measurements. It is fast and accurate, requiring the knowledge of overspecified steady-state temperature and heat flux or heat transfer coefficients over at least a portion of the boundary. The boundary element method was used to determine the field of the Kirchhoff transform function and its inversion yielded values of thermal conductivity at the locations and temperatures of the instrument readings. Several different inversion procedures were attempted, including regularization, finite differencing, and least-squares fitting with basis functions. The program was very accurate when the data was without error. For most of the inversion procedures it did not excessively amplify input temperature measurement errors when those errors were less than one to five percent standard deviation. The program was found to be less sensitive to measurement errors in heat fluxes than to errors in temperatures. The accuracy of the algorithm was greatly increased with the use of a priori knowledge about the thermal conductivity basis functions. One computational solution required only several seconds on a personal computer.

Acknowledgments

The authors are grateful for the NASA-Penn State Space Propulsion Engineering Center Graduate Student Fellowship facilitated by Prof. Charles Merkle, the National Science Foundation Grant DMI-9522854 monitored by Dr. George Hazelrigg, the NASA Lewis Research Center Grant NAG3-1995 facilitated by Dr. John Lytle and administered by Dr. Cestus Civinskas, and for ALCOA Foundation Faculty Fellowship administered by Dr. Yimin Ruan.

Nomenclature

- F = objective function
- $[G]$ = geometric coefficient matrix
- $[H]$ = geometric coefficient matrix
- h = thermal convection coefficient
- k = thermal conductivity
- Q = heat flux
- q = Kirchhoff's heat flux
- $\{Q\}$ = vector of Kirchhoff's heat fluxes
- R = random number
- T = temperature
- u = Kirchhoff's heat function
- $\{U\}$ = vector of Kirchhoff's heat functions
- z = coordinate

Greek Letters

- α = coefficient of steepness of k - T curve
 β = coefficient of non-linearity of k - T curve
 Γ = boundary or surface of an object
 γ = Twomey regularization parameter
 σ = standard deviation

Superscripts

- meas = measured or specified value
comp = computed or predicted value

Subscripts

- analyt = analytic
cold = cold boundary
hot = hot boundary
max = maximum value
min = minimum value
0 = reference value
1,2 = end points of an interval

References

- [1] Annual Book of Standards, 1997, Section 4, Vol. 04.06, *Thermal Insulation; Environmental Acoustics*, ASTM Designation: C 177-97.
- [2] Beck, J. V., Blackwell, B., and St. Clair, C. R., 1985, *Inverse Heat Conduction: Ill-Posed Problems*, John Wiley and Sons, New York.
- [3] Alifanov, O. M., 1994, *Inverse Heat Transfer Problems*, Springer-Verlag, Berlin.
- [4] Artyukhin, E. A., 1993, "Iterative Algorithms for Estimating Temperature-Dependent Thermophysical Characteristics," *Proceedings of Inverse Problems in Engineering, Theory and Practice*, N. Zabarar, et al., eds., ASME, New York, pp. 101–108.
- [5] Beck, J. V., and Arnold, K. J., 1997, *Parameter Estimation in Engineering and Science*, John Wiley and Sons, New York.
- [6] Orlande, H. R. B., and Ozisik, M. N., 1993, "Determination of the Reaction Function in a Reaction-Diffusion Parabolic Problem," *Inverse Problems in Engineering: Theory and Practice*, N. Zabarar et al., eds., ASME, New York, pp. 117–124.
- [7] Dantas, L. B., and Orlande, H. R. B., 1996, "A Function Estimation Approach for Determining Temperature-Dependent Thermophysical Properties," *Inverse Probl. Eng.*, **3**, No. 4, pp. 261–280.
- [8] Lam, T. T., and Yeung, W. K., 1995, "Inverse Determination of Thermal Conductivity for One-Dimensional Problems," *J. Thermophys. Heat Transfer*, **9**, No. 2, pp. 335–344.
- [9] Yang, C.-Y., 1997, "Non-Iterative Solution of Inverse Heat Conduction Problems in One Dimension," *Commun. Numer. Meth. Eng.*, **13**, pp. 419–427.
- [10] Huang, C.-H., Yan, J.-Y., and Chen, H.-T., 1995, "Function Estimation in Predicting Temperature-Dependent Thermal Conductivity Without Internal Measurements," *AIAA J. Thermophys. Heat Transf.*, **9**, No. 4, Oct.–Dec., pp. 667–673.
- [11] Sawaf, B., Ozisik, M. N., and Jarny, Y., 1995, "An Inverse Analysis to Estimate Linearly Temperature Dependent Thermal Conductivity Components and Heat Capacity of an Orthotropic Medium," *Int. J. Heat Mass Transf.*, **38**, No. 16, pp. 3005–3010.
- [12] Arpaci, V. S., 1966, *Conduction Heat Transfer*, Addison-Wesley, Reading, MA.
- [13] Hansen, P. C., 1997, *Rank-Deficient and Discrete Ill-Posed Problems: Numerical Aspects of Linear Inversion*, SIAM, Philadelphia, PA.
- [14] Dulikravich, G. S., and Martin, T. J., 1996, "Inverse Shape and Boundary Condition Problems and Optimization in Heat Conduction," *Advances in Numerical Heat Transfer*, W. J. Minkowycz and E. M. Sparrow, eds., Taylor & Francis, London, pp. 324–367.
- [15] Martin, T. J., and Dulikravich, G. S., 1997, "Non-Iterative Inverse Determination of Temperature-Dependent Heat Conductivities," *Symposium on Inverse Design Problems in Heat Transfer and Fluid Flow*, Vol. 2, G. S. Dulikravich, and K. A. Woodbury, eds., ASME, New York, pp. 141–150.
- [16] Banerjee, P. K., and Raveendra, S. T., 1981, *Boundary Element Methods in Engineering Science*, McGraw-Hill, London.
- [17] Brebbia, C. A., 1978, *The Boundary Element Method for Engineers*, John Wiley and Sons, New York.
- [18] Martin, T. J., and Dulikravich, G. S., 1996, "Inverse Determination of Boundary Conditions in Steady Heat Conduction with Heat Generation," *ASME J. Heat Transfer*, **118**, No. 3, pp. 546–554.
- [19] Brebbia, C. A., and Dominguez, J., 1989, *Boundary Elements: An Introductory Course*, McGraw-Hill, New York.
- [20] Tikhonov, A. N., and Arsenin, V. Y., 1977, *Solutions of Ill-Posed Problems*, V. H. Winston, Washington, DC.
- [21] Golub, G. H., and Van Loan, C. F., 1996, *Matrix Computations*, 3rd Ed., Johns Hopkins Press, Baltimore, MD.
- [22] Press, W. H., Teukolsky, S. A., Vetterling, W. T., and Flannery, B. P., 1986, *Numerical Recipes in FORTRAN, The Art of Scientific Computing*, 2nd Ed., Cambridge University Press, Cambridge, UK.
- [23] Twomey, S., 1963, "On the Numerical Solution of Fredholm Integral Equations of the First Kind by the Inversion of the Linear System Produced by Quadrature," *J. Assoc. Comput. Mach.*, **10**, No. 1, pp. 78–101.
- [24] Barsky, B. A., 1988, *Computer Graphics and Geometric Modeling Using Beta-Splines*, Springer-Verlag, Berlin.
- [25] Chapman, A. J., 1960, *Heat Transfer*, McMillan, New York.
- [26] Ho, C. Y., Powell, R. W., and Liley P. E., 1974, Thermal Conductivity of the Elements: A Comprehensive Review, *Journal of Physical and Chemical Reference Data*, Vol. 3, Supplement No. 1.

Inverse Convection Problem for Determining Wall Heat Flux in Annular Duct Flow

H.-Y. Li¹

e-mail: hyl@huafan.hfu.edu.tw

W.-M. Yan

Department of Mechanical Engineering,
Hua Fan University,
Shihtin, Taipei, Taiwan 22305, R.O.C.

An inverse problem for unsteady forced convection in an annular duct is presented. The simulated temperature data taken at the outer wall are used to estimate the time-dependent axially varying surface heat flux distribution at the inner wall of the annular passage. No prior information on the functional form of the unknown wall heat flux is needed in the inverse method. The effects of the functional form of the wall heat flux, the number of the measurement points, and the measurement errors on the accuracy of the estimation are investigated. It is shown that the reconstruction of the timewise and spatial variations of the wall heat flux is satisfactory even if the estimated function is not smooth. [S0022-1481(00)01003-3]

Keywords: Annular Flow, Forced Convection, Heat Transfer, Inverse, Laminar

Introduction

Inverse heat conduction problems concerned with the determination of the thermal boundary conditions, the initial condition, or the thermal properties of a heated body have been generally treated in the last few decades. The texts by Beck et al. [1] and Alifanov [2] give an excellent comprehensive review about inverse heat conduction problems. While inverse heat conduction problems are now well documented, inverse problems of heat convection have just begun to receive much attention. Raghunath [3], Bokar and Ozisik [4], and Liu and Ozisik [5] considered the inverse convection problem of determining the inlet temperature of a thermally developing hydrodynamically developed laminar flow between parallel plates from temperature measurements taken downstream of the entrance. Moutsoglou [6] investigated the steady-state inverse forced convection problem between parallel flat plates. He determined the boundary heat flux of the top wall from measured temperature data at the bottom wall by using the straight inversion and the whole domain regularization schemes. Huang and Ozisik [7] determined the spacewise variation of the wall heat flux for laminar flow through a parallel plate duct from temperature data taken inside the fluid at several different locations along the flow. Liu and Ozisik [8] estimated the timewise variation of the wall heat flux for transient turbulent forced convection inside parallel plate ducts from simulated transient temperature data. The unknown wall heat fluxes or inlet temperatures to be estimated are of one variable in these inverse convection problems. Convective heat transfer in annular flows is important in many engineering applications, including, among others, heat exchangers, nuclear reactors, and cooling of electronic systems. The inverse analysis provides an appropriate way to determine crucial parameters in these applications when direct measurements of the desired quantities, such as the inlet temperature or the wall heat flux, are not possible.

In the present study, the conjugate gradient method is adopted for the estimation of the inner wall heat flux for unsteady laminar forced convection in an annular duct from the temperature measurements taken at the outer wall. The unknown wall heat flux to be estimated is a function of time and space. No prior information is needed for the functional form of the wall heat flux in the inverse analysis.

Analysis

Direct Problem. The problem considered here is the laminar hydrodynamically developed flow inside an annular duct (see Fig. 1). As shown in the figure, two concentric tubes of circular cross section have inner radius r_i and outer radius r_o , respectively. Flow enters the annular passage with a uniform temperature T_e and fully developed velocity profile $u(r)$. Initially, the whole system is maintained at a uniform temperature T_e . At time $t > 0$, the inner wall is suddenly subjected to a heat flux $q(x, t)$, while the outer wall is kept thermally insulated. The heat exchange between the flow and wall starts to occur. In this study, the properties of the fluid are assumed to be constant. Besides, only high Peclet number flow is treated here so that the axial fluid conduction is negligibly small. It is intended to provide a first step toward future work, in which these effects will be considered. Then, by introducing the following dimensionless quantities

$$\begin{aligned} \xi &= \frac{x}{D_h \text{Pe}} & \eta &= \frac{r}{r_o} \\ \tau &= \frac{\alpha t}{D_h^2} & U &= \frac{u}{\bar{u}} \\ \theta &= \frac{k(T - T_e)}{D_h q_{\text{ref}}} & \lambda &= \frac{r_i}{r_o} \\ \text{Pe} &= \frac{\bar{u} D_h}{\alpha} & Q &= \frac{q}{2(1 - \lambda) q_{\text{ref}}} \\ D_h &= 2(r_o - r_i) & U &= \frac{2 \left[1 - \eta^2 - \left(\frac{1 - \lambda^2}{\ln \lambda} \right) \ln \eta \right]}{1 + \lambda^2 + \frac{1 - \lambda^2}{\ln \lambda}}, \end{aligned} \quad (1)$$

the governing equation in dimensionless form for the problem is given by

$$\frac{\partial \theta}{\partial \tau} + U \frac{\partial \theta}{\partial \xi} = 4(1 - \lambda)^2 \frac{1}{\eta} \frac{\partial}{\partial \eta} \left(\eta \frac{\partial \theta}{\partial \eta} \right) \quad (2a)$$

with the initial condition and the boundary conditions

$$\theta(\xi, \eta, 0) = 0 \quad (2b)$$

$$\theta(0, \eta, \tau) = 0 \quad (2c)$$

¹To whom correspondence should be addressed.

Contributed by the Heat Transfer Division for publication in the JOURNAL OF HEAT TRANSFER and presented at the 1999 National Heat Transfer Conference. Manuscript received by the Heat Transfer Division, May 17, 1999; revision received, February 29, 2000. Associate Technical Editor: D. Zumbrennen.

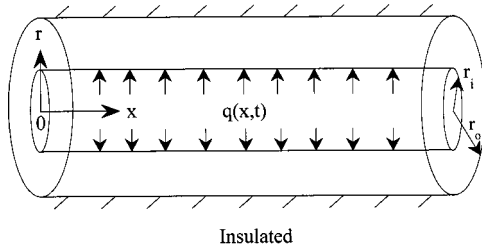


Fig. 1 Geometry and coordinates

$$\frac{\partial \theta(\xi, 1, \tau)}{\partial \eta} = 0 \quad (2d)$$

$$\frac{\partial \theta(\xi, \lambda, \tau)}{\partial \eta} = Q(\xi, \tau). \quad (2e)$$

The direct problem considered here is to determine the temperature distribution in the flow field, while the velocity distribution, the initial condition, and the boundary conditions are given. The problem defined by the foregoing equations is solved by the finite difference technique ([9]). The solution is marched in the time and the downstream directions. A fully implicit numerical scheme in which the unsteady energy storage term is approximated by the backward difference, the axial convection term by the upwind difference, and the radial diffusion term by the central difference is employed to transform Eqs. (2) into the finite difference equations. This system of equations is tridiagonal, which can be solved efficiently by the Thomas algorithm ([9]).

Inverse Problem. For the inverse problem, the temperature data at the outer wall are provided as an additional input, but the heat flux at the inner wall $Q(\xi, \tau)$ is unknown. The reconstruction of the wall heat flux from the knowledge of the measured temperature data can be obtained by minimizing the objective function

$$J = \sum_{i=1}^M \sum_{k=1}^N (\theta_{i,k} - Z_{i,k})^2 \quad (3)$$

where $\theta_{i,k} = \theta(\xi_i, 1, \tau_k)$ is the calculated temperature for an estimated $Q(\xi, \tau)$ and $Z_{i,k} = Z(\xi_i, 1, \tau_k)$ is the measured temperature taken at the outer wall. M and N are the numbers of the measured data in the ξ and τ -directions, respectively.

The iterative process based on the conjugate gradient method ([10]) is used to determine the unknown wall heat flux $Q(\xi, \tau)$

$$Q_{m,n}^{p+1} = Q_{m,n}^p - \beta^p d_{m,n}^p \quad (4)$$

where $Q_{m,n} = Q(\xi_m, \tau_n)$, β^p is the step size, $d_{m,n}^p$ is the direction of descent which is determined from

$$d_{m,n}^p = \left(\frac{\partial J}{\partial Q_{m,n}} \right)^p + \gamma^p d_{m,n}^{p-1} \quad (5)$$

and the conjugate coefficient γ^p is computed from

$$\gamma^p = \frac{\sum_{m=1}^M \sum_{n=1}^N \left[\left(\frac{\partial J}{\partial Q_{m,n}} \right)^p \right]^2}{\sum_{m=1}^M \sum_{n=1}^N \left[\left(\frac{\partial J}{\partial Q_{m,n}} \right)^{p-1} \right]^2} \quad \text{with } \gamma^0 = 0. \quad (6)$$

Here, $\partial J / \partial Q_{m,n}$ is the gradient of the objective function. It is determined by differentiating Eq. (3) with respect to $Q_{m,n}$ to obtain

$$\frac{\partial J}{\partial Q_{m,n}} = 2 \sum_{i=1}^M \sum_{k=1}^N (\theta_{i,k} - Z_{i,k}) \frac{\partial \theta_{i,k}}{\partial Q_{m,n}}. \quad (7)$$

The step size is determined from

$$\beta^p = \frac{\sum_{i=1}^M \sum_{k=1}^N (\theta_{i,k}^p - Z_{i,k}) \sum_{m=1}^M \sum_{n=1}^N \left(\frac{\partial \theta_{i,k}}{\partial Q_{m,n}} \right)^p d_{m,n}^p}{\sum_{i=1}^M \sum_{k=1}^N \left[\sum_{m=1}^M \sum_{n=1}^N \left(\frac{\partial \theta_{i,k}}{\partial Q_{m,n}} \right)^p d_{m,n}^p \right]^2} \quad (8)$$

where $\partial \theta_{i,k} / \partial Q_{m,n}$ is the sensitivity coefficient. To calculate the sensitivity coefficient, we differentiate the direct problem with respect to $Q_{m,n}$ to obtain the sensitivity problem, i.e.,

$$\frac{\partial}{\partial \tau} \left(\frac{\partial \theta}{\partial Q_{m,n}} \right) + U \frac{\partial}{\partial \xi} \left(\frac{\partial \theta}{\partial Q_{m,n}} \right) = 4(1-\lambda)^2 \frac{1}{\eta} \frac{\partial}{\partial \eta} \left(\eta \frac{\partial}{\partial \eta} \left(\frac{\partial \theta}{\partial Q_{m,n}} \right) \right) \quad (9a)$$

$$\frac{\partial \theta(\xi, \eta, 0)}{\partial Q_{m,n}} = 0 \quad (9b)$$

$$\frac{\partial \theta(0, \eta, \tau)}{\partial Q_{m,n}} = 0 \quad (9c)$$

$$\frac{\partial}{\partial \eta} \left(\frac{\partial \theta(\xi, 1, \tau)}{\partial Q_{m,n}} \right) = 0 \quad (9d)$$

$$\frac{\partial}{\partial \eta} \left(\frac{\partial \theta(\xi, \lambda, \tau)}{\partial Q_{m,n}} \right) = \hat{u}(\xi - \xi_m, \tau - \tau_n) \quad (9e)$$

for $m = 1, 2, \dots, M$, $n = 1, 2, \dots, N$, where

$$\hat{u}(\xi - \xi_m, \tau - \tau_n) = \begin{cases} 1 & \xi = \xi_m, \tau = \tau_n \\ 0 & \text{otherwise} \end{cases} \quad (9f)$$

The solution procedure for θ can be applied for $\partial \theta / \partial Q_{m,n}$, since the governing equation, initial condition, and boundary conditions for $\partial \theta / \partial Q_{m,n}$ are similar to those for θ .

If the problem contains no measurement errors, the condition

$$J(Q_{m,n}^p) < \delta \quad (10)$$

can be used for terminating the iterative process, where δ is a small specified positive number. However, the measured temperature data contain measurement errors. Following the computational experience, we use the discrepancy principle ([11])

$$J(Q_{m,n}^p) < MN\sigma^2 \quad (11)$$

as the stopping criterion, where σ is the standard deviation of the measurement errors.

The computational procedure for the inverse convection problem is summarized as follows:

- Step 1: Solve the sensitivity problem to calculate the sensitivity coefficient $\partial \theta_{i,k} / \partial Q_{m,n}$.
- Step 2: Pick an initial guess $Q_{m,n}^0$ and set $p = 0$.
- Step 3: Solve the direct problem to compute $\theta_{i,k}$.
- Step 4: Calculate the objective function. Terminate the iteration process if the specified stopping criterion is satisfied. Otherwise go to Step 5.
- Step 5: Knowing $\partial \theta_{i,k} / \partial Q_{m,n}$, $\theta_{i,k}$, and $Z_{i,k}$, compute the gradient of the objective function $\partial J / \partial Q_{m,n}$.
- Step 6: Knowing $\partial J / \partial Q_{m,n}$, compute γ^p and $d_{m,n}^p$.
- Step 7: Knowing $\partial \theta_{i,k} / \partial Q_{m,n}$, $\theta_{i,k}$, $Z_{i,k}$, and $d_{m,n}^p$, compute β^p .
- Step 8: Knowing β^p and $d_{m,n}^p$, compute $Q_{m,n}^{p+1}$. Set $p = p + 1$ and go to Step 3.

Results and Discussion

The accuracy of the inverse algorithm for the estimation of the inner wall heat flux is examined for four test examples by using simulated measured temperature data at the outer wall. The simu-

Table 1 Comparison of $\theta(1,1,\tau)$ for various grid arrangements

| τ | $\theta(1,1,\tau)$ | | |
|--------|--------------------------|--------------------------|--------------------------|
| | $21 \times 21 \times 21$ | $41 \times 41 \times 41$ | $81 \times 81 \times 81$ |
| 0.3 | 1.07889 | 0.97874 | 0.91824 |
| 0.5 | 2.63416 | 2.63966 | 2.65034 |
| 0.8 | 3.63838 | 3.74104 | 3.79660 |
| 1 | 2.67688 | 2.75278 | 2.78851 |

lated measured temperature data, Z , are generated by adding random errors to the exact temperature, θ , computed from the solution of the direct problem

$$Z = \theta + \sigma \zeta \quad (12)$$

where σ is the standard deviation of the measurement data, ζ is a random variable of normal distribution with zero mean and unit standard deviation. In the present study, the radius ratio λ is fixed to be 0.5. Equally spaced measurements are taken both in $0 \leq \xi \leq 1$ and $0 \leq \tau \leq 1$ for all the examples considered. The data are used as input to reconstruct the unknown wall heat flux in the inverse problem. We examine the effects of the functional form of the wall heat flux, the number of the measurement points, and the measurement errors on the accuracy of the estimation. Different grid arrangements are used to ensure that the solution of the direct problem is grid independent. The results obtained with various grid points for the wall heat flux of example 1 are given in Table 1. It is found that the deviations in $\theta(1, 1, \tau)$ calculated with grid $41 \times 41 \times 41$ and $81 \times 81 \times 81$ are always less than 6.6 percent. The $41 \times 41 \times 41$ grid points are used for the solution of the direct problem to illustrate the inverse methodology by considering numerical accuracy, computational time, and computer memory for the inverse analysis. To validate the prediction of the model, simulated measured temperature data are used as input for the estimation of the inner wall heat fluxes. Comparisons between the estimated and exact values of the inner wall heat fluxes are made in the paper. The estimation of the wall heat flux from the simulated measured temperature data with no measurement errors, i.e., $\sigma=0$ is examined first. As a result, the estimated solutions converge graphically to the exact values of the wall heat fluxes.

In the first example, the spatial and timewise variations of the unknown wall heat flux are considered to be sinusoidal functions

$$Q(\xi, \tau) = 10 \sin(\pi \xi) \sin(\pi \tau). \quad (13)$$

Figures 2 and 3 show the exact and estimated results of the inner wall heat flux at $\tau=0.2$, $\tau=0.5$, and $\tau=0.9$ for simulated experimental data containing errors of standard deviation $\sigma=0.01$ and

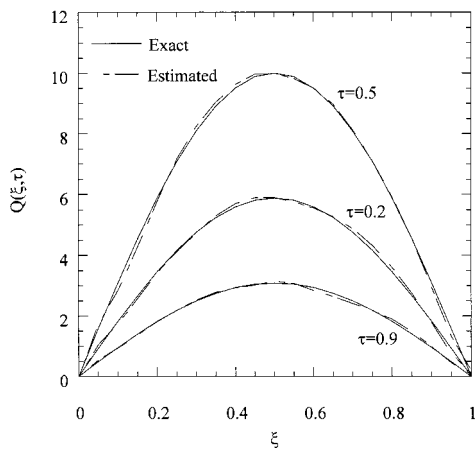


Fig. 2 The exact and estimated wall heat fluxes for $\sigma=0.01$, $M=41$, $N=41$

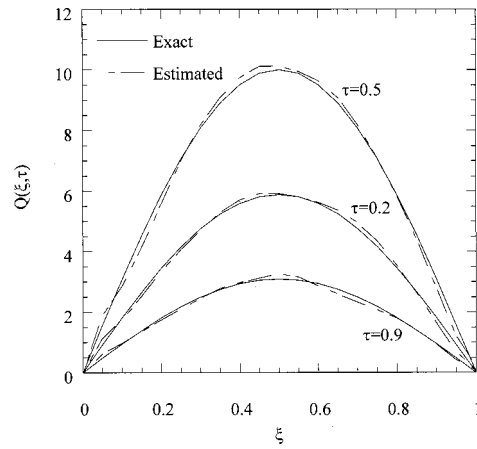


Fig. 3 The exact and estimated wall heat fluxes for $\sigma=0.02$, $M=41$, $N=41$

$\sigma=0.02$, respectively. The standard deviations of the measured data are taken to be 0.01 and 0.02, which correspond to 0.7 percent and 1.4 percent relative errors based on the maximum dimensionless measured temperature. Because the sinusoidal functions are smooth, the wall heat flux is well reconstructed from temperature measurements taken at the outer wall. It is noted that the accuracy of the estimation decreases as σ increases. In this paper, the inverse convection problem is solved in dimensionless form. To get some ideal of the corresponding dimensional variables, we consider air at $T_e=300$ K enters an annular duct of inner radius $r_i=0.01$ m, outer radius $r_o=0.02$ m, and length $L=3.6$ m. The mean velocity \bar{u} , the total experimental time t_f , and the reference heat flux q_{ref} are taken as 0.2 m/s, 18 s, and 100 W/m², respectively. If 41 measurement points are taken both in $0 \leq \xi \leq 1$ and $0 \leq \tau \leq 1$, it corresponds to a sensor spacing of $\Delta x=0.09$ m and a sampling rate of $\Delta t=0.45$ s. The actual temperature errors are $\pm 0.55^\circ\text{C}$ and $\pm 1.1^\circ\text{C}$ for $\sigma=0.01$ and $\sigma=0.02$, respectively. These values are larger than the typical value for thermocouple measurement error, i.e., $\pm 0.25^\circ\text{C}$. Figure 4 is intended to illustrate the effects of the numbers of the measurement points M and N on the accuracy of the estimation. In this case, M and N are both taken as 21. Comparing Fig. 4 with Fig. 2, it is noted that increasing the measurement points from 21×21 to 41×41 improves the accuracy significantly. The measurement errors trend to become more correlated as the sampling rate increases and the distance between the sensors decreases ([1]). Very high correlation between measurement data provides less information for the inverse

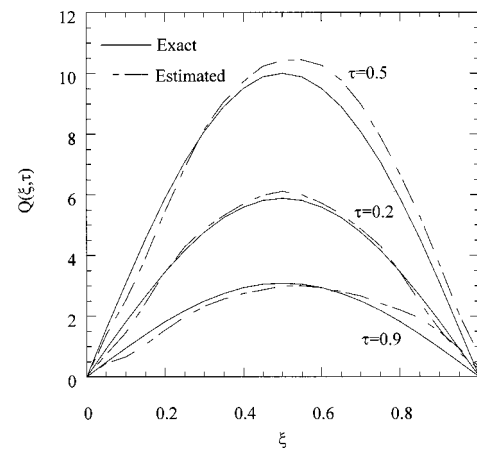


Fig. 4 The exact and estimated wall heat fluxes for $\sigma=0.01$, $M=21$, $N=21$

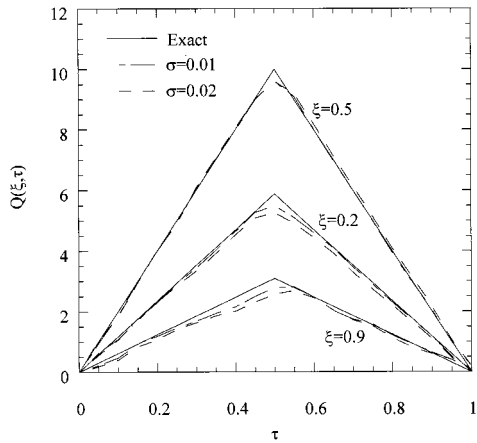


Fig. 5 The exact and estimated wall heat fluxes for $\sigma=0.01$ and $\sigma=0.02$, $M=41$, $N=41$

analysis. The computational time and memory also increase under such circumstances. As a result, 41×41 measurement points are used for all of the results presented in this paper except in Fig. 4.

In the second example, the wall heat flux with a triangular timewise variation and sinusoidal spatial variation is considered,

$$Q(\xi, \tau) = \begin{cases} 20\tau \sin(\pi\xi) & 0 \leq \tau \leq 0.5 \\ 20(1-\tau) \sin(\pi\xi) & 0.5 \leq \tau \leq 1 \end{cases} \quad (14)$$

The inverse solutions at $\xi=0.2$, $\xi=0.5$, and $\xi=0.9$ are shown in Fig. 5 from the measured temperature data. The agreement between the estimated and the exact values of the wall heat flux is satisfactory for both $\sigma=0.01$ and $\sigma=0.02$. The prediction of the wall heat flux is less accurate near $\tau=0.5$ because the wall heat flux is not smooth there. The inverse solutions when the measurements are taken inside the fluid are also examined. Figures 6 and 7 show the sensitivity coefficient $\partial\theta(\xi, \eta, \tau)/\partial Q_{2,2}$ at different sensor locations, i.e., $\eta=1$ and $\eta=0.5$, respectively. The magnitude of the sensitivity coefficient increases as the distance between the inner wall and the sensors decreases. As expected, it is shown that the accuracy of the estimation can be improved significantly when the sensors are located close to the inner wall. However, from the experimental point of view, it is desirable to avoid sensors within the fluid, which will disturb the flow field and introduce errors.

In the third example, the unknown wall heat flux is assumed to be a function with a sinusoidal timewise variation and triangular spatial variation

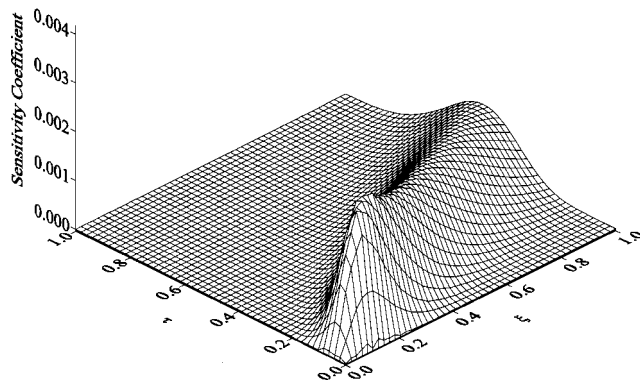


Fig. 6 The sensitivity coefficient $\partial\theta(\xi, 1, \tau)/\partial Q_{2,2}$ used in the inverse analysis when the measurements are taken at $\eta=1$

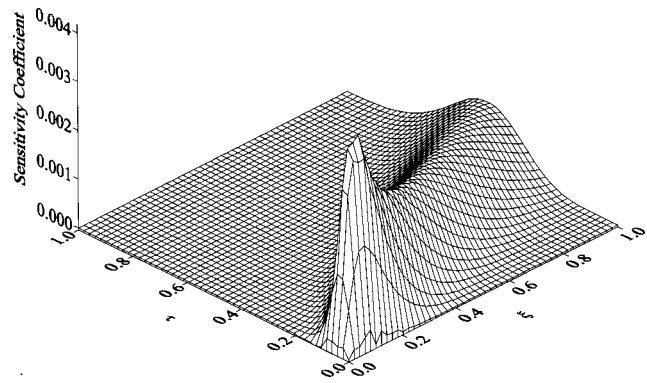


Fig. 7 The sensitivity coefficient $\partial\theta(\xi, 0.5, \tau)/\partial Q_{2,2}$ used in the inverse analysis when the measurements are taken at $\eta=0.5$

$$Q(\xi, \tau) = \begin{cases} 20\xi \sin(\pi\tau) & 0 \leq \xi \leq 0.5 \\ 20(1-\xi) \sin(\pi\tau) & 0.5 \leq \xi \leq 1 \end{cases} \quad (15)$$

Figure 8 shows the estimation of the spatial variation of the wall heat flux at $\tau=0.2$, $\tau=0.5$, and $\tau=0.9$ for simulated experimental data with $\sigma=0.01$ and $\sigma=0.02$, respectively. Overall, it can be seen that the estimation of the wall heat flux is satisfactory. As expected, the prediction of the wall heat flux is less accurate near $\xi=0.5$.

In the final example, the unknown wall heat flux is assumed to vary in the form

$$Q(\xi, \tau) = \begin{cases} 30\tau \cos\left(\frac{\pi}{2}\xi\right) & 0 \leq \tau \leq 0.5 \\ 20(1-\tau) \cos\left(\frac{\pi}{2}\xi\right) & 0.5 < \tau \leq 1 \end{cases} \quad (16)$$

which is difficult to predict for the inverse analysis due to the discontinuity presents in the function. Figure 9 shows the exact and estimated results of the inner wall heat flux at $\xi=0.2$, $\xi=0.5$, and $\xi=0.9$ for simulated experimental data containing errors of standard deviation $\sigma=0.02$. The prediction is less accurate near $\tau=0.5$ where the wall heat flux is not continuous. The accuracy of the estimation can be improved if the sensors are located closer to the inner wall or the measurement errors are reduced. In this paper, the sensitivity problem can be solved once for given M and N . The CPU time required for the sensitivity problem with $M=41$ and $N=41$ is 11 minutes on a personal computer with an

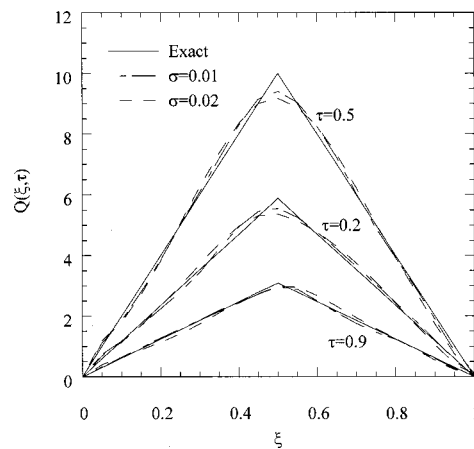


Fig. 8 The exact and estimated wall heat fluxes for $\sigma=0.01$ and $\sigma=0.02$, $M=41$, $N=41$

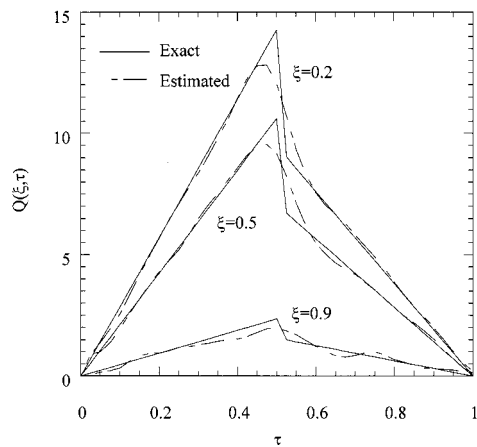


Fig. 9 The exact and estimated wall heat fluxes for $\sigma=0.02$, $M=41$, $N=41$

Intel Pentium II 233 MHz processor. If the sensitivity coefficients are given as input, the computational time required for each case of the inverse problem varies from 8 to 105 seconds.

Conclusion

An inverse convection method for estimating the inner wall heat flux for unsteady laminar forced convection in an annular duct has been presented. The unknown wall heat flux is a function of time and space. No prior information is needed for the functional form of the wall heat flux in the inverse analysis. Different timewise and spatial variations of the wall heat fluxes are used to illustrate the accuracy of the method. The reconstruction of the wall heat flux is satisfactory when simulated exact or noisy data are input to the inverse analysis. As expected, the prediction of the wall heat flux is less accurate if the estimated function is not smooth.

Acknowledgment

The support of this work by the National Science Council of the Republic of China under Contract No. NSC 88-2212-E-211-003 is gratefully acknowledged.

Nomenclature

D_h = hydraulic diameter
 d = direction of descent
 J = objective function

k = thermal conductivity
 M = the number of the measured data in the ξ -direction
 N = the number of the measured data in the τ -direction
 Pe = Peclet number
 Q = dimensionless wall heat flux
 q = wall heat flux
 q_{ref} = reference heat flux
 r = radial coordinate
 T = temperature
 t = time
 U = dimensionless velocity
 u = velocity
 \bar{u} = mean velocity
 x = axial coordinate
 Z = measured temperature data
 α = thermal diffusivity
 β = step size
 η = dimensionless radial coordinate
 λ = radius ratio
 γ = conjugate coefficient
 θ = dimensionless temperature
 σ = standard deviation
 τ = dimensionless time
 ξ = dimensionless axial coordinate
 ζ = random variable

References

- [1] Beck, J. V., Blackwell, B., and Clair, C. R. St., Jr., 1985, *Inverse Heat Conduction: Ill-Posed Problems*, John Wiley and Sons, New York.
- [2] Alifanov, O. M., 1994, *Inverse Heat Transfer Problems*, Springer-Verlag, New York.
- [3] Raghunath, R., 1993, "Determining Entrance Conditions From Downstream Measurements," *Int. Commun. Heat Mass Transfer*, **20**, pp. 173–183.
- [4] Bokar, J. C., and Ozisik, M. N., 1995, "An Inverse Analysis for Estimating the Time-Varying Inlet Temperature in Laminar Flow Inside a Parallel Plate Duct," *Int. J. Heat Mass Transf.*, **38**, pp. 39–45.
- [5] Liu, F. B., and Ozisik, M. N., 1996, "Estimation of Inlet Temperature Profile in Laminar Duct Flow," *Inv. Probl. Eng.*, **3**, pp. 131–143.
- [6] Moutsoglou, A., 1990, "Solution of an Elliptic Inverse Convection Problem Using a Whole Domain Regularization Technique," *J. Thermophys. Heat Transfer*, **4**, pp. 341–349.
- [7] Huang, C. H., and Ozisik, M. N., 1992, "Inverse Problem of Determining Unknown Wall Heat Flux in Laminar Flow Through a Parallel Plate Duct," *Numer. Heat Transfer, Part A*, **21**, pp. 55–70.
- [8] Liu, F. B., and Ozisik, M. N., 1996, "Inverse Analysis of Transient Turbulent Forced Convection Inside Parallel-Plate Ducts," *Int. J. Heat Mass Transf.*, **39**, pp. 2615–2618.
- [9] Patankar, S. V., 1980, *Numerical Heat Transfer and Fluid Flow*, Hemisphere, Washington, DC.
- [10] Hestenes, M. R., 1980, *Conjugate Direction Methods in Optimization*, Springer-Verlag, New York.
- [11] Alifanov, O. M., 1974, "Solution of an Inverse Problem of Heat Conduction by Iteration Methods," *J. Eng. Phys.*, **26**, pp. 471–476.

Heat Transfer and Pressure Drop of Laminar Flow in Horizontal Tubes With/Without Longitudinal Inserts

S.-S. Hsieh

Sun Yat-Sen Professor of Mechanical Engineering,
Dean of Engineering,
Fellow ASME

I.-W. Huang

Graduate Student,
Department of Mechanical Engineering

National Sun Yat-Sen University,
Kaohsiung, Taiwan R.O.C.

Heat transfer and pressure drop characteristics of water flow in horizontal tubes with/without longitudinal inserts used as a heat exchanger tubing was experimentally studied. Testing was performed on bare tubes and tubes with square and rectangular as well as crossed-strip inserts with aspect ratios $AR=1$ and 4 and varied ratios of inlet mixed mean temperature to wall temperature of 0.88 to 0.97. The Reynolds number ranged from approximately 250 to 1750 for flow visualization and from 1700 to 4000 for the pressure drop and heat transfer measurements. Flow visualization, using a dye injection method, revealed a highly complex flow pattern including a secondary flow formed in the cross section for crossed-strip inserts. The thermal entrance length was found and correlated in terms of Re for this type of inserted tubes. The enhancement of heat transfer as compared to a conventional bare tube at the same Reynolds number based on the hydraulic diameter was found to be about a factor of 16 at $Re \leq 4000$, while the friction factor rise was only about a factor of 4.5 at $Re \leq 4000$. [S0022-1481(00)01303-7]

Keywords: Augmentation, Forced Convection, Heat Exchangers, Heat Transfer

1 Introduction

The efficiency and economic competitiveness of many industry processes depend, to a great extent, on the performance of heat exchangers. Consequently, there is considerable engineering effort directed toward the development of high performance heat exchangers. Improvement in performance may result in a heat exchanger of a smaller size. For a heat exchanger of a fixed size, improved performance may allow for either an increased heat transfer rate or a decrease in temperature difference between the process fluids, the latter allowing for more efficient utilization of thermodynamic availability.

As a practically used displaceable device, a longitudinal rectangular plate is often inserted in the tubes of heat exchangers to enhance tube-side heat transfer. Solanki et al. [1,2] conducted experimental and theoretical studies for laminar forced convection in tubes with polygon inner cores. Chen and Hsieh [3] numerically studied laminar mixed convection in a horizontal tube with a longitudinal square core.

Most studies have been concerned with fully developed conditions. However, it was unclear how the flow develops to the final states for laminar or turbulent convection in a horizontal tube, especially with a longitudinal strip in its core. The developing process would not only provide insight into the complicated physics involved, but also legitimize the fully developed solution. Recently, Hsieh and Wen [4] did a numerical study for laminar developing flow in a horizontal tube with strip-type inserts. Further, Wu [5] and Liu [6] reported experimentally a two-part study for turbulent air flow in a horizontal tube with longitudinal inserts. However, the literature on experimental studies dealing with developing laminar convection tube flow with a longitudinal insert is relatively scarce.

The purpose of the present work is to extend the previous studies ([5,6]) for turbulent flow to the developing laminar tube flow and heat transfer with strip type inserts. The geometry and dimensions of the inserts used in this study are shown in Fig. 1. These inserts were chosen to simulate the applications in waste heat recovery system as a recuperator. The inserts were made from Plexiglas and considered to be adiabatic. The Reynolds number range of the experiments was from 250 to 4000 and the Prandtl number for the heat transfer study was extended from 2.4 to 4.6. The geometric size (e.g., H and L) as well as operating condition (e.g., developing flow and developed flow) is totally different from those of Solanki et al. [1,2] and Chen and Hsieh [3].

2 Experimental Setup and Procedure

Figure 2 shows a schematic drawing of the experimental apparatus. There are two test systems; one is for flow visualization, and one is for pressure drop and heat transfer measurements. This means two different, but complementary, apparatuses were employed for the present experiments.

2.1 Flow Visualization. The experimental setup used an available constant-head reservoir (12-m height) containing about 3000 L of city water that was supplied with water through an inlet at the bottom (see Fig. 2 for details). An overflow control valve maintained a constant head in the tank. The water from the outlet passed through a flowmeter first and then to a transparent Plexiglas tube (14-mm dia. with 2 mm in thickness), where the actual experimentation was carried out. The flow in the tube, and therefore the Reynolds number, was measured by a rotameter.

Longitudinal strips were inserted into the transparent tube. The strips were also made from Plexiglas as shown in Fig. 1. All inserts were closely bonded to the tube to insure a tight "spill-over" proof seal (i.e., no leak). The visualization of the flow patterns was aided by injection of colored (blue) dye into the tube. The dyes were introduced through the upstream plenum and ejected from a tube of 1-mm dia. hypodermic tubes right at the water inlet with great care to keep the disturbance due to the dye to minimum. Formulations of this type resist breakup under highly

Contributed by the Heat Transfer Division for publication in the JOURNAL OF HEAT TRANSFER. Manuscript received by the Heat Transfer Division, Jan. 8, 1999; revision received, Dec. 14, 1999. Associate Technical Editor: J. Han.

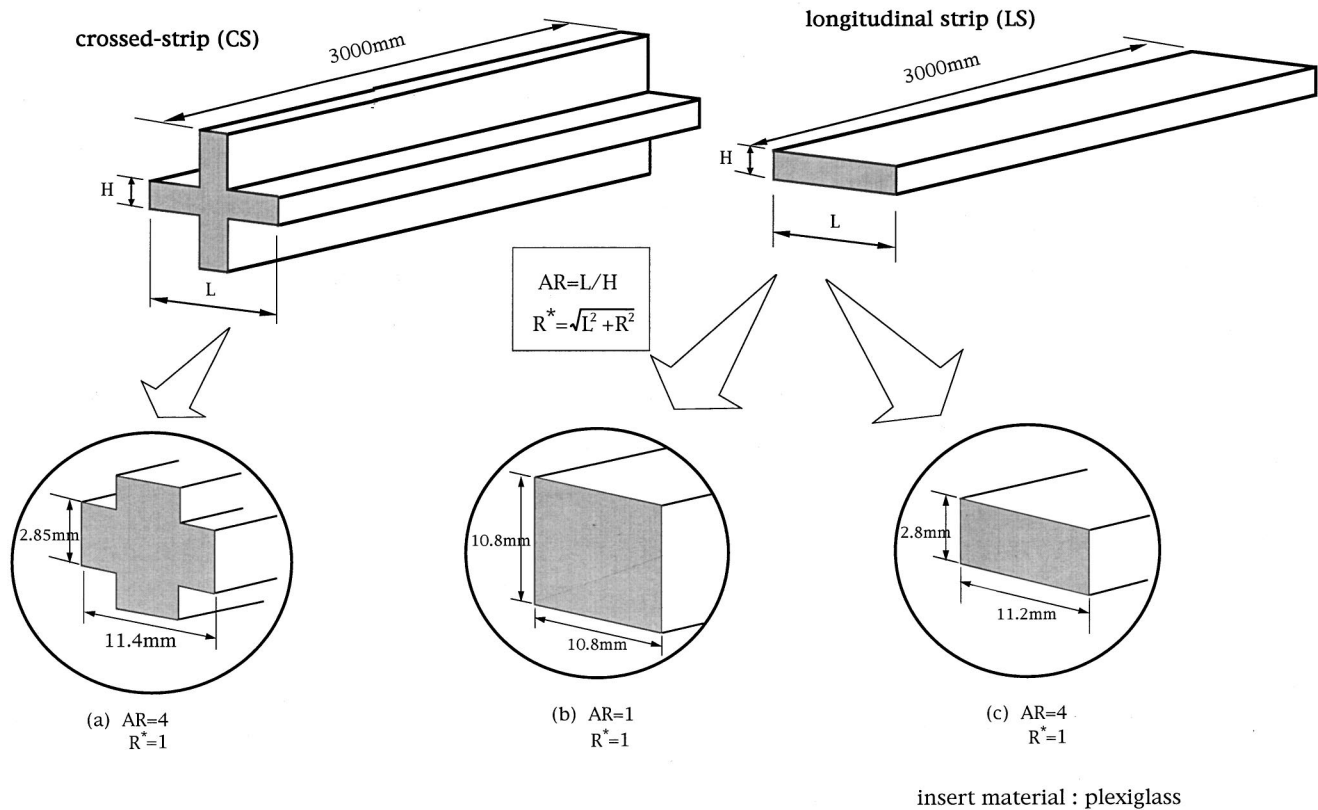


Fig. 1 The geometry and dimensions of the inserts used in this study

turbulent conditions ([7]). This was done to identify the different types of flow that might exist near the wall and the insert. The dyes facilitated observation of the behavior of different layers of fluid. Table 1 gives the geometric parameters and operating ranges that were used for flow visualization. Due to the refraction of the

circular tube, special treatment (e.g., using concave/or convex lens) was made to avoid this effect. The experiments were carried out several times to verify satisfactory repeatability of flow patterns. The lighting was provided by one LPL-BROM CINE 500W floodlight. The still pictures were taken using Cannon-AE1 cam-

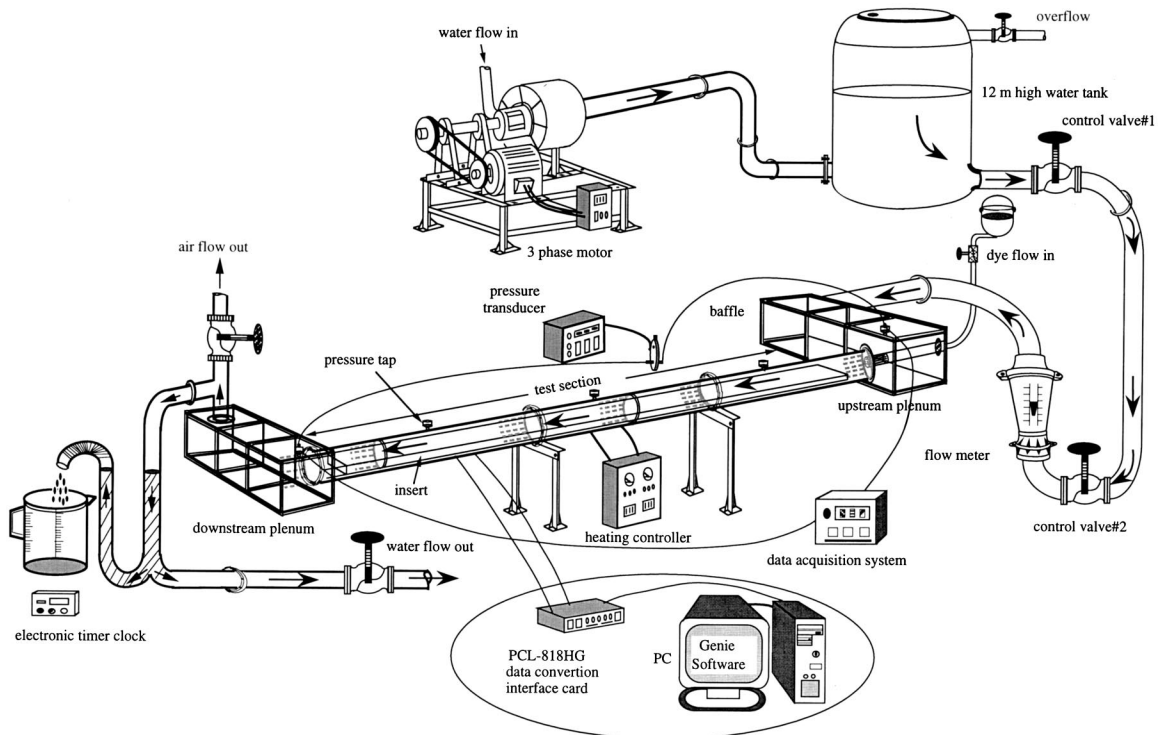
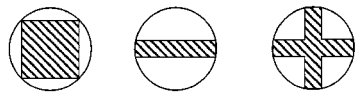


Fig. 2 The schematic of the present experimental apparatus

Table 1 Geometric parameters and operating ranges for flow visualization study

| Parameter | Range or value |
|---|--|
| Reynolds number, Re | 250-1750 |
| Inlet water temperature (°C) | 26±0.5 |
| Outlet water temperature (°C) | 26±0.5 |
| Average temperature (°C) | 26 |
| Mean velocity, u_m (m/s) | 0.0614(CS,AR=4)-0.413(LS,AR=1) |
| Aspect ratio, AR | 1,4 |
| Mass flow ratio,(kg/s) | 0.000262(LS,AR=1)-0.00784(LS,AR=4) |
| Geometry of test tubes ($D_o=15.88$ mm, $D_i=13.84$ mm) |  $D = 1.56$ mm LS(AR=1) $D = 6.66$ mm LS(AR=4) $D = 4.2$ mm CS(AR=4) |

era with an exposure time of 1/4000~1/500 s with ISO 400 Eastman Kodak 35-mm color slide films. In fact, good flow visualization images are obtained from the contrast between fluid with and without the dye.

2.2 Pressure Drop and Heat Transfer Measurements.

The experiments for determining heat transfer coefficients and friction factor for water flowing in a horizontal duct is shown in Fig. 2. The duct was made of 14 mm (±0.1-mm) dia. with a 2-mm thick copper tube. Heat transfer and pressure drop tests were done independently. Both used water as the working fluid. The pressure drop experiments were done adiabatically. Inlet and

outlet pressures were measured with a piezoresistive-type transducer, respectively, and differential pressure at a 100-mm interval each across the channel is measured with a strain-gauge-type transducer. The test section is formed by the tubes with and without inserts. Unlike flow visualization tests, the inserts here were fabricated from copper plate 3000-mm (±0.5-mm) long. In machining, care was taken to achieve a hydrodynamically smooth surface finish on the inserts. The side view of the test section shows the assembled relative positions of the front and end tubes which form the test duct. As seen in Fig. 3 the inserts were positioned in such a way that the upstream and downstream plenums were properly flanged by the adjustment screws. The entering flow was calmed by the baffles in the upstream plenum before it entered the duct. An assembled view of the joining of the respective inlet and exit ends of the test section was shown in Fig. 3. Table 2 lists the geometric parameters and operating range used in heat transfer and pressure drop measurements.

The test tube includes a heating part that has a double-tube structure and is between the tube exit and 3000 mm upstream from the exit. The inner tube of the heating part which is the test tube of $D = 14$ mm is made of 1-mm-thick copper plate. A cartridge heater was composed of four heating elements and was filled into the gap between the inner and outer tube which results in that the air existing in the gap between inner and outer tube was preheated and a constant heat flux condition was reached eventually. The wire (1.8-mm gauge) chosen as a heating element was made of a nickel-chrome alloy. The heating element is 6.83 mm in diameter. A detail of the manifolds that illustrates the heating element is also shown in Fig. 3. The test inserts were inserted into the test tube. The test tube had a fitting added to each end for attachment. The locations of the thermocouples (total 84 thermocouples) used to measure the test section wall temperature distributions as well as flowing water temperature inside the tube at particular positions along downstream distance are positioned as the same as Liu [6]. Temperatures measured at these locations provided experimental confirmation of the establishment of fully

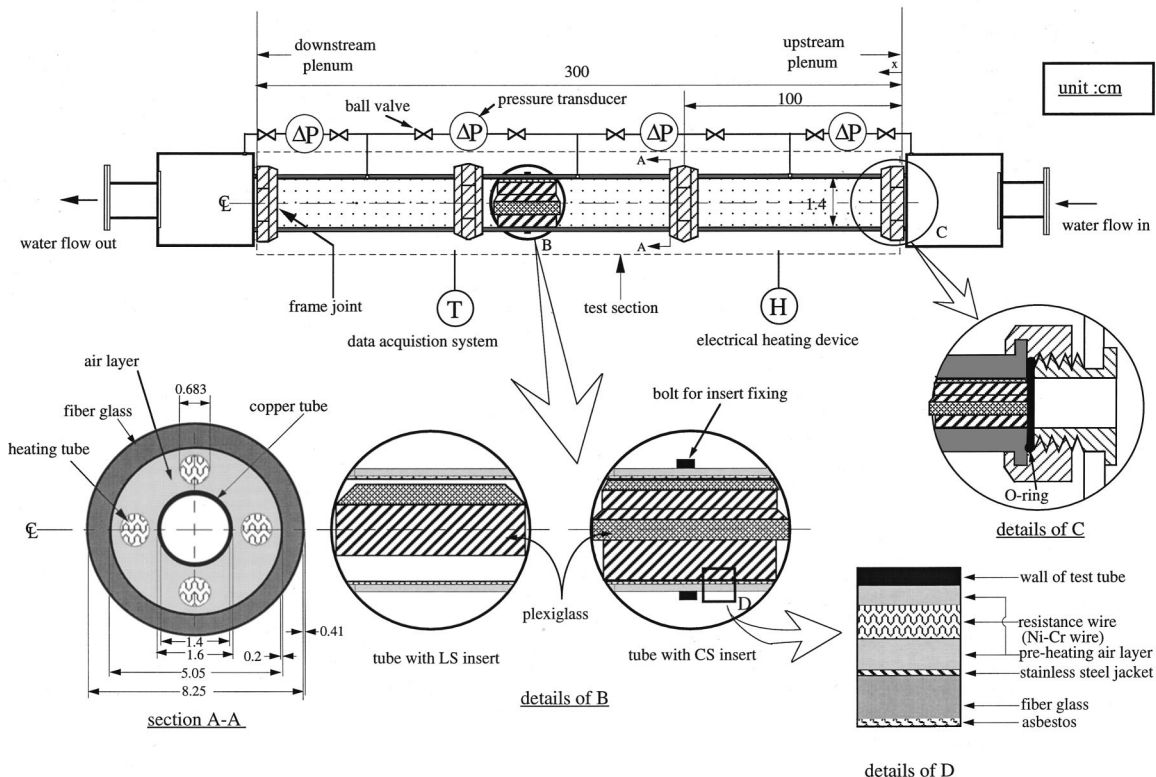


Fig. 3 Test section details

Table 2 Experimental parameters and operating ranges

| conditions | pressure drop | heat transfer |
|---|------------------------------------|------------------------------------|
| Reynolds number, Re | 1700-4000 | 1700-4000 |
| Inlet water temperature(°C) | 26±0.5 | 27.5 |
| Outlet water temperature(°C) | 26±0.5 | 39.39(bare)-75.87(LS,AR=1) |
| Ratio of inlet mean temperature to wall temperature | ————— | 0.88-0.97 |
| Average temperature(°C) | 26 | 33.45(bare)-51.68(LS,AR=1) |
| Prandtl number, Pr | 5.88 | 2.4-4.6 |
| Aspect ratio, AR | 1,4 | 1,4 |
| Mass flow rate, (kg/s) | 0.000262(LS,AR=1)-0.00784(LS,AR=4) | 0.000262(LS,AR=1)-0.00784(LS,AR=4) |
| Net heat flow rate, Q(W) | ————— | 2743, 3429, 4115 |
| Wall heat flux, q _w (W/m ²) | ————— | 18287, 22860, 27433 |

developed flow. Fine gauge (≅0.1 mm) specially calibrated Type K type thermocouples were employed with the intent of minimizing the disturbance of the temperature field in the vicinity of the thermocouple junctions. The thermocouples were installed in holes drilled into the back side of the tube walls to within 2 mm of the surface. Five thermocouples, respectively, positioned just upstream and downstream of the tube inlet and outlet were used to measure the temperature at respective positions incorporated with the corresponding velocity measurements to calculate the inlet and outlet bulk mean temperatures.

Electric power was supplied to the test section heating wire by one circuit. The source of power for this circuit was an autotransformer, supplied from a standard 220V, 60-cycle a.c. wall outlet. These autotransformers were designed for a load voltage output of 0–220 V, with a maximum current of 40 amps.

Water flow rates were measured by rotameter (0.5~3 L/min). This gives the tube-side Reynolds number range from 1700 to 4000. The pressure drop along the entire test section was measured by means of static manometers. In all, five taps were stationed 100 mm apart. The pressure taps were connected by flexible PVC tubing to the monometer. All measurements were made under steady-state conditions. The fluid properties were calculated as the average between the inlet and outlet bulk temperature. Generally, it took 1.5 hours to reach steady state at Re=1700.

After the establishment of an overflow from the constant head tank and filling the plenum chambers, the flow control valve was opened to the maximum flow rate in order to wash any air bubbles or pockets out of the test duct which may have formed while the system was at rest. The flow control valve was then adjusted to the desired flow rate for the run as measured by the rotameter. The inlet bulk temperature was then measured and recorded. Next, heating was initiated by the adjustment of the autotransformers to predetermined voltage outputs. Data acquisition began after steady state operation was achieved.

3 Data Reduction

The primary goal of this experiment was to determine the possible flow pattern and fully developed Nusselt numbers for water flowing in tubes with and without inserts. The independent parameters for heat transfer measurement were the Reynolds number, the Prandtl number and the ratio of inlet mixed mean temperature to wall temperature while for flow visualization the independent parameters were Reynolds number and downstream position. The

viscosity and the Prandtl number of the water, which are strongly temperature dependent, as stated before, were evaluated at the average bulk temperature.

The tube side local heat transfer coefficient and Nusselt number due to pure forced convection were calculated as

$$Q_{net} = h_x A_s (T_{wx} - T_{bx})$$

$$q'' = Q_{net} / A_s, \quad A_s = \pi D_o l \quad (1)$$

$$Nu_x = \frac{h_x D_i}{k_f}$$

where k_f is the thermal conductivity of water and A_s is the area of the heated region of the water tubes ($= \pi D_o l$). The local net heat transfer rate Q_{net} was the electrical power generated from the heater with the heat loss to the outside of the test channel deducted (including conduction and radiation heat losses). The sum of these two losses was found to be less than ten percent of the total heat input at the worst case.

Buoyancy effect was considered negligible since the water was used as the working fluid. Actually, the Richardson number (Gr/Re^2) was computed for the worst case ($Re=1700$, $Q_{net}=3429$ W with strip type insert of $AR=1$) and it was found to be about 0.1. T_{wx} was calculated based on the average of several circumferential (four for LS inserts; six for CS inserts) temperature readings.

T_{bx} is obtained by energy balance at any streamwise tube location, defined as $T_{bx} = T_{bi} + q''_w (\pi D \Delta X / \dot{m} C_p)$ where ΔX is the stream distance from the beginning of heating for the streamwise station of interest, \dot{m} is the water mass flow rate and C_p is water specific heat. The effect of the inserts acted as fins only when the width of the insert is close to the inside diameter. However, such effect as the modifying the temperature of the water in the tube was considered negligible ([8]) especially for that the Plexiglas insert was chosen.

The determination of fully developed Nusselt numbers from the experimental data begins with the calculation of the local bulk temperature rise based on an energy balance on the flowing water. The calculated and measured local water bulk mean temperatures at a particular downstream distance from the inlet was found to be in good agreement within ±5 percent. The present results consisted of 108 data sets obtained from four different tubes.

The Darcy friction factor was evaluated using the pressure drop in conjunction with the following equation:

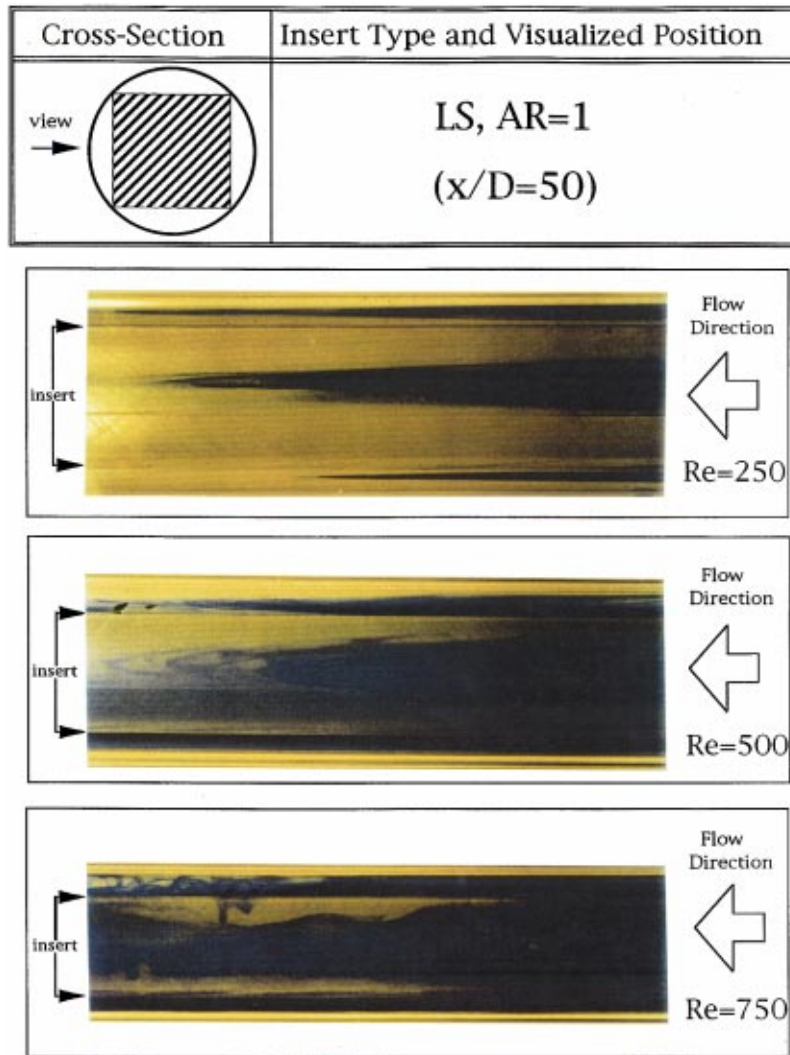


Fig. 4 Visualized flow pattern for LS insert of AR=1 at $x/D=50$ for different Re

$$f = \frac{(\Delta P/l)D_1}{\frac{1}{2}\rho u_m^2} \quad (2)$$

where u_m is nominal (bulk) average velocity of the fluid, l is the length of the test tube, and ρ is the density of the fluid.

4 Experimental Uncertainty

Before the experiments, all the thermocouples were calibrated in a constant temperature bath to ensure the measurement accuracy of $\pm 0.1^\circ\text{C}$. The voltage input to each finned-type heater was measured with a sensitivity of ± 0.5 mV and an accuracy of ± 0.5 percent. Several runs were conducted in which the voltage and the current for the circuit were measured, and the calculated power output was highly stable. This procedure resulted in a maximum uncertainty of ± 1 percent for the calculated power output. The thermophysical properties of the water were assigned an uncertainty of ± 1 percent. This was based on the latest values evaluated at proper temperature and pressure.

An error analysis using the method of Moffat [9] was performed to determine the uncertainty in the experimental data. The single largest contributor to uncertainty in the Reynolds number (1700 to 4000) was the measurement of the volumetric flow rate. The resulting maximum uncertainty in Re and f is 4.9 and 5.3 percent, respectively. The majority of the error in Nu can be

traced to the uncertainty in the convective heat transfer and is due mainly to the simplified analysis for the conduction loss correction. Although the conduction loss through the insert can probably be estimated to be within two to three percent accuracy, these losses are so small that this might be considered negligible. The estimated error in the temperature difference is 0.2°C . The resulting maximum uncertainty in Nu is six percent.

5 Results and Discussion

5.1 Flow Visualization. Flow visualization was conducted at a particular position chosen in such a way that a hydrodynamically fully developed condition was reached to deduce the main flow features and to observe the influence of the insert geometry on the flow pattern. There are small separation zones near the fronts of the sides of the inserts but we don't think it would affect the downstream flow at each corresponding fully developed region much. Although the visual results depend on where ink was injected, typical photographic sequences are obtained and shown in Figs. 4 to 6. The corresponding sketches are shown in Fig. 7. The following inferences on the effects of the insert geometry and Re can be drawn from these figures.

1 At low Re, the traditional "laminar" type flow pattern is clearly seen (Figs. 4, 5, and 6).

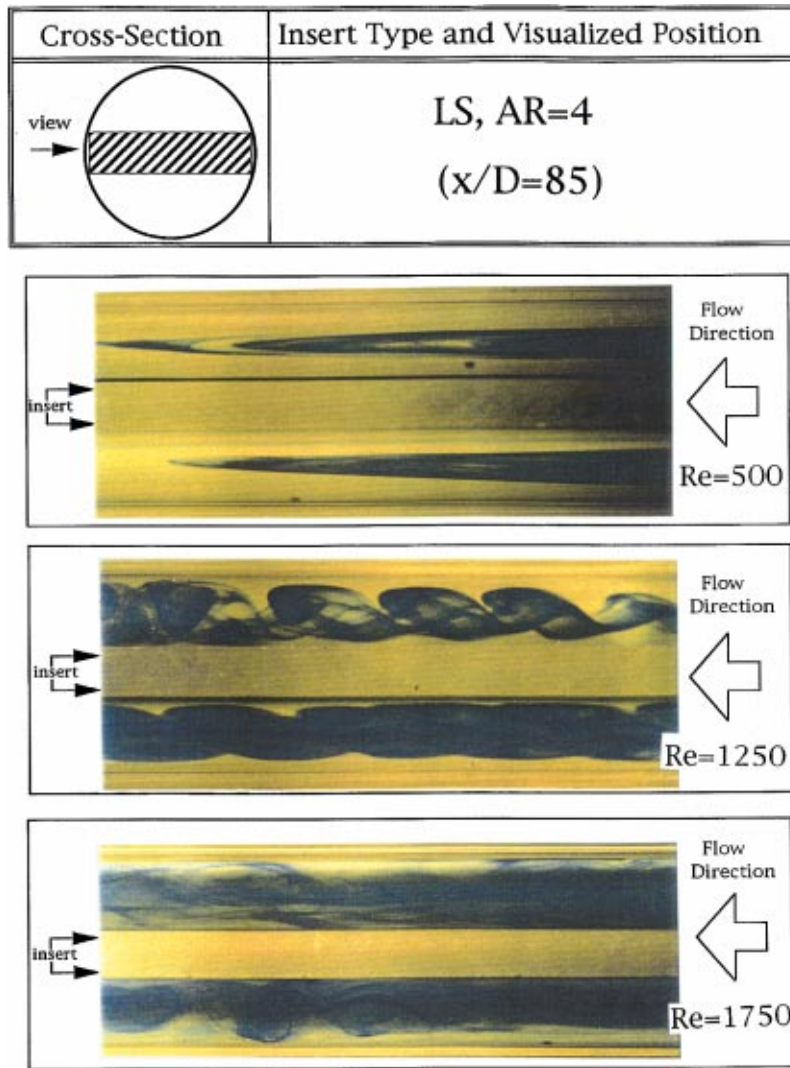


Fig. 5 Visualized flow pattern for LS insert of AR=4 at $x/D=85$ for different Re

2 Slight differences in the patterns evolve as the flow moves downstream, but the major changes occur from one geometry to another and with Re as well (Figs. 4, 5, and 6).

3 As Re increases, the onset of transition to turbulence occurs followed by the sequence of LS ($AR=1$), CS ($AR=4$), and LS ($AR=4$) insert (Figs. 4, 5, and 6).

4 Dye injection tests conducted in a bare tube (not shown here) indicated the presence of laminar flow well up to $Re=2300$ which is larger than the present worst case of $Re=1750$ for LS insert of $AR=4$ (Fig. 5).

5 Tests at $Re>1250$ for LS insert of $AR=4$ result in high enough turbulence that the dyes are thoroughly mixed. It also suggests that both rotational and crossover patterns exist in flow over a strip-type insert (Figs. 5 and 6) which result in a helical-like motion of the fluid. The reasons for this are not understood at this stage. Since no further attempt has as yet been made in this work to visualize or to otherwise study the characteristics of the flow past an insert in an open literature, it may provide some physical insight in this regard even under present situation. The flow patterns viewed on different sides of the inserts are not same and not symmetric with respect to the tube centerline. These are expected and may be caused by experimental errors.

In general, based on the present side view, these flow patterns imply that there are symmetric cells. Also, as Re increases, it seems that the strength of symmetric vortices was enhanced. Ap-

parently, these vortices were stretched by a velocity gradient in the main flow and advected downstream (see, for example, Fig. 6 at $Re=750$). It is conjectured ([4]) that Fig. 4 basically shows two pairs of symmetric vortex cells inside the cross section for the LS insert of $AR=1$. This is perhaps because a secondary flow was formed and was due to the complex interaction among shear forces and the geometry of the insert. The similar situation was also found in Figs. 5 and 6 at low $Re(\leq 500)$. However, it seems that the flow becomes more irregular and chaotic at $Re \geq 750$. It also seems that, however, the turbulence intensity shown in Fig. 5 is much higher than the one shown in Fig. 4 for LS insert of $AR=1$ due to the presence of more irregular motions in Fig. 5 with $AR=4$. This is perhaps due to a higher corresponding Re in Fig. 5. But, most importantly, it indicates that the LS insert with $AR=4$ seems to have stronger local turbulence compared with the other two inserted tubes, i.e., CS ($AR=4$) and LS ($AR=1$). Actually, the main flow in tubes with LS insert of $AR=4$ has a higher spatially averaged velocity, which results in a higher heat transfer. This can also be seen later.

In summary, the present complex flow pattern in the inserted tubes can be possibly attributed to a drag on the disruption due to possible vortex cell formation in cross section and an increase in turbulent intensity caused by the shear layer (also different mean velocities in the passages around the inserts).

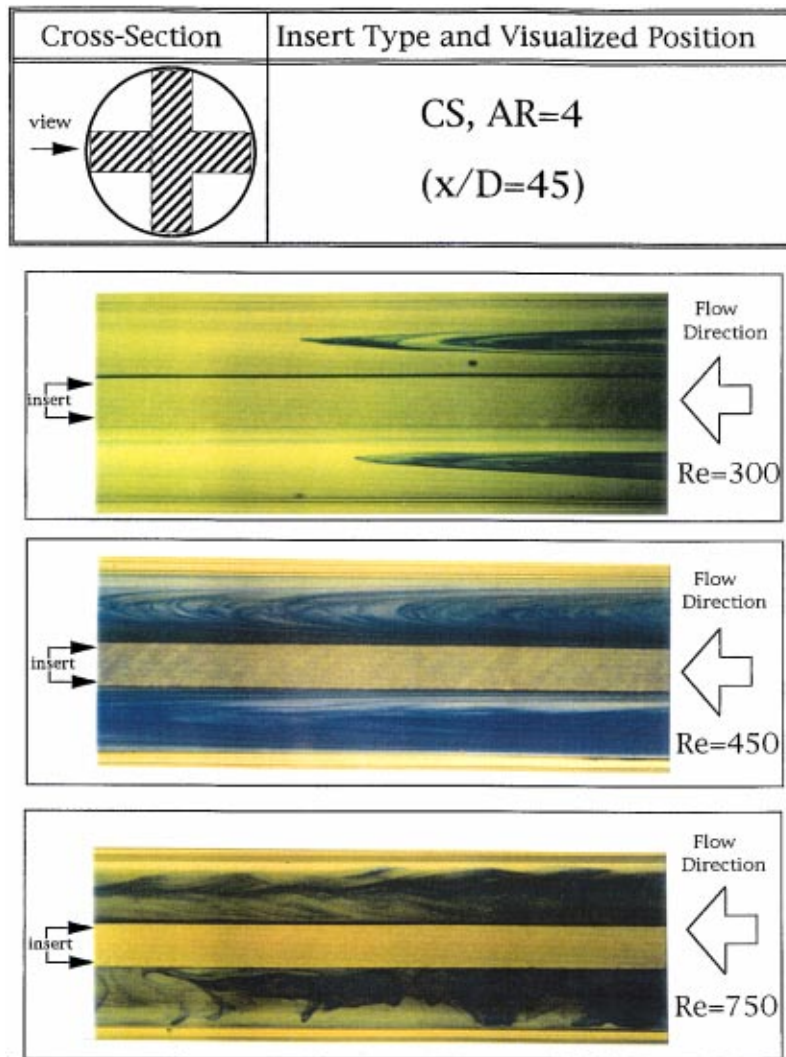


Fig. 6 Visualized flow pattern for LS insert of AR=4 at $x/D=45$ for different Re

5.2 Pressure Drop and Heat Transfer Measurements

5.2.1 Temperature Distribution and Nusselt Numbers. Temperature distribution along streamwise distance was measured and a representative dimensionless temperature distribution ($Re=2300$, $Q_{net}=3429$ W, and $q_w=22860$ W/m²) plot is shown in Fig. 8. In this figure, the ordinate variable is the nondimensionalized temperature difference T^* , defined as $T-T_{bi}/Q_{net}/lk_f$. The abscissa variable in Fig. 8 is known as the inverse Graetz number and is a dimensionless representation of the linear axial coordinate.

For the longitudinally constant heat flux boundary condition of the present study as evidenced by this figure, the thermally fully developed region is characterized by wall and mean bulk water temperature that increased linearly as a function of longitudinal downstream position. The most important portion of the wall temperature distribution is the central portion ($x^*\geq 4\times 10^{-3}$ for all the cases considered) through which a straight line has been fitted parallel to the line representing the bulk temperature. The vertical distance between this line segment and the bulk temperature line indicates the wall-to-bulk temperature difference used to calculate the fully developed heat transfer coefficient. The entrance effect on heat transfer enhancement can also be explained by such difference and it was also clearly noted especially for tubes with inserts.

From Fig. 8, one can see that the bare tube has the largest temperature difference followed by LS (AR=4), CS (AR=4), and LS (AR=1). This is the same as reported by Liu [6] for turbulent air flow. Keeping the other parameters fixed, the smallest temperature difference in Fig. 8 indicates the best heat transfer performance one may obtain. This is partly because the LS insert with AR=1 provides a larger heat transfer area and partly because LS inserts with AR=1 have a higher convective heat transfer due to higher average velocity. In fact, the ratios of surface area of the tubes with and without inserts are 1.94 for LS (AR=1), 2.3 for CS (AR=4), and 1.8 for LS (AR=4), respectively. The increase in heat transfer coefficient due to heat transfer area is counterbalanced by the lower heat transport capability due to a lower average velocity for CS insert as compared to the LS inserts. At this stage, the heat transfer increases with an insert for a variety of reasons. The blockage of the flow due to the presence of the insert increases the flow velocity. The cross flow patterns of the fluid (based on flow visualization) by the presence of the insert improves the mixing.

Figure 9 shows the local Nu along the downstream distance and the onset of the fully developed Nusselt number value plot, ranging from $42D$ to $100D$, depending on the tube inside geometry. A fully developed value (i.e., thermal entrance length, L_e) was determined when the variation of two consecutive Nu_x was less than

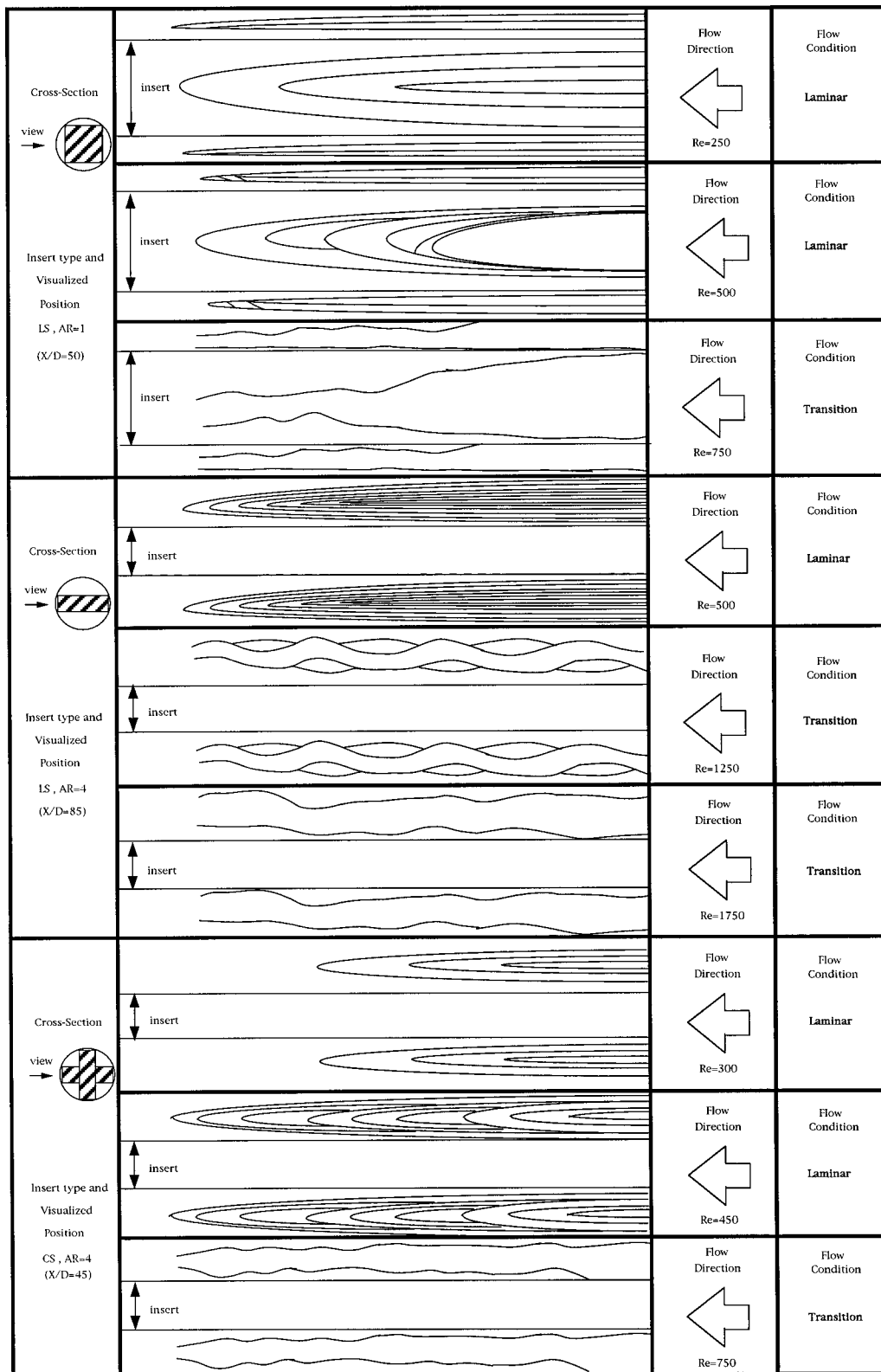


Fig. 7 Accompanying sketches of the corresponding plots

one percent. The sequence is that the CS insert with $AR=4$ has the earliest incipience of fully developed value followed by LS ($AR=1$), LS ($AR=4$), and the bare tube. The f_{dp} value of each tube is correlated in terms of Re in the form

$$\frac{L_e}{D} = C(Re)^m. \quad (3)$$

The values for constant C and exponent m are tabulated in Table 3. Within ± 8 percent accuracy, one obtains $m=0.2993 \pm 0.048$. This suggests that Reynolds number dependence on thermal entrance length is not altered for all the four cases under consideration.

The fully developed Nusselt numbers are plotted against Re in Fig. 10. The effect of insert on Nu is shown in Fig. 10. The

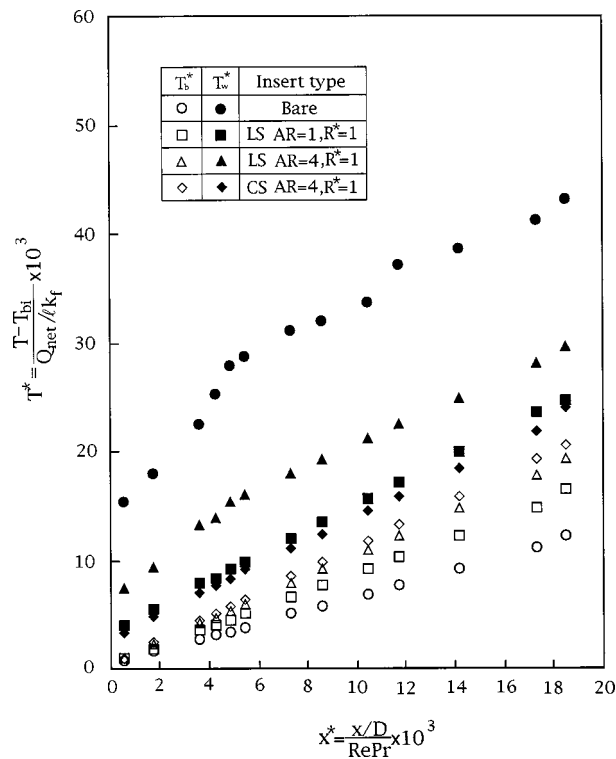


Fig. 8 Local dimensionless wall and bulk temperature distribution at $Q_{net} = 3429 \text{ W}$ and $q_w = 22,860 \text{ W/m}^2$

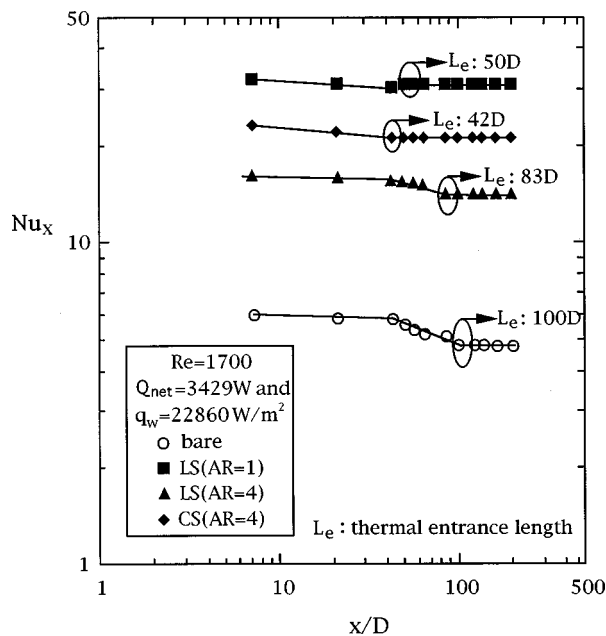


Fig. 9 Nu_x versus x/D

Table 3 Constants for thermal entrance length correlation $L_e/D = c Re^m$

| insert type \ constant | Bare tube | LS(AR=1) | LS(AR=4) | CS(AR=4) | Average |
|------------------------|-----------|----------|----------|----------|--------------------|
| C | 7.42 | 7.34 | 7.79 | 5.47 | — |
| m | 0.35 | 0.258 | 0.315 | 0.274 | 0.2993 ± 0.048 |

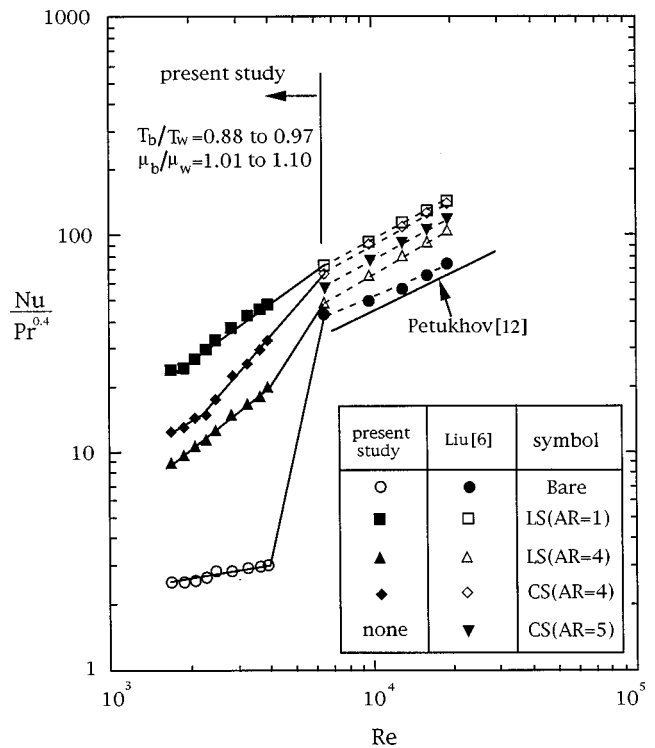


Fig. 10 Nusselt numbers versus Re . Reference cited in figure is Ref. [12].

corresponding bare tube values are also plotted for reference. It should be noted that the fluid Prandtl number changed along the tube; therefore, the left ordinate was so chosen as $Nu/Pr^{0.4}$. However, the effect of Prandtl number was not considered because the change of Pr seems not big. In fact, the value of μ_b/μ_w is around 1.01 to 1.10 in the present work. Figure 10 shows that slope of the $Nu/Pr^{0.4}$ versus Re graph is almost constant even at the low Re ($Re \approx 1000$) end, indicating a departure from laminar behavior at these low Re values. Incorporating with the data from Liu [6] there is a transition region ($4000 \leq Re \leq 6500$) as would be expected for the bare tube, except for the tubes with LS inserts of $AR=1$. Transition from laminar to turbulent flow occurred at lower Reynolds number (e.g., $Re \approx 3600$ for the LS insert of $AR=1$) than for the bare tube ($Re \approx 4000$). The increase in Nusselt number (compared to that of bare tube) of up to 16 is possible in the low Re region ($Re \approx 4000$) by using the inserted tubes; however, this value goes down to 2.3 or so in the turbulent regime ($Re \approx 19,500$). The highest enhancement levels in the Nusselt number over bare tube values are noted in the laminar regime. This behavior is expected because, as stated earlier, in the flow visualization for laminar flow, the dominant thermal resistance is not limited to a thin boundary layer adjacent to the flow. Consequently, the present insert geometry mixing the gross flow is more

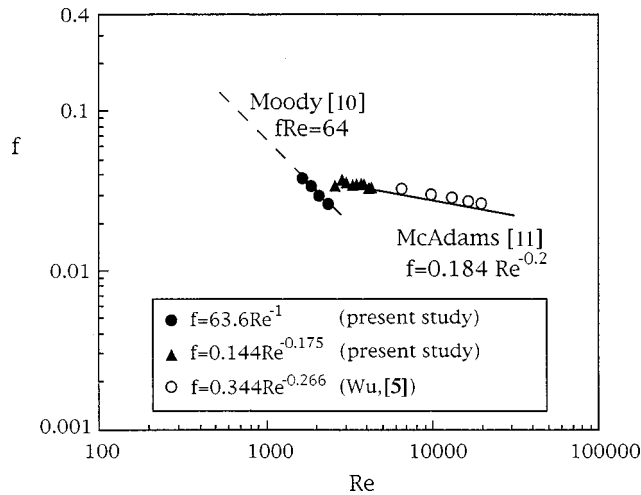


Fig. 11 Friction factor results for the case of smooth tube

effective in laminar flow than in turbulent flow. Moreover, good agreement with the predictions of the Petukhov correlation can be seen for testing (data from [6]) in the Reynolds number range of 6500 to 19,500 for the bare tubes without inserts.

5.2.2 Pressure Drop (Friction Factor). Figure 11 shows the isothermal friction factor calculated from the pressure drop measurements. Data on bare tubes with different Re are also presented in Fig. 11. The present measured values and values obtained from Hsieh and Wu [5] are presented for $6500 \leq Re \leq 19,500$. For the laminar regime, the correlation developed by Moody [10] was used as a reference. As can be seen from the figure, the results agree well with the prediction of $64/Re$ for laminar flow. For the turbulent regime, the correlation developed by McAdams [11] was used ($0.184 Re^{-0.2}$). Transition occurs in bare tubes between 2000 and 4000. It is found in Fig. 11 that there is good agreement between the bare tube friction factors presently obtained and the corresponding values in the literature.

Typical results for the friction factors in the tube with inserts, the corresponding bare tube values, and the ratio of the two are presented in Fig. 12. In Fig. 12 the ordinates on left and right sides refer to the friction factor, and friction factor increase (the corre-

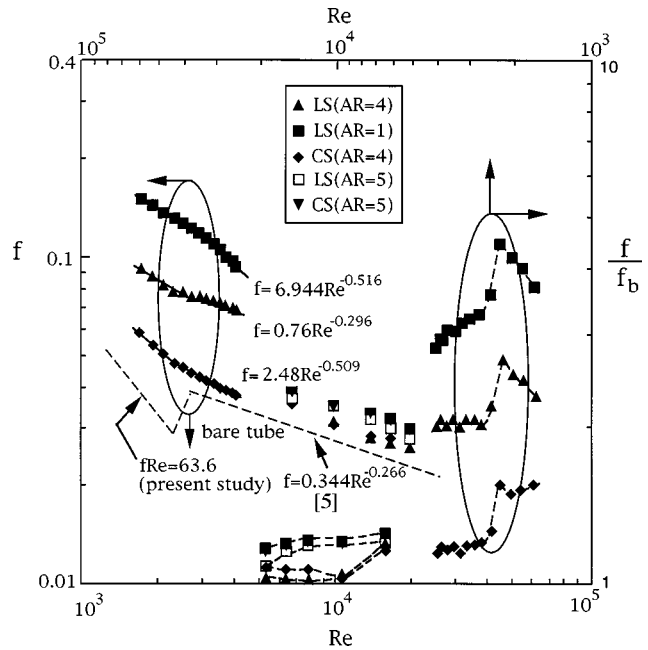


Fig. 12 Friction factor f and ratio f/f_b

sponding Re read from the top abscissa), respectively. In Fig. 12 for tubes with inserts, the curves for f with inserts are almost parallel to the corresponding f without inserts in the high range Re ($Re > 4000$). At $Re < 4000$, the slope undergoes an abrupt transition representing a change in the flow characteristics.

Among three tubes with inserts, it is found that the trend shown in tubes with CS insert of $AR=4$ seems much like the corresponding f curve. However, the other two curves of tubes with LS ($AR=1$) and LS ($AR=4$) show different slopes.

The transition Re value is lower ($2000 \leq Re \leq 2500$) than the value expected for a bare tube ($2300 \leq Re \leq 4000$). This change is also clearly reflected in the friction factor increase plot. The increase in the low Re range is about 1.5~3.0 times the bare tube value. Moreover, the differences for three tubes with inserts in the friction factor at $Re > 4000$ could not be distinguished.

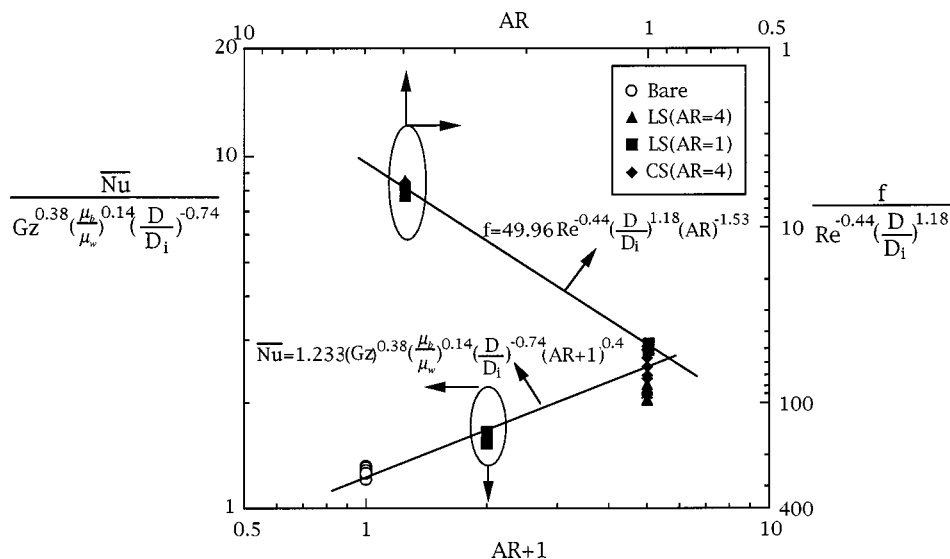


Fig. 13 Correlation of Nusselt number (with bare tube) and friction factor (without bare tube) for inserted tubes in the present study

5.3 Correlations of the Relevant Parameters. It is evident from Figs. 10 and 12 that the friction factor and the Nusselt number for the tubes with inserts is a function of Re and the geometric parameters of the insert. Therefore, the f and tube average \overline{Nu} can be correlated in Fig. 13 using the following relationship:

$$f = 49.96 \text{Re}^{-0.44} (D/D_i)^{1.18} (AR)^{-1.53}$$

and

$$\overline{Nu} = 1.233 (\text{Gz})^{0.38} (\mu_b/\mu_w)^{0.14} (D/D_i)^{-0.74} (AR+1)^{0.41}.$$

The correlation was derived using standard procedures. The exact ratio effect on f and \overline{Nu} is clearly noted. Since the conventional $f = 64/\text{Re}$ for bare tube is very known, the f correlation does not include the tubes without inserts. Although the range of μ_b/μ_w of the present study was limited as mentioned before, its effect is well known (assuming 0.14 as exponent) and is, therefore, included for completeness. The insert effect on both f and \overline{Nu} is also observed based on the exponents of (D/D_i) and AR each.

6 Conclusions

The study of flow using three kinds of inserts in a horizontal circular tube in the ranges of $250 < \text{Re} < 4000$ and $2.4 \leq \text{Pr} \leq 4.6$ has shown

1 early or transition to turbulence occurs in the inserted tubes for some cases.

2 the complex flow pattern in the inserted tubes is perhaps due to a drag by vortex formation and an increase in turbulent intensity by shear layer in the presence of the insert.

3 heat transfer enhancement can be up to 16 times larger, while the friction factor is about 4.5 times larger at the same Reynolds numbers based on hydraulic diameter. This results in that the conventional enhancement level (η) can reach a value of 4. This is higher than the corresponding study for turbulent flow which was found to be 2~3.

4 a general correlation of Re, D/D_i , and AR on f and \overline{Nu} was developed for tubes with inserts.

Acknowledgment

This work was supported by a research grant (NSC 88-2212-E110-039) from the National Science Council, Taiwan, R.O.C.

References

- [1] Solanki, S.-C., Saini, J.-S., and Gupta, C.-P., 1985, "An Experimental Investigation of Fully Developed Laminar Flow in a Non-Circular Annulus," Eighth National Conference on Heat Mass Transfer, HMTA 34-85, Visakhapatnam.
- [2] Solanki, S.-C., Prekash, S., Saini, J.-S., and Gupta, C.-P., 1987, "Forced Convection Heat Transfer in Doubly Connected Ducts," *Int. J. Heat Fluid Flow*, **8**, pp. 107-110.
- [3] Chen, J.-D., and Hsieh, S.-S., 1991, "Assessment Study of Longitudinal Rectangular Plate Inserts as Tubeside Heat Transfer Augmentative Device," *Int. J. Heat Mass Transf.*, **34**, pp. 2545-2553.
- [4] Hsieh, S.-S., and Wen, M.-Y., 1996, "Developing Three-Dimensional Laminar Mixed Convection in a Circular Tube Inserted with Longitudinal Strips," *Int. J. Heat Mass Transf.*, **19**, pp. 299-310.
- [5] Wu, F.-Y., 1996, "Turbulent Flow and Pressure Drop in a Horizontal Circular Tube With Strip-Type Inserts," Masters thesis, Department of Mechanical Engineering, National Sun Yat-Sen University (in Chinese).
- [6] Liu, M.-H., 1996, "Turbulent Heat Transfer in a Horizontal Circular Tube With Strip-Type Inserts," MS thesis, Department of Mechanical Engineering, National Sun Yat-Sen University (in Chinese).
- [7] Hoyt, J. W., and Sellin, R. H. J., 1997, "Flow Over Tube Banks: A Visualization Study," *ASME J. Fluids Eng.*, **119**, pp. 480-483.
- [8] Chen, J.-D., and Hsieh, S.-S., 1992, "Laminar Forced Convection in Circular Duct Inserted with a Longitudinal Rectangular Plate," *AIAA J. Thermophys. Heat Transf.*, **6**, pp. 177-179.
- [9] Moffat, R. J., 1988, "Describing the Uncertainties in Experimental Results," *Exp. Therm. Fluid Sci.*, **1**, pp. 3-17.
- [10] Moody, L. F., 1944, "Friction Factor for Pipe Flow," *Trans. ASME*, **66**, pp. 671-684.
- [11] McAdams, W. H., 1954, *Heat Transmission*, 3rd Ed., McGraw-Hill, New York.
- [12] Petukhov, B. S., 1970, "Heat Transfer and Friction in Turbulent Pipe Flow With Variable Physical Properties," *Advances in Heat Transfer*, J. P. Hartnett and T. F. Irvine, eds., Academic Press, San Diego, CA, pp. 504-564.

Effect of Double Dispersion on Mixed Convection Heat and Mass Transfer in Non-Darcy Porous Medium

P. V. S. N. Murthy¹

Department of Mathematics,
I.I.T.—Madras,
Madras 600 036, India

Similarity solution for the problem of hydrodynamic dispersion in mixed convection heat and mass transfer from vertical surface embedded in porous media has been presented. The flow induced by the density variations is comparable with the freestream flow. The heat and mass transfer in the boundary layer region for aiding and opposing buoyancies in both aiding and opposing flows has been analyzed. The structure of the flow, temperature, and concentration fields in the Darcy and non-Darcy porous media are governed by complex interactions among the diffusion rate (Le) and buoyancy ratio (N) in addition to the flow driving parameter (Ra/Pe). The flow, temperature, and concentration fields are analyzed and the variation of heat and mass transfer coefficients with the governing parameters are presented. [S0022-1481(00)00703-9]

Keywords: Boundary Layer, Dispersion, Heat Transfer, Mass Transfer, Mixed Convection, Porous Media

1 Introduction

Thermal and solutal transport by fluid flowing through a porous matrix is a phenomenon of great interest from both the theory and application point of view. Heat transfer in the case of homogeneous fluid-saturated porous media has been studied with relation to different applications like dynamics of hot underground springs, terrestrial heat flow through aquifer, hot fluid and ignition front displacements in reservoir engineering, heat exchange between soil and atmosphere, flow of moisture through porous industrial materials, and heat exchanges with fluidized beds. Mass transfer in isothermal conditions has been studied with applications to problems of mixing of fresh and salt water in aquifers, miscible displacements in oil reservoirs, spreading of solutes in fluidized beds and crystal washers, salt leaching in soils, etc. Prevention of salt dissolution into the lake waters near the sea shores has become a serious problem of research.

Coupled heat and mass transfer phenomenon in porous media is gaining attention due to its interesting applications. The flow phenomenon is relatively complex rather than that of the pure thermal convection process. Processes involving heat and mass transfer in porous media are often encountered in the chemical industry, in reservoir engineering in connection with thermal recovery process, and in the study of dynamics of hot and salty springs of a sea. Underground spreading of chemical wastes and other pollutants, grain storage, evaporation cooling, and solidification are the few other application areas where the combined thermo-solutal natural convection in porous media are observed. Combined heat and mass transfer by free convection under boundary layer approximations has been studied by Bejan and Khair [1], Lai and Kulacki [2], and Murthy and Singh [3]. Coupled heat and mass transfer by mixed convection in Darcian fluid-saturated porous medium has been analyzed by Lai [4]. The free convection heat and mass transfer in a porous enclosure has been studied recently by Angirasa et al. [5].

The porous medium inertial effects have been proved to be important for moderate and fast flows, i.e., when the pore diameter-dependent Reynolds number is greater than the order of unity. For low-porosity media, the Forchheimer flow model has been proved to be appropriate and it has been widely used in the works of Vafai and Tien [6,7], Whitaker [8], etc. When the inertial effects are prevalent, the thermal and solutal dispersion effects become important, and these effects are very significant in forced and mixed convection flows and in vigorous natural convection flows as well. Thermal dispersion effects have been studied at length by researchers such as Bear [9], Kvernfold and Tyvand [10], Plumb [11], Hong and Tien [12], Hong et al. [13], Cheng and Vortmeyer [14], Lai and Kulacki [15], Amiri and Vafai [16], Gorla et al. [17], and Murthy and Singh [18,19]. A brief review on thermal dispersion can be found in Bear [9] and Nield and Bejan [20]. Kvernfold and Tyvand [10] argued that better agreement between the theoretical prediction and experimental data can be obtained when thermal dispersion effects are taken into consideration appropriately.

Coupled heat and mass transfer phenomenon in non-Darcy flows are studied by Karimi-Fard et al. [21] and Murthy and Singh [3]. The complexity of the flow increases when higher order effects like thermal and solutal dispersion, wall channeling, and porosity variations are considered in the medium. A numerical study of double-diffusive free-convection heat and mass transfer in a square cavity filled with a porous medium has been done by Karimi-Fard et al. [21]. A more general flow equation (Darcy-Forchheimer-Brinkman), coupled with energy and concentration equations, are solved using a finite volume technique. The investigation showed that the inertial and boundary effects have a profound effect on the double-diffusive convection. The study is valid for $N=1$ and it neglected the effect of double dispersion which is most important in the non-Darcy mixed convection. A similarity solution has been presented in Murthy and Singh [3] for the free-convection heat and mass transfer in a Forchheimer porous medium.

The effect of solutal and thermal dispersion effects in homogeneous and isotropic Darcian porous media has been analyzed by Dagan [22]. A systematic derivation of the governing equations with various types of approximations used in applications has been presented. Using scale analysis arguments, Telles and Tre-

¹Present address: Department of Mathematics and Humanities, REC Warangal, A.P., 506 004, India. E-mail: pvsnm@recw.ernet.in

Contributed by the Heat Transfer Division for publication in the JOURNAL OF HEAT TRANSFER. Manuscript received by the Heat Transfer Division, April 20, 1999; revision received, January 18, 2000. Associate Technical Editor: C. Beckermann.

visan [23] analyzed the double-dispersion phenomenon in a free-convection boundary layer adjacent to a vertical wall in a Darcian fluid-saturated porous medium. Depending on the relative magnitude of the dispersion coefficients, four classes of flow were identified and the heat and mass transfer has been studied.

In the present paper, the effect of hydrodynamic dispersion on mixed convection heat and mass transfer near a vertical surface embedded in a porous medium has been analyzed under boundary layer approximations using the similarity solution technique. The mixed convective flow is promoted by the uniform freestream and density variations due to the combination of temperature and concentration gradients. The Forchheimer flow model is considered and the porous medium porosity is assumed to be low so that the boundary effects in the medium may be neglected. The heat and mass transfer in the boundary layer region has been analyzed for aiding and opposing buoyancies for both the aiding and opposing flows. The flow, temperature, and concentration fields in Darcy and non-Darcy porous media are observed to be governed by complex interactions among the diffusion rate (Le), buoyancy ratio (N), and Pe_γ and Pe_ζ , the dispersion thermal and solutal diffusivity parameters, in addition to the flow driving parameter Ra/Pe . Due to dispersion effects, heat transfer is enhanced whereas the mass transfer coefficient becomes less predictable.

2 Governing Equations

Mixed convection heat and mass transfer from the impermeable vertical flat wall in a fluid-saturated porous medium is considered for the study and the schematic is shown in Fig. 1 (reproduced from Lai [4]). The x -axis is taken along the plate and y -axis is normal to it. The wall is maintained at constant temperature and concentration, T_w and C_w , respectively, and these values are assumed to be greater than the ambient temperature and concentration, T_∞ and C_∞ , respectively. The governing equations for the boundary layer flow, heat, and mass transfer from the wall $y=0$ into the fluid-saturated porous medium $x \geq 0$ and $y > 0$ (after making use of the Boussinesq approximation) are given by

$$\frac{\partial u}{\partial y} + \frac{c\sqrt{K}}{\nu} \frac{\partial u^2}{\partial y} = \left(\frac{Kg\beta_T}{\nu}\right) \frac{\partial T}{\partial y} + \left(\frac{Kg\beta_c}{\nu}\right) \frac{\partial C}{\partial y} \quad (1)$$

$$u \frac{\partial T}{\partial x} + v \frac{\partial T}{\partial y} = \frac{\partial}{\partial y} \left(\alpha_e \frac{\partial T}{\partial y} \right) \quad (2)$$

$$u \frac{\partial C}{\partial x} + v \frac{\partial C}{\partial y} = \frac{\partial}{\partial y} \left(D_e \frac{\partial C}{\partial y} \right) \quad (3)$$

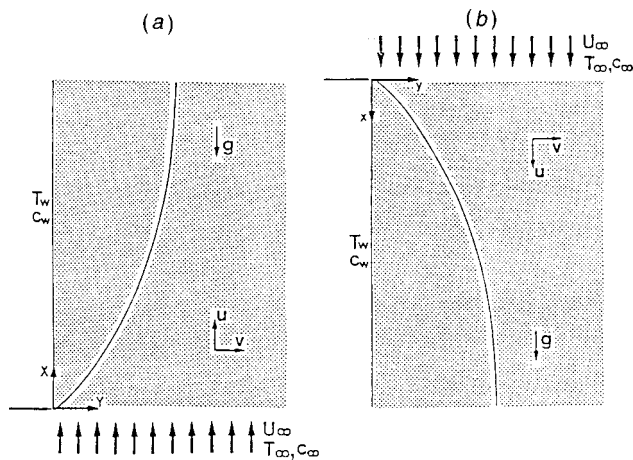


Fig. 1 Coupled heat and mass transfer by mixed convection from a vertical plate in a saturated porous medium (reproduced from Lai [4])

with the boundary conditions

$$\left. \begin{aligned} y=0: & \quad v=0, \quad T=T_w, \quad C=C_w \\ y \rightarrow \infty: & \quad u=U_\infty, \quad T=T_\infty, \quad C=C_\infty \end{aligned} \right\} \quad (4)$$

Here x and y are the Cartesian coordinates, u and v are the averaged velocity components in x and y -directions, respectively, T is the temperature, C is the concentration, β_T is the coefficient of thermal expansion, β_c is the coefficient of solutal expansion, ν is the kinematic viscosity of the fluid, K is the permeability, c is an empirical constant, g is the acceleration due to gravity, and α_e and D_e are the effective thermal and solutal diffusivities, respectively. The subscripts w and ∞ indicate the conditions at the wall and at the outer edge of the boundary layer, respectively.

Following Telles and Trevisan [23], the expressions for α_e and D_e can be written as $\alpha_e = \alpha + \gamma du$ and $D_e = D + \zeta du$, where α and D are the molecular thermal and solutal diffusivities, respectively, whereas γdu and ζdu represent dispersion thermal and solutal diffusivities, respectively. The above model for thermal dispersion has been used extensively by researchers like Plumb [11], Hong et al. [13], Hong and Tien [12], Lai and Kulacki [2,15], Murthy and Singh [18,19,24] in studies of convective heat transfer in non-Darcy porous media. For moderate and high Peclet number flows, a linear variation of the thermal and solutal dispersions with velocity has been proved to be reasonable, see, for example, Saffman [25] and Bear [9]. Similar representation for solutal dispersion can be seen in Dagan [22].

Making use of the following transformation

$$\eta = \frac{y}{x} Pe_x^{1/2}, \quad f(\eta) = \frac{\psi}{\alpha Pe_x^{1/2}}, \quad \theta(\eta) = \frac{T - T_\infty}{T_w - T_\infty},$$

$$\phi(\eta) = \frac{C - C_\infty}{C_w - C_\infty},$$

the governing Eqs. (1)–(3) become

$$f'' + 2F_o Pe f' f'' = \pm \frac{Ra}{Pe} [\theta' + N \phi'] \quad (5)$$

$$\theta'' + \frac{1}{2} f \theta' + Pe_\gamma (f' \theta'' + f'' \theta') = 0 \quad (6)$$

$$\phi'' + \frac{Le}{2} f \phi' + Le Pe_\zeta (f' \phi'' + f'' \phi') = 0 \quad (7)$$

and the boundary conditions (4) transform into

$$\left. \begin{aligned} \eta=0: & \quad f=0, \quad \theta=1, \quad \phi=1 \\ \eta \rightarrow \infty: & \quad f'=1, \quad \theta=0, \quad \phi=0 \end{aligned} \right\} \quad (8)$$

The important parameters involved in the present study are the local Peclet number $Pe_x = U_\infty x / \alpha$, the local Darcy-Rayleigh number $Ra_x = Kg\beta_T \theta_w x / \alpha \nu$, which is defined with reference to the temperature difference alone, $Pe = U_\infty d / \alpha$ and $Ra = Kg\beta_T \theta_w d / \alpha \nu$, are the pore diameter-dependent Peclet and Rayleigh numbers, respectively. The inertial parameter is $F_o Pe = (c\sqrt{K}\alpha/d\nu)(U_\infty d/\alpha) = c\sqrt{K}U_\infty/\nu$ (in the present study, $F_o Pe$ is varied as a single parameter), the buoyancy ratio is $N = \beta_c \phi_w / \beta_T \theta_w$, and the diffusivity ratio is $Le = \alpha/D$. The Lewis number is nothing but the ratio of the Schmidt number (ν/D) and Prandtl number (ν/α). The flow governing parameter is Ra/Pe and is independent of x . $Ra/Pe=0$ represents the forced convection flow. The flow asymptotically reaches the free convection flow limit as this parameter tends to ∞ . Pe_γ and Pe_ζ represent thermal and solutal dispersion parameters, respectively, and are defined here as $Pe_\gamma = \gamma U_\infty d / \alpha$ and $Pe_\zeta = \zeta U_\infty d / \alpha$. It is worth mentioning that the thermal dispersion parameter Pe_γ has been treated as γPe in the works of Lai and Kulacki [26] where the coefficients of thermal dispersion have been assigned values in the range 1/7 to 1/3. Researchers like Gorla et al. [17], Hong and Tien [12], and

Hong et al. [13], who worked extensively on thermal dispersion effects, treated them as a single parameter ($DS = \gamma Ra$), as the value of γ depends on the experiment. In the present investigation also, we consider the thermal and solutal dispersion parameters Pe_γ and Pe_ζ with γ and ζ included in the parameters. In Eq. (5), the positive and negative signs represent aiding and opposing flows, respectively. $N > 0$ indicates the aiding buoyancy and $N < 0$ indicates the opposing buoyancy.

3 Results and Discussion

The resulting ordinary differential Eqs. (5)–(7) are integrated by giving appropriate initial guess values for $f'(0)$, $\theta'(0)$, and $\phi'(0)$ to match the values with the corresponding boundary conditions at $f'(\infty)$, $\theta(\infty)$, and $\phi(\infty)$, respectively. NAG software (D02HAFE routine) is used for integrating the corresponding first-order system of equations and shooting and matching the initial and boundary conditions. The results are observed up to an accuracy of 5.0×10^{-6} . Extensive calculations have been performed to obtain the flow, temperature, and concentration fields for a wide range of parameters $0 \leq F_o Pe \leq 2$, $0 \leq Ra/Pe \leq 100$, $-1 < N \leq 4$, $0.01 \leq Le \leq 100$, $0 \leq Pe_\gamma \leq 5$, and $0 \leq Pe_\zeta \leq 5$. As an indication of proper formulation and accurate calculation, the results obtained here are compared with previously published analytical results.

With $F_o Pe = 0$, $Pe_\gamma = 0$, and $Pe_\zeta = 0$, the present problem reduces to heat and mass transfer by Darcian mixed convection in porous media analyzed by Lai [4]. By setting the parameters $N = 0$, $Le = 1$, and $Pe_\zeta = 0$, the problem reduces to that of non-Darcian mixed convection along a vertical wall in a saturated porous medium, which has been studied by Lai and Kulacki [15]. The comparison showed that the present results match exactly with the results presented in the above works. When N is comparable with -1 , the temperature and concentration buoyancy effects are of the same order of magnitude and in opposing directions. Due to this, the resulting flow does not have the parallel double boundary layer structure. Contrary to what has been reported by Bejan and Khair [1], Lai and Kulacki [2] and Murthy and Singh [3] found similarity solutions for $Le = 1$ and $-1 < N < 0$, and the solutions in the range of $N < -1$ are impossible. These contradictions are resolved clearly in Lai and Kulacki [2]. In fact, the results presented below uncover some interesting facts regarding the flow field in the boundary layer, heat, and mass transfer coefficients.

3.1 Aiding Flow. When buoyancy is aiding the flow, for $N > 0$ (aiding buoyancy case) the tangential velocity evolves from nonzero wall velocity to uniform freestream velocity for all values of $Le > 0$. In the case of opposing buoyancy ($N < 0$), when $Le > 1$, the flow field follows the same pattern. But when $0 < Le < 1$, a distinct feature is observed. The vertical component of velocity attains negative values near the wall and well inside the boundary layer. Far from the wall it attains its outer edge boundary condition. This may be explained as follows. When $N < 0$ the downward species buoyancy overpowers the upward thermal buoyancy and $Le < 1$ results in larger solutal diffusion than the thermal diffusion. The favorable action of Ra/Pe to the flow field is countered by the opposing buoyancy ($N < 0$) and also by the higher solutal diffusivity ($Le < 1$). The flow reversal is seen when the later effects dominate the flow favoring mixed convection parameter. This phenomena is clearly seen in Figs. 2 and 3. In these figures the tangential velocity component is plotted against similarity variable for $-1 < N < 0$ and $0 < Le < 1$.

The Ra/Pe values indicated in the figures correspond to the minimum Ra/Pe for which flow reversal occurred under the fixed values of other parameters. For fixed Le , this value of Ra/Pe increases with the decrease in the value of the buoyancy ratio. For fixed value of buoyancy ratio N , this value of Ra/Pe increases with the increase in the value of the diffusion ratio Le . This phenomena is seen in both Darcy and non-Darcy mixed convection flows. It is

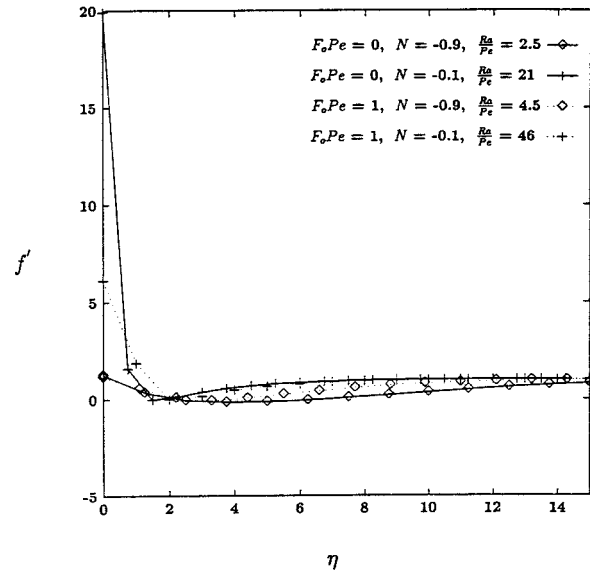


Fig. 2 Nondimensional velocity profiles $f'(\eta)$ for $-1 < N < 0$, $Le = 0.1$ (aiding flow)

also clear from both these figures that the inertial effects delay the occurrence of this phenomena. The work by Lai [4] did not reveal this phenomenon; recently Angirasa et al. [5] noticed flow reversal for $N = -0.5$ and -1.5 when $Le < 1$ in their study of free-convection heat and mass transfer in a fluid-saturated porous enclosure. They observed this phenomenon at large values of the flow-governing Rayleigh number. Mahajan and Angirasa [27] reported similar observations in connection with free-convection heat and mass transfer in the case of opposing buoyancies in clear fluids also.

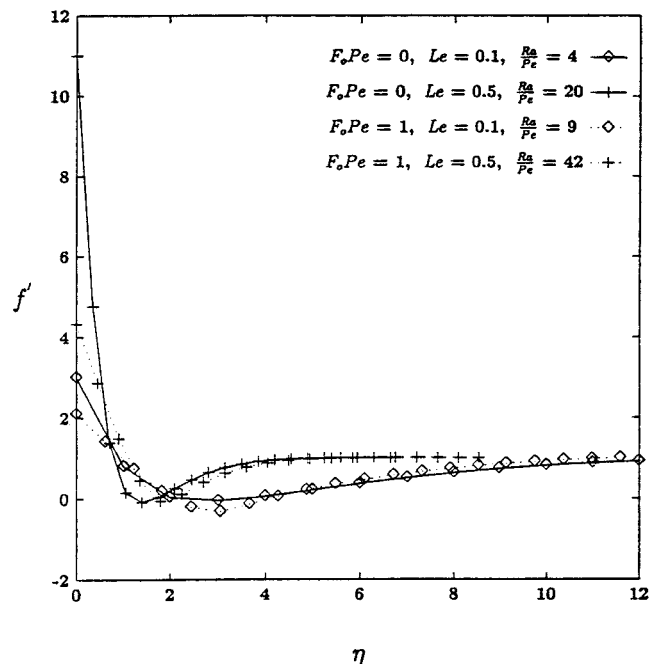


Fig. 3 Nondimensional velocity profiles $f'(\eta)$ for $0 < Le < 1$, $N = -0.5$ (aiding flow)

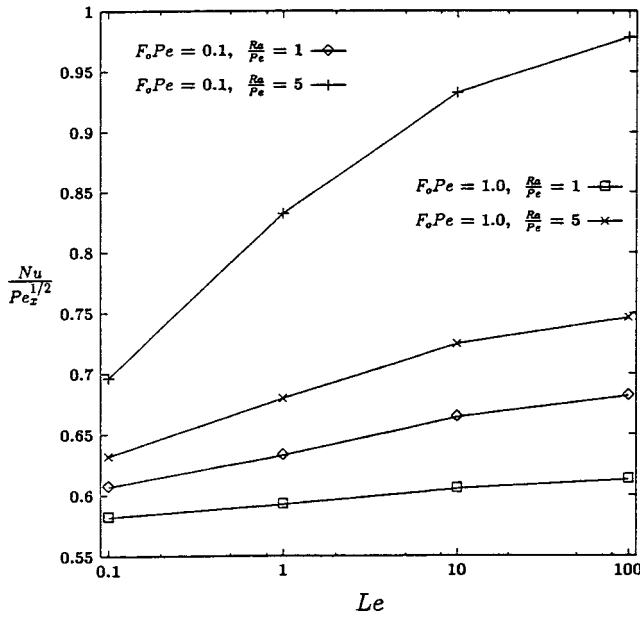


Fig. 4 Heat transfer coefficient as a function of Lewis number when $N < 0$. Here $N = -0.5$, $Pe_\gamma = 0 = Pe_\zeta$ (aiding flow).

Now the heat and mass transfer coefficients, in terms of the Nusselt and Sherwood numbers in the presence of thermal and solutal dispersion diffusivities, can be written as

$$\frac{Nu}{Pe_x^{1/2}} = -[1 + Pe_\gamma f'(0)]\theta'(0), \quad (9)$$

$$\frac{Sh}{Pe_x^{1/2}} = -[1 + Pe_\zeta f'(0)]\phi'(0). \quad (10)$$

With $F_oPe = 0$, $Pe_\gamma = 0$, and $Pe_\zeta = 0$, the observations made here are consistent with those reported by Lai [4]. It is observed that for $Le > 1$, the heat transfer coefficient increases for $N < 0$ and it decreases for $N > 0$. For $Le < 1$, the situation is reversed. For Pe_γ

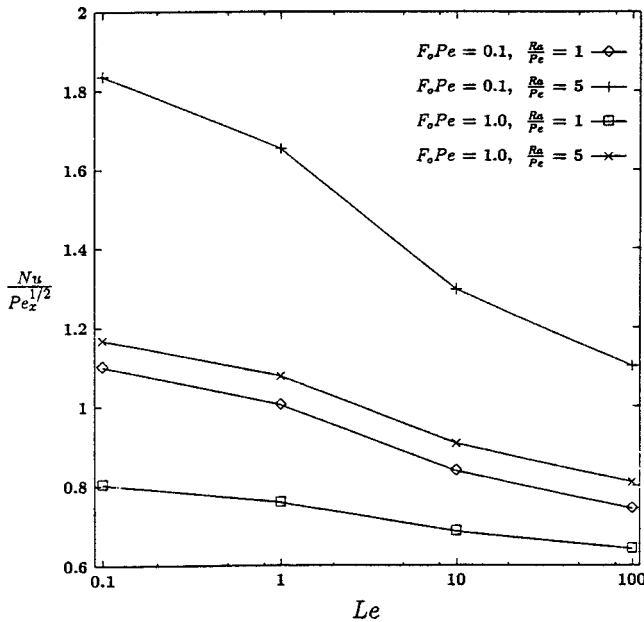


Fig. 5 Heat transfer coefficient as a function of Lewis number when $N > 0$. Here, $N = 4.0$, $Pe_\gamma = 0 = Pe_\zeta$ (aiding flow).

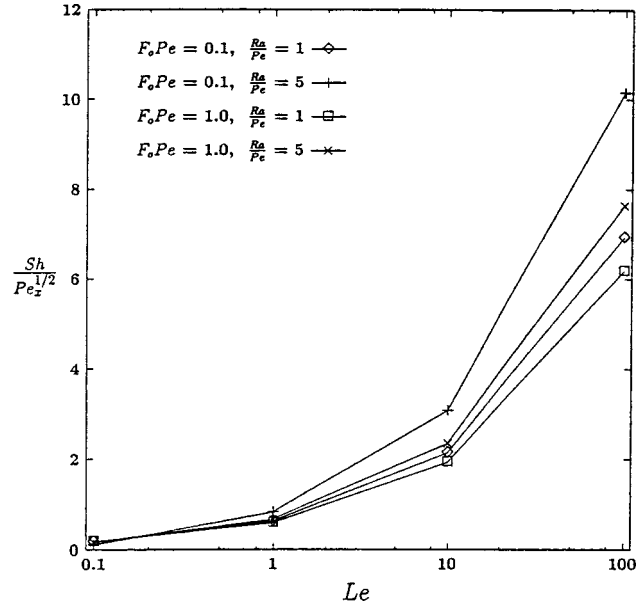


Fig. 6 Mass transfer coefficient as a function of Lewis number when $N < 0$. Here $N = -0.5$, $Pe_\gamma = 0 = Pe_\zeta$ (aiding flow).

$= 0$ and $Pe_\zeta = 0$, the Eqs. (9) and (10) reduce to $Nu/Pe_x^{1/2} = -\theta'(0)$ and $Sh/Pe_x^{1/2} = -\phi'(0)$. The effect of diffusivity ratio and the buoyancy ratio on heat and mass transfer coefficients is plotted in Figs. 4–7 for two values of inertial parameter $F_oPe = 0.1$ (near Darcy-region) and $F_oPe = 1.0$ (non-Darcy region). The inertial effects always decrease the heat and mass transfer coefficients in both opposing and aiding buoyancies. The increase in the value of the mixed convection parameter increases the heat and mass transfer rates. It is clearly seen from these figures that the convection favoring effect of Ra/Pe is countered by the microscopic drag due to the increase in the inertial parameter. The heat transfer coefficient is observed to increase with the diffusivity ratio in the opposing buoyancy case whereas it decreases in the aiding buoyancy case. This is clearly seen from

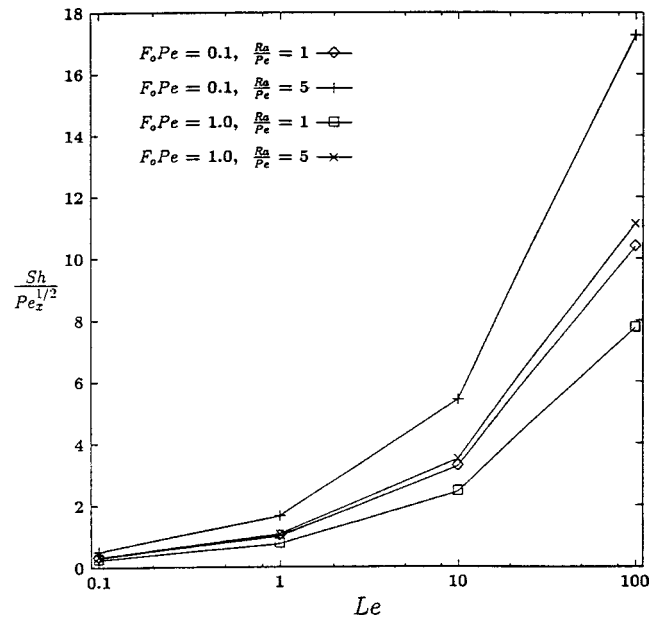


Fig. 7 Mass transfer coefficient as a function of Lewis number when $N > 0$. Here, $N = 4.0$, $Pe_\gamma = 0 = Pe_\zeta$ (aiding flow).

Table 1 $-\theta'(0)$ for $N=-0.5$, $F_oPe=1.0$ and $Pe_z=0$

| Ra/Pe | $f'(0)$ | Le=1 | | | Le=10 | | |
|-------|---------|---------------|---------------|---------------|---------------|---------------|---------------|
| | | $Pe_\gamma=0$ | $Pe_\gamma=1$ | $Pe_\gamma=5$ | $Pe_\gamma=0$ | $Pe_\gamma=1$ | $Pe_\gamma=5$ |
| 0 | 1.0 | 0.5642 | 0.3989 | 0.2303 | 0.5642 | 0.3989 | 0.2303 |
| 1 | 1.1583 | 0.5922 | 0.4027 | 0.2305 | 0.6054 | 0.4151 | 0.2368 |
| 5 | 1.6794 | 0.6793 | 0.4186 | 0.2354 | 0.7244 | 0.4544 | 0.2500 |
| 10 | 2.1926 | 0.7580 | 0.4344 | 0.2405 | 0.8247 | 0.4801 | 0.2568 |
| 20 | 3.0 | 0.8706 | 0.4557 | 0.2465 | 0.9617 | 0.5069 | 0.2627 |
| 50 | 4.7262 | 1.0768 | 0.4870 | 0.2541 | 1.203 | 0.5387 | 0.2684 |
| 100 | 6.7284 | 1.2797 | 0.5096 | 0.2588 | 1.4347 | 0.5581 | 0.2713 |

Table 2 $-\theta'(0)$ for $N=1.0$, $F_oPe=1.0$ and $Pe_z=0$

| Ra/Pe | $f'(0)$ | Le=1 | | | Le=10 | | |
|-------|---------|---------------|---------------|---------------|---------------|---------------|---------------|
| | | $Pe_\gamma=0$ | $Pe_\gamma=1$ | $Pe_\gamma=5$ | $Pe_\gamma=0$ | $Pe_\gamma=1$ | $Pe_\gamma=5$ |
| 0 | 1.0 | 0.5642 | 0.3989 | 0.2303 | 0.5642 | 0.3989 | 0.2303 |
| 1 | 1.5616 | 0.6603 | 0.3892 | 0.1984 | 0.6377 | 0.3706 | 0.1901 |
| 5 | 3.0 | 0.8706 | 0.3771 | 0.1695 | 0.8083 | 0.3411 | 0.1576 |
| 10 | 4.217 | 1.0203 | 0.3714 | 0.1609 | 0.9358 | 0.3323 | 0.1494 |
| 20 | 6.0 | 1.2097 | 0.3657 | 0.1552 | 1.1012 | 0.3269 | 0.1449 |
| 50 | 9.6119 | 1.5295 | 0.3585 | 0.1507 | 1.3837 | 0.3234 | 0.1423 |
| 100 | 13.7215 | 1.8237 | 0.3535 | 0.1488 | 1.6492 | 0.3221 | 0.1415 |

Figs. 4 and 5. For fixed values of other parameters, the magnitude of $Nu/Pe_x^{1/2}$ for $N>0$ is higher than that for $N<0$ for all values of Le considered in the study. This clearly indicates that the buoyancy ratio has significant effect on the heat transfer coefficient than the diffusivity ratio. Figures 6 and 7 clearly indicate the favorable effect of the Lewis number on the mass transfer coefficient in both opposing and aiding buoyancies. Uniform trend in the Sherwood number results is observed with increase in the buoyancy ratio N from -1 to 4 .

The variation of the heat transfer coefficient with Ra/Pe for nonzero values of Pe_γ is studied for a wide range of values of Le . The effect of thermal dispersion on the heat transfer is studied keeping $Pe_z=0$. Consistent with the results presented in Lai and Kulacki [15] and Hong and Tien [12], the value of $-\theta'(0)$ decreases as the thermal dispersion coefficient Pe_γ increases. Also

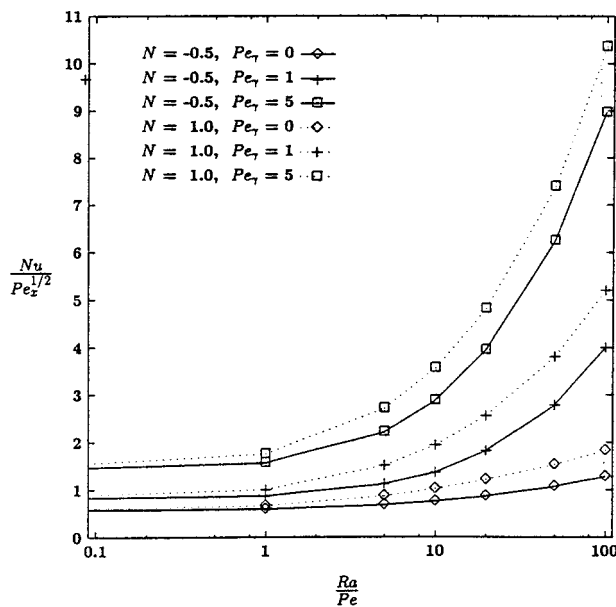


Fig. 8 Heat transfer coefficient as a function of Ra/Pe when $F_oPe=1.0$, $Le=1.0$, $Pe_z=0$ (aiding flow)

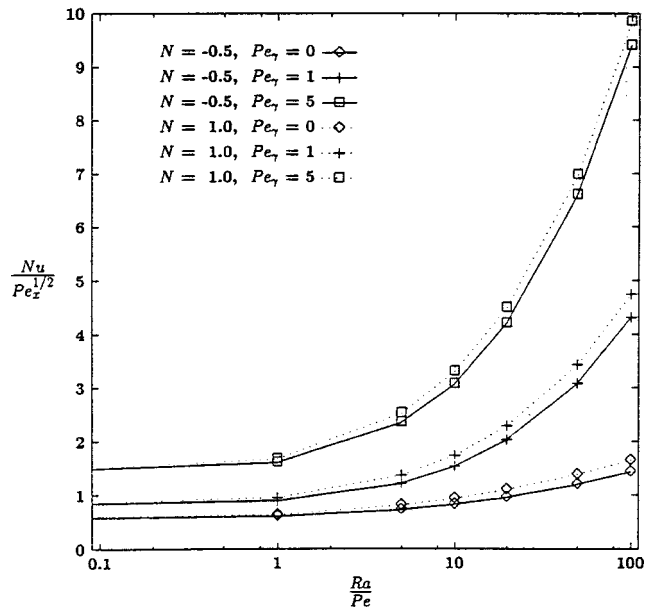


Fig. 9 Heat transfer coefficient as a function of Ra/Pe when $F_oPe=1.0$, $Le=10.0$, $Pe_z=0$ (aiding flow)

for large Pe_γ , in a very small region near the wall, the temperature gradient is greatly increased and as a result heat transfer is greatly enhanced due to thermal dispersion. The wall temperature gradient values for $F_oPe=1$, for two values of $N=-0.5$ and 1.0 are presented in Tables 1–2. The value of $f'(0)$ is dependent on F_oPe and this is evident from the previous studies as well. From these two tables, it is also clear that $f'(0)$ depends on the buoyancy ratio N . The heat transfer coefficient written in terms of the Nusselt number using Eq. (9) is calculated from the values of $-\theta'(0)$ for the nonzero dispersion coefficient and is plotted in Figs. 8–9 for $Le=1.0$ and 10.0 , respectively. Figures clearly indicate the favorable influence of thermal dispersion on the heat transfer results. The $Nu/Pe_x^{1/2}$ value increases with increasing Ra/Pe . Aiding buoyancy favors the heat transfer, whereas this favorable action is aided by increasing the value of Le when $N<0$ and is suppressed by an increase in the value of Le when $N>0$. This is evident from the Figs. 8–9. These results are in agreement with the results reported by Lai [4].

The effect of solutal dispersion on the mass transfer coefficient has been analyzed keeping $Pe_\gamma=0$. The values of $-\phi'(0)$ have been tabulated for $F_oPe=1$ and for two values of $N=-0.5$ and 1.0 in Tables 3–4. Analogous to the pure thermal convection process, the value of $-\phi'(0)$ decreases with increasing values of Pe_z . Interestingly, at large Pe_z , for large values of Ra/Pe , in a relatively large region (larger than that observed for thermal gradients) near the wall, the concentration gradient is greatly increased. But, against this expectation, peculiar behavior in the mass transfer coefficient is observed. The imbalance between the

Table 3 $-\phi'(0)$ for $N=-0.5$, $F_oPe=1.0$ and $Pe_\gamma=0$

| Ra/Pe | $f'(0)$ | Le=1 | | | Le=10 | | |
|-------|---------|---------------|---------------|---------------|---------------|---------------|---------------|
| | | $Pe_\gamma=0$ | $Pe_\gamma=1$ | $Pe_\gamma=5$ | $Pe_\gamma=0$ | $Pe_\gamma=1$ | $Pe_\gamma=5$ |
| 0 | 1.0 | 0.5642 | 0.3989 | 0.2303 | 1.7841 | 0.5379 | 0.2498 |
| 1 | 1.1583 | 0.5922 | 0.3888 | 0.2062 | 1.9329 | 0.512 | 0.2208 |
| 5 | 1.6794 | 0.6793 | 0.3555 | 0.1463 | 2.3534 | 0.4463 | 0.1534 |
| 10 | 2.1926 | 0.758 | 0.3258 | 0.105 | 2.7009 | 0.3992 | 0.1109 |
| 20 | 3.0 | 0.8706 | 0.2835 | 0.0716 | 3.1686 | 0.3441 | 0.0769 |
| 50 | 4.7262 | 1.0768 | 0.219 | 0.0483 | 3.9815 | 0.2678 | 0.0515 |
| 100 | 6.7284 | 1.2797 | 0.1801 | 0.0383 | 4.7585 | 0.2168 | 0.0403 |

Table 4 $-\phi'(0)$ for $N=1.0$, $F_oPe=1.0$ and $Pe_\gamma=0$

| Ra/Pe | $f'(0)$ | Le=1 | | | Le=10 | | |
|-------|---------|---------------|---------------|---------------|---------------|---------------|---------------|
| | | $Pe_\gamma=0$ | $Pe_\gamma=1$ | $Pe_\gamma=5$ | $Pe_\gamma=0$ | $Pe_\gamma=1$ | $Pe_\gamma=5$ |
| 0 | 1.0 | 0.5642 | 0.3989 | 0.2303 | 1.7841 | 0.5379 | 0.2498 |
| 1 | 1.5616 | 0.6603 | 0.3892 | 0.1984 | 2.1381 | 0.4773 | 0.2078 |
| 5 | 3.0 | 0.8706 | 0.3771 | 0.1695 | 2.8864 | 0.4215 | 0.1728 |
| 10 | 4.217 | 1.0203 | 0.3714 | 0.1609 | 3.4061 | 0.4018 | 0.1629 |
| 20 | 6.0 | 1.2097 | 0.3657 | 0.1552 | 4.0548 | 0.3858 | 0.1564 |
| 50 | 9.6119 | 1.5295 | 0.3585 | 0.1507 | 5.1295 | 0.3698 | 0.1514 |
| 100 | 13.7215 | 1.8237 | 0.3535 | 0.1488 | 6.1278 | 0.3607 | 0.1492 |

Lewis number and buoyancy parameter influence more against the enhancement of mass transfer results. For $Pe_\zeta=0$, the value of $-\phi'(0)$ increases with increasing values of Ra/Pe for all values of Le and N. For large Pe_ζ , the value of $-\phi'(0)$ decreases rapidly to near zero values with increasing Ra/Pe.

The mass transfer results are not straightforward for analysis. The complex interaction between Le, N, Pe_ζ , and Ra/Pe show complex behavior for $Sh/Pe_x^{1/2}$ curves. The results presented in the Figs. 10 and 11 are for Le=1 and 10 with $F_oPe=1$ and $Pe_\gamma=0$. In the case of aiding buoyancy, when Le=1, the mass transfer coefficient increases with Ra/Pe and the dispersion mechanism augments the mass transfer. In fact, these curves are same as the curves presented for $N=1.0$ in Fig. 8 (see the Eqs. (5)–(7) with Le=1). But this is not the case in the opposing buoyancy. When $N < 0$ and Le=1, $Sh/Pe_x^{1/2}$ increases with Ra/Pe for $Pe_\zeta=0$ and $Pe_\zeta=1$. When $Pe_\zeta=5$, it increases with Ra/Pe up to the value 5 and then decreases thereafter. Its value becomes less than the corresponding value for $Pe_\zeta=1$ from Ra/Pe=20 onwards; it may be inferred that the strength of the solutal dispersion becomes insignificant at higher values of Ra/Pe in the case of opposing buoyancy.

Unlike when Le=1, for Le>1, even for $N > 0$, there is no clear pattern for the mass transfer results. From Fig. 11 it can be observed that the curve for $Pe_\zeta=1$ is always at a lower level than that for $Pe_\zeta=0$. Also, the curve for $Pe_\zeta=5$ is at a lower level up to Ra/Pe=5 and from that point onwards the $Sh/Pe_x^{1/2}$ values are greater than the corresponding values of that for $Pe_\zeta=0$. This shows clearly that in the aiding buoyancy case, for moderate to

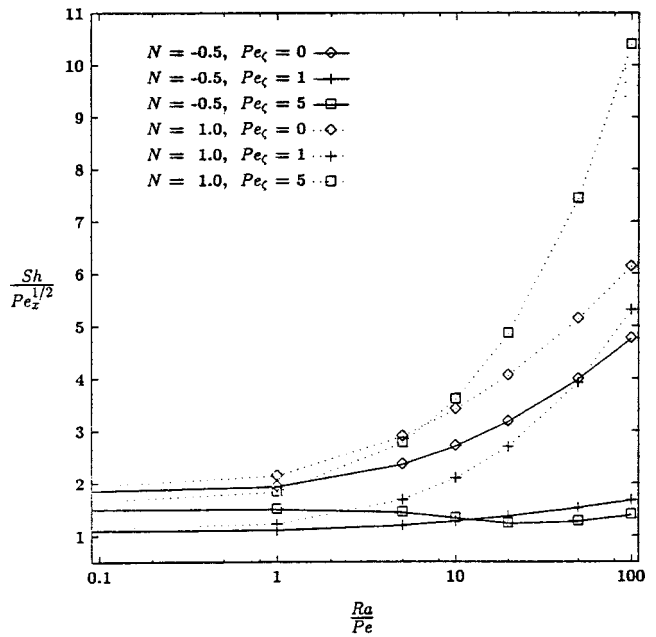


Fig. 11 Mass transfer coefficient as a function of Ra/Pe when $F_oPe=1.0$, $Le=10.0$, $Pe_\gamma=0$ (aiding flow)

large values of Le, the effect of the dispersion parameter is not favorable for the mass transfer up to a certain low value of Ra/Pe. Also, there exists a critical value of Ra/Pe after which the dispersion effects are significant in the mass transfer mechanism. With Le=10 and $N < 0$, the $Sh/Pe_x^{1/2}$ curve for $Pe_\zeta=0$ is always at a higher level than that for $Pe_\zeta=1$ and 5. This shows that as the value of the Lewis number increases, the dispersion effects reduce the mass transfer rate at moderate and higher values of Ra/Pe in the opposing buoyancy. Thus the complex interactions between F_oPe , Le, N, Ra/Pe and the pair Pe_γ and Pe_ζ prevent us from making any general statement about the mass transfer mechanism.

3.2 Opposing Flow. The flow field becomes more complex when the freestream flow is opposing the buoyancy. Like in the

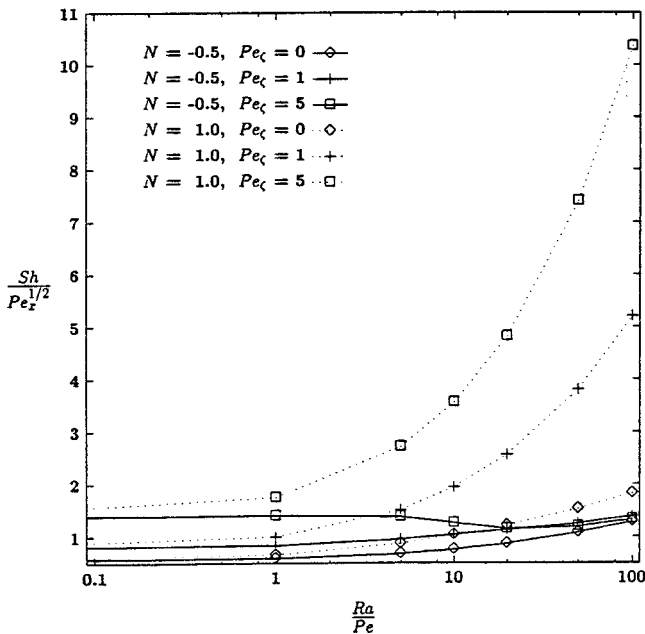


Fig. 10 Mass transfer coefficient as a function of Ra/Pe when $F_oPe=1.0$, $Le=1.0$, $Pe_\gamma=0$ (aiding flow)

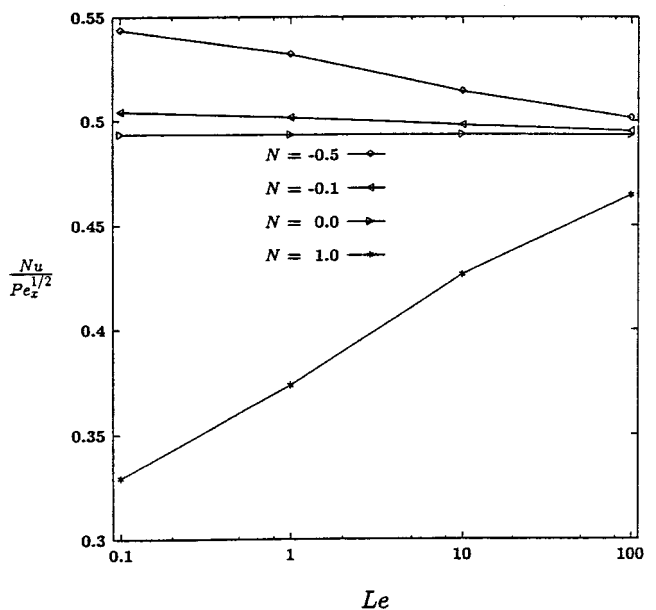


Fig. 12 Heat transfer coefficient as a function of Le for various values of N when $Pe_\gamma=0=Pe_\zeta$, $Ra/Pe=1.0$, $F_oPe=1.0$ (opposing flow)

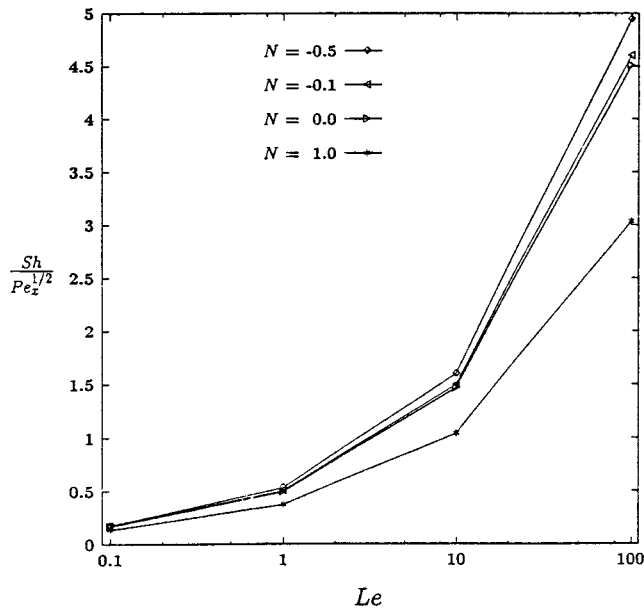


Fig. 13 Mass transfer coefficient as a function of Le for various values of N when $Pe_\gamma=0=Pe_\zeta$, $Ra/Pe=1.0$, $F_oPe=1.0$ (opposing flow)

aiding flow case, the wall velocity depends only on the inertial parameter and the buoyancy ratio. It is independent on the Lewis number. Flow separation is the most common feature observed in the opposing flows. The flow separation point also depends on the buoyancy ratio. In the absence of thermal and solutal dispersion effects, the separation point in the Darcy flow ($F_oPe=0$) is seen to occur at $Ra/Pe=2.0, 1.1, 1, 0.5$ for $N=-0.5, -0.1, 0, 1.0$, respectively. In the Forchheimer flow ($F_oPe=1.0$) the occurrence of the flow separation is delayed, the separation points are observed to occur at $Ra/Pe=4.0, 2.3, 2.0, 1.0$ for $N=-0.5, -0.1, 0, 1.0$, respectively. The presence of thermal and solutal dispersion

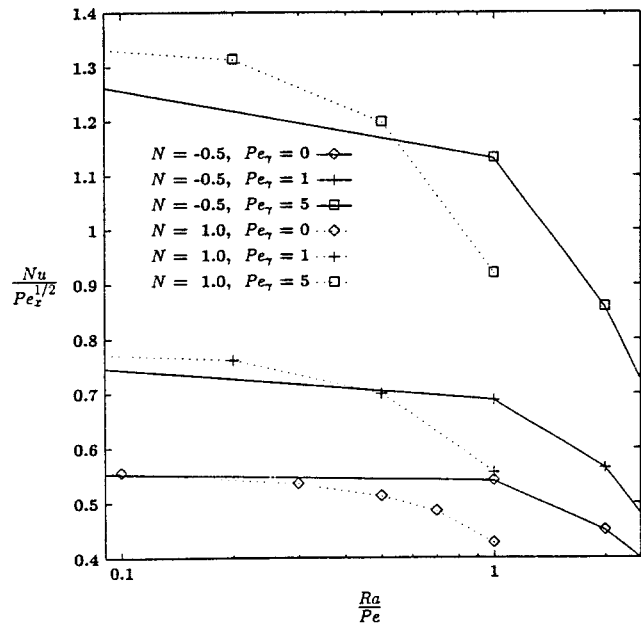


Fig. 15 Heat transfer coefficient as a function of Ra/Pe in the presence of thermal dispersion effects in non-Darcy flow. Here $F_oPe=1.0$, $Le=10.0$, $Pe_\zeta=0$ (opposing flow).

diffusivity will not alter the point of flow separation in both Darcy and non-Darcy flows.

The heat and mass transfer coefficients in opposing flow are presented in Figs. 12–17. As expected, the heat transfer decreases with Le for opposing buoyancy, whereas it increases with Le for aiding buoyancy. It is just a reverse mechanism to the aiding flow case and is clearly seen in Fig. 12. The $Nu/Pe_x^{1/2}$ values for the opposing buoyancy are at higher level than those for aiding buoyancy. It is evident from the Fig. 13 that the mass transfer coefficient increases with Le here also, the $Sh/Pe_x^{1/2}$ values in opposing buoyancy are at higher level than those in aiding buoyancy. Aid-

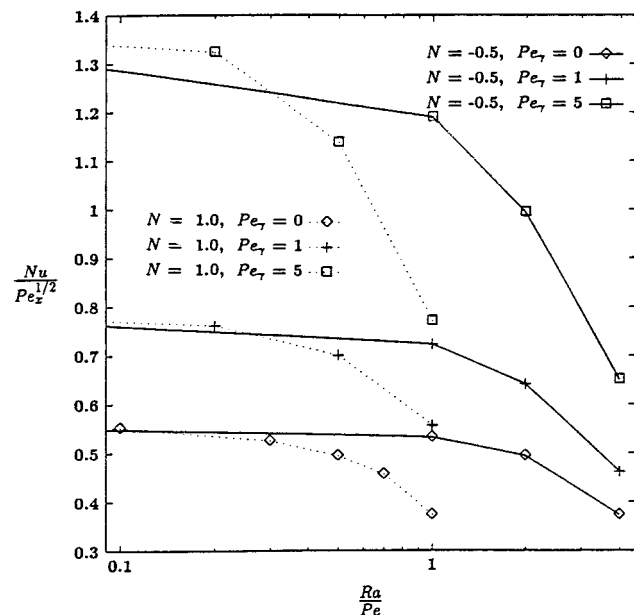


Fig. 14 Heat transfer coefficient as a function of Ra/Pe in the presence of thermal dispersion effects in non-Darcy flow. Here $F_oPe=1.0$, $Le=1.0$, $Pe_\zeta=0$ (opposing flow).

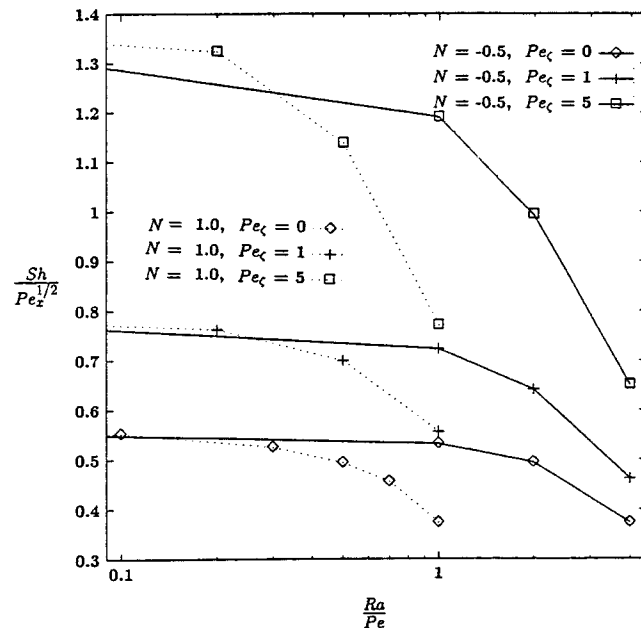


Fig. 16 Mass transfer coefficient as a function of Ra/Pe in the presence of solutal dispersion effects in non-Darcy flow. Here $F_oPe=1.0$, $Le=1.0$, $Pe_\gamma=0$ (opposing flow).

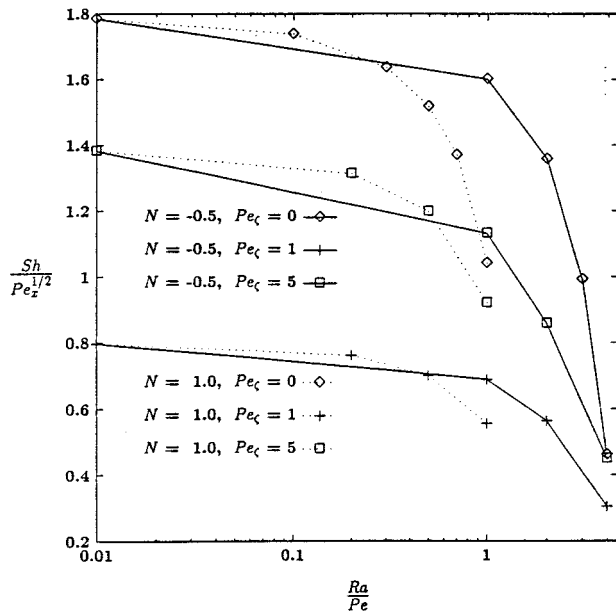


Fig. 17 Mass transfer coefficient as a function of Ra/Pe in the presence of solutal dispersion effects in non-Darcy flow. Here $F_oPe=1.0$, $Le=10.0$, $Pe_\gamma=0$ (opposing flow).

ing buoyancy is hindrance to the free stream flow in the opposing flow case, so a reduction in the transport quantities is observed.

The variation of $Nu/Pe_x^{1/2}$ with Ra/Pe in the opposing flow is plotted in Figs. 14–15 with $F_oPe=1$ for different values of N and Pe_γ . Thermal dispersion enhances the heat transfer rate in both $N>0$ and $N<0$ for all values of $Le>0$. Interestingly, for fixed Le , and nonzero Pe_γ , there exists one critical value of Ra/Pe before which the $Nu/Pe_x^{1/2}$ for $N=1.0$ is more than that for $N=-0.5$ and after which its reverse is seen. These arguments are evident from Figs. 14–15.

The $Sh/Pe_x^{1/2}$ is plotted against Ra/Pe for $F_oPe=1$ and for six combinations of Pe_ζ and N in Figs. 16–17. Here also, the mass transfer coefficient decreases with Ra/Pe , the dispersion effect enhances the mass transfer, and the existence of critical Ra/Pe for which the dual behavior of the mass transfer coefficient is observed. In the opposing flow also, the complex interactions between these parameters do not permit a clear pattern for the heat and mass transfer results.

Conclusions

Similarity solution for hydrodynamic dispersion in mixed convection heat and mass transfer near vertical surface embedded in a porous medium has been presented. The heat and mass transfer in the boundary layer region has been analyzed for aiding and opposing buoyancies in both the aiding and opposing flows. The structure of the flow, temperature, and concentration fields in the Darcy and non-Darcy porous media are governed by complex interactions among the diffusion rates (Le) and buoyancy ratio (N) in addition to the flow driving parameter (Ra/Pe). Extensive calculations for a wide range of these parameters are performed. For small values of Le in the opposing buoyancy, flow reversal near the wall is observed. The heat transfer coefficient always increases with Ra/Pe . Thermal dispersion favors the heat transfer. As Le increases, the effect of solutal dispersion on the nondimensional mass transfer coefficient becomes less predictable in both aiding and opposing buoyancies. In the opposing flow case, the flow separation point is observed to depend on the inertial parameter and buoyancy ratio. A reduction in the heat and mass transfer

coefficients is seen with increasing values of Ra/Pe . Here also the Lewis number has complex impact on the heat and mass transfer mechanism.

Acknowledgments

My sincere thanks to the reviewers for their encouraging comments and constructive suggestions to improve the manuscript. I thank Prof. A. Avudainayagam, Department of Mathematics, IIT–Madras for his constant encouragement and support during my post-doctoral research. I sincerely acknowledge the CSIR (INDIA) for its financial support in carrying out this research.

Nomenclature

- c = inertial coefficient
- C = concentration
- d = pore diameter
- D = mass diffusivity
- D_e = effective mass diffusivity
- f = nondimensional stream function
- $F_oPe = c\sqrt{K}U_\infty/\nu$, parameter representing non-Darcian effects
- g = acceleration due to gravity
- K = permeability
- $Le = \alpha/D$, Lewis number
- $N = \beta_C\phi_w/\beta_T\theta_w$, buoyancy ratio
- $Nu/Pe_x^{1/2}$ = nondimensional heat transfer coefficient; ref Eq. (9)
- $Sh/Pe_x^{1/2}$ = nondimensional mass transfer coefficient; ref Eq. (10)
- Pe_x = local Peclet number $u_\infty x/\alpha$
- $Pe = u_\infty d/\alpha$
- $Pe_\gamma = \gamma U_\infty d/\alpha$, parameter representing thermal dispersion effects
- $Pe_\zeta = \zeta U_\infty d/\alpha$, parameter representing solutal dispersion effects
- Ra_x = modified Rayleigh number, $Kg\beta_T\theta_w x/\alpha\nu$
- $Ra = Kg\beta_T\theta_w d/\alpha\nu$
- T = temperature
- u, v = velocity components in x and y -directions, respectively
- x, y = Cartesian coordinates

Greek Symbols

- α = molecular thermal diffusivity
- α_e = effective thermal diffusivity
- β_T = thermal expansion coefficient
- β_C = solutal expansion coefficient
- η = similarity variable
- ν = kinematic viscosity
- ψ = stream function
- θ = nondimensional temperature
- ϕ = nondimensional concentration
- γ = coefficient of dispersion thermal diffusivity
- ζ = coefficient of dispersion solutal diffusivity

Subscripts

- w = evaluated at wall
- ∞ = evaluated at the outer edge of the boundary layer

References

- [1] Bejan, A., and Khair, K. R., 1985, "Heat and Mass Transfer by Natural Convection in a Porous Medium," *Int. J. Heat Mass Transf.*, **28**, pp. 909–918.
- [2] Lai, F. C., and Kulacki, F. A., 1991a, "Coupled Heat and Mass Transfer by Natural Convection From Vertical Surfaces in Porous Media," *Int. J. Heat Mass Transf.*, **34**, pp. 1189–1194.
- [3] Murthy, P. V. S. N., and Singh, P., 1998, "Heat and Mass Transfer by Natural Convection in a Non-Darcy Porous Medium," *Acta Mech.*, accepted for publication.
- [4] Lai, F. C., 1991, "Coupled Heat and Mass Transfer by Mixed Convection From a Vertical Plate in a Saturated Porous Medium," *Int. Commun. Heat Mass Transfer*, **18**, pp. 93–106.

- [5] Angirasa, D., Peterson, G. P., and Pop, I., 1997, "Combined Heat and Mass Transfer by Natural Convection With Opposing Buoyancy Effects in a Fluid Saturated Porous Medium," *Int. J. Heat Mass Transf.*, **40**, pp. 2755–2773.
- [6] Vafai, K., and Tien, C. L., 1981, "Boundary and Inertia Effects on Flow and Heat Transfer in Porous Media," *Int. J. Heat Mass Transf.*, **24**, pp. 195–203.
- [7] Vafai, K., and Tien, C. L., 1982, "Boundary and Inertia Effects on Convective Mass Transfer in Porous Media," *Int. J. Heat Mass Transf.*, **25**, pp. 1183–1190.
- [8] Whitaker, S., 1997, "The Forchheimer Equation: A Theoretical Development," *Transp. Porous Media*, **25**, pp. 27–61.
- [9] Bear, J., 1972, *Dynamics of Fluids in Porous Media*, Elsevier, New York.
- [10] Kvernfold, O., and Tyvand, P., 1980, "Dispersion Effect on Thermal Convection in Porous Media," *J. Fluid Mech.*, **99**, pp. 673–686.
- [11] Plumb, O. A., 1981, "The Effect of Thermal Dispersion on Heat Transfer in Packed Bed Boundary Layers," *ASME-JSME Joint Thermal Conference Proceedings*, Vol. 2, ASME, New York, pp. 17–21.
- [12] Hong, J. T., and Tien, C. L., 1987, "Analysis of Thermal Dispersion Effect on Vertical Plate Natural Convection in Porous Media," *Int. J. Heat Mass Transf.*, **30**, pp. 143–150.
- [13] Hong, J. T., Yamada, Y., and Tien, C. L., 1987, "Effect of Non-Darcian and Non-Uniform Porosity on Vertical Plate Natural Convection in Porous Media," *ASME J. Heat Transfer*, **109**, pp. 356–362.
- [14] Cheng, P., and Vortmeyer, D., 1988, "Transverse Thermal Dispersion and Wall Channeling in a Packed Bed With Forced Convection Flow," *Chem. Eng. Sci.*, **43**, pp. 2523–2532.
- [15] Lai, F. C., and Kulacki, F. A., 1991b, "Non-Darcy Mixed Convection Along a Vertical Wall in Saturated Porous Medium," *ASME J. Heat Transfer*, **113**, pp. 252–255.
- [16] Amiri, A., and Vafai, K., 1994, "Analysis of Dispersion Effects and Non-Thermal Equilibrium, Non-Darcian, Variable Porosity Incompressible Flow Through Porous Media," *Int. J. Heat Mass Transf.*, **37**, pp. 936–954.
- [17] Gorla, R. S. R., Bakier, A. Y., and Byrd, L., 1996, "Effects of Thermal Dispersion and Stratification on Combined Convection on a Vertical Surface Embedded in a Porous Medium," *Transp. Porous Media*, **25**, pp. 275–282.
- [18] Murthy, P. V. S. N., and Singh, P., 1997, "Effect of Viscous Dissipation on a Non-Darcy Natural Convection Regime," *Int. J. Heat Mass Transf.*, **40**, pp. 1251–1260.
- [19] Murthy, P. V. S. N., and Singh, P., 1997, "Thermal Dispersion Effects on Non-Darcy Natural Convection Over Horizontal Plate With Surface Mass Flux," *Arch. Appl. Mech.*, **67**, pp. 487–495.
- [20] Nield, D. A., and Bejan, A., 1992, *Convection in Porous Media*, Springer-Verlag, New York.
- [21] Karimi-Fard, M., Charrier-Mojtabi, M. C., and Vafai, K., 1997, "Non-Darcian Effects on Double-Diffusive Convection Within a Porous Medium," *Numer. Heat Transfer, Part A*, **31**, pp. 837–852.
- [22] Dagan, G., 1972, "Some Aspects of Heat and Mass Transport in Porous Media," *Developments in Soil Science: Fundamentals of Transport Phenomena in Porous Media*, International Association for Hydraulic Research, Elsevier, London, pp. 55–63.
- [23] Telles, R. S., and Trevisan, O. V., 1993, "Dispersion in Heat and Mass Transfer Natural Convection Along Vertical Boundaries in Porous Media," *Int. J. Heat Mass Transf.*, **36**, pp. 1357–1365.
- [24] Murthy, P. V. S. N., and Singh, P., 1997, "Thermal Dispersion Effects on Non-Darcy Natural Convection With Lateral Mass Flux," *Heat Mass Transfer*, **33**, pp. 1–5.
- [25] Saffman, P. G., 1960, "Dispersion due to Molecular Diffusion and Macroscopic Mixing in Flow Through a Network of Capillaries," *J. Fluid Mech.*, **7**, pp. 194–208.
- [26] Lai, F. C., and Kulacki, F. A., 1989, "Thermal Dispersion Effects on Non-Darcy Convection Over Horizontal Surfaces in Saturated Porous Media," *Int. J. Heat Mass Transf.*, **32**, pp. 356–362.
- [27] Mahajan, R. L., and Angirasa, D., 1993, "Combined Heat and Mass Transfer by Natural Convection With Opposing Buoyancies," *ASME J. Heat Transfer*, **115**, pp. 606–612.

Laminar Natural Convection in Isosceles Triangular Enclosures Heated From Below and Symmetrically Cooled From Above

G. A. Holtzman

Department of Mechanical Engineering,
The University of Texas at Austin,
Austin, TX 78712

R. W. Hill

Assoc. Mem. ASME
Department of Mechanical and Aerospace
Engineering,
University of Missouri-Columbia,
Columbia, MO 65211
e-mail: hillrw@missouri.edu

K. S. Ball

Mem. ASME
Department of Mechanical Engineering,
The University of Texas at Austin,
Austin, TX 78712
e-mail: kball@burst.me.utexas.edu

A numerical study of natural convection in an isosceles triangular enclosure with a heated horizontal base and cooled upper walls is presented. Nearly every previous study conducted on this subject to date has assumed that the geometric plane of symmetry is also a plane of symmetry for the flow. This problem is re-examined over aspect ratios ranging from 0.2 to 1.0 and Grashof numbers from 10^3 to 10^5 . It is found that a pitchfork bifurcation occurs at a critical Grashof number for each of the aspect ratios considered, above which the symmetric solutions are unstable to finite perturbations and asymmetric solutions are instead obtained. Results are presented detailing the occurrence of the pitchfork bifurcation in each of the aspect ratios considered, and the resulting flow patterns are described. A flow visualization study is used to validate the numerical observations. Computed local and mean heat transfer coefficients are also presented and compared with results obtained when flow symmetry is assumed. Differences in local values of the Nusselt number between asymmetric and symmetric solutions are found to be more than 500 percent due to the shifting of the buoyancy-driven cells.

[S0022-1481(00)02503-2]

Keywords: Computational, Enclosure Flows, Heat Transfer, Instability, Natural Convection

Introduction

In this study, consideration is given to laminar natural convection in an isosceles triangular enclosure heated from below with symmetric boundary conditions. The situation simulates the nighttime heating of an attic space. Previous studies of this topic have been performed both numerically and experimentally. Several earlier studies have been performed for triangular enclosures in general ([1–3]), but the focus of this paper is on isosceles triangular enclosures with symmetric temperature boundary conditions heated from below.

In modeling natural convection in an isosceles triangular enclosure, nearly every numerical study previously reported in the literature employed a symmetry condition at the midplane and performed the simulations using only one half of the physical domain. Akinsete and Coleman [4] used a finite difference representation of the steady-state stream function, vorticity, and energy equations with an adiabatic boundary condition for the vertical wall in a right triangular enclosure, and made the claim that the problem could also represent the case for an isosceles triangular enclosure due to symmetry. Poulikakos and Bejan [5] used a similar numerical approach, except that transient simulations were performed and an actual symmetry condition was used at the midplane for Gr up to 10^5 and $A = 0.2$ to 1.0 . The use of the symmetry condition for this problem was continued by Ghassemi and Roux [6], Salmun [7], and Hasani and Chung [8].

Del Campo et al. [9] numerically modeled natural convection in triangular enclosures using a Galerkin finite element method with a stream function-vorticity formulation of the steady-state

equations of motion for $A = 0.2$ to 20 and $Gr = 10^3$ to 10^6 . For the cases they considered with symmetric boundary conditions and heating from below, no symmetry assumption was made. Triangular elements with linear interpolation were used, and the resulting graded mesh was very symmetric. The solutions obtained were all symmetric about the midplane.

A continuing source of discrepancies in the literature is the calculation of average Nu (average dimensionless temperature gradient) along the base for the triangular enclosure. Akinsete and Coleman [4] recognized the existence of unbounded heat transfer at the corner of the enclosure where a temperature discontinuity exists, and calculated the limiting value of Nu using a method outlined by Collatz [10]. Poulikakos and Bejan [5] proposed starting the integration of the temperature gradient from a set distance away from the corner, thereby avoiding the singularity. Del Campo et al. [9] proposed a convective Nu defined as the difference between Nu for the case considered and Nu for pure conduction (using the same grid resolution). Salmun [7] and Hasani and Chung [8] did not specifically discuss the problem of the singularity and reported similar results for their average Nu due to having used the same grid resolutions.

A limited number of laboratory experiments have been conducted for natural convection in triangular enclosures with base heating. One experiment reported in the literature involving symmetric temperature boundary conditions for an isosceles triangular enclosure and base heating was done by Flack [11]. The flow was reported as ‘turbulent’ for $Gr = 3 \times 10^5$ with $A = 0.58$ and for $Gr = 8.9 \times 10^5$ with $A = 1.0$. Nu values were inferred using a Wollaston prism schlieren interferometer. Flow patterns were determined qualitatively using a particle-based visualization technique and quantitative measurements were taken using a laser velocimeter. For the heated base experiments, no mention was made as to the symmetry of the flow. Poulikakos and Bejan [12] conducted

Contributed by the Heat Transfer Division for publication in the JOURNAL OF HEAT TRANSFER and presented at the 1998 IMECE, Anaheim. Manuscript received by the Heat Transfer Division, Sept. 11, 1998; revision received, Jan. 6, 2000. Associate Technical Editor: R. Dougllass.

experiments in a right triangular enclosure with an insulated vertical wall, and noted that the flow phenomenon should be similar to that found in a symmetric triangular space.

The purpose of this paper is to provide steady-state numerical results considering the entire triangular region without symmetry assumptions. Removing the symmetry assumption leads to new results; specifically, the occurrence of symmetry breaking pitchfork bifurcations. Local and mean heat transfer coefficients are presented, and compared with results in which a symmetric flow pattern is assumed. Flow visualization results from laboratory experiments are also provided to qualitatively confirm the numerical observations.

Numerical Model

A long air-filled triangular enclosure ($Pr=0.71$) is considered such that the region of interest is two-dimensional with cross section and boundary conditions as shown in Fig. 1. The Cartesian two-dimensional Navier-Stokes and energy equations are solved in nondimensional form assuming constant properties using the commercial finite element code FIDAP, version 7.6 (Fluent, Inc., Lebanon, NH) subject to the Boussinesq approximation.

The boundary conditions for the base, the left side, and the right side, respectively, are

$$U = V = 0 \quad \text{and} \quad \theta = 1 \quad \text{at} \quad -\frac{1}{A} \leq X \leq \frac{1}{A}, \quad Y = 0 \quad (1)$$

$$U = V = 0 \quad \text{and} \quad \theta = 0 \quad \text{at} \quad -\frac{1}{A} \leq X \leq 0, \quad Y = AX + 1 \quad (2)$$

$$U = V = 0 \quad \text{and} \quad \theta = 0 \quad \text{at} \quad 0 \leq X \leq \frac{1}{A}, \quad Y = -AX + 1 \quad (3)$$

In the present work, Gr up to 10^5 is considered for aspect ratios of $A = 1.0, 0.5,$ and 0.2 . Though others have numerically considered higher Gr , the maximum of $Gr = 10^5$ was chosen here due to the experimental work of Flack [11] in which unsteady flow was reported between $Gr = 10^5$ and 10^6 . The steady-state form of the Navier-Stokes and energy equations were solved subject to the above boundary conditions using a convergence criterion of 10^{-6} for the rms norm of the difference between successive solution vectors normalized by the last solution vector for each dependent variable. Convergence criteria down to 10^{-10} were used for select cases and found to result in negligible solution differences from the chosen criterion. To avoid exceeding the available computer memory, the successive substitution solution approach was used for the relatively coarse grid resolution cases, whereas the segregated solver was used for the relatively fine grid resolutions ([13]). Both the segregated and successive substitution approaches were used on selected cases to ensure that the results were not dependent on the approach chosen. To confirm that the steady-state assumption was appropriate, transient solutions of the equations were performed at $Gr = 10^5$ for each aspect ratio, and the solutions were found to be steady. The flow visualization studies (discussed later) confirm that the flow at $Gr = 10^5$ with $A = 0.5$ is steady; transition to unsteady flow is observed experimentally just above $Gr = 10^5$.

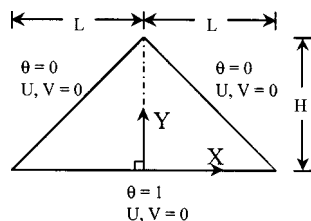


Fig. 1 Physical domain and boundary conditions

The computational domain was discretized with a paved mesh of quadratic triangular elements, and the pressure solution was carried out using a discontinuous pressure approximation ([13]). The elements were formed by distributing points evenly (no grading) along each edge of the computational domain, and the FIDAP paved meshing algorithm was used to generate all grids. The grids generated in this manner were not symmetric about the geometric plane of symmetry, but the elements were reasonably evenly distributed. Grid independence tests were performed on key parameters of this study such as the maximum x -component of velocity at the geometric symmetry plane, local and average convective Nusselt numbers along the base, and the onset of the bifurcation. As a result of this grid study, the detailed results reported here had 120, 200, and 260 segments (or half as many quadratic elements) along the base for $A = 1.0, 0.5,$ and 0.2 , respectively. The adequacy of the grids chosen is demonstrated in the grid independence study provided at the end of the results section.

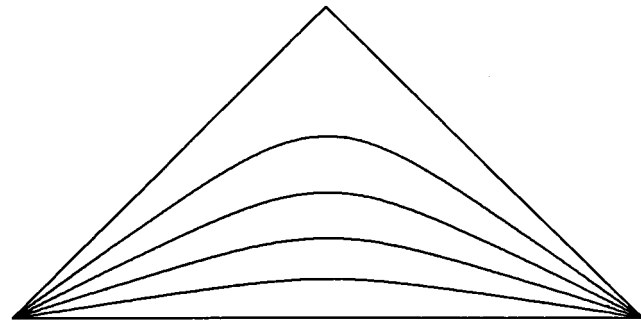
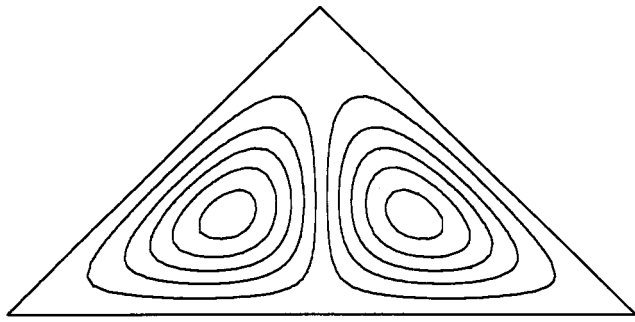
Flow Visualization Study

To confirm the numerical predictions of the flow patterns and the existence of a symmetry-breaking bifurcation, a flow visualization study was conducted. Smoke was slowly injected into an air-filled triangular enclosure, having a height of 56 mm, half-length of 112 mm, and a depth of 327 mm (resulting in an aspect ratio of $A = 0.5$). The ends of the enclosure were sealed by Plexiglas plates. The enclosure was constructed of 20-mm-thick aluminum plates with milled passageways for circulating fluid to maintain isothermal surfaces and to impose a temperature difference between the base and upper walls. Fine-gage (0.005-in.) Type K thermocouples, calibrated to reduce experimental uncertainty, were potted to the aluminum plates using high thermal conductivity paste. In the middle of the enclosure, two Plexiglas-covered slits separated by approximately 86 mm in the third dimension (depth) allowed different cross-sectional planes of the enclosure to be illuminated by He-Ne laser sheets, providing the visualization of the flow. By comparing the smoke patterns at the two depths, the flow was confirmed to be two-dimensional for the range of Gr considered. The primary experimental uncertainty affecting Gr was the uncertainty in the measured temperature difference, estimated to be approximately ± 0.1 K based on multiple measurements of a steady variable ([14]). This corresponds to an uncertainty of ± 275 in Gr (for air at 300 K).

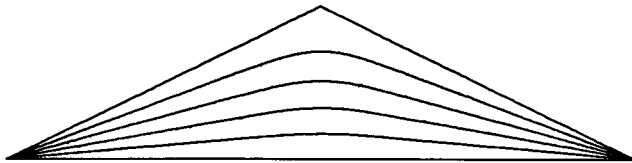
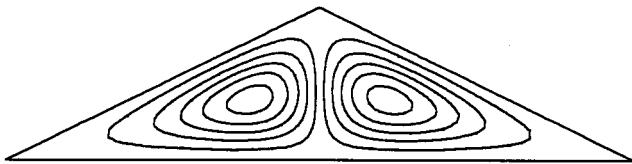
Results and Discussion

Symmetric Flow. The assumption of symmetric flow in the isosceles triangle used by other researchers in defining their numerical models is in fact correct for low values of Gr . In Fig. 2, the streamlines and temperature contours of the flow are shown for $Gr = 10^3$ and for $A = 1.0, 0.5,$ and 0.2 , respectively. At this value of Gr , for each aspect ratio the computed flow is symmetric with respect to the geometric midplane. The flow rises in the center of the enclosure and falls along each cold inclined side creating mirror image structures that rotate clockwise in the right half and counterclockwise in the left half. The temperature profiles for $Gr = 10^3$ are very close to those of the conduction solution, indicating that convection is not important. Figure 3 shows the flow visualization for $A = 0.5$ and $Gr = 5000$, revealing the existence of a nearly symmetric flow pattern. Note that this value of Gr (within experimental uncertainty) is less than the numerically predicted critical value, $Gr_c = 8930$, discussed later. The slight deviation from perfect symmetry is attributed to the difficulty in achieving perfectly symmetric experimental conditions.

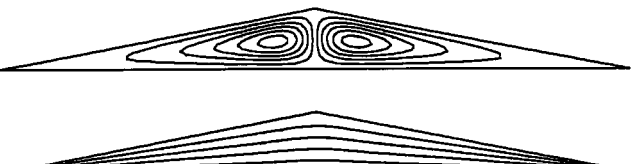
For $A = 1.0$ and $Gr = 10^4$, the increased buoyancy forces at this higher value of Gr generate stronger counter rotating convective cells, but the flow remains symmetric about the geometric midplane (results not shown here). The streamlines are qualitatively similar to those for $Gr = 10^3$, but the temperature contours are displaced upward from their location at $Gr = 10^3$ near the center of



(a)



(b)



(c)

Fig. 2 Streamline (upper) and temperature (lower) profiles for $Gr=10^3$: (a) $A=1.0$; ($\Delta\psi=0.0252$, $\Delta\theta=0.2$), (b) $A=0.5$; ($\Delta\psi=0.0374$, $\Delta\theta=0.2$), and (c) $A=0.2$; ($\Delta\psi=0.0316$, $\Delta\theta=0.2$)

the enclosure causing a local decrease in Nu_c . It is noted that the horizontal component of velocity is zero everywhere along the midplane for these symmetric results. For the other two aspect ratios, the flow at $Gr=10^4$ is not symmetric and is discussed in the next two sections.

Pitchfork Bifurcation. As the Grashof number is increased above a critical value the flow is observed to undergo a supercritical pitchfork bifurcation, in which case one of two possible mirror image asymmetric solutions are obtained. For these asymmetric solutions, the horizontal velocity along the midplane of the triangle is nonzero. Thus, the branch point of the pitchfork can be

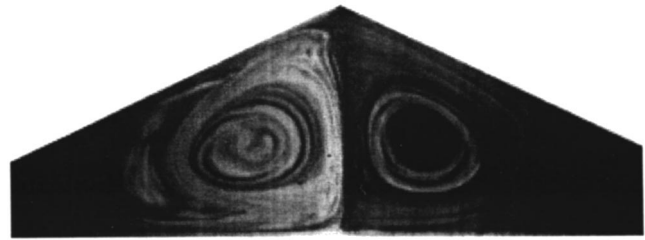


Fig. 3 Symmetric experimental flow pattern for $Gr=5 \times 10^3$ and $A=0.5$

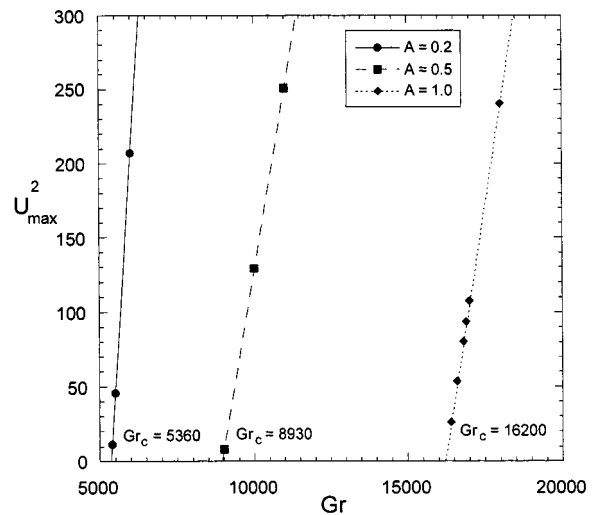


Fig. 4 Determination of Gr_c for each aspect ratio using maximum horizontal velocity at the geometric symmetry plane

determined by extrapolating to zero the square of the maximum value of the horizontal velocity at the midplane for values of Gr above the critical value as shown in Fig. 4. The values of Gr_c obtained using this method are also reported on the figure. Gr_c is found to decrease with decreasing A .

The existence of multiple solutions necessitates that particular care be exercised in obtaining solutions above Gr_c , because both symmetric and asymmetric solutions can be obtained depending upon the solution approach. From past experience, if all aspects of the solution technique are perfectly symmetric, then symmetric solutions can be obtained at parameters above the pitchfork bifurcation point ([15]). However, these symmetric solutions are unstable and will evolve to a stable asymmetric solution if a finite perturbation is applied. These finite perturbations may be a slight tilting of the enclosure for a few iterations followed by a return to vertical, asymmetries imposed by using an asymmetric grid distribution, or the use of a solution algorithm that imposes slight asymmetries in the results (Gauss-Seidel iteration, for example). For the cases considered here, if started from symmetric initial conditions with no tilting of the enclosure, during iterative solutions of the steady-state equations the flow would initially evolve toward a symmetric solution, reaching (in some cases) residuals of less than 10^{-5} . However, when Gr was above the critical value, as the computations were continued the residual would start to rise and then decrease again, this time converging to one of the two stable asymmetric results. Similar behavior was seen in the transient cases run above Gr_c , where the solution would initially evolve towards a symmetric result, then deviate to an asymmetric solution before reaching a steady state. It is thus concluded that above Gr_c , the asymmetric solutions in the triangular enclosure

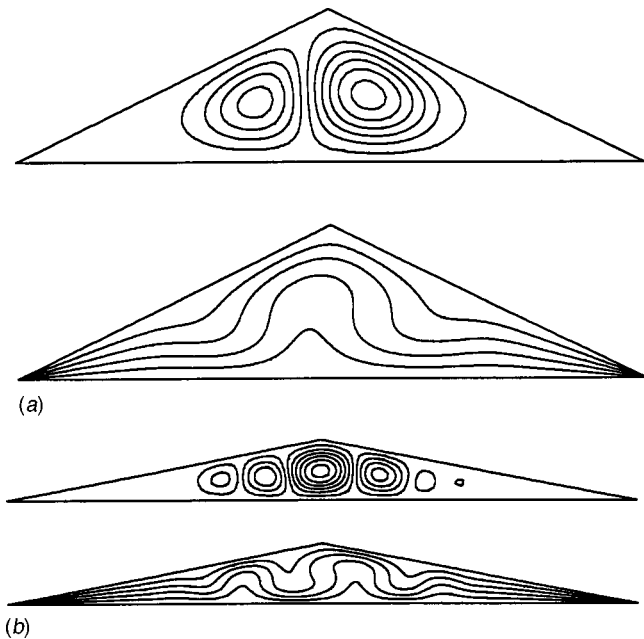


Fig. 5 Streamline (upper) and temperature (lower) profiles for $Gr=10^4$: (a) $A=0.5$ ($\Delta\psi=1.11$, $\Delta\theta=0.2$), and (b) $A=0.2$ ($\Delta\psi=1.57$, $\Delta\theta=0.2$)

are stable to finite perturbations whereas the symmetric ones are not. Del Campo et al. [9], who considered an isosceles triangular domain above Gr_c , did not find any asymmetric solutions. In light of the nonuniform iterative convergence behavior observed for these cases, one possibility to explain this fact might be that the iterative convergence criteria used by del Campo et al. were too large.

Flow and Temperature Field Above Gr_c . As Gr is increased above Gr_c for the aspect ratio in question, the flow pattern becomes increasingly asymmetric and the number of circulation cells is observed to increase. As noted above, at $Gr=10^4$ and $A=1.0$, the flow is below the critical value and remains symmetric. However, for $A=0.5$ and 0.2 , the flow is asymmetric (Fig. 5). For $A=0.5$ and $Gr=10^4$ (just above Gr_c) as shown in Fig. 5(a), the central plume is shifted slightly to one side of the midplane and the clockwise (right) circulation cell is larger than the other cell. The temperature contours are shifted upward and spaced relatively far apart near the base of the plume, indicating a reduction in heat transfer at that location relative to the pure conduction case. The temperature gradients are increased near the base where the cold plumes falling from the upper surfaces impinge upon the base. For the smaller aspect ratio $A=0.2$ and $Gr=10^4$, many more circulation cells and plumes exist, as seen in Fig. 5(b). By comparing the streamline and temperature profiles of Fig. 5(b), it is clear that the center circulation cell is rotating counterclockwise. The cells to the left and right of this center cell alternate in direction of rotation with decreasing strength. The experimental flow visualization results for $Gr=10^4$ are provided in Fig. 6, and these results qualitatively agree quite well with the numerical results for $A=0.5$ shown in Fig. 5(a).

For all aspect ratios at $Gr=10^5$ (Fig. 7), a central circulation cell exists with counterrotating cells to either side. In each case, the regions of small temperature gradients near the base are displaced away from the midplane along with the plume. For $A=1.0$, one circulation cell dominates the other and the central plume is shifted to one side, rises up to meet the cold sloping wall, and continues upward toward the top of the triangle as seen in Fig. 7(a). For $A=0.5$ with $Gr=10^5$ shown in Fig. 7(b), a central circulation cell rotating clockwise exists near the midplane of the

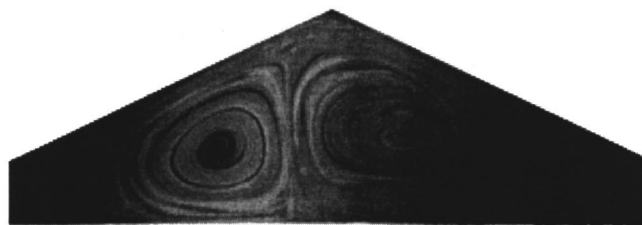


Fig. 6 Experimental flow pattern for $Gr=10^4$ and $A=0.5$

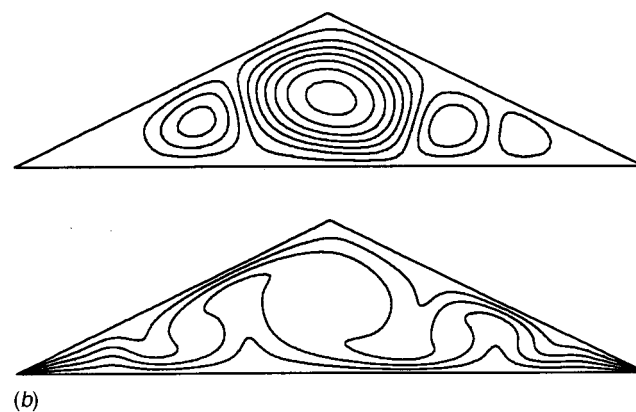
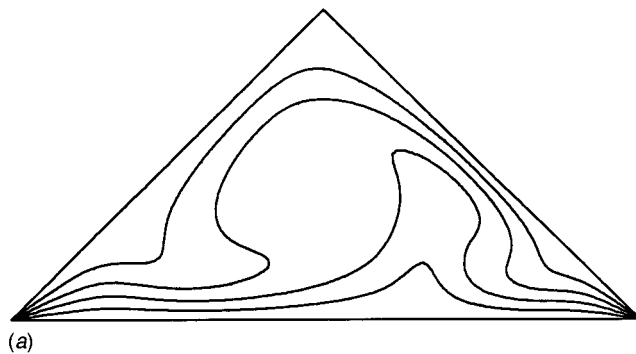
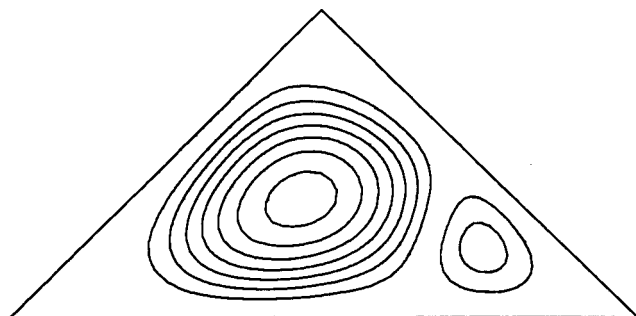


Fig. 7 Streamline (upper) and temperature (lower) profiles for $Gr=10^5$: (a) $A=1.0$ ($\Delta\psi=3.34$, $\Delta\theta=0.2$), (b) $A=0.5$ ($\Delta\psi=4.93$, $\Delta\theta=0.2$), and (c) $A=0.2$ ($\Delta\psi=6.73$, $\Delta\theta=0.2$)

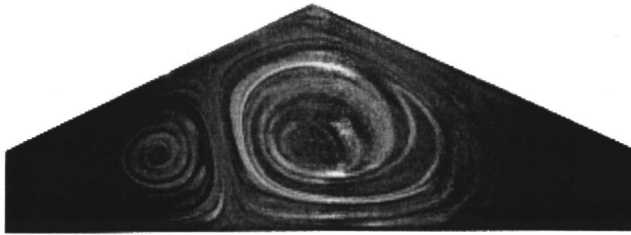


Fig. 8 Experimental flow pattern for $Gr=10^5$ and $A=0.5$

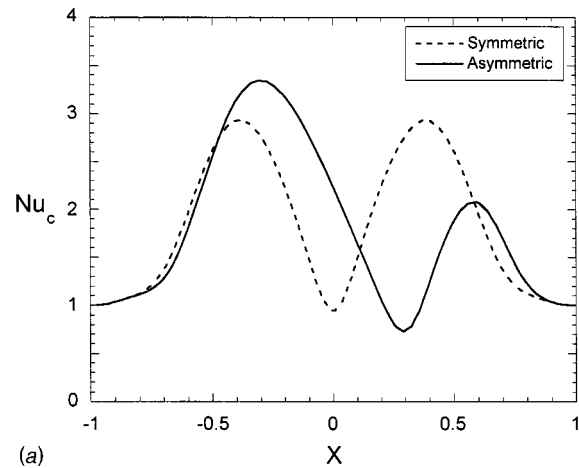
geometry with counterrotating cells to either side. The flow and temperature profiles for the smaller aspect ratio $A=0.2$ are more complex at $Gr=10^5$, where several circulation cells are on either side of the central one, and many plumes alternately rise and fall throughout the domain, as seen in Fig. 7(c). (It should be emphasized that the results shown are not unique, but are one of the two possible mirror image solutions.) Experimental smoke visualization results for $Gr=10^5$ are provided in Fig. 8 which agree qualitatively very well with the numerical results for the same conditions provided in Fig. 7(b).

Heat Transfer. As noted above in the Introduction, the local Nu (dimensionless temperature gradient) is unbounded at the corners of the triangular geometry where the hot base meets the cold side walls. Therefore, determination of an average Nu by a direct integration of the dimensionless temperature gradient starting from the closest node to the tip (since the gradient is undefined at the tip) would yield highly grid dependent results. The average Nu would be increasingly dominated by the singularity as the grid is refined. This detail has been poorly handled by most of the researchers who have considered the problem numerically resulting in grid-dependent results that cannot be directly compared. To focus on the effect of the fluid motion on the heat transfer and to avoid the issue of unbounded heat transfer at the tip region, a convective Nusselt number, Nu_c , is defined as the ratio of Nu at a given Gr to Nu for the corresponding conduction solution ($Gr=0$). The Nusselt number here is computed by evaluating the dimensionless temperature gradient on the wall at the finite element Gauss points. By considering the heat transfer in this way, both the local and average Nu_c asymptotically approach unity as Gr is decreased. Nu_c thus represents the increase (or local decrease if it is less than unity) in heat transfer relative to the case for pure conduction and converges both locally and in an average sense as the grid is refined. Table 1 summarizes $Nu_{c,avg}$ along the base for each aspect ratio as a function of Gr , and it is seen that decreasing the aspect ratio increases $Nu_{c,avg}$ for a given Gr . This $Nu_{c,avg}$ is computed by simply summing all of the local values for Nu_c and dividing by the number of values (made possible since the Nu_c values are located at the Gauss points). The increase in Nu_c with decreasing A is attributed to the multicellular flow pattern described above.

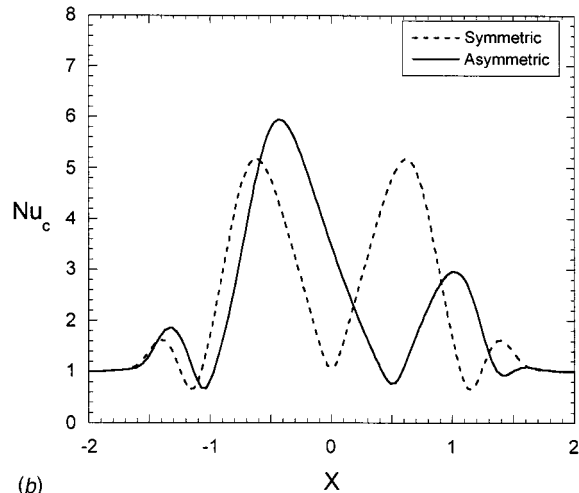
Effect of the Symmetry Assumption. To highlight the differences in the local heat transfer depending on whether one assumes a symmetry condition, computations were also performed for selected cases using a symmetry assumption. Note that the solutions assuming symmetry used the same number of elements along the base half-length as for the solutions not assuming flow

Table 1 Average convective Nusselt numbers

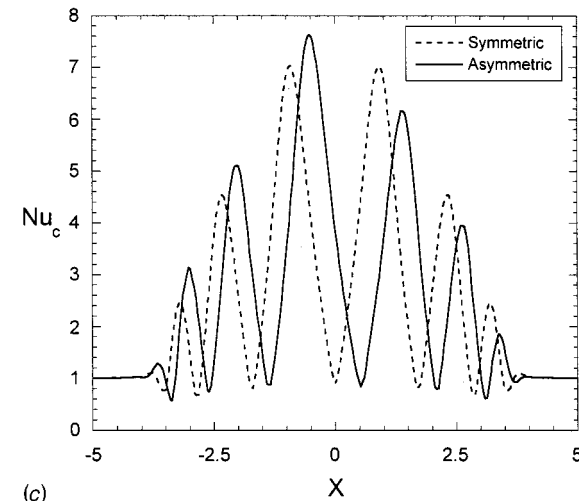
| A | $Gr=10^3$ | $Gr=10^4$ | $Gr=10^5$ |
|-----|-----------|-----------|-----------|
| 1.0 | 1.0 | 1.07 | 1.80 |
| 0.5 | 1.0 | 1.20 | 2.19 |
| 0.2 | 1.0 | 1.28 | 2.48 |



(a)



(b)



(c)

Fig. 9 Nu_c along the base for asymmetric and symmetric solutions at $Gr=10^5$ (a) $A=1.0$, (b) $A=0.5$, and (c) $A=0.2$

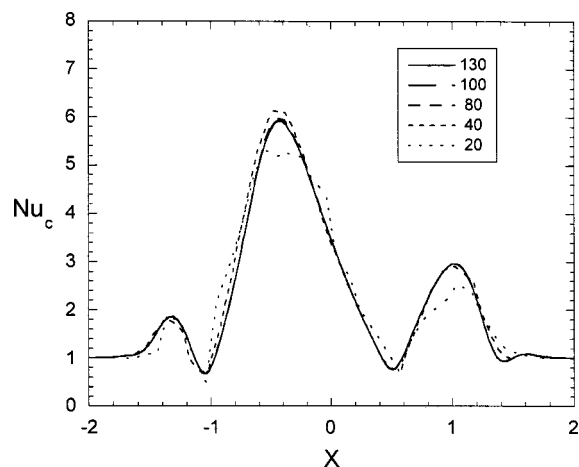
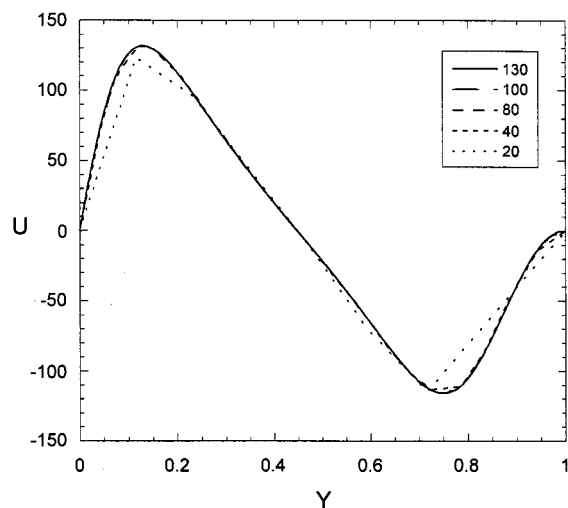
symmetry. Figure 9 shows the local Nu_c across the base for both the symmetric and asymmetric cases at $Gr=10^5$ with $A=1.0, 0.5$, and 0.2 . Nu_c drops below unity near $X=0.3$ in the asymmetric case with $A=1.0$, as seen in Fig. 9(a), where a rising plume is located (Fig. 7(a)). The falling plumes, which impinge on the base, cause a local increase in heat transfer and a clear increase in the temperature gradients. This effect is also seen for $A=0.5$ (Figs. 9(b) and 7(b)), where the number of upward plumes is

Table 2 Change in average Nu_c for $Gr=10^5$ and $A=0.5$

| Segments Along the Base | $Nu_{c,avg}$ | Percent Change |
|-------------------------|--------------|----------------|
| 80 | 2.252 | 2.99 |
| 160 | 2.201 | 0.658 |
| 200 | 2.193 | 0.258 |
| 260 | 2.187 | ... |

three, as shown by inspection of the temperature contours, or by noting the number of minima in the plot of Nu_c . As indicated in Fig. 9(c), the flow pattern for $A=0.2$ is much more complex, and the number of upward plumes is seen to be 6, as evident in either Figs. 9(c) or 7(c).

In Fig. 9, the maximum value of Nu_c is seen to be higher for the asymmetric cases. Additionally, the percent differences in Nu_c for the asymmetric and symmetric cases shown in Fig. 9 can be more than 250–550 percent depending upon location and aspect ratio due to the different locations of the convective cells in the asymmetric and symmetric cases. However, when integrating the local values of Nu_c for both the symmetric and asymmetric solutions, the difference between $Nu_{c,avg}$ in each case is only found to be

**Fig. 10 Nu_c along the base for $A=0.5$, $Gr=10^5$ using different grid resolutions****Fig. 11 Horizontal velocity profile at the geometric symmetry plane for $A=0.5$, $Gr=10^5$ using different grid resolutions**

about 2.5 to 5.0 percent. The peak value of Nu_c is greater by 6 to 12 percent for the asymmetric case compared to the symmetric one. Thus, by assuming the flow to be symmetric about the geometric symmetry plane, the predicted local heat transfer is much different than for the simulations without symmetry. However, the error in predicted overall heat transfer by assuming a symmetry condition is relatively small.

Grid Independence Study. To ensure the accuracy of the numerical results a grid independence study was performed. For each grid and aspect ratio, proportional numbers of elements were used for each side of the enclosure according to the side lengths. Important parameters such as the horizontal velocity component along the symmetry plane, Gr_c , and both local and average Nu_c were calculated at several grid resolutions and compared. The grids for the results reported in this paper were chosen such that the percent change in $Nu_{c,avg}$ for each aspect ratio was less than 0.5 percent. For an aspect ratio of 0.5, the chosen grid had 200 segments across the base, as shown in Table 2. Likewise, for $A=1.0$ and 0.2, the grids chosen had 120 and 260 segments across the base, respectively.

To verify that the grid resolutions based on this criterion were adequate for resolving local quantities, additional grid studies were performed for each of the cases included in this study. Typical results are shown for $A=0.5$ and $Gr=10^5$ in Figs. 10–11, which show Nu_c along the base and the nondimensional horizontal velocity along the midplane of the triangle, respectively, for each of the grids used. The local values of Nu_c and the horizontal velocity are observed to converge to one profile as the grid is refined. Similar trends were observed for all other cases considered.

To determine the sensitivity of Gr_c to grid resolution, the extrapolation procedure described earlier was repeated for different grids for $A=1.0$. For doubling the grid from 60 to 120 segments along the base, the percent change in the critical Grashof number was less than 0.1 percent indicating that the reported Gr_c is grid independent for $A=1.0$. Based on the other grid tests performed, it is expected that the reported values of Gr_c for $A=0.5$ and $A=0.2$ are similarly grid independent.

Conclusions

Numerical results for laminar natural convection in an isosceles triangular enclosure heated from below, considering the complete physical domain (i.e., using no symmetry assumptions), are presented for three aspect ratios. At low Gr , symmetric solutions are obtained indicating that a symmetry assumption is valid. As Gr is increased, a pitchfork bifurcation is observed in which two steady asymmetric mirror image solutions can be obtained. Critical values of Gr have been determined for $A=1.0$, 0.5, and 0.2 with Gr_c increasing as A increases. The local convective Nusselt numbers along the base between asymmetric and symmetric cases can differ by up to 550 percent due to shifting of the convective cells, but differences in the averaged quantities are no more than five percent. All of the results reported in this paper are based on the assumption that the flow is two-dimensional near the center of the enclosure. Flow visualization studies provide validation of this assumption and the numerically predicted occurrence of the pitchfork bifurcation for a geometry with $A=0.5$. As Gr is increased, the flow will undoubtedly become three-dimensional and unsteady.

Nomenclature

- A = aspect ratio, H/L
- Gr = Grashof number, $g\beta\Delta TH^3/\nu^2$
- Gr_c = critical Grashof number
- L = half-length of the enclosure
- Nu = Nusselt number, hH/k
- Nu_c = convective Nusselt number
- $Nu_{c,avg}$ = average convective Nusselt number
- T_C = cold surface temperature

T_H = hot surface temperature
 ΔT = temperature difference, $T_H - T_C$
 U = dimensionless velocity in the x -direction, uH/ν
 V = dimensionless velocity in the y -direction, vH/ν
 X = dimensionless x -coordinate, x/H
 Y = dimensionless y -coordinate, y/H
 θ = dimensionless temperature, $(T - T_C)/(T_H - T_C)$

References

- [1] Flack, R. D., Konopnicki, T. T., and Rooke, J. H., 1979, "The Measurement of Natural Convective Heat Transfer in Triangular Enclosures," *ASME J. Heat Transfer*, **101**, pp. 648–654.
- [2] Karyakin, Y. E., and Sokovishin, Y. A., 1985, "Unsteady Natural Convection in a Triangular Enclosure," *Fluid Dyn.*, **20**, pp. 811–815.
- [3] Karyakin, Y. E., Sokovishin, Y. A., and Martynenko, O. G., 1988, "Transient Natural Convection in Triangular Enclosures," *Int. J. Heat Mass Transf.*, **31**, pp. 1759–1766.
- [4] Akinsete, V. A., and Coleman, T. A., 1982, "Heat Transfer by Steady Laminar Free Convection in Triangular Enclosures," *Int. J. Heat Mass Transf.*, **25**, pp. 991–998.
- [5] Poulidakos, D., and Bejan, A., 1983, "The Fluid Dynamics of an Attic Space," *J. Fluid Mech.*, **131**, pp. 251–269.
- [6] Ghassemi, M., and Roux, J. A., 1989, "Numerical Investigation of Natural Convection Within a Triangular Shaped Enclosure," *Heat Transfer in Convective Flows*, R. K. Shah, ed., ASME, New York, pp. 169–175.
- [7] Salmun, H., 1995, "Convection Patterns in a Triangular Domain," *Int. J. Heat Mass Transf.*, **38**, pp. 351–362.
- [8] Hasani, S. M. F., and Chung, B. T. F., 1997, "Laminar Natural Convection in a Triangular Enclosure," *Proceedings of the ASME Ocean Engineering Division*, D. T. Valentine, and C. C. Jahnke, eds., ASME, New York, pp. 107–116.
- [9] Del Campo, E. M., Sen, M., and Ramos, E., 1988, "Analysis of Laminar Natural Convection in a Triangular Enclosure," *Numer. Heat Transfer*, **13**, pp. 353–372.
- [10] Collatz, L., 1966, *The Numerical Treatment of Differential Equations*, Springer-Verlag New York.
- [11] Flack, R. D., 1980, "The Experimental Measurement of Natural Convection Heat Transfer in Triangular Enclosures Heated or Cooled From Below," *ASME J. Heat Transfer*, **102**, pp. 770–772.
- [12] Poulidakos, D., and Bejan, A., 1983, "Natural Convection Experiments in a Triangular Enclosure," *ASME J. Heat Transfer*, **105**, pp. 652–655.
- [13] *FIDAP Reference Manuals*, 1996, Fluent, Inc., Lebanon, NH.
- [14] Moffat, R. J., 1982, "Contribution to the Theory of Single-Sample Uncertainty Analysis," *ASME J. Fluids Eng.*, **104**, pp. 250–258.
- [15] Hill, R. W., and Ball, K. S., 1997, "Chebyshev Collocation Analysis of Axisymmetric Flow and Heat Transfer between Counter-Rotating Disks," *ASME J. Fluids Eng.*, **119**, pp. 940–947.

Inverse Design Model for Radiative Heat Transfer

J. R. Howell

e-mail: jhowell@mail.utexas.edu

O. A. Ezekoye

J. C. Morales

Department of Mechanical Engineering,
The University of Texas at Austin,
Austin, TX 78714-1063

Inverse solution techniques are applied to the design of heat transfer systems where radiation is important. Various solutions using inverse methods are demonstrated, and it is argued that inverse design techniques provide an alternative to conventional iterative design methods that is more accurate and faster, and can provide a greatly improved first estimate of a thermal design. This estimate can then be used as a trial design in more complete thermal analysis programs for predicting system behavior, eliminating many faulty first design trials. [S0022-1481(00)02703-1]

Keywords: Furnaces, Heat Transfer, Inverse, Radiation

Introduction

The presence of significant radiative transfer in high-temperature engineering systems greatly complicates the modeling process. Radiative energy transfer is inherently described by integral terms. Introducing the radiative flux divergence makes the energy equation, which is necessary for thermal system modeling, into an integro-differential equation that is highly nonlinear. Detailed first-principles design of these systems is thus difficult, and is only now becoming common because of the power of contemporary numerical methods and computer capacity. Conventional design of complex thermal systems involving significant radiative transfer still relies to a great extent on experience and prior art. Such an approach requires specification of the system geometry, boundary conditions on each boundary and material properties. These conditions are called the "assumed design set." In contemporary design, the design set is then used along with the governing equations to predict system behavior. If the predicted behavior is satisfactory, then the design set is accepted; if not, some values within the design set are changed, and the prediction is repeated. Iteration proceeds in this way until a design set is achieved that satisfactorily meets the system requirements.

Modern simulation tools that solve the coupled equations of energy, mass, and momentum transfer including the effects of chemical reaction and radiative transfer in participating media can provide accurate prediction of the behavior of environmental and energy systems. These tools require the input information noted above as a design set; i.e., geometry, boundary conditions and properties, along with initial conditions if transient behavior is to be predicted. The flexibility and accuracy of these sophisticated tools demands computer speed and capacity, and the cost of an accurate and detailed simulation for even a single design set can be large. Typical design codes for commercial utility boilers that include participating media may involve over 500,000 surface and volume elements for sufficient spatial resolution, and require solution of the coupled momentum, energy (including the effects of radiation in participating media), continuity, and chemical species equations. Because of the time and cost of each of these simulations, satisfactory final design may be limited to a choice from among a small number of design sets. Clearly, the designer should have the best possible initial design set so that the number of cases needed to achieve the desired design outcomes is minimized.

Here, we examine inverse methods for obtaining an approximate initial design set for use in the sophisticated available design tools. This will greatly improve the practical design of thermal and environmental systems, particularly those involving significant radiative energy transfer.

Inverse Design

The analytical/numerical methods for conventional thermal analysis developed in the past have most often focused on mathematically well-behaved methods. These methods require one boundary condition to be prescribed on each boundary of the system, and the system geometry and properties must be given. The thermal behavior of the control volume can then be predicted. We might define this class of analytical design methods as "forward" solution techniques, where we proceed from a defined set of properties and conditions to predict system behavior.

In contrast, an inverse design methodology allows specification of the desired *outcome* of a design, and then *determines* the design set (or some portion of the design set) that will provide this outcome. Inverse design shares some characteristics with inverse methods used in experimental methods, where a measurement at a boundary is used to infer conditions within the system or at another boundary as in [1–12]. However, inverse design has significant differences that require modification of the methods developed for inverse experimental analysis.

Examples of inverse design problems are in [13,14]. These researchers have examined how the transient thermal boundary conditions on the exterior of a casting could be varied in order that the freezing boundary within the casting could progress at a uniform rate and thus provide uniform grain structure and improved final castings.

Here, we concentrate on providing an *initial* design set for thermal systems and equipment when significant radiative transfer is present. That is, what is the best placement of energy sources (within a volume or on boundaries) or the best geometry for a thermal system that will produce the desired output from the thermal system. This type of design problem is usually steady-state, multidimensional, and incorporates multiple modes of heat transfer.

Inverse design sounds as if it is the perfect design tool. However, when inverse design is actually applied, an immediate difficulty arises. The mathematical model for inverse design usually requires that the known conditions on one or more surfaces of the system under study be *overspecified*; e.g., both temperature and heat flux may be specified on the material passing through an annealing furnace. On one or more other surfaces, *no* boundary condition is initially specified; indeed, the objective is to determine that boundary condition (e.g., heater temperature or net radiative flux) that will provide the conditions on the overspecified surface. Unfortunately, this type of model leads to formulations that are ill-conditioned mathematically; that is, the solutions from inverse analysis may be multivalued, sensitive to small perturbations in input values, and in general require more sophisticated mathematical tools than are required for conventional forward solutions. When radiative transfer is significant, the governing equa-

Contributed by the Heat Transfer Division for publication in the JOURNAL OF HEAT TRANSFER. Manuscript received by the Heat Transfer Division, Oct. 25, 1999; revision received, Apr. 19, 2000. Associate Technical Editor: P. Menguc.

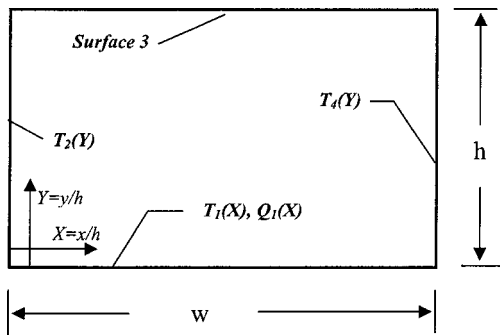


Fig. 1 Geometry for an inverse radiative transfer problem

tions are integral or integral-differential equations. In their finite difference form, these equations provide a set of coupled highly nonlinear equations. When placed in matrix form, the radiative exchange among elements causes the matrix of coefficients to be full rather than tridiagonal or sparse as is common in the absence of radiative transfer.

An illustrative example of a simple inverse radiation problem is the rectangular enclosure shown in Fig. 1.

Here, in a typical inverse design problem, both the heat flux and temperature on surface 1 are specified, and the designer wishes to know the temperature distribution required on surface 3 to provide these conditions. The surfaces are gray and diffuse, and no radiatively participating medium is present within the enclosure. The J_i is the radiosity (emitted plus reflected radiant flux) leaving surface i . When the net energy exchange equations for radiative transfer are written for an element on surface 1, the result is

$$q_1(x) - \varepsilon_1 \sigma T_1^4(x) = \varepsilon_1 \sum_{i=1}^4 \int_0^{L_i} J_i(\xi_i) K(x, \xi_i) dA_i \quad (1)$$

where the summation is over the bounding surfaces of the enclosure and the integration is over an individual bounding surface. Because both the dimensionless temperature distribution $T_1(X)$ and dimensionless total radiative flux distribution $Q_1(X)$ on surface 1 have been specified, the left-hand side of Eq. (1) is therefore known. Equation (1) thus has the characteristics of a Fredholm integral equation of the first kind, and its appearance in the equation set for the inverse problem causes the problem to be ill-conditioned. For forward problems, one and only one BC is prescribed on each surface, and equations of this type do not appear.

The kernel of the integral, $K(x, \xi_i)$ has the general form (with no attenuating medium present) of $K(x, \xi_i) = \cos \theta_1 \cos \theta_i / \pi S_{1-i}^2$, where θ is the angle between the line connecting a surface element on surface 1 and a surface element on surface i and the outward facing normal from these elements. The distance between the elements is S_{1-i} . If an absorbing-emitting, cold medium with uniform properties is present between the elements, then the form given for the kernel is multiplied by $\exp(-aS_{1-i})$, where a is the linear absorption coefficient of the medium.

For many physical systems the linear inverse problem resulting from discretization of the integral equations describing radiative exchange in the absence of conduction or convection can be formulated in terms of a matrix operator \mathbf{A} and a vector of unknowns \mathbf{X} ,

$$\mathbf{A}\mathbf{X} = \mathbf{b}. \quad (2)$$

In surface radiation problems, the vector \mathbf{X} contains the unknown radiosity distributions on all surfaces as well as the unknown temperature distribution on the U_k (unknown) surface. Mathematically, inverse thermal design requires solving sets of equations that include Fredholm integral equations of the first kind as shown in Eq. (1). These are known to have multiple so-

lutions that are susceptible to oscillations. Exact solution by matrix inversion is usually not possible because the matrix of coefficients is then nearly singular. In contrast, forward design of radiative transfer problems requires solution of sets of Fredholm integral equations of the *second* kind whose solutions are well behaved. Further, for problems involving radiative transfer the matrix \mathbf{A} is usually full, in contrast to inverse problems that involve only conduction or convection, where the matrix is sparse or banded, allowing relatively fast solution algorithms to be used.

Solution Techniques for Inverse Problems With Radiation.

The use of direct matrix inversion, inverse Monte Carlo techniques, the Tikhonov method, truncated singular value decomposition (TSVD), modified truncated singular value decomposition (MTSVD), artificial neural networks, and the conjugate gradient method have all been used to solve problems with the form similar to that encountered in inverse radiative design ([15–17]).

For forward problems, direct matrix inversion by Gaussian elimination, Cholesky, LU decomposition and QR factorization are widely used ([18]). Some inverse problems can be solved by direct matrix inversion over a limited range of parameters, or if a large error can be tolerated in the solution.

The extensive work on inverse analysis of conduction problems by Beck et al. [19,20] has laid the groundwork for many solution techniques that can be applied to more general inverse problems. This work has been in cooperation with and has drawn upon a considerable body of work in Russia ([20]). Recent monographs ([21–24]) have further explored techniques for solving inverse problems that arise in property measurement, remote sensing, structural dynamics, and conduction heat transfer.

A rank revealing decomposition such as *singular value decomposition* (SVD) allows the study of the degree of ill-conditioning of linear systems. SVD is a matrix operation in which a matrix \mathbf{A} is decomposed into a product of three matrices, \mathbf{U} , \mathbf{W} and \mathbf{V} . \mathbf{U} and \mathbf{V} are orthonormal; i.e., they possess the property that $\mathbf{U}^T\mathbf{U} = \mathbf{V}^T\mathbf{V} = \mathbf{I}$, where \mathbf{I} is the identity matrix. The \mathbf{W} is the diagonal matrix composed of the singular values of the matrix \mathbf{A} . Hansen [24] describes details of the decomposition and software for carrying it through, along with a very clear discussion of the mathematical background of SVD.

The singular values w_i form a nonnegative diagonal of \mathbf{W} with decreasing numerical values, and examination of their relative magnitudes provides an important measure of whether \mathbf{A} itself can be readily inverted. \mathbf{A} need not be square to apply SVD, which adds greatly to the utility (since we can examine behavior when equations and unknowns are unequal, i.e., *rank deficient* problems). The ratio of the largest to the smallest singular values, w_1/w_N , where N is the rank of \mathbf{A} , is called the *condition number* of matrix \mathbf{A} . The larger the condition number, the more difficult will be conventional matrix inversion of \mathbf{A} . If the equation set is truly singular, one or more singular values will be zero indicating the impossibility of direct solution by straightforward matrix inversion of the complete matrix \mathbf{A} .

The availability and power of SVD is the basis for a number of methods for treating ill-conditioned equation sets of the type that arise in inverse design, including truncated singular value decomposition (TSVD) and modified TSVD. SVD may also be used as an aid to interpreting the results and increasing the efficiency of Tikhonov regularization. These methods, along with the application of the conjugate gradient approach, will now be discussed in more detail.

Regularization. As a result of discretization, the set of integral equations describing radiative transfer has been transformed into a set of linear algebraic equations. However, the ill-posed nature of the system for the case of inverse design problems has not been addressed, and an infinite-dimensional (continuous) ill-posed problem has only been transformed into a *discrete ill-posed problem*. Hansen [25] indicates that a discrete system $\mathbf{A}\mathbf{X} = \mathbf{b}$ is ill-posed if the following criteria are satisfied:

- 1 The singular values of \mathbf{A} decay gradually toward zero.
- 2 The ratio of the largest to the smallest nonzero singular value (condition number) of matrix \mathbf{A} is large.

The first criterion indicates that there is no “nearby” problem with a well-conditioned matrix of coefficients and with well-determined rank. The second criterion similarly implies that matrix \mathbf{A} is ill-conditioned, i.e., the solution is potentially unstable to perturbation in the data. These two criteria do not imply that a meaningful solution cannot be obtained, but that standard methods such as Gaussian elimination, LU or QR factorization cannot be used in a straightforward manner, particularly if a meaningful (useful) solution is to be obtained. Instead, more elaborate methods must be applied. Numerical methods that can solve this type of problem are the so-called *regularization methods*.

Because of the gradual decay of the singular values of \mathbf{A} , the discrete system is essentially undetermined. Therefore, it is necessary to include additional information regarding the solution to stabilize the problem and to single out a useful and stable solution. Even though there are many types of additional constraints that can be imposed on the solution, by far the most dominant is to require that the l_2 -norm, or some other suitable norm, be small. In addition, the constraint imposed by the system of equations, i.e., $\mathbf{AX}=\mathbf{b}$, must be relaxed in order to accommodate the regularizing constraint.

The regularization process is thus an attempt to reduce the fluctuations of the solution introduced by the ill-conditioned nature of the equations, which is called the *perturbation error*, while not introducing too much error through over-smoothing of the solution and thus introducing *regularization error*. Finding the best solution \mathbf{X}^* that provides a reasonable tradeoff between these two errors is the goal of most inverse solution methods.

A measure of the perturbation error is the l_2 -norm of the solution, defined by

$$l_2(\mathbf{X}^*) = \|\mathbf{L}(\mathbf{X} - \mathbf{X}^*)\|_2 \quad (3)$$

where \mathbf{L} is the smoothing operator used on the data (usually the identity matrix or first or second derivative) and \mathbf{X} is the required design solution. If \mathbf{L} is taken to be the identity matrix, then the l_2 -norm becomes the mean variance of the calculated solution relative to the imposed design requirement, and corresponds to zeroth-order regularization. If \mathbf{L} is taken as the first or second derivative operator, these correspond to first and second-order regularization, respectively.

The regularization error is taken to be the residual norm of the solution, R , given by

$$R = \|\mathbf{AX}^* - \mathbf{b}\|_2. \quad (4)$$

If $\mathbf{X}^* = \mathbf{X}$, then there is no regularization error as the exact and regularized solution will be equal, and the matrix equation is exactly satisfied; however, the more the solution is regularized by introducing smoothing, the larger will be the residual norm R .

The goal of the regularizing algorithm is thus to obtain a balance between minimizing the fluctuations in the solution as measured by the l_2 -norm while simultaneously introducing the smallest possible residual norm.

Since the introduction of the concept of regularization by Tikhonov in the early 1960s ([26,27]), several methodologies have been developed to compute or estimate the solution of ill-posed problems. Hansen [25] presents a brief summary of several algorithms that can be classified into two groups: direct and iterative methods. Direct methods are those that reformulate the problem by introducing additional constraints and estimate the solution by using standard linear solvers for the new problem. On the other hand, iterative regularization is based on the inherent regularizing property of linear solvers when applied directly to the original system of equations. During initial iterations the low frequency components are resolved, while high frequency components associated with the solution are found late during the iterative process or before the solution starts to diverge. Then, if the iterative pro-

cedure is stopped/halted before the high frequency components are resolved or incipient divergence starts, a self-regularized solution is obtained ([28]).

The most popular regularization algorithm is the one known as *Tikhonov regularization* ([26,27]). This method is also called the Phillips-Twomey or the constrained linear inversion method ([18]). In addition, methods based on singular value decomposition (SVD) have gained popularity among other direct methods. The use of SVD based methods offers several advantages since it allows study of singular value spectrum of the matrix \mathbf{A} , and, therefore, determination of the degree of ill-conditioning of the system under consideration.

For inverse design, the best solution must be chosen based on some criterion; normally, this is some criterion for tradeoff between the perturbation error (Eq. (3)) and the regularization error (Eq. (4)). However, this is not in itself sufficient for the designer. It is also necessary that the chosen solution meet two other design conditions. First, the l_2 -norm based on direct comparison with the prescribed input conditions must be within some allowable design criterion. This must be met regardless of the value of the l_2 -norm of Eq. (3) used in choice of the “best” solution from a particular regularization method. Secondly, the chosen design solution must meet prescribed or heuristic conditions that the designer believes are appropriate, such as smoothness of solutions or solutions that meet some other desirable conditions such as not exceeding a maximum materials temperature. That is, the designer may choose a solution with a larger l_2 -norm based on comparison with the prescribed input conditions if that solution has other desirable attributes. Thus, the chosen design solution may differ from the “best” regularized solution obtained by any of the methods to be discussed. This is a fundamental difference from experimentally based inverse problems, where the goal is to find the very best solution that matches the measured input values.

We now examine the details of four methods for treating inverse problems made up of sets of linear algebraic equations. The proofs of the mathematical characteristics of these methods are carefully laid out in the excellent monograph by Hansen [24].

Truncated Singular Value Decomposition. The use of SVD and the examination of the set of singular values shows why the matrix \mathbf{A} is ill-conditioned. One use of this information is that it allows us to find a problem that can be solved by simply truncating the set of singular values to a smaller set that has an acceptable condition number. The corresponding matrix \mathbf{A}^* can then be generated, inverted to provide the inverted truncated matrix \mathbf{A}^{*-1} , and the solution

$$\mathbf{X}^* = \mathbf{A}^{*-1} \mathbf{b} \quad (5)$$

can be generated. The solution \mathbf{X}^* will not be exact, because some information has been deleted by throwing away the smaller singular values. However, the solution can be obtained, and it can be made well behaved if a sufficient number of small singular values are truncated. The accuracy of the solution for \mathbf{X}^* is then found. The forward problem is solved by deleting one of the extra boundary conditions used in the inverse solution, and inserting \mathbf{X}^* as the boundary condition on the boundary with no originally prescribed condition. Either prescribed condition may be retained on the design surface, but the known temperature is usually chosen because it is an easier condition to apply in forward solutions. However, because forward solutions are unique, retaining either condition will provide the same result in the forward calculation. The result of the forward solution can then be compared with the required extra boundary condition.

The first step is to determine the singular value decomposition for \mathbf{A} . A truncated solution is then computed by neglecting the $n-p$ smallest singular values of matrix \mathbf{A} , constituting the truncated singular value decomposition (TSVD) method. Thus,

$$\mathbf{X}^* = \mathbf{X}_p = \sum_{i=1}^p \frac{\mathbf{v}_i \mathbf{u}_i^T \mathbf{b}}{w_i} \quad (6)$$

Modified Truncated Singular Value Decomposition. An improvement to TSVD is the modified truncated singular value decomposition (MTSVD) method [29]. This regularization algorithm is a two-step procedure. First, an initial approximation is obtained by computing a truncated singular value decomposition (TSVD), i.e., discard singular values below a given threshold and its corresponding singular vectors as for Eq. (6). As a second step, a correction term to \mathbf{X}_p is computed from the remaining singular values and its corresponding singular vectors, i.e., from the null space of matrix \mathbf{A} . In this step, information concerning additional constraints or smoothing characteristics is introduced.

The correction term is calculated after solving the following least-squares problem for \mathbf{Z}_p

$$\min \|\mathbf{L}\mathbf{V}_p \mathbf{Z}_p - \mathbf{L}\mathbf{X}_p\|_2 \quad (7)$$

where the matrix \mathbf{L} represents the smoothing operator that is being applied on the solution and $\mathbf{Z}_p = (\mathbf{L}\mathbf{V}_p)^T \mathbf{L}\mathbf{X}_p$. Here, a second derivative finite difference operator is used, i.e., \mathbf{L} is given by

$$\mathbf{L} = \begin{bmatrix} 0 & & & & 0 \\ 1 & -2 & 1 & & \\ & \cdot & \cdot & \cdot & \\ & & & 1 & -2 & 1 \\ 0 & & & & & 0 \end{bmatrix} \quad (8)$$

and the matrix \mathbf{V}_p is formed by the remaining $n-p$ singular vectors, i.e.,

$$\mathbf{V}_p \equiv [\mathbf{v}_{p+1}, \dots, \mathbf{v}_n] \quad (9)$$

Then, the correction term is calculated by

$$\mathbf{X}_{C,p} = \mathbf{V}_p \mathbf{Z}_p \quad (10)$$

The MTSVD or \mathbf{L} -order regularized solution is obtained by subtracting the correction term from the initial estimate, that is

$$\mathbf{X}_{L,p} = \mathbf{X}_p - \mathbf{X}_{C,p} \quad (11)$$

This procedure is then repeated for the next larger value of p , and the procedure is continued until the solution converges to a smooth result and further increases in p result in the appearance of unacceptable oscillations in the solution. The initial value of p is usually the one for which the distribution of singular values starts to decay rapidly.

We have found that MTSVD works well for radiative surface interchange problems. However, for more complex systems with volume-volume interchange as for participating media, it is difficult to assemble the equations in such a way as to allow straightforward application of the minimization step.

Tikhonov Regularization. Solution of ill-posed problems began after the pioneering works of A. N. Tikhonov in the 1960s ([21,26,27]). His method of regularization considerably broadened the bounds of effective practical use of ill-posed problems in physical sciences. The main idea of the Tikhonov regularization method is to introduce a side constraint in order to stabilize or regularize the problem. Usually, this side constraint is linear, and allows the inclusion of an initial estimate, if available. The side constraint involves a norm that can be defined as

$$\Psi_i(\mathbf{X}) = \|\mathbf{L}_i(\mathbf{X} - \mathbf{X}_0)\|_2^2 \quad (12)$$

where \mathbf{L}_i approximates the i th derivative operator and \mathbf{X}_0 is an initial (biased) solution estimate. For $i=0$, the identity operator is assumed. The Tikhonov regularization method minimizes the functional $\Phi_\alpha(\mathbf{X})$, which is defined as

$$\Phi_\alpha(\mathbf{X}) = \|\mathbf{A}\mathbf{X} - \mathbf{b}\|_2^2 + \sum_{i=0}^q \alpha_i^2 \|\mathbf{L}_i(\mathbf{X} - \mathbf{X}_0)\|_2^2 = R^2 + \sum_{i=0}^q \alpha_i^2 \Psi_i(\mathbf{X}) \quad (13)$$

Therefore, the solution, \mathbf{X}_α is a function of the regularization parameter α and the initial solution \mathbf{X}_0 . Clearly, a large α represents a highly regularized solution with a small semi-norm as indicated by Eq. (13), while a small α has the reverse effect. That is, the solution minimizes the residual (first term on the right-hand side of Eq. (13)), but it is unstable to perturbations in the data. Thus, the selection of α is an important part of the regularization process and it must be selected carefully.

The selection of the initial estimate \mathbf{X}_0 is less critical, although it can be used in design to provide a better final solution. A choice of $\mathbf{X}_0 = 0$ introduces no bias; other choices and their effects are discussed below.

Minimization of Eq. (13) with respect to \mathbf{X} implies that

$$\Phi'_\alpha(\mathbf{X}) = 2\mathbf{A}^T(\mathbf{A}\mathbf{X} - \mathbf{b}) + 2 \sum_{i=0}^q \alpha_i^2 \mathbf{L}_i^T \mathbf{L}_i(\mathbf{X} - \mathbf{X}_0) \quad (14)$$

At the minimum, Φ'_α should be zero, thus Eq. (14) can be rearranged as

$$\mathbf{A}^T \mathbf{A} \mathbf{X} + \sum_{i=0}^q \alpha_i^2 \mathbf{L}_i^T \mathbf{L}_i \mathbf{X} = \mathbf{A}^T \mathbf{b} + \sum_{i=0}^q \alpha_i^2 \mathbf{L}_i^T \mathbf{L}_i \mathbf{X}_0 \quad (15)$$

For example, what is called standard Tikhonov regularization is the case when the series is terminated at $q=0$, thus \mathbf{L}_i becomes the identity matrix \mathbf{I} . That is,

$$(\mathbf{A}^T \mathbf{A} + \alpha_0^2 \mathbf{I}) \mathbf{X} = \mathbf{A}^T \mathbf{b} + \alpha_0^2 \mathbf{X}_0 \quad (16)$$

Another example is the second-order regularization method, for which $q=2$, $\alpha_0 = \alpha_1 = 0$, leaving α_2 as the only regularization parameter.

$$(\mathbf{A}^T \mathbf{A} + \alpha_2^2 \mathbf{L}_2^T \mathbf{L}_2) \mathbf{X} = \mathbf{A}^T \mathbf{b} + \alpha_2^2 \mathbf{L}_2^T \mathbf{L}_2 \mathbf{X}_0 \quad (17)$$

To complete the regularization procedure, the regularization parameter α has to be determined. There are several ways to find the optimal value ([25]).

The L -curve is perhaps the most convenient graphical tool for analysis of discrete ill-posed problems. It is a plot of the semi-norm used as a side constraint, $\|\mathbf{L}_i(\mathbf{X} - \mathbf{X}_0)\|$, versus the corresponding residual norm, $\|\mathbf{A}\mathbf{X} - \mathbf{b}\|$, for different values of the regularization parameter α . In this way, the L -curve displays the compromise between minimization of both quantities. This curve is very important since it divides the first quadrant into two regions. Hansen [25] indicates that it is impossible to construct any regularized solution that corresponds to a point below the L -curve; therefore, any regularized solution either lies on or above the L -curve. When plotted in log-log scale, the curve almost always has a characteristic L-shaped appearance with a distinct corner separating the vertical and the horizontal part of the curve. This corner corresponds to the near optimal value for the regularization parameter α . Unfortunately, the present study has found that the solutions corresponding to this corner have undesirable oscillations and in some circumstances some components of the solution vector become negative. Since these components represent the outgoing radiative energy, which is defined as positive, negative values are unacceptable on physical grounds, although they may provide a mathematically acceptable solution. For larger values of the regularization parameter, the solution has less or no oscillations, but at the expense of a larger residual error.

Note that if the initial solution estimate \mathbf{X}_0 is taken as exactly equal to the solution \mathbf{X} , then the value of α becomes indeterminate (see Eqs. (13–15)). In that case, the solutions from Tikhonov regularization reduce to the solutions of Eq. (2). Because these solutions are known to be unstable, a further regularization, perhaps through TSVD (Eq. (6)), must be applied to obtain a solu-

tion. The condition $\mathbf{X}_0 = \mathbf{X}$ is, of course, an unlikely scenario, as the exact solution is not known a priori. If it is, there is no reason to be solving the problem.

Because of the nondimensional form of the relations used here, the values of \mathbf{X}_0 should have certain attributes in order to bias the regularization result toward a useful design solution. Because of the nondimensionalized forms for the temperatures, radiosities, or radiative fluxes on heater surfaces, \mathbf{X}_0 is expected to be positive and of order unity, and we also strive to have solutions that are smooth. In the absence of other information, a value of $\mathbf{X}_0 = [1]$ is a reasonable choice.

To determine the value of the regularization parameter α for standard Tikhonov regularization, Eq. (13) must be solved for several values of α . This process is time-consuming and can be avoided by using the singular value decomposition of matrix \mathbf{A} ([29]). The first step is to determine the singular value decomposition for \mathbf{A} , that is to compute the left singular vectors \mathbf{u} , the singular values w_i and the right singular vectors \mathbf{v} . So \mathbf{A} can be expressed as

$$\mathbf{A} = \mathbf{U}\mathbf{W}\mathbf{V}^T = \sum_{i=1}^n \mathbf{u}_i w_i \mathbf{v}_i^T \quad (18)$$

where n is the total number of unknown radiosities. Then, a solution for a fixed α can be computed by introducing the filters f_i , which can be evaluated using

$$f_i = \frac{w_i^2}{w_i^2 + \alpha^2} \quad (19)$$

Thus, the regularized solution for a fixed α , \mathbf{X}_α , can be computed by

$$\mathbf{X}_\alpha = \sum_{i=1}^n f_i \frac{\mathbf{v}_i \mathbf{u}_i^T \mathbf{b}}{w_i} = \sum_{i=1}^n \frac{w_i}{w_i^2 + \alpha^2} \mathbf{v}_i \mathbf{u}_i^T \mathbf{b} \quad (20)$$

After a solution for a fixed regularization parameter is obtained, additional solutions can be computed by only recomputing the filters f_i and the matrix multiplications involved in Eq. (20).

Conjugate Gradient Method. The conjugate gradient method is an iterative technique for producing regularized solutions that avoids the explicit decomposition of the matrix \mathbf{A} . Matrix decompositions such as SVD are inherently time-consuming for large matrices, but are an inherent part of the TSVD, MTSVD and Tikhonov methods. Therefore, conjugate gradient solutions are often the method of choice for multidimensional problems. We shall see that the conjugate gradient approach offers particular advantages for multimode problems where solutions to nonlinear equation sets are required. Hansen [24] points out that the operations used in conjugate gradient regularization (CGR) lend themselves to parallelization.

The number of iterations performed, n , acts as the regularization parameter ([24] pg. 142), as the iterations serve to filter the higher frequency oscillations in the solution. Thus, a series of regularized solutions is automatically produced during the solution—a boon for the designer, who can choose among them based on other criteria than simply taking the solution with the smallest l_2 -norm.

If the initial guess for the CGR algorithm is taken as $\mathbf{X}^{(0)} = 0$, the auxiliary vector \mathbf{d} has starting value $\mathbf{d}^{(0)} = \mathbf{A}^T - \mathbf{r}^{(0)}$, and the residual vector is defined as $\mathbf{r}^{(n)} = \mathbf{b} - \mathbf{A}\mathbf{X}^{(n)}$ so that $\mathbf{r}^{(0)} = \mathbf{b} - \mathbf{A}\mathbf{X}^{(0)}$, then the CGR algorithm that is stable for inverse problems is given by the following five steps ([24]):

$$\begin{aligned} \alpha_n &= \frac{\|\mathbf{A}^T \mathbf{r}^{(n-1)}\|_2^2}{\|\mathbf{A}\mathbf{d}^{(n-1)}\|_2^2} \\ \mathbf{X}^{(n)} &= \mathbf{X}^{(n-1)} + \alpha_n \mathbf{d}^{(n-1)} \\ \mathbf{r}^{(n)} &= \mathbf{r}^{(n-1)} - \alpha_n \mathbf{A}\mathbf{d}^{(n-1)} \end{aligned} \quad (21)$$

$$\beta_n = \frac{\|\mathbf{A}^T \mathbf{r}^{(n)}\|_2^2}{\|\mathbf{A}^T \mathbf{r}^{(n-1)}\|_2^2}$$

$$\mathbf{d}^{(n)} = \mathbf{A}^T \mathbf{r}^{(n)} + \beta_n \mathbf{d}^{(n-1)}$$

The solution norm at each iteration $\|\mathbf{X}^{(n)}\|_2$ will increase monotonically with n , and the residual norm $\|\mathbf{r}^{(n)}\|_2$ will decrease monotonically with n if $\mathbf{X}^{(0)} = 0$. This behavior can be used to establish an L-curve and provide a criterion for stopping the iterative process.

Prior Research on Inverse Radiative Design. Recent research has centered on inverse solutions of design problems where radiative transfer is dominant. Recent reviews of the literature are available on enclosure problems where no participating medium is present ([15]), or where a participating medium is present ([17]).

A zonal method is used in [30] to formulate the radiative transfer in a rectangular enclosure containing an isothermal absorbing-emitting medium, and the characteristics (temperature and heat flux distributions) on the Uk surface were found. The Jacobi and Gauss-Seidel iterative solution methods were used, with the former providing the more stable and accurate results.

TSVD was used to solve some interesting two-dimensional furnace design problems, and found to work well ([31]). Two constraints (net radiative flux and temperature distributions) were imposed on all surface boundaries, and the volumetric energy generation rate distribution in the medium necessary to satisfy those constraints was sought. Radiative equilibrium was invoked in some of the medium volume elements in order to make the number of equations and unknowns equal. Then, the number of volume elements where radiative equilibrium was invoked was reduced, so the number of unknowns was larger than the number of equations, and the TSVD provided a solution that minimized the sum of the squares of the medium element temperatures. As the number of unknowns became still greater, oscillations were found in the solutions.

In [17], an inverse problem was solved in which all boundaries except one were adiabatic; the remaining boundary was a TQ boundary with emissivity of 0.5. The required medium temperature and source distributions were found that provided these given boundary conditions. TSVD was used for the inversion.

Various investigators ([32–35]) have used the modified truncated singular value decomposition method (MTSVD). The implementation of MTSVD for three-dimensional configurations showed that if a large number of surfaces is used in the computations, then TSVD and MTSVD require considerable memory storage and computer time to handle the required singular value decomposition (SVD).

The discrete ordinates method along with a conjugate gradient approach was used to find the net source distribution in an absorbing-emitting-scattering medium contained in a two-dimensional enclosure ([36]). Measured boundary intensities at the boundary midpoints were used as input to the inverse problem. Although this is not an application of inverse techniques to thermal design, it demonstrates the usefulness of the conjugate gradient technique in inverse problems.

A detailed study of inverse design techniques was carried out in [34], concentrating in particular on a comparison of the MTSVD and Tikhonov methods for two and three-dimensional enclosure problems with an absorbing-emitting medium.

In [32,37], MTSVD along with the Monte Carlo-based READ method ([38]) for computing exchange areas for the Hottel zone method were used to solve inverse problems. One practical problem was the temperature distribution needed for heaters to obtain a uniform heat flux and temperature on the material on the bottom of an industrial furnace.

Tikhonov regularization was used on an inversely posed problem to optimize a furnace design ([39]). The author noted the

existence of nonphysical (negative) radiosities for certain configurations, and also noted that greater regularization was required as the grid resolution was increased.

Inverse Solutions

We have investigated the general problem posed in Fig. 1 in some detail. We examined the effects of boundary condition choices and parameter variations on the solutions. We then considered the choice of solution methodology on the results. Finally we investigated the effects of grid choice and on the overall accuracy of the design. The tradeoffs naturally present between accuracy in achieving the desired design versus generation of non-physical designs are discussed.

Before discussing the inverse problem, solutions are given for the forward problem for dimensionless temperatures $T = t/t_{\text{ref}}$ specified on the enclosure as $T_{\text{top}} = T_3 = 2$, $T_2 = T_4 = 1.5$, and $T_1 = T_{\text{bottom}} = 1.0$, all surfaces black, and an aspect ratio $A = h/w = 0.5$. The dimensionless net radiative flux $Q_1(X) = q_{\text{net}}(x)/\sigma t_{\text{ref}}^4$ on the bottom surface was found. The result for this traditional forward problem is shown in Fig. 2, for various numbers of elements N on the surfaces. For 20 or more elements on each surface, the results are essentially unchanged, as confirmed by computing the l_2 -norm as a function of number of increments.

Now, a series of inverse problems is solved using second order Tikhonov regularization in which the net flux on surface 1 as found by the forward solution, Fig. 2, is imposed, while varying other conditions. For example, Fig. 3 shows the temperatures on surface 3 found by inverse solution when the temperatures on the two side walls are changed from the original value of 1.5. For the value of $T_2 = T_4 = 1.5$, the original condition of $T_3(X) = 2$ is recovered, as expected. However, as the side-wall temperatures are lowered, the temperature distribution on the top surface must vary to compensate and provide the necessary radiative flux on the bottom surface.

The results of Tikhonov regularization depend on the choice of the regularization parameter α . In Fig. 4, the accuracy of the heat flux prediction is shown as a function of this parameter for the cases of different wall temperatures. The error in the predicted and imposed radiative flux becomes greater as the imposed side wall temperatures deviate more from the original forward problem. The line separating the regions marked "oscillations" and "over-regularized" is derived from the L-curves for these solu-

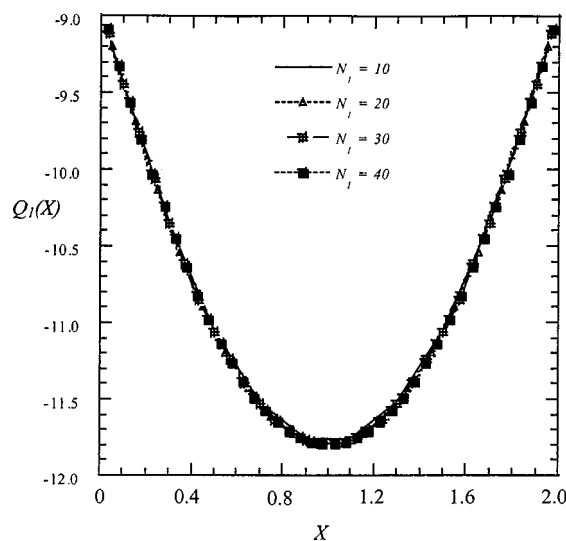


Fig. 2 Net dimensionless radiative flux $Q_1(X) = q_{\text{net}}(x)/\sigma t_{\text{ref}}^4$ on bottom surface of black rectangular enclosure with $T_{\text{top}} = T_3 = 2$, $T_2 = T_4 = 1.5$, and $T_1 = T_{\text{bottom}} = 1.0$, aspect ratio $A = h/w = 0.5$

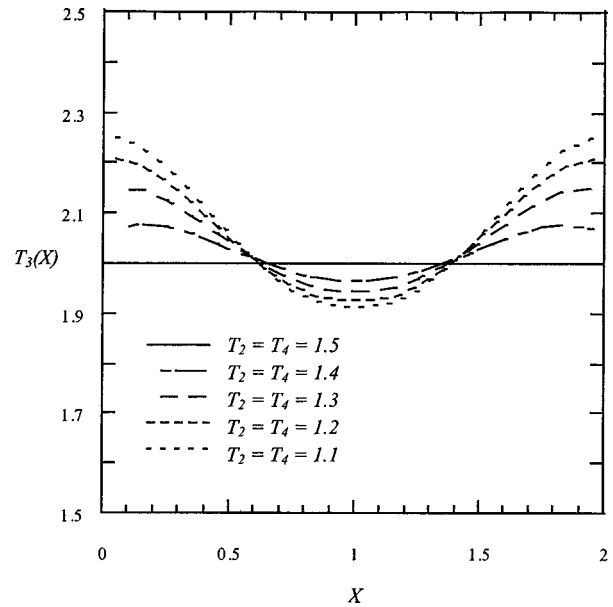


Fig. 3 Temperature distribution on top surface of black rectangular enclosure for various side-wall temperatures, $T_1 = T_{\text{bottom}} = 1.0$, imposed net dimensionless radiative flux $Q_1(X)$ from Fig. 2, aspect ratio $A = h/w = 0.5$

tions, but is approximate. It was chosen by examining the solutions for a range of α values, and noting when oscillations begin to appear.

The solutions shown in Fig. 3 would be very difficult to obtain using iterative forward solutions, but are shown by Fig. 4 to provide heat flux values very near to the imposed condition (generally within one percent). Similar solutions have been obtained for various imposed emissivity values on the side walls ([35]).

Similar solutions to those produced by the Tikhonov method can be generated using other inversion techniques. A comparison of predictions by different solution methods is shown in Fig. 5 for

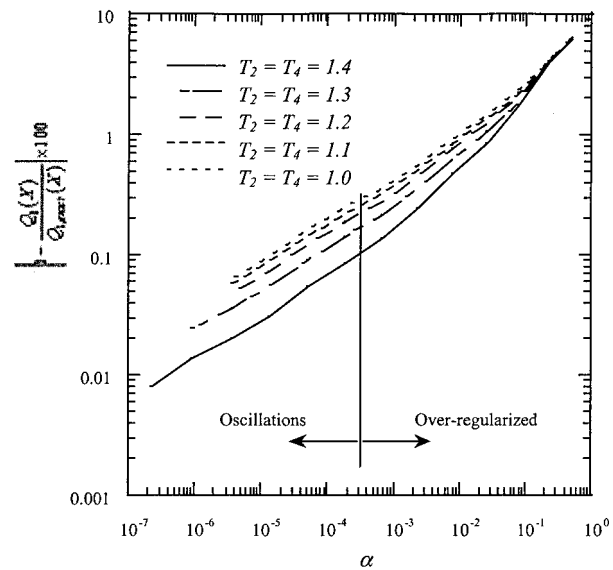


Fig. 4 Error in predicted heat flux on bottom surface versus regularization parameter α using temperature distributions on top surface of black rectangular enclosure for various side-wall temperatures from Fig. 4, $T_1 = T_{\text{bottom}} = 1.0$, imposed net dimensionless radiative flux $Q_1(X)$ from Fig. 2, aspect ratio $A = h/w = 0.5$

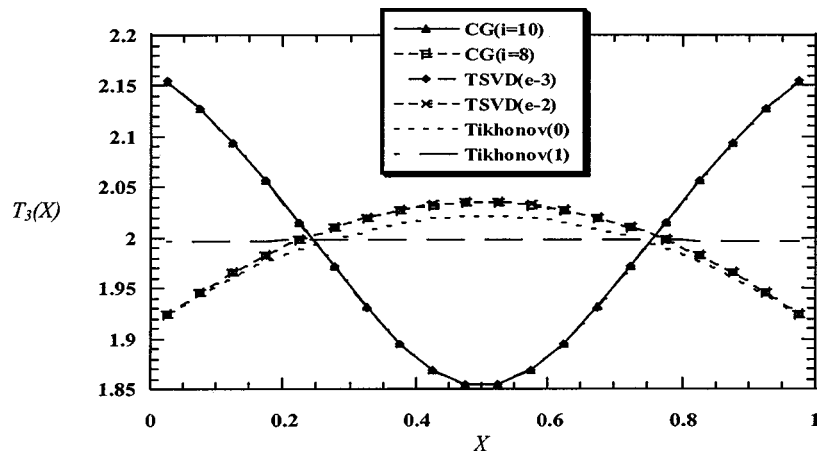


Fig. 5 Comparison of predicted top surface temperature $T_3(X)$ in square enclosure by 3 methods

an inverse radiative heat transfer problem. In this problem the unknown nondimensional temperature, $T_3(X)$, on the Uk top surface is to be predicted in a square (two-dimensional) enclosure with the bottom surface specified as the design surface. There is no participating medium and all surfaces are diffuse-gray and have an emissivity of 0.9. Each surface is segmented into 20 increments. Side walls are at $T_2 = T_4 = 1.5$, the bottom wall is at $T_1 = 1.0$ and has a parabolic dimensionless heat flux distribution $Q_1(X) = 3.2X^2 - 3.2X - 6.8$. These solutions all have less than one percent maximum difference from the prescribed $Q_1(X)$.

The Tikhonov 0th order solution gives good agreement with both the conjugate gradient method with eight iterations and the truncated singular value decomposition (TSVD) with p singular values greater than 10^{-2} . If we add two more iterations to the CG method and retain additional singular values greater than 10^{-3} in the TSVD, the solutions are slightly more accurate, but give a different shape and possibly a less desirable (less smooth) design solution. Figure 5 points out an important distinction between inverse problems applied to design and those in property measure-

ment and control. In design, any solution that provides the desired outcome may be acceptable, and the designer may pick the one that is simplest to implement.

The inversion methodology used for the base transparent case can be applied to a problem in which an absorbing cold isothermal medium at $T=0$ and optical thickness $\tau = ah$ is placed in the enclosure. Again, the side walls are at $T_2 = T_4 = 1.5$, the heat flux on bottom surface 1 is as shown in Fig. 2, and we wish to determine the temperature distribution on the top surface, $T_3(X)$. The results are in Fig. 6, and the accuracy of the solution is in Fig. 7.

As the optical thickness increases, the attenuation by the medium requires greater and greater temperatures on the top surface to provide the necessary radiative flux to the bottom surface. Again, these solutions would be quite tedious to obtain using iterative forward solutions. Figure 7 shows that the accuracy of the inverse solutions becomes poorer as the attenuation (optical thickness) becomes large. Note that the functional dependence of the

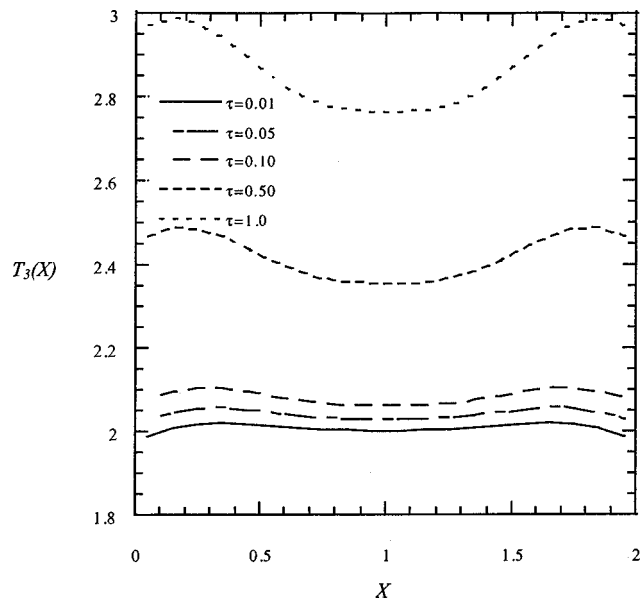


Fig. 6 Temperature distribution on top surface of black rectangular enclosure containing a gray cold gas with optical thickness $\tau = ah$; $T_1 = T_{\text{bottom}} = 1.0$, imposed net dimensionless radiative flux $Q_1(X)$ from Fig. 3, aspect ratio $A = h/w = 0.5$

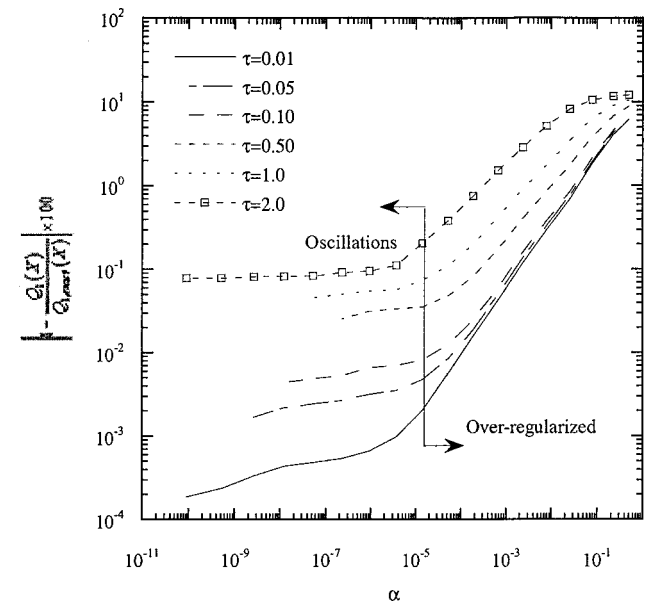


Fig. 7 Error in predicted heat flux on bottom surface versus regularization parameter α using temperature distributions on top surface of black rectangular enclosure for various medium optical thicknesses from Fig. 6, $T_1 = T_{\text{bottom}} = 1.0$, imposed net dimensionless radiative flux $Q_1(X)$ from Fig. 3, aspect ratio $A = h/w = 0.5$

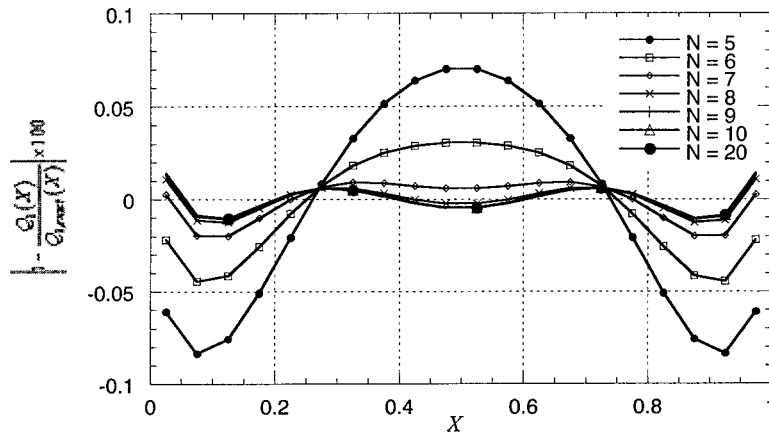


Fig. 8 Error in predicted dimensionless heat flux distribution $Q_1(X)$ for various levels of surface grid refinement

error on the regularization parameter is different from the transparent cases in the participating cases. Physically, as the optical thickness increases, the energy from the top wall is greatly attenuated before affecting the bottom wall and has smaller influence on the bottom surface. This results in greater uncertainty in the top wall temperature results. Similar solutions were obtained by using the MTSVD method ([35]).

Grid Effects. As with all numerical methods, tradeoffs also exist for inverse problems among grid size, relative error and computational costs. Unlike other numerical methods, the interplay between these parameters in inverse solutions is not well understood or characterized. As an example, Fig. 8 shows the error in the heat flux on the design surface based on predicted surface 3 temperatures. The error initially decreases with increasing grid resolution and then approaches a constant error value independent of further resolution. This is in contrast to forward problems where the total error tends to decrease with increased grid resolution until the errors reach the machine error limits. It appears that roundoff errors from the inversion process (i.e., regularization) become larger than truncation errors very quickly in the inverse formulation.

Existence of Solutions. Nonphysical results may be generated in two fundamentally different ways when solving an inverse problem. First, unlike inverse analysis of experimental data where a boundary measurement is used to infer physical properties or other system conditions, it is possible to pose conditions (the design set) for a design problem that have no physical solution. In such cases, the overall problem formulation cannot be satisfied without the “solution” predicting nonphysical results such as negative absolute temperatures, negative radiosities, etc.

In Fig. 9 an example of the generation of nonphysical results is shown. A rectangular enclosure with aspect ratio A has a surface at the top with unknown thermal conditions and a design surface at the bottom. The aspect ratio of this enclosure is varied from 0.5 to 0.7. For a fixed pre-specified error criterion (based on the ability of the predicted solution to satisfy the design conditions), the predicted radiosity distribution on the top surface begins to oscillate at larger aspect ratios, and takes negative values at the edges. The radiosity, composed of emitted plus reflected radiation, must be positive in a real system. Physical results can be generated for the 0.7 aspect ratio if the error criterion is significantly relaxed (curve with the x markers). These results imply that for some cases, a design solution cannot be found within a specified tolerance without the predicted unknown solution becoming nonphysical.

The other way that nonphysical results may be generated in inverse analysis is through an inappropriate choice of solution

procedure for the particular problem. As previously noted, solutions to ill-conditioned systems are extremely sensitive to perturbations in the input parameters and roundoff errors in the computational procedure. Improper selection of the solution methodology or any number of other factors (e.g., over-regularization, grid choice, etc.) may generate a nonphysical solution. It is important to distinguish between the two possibilities for creating nonphysical solutions. It will be valuable to develop an approach that is (a) independent of solution methodology and (b) will identify and eliminate problem specifications that have no physical solutions.

Three-Dimensional Solutions. The numerical techniques described and used in previous sections can be applied to problems in three-dimensional enclosures. As previously noted, it is not unusual to use 500,000 computational elements in a three-dimensional forward design of an industrial furnace. It is most likely that an inverse design tool that extends the techniques shown above would be used early in the design stage of a furnace or heater system to specify approximate heater conditions that could be refined further with detailed forward calculations. In general then, we would assume that a relatively coarse grid would be used for the inverse solution and that a finer grid would be used in the forward cycle of the design project to make de-

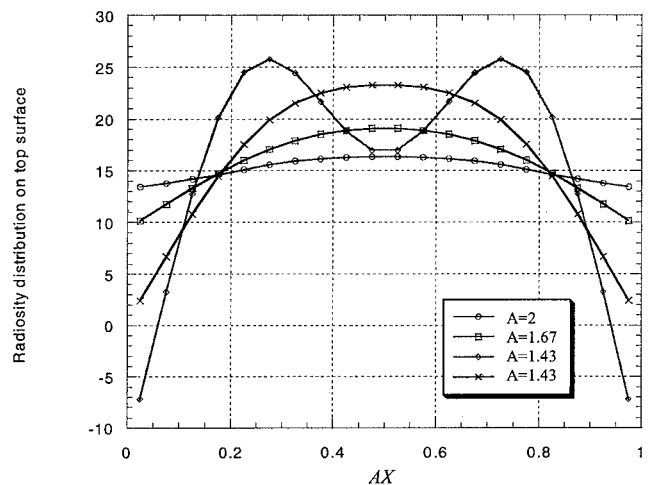


Fig. 9 Radiosity distribution along unknown surface with geometry aspect ratio $A = w/h$ as a parameter

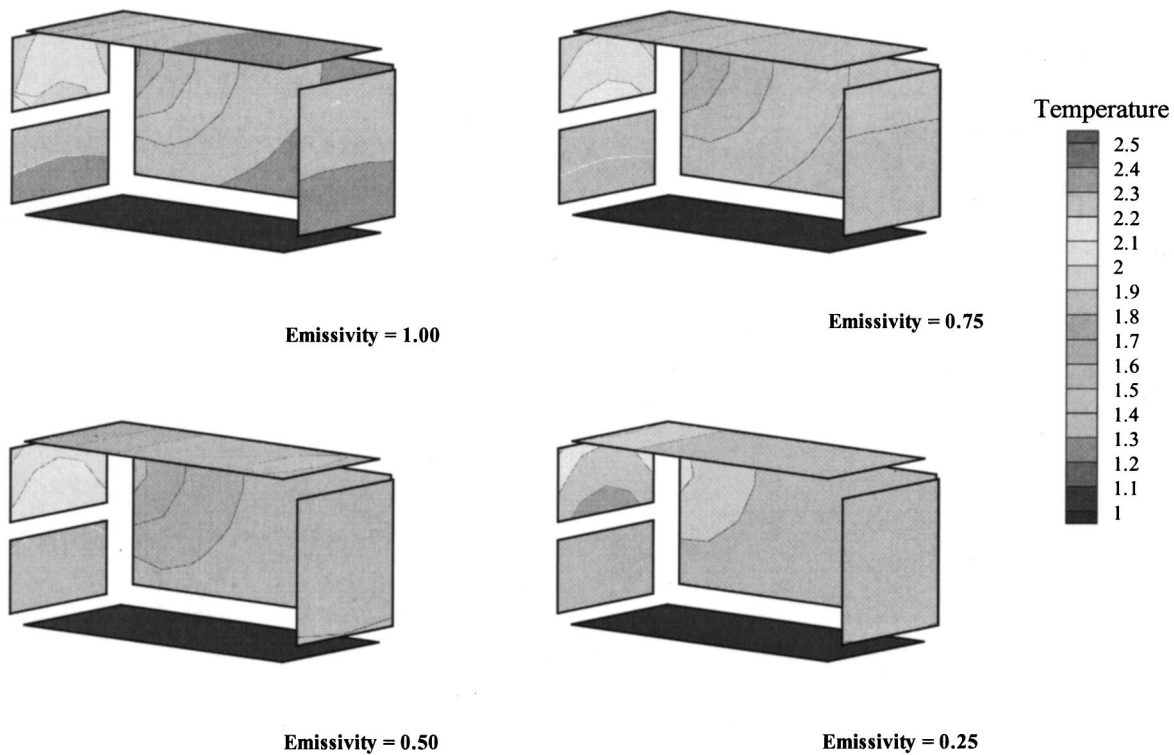


Fig. 10 Temperature profiles on the interior surfaces of a radiantly heated process furnace enclosing a transparent medium by inverse analysis. All surfaces adiabatic except upper half of left end (the heater) and the bottom surface, which is at uniform temperature and given heat flux distribution. Heater temperature profiles are for cases when the bottom surface emissivity is varied as shown.

tailed modifications. By adopting a coarse-grid-based inverse solution, the relative computational cost of the inversion process is manageable.

Shown in Fig. 10 is a three-dimensional rectangular enclosure with no participating medium. The radiative heater is on the upper half of the left-hand end of the enclosure. It is desired to maintain the bottom surface at prescribed heat flux and dimensionless temperature of 1.0. All other surfaces except the bottom and top-left-end are adiabatic. The computed surface temperature profiles required on the heater surface and resulting on the other enclosure surfaces are shown for various emissivities on the bottom surface.

This three-dimensional calculation was performed on an IBM RS6000 computer system and required two to five minutes of CPU time per case. This example shows the power of inverse design in the design process, as using forward solutions to determine the correct temperature distributions for achieving the desired conditions on the bottom surface would be extremely tedious. For problems with participating media, the number of elements and the matrix size become much larger than for this surface radiation problem. Some of the inversion techniques may become intractable in this case because the matrices are full or nearly full, and matrix operations such as SVD become very time-consuming.

An important consideration is the relative time to generate a forward solution compared with an inverse solution. For example, if a few hundred forward solutions can be carried out in the same time as an inverse solution, then inverse solution for design becomes impractical, as an iterative forward solution can be done more cheaply in terms of computer time. Morales [35] compared the time for the forward, MTSVD and Tikhonov solutions for the problem described in Figs. 1–5, using 100 through 800 surface nodes. These two methods are the slowest of the four methods outlined in this paper; TSVD is generally faster than MTSVD, and the conjugate gradient approach is faster than the other three.

Thus, Morale's results provide a reasonable guide. He shows that, for all cases studied, between 1.9 and 3.5 forward solutions could be carried out per inverse MTSVD solution, and between 2.8 and 5.5 against Tikhonov. It is unlikely that accurate solutions could be obtained with so few forward iterations; in addition, the multiple solutions available from the inverse approach would be missed.

Conclusions

Inverse design techniques as outlined in this paper hold the promise of providing a good initial design that can then be more carefully analyzed by conventional detailed prediction of performance. This should greatly reduce the cost involved in the conventional process, and may become a useful tool among the skills of future designers. Inverse design techniques may also produce a better final design in many cases because the conditions assumed for final traditional design can be much closer to the optimum set.

The development of inverse design methods for thermal fluid systems will represent a significant departure in the design process from the present approaches. There are many hurdles to be cleared before both designers and researchers in the thermal fluid area apply inverse methods to the wide range of system design problems that exist. It is first necessary to bridge a gap between the theoretical developments in the mathematics of inverse methods and applications to real engineering systems. Following that, issues such as accuracy, grid dependence, and constraints that are relevant to engineers must be adequately documented and resolved.

We believe that the design process is almost always better approached by an inverse technique; indeed, design would probably have been developed along these philosophical lines in the past except for the mathematical problems inherent in inverse analysis,

and the development of inverse design methods for thermal fluid systems involving significant radiation represents an important design alternative to the present approaches.

Acknowledgments

The authors acknowledge the support of IHI, Inc. and the Texas Higher Education Coordinating Board (Grant ARP-218).

Nomenclature

- a = radiative linear absorption coefficient, m^{-1}
 A = area, m^2 ; aspect ratio, h/w
 \mathbf{A} = matrix of coefficients
 \mathbf{A}^* = truncated matrix of coefficients
 \mathbf{b} = vector of known quantities
 \mathbf{d} = auxiliary vector in conjugate gradient algorithm, Eq. (21).
 F = radiation configuration factor
 h = distance between parallel plates, m
 \mathbf{I} = identity matrix
 i = singular value index
 J = radiosity, W/m^2
 K = kernel of integral equation
 \mathbf{L} = smoothing operator
 N = number of enclosure surface elements
 n = number of iterations
 p = number of retained singular values
 q = energy flux, W/m^2
 R = residual norm, Eq. (3)
 \mathbf{r} = residual vector, Eq. (21)
 Q = dimensionless radiative energy flux, $q_{rad}/\sigma t_{ref}^4$
 t = absolute temperature, K
 T = normalized temperature, t/t_{ref}
 \mathbf{U} = orthogonal matrix
 \mathbf{V} = orthogonal matrix
 \mathbf{u}, \mathbf{v} = column vectors for orthonormal vectors used in SVD
 w = singular value; width of plate, m
 \mathbf{W} = matrix of singular values
 \mathbf{X} = solution vector
 \mathbf{X}^* = regularized solution vector
 X = dimensionless coordinate position, x/h
 Y = dimensionless coordinate position, y/h
 x = coordinate distance, m
 y = coordinate distance, m
 Z = smoothing vector

Greek Symbols

- α = Tikhonov regularization parameter, Eq. (13); parameter in CGR algorithm, Eq. (21)
 ε = surface emissivity
 Ψ = norm of side constraint, Eq. (12)
 Φ = Tikhonov regularization function
 σ = Stefan-Boltzmann constant, $5.67 \times 10^{-8} W/m^2 \cdot K^4$
 τ = optical thickness, ah
 ξ = arbitrary coordinate, m

Subscripts

- C = correction term
 i = index of surface subdivisions or singular values; i th derivative
 N = rank of coefficient matrix
 n = iteration number
 p = based on p retained singular values
 rad = radiative
 0 = initial estimate
 $1,2,3,4$ on surfaces 1,2,3 or 4

References

- [1] Farag, I. H., 1979, "Temperature Profiles in Combustion Gases by Inversion: Review and Approach," ASME Paper 79-HT-21, ASME, New York.
- [2] Matthews, L. K., Viskanta, R., and Incropera, F., 1984, "Development of Inverse Methods for Determining Thermophysical Properties of High-Temperature Fibrous Materials," *Int. J. Heat Mass Transf.*, **27**, No. 4, pp. 487–495.
- [3] Wu, W. J., and Mulholland, G. P., 1989, "Two-Dimensional Inverse Radiation Heat Transfer Analysis Using Monte Carlo Techniques," *Heat Transfer Phenomena in Radiation, Combustion and Fires*, R. K. Shah, ed., ASME, New York.
- [4] Lin, J.-D., and Tsai, J.-H., 1991, "Comparison of P1 and S-P Two Flux Approximations in Inverse Scattering Problems," ASME Paper 91-WA-HT-13, ASME, New York.
- [5] Subramaniam, S., and Mengüç, M. P., 1991, "Solution of the Inverse Radiation Problem for Inhomogeneous and Anisotropically Scattering Media Using a Monte Carlo Technique," *Int. J. Heat Mass Transf.*, **34**, No. 1, pp. 253–266.
- [6] Li, H. Y., and Özişik, M. N., 1992, "Estimation of the Radiation Source Term With a Conjugate-Gradient Method of Inverse Analysis," *J. Quant. Spectrosc. Radiat. Transf.*, **48**, No. 3, pp. 237–244.
- [7] Tsai, J.-H., 1993, "Inverse Scattering Problem With Two Flux Methods," *Int. Commun. Heat Mass Transfer*, **20**, pp. 585–596.
- [8] Hendricks, T. J., and Howell, J. R., 1994, "Inverse Radiative Analysis to Determine Spectral Radiative Properties Using the Discrete Ordinates Method," *Proc. 10th International Heat Transfer Conference*, Vol. 2, Institute of Chemical Engineers, Rugby, U.K., pp. 75–80.
- [9] Jones, M. R., Curry, B. P., Brewster, M. Q., and Leong, K. H., 1994, "Inversion of Light-Scattering Measurements for Particle Size and Optical Constants: Theoretical Study," *Appl. Opt.*, **33**, No. 18, pp. 4025–4041.
- [10] Jones, M. R., Tezuka, A., and Yamada, Y., 1995, "Thermal Tomographic Detection of Inhomogeneities," *ASME J. Heat Transfer*, **117**, pp. 969–975.
- [11] McCormick, N. J., 1997, "Analytical Solutions for Inverse Radiative Transfer Optical Property Estimation," *Proc. ASME Heat Transfer Division*, Vol. 3, ASME, New York, pp. 367–371.
- [12] Kudo, K., Kuroda, A., Ozaki, E., and Oguma, M., 1997, "Estimation of Absorption Coefficient Distribution in Two-Dimensional Gas Volume by Solving Inverse Radiative Property Value Problem," *Radiative Transfer-II: Proc. Second Int. Symp. on Radiation Transfer*, M. P. Mengüç, ed., Begell House, New York.
- [13] Frankel, J. I., and Keyhani, M., 1996, "A New Approach for Solving Inverse Solidification Design Problems," *Numer. Heat Transfer, Part B*, **30**, No. 2, pp. 161–177.
- [14] Yang, G. Z., and Zabarar, N., 1998, "The Adjoint Method for an Inverse Design Problem in the Directional Solidification of Binary Alloys," *J. Comput. Phys.*, **140**, pp. 432–452.
- [15] França, F., Morales, J. C., Oguma, M., and Howell, J. R., 1998, "Inverse Design of Radiating Systems Dominated by Radiative Transfer," *Radiative Transfer II: Proc. Second Int. Symp. Radiative Heat Transfer*, M. P. Mengüç, ed., Begell House, New York.
- [16] Franca, F., Morales, J. C., Oguma, M., and Howell, J. R., 1998, "Inverse Design of Thermal Systems With Radiation," Invited keynote lecture, *Heat Transfer 1998, Proc. 11th Int. Heat Transfer Conf.*, Vol. I, J. S. Lee, ed., Taylor and Francis, New York, pp. 213–221.
- [17] França, F., Morales, J. C., Oguma, M., and Howell, J. R., 1998, "Inverse Radiation Heat Transfer Within Enclosures With Participating Media," *Proc. 1998 11th Int. Heat Trans. Conf.*, J. S. Lee, ed., Taylor and Francis, New York, Vol. 7, pp. 433–438.
- [18] Press, W. H., Teukolsky, S. A., Vetterling, W. T., and Flannery, B. P., 1992, *Numerical Recipes in FORTRAN: The Art of Scientific Computing*, Cambridge University Press, New York.
- [19] Beck, J. V., Blackwell, B., and St. Clair, Jr., 1995, *Inverse Heat Conduction: Ill-Posed Problems*, John Wiley and Sons, New York.
- [20] Beck, J. V., Alifanov, O. M., Woodbury, K. A., Artyukhin, E. A., and McCormick, N., 1992, "Joint American-Russian NSF Workshop on Inverse Problems in Heat Transfer," Final Report MSU-ENGR-92-008, Michigan State University.
- [21] Alifanov, O. M., 1994, *Inverse Heat Transfer Problems*, Springer-Verlag, Berlin.
- [22] Alifanov, O. M., Artyukhin, E. A., and Rumyantsev, S. V., 1995, *Extreme Methods for Solving Ill-Posed Problems With Applications to Inverse Heat Transfer Problems*, Begell House, New York.
- [23] Trujillo, D. M., and Busby, H. R., 1997, *Practical Inverse Analysis in Engineering*, CRC Press, Boca Raton, FL.
- [24] Hansen, P. C., 1998, *Rank-Deficient and Discrete Ill-Posed Problems: Numerical Aspects of Linear Inversion*, SIAM, Philadelphia, PA.
- [25] Hansen, P. C., 1992, "Numerical Tools for Analysis and Solution of Fredholm Integral Equations of the First Kind," *Inverse Probl.*, **8**, pp. 849–872.
- [26] Tikhonov, A. N., 1963, "Solution of Incorrectly Formulated Problems and the Regularization Method," *Sov. Math. Dokl.*, **4**, pp. 1035–1038 (English translation 1963, *Dokl. Akad. Nauk. SSSR*, **151**, pp. 501–504).
- [27] Tikhonov, A. N., Goncharsky, A. V., Stepanov, V. V., and Yagola, A. C., 1995, *Numerical Methods for the Solution of Ill-Posed Problems*, Kulwer Academic, Boston.
- [28] Hanke, M., 1995, *Conjugate Gradient Type Methods for Ill-Posed Problems*, John Wiley and Sons, New York.
- [29] Hansen, P. C., Sekii, T., and Shibahashi, H., 1992, "The Modified Truncated

- SVD Method for Regularization in General Form,” *SIAM J. Sci. Stat. Comput.*, **13**, No. 5, pp. 1142–1150.
- [30] França, F., and Goldstein, L., 1996, “Application of the Zoning Method in Radiative Inverse Problems,” *Brazilian Congress of Engineering and Thermal Sciences, ENCIT 96*, Florianopolis, Brazil.
- [31] Kudo, K., Kuroda, A., Eid, A., Saito, T., and Oguma, M., 1996, “Solution of the Inverse Radiative Load Problems by the Singular Value Decomposition,” *Radiative Transfer-I: Proc. First Int. Symp. on Radiation Transfer*, M. P. Mengüç, ed., Begell House, New York, pp. 568–578.
- [32] Matsumura, M., Morales, J. C., and Howell, J. R., 1998, “Optimal Design of Industrial Furnaces by Using Numerical Solution of the Inverse Radiation Problem,” *Proc. 1998 Int. Gas Research Conf.*, San Diego, Nov.
- [33] Morales, J. C., Harutunian, V., Oguma, M., and Howell, J. R., 1996, “Inverse Design of Radiating Enclosures With an Isothermal Participating Medium,” *Radiative Transfer I:—Proc. First Int. Symp. on Radiative Heat Transfer*, M. P. Mengüç, ed., Begell House, New York, pp. 579–593.
- [34] Morales, J. C., Matsumura, M., Oguma, M., and Howell, J. R., 1997, “Computation of Inverse Radiative Heat Transfer Within Enclosures,” *Proc. 1997 ASME National Heat Transfer Conference*, ASME, New York.
- [35] Morales, J. C., 1998, “Radiative Transfer Within Enclosures of Diffuse Gray Surfaces: The Inverse Problem,” Ph.D. dissertation, Department of Mechanical Engineering, The University of Texas at Austin, Austin, TX.
- [36] Li, H. Y., 1997, “Inverse Radiation Problem in Two-Dimensional Rectangular Media,” *AIAA J. Thermophy. Heat Transf.*, **11**, No. 4, pp. 556–561.
- [37] Matsumura, M., 1997, “Optimal Design of Industrial Furnaces by Using Numerical Solution of the Inverse Radiation Problem,” M.S. thesis, Department of Mechanical Engineering, The University of Texas at Austin, Austin, TX.
- [38] Yang, W.-J., Taniguchi, H., and Kudo, K., 1995, “Radiative Heat Transfer by the Monte Carlo Method,” *Advances in Heat Transfer*, **27**, J. P. Hartnett, and T. F. Irvine, eds., Academic Press, San Diego.
- [39] Jones, M. R., 1999, “Inverse Analysis of Radiative Heat Transfer Problems,” *ASME J. Heat Transfer*, **121**, pp. 481–484.

Comparison of Monte Carlo Surface Exchange With Radiative Continuum Results in Large Particle Dispersions

E. Nisipeanu

P. D. Jones

Mechanical Engineering Department,
Auburn University,
Auburn University, AL 36849-5341

A Monte Carlo technique follows radiation intensity rays through a dispersion of particles. Rays reflect from and are absorbed by the surfaces of the particles that they encounter. Transmitted radiative fluxes are compared with Monte Carlo simulations of a radiative continuum, using properties from both independent and correlated scattering theories. Whereas both discontinuous (surface) and continuous representations of the medium yield similar results for high porosities (low volume fractions), the continuous representation yields transmission overpredictions for porosities less than 0.9, using independent scattering properties, and for porosities less than 0.7, using correlated scattering properties. The overprediction is less severe for less reflective particle surfaces. [S0022-1481(00)01603-0]

Keywords: Heat Transfer, Monte Carlo, Participating Media, Particulate, Radiation

Introduction

Transmission of thermal radiation through clouds of optically large particles is often solved by assuming a radiative continuum. The radiative transfer equation (RTE) is solved using appropriate overall properties for extinction coefficient, scattering albedo, and scattering phase function. In this work, the real discontinuous nature of such media is preserved and the multitude of particles are considered to experience surface radiative exchange between each one of them. The approach is simple in concept though somewhat exacting in practice: A Monte Carlo simulation of a large number of energy bundles passes through the entire medium, interacting with solid particles along the way. The results of this work should be useful in determining where the radiative continuum assumption breaks down for media such as fluidized beds, dispersed suspensions, porous solids, and other discrete (or discontinuous) media, although the medium characterization will not support the packed bed limit, and hence only qualitative conclusions may be drawn for that case. Potentially, this work could serve as a benchmark to improve dependent scattering theory, thus expanding the applicable range for radiative continuum modeling.

Previous works with discontinuous (i.e., discrete or noncontinuum) models usually address a dense particulate suspension and treat it as a regular assembly of cells of identical geometry. Vortmeyer [1] reviews a series of such radiative models, concluding that identical cell models are only applicable if the optical thickness of the medium is very large and direct incidence from non-neighboring cells can be safely neglected. An example of this approach is given by Chan and Tien [2], which analyzes radiative transfer through packed beds by determining the scattering diagram of a unit cell. Solutions are obtained using Monte Carlo sampling techniques, though the radiative flux incident on each neighboring cell is considered to be diffuse. Similar work is reported in Kudo et al. [3], which examines different types of packing and variations in volume fraction. In the present work, the unit cell of fixed geometry is avoided, and both optically thick and thin

participating media have been studied. By allowing random fluctuations in locations, ray effects from particle arrangement lattices are avoided.

Tien [4] gives an extensive overview of radiative transfer in packed and fluidized beds, comparing experimental results to both continuous models (modified by application of dependent scattering theory) and discontinuous cell models. The Monte Carlo models of Kudo et al. [3] and Yang et al. [5] are found to compare best with the packed bed experimental results of Chen and Churchill [6], although neither applies over the entire range of particle diameter to bed thickness ratio. (Experimental results for high solid fraction dispersions which are not packed are not available.) Yang et al. [5] examines a random packing of spheres in the entire medium instead of using a cell model. The average penetration distance of a photon before its absorption or scattering is evaluated as a function of extinction coefficient. The extinction coefficient is determined, using a Monte Carlo technique, as the fraction of energy bundles intercepted by spheres during travel through a predetermined distance. Singh and Kaviany [7] examine a (nonpacked) suspension of spheres in a regular, staggered arrangement. A full Monte Carlo approach is employed, and randomly oriented bundles of energy are allowed to interact with spheres in their paths. Particle properties are restricted to directional independence, and periodic boundary conditions are applied in the lateral directions to simulate a one-dimensional bed. In order to speed up the solution convergence, an energy partitioning method is used rather than a random number to decide whether a bundle is absorbed or reflected at an impact point. Palmer et al. [8] apply an approach similar to that of the present work, in that arrays of cylindrical reflector elements are modeled both as a collection of discrete surfaces, and also as an equivalent radiative continuum. Significant differences in results are found between the two cases.

The present work might be viewed as an extension of Singh and Kaviany [7] to a less restricted case. A three-dimensional suspension of spherical particles in a pseudo-random arrangement is modeled by a Monte Carlo ray tracing procedure throughout the entire medium to evaluate radiative transfer through the suspension for a large range of radiative and geometrical parameters. The domain of interest consists of a cube of variable size, where the bottom face is a hot, isothermal, black surface, and the top face is a black surface at zero temperature. The side walls are

Contributed by the Heat Transfer Division for publication in the JOURNAL OF HEAT TRANSFER. Manuscript received by the Heat Transfer Division, April 20, 1998; revision received, February 14, 2000. Associate Technical Editor: D. Kaminski.

perfect specular reflectors to account for rays traveling into the cube from neighboring regions. Any other boundary conditions can be employed since no simplification towards one or two-dimensional simulations is made. The spherical particles may be either specular, diffuse, or partially specular reflectors which absorb and emit radiation. The directional distribution of radiant propagation in the medium as a system is tracked, and variation of the radiative properties of specular particles with the local (particle surface) polar angle is considered.

Analysis

The following analysis is applied to a gray medium in thermal and radiative equilibrium in order to illustrate the essential processes of radiative propagation by surface reflection within the complex morphology of the medium. With appropriate attention to the emissive term and spectral indices of refraction, a nongray case could be considered. With coupling to an energy equation, combined mode cases could be considered.

Features of the Discontinuous Model. A uniform three-dimensional mesh is generated in the medium, and a spherical particle is associated with each node. The sphere centers (x_c, y_c, z_c) are located in random positions about the node according to

$$\begin{aligned} x_c &= x_c + \left(\frac{\Delta x}{2} - r_s \right) (2R_x - 1) \\ y_c &= y_c + \left(\frac{\Delta y}{2} - r_s \right) (2R_y - 1) \\ z_c &= z_c + \left(\frac{\Delta z}{2} - r_s \right) (2R_z - 1) \end{aligned} \quad (1)$$

where R_x, R_y, R_z are random numbers between 0 and 1. Overlapping of particles is automatically avoided. Thus the medium is pseudo random, in that each particle must stay within a defined cell, although it takes on a random location within that cell. As compared to a fully random distribution of particles, the pseudo-random distribution has the advantage of maintaining a uniform number density, while allowing neighboring particles to be located randomly with respect to each other. This limits unnecessary streaming effects caused by uneven number densities, and reduces the number of particle distribution realizations which must be simulated before results converge. However, the pseudo-random distribution becomes less random as the ratio of particle diameter to cell size increases, and the particles become effectively fixed in space within the cell boundaries. Thus, while the pseudo-random

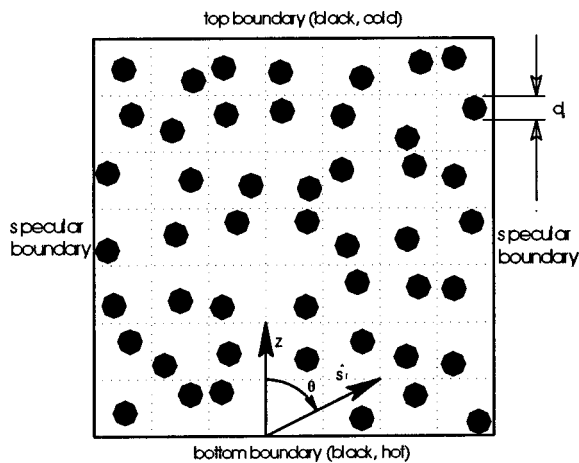


Fig. 1 Two-dimensional view of the particle suspension computational field

distribution works well for nonpacked dispersions, it can only qualitatively model a randomly packed bed, and only for cubic packing geometries.

All the dimensions of the problem are normalized by the side length of a nodal cube. Consequently, the dimensionless side length of the medium is given by the number of particles in each direction. The dimensionless diameter of the spherical particles d_s (actual diameter divided by nodal cube side length) can be varied between 0 and 1 (Fig. 1). The former case represents a uniformly distributed, disperse particulate medium. In the latter case, the spheres touch each other and the medium has the lowest possible porosity for the present implementation of the model (simple cubic), although this gives too structured an array and too much porosity to actually be used in packed bed cases. After the release of each energy bundle at the bottom boundary, or after each impact on the side boundaries, the position of the particles in the medium is changed in order to maintain independence from a particular array of particle locations.

Monte Carlo Method. The Monte Carlo technique starts by releasing energy bundles from the bottom boundary and then tracing them until they are absorbed by a particle or by a boundary. Locations of the emission points on the lower boundary and directions of emission are determined using Monte Carlo direct simulations. For a diffuse, isotropic bottom boundary, the directions of emission are ([9])

$$\begin{aligned} \psi &= 2\pi R_\psi \Rightarrow \psi \in [0, 2\pi) \\ \theta &= \sin^{-1}(\sqrt{R_\theta}) \Rightarrow \theta \in \left[0, \frac{\pi}{2}\right]. \end{aligned} \quad (2)$$

The coordinates of the energy bundle after it travels a distance P are

$$\begin{aligned} x &= x_d + l_1 P \\ y &= y_d + l_2 P \\ z &= z_d + l_3 P \end{aligned} \quad (3)$$

where $l_1 = \sin \theta \cos \psi$, $l_2 = \sin \theta \sin \psi$, and $l_3 = \cos \theta$ are the direction cosines of the ray. To determine the coordinates of the intersection point with a spherical particle, x , y , and z are substituted into the spherical surface equation:

$$(x - x_c)^2 + (y - y_c)^2 + (z - z_c)^2 = r_s^2. \quad (4)$$

The discriminant of the second-order equation in P is computed. If this discriminant is positive, the equation has real roots and the solution is the smaller of the two ([2]), the other impact point being impossible for opaque particles since the energy bundles do not penetrate the particles.

The spherical particles may be considered to be either diffuse or specular reflectors, or a combination of these. If the particles are specular, then directionally dependent reflectivity and absorptivity functions are predicted by Fresnel's equations, which depend upon the complex index of refraction of the particle material ([9]). The incident polar and azimuthal angles at a spherical particle surface are computed from the direction of the in-coming ray and the normal at the surface. The direction of a reflected ray is found from Snell's law as

$$\hat{s}_r = \hat{s}_i + 2|\hat{s}_i \cdot \hat{n}| \hat{n} \quad (5)$$

in which the unit sphere surface normal $\hat{n} (n_1, n_2, n_3)$ is

$$\hat{n} = \frac{x - x_c}{r_s} \hat{i} + \frac{y - y_c}{r_s} \hat{j} + \frac{z - z_c}{r_s} \hat{k}. \quad (6)$$

For diffuse reflectors, random polar and azimuthal reflection angles are simply generated by the Monte Carlo method in the local coordinate system. However, in order to keep track of the

bundle trajectory, the direction cosines in the overall medium coordinate system must be determined. The direction of the reflected ray is

$$\hat{\mathbf{s}}_r = \underbrace{\sin \theta_r \cos \psi_r}_{l_{111}} \hat{\mathbf{t}}_1 + \underbrace{\sin \theta_r \sin \psi_r}_{l_{112}} \hat{\mathbf{t}}_2 + \underbrace{\cos \theta_r}_{l_{113}} \hat{\mathbf{n}} \quad (7)$$

where l_{111} , l_{112} , and l_{113} are the local direction cosines. $\hat{\mathbf{t}}_1$, $\hat{\mathbf{t}}_2$ are two unit tangent vectors at the point of impact and perpendicular to each other, where

$$\hat{\mathbf{t}}_1 = \frac{\hat{\mathbf{v}} \times \hat{\mathbf{n}}}{|\hat{\mathbf{v}} \times \hat{\mathbf{n}}|}, \quad \hat{\mathbf{t}}_2 = \frac{\hat{\mathbf{n}} \times \hat{\mathbf{t}}_1}{|\hat{\mathbf{n}} \times \hat{\mathbf{t}}_1|} \quad (8)$$

and $\hat{\mathbf{v}}$ is an arbitrary vector.

At its interaction with a particle, the energy bundle can be absorbed instead of reflected. Since α_s , the absorptivity of a particle, can be seen as the probability of absorption of a bundle at the interaction point, a random number R_a between 0 and 1 is generated and if $R_a < \alpha_s$, then the energy bundle is absorbed. At radiative and particle thermal equilibrium, for any energy bundle absorbed by a sphere, another one is emitted by the same sphere from a random position on its surface and in a random direction. The polar and azimuthal angles corresponding to this random position are

$$R_\theta = \frac{\int_0^{2\pi} \int_0^{\theta_c} \sin \theta d\theta d\psi}{\int_0^{2\pi} \int_0^\pi \sin \theta d\theta d\psi} = \frac{1 - \cos \theta_c}{2} \Rightarrow \theta_c = \cos^{-1}(1 - 2R_\theta)$$

$$R_\psi = \frac{\int_0^{\psi_c} d\psi}{\int_0^{2\pi} d\psi} \Rightarrow \psi_c = 2\pi R_\psi \quad (9)$$

and the random position is

$$\begin{aligned} x &= x_c + r_s \sin \theta_c \cos \psi_c \\ y &= y_c + r_s \sin \theta_c \sin \psi_c \\ z &= z_c + r_s \cos \theta_c \end{aligned} \quad (10)$$

The emission direction is determined from relations similar to Eq. (2).

If Eq. (4), with x , y , and z obtained from Eq. (3), has no real solution P , then the energy bundle strikes one of the bounding surfaces. In order to account for the contribution in radiative transfer from the regions beyond the computational domain, the side walls are considered to be perfect specular reflectors. This means that each time a ray strikes one of the side walls, it reflects according to Snell's law. The energy bundles that end up back on the bottom face are absorbed and their history ends at this point. The energy bundles that manage to get to the top boundary are recorded together with the corresponding incident angles with a precision of one degree. Examples of directional flux output are shown in Fig. 2. Note that Fig. 2 shows directional flux in 1-deg increments for a simulation of 10^5 total bundles (approximately 800 CPU hrs.). Hence, the average number of bundles represented by each point in Fig. 2 is only about 10^3 . This accounts for the somewhat uneven appearance of Fig. 2. Flux integrated over all directions is, of course, much smoother. The total number of energy bundles absorbed by the top boundary is used to determine the dimensionless hemispherical radiative flux at the top boundary.

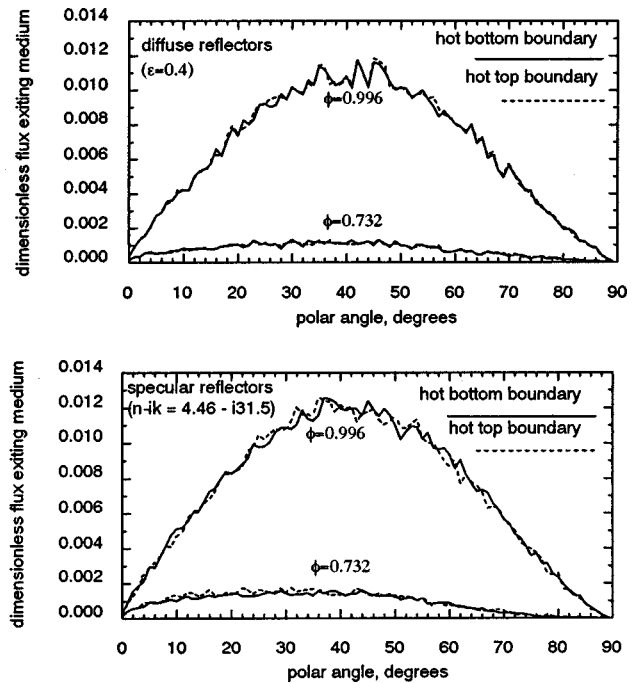


Fig. 2 Directional distribution of the dimensionless radiative flux in two cases: energy bundles released from the bottom; and from the top boundary, respectively

Monte Carlo techniques are notorious for CPU time consumption. Care is taken to check for collisions only with particles in the octant of a generated or reflected direction, and to consider particles for collision in order of distance from a beam origin. Using an Ultra2 Model 2200—dual 200MHz UltraSPARC processor, CPU times of roughly 0.5 min per energy bundle are achieved.

As a means of verification, the present model was operated for a limiting case of a medium with a single sphere. Analytic solutions for both perfectly emitting and perfectly reflecting spheres are within one percent of model predictions for all porosities. Based on these studies, a base simulation of 10^5 energy bundles was chosen.

Results and Discussion

Figures 3 and 4 show the dimensionless flux on the top boundary (analogous to transmission for the case of a black bottom boundary), for media comprised of diffusely reflecting particles with $\epsilon=0.4$ (Fig. 3), and of specularly reflecting particles with $n=4.46$, $k=31.5$ (Fig. 4, representative of a highly reflective metal). Porosity is varied by altering the size of the particles. The variation of dimensionless flux with the parameter H/d_s (medium height to particle diameter ratio, which for fixed porosity is directly proportional to optical thickness) has the same trend for either diffuse or specular particles. Figures 3 and 4 show analogous results computed by a Monte Carlo solution of the RTE, which assumes a radiative continuum. The properties of the continuous model are determined by independent scattering theory:

$$\omega = \rho_s$$

$$\beta = Q_{ext} \pi r_s^2 N_v$$

$$\Phi = 1; \quad \text{specularly scattering media}$$

$$\Phi = \frac{8}{3\pi} (\sin \Theta - \Theta \cos \Theta); \quad \text{diffusely scattering media.} \quad (11)$$

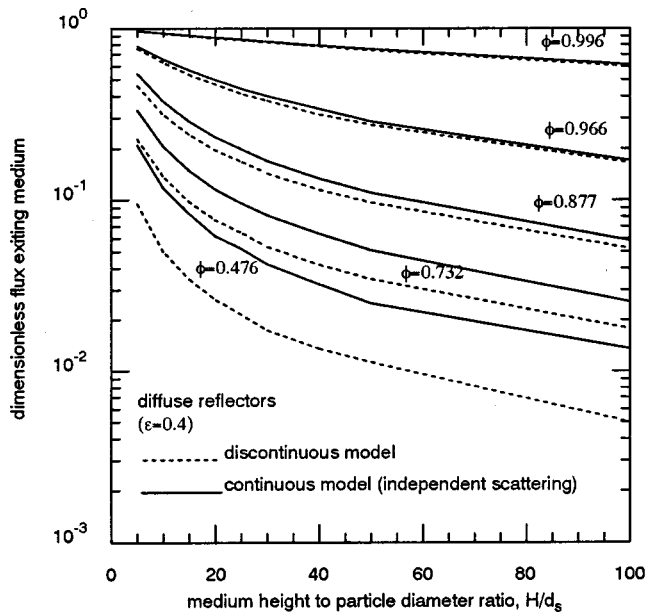


Fig. 3 Comparison of Monte Carlo solutions for discontinuous and continuous models (independent scattering theory) at different porosities—the diffuse case

For large spheres ($2\pi r_s/\lambda \gg 1$), diffraction causes radiative energy to be scattered forward within a very narrow angle ([9]) from the direction of transmission. Thus diffraction can be neglected and treated as transmission. It is also neglected in the discontinuous model. Hence, for large particles without diffraction $Q_{ext} = 1$. For the arrangement in this model, the dimensionless $N_v = 1$, where N_v is the number density defined by the number of the spheres in the volume (unity) of the bed. Since thermal radiation is basically infrared, the assumption of large spheres is satisfied for $r_s > 10 \mu\text{m}$.

For high porosities (>0.9) the continuous and discontinuous models (RTE and surface radiation) produce similar results,

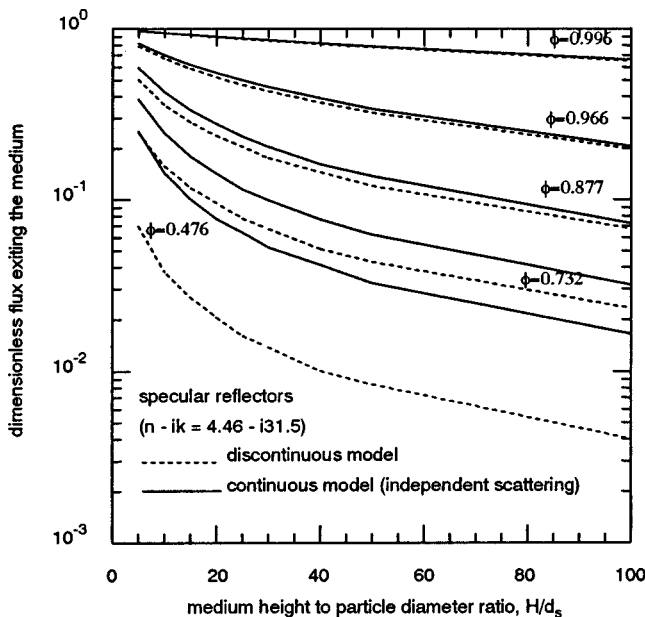


Fig. 4 Comparison of Monte Carlo solutions for discontinuous and continuous models (independent scattering theory) at different porosities—the specular case

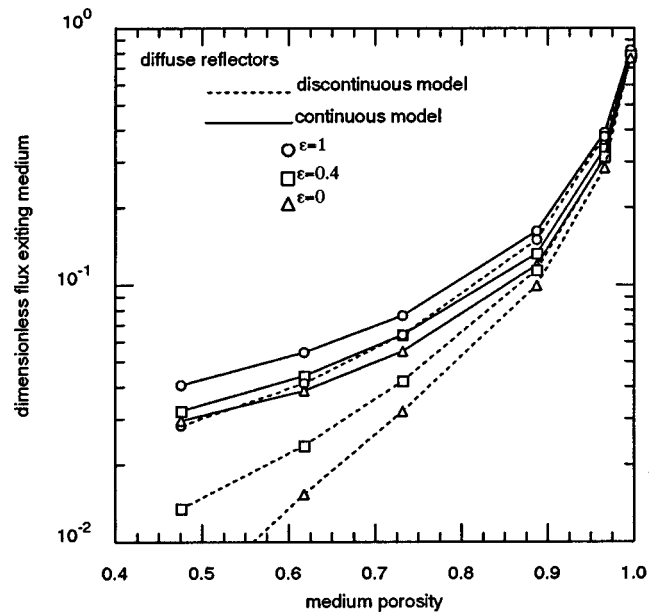


Fig. 5 Comparison of Monte Carlo solutions for discontinuous and continuous models for different particle radiative properties—the diffuse case

whereas differences appear for lower porosities. That is, while a radiative continuum solution (RTE) using independent scattering is a good approximation for high porosity particle suspensions, such a solution severely overestimates radiative transmission through lower porosity suspensions. Note that transmittance in Figs. 3 and 4 is shown on a log scale. The continuum approach treats the medium as being composed of a multitude of point scatterers and having a certain extinction coefficient. As the particles become larger relative to their computational cell (decreasing porosity), they cannot be approximated as point scatterers and the continuum approach breaks down. Note in Figs. 3 and 4 that the difference between the continuous and discontinuous models varies only slightly with H/d_s (medium thickness; number of ball rows). Thus, it may be inferred that the coarseness (ball size relative to medium thickness) of the medium has only a slight effect on the validity of the continuum assumption.

RTE results were also computed using the dependent scattering theory of Kamiuto ([10], not shown). Dependent scattering improves the RTE results, delaying divergence between the continuous and discontinuous results to $\phi < 0.7$, though in other respects following the same trends as Figs. 3 and 4. Porosities of $\phi < 0.7$ might be considered to come into a range where the pseudo-random medium starts to exhibit a tendency towards streaming effects due to the constraint of larger particles within a fixed volume computational cell. However, it should be noted that streaming effects (through the pseudo-random medium) would tend to increase transmittance, whereas all results reported here show a transmittance for the discontinuous simulation which is lower than that predicted by continuum methods. If discontinuous effects are unimportant, then correlated scattering theory should work as well for a simple cubic packed bed ($\phi = 0.476$) as for a randomly packed bed, except for perhaps a bit more transmittance in the cubic bed, as allowed by streaming effects. And yet it is the continuum model which gives the overprediction.

The effect on transmittance of differing particle radiative properties is shown in Figs. 5 and 6 for diffuse and specular reflectors, respectively, for $H/d_s = 40$. For diffuse reflectors, results for several values of particle emittance are shown. For specular reflectors, four cases are considered: high reflectance metallic (Al); low reflectance metallic (Ni); high reflectance dielectric ($n = 6$); and low reflectance dielectric ($n = 1$). Figure 5 shows that divergence

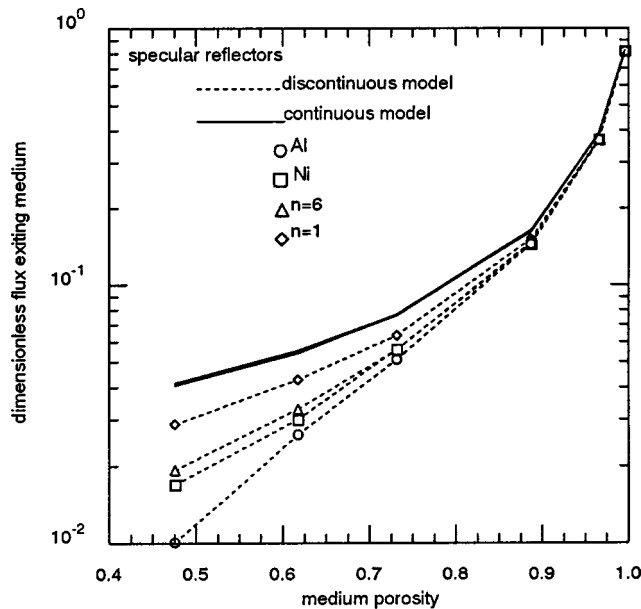


Fig. 6 Comparison of Monte Carlo solutions for discontinuous and continuous models for different particle radiative properties—the specular case

between the discontinuous (surface radiation Monte Carlo) and continuum assumption (RTE) results increases with decreasing particle emittance as well as decreasing porosity. Figure 6 shows that divergence increases for higher reflectance particles and also for more metallic particles. Figure 6 confirms that for isotropic scattering in the continuous model, particle surface properties are not important ([9]). Since the difference between them is insignificant, identifying marks are omitted from the continuum results lines in Fig. 6. Figure 6 demonstrates that there is a significant effect of particle surface properties in dispersed media, as predicted by Monte Carlo simulation.

Figure 7 compares the present results with those of Singh and Kaviany [7], which considers a fixed (staggered) particle arrangement (instead of pseudo random), with periodic lateral boundary

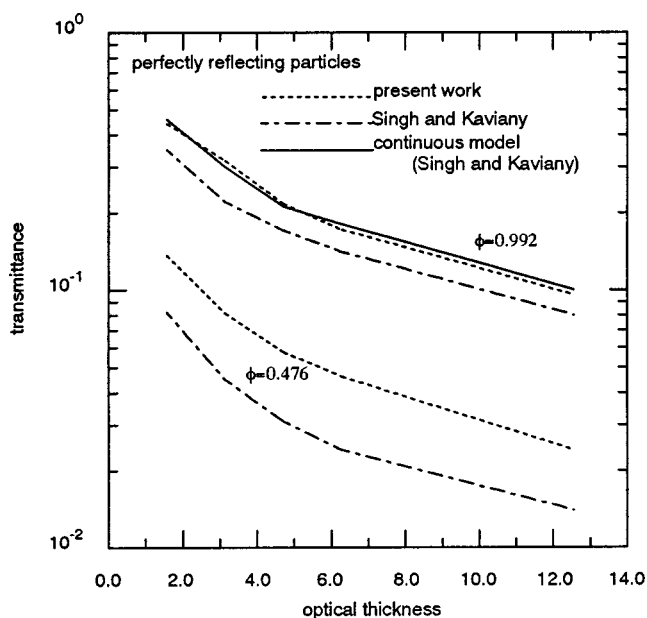


Fig. 7 Comparison with Singh and Kaviany model

conditions (instead of specularly reflecting boundaries on a wide mesh), and energy partitioning (instead of probability-based absorption). Transmittance is plotted against optical thickness, $\tau = 1.5(1 - \varphi)H/d_s$. The present model predicts consistently higher transmittances, and gives results for high porosity which are similar for the discontinuous and the continuous approaches. The Singh and Kaviany model predicts lower transmittances than the continuous model even for the highest considered porosity. The differences shown in Fig. 7 are interesting in that they indicate potential difficulties in setting up a truly confirming experiment.

Conclusions

Given a sufficient number of energy bundles and assuming the absence of modeling errors, the Monte Carlo method might be considered to offer the most correct solution to radiative transfer problems that can be available ([11]). The present full Monte Carlo simulation of surface radiation interaction with a pseudo-randomly arranged suspension of optically large, spherical, opaque particles shows that radiative continuum models do not correctly predict the behavior of such media at low porosity (dense suspensions), or for reflective (low emittance) particles. This may be due to the fact that as particles attain finite diameters with respect to the interparticle distance, the medium becomes significantly inhomogeneous and might not be properly described by the homogeneous continuum model with properties determined by the independent scattering theory. The discrepancy can be improved by using correlated scattering to develop the effective continuum properties of the medium, though divergence between continuous and discontinuous simulations still occurs. It is also found that deviation between the continuous (RTE) and the discontinuous (surface radiation) models depends only slightly on the coarseness of the medium (expressed here by H/d_s).

Nomenclature

- d_s = dimensionless particle diameter
- H = dimensionless medium depth
- $\hat{i}, \hat{j}, \hat{k}$ = unit vectors in x, y, z directions
- k = absorptive index
- l_1, l_2, l_3 = direction cosines
- n = refractive index
- \hat{n} = unit surface normal
- n_1, n_2, n_3 = normal components in x, y, z directions
- N_v = number density
- P = dimensionless pathlength
- Q_{ext} = extinction efficiency
- q_1, q_2 = dimensionless hemispherical radiative flux reflected and transmitted, $(\text{flux}/\sigma T_1^4)$
- r_s = dimensionless particle radius
- R_x, R_y, R_z = random numbers between 0 and 1
- $R_\alpha, R_\theta, R_\psi$ = random numbers between 0 and 1
- \hat{s}_i, \hat{s}_r = incident and reflected ray direction vector
- \hat{t}_1, \hat{t}_2 = unit vectors tangent to the particle surface
- T_1, T_2 = bottom and top boundary temperatures, K
- \hat{v} = arbitrary vector
- x, y, z = dimensionless energy bundle coordinates
- x_c, y_c, z_c = dimensionless sphere center coordinates
- $\Delta x, \Delta y, \Delta z$ = dimensionless side length of unit cell

Greek Symbols

- α = absorptivity
- ε = emissivity
- θ = polar angle
- Θ = angle between incident and scattered rays
- ρ_s = particle reflectivity
- σ = Stefan-Boltzmann constant, $5.67 \times 10^{-8} \text{ W/m}^2 \text{ K}^4$
- τ = optical thickness
- φ = porosity
- Φ = scattering phase function

ψ = azimuthal angle
 ω = scattering albedo

Subscripts

c = particle center
 d = departure point
 i, r = incident, reflected
 l = local
 s = sphere (spherical particle)
 v = volume
 x, y, z = x, y, z directions
 θ, ψ = polar, azimuthal directions
1, 2 = bottom, top boundaries
1, 2, 3 = perpendicular directions in local coordinate system

References

- [1] Vortmeyer, D., 1978, "Radiation in Packed Solids," *Proceedings, 6th International Heat Transfer Conference* (Toronto), Vol. 6, Hemisphere, Washington, DC, pp. 525–539.
- [2] Chan, C. K., and Tien, C. L., 1974, "Radiative Transfer in Packed Spheres," *ASME J. Heat Transfer*, **96**, pp. 52–58.
- [3] Kudo, K., Yang, W. J., Taniguchi, H., and Hayasaka, H., 1987, "Radiative Heat Transfer in Packed Spheres by Monte Carlo Method," *Heat Transfer in High Technology and Power Engineering*, Hemisphere, New York, pp. 529–540.
- [4] Tien, C. L., 1988, "Thermal Radiation in Packed and Fluidized Beds," *ASME J. Heat Transfer*, **110**, No. 4(B), pp. 1230–1242.
- [5] Yang, Y. S., Howell, J. R., and Klein, D. E., 1983, "Radiative Heat Transfer Through a Randomly Packed Bed of Spheres by the Monte Carlo Method," *ASME J. Heat Transfer*, **105**, No. 2, pp. 325–332.
- [6] Chen, J. C., and Churchill, S. W., 1963, "Radiant Heat Transfer in Packed Beds," *AIChE. J.*, **9**, pp. 35–41.
- [7] Singh, B. P., and Kaviany, M., 1991, "Independent Theory Versus Direct Simulation of Radiation Heat Transfer in Packed Beds," *Int. J. Heat Mass Transf.*, **34**, No. 11, pp. 2869–2882.
- [8] Palmer, B. J., Drost, M. K., and Welty, J. R., 1996, "Comparison of Equation of Transfer With Simulations on Large Arrays of Cylindrical Reflector Elements," *Numer. Heat Transfer, Part B*, **30**, No. 3, pp. 271–289.
- [9] Modest, M. F., 1993, *Radiative Heat Transfer*, McGraw-Hill, New York.
- [10] Kamiuto, K., 1990, "Correlated Radiative Transfer in Packed-Sphere Systems," *J. Quant. Spectrosc. Radiat. Transf.*, **43**, No. 1, pp. 39–43.
- [11] Howell, J. R., 1988, "Thermal Radiation in Participating Media: The Past, the Present, and Some Possible Futures," *ASME J. Heat Transfer*, **110**, No. 4(B), pp. 1220–1229.

Pool Boiling Heat Transfer From Plain and Microporous, Square Pin-Finned Surfaces in Saturated FC-72

K. N. Rainey

Department of Mechanical
and Aerospace Engineering,
The University of Texas at Arlington,
Arlington, TX 76019-0023

S. M. You

Associate Professor,
School of Mechanical
and Aerospace Engineering,
Seoul National University,
Seoul 151-742, Korea
e-mail: smyou@snu.ac.kr

The present research is an experimental study of “double enhancement” behavior in pool boiling from heater surfaces simulating microelectronic devices immersed in saturated FC-72 at atmospheric pressure. The term “double enhancement” refers to the combination of two different enhancement techniques: a large-scale area enhancement (square pin fin array) and a small-scale surface enhancement (microporous coating). Fin lengths were varied from 0 (flat surface) to 8 mm. Effects of this double enhancement technique on critical heat flux (CHF) and nucleate boiling heat transfer in the horizontal orientation (fins are vertical) are investigated. Results showed significant increases in nucleate boiling heat transfer coefficients with the application of the microporous coating to the heater surfaces. CHF was found to be relatively insensitive to surface microstructure for the finned surfaces except in the case of the surface with 8-mm-long fins. The nucleate boiling and CHF behavior has been found to be the result of multiple, counteracting mechanisms: surface area enhancement, fin efficiency, surface microstructure (active nucleation site density), vapor bubble departure resistance, and re-wetting liquid flow resistance. [S0022-1481(00)02603-7]

Keywords: Boiling, Enhancement, Experimental, Finned Surfaces, Heat Transfer

Introduction

For the past three decades, microprocessor technology has produced increasingly denser and faster chips. These advances in chip design have also produced increased power dissipation requirements. To handle the increased heat dissipation requirements of these chips, direct liquid immersion cooling, involving boiling heat transfer between the chips and the coolant, is considered a practical method for handling the large amount of heat generated from high watt density devices (Bar-Cohen [1]). Compared with forced convection cooling schemes (both single and two-phase), pool boiling heat transfer is considered to be the more attractive alternative because it is generally less complex and easier to seal. However, pool boiling must rely on enhancement techniques to achieve the high heat flux requirements predicted for future electronics.

Large-scale area enhancement using a single or an array of fins is one such method that has been studied for the enhancement of pool boiling heat transfer. Haley and Westwater [2] studied a 6.4-mm diameter, 30.6-mm long single horizontal copper fin in isopropyl alcohol and R-113 and found that multiple stable boiling modes could occur simultaneously and at adjacent positions along a fin, thus showing the highly complex nature of boiling from fins. As a result, Lai and Hsu [3], and more recently Liaw and Yeh [4], have presented theoretical models of multiple-mode boiling from single fins in order to study this phenomenon.

Klein and Westwater [5] provided the first experimental study of boiling from a multiple pin fin array. Using 6.4-mm diameter, 19 and 28.6-mm long copper cylindrical pin fins positioned horizontally in R-113 and water, they found that a fin spacing of only about 1.6 mm was wide enough to allow all fins to behave independently, even for nine or ten fin arrays. Mudawar and Anderson [6] also studied single and multiple copper pin finned surfaces in

FC-72 and FC-87 and found that their single fin modeling approach could be extended to predict the boiling curves of their multiple fin surfaces with reasonable accuracy. Kumagai et al. [7] produced an extensive study of boiling from relatively small copper rectangular fin arrays. They tested various fin lengths (0 to 10 mm), thicknesses (0.2 to 1.5 mm), and spacings (0.28 to 2 mm) as well as base surface orientation in R-113 and determined an “optimized” fin array design. Later, Yeh [8] proposed a design method to obtain an optimum array of longitudinal rectangular fins. Kumagai et al. [7] also found that the longitudinal fin orientation (base surface is vertical) provided better, more stable heat transfer performance than the vertical fin orientation (base surface horizontal). On the other hand, Guglielmini et al. [9] found that the vertical fin orientation of their copper square pin fin array surfaces (0.4 and 0.8 mm width and spacing, 3 mm long) provided slightly better heat transfer performance than the longitudinal orientation.

Another method which has been studied extensively for the enhancement of pool boiling heat transfer is small-scale surface enhancement using a variety of techniques: surface roughening, mechanically produced reentrant type surfaces, porous metallic coatings, and microporous coatings as well as others. Two methods of particular interest are surface roughening and microporous coatings. Due to severe aging effects, surface roughening has received little sustained interest. Chaudri and McDougall [10] measured the long-term nucleate boiling performance of an abrasive treated tube and found only temporary benefits. Nishikawa et al. [11] also observed that the effects of surface roughness diminish with increasing pressure. A relatively new method for surface enhancement is the microporous coating developed by O'Connor and You [12] and Chang and You [13,14]. The coating is a surface treatment technique used to increase vapor/gas entrapment volume and active nucleation site density by forming a porous structure with cavities much smaller than conventional metallic porous coatings. Chang and You [15] have shown that, compared to a plain surface, the microporous coated surface augmented

Contributed by the Heat Transfer Division for publication in the JOURNAL OF HEAT TRANSFER. Manuscript received by the Heat Transfer Division, June 18, 1999; revision received, Apr. 17, 2000. Associate Technical Editor: T. Chu.

nucleate boiling heat transfer coefficients by about 330 percent and increased critical heat flux (CHF) by approximately 100 percent.

The objective of the present work is to investigate the pool boiling heat transfer performance of a double enhancement technique which utilizes a multiple square pin fin array on a horizontal flat surface with a microporous coating surface enhancement. By combining a small-scale surface enhancement with a large-scale area enhancement, the overall heat transfer performance could potentially be increased beyond the heat transfer performance obtained using only one method. To the authors' knowledge, no research has been done on the combination of micron-scale surface enhancements with fin arrays. The heater surfaces are machined from solid copper blocks. An initial matrix of five different fin lengths were considered: 0 (flat surface), 1, 2, 4, and 8 mm. Additional fin lengths of 0.25 and 0.5 mm for the microporous coated surface were added to better understand the effect of fin length on CHF. All testing is performed in saturated FC-72 at atmospheric pressure, under increasing heat flux conditions, and with the base surface in the horizontal upward-facing orientation (fins are vertical).

Experimental Apparatus and Procedure

Test Facility. The pool boiling test facility used for the present work is shown in Fig. 1. The test liquid, saturated FC-72 at atmospheric pressure, was contained within a stainless steel pressure vessel, 406 mm high and 154 mm in diameter, which was heated by three band heaters located on the sides and bottom of the chamber. A cartridge heater was located in the bottom of the chamber to provide additional heating during degassing and prior to tests. The test vessel was insulated with 15-mm-thick foam insulation. An external water-cooled condenser was used throughout the testing to prevent loss of test liquid. A copper-constantan thermocouple was placed within the test vessel to measure bulk liquid temperature. Atmospheric pressure was maintained by venting the vessel to ambient. The test heater assembly was mounted to a stainless steel support bar and immersed in the test liquid. The test liquid surface was maintained at approximately 150 mm above the test heater.

A DC power supply was connected in series with a shunt resistor and the test heater. The shunt resistor, rated at 100 mV and 10 A, was used to determine the current in the electric circuit. A measured voltage drop across the test heater was used to calculate the heat flux applied to the test heater.

The test heater design is shown in Fig. 2. The heating element is a thin tantalum film and a titanium nitride film. The heating element was sputtered onto a 0.5-mm-thick silicon nitride coated silicon wafer along with copper for solder connections. The total heating element electrical resistance was about 20 Ω . The heating element side of the wafer was soldered to copper tape for the power lead connections while the other side of the wafer was soldered to the finned copper block. The finned copper blocks were machined from solid pieces of copper with a 10 mm \times 10 mm \times 2 mm base surface and 0, 0.25, 0.5, 1, 2, 4, and 8 mm fin lengths, L . A 5 \times 5 array of square pin fins with a fin thickness, t , of 1 mm and fin spacing, b , of 1 mm was machined on the surface using a high-speed steel slitting saw blade. The base of the copper block contains two thermocouple wells centered in the base surface and spaced 5 mm apart and 5 mm deep. The copper/heater assembly was attached to a Teflon substrate (10 mm thick) using a 3M epoxy (1832L-B/A, $k \approx 0.067$ W/m-K). The completed test heater was then mounted in a Lexan frame and surrounded by 3M epoxy to generate a flush-mounted heating surface. The surface condition of the finned heaters is "machine roughened." The flat surface was also created using the same machining process in order to obtain a comparable surface roughness. All surfaces were cleaned with acetone prior to testing.

For the microporous coated heater tests, the coating used is the ABM coating introduced by Chang and You [14]. The mi-

croporous coating technique was previously developed by O'Connor and You [12], further refined by Chang and You [13,14], and patented by You and O'Connor [16]. The coating is a surface treatment technique used to increase vapor/gas entrapment volume and active nucleation site density by forming a porous structure of about 0.1–1 μ m size cavities. The ABM coating was named from the initial letters of its three components: Aluminum particles/Devcon Brushable Ceramic epoxy/Methyl-Ethyl-Keytone (M.E.K.). The mixture of the three components was spray-coated over the finned surfaces using an Iwata HP-C airbrush. After the carrier (M.E.K.) evaporated, the resulting coated layer consisted of microporous structures with aluminum particles (1 to 20 μ m in diameter) and a binder (Devcon Brushable Ceramic), having a thickness of ≈ 50 μ m. The microporous coating

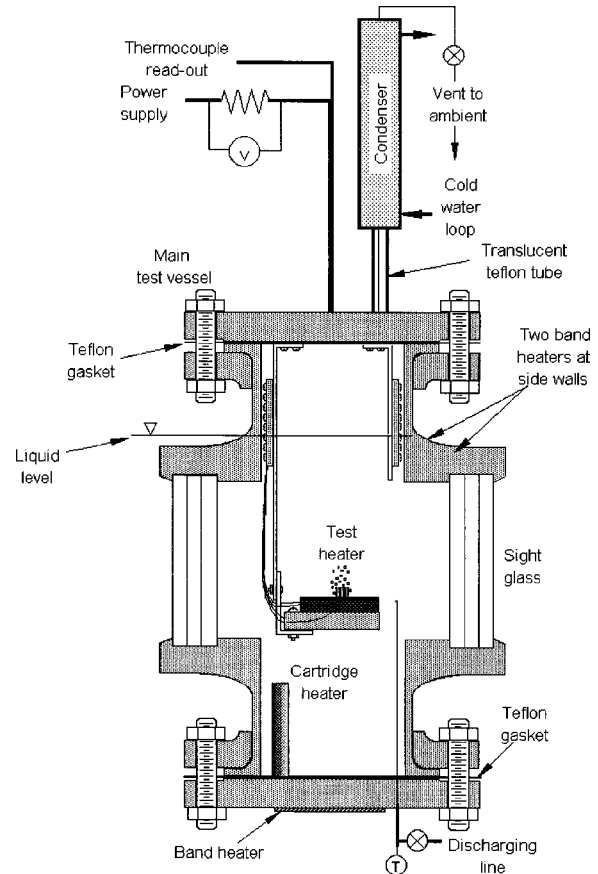


Fig. 1 Schematic of test apparatus

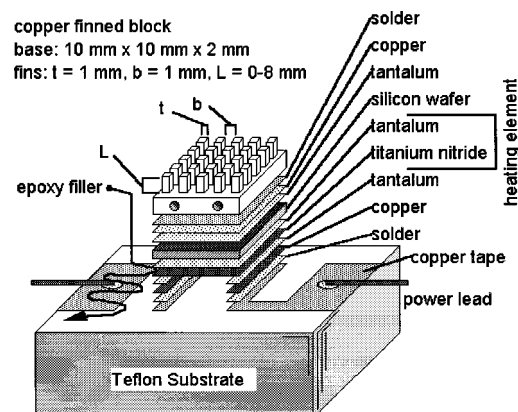


Fig. 2 Test heater design

provides no significant increase of the heat transfer surface area. Detailed descriptions of the coating are provided by O'Connor and You [12] and Chang and You [13,14].

Test Procedure. The test chamber was heated to the test liquid's saturation temperature using the three band heaters and the cartridge heater. Once at its saturation temperature, the test liquid was boiled vigorously for two hours in order to remove dissolved gases before testing. Boiling curves were then generated for each surface tested. There was a two-hour delay between runs to allow the heater and test section to return to steady state. Three consecutive runs were conducted for each heater tested. Identical boiling curves for each surface assured the consistency and repeatability of the data.

Heat flux was controlled by voltage input. After each voltage change (heat-flux increment), a 15-second delay was imposed before initiating data acquisition. After the delay, the computer repeatedly collected and averaged 125 base surface temperature measurements over 15 seconds until the temperature difference between two consecutive averaged temperature measurements for all thermocouples was less than 0.2 K. The test section at this point was assumed to be at steady state. Steady-state condition was usually reached approximately 45 seconds after each heat-flux increment. After reaching steady state, the heater surface and bulk fluid temperatures were measured and the heat flux was calculated. For heat flux values greater than ≈ 80 percent of q''_{CHF} , instantaneous surface temperature was monitored for 45 seconds after each increment to prevent heater burnout. Each instantaneous surface temperature measurement was compared with the previous steady-state surface temperature measurement. If a temperature difference larger than 20 K was detected, q''_{CHF} was assumed and the power shut off. The q''_{CHF} value was computed as the steady-state heat flux value just prior to power supply shut-down plus half of the increment.

Experimental Uncertainty. Uncertainties for the heat-flux and temperature measurements were estimated for the present heater. Substrate conduction losses were estimated based on the values reported by O'Connor and You [12], whose heater had a similar construction as the present one. Taking into account both measurement and substrate conduction errors, the uncertainty in heat flux (q''_b) was estimated as 16, 6.0, 6.1, and 6.2 percent at 0.5, 16, 80, and 120 W/cm², respectively. In addition, temperature measurement uncertainty was estimated considering thermocouple calibration error, temperature correction for the embedded thermocouples, and thermocouple resolution error. The uncertainty for temperature measurement was ± 0.4 K.

Results and Discussion

The effects of combining an area enhancement (square pin fins) and a surface enhancement (microporous coating) were investigated utilizing 1 cm² (10 mm \times 10 mm) copper base surfaces with different fin lengths: 0 (flat surface), 1, 2, 4, and 8 mm. Both plain and microporous coated finned surfaces were tested in saturated FC-72 at 1 atm. All testing was performed under increasing heat flux conditions and in the horizontal, upward facing orientation. Additional fin lengths of 0.25 and 0.5 mm for the microporous coated surface were tested to better understand the behavior of q''_{CHF} at fin lengths between 0 and 1 mm.

Effect of Surface Microstructure for Flat Surfaces. The effect of surface microstructure on pool nucleate boiling heat transfer and q''_{CHF} was investigated by comparing the present plain machine roughened flat surface with a highly polished plain surface previously tested by Chang and You [15] and a microporous (ABM) coated surface previously tested by Chang and You [14]. Figure 3 illustrates the flat surface pool boiling test results with the three different surface conditions. The single-phase natural convection data of all of the surfaces exhibited comparable heat

transfer coefficients showing negligible surface microstructure effects. The incipient superheat values showed a decreasing trend with increased "surface roughness." The incipient superheat values for the present plain machine roughened surface varied within a range of 16 to 28 K for three consecutive runs while Chang and You [15] reported a range of 25 to 40 K for their highly polished surface and Chang and You [14] reported incipient superheats to be less than 10 K for their ABM surface. O'Connor and You [12] attributed the decrease in incipient superheat for their microporous coating compared to plain surfaces primarily to the presence of larger embryonic bubble diameters produced by increased vapor/gas entrapment in the microstructure. The rougher surface of the present machine roughened surface is expected to have larger cavities (larger embryonic bubble sizes) than the highly polished surface and thus exhibit decreased incipient superheats. The nucleate boiling curves of the three surfaces show significant increases in heat transfer coefficient relative to increasing surface roughness. For instance, at 10 W/cm², the machine roughened and microporous coated surfaces exhibited heat transfer coefficients that were 80 percent and 300 percent higher than the highly polished surface, respectively. Chang and You [14] attributed the better heat transfer performance of the microporous coated surface to increased external vaporization, smaller departing bubble sizes, and higher bubble departure frequencies produced from the microporous structure.

As shown in Fig. 3, the surface microstructure significantly affects q''_{CHF} as well as incipience and nucleate boiling performance. The q''_{CHF} values for the present machine roughened surface ranged from 18.7 to 19.1 W/cm² while Chang and You [15] reported a range of 13.2 to 16.0 W/cm² for their highly polished surface and Chang and You [14] show a range of about 25.3 to 26.5 W/cm² for their microporous coated surface. In comparison, Zuber's [17] correlation given by

$$q''_{CHF,Z} = \frac{\pi}{24} h_{lv} \rho_v^{1/2} [g \sigma (\rho_l - \rho_v)]^{1/4} \quad (1)$$

predicts $q''_{CHF,Z} = 15.1$ W/cm² for saturated FC-72 at atmospheric pressure. Since Zuber's [17] correlation does not take into account the effects of surface microstructure, it fails to accurately predict q''_{CHF} for enhanced surfaces. Chang and You [13] classified particle enhancement coatings into two groups: microporous and porous. If the coating thickness was less than the superheated liquid

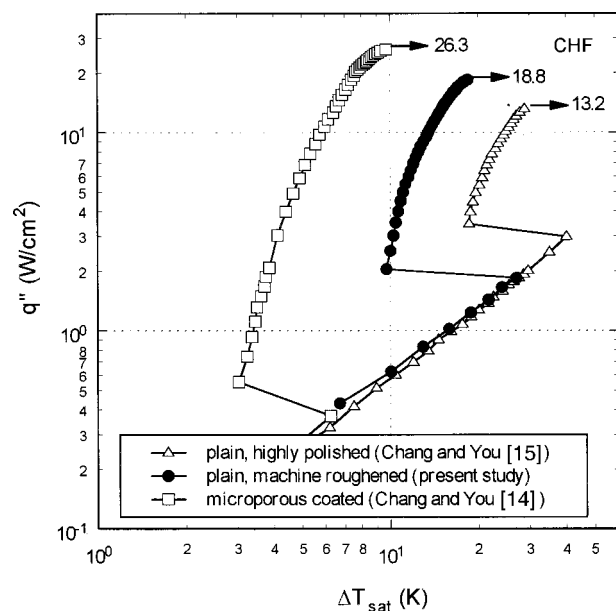


Fig. 3 Surface microstructure effect for flat surfaces

layer thickness, it was termed “microporous” while coatings with thicknesses greater than the superheated liquid layer thickness were called “porous.” Using Zuber’s [17] hydrodynamic model of q''_{CHF} , Polezhaev and Kovalev [18] tried to explain the enhancement on q''_{CHF} of porous coatings as due to the structure of the coating influencing the vapor jet spacing rather than the Taylor wavelength. Tehvor [19] used Haramura and Katto’s [20] macro-layer dryout model of q''_{CHF} to explain the enhancement on q''_{CHF} of porous coatings as due to an increase in the macrolayer evaporation time caused by the presence of the porous layer. Although these hypotheses could explain the microporous coated surface results, neither of them explains the enhancement of q''_{CHF} observed in Fig. 3 for the machine roughened surface. This indicates that the enhancement of q''_{CHF} for plain, roughened surfaces is primarily due to the increased number of active nucleation sites provided by the microstructure.

Method for Analyzing Experimental Finned Surface Data. Prior to discussing the results of the finned surfaces, a method for determining the surface averaged heat transfer coefficient, \bar{h} , and the heat sink efficiency (also called the overall surface efficiency), η_o , from the experimental data must be established. For a finned surface, the heat sink efficiency is given by

$$\eta_o = 1 - \frac{A_f}{A_t} (1 - \eta_f) = \frac{q''_t}{\bar{h} \Delta T_b} \quad (2)$$

where the individual fin efficiency is $\eta_f = \tanh(mL_c)/mL_c$. For a square pin fin $L_c = L + t/4$ and $m = (4\bar{h}/kt)^{1/2}$; Eq. (2) can be numerically solved for \bar{h} since all other variables are known. Once \bar{h} is known, η_o can be calculated. This method is used to calculate \bar{h} and η_o in the following analysis of the present finned surface experimental data. Although this one-dimensional approach for the finned surface data reduction is not considered very accurate, it is believed to provide a good means for the comparison of the boiling behavior between the plain and microporous finned surfaces.

Plain, Finned Surface Nucleate Boiling Results. The boiling curves of the plain finned surfaces with different fin lengths are shown in Fig. 4. Unless otherwise noted, “plain” refers to the uncoated, machine-roughened surface discussed previously. In this graph, the heat flux based on the total finned surface area (fin and base surface area) is plotted versus the base surface superheat. Since boiling fins can have non-uniform heat transfer coefficients (Srinivasan and Shah [21]) and thus temperature variations, the surface superheat based on the temperature at the base of the fins ($\Delta T_b = T_b - T_{sat}$) is used. T_b is taken to be the temperature at the top of the base surface (1 mm above the thermocouple location). A one-dimensional correction was applied to the thermocouple measurements in order to obtain T_b . The flat surface data serves as a reference for comparison. The single-phase natural convection data for all surfaces show only a small degree of scatter that is the result of uncertainties in surface area and temperature measurement. For all of the finned surfaces, boiling generally initiated in a “patchy,” localized fashion and spread to the rest of the surface as the heat flux was increased. For a given surface, the boiling initiated in the same locations for all runs indicating the presence of “preferred” nucleation sites produced by the machining process. These preferred sites were generally at the fin edges and explain the virtual absence of temperature overshoots.

The nucleate boiling performance of the plain surfaces shows some interesting trends. From Fig. 4, it can be seen that the boiling curves are showing different behaviors relative to fin length. The $L = 1, 2,$ and 4 mm surfaces are nearly coincident and show comparable heat transfer performance up to q''_{CHF} while the $L = 8$ mm surface shows a significant degradation in heat transfer performance. The significant degradation of the $L = 8$ mm surface relative to the other finned surfaces indicates the presence of an

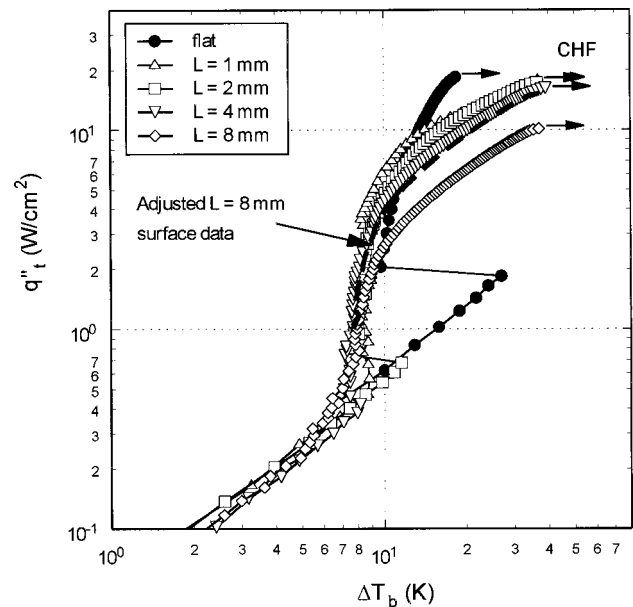


Fig. 4 Plain, finned surface boiling curves based on total surface area

additional heat transfer degradation mechanism not seen in the $L = 1, 2,$ and 4 mm surface data. This behavior was seen to be repeatable, even for different surfaces. Kumagai et al. [7] observed that boiling did not occur at the fin tips of their longest rectangular finned surface in R-113 even near q''_{CHF} . Although the heat transfer mode at the fin tips in the present study could not be determined, it is believed that the degradation in heat transfer performance is due to a non-boiling region near the fin tips (surface temperature too low to sustain boiling). This degradation mechanism decreases the active or “effective” nucleate boiling heat transfer surface area and, therefore, shifts the boiling curve of the $L = 8$ mm surface downward when plotted based upon total area, as seen in Fig. 4. By assuming that the effective surface area of the $L = 8$ mm surface is approximately equivalent to the total surface area of an $L \approx 5$ mm surface (shown as a dashed line in Fig. 4), the boiling curve of the $L = 8$ mm surface became nearly coincident with the $L = 1, 2,$ and 4 mm surfaces. This indicates that only about 60 percent of the $L = 8$ mm surface is effectively transferring heat and that $L \approx 5$ mm is the optimum fin length for the present plain, finned surfaces.

The fin tip wall superheat value of the $L = 8$ mm surface at the last steady-state point prior to CHF was estimated at 12 K using a standard one-dimensional steady-state conduction analysis and assuming that the heat transfer coefficient along the fin is constant (the average value shown in Fig. 5). Although the estimate is not considered very accurate, it shows that the fin tip temperature is very near the minimum temperature required for nucleation, which supports the previous conjecture of a non-boiling fin tip condition.

Below $q''_t \approx 7$ W/cm² ($L = 1, 2,$ and 4 mm cases), the finned surfaces in Fig. 4 show boiling curve slopes approximately equal to the flat surface boiling curve indicating comparable nucleate boiling behavior. However, at heat fluxes above $q''_t \approx 7$ W/cm², the boiling curves show a noticeable decrease in slope. Similar trends were seen in the boiling curves of Kumagai et al. [7] and Guglielmini et al. [9]. Haley and Westwater [2] have shown that stable film, transition, and nucleate boiling along with free convection can occur simultaneously and at adjacent positions along a single, horizontal fin in isopropyl alcohol and R-113. However, visual observations as well as the relatively low wall superheats above $q''_t \approx 7$ W/cm² indicate that initiation of localized film boil-

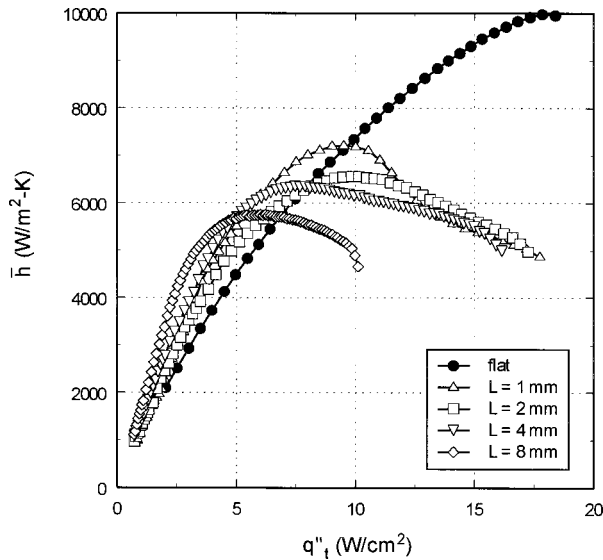


Fig. 5 Plain, finned surface average heat transfer coefficients

ing at the base of the fins is not the cause of the observed slope changes. Instead, it is believed that the degradation is primarily the result of increased bubble departure resistance due to the presence of the fins. The heat sink geometry increases the vapor bubble residence time by providing resistance to the departing bubbles. The longer bubble residence time increases the flow resistance on the approaching re-wetting liquid causing liquid starvation and ultimately producing a temporal localized dry-out situation near the base of the fins. This would cause a decrease in the heat transfer coefficient and increase in the base surface temperature, as seen in Fig. 4. Also, the flow path blockage provided by the fins further increases the re-wetting liquid flow resistance, however, this effect is believed to be small compared to the effect of the longer bubble residence time.

The average heat transfer coefficient, \bar{h} , and the heat sink efficiency, η_o , of the plain finned surfaces were calculated based upon previous discussions and plotted versus the total surface area heat flux in Figs. 5 and 6, respectively (the flat surface is assumed to have a heat sink efficiency equal to 1). At heat fluxes below $q''_t \approx 5 \text{ W/cm}^2$, the finned surfaces in Fig. 5 show a sizable in-

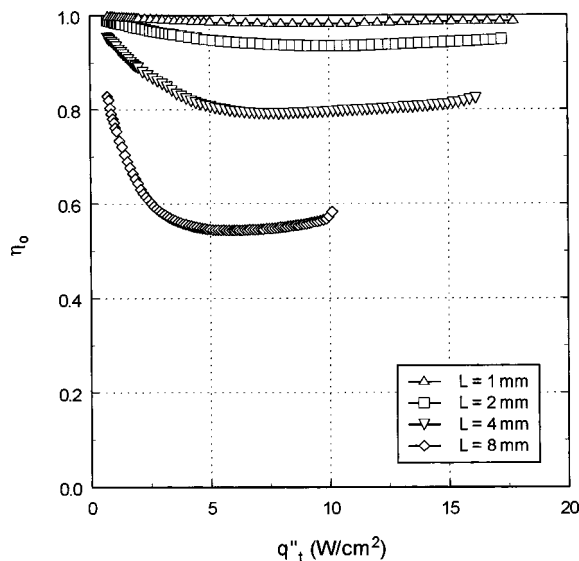


Fig. 6 Plain, finned surface heat sink efficiency

crease in the average heat transfer coefficient over the flat surface data. This is most likely due to a larger number of active nucleation sites than the flat surface created by the machining of the fins. Between $q''_t \approx 5\text{--}10 \text{ W/cm}^2$, the finned surfaces reach a maximum \bar{h} value and then decrease with increasing heat flux while η_o reaches a minimum value and then increases slightly with increasing heat flux. This behavior corresponds to the degradation in heat transfer from the increased re-wetting fluid resistance discussed previously. The more rapid decline in \bar{h} with increasing q''_t of the $L=8 \text{ mm}$ surface shows the further degradation in heat transfer performance caused by a reduction in effective boiling area from poor heat sink efficiency (less than 60 percent as shown in Fig. 6) which has also previously been discussed.

The heat flux based on the base (or projected) surface area, which is considered most useful for microelectronics cooling applications, is plotted in Fig. 7. Figure 7 shows that for surfaces with fin lengths from 1 to 4 mm the heat transfer performance improve proportional to surface area. However, any further increase in fin length does not significantly improve the heat transfer performance due to a reduction in the effective area for nucleate boiling as shown by the $L=8 \text{ mm}$ surface.

Microporous, Finned Surface Nucleate Boiling Results.

The boiling curves of the microporous coated finned surfaces with different fin lengths are shown in Fig. 8. The heat flux based on the base surface area is plotted along with the plain, flat surface data from Fig. 7 for reference. For clarity, only the nucleate boiling portion of the finned surfaces' boiling curves is shown. The nucleate boiling performance of the microporous coated surfaces (flat to $L=8 \text{ mm}$) show significantly lower surface superheats than the plain surfaces. This shows the superior nucleate boiling characteristics of the microporous coated surfaces over the plain surfaces, which has already been discussed in detail by Chang and You [13–15]. However, the most striking feature of the microporous coated surface results is that the nucleate boiling curves of all fin lengths, including the flat surface, appear to collapse to one curve when plotted relative to the base surface. This shows that the nucleate boiling heat transfer coefficient (based upon a given base area) can be increased with the application of the microporous coating, however, no further improvement is gained by increasing the fin length. Chang and You [22] have observed that the heat transfer performance of microporous coated surfaces un-

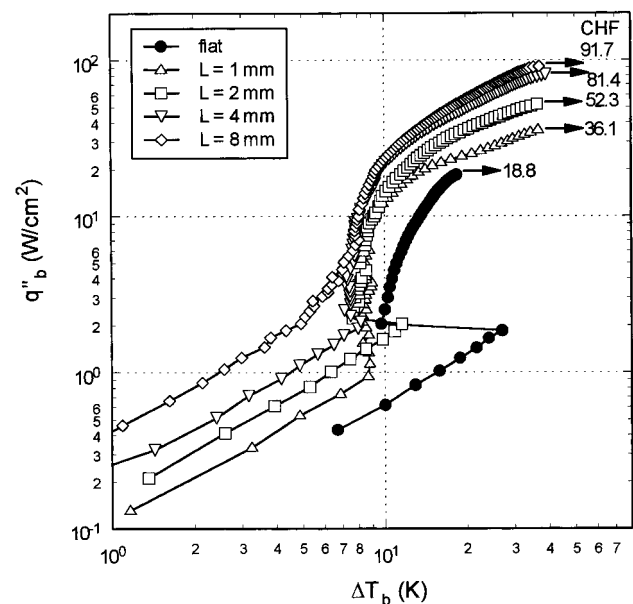


Fig. 7 Plain, finned surface boiling curves based on base surface area

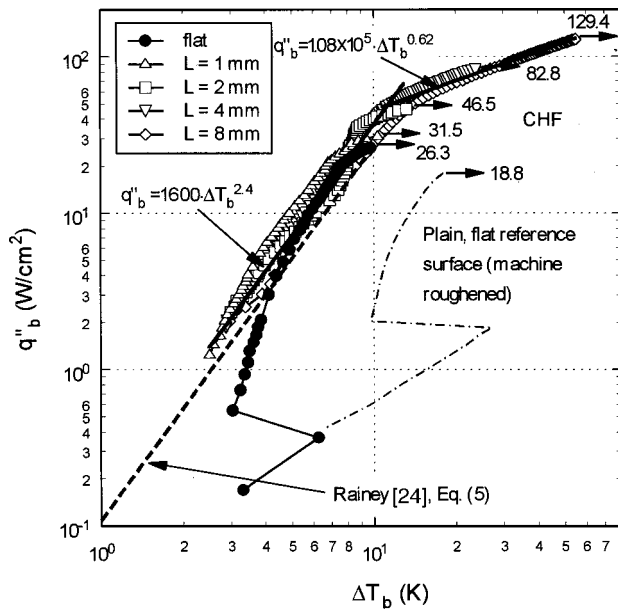


Fig. 8 Microporous coated, finned surface boiling curves based on base surface area

der saturated nucleate boiling conditions is unaffected by changes in either surface area or inclination, therefore, it is interesting to see that the nucleate boiling heat transfer performance of the present microporous coated finned surfaces is unaffected by changes in fin length. In general, the heat transfer surface area does not affect nucleate boiling performance unless the number of active nucleation sites becomes limited and does not increase with increasing heat flux. In contrast to the plain finned surfaces in Fig. 7, the microporous coated finned surfaces' boiling curves in Fig. 8 are nearly coincident indicating that the microporous coating removes this form of surface area dependency by providing a much higher number of active nucleation sites. The effect of changes in surface area only becomes evident at q''_{CHF} , which is discussed later.

Another interesting feature of the microporous coated surfaces is the noticeable change in slope at $q''_b \approx 50 \text{ W/cm}^2$. As discussed previously, a similar trend was observed in the plain surface data in Fig. 7 but at much lower heat flux values and was attributed to the presence of a temporal dry-out situation caused by increased bubble departure resistance. It is postulated that the same degradation mechanism is responsible for the change in slope of the microporous coated surfaces' boiling curves shown in Fig. 8. O'Connor and You [12] observed that a number of small bubbles near the surface of their microporous coated horizontal flat heater fed large hovering vapor mushrooms just prior to q''_{CHF} . This bubble departure behavior provides a more stable heat removal mechanism and delays the formation of the temporal dry-out situation due to increased vapor bubble residence time. A simple two line power-law curve-fit (a simplified form of Rohsenow's [23] correlation) given by

$$q''_b = 1600 \cdot \Delta T_b^{2.4} \quad \text{for } q''_b < 5 \times 10^5 \text{ W/m}^2 \quad (3)$$

$$q''_b = 1.08 \times 10^5 \cdot \Delta T_b^{0.62} \quad \text{for } q''_b > 5 \times 10^5 \text{ W/m}^2 \quad (4)$$

is proposed to approximate the nucleate boiling curves of the microporous coated, finned surfaces shown in Fig. 8. The curve fit developed by Rainey [24] for microporous coated flat surfaces of different sizes and various inclination angles is also shown in Fig. 8 and is given by

$$q''_b = 1100 \cdot \Delta T_b^{2.4} \quad (5)$$

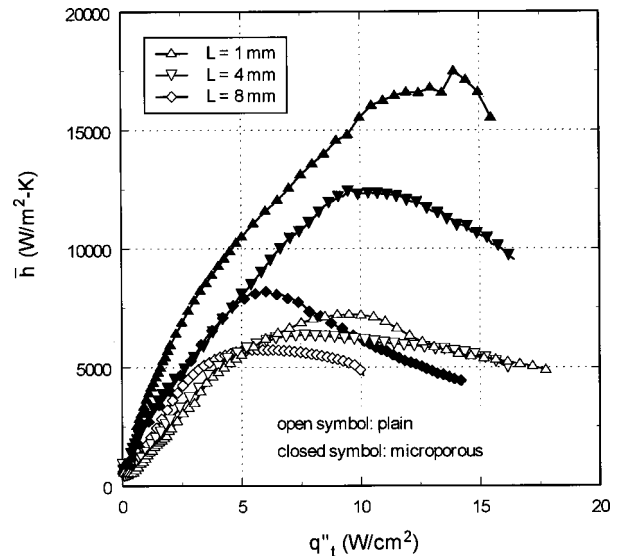


Fig. 9 Plain/microporous coated, finned surface average heat transfer coefficients

Rainey's curve fit compares well with the present curve fit given by Eq. (3). Historically, the exponent on ΔT_b has been taken to be about 3 for nucleate boiling (Rohsenow [23]) and 0.75 for laminar film boiling (Bromley [25] and Berenson [26]). The exponent of 2.4 on ΔT_b when $q''_b < 50 \text{ W/cm}^2$ indicates that the primary heat transfer mode is nucleate boiling while the exponent of 0.62 on ΔT_b when $q''_b > 50 \text{ W/cm}^2$ indicates the presence of the temporal dry-out situation previously discussed.

To better compare the effect of the microporous coating on the nucleate boiling performance, the average heat transfer coefficient based on the total surface area of the $L=1, 4,$ and 8 mm microporous coated surfaces is plotted alongside the corresponding plain surface data in Fig. 9. The much higher heat transfer coefficients of the microporous coated surfaces illustrate the profound effect that the microporous coating has on the boiling performance. The maximum heat transfer coefficients for the $L=4$ and 8 mm microporous coated surfaces occurred at about the same heat flux value as the slope change ($q''_b \approx 50 \text{ W/cm}^2$) and signifies the point at which the temporal dry-out situation begins to occur at the base of the fins. Although the heat transfer coefficient is much higher for the microporous coated surfaces, the heat sink efficiency is only mildly reduced by about ten percent (not shown). This shows that the differences in nucleate boiling heat transfer performance between the plain and microporous coated surfaces is primarily due to the differences in surface microstructure.

Effect of Fin Length on CHF. Figure 10 shows the effect of fin length on q''_{CHF} relative to the base surface area. Zuber's [17] correlation, Eq. (1), is also plotted (by multiplying $q''_{CHF,Z}$ by A_f/A_b) for reference. The plain surfaces appear to show a direct relationship between $q''_{b,CHF}$ and fin length (constant $q''_{f,CHF}$), for fin lengths up to 4 mm . However, when increasing the fin length further, $q''_{b,CHF}$ deviates from this trend showing significant degradation. The dashed trendline in Fig. 10 illustrates this behavior. The degradation in q''_{CHF} is consistent with early discussions regarding the degradation in nucleate boiling performance of the plain surfaces due to a non-boiling region at the tips of the fins and appears to support the previously estimated optimum or transition point of $L \approx 5 \text{ mm}$. Kumagai et al.'s [7] data shows a similar transition behavior in saturated R-113.

The microporous coated surfaces' $q''_{b,CHF}$ values, also shown in Fig. 10, appear to show a different behavior with fin length than

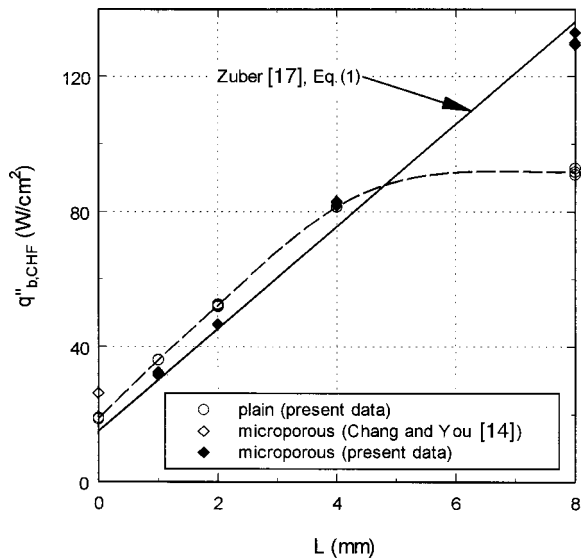


Fig. 10 Critical heat flux versus fin length

the machined surfaces. From 1 to 8-mm fin lengths, $q''_{b,CHF}$ appears to follow a direct relationship with fin length. At a fin length of 8 mm, the effects of surface enhancement on q''_{CHF} in Fig. 10 again becomes a factor. The microporous coated $L=8$ mm surface repeatedly showed no degradation in $q''_{b,CHF}$ as was observed in the plain surface results. This seems to be due to the microporous coating's nucleation enhancement characteristics. The relatively low fin-tip temperatures of the $L=8$ mm surfaces may be too low to sustain nucleate boiling on the plain surface but are high enough to sustain nucleate boiling on the microporous coated surface. Applying the same one-dimensional conduction analysis used for the plain surface, the fin-tip wall superheat (ΔT_{su}) of the microporous $L=8$ mm surface at the last steady-state point prior to CHF was roughly estimated at 19 K. Unlike the plain $L=8$ mm surface, this estimated temperature is much higher than the minimum temperature required for nucleation, indicating a boiling fin-tip condition. However, it is expected that the microporous coated surfaces would experience degradation in q''_{CHF} similar to the plain surfaces at fin lengths greater than 8 mm.

Decreasing the fin length from 1 to 0 mm in Fig. 10 appears to show a moderate deviation in q''_{CHF} behavior for the microporous coated surfaces. To investigate this behavior, two additional microporous coated surfaces with fin lengths of 0.25 and 0.5 mm were tested and plotted in Fig. 11. The low fin length region of Fig. 10 is shown in Fig. 11. The q''_{CHF} data is normalized with respect to $q''_{CHF,Z}$. As can be seen from Fig. 11, $q''_{t,CHF}$ for the microporous coated surfaces drastically decreases with the addition of fins and then becomes relatively constant with values similar to Zuber's [17] correlation. While q''_{CHF} for the flat surfaces is significantly affected by enhancement of the surface microstructure (as shown in Fig. 3), the comparable q''_{CHF} values of the plain and microporous finned surfaces indicate insensitivity to surface enhancement. This indicates that q''_{CHF} for the present microporous coated finned surfaces is limited by hydrodynamic mechanisms rather than by the surface microstructure (number of active nucleation sites). Unlike flat surfaces, finned surfaces have adjacent and opposing walls, which increases the level of bubble crowding at a given heat flux. As the heat flux approaches q''_{CHF} , the increased bubble crowding would more effectively block the re-wetting liquid flow and could cause q''_{CHF} to occur at a lower heat flux than an equivalent flat surface as was seen in Fig. 11 for the microporous coated surfaces.

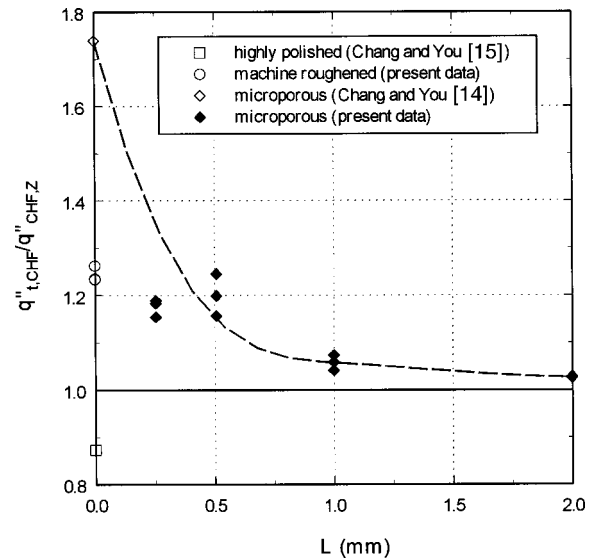


Fig. 11 Normalized critical heat flux versus fin length in the short fin region

Conclusions

The pool boiling heat transfer performance of a "double enhancement" technique which combined a surface enhancement (microporous coating) and an area enhancement (square pin fins) was investigated using 1-cm² flush-mounted copper surfaces. The effects of surface microstructure on the nucleate boiling curve were also investigated using three different surface conditions: plain polished (from Chang and You [15]), plain machine roughened (present study), and microporous coated (Chang and You [14]). All tests were performed in saturated FC-72 at atmospheric pressure under increasing heat flux conditions.

- The effects of surface roughness on the pool boiling heat transfer of flat surfaces were found to be significant throughout the entire nucleate boiling curve. An increase in surface roughness produced a decrease in incipient superheat and temperature overshoot and significantly increased the nucleate boiling heat transfer coefficients and CHF. The effects are considered to be directly related to active nucleation site density differences.
- For the plain finned surfaces, the heat transfer performance can be significantly enhanced with the addition of square pins up to a fin length of about 5 mm. Above 5 mm, it is believed that the surface temperature of the tip portion of the fins is too low to sustain boiling which reduces the "effective" boiling area and provides no additional improvements in heat transfer performance.
- The microporous coated finned surfaces provide significantly higher heat transfer coefficients over the plain finned surfaces. In addition, the nucleate boiling curves of the microporous coated surfaces collapse to one line regardless of fin length (for fin lengths up to 8 mm) and are well correlated with a two-line power-law curve fit.
- It is believed that the presence of the pin fins produces a resistance to vapor bubble departure, which increases the bubble residence time and causes a change in boiling curve slope of both the plain and microporous finned surfaces. The longer bubble residence time would also increase the flow resistance on the approaching re-wetting liquid causing liquid starvation and ultimately produce a temporal localized dry-out situation near the base of the fins.
- At fin lengths up to 4 mm, the CHF behavior for the present finned surfaces appears to be independent of surface microstructure. As a result, Zuber's [17] correlation provides a good estimate of CHF for both the plain and microporous coated finned surfaces.

At a fin length of 8 mm, the plain finned surfaces deviate from this trend due to the non-boiling tip condition previously stated; however, the microporous coated surface does not deviate due to the superior nucleation characteristics of the microporous coating.

Acknowledgments

The Texas Higher Education Coordinating Board primarily supported this study: Advanced Research/Technology Program grant number 003656-014. The Advanced Technology Group of Nortel provided additional support. The authors extend their thanks to the 3M Industrial Chemical Products Division for the donation of FC-72 test liquid.

Nomenclature

- A = area, m^2
 b = fin spacing, m
 g = acceleration due to gravity, m/s^2
 \bar{h} = average heat transfer coefficient, W/m^2-K
 h_{lv} = latent heat of vaporization, J/kg
 k = thermal conductivity, $W/m-K$
 L = fin length, m
 L_c = corrected fin length, m
 m = fin efficiency parameter
 q'' = heat flux, W/m^2
 t = fin width (thickness), m
 T = temperature, K
 ΔT_{sat} = surface superheat; $T_w - T_{sat}$, K
 ΔT_b = base surface superheat; $T_b - T_{sat}$, K
 η_f = individual fin efficiency
 η_o = heat sink efficiency
 ρ = density, kg/m^3
 σ = surface tension, N/m

Subscripts

- CHF = critical heat flux
 b = base surface
 l = saturated liquid
 sat = saturated conditions
 t = total surface
 v = saturated vapor
 w = heater surface (wall)
 Z = CHF prediction of Zuber [17]

References

- [1] Bar-Cohen, A., 1992, "State-of-the-Art and Trends in the Thermal Packaging of Electronic Equipment," *ASME J. Electron. Packag.*, **114**, pp. 254–270.
 [2] Haley, K. W., and Westwater, J. W., 1966, "Boiling Heat Transfer from a Single Fins," *Proceedings of the 3rd International Heat Transfer Conference*, Vol. 3, Chicago, pp. 245–253.
 [3] Lai, F. S., and Hsu, Y. Y., 1967, "Temperature Distribution in a Fin Partially

- Cooled by Nucleate Boiling," *AIChE J.*, **13**, No. 4, pp. 817–821.
 [4] Liaw, S. P., and Yeh, R. H., 1994, "Fins With Temperature Dependent Surface Heat Flux-II. Multi-Boiling Heat Transfer," *Int. J. Heat Mass Transf.*, **37**, No. 10, pp. 1517–1524.
 [5] Klein, G. J., and Westwater, J. W., 1971, "Heat Transfer From Multiple Spines to Boiling Liquids," *AIChE J.*, **17**, No. 5, pp. 1050–1056.
 [6] Mudawar, I., and Anderson, T. M., 1993, "Optimization of Enhanced Surfaces for High Flux Chip Cooling by Pool Boiling," *ASME J. Electron. Packag.*, **115**, pp. 89–100.
 [7] Kumagai, S., Jho, S. G., Hirono, Y., Shimada, R., and Takeyama, T., 1987, "Boiling Heat Transfer From Circular Surfaces With Rectangular Fin Array," *Heat Transf. Jpn. Res.*, **16**, No. 2, pp. 69–81.
 [8] Yeh, R. H., 1997, "Analysis of Thermally Optimized Fin Array in Boiling Liquids," *Int. J. Heat Mass Transf.*, **40**, No. 5, pp. 1035–1044.
 [9] Guglielmini, G., Misale, M., and Schenone, C., 1996, "Experiments on Pool Boiling of a Dielectric Fluid on Extended Surfaces," *Int. Commun. Heat Mass Transfer*, **23**, No. 4, pp. 451–462.
 [10] Chaudri, I. H., and McDougall, I. R., 1969, "Aging Studies in Nucleate Pool Boiling of Isopropyl Acetate and Perchloroethylene," *Int. J. Heat Mass Transf.*, **12**, pp. 681–688.
 [11] Nishikawa, K., Fujita, Y., Ohta, H., and Hidaka, S., 1982, "Effect of the Surface Roughness on the Nucleate Boiling Heat Transfer Over the Wide Range of Pressure," *Proceedings of the 7th International Heat Transfer Conference*, Munich, Germany, pp. 61–66.
 [12] O'Connor, J. P., and You, S. M., 1995, "A Painting Technique to Enhance Pool Boiling Heat Transfer in FC-72," *ASME J. Heat Transfer*, **117**, pp. 387–393.
 [13] Chang, J. Y., and You, S. M., 1997, "Boiling Heat Transfer Phenomena From Micro-Porous and Porous Surfaces in Saturated FC-72," *Int. J. Heat Mass Transf.*, **40**, No. 18, pp. 4437–4447.
 [14] Chang, J. Y., and You, S. M., 1997, "Enhanced Boiling Heat Transfer From Micro-Porous Surfaces: Effects of a Coating Composition and Method," *Int. J. Heat Mass Transf.*, **40**, No. 18, pp. 4449–4460.
 [15] Chang, J. Y., and You, S. M., 1996, "Heater Orientation Effects on Pool Boiling of Micro-Porous-Enhanced Surfaces in Saturated FC-72," *ASME J. Heat Transfer*, **118**, pp. 937–943.
 [16] You, S. M., and O'Connor, J. P., 1998, "Boiling Enhancement Paint," U. S. Patent #5814392.
 [17] Zuber, N., 1959, "Hydrodynamic Aspects of Boiling Heat Transfer," AEC Report No. AECU-4439, Physics and Mathematics.
 [18] Polezhaev, Y. V., and Kovalev, S. A., 1990, "Modeling Heat Transfer With Boiling on Porous Structures," *Therm. Eng.*, **37**, No. 12, pp. 617–620.
 [19] Tehver, J., 1992, "Influences of Porous Coating on the Boiling Burnout Heat Flux," *Recent Adv. Heat Transfer*, pp. 231–242.
 [20] Haramura, Y., and Katto, Y., 1983, "A New Hydrodynamic Model of the Critical Heat Flux, Applicable Widely to Both Pool and Forced Convective Boiling on Submerged Bodies in Saturated Liquids," *Int. J. Heat Mass Transf.*, **26**, pp. 389–399.
 [21] Srinivasan, V., and Shah, R. K., 1997, "Fin Efficiency of Extended Surfaces in Two-Phase Flow," *Int. J. Heat Mass Transf.*, **18**, No. 4, pp. 419–429.
 [22] Chang, J. Y., and You, S. M., 1997, "Pool Boiling Heat Transfer From Inclined, Micro-Porous Surfaces Simulating Microelectronic Devices," *Proceedings of the INTERpack '97*, E. Suhir, et al., eds, ASME, New York, pp. 2055–2063.
 [23] Rohsenow, W. M., 1962, "A Method of Correlating Heat Transfer Data for Surface Boiling of Liquids," *ASME J. Heat Transfer*, **74**, pp. 969–975.
 [24] Rainey, K. N., 1999, "Pool Boiling Heat Transfer from Plain and Microporous Finned Surfaces in Saturated FC-72," M.S. thesis, The University of Texas at Arlington, Arlington, Texas.
 [25] Bromley, J. A., 1950, "Heat Transfer in Stable Film Boiling," *Chem. Eng. Prog.*, **46**, No. 5, pp. 221–227.
 [26] Berenson, P. J., 1961, "Film Boiling Heat Transfer From a Horizontal Surface," *ASME J. Heat Transfer*, **83**, p. 351.

Optical Properties in the Visible of Overfire Soot in Large Buoyant Turbulent Diffusion Flames

S. S. Krishnan

K.-C. Lin

G. M. Faeth¹

3000 Francois-Xavier Bagnoud Building
e-mail: gmfaeth@umich.edu

Department of Aerospace Engineering,
The University of Michigan,
Ann Arbor, MI 48109-2140

Nonintrusive measurements of the optical properties of soot at visible wavelengths (351.2–800.0 nm) were completed for soot in the overfire region of large (2–7 kW) buoyant turbulent diffusion flames burning in still air at standard temperature and pressure, where soot properties are independent of position and characteristic flame residence time for a particular fuel. Soot from flames fueled with gaseous (acetylene, ethylene, propylene, and butadiene) and liquid (benzene, cyclohexane, toluene, and n-heptane) hydrocarbon fuels were studied. Scattering and extinction measurements were interpreted to find soot optical properties using the Rayleigh-Debye-Gans/polydisperse-fractal-aggregate theory after establishing that this theory provided good predictions of scattering patterns over the present test range. Effects of fuel type on soot optical properties were comparable to experimental uncertainties. Dimensionless extinction coefficients were relatively independent of wavelength for wavelengths of 400–800 nm and yielded a mean value of 8.4 in good agreement with earlier measurements. Present measurements of the refractive index function for absorption, $E(m)$, were in good agreement with earlier independent measurements of Dalzell and Sarofim and Stagg and Charalampopoulos. Present values of the refractive index function for scattering, $F(m)$, however, only agreed with these earlier measurements for wavelengths of 400–550 nm but otherwise increased with increasing wavelength more rapidly than the rest. The comparison between present and earlier measurements of the real and imaginary parts of the complex refractive index was similar to $E(m)$ and $F(m)$. [S0022-1481(00)02203-9]

Keywords: Combustion, Fire, Flame, Participating Media, Radiation

Introduction

Information about the optical properties of soot is needed to develop reliable nonintrusive (optical) measurements of soot properties and estimates of continuum radiation due to soot in flame environments. Substantial information about the optical properties of soot is already known, as follows: Soot consists of nearly monodisperse spherical primary particles that collect into mass fractal aggregates having broad size distributions, soot primary particle diameters and aggregate sizes vary widely but soot fractal properties appear to be relatively universal, soot optical properties in the visible can be approximated reasonably well by Rayleigh-Debye-Gans scattering from polydisperse mass fractal aggregates (called RDG-PFA theory), and current estimates of soot optical properties in flame environments are mainly limited by excessive uncertainties about soot refractive index properties (see Faeth and Köylü [1] and references cited therein). Motivated by these observations, the objective of the present investigation was to measure soot optical properties at visible wavelengths, emphasizing dimensionless extinction coefficients and refractive indices.

Earlier studies of soot dimensionless extinction coefficient and refractive index properties in the visible are briefly reviewed in the following, more details can be found in Charalampopoulos [2], Faeth and Köylü [1], Jullien and Botet [3], Köylü and Faeth [4], Tien and Lee [5], Viskanta and Mengüç [6], and references cited therein. Some past determinations of soot refractive indices involve *ex situ* reflectivity measurements of compressed soot samples ([7–9]); these results have been questioned, however, due to potential changes of soot properties caused by sample collec-

tion and compression as well as potential effects of surface irregularities on measured reflectance properties ([2,5,9]). In order to avoid these error sources, other studies involved *in situ* measurements of extinction and scattering ([2,10–12]); unfortunately, these studies have a number of deficiencies as well: Soot structure generally was not characterized, Rayleigh and Mie scattering approximations were used to analyze the measurements that have not proven to be very effective for soot aggregates, questionable approximations involving either graphitic-based dispersion models or Kramers-Krönig causality relationships were adopted in some cases, and there has only been limited consideration of effects of fuel type on soot refractive index properties ([1,13–16]).

A recent study of the refractive index properties of soot due to Wu et al. [17] sought to resolve concerns about earlier work. These experiments considered soot emitted from buoyant turbulent diffusion flames in the long residence time regime where soot properties are relatively independent of position in the fuel-lean (overfire) region and residence time ([18–19]). Measurements included soot density, structure, gravimetric volume fraction, and scattering and absorption properties. These data were analyzed to find soot dimensionless extinction coefficients, fractal dimensions, and refractive index properties based on RDG-PFA scattering theory. RDG-PFA theory was successfully evaluated and soot refractive indices were independent of fuel type and in good agreement with earlier work. On the other hand, dimensionless extinction coefficients were significantly smaller (by 40 percent) than earlier measurements reported by Dobbins et al. [20] and Choi et al. [21]. This last difficulty clearly raises concerns about the associated measurements of refractive index properties reported by Wu et al. [17].

In view of these observations, the present study of soot optical properties in the visible was undertaken, considering soot emitted from buoyant turbulent diffusion flames in the long residence time

¹To whom correspondence should be addressed.

Contributed by the Heat Transfer Division for publication in the JOURNAL OF HEAT TRANSFER. Manuscript received by the Heat Transfer Division, August 4, 1999; revision received, Feb. 14, 2000. Associate Technical Editor: J. Gore.

regime. The approach was similar to Wu et al. [17] where measurements of gravimetric soot volume fractions and soot extinction and scattering properties were analyzed using RDG-PFA theory to find dimensionless extinction coefficients, fractal dimensions, and refractive index properties. Flame conditions included a variety of gaseous and liquid hydrocarbon fuels burning in still air.

Experimental Methods

Apparatus. Present test flames were large buoyant turbulent diffusion flames burning in still air within the long residence time regime. The test flames were provided by gas and liquid-fueled burners injecting fuel gases vertically upward. Soot properties were measured by collecting the combustion products in a hood having a 152-mm diameter vertical exhaust duct. Measurements were made at the exit of the exhaust duct where properties across the flow were nearly uniform; nevertheless, soot concentrations were measured along the optical path so that extinction measurements could be referenced to conditions at the duct axis where all other optical measurements were made. Note that using a collection system in this way does not affect soot structure and optical properties because they are universal in the overfire region for present test conditions ([14]). A water-cooled burner having a diameter of 50 mm described by Sivathanu and Faeth [18] was used for the gas-fueled flames. Uncooled burners having diameters of 51 and 102 mm were used for the liquid-fueled flames, adjusting the fuel flow rate to attain steady pool fires with the liquid surface roughly 10–20 mm below the burner exit.

Sampling Measurements. Aside from routine sampling measurements of gas temperatures and compositions at the measuring location, sampling measurements included soot structure and gravimetric volume fractions. Other soot properties of interest during the present study, e.g., soot density and composition, were drawn from Köylü and Faeth [14,19] and Wu et al. [17] for similar soot populations.

Soot structure was found by thermophoretic sampling and analysis using transmission electron microscopy (TEM), following Köylü and Faeth [19]. Sampling was carried by inserting TEM grids into the flow at the exhaust duct axis. Sampling times were selected to achieve less than ten percent coverage of the grid surface with soot in order to avoid overlapping aggregates on the grid. Effects of aggregate size on sampling bias were less than 20 percent from estimates based on Rosner et al. [22]. Samples of 400 primary particles selected from more than 50 aggregates were used to find the mean value of d_p with an experimental uncertainty less than two percent (95 percent confidence).

Gravimetric volume fractions were measured following Wu et al. [17]. This involved sampling the flow and measuring the volumes of soot and gas collected. The sampling probe was aligned with the exhaust duct axis and had a 13-mm-diameter inlet connected to a 47-mm-diameter Gelman filter. The filter was connected to a vacuum pump through a flowmeter and valve. The flowmeter was fitted with a manometer and calibrated over the required range of inlet pressures and flow rates using a wet test meter. Soot samples were collected for a timed period using two filters, one in the filter holder and the second to mechanically collect soot from the sample line and filter holder. The mass of soot was found by weighing the filters before and after sampling using an electronic balance. Given these measurements, the soot volume fraction could be computed from the known soot density. Sample times were lengthy and several samples along the optical path and repeat samples were required; therefore, a laser extinction system was used across the sampling duct exit to insure that flame conditions were accurately repeated. In addition, gravimetric soot volume fractions were measured at more locations along the optical path than before. These two changes from the approach used by Wu et al. [17] are felt to be mainly responsible for better

agreement between present and past measurements of the dimensionless extinction coefficients of soot than before.

Optical Measurements. Soot scattering and extinction properties were measured following Köylü and Faeth [14,15]. Light sources used for measurements at various wavelengths were as follows: 351.2, 457.9, 488.0, and 514.5 nm using an argon-ion laser (4W, Coherent Innova 90-4); 632.8 nm using a He-Ne laser (28 mW, Melles Griot MG53036); 405.0 nm using a mercury lamp (100W, Oriel 6333); and 800.0 nm (for extinction measurements only) using a laser diode (700 mW, SDL-2360-P3). The incident beams were passed through a polarization rotator and mechanical chopper and then focused at the axis of the exhaust duct. The collecting optics for scattering measurements were mounted on a turntable so that scattering angles of 5–160 deg could be considered. The collecting optics had a collection angle of 0.7 msr, dichroic sheet polarizer filters (1 and 10 nm bandwidths for laser and lamp sources, respectively), neutral density filters and a photodetector. The extinction measurements employed similar but rigidly mounted collection optics, designed following Manickavasagam and Mengüç [23] to reduce contributions of forward scattering to less than one percent. An optical system housing and darkroom conditions in the laboratory minimized optical noise due to ambient lighting.

Rayleigh scattering from propane gas was used to provide an absolute calibration of the scattering measurements. Absolute differential scattering cross sections of soot were found from ratios of the detector signal for soot and propane, based on the Rayleigh scattering properties of propane from Rudder and Bach [24] and Dyer [25]. Total volumetric scattering cross sections were found by integrating volumetric differential scattering cross sections over the spherical surface while extrapolating to find contributions in the near forward and backward scattering directions as discussed by Wu et al. [17]; the corrections of the total volumetric scattering cross sections due to these extrapolations did not exceed 25 percent.

Theoretical Methods

Dimensionless Extinction Coefficients. The dimensionless extinction coefficient is a useful optical property that provides a simple relationship between extinction and soot volume fractions ([20,21]). This parameter was found for present test conditions based on Dobbins et al. [20], as follows:

$$K_e = -\lambda \ln(I/I_o)/(Lf_v) \quad (1)$$

Values of f_v were nearly constant (varying 14 to 20 percent) over the present optical path; nevertheless, an appropriate average value was used in Eq. (1) based on several gravimetric measurements of f_v along the path. Experimental uncertainties of K_e (95 percent confidence) varied between 14 percent (acetylene at 351.2 nm) and 24 percent (n-heptane at 800 nm), dominated by uncertainties in the soot volume fraction determinations along the optical path.

Refractive Index Properties. Measurements of refractive index properties were based on RDG-PFA theory, adopting the approach of Wu et al. [17], therefore, only results from RDG-PFA theory specifically used during the present study are discussed in the following. The main assumptions of RDG-PFA theory are as follows: Individual primary particles satisfy the Rayleigh scattering approximation, soot aggregates satisfy the Rayleigh-Debye-Gans (RDG) scattering approximation, primary particles are spherical and monodisperse, primary particles just touch one another, the number of primary particles per aggregate satisfies a log-normal probability distribution function, and the aggregates are mass fractal-like objects that satisfy the following relationship ([3]):

$$N = k_f(R_g/d_p)^{D_f} \quad (2)$$

These approximations have proven to be satisfactory during past evaluations for soot at a variety of conditions ([14–16,19]); they were also evaluated by comparing predicted and measured scattering patterns during the present investigation, as discussed later.

Values of the measured volumetric vv scattering cross section, $\bar{Q}_{vv}^a(qd_p)$, satisfied power-law behavior at large angles, similar to results illustrated for soot emitted from gas fueled flames by Wu et al. [17]. Thus, values of the fractal dimension, D_f , needed to find the refractive index function for scattering, $F(m)$, were found based on the results of RDG-PFA theory in the large-angle regime, as follows:

$$D_f = -d \ln(\bar{Q}_{vv}^a(p d_p)) / d \ln(q d_p) \quad (3)$$

where all parameters on the right-hand side of Eq. (3) are known from the measurements. Experimental uncertainties (95 percent confidence) of the D_f measurements are less than five percent.

Values of the refractive index function for absorption, $E(m)$, were found from RDG-PFA theory, as follows:

$$E(m) = \lambda(\bar{Q}_e^a - \bar{Q}_s^a) / (6 \pi f_v) \quad (4)$$

where \bar{Q}_e^a and \bar{Q}_s^a are the measured volumetric extinction and total scattering cross sections while f_v is the gravimetrically measured soot volume fraction. Experimental uncertainties (95 percent confidence) of $E(m)$ varied between 14 percent (acetylene at 351.2 nm) and 24 percent (n-heptane at 632.8 nm). Corresponding values of the refractive index function for scattering, $F(m)$, were found from RDG-PFA theory in the large-angle regime, as follows:

$$F(m) = 2\lambda^4 (q d_p)^{D_f} \bar{Q}_{vv}^a(q d_p) / (3 \pi^3 k_f f_v) \quad (5)$$

where all parameters on the right-hand side of this equation are either known or measured after adopting $k_f=8.5$ based on the measurements of Köylü et al. [26] for soot similar to the present measurements; e.g., soot emitted from large buoyant turbulent-diffusion flames in the long residence time regime and fueled with acetylene, propylene, ethylene, and propane. The experimental uncertainties (95 percent confidence) of $F(m)$ varied between 19 percent (acetylene at 351.2 nm) and 26 percent (n-heptane at 632.8 nm). Finally, given values of $E(m)$ and $F(m)$, their definitions provide two equations to solve for the real and imaginary parts of the soot refractive index, $m=n+i\kappa$; the experimental uncertainties of n and κ are comparable to $E(m)$ and $F(m)$, respectively.

Results and Discussion

Test Conditions. Present test conditions are summarized in Table 1. The flames involved both gaseous (acetylene, ethylene, propylene, butadiene) and liquid (benzene, cyclohexane, toluene,

Table 1 Summary of test conditions^a

| Fuel | Formula (-) | M (kg/kgmol) | d (mm) | \dot{Q} (kW) | t_r^b (ms) |
|-----------------------|--------------------------------|----------------|----------|----------------|--------------|
| Gas-fueled flames: | | | | | |
| Acetylene | C ₂ H ₂ | 26.04 | 50 | 6.16 | 329 |
| Ethylene | C ₂ H ₄ | 28.05 | 50 | 5.14 | 317 |
| Propylene | C ₃ H ₆ | 42.08 | 50 | 6.58 | 333 |
| Butadiene | C ₄ H ₆ | 54.09 | 50 | 1.70 | 254 |
| Liquid-fueled flames: | | | | | |
| Benzene | C ₆ H ₆ | 78.11 | 51 | 3.40 | 292 |
| Cyclohexane | C ₆ H ₁₂ | 84.16 | 102 | 5.00 | 315 |
| Toluene | C ₇ H ₈ | 92.13 | 51 | 2.50 | 274 |
| n-Heptane | C ₇ H ₁₆ | 100.20 | 102 | 4.10 | 303 |

^aSoot properties measured in the overfire region of buoyant turbulent diffusion flames burning in still air in the long residence time regime with ambient pressures and temperatures of 99±0.5 kPa and 298±3 K, respectively. Listed in the order of increasing molecular weight for gas and liquid fuels, respectively.

^bComputed from correlation of Sivathanu and Faeth [18].

Table 2 Summary of soot structure properties^a

| Fuel | d_p (nm) | \bar{N} | N_g | σ_g | $D_f(\sigma_D)^b$ |
|-----------------------|-----------------|-----------|-------|------------|-------------------|
| Gas-fueled flames: | | | | | |
| Acetylene | 47 | 417 | 214 | 3.3 | 1.79(0.01) |
| Ethylene | 32 | 467 | 290 | 2.7 | 1.80(0.01) |
| Propylene | 41 | 460 | 227 | 3.0 | 1.79(0.02) |
| Butadiene | 42 ^c | ... | ... | ... | 1.79(0.03) |
| Liquid-fueled flames: | | | | | |
| Benzene | 50 | 552 | 261 | 3.5 | 1.77(0.05) |
| Cyclohexane | 37 ^c | ... | ... | ... | 1.80(0.06) |
| Toluene | 51 | 526 | 252 | 3.2 | 1.79(0.07) |
| n-Heptane | 35 | 260 | 173 | 2.4 | 1.79(0.06) |

^aSoot in the overfire region of buoyant turbulent diffusion flames burning in still air in the long residence time regime with ambient pressures and temperatures of 99 ± 0.5 kPa and 298 ± 3 K, respectively. Soot density of 1880 kg/m³ from Wu et al. [17]; $k_f=8.5$ with a standard deviation of 0.5 from Köylü et al. [26]. Values of d_p , \bar{N} , N_g , and σ_g from Köylü et al. [27] and Köylü and Faeth [14] except when noted otherwise. Listed in order of increasing molecular weight for gas and liquid fuels, respectively.

^bFrom present scattering measurements in the wide-angle regime averaged over wavelengths of 351.2–632.8 nm with standard deviations for each fuel in parentheses.

^cFrom present TEM measurements.

n-heptane) hydrocarbon fuels burning in still air from burners having diameters of 50–102 mm with heat release rates of 2–7 kW. Characteristic residence times were computed using the correlation of Sivathanu and Faeth [18] finding values of 254–333 ms which places present flames in the long residence time regime ([19]). Present measurements were confined to the fuel-lean overfire region of the flames.

Soot structure properties for present test conditions are summarized in Table 2. Primary particle diameters are in the range 32–51 nm, with standard deviations of 17–21 percent of mean values and were reasonably monodisperse as concluded by Köylü and Faeth [19] for similar conditions. For the present ranges of primary particle diameters and wavelengths, values of the primary particle size parameters, $x_p=2\pi d_p/\lambda$, were in the range 0.16–0.46, with the maximum value being the largest yet considered for evaluating RDG-PFA predictions of soot optical properties. The mean numbers of primary particles per aggregate were known for soot from a number of the fuels from Köylü and Köylü and Faeth [14] and these values are summarized in the table. The values of d_p and \bar{N} yield typical aggregate dimensions of 1000–10,000 nm which is larger than the visible wavelength range and provides significant potential for scattering ([1]). Values of the fractal dimensions were measured as described in connection with Eq. (3) and were found to be properly independent of wavelength for a given fuel within experimental uncertainties; therefore, mean values of D_f for each fuel are summarized in the table. It is evident that effects of fuel type are also small, yielding a mean value of $D_f=1.79$ with a standard deviation of 0.05 when averaged over all wavelengths and fuels.

Dimensionless Extinction Coefficients. Present measurements of dimensionless extinction coefficients are plotted as a function of fuel type (fuel molecular weight) and wavelength in Fig. 1. The mean value of present measurements averaged over all fuels and wavelengths is 8.4 with a standard deviation of 1.5. In addition, the mean value averaged over all fuels at each wavelength is shown as a dashed line on the plots for reference purposes. These average values of K_e at each wavelength considered during the present measurements are summarized in Table 3. There is a tendency for overfire soot from acetylene and n-heptane to yield dimensionless extinction coefficients near uncertainty limits that are smaller and larger than the rest, respectively. It is felt, however, that these differences may be due to experimental difficulties. In particular, acetylene soot involved the presence of a tarry residue not seen for soot from the other fuels which could

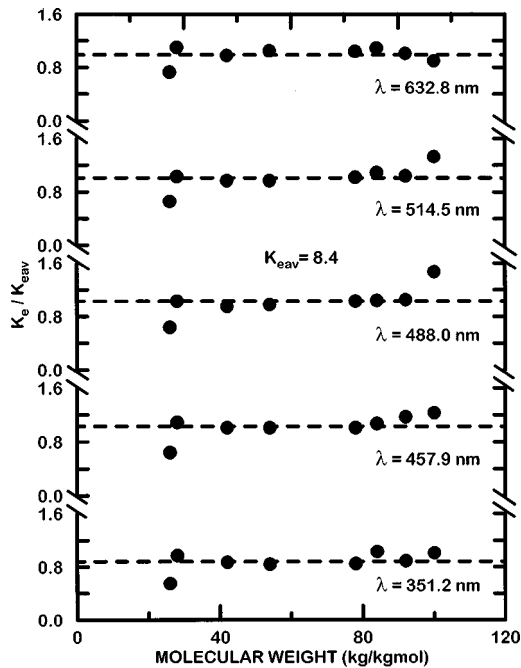


Fig. 1 Measured dimensionless extinction coefficients of soot in the visible as a function of fuel molecular weight and wavelength

cause overestimation of the soot volume fraction while n-heptane measurements involved small soot concentrations and signal-to-noise ratios of extinction measurements. Thus, in view of the rather similar values of dimensionless extinction coefficients of the other six fuels, it is concluded that effects of soot type on this parameter are small. Similar small effects of fuel type were also observed by the soot refractive index properties considered during the present investigation as will be discussed subsequently. Notably, Sivathanu et al. [28] find similar relatively small effects of fuel type on the specific absorption coefficients of soot in premixed flames fueled with methane, propane, and ethylene.

Values of the dimensionless extinction coefficient, averaged over all the fuels at each wavelength, are plotted as a function of wavelength in Fig. 2. Other measurements of K_e for soot formed from the combustion of crude oil from Dobbins et al. [20] and from the combustion of acetylene from Choi et al. [21] are also shown on the plot for comparison with the present measurements. Clearly, the results of all three studies are in excellent agreement. In addition, the results of Choi et al. [21] tend to support the idea that present results for acetylene were affected by the tarry resi-

Table 3 Refractive index properties and dimensionless extinction coefficients in the visible^a

| λ (nm) | $E(m)$ | $F(m)$ | $F(m)/E(m)^d$ | n | κ | K_e |
|--------------------|-------------------------|-------------------------|---------------|------|----------|-----------------------|
| 351.2 | 0.24(0.06) | 0.13(0.03) | 0.63 | 1.38 | 0.44 | 7.4(1.3) |
| 405.0 ^b | ... | ... | 0.76 | ... | ... | 8.8(1.0) ^e |
| 457.9 | 0.27(0.06) ^c | 0.26(0.07) ^c | 0.87 | 1.64 | 0.62 | 8.7(1.5) |
| 488.0 | 0.28(0.04) | 0.25(0.07) | 0.93 | 1.60 | 0.62 | 8.7(1.9) |
| 514.5 | 0.29(0.04) | 0.27(0.06) | 0.98 | 1.62 | 0.66 | 8.6(1.5) |
| 632.8 | 0.27(0.04) | 0.44(0.15) | 1.17 | 1.99 | 0.89 | 8.4(1.0) |
| 800.0 ^b | ... | ... | ... | ... | ... | 9.3(1.5) ^f |

^aStandard deviations are shown in brackets.

^bOnly extinction measurements were made at 405.0 and 800.0 nm.

^cBenzene and toluene were excluded at 457.9 nm.

^dValues of $F(m)/E(m)$ were obtained from the correlation for all fuels in studies made in the visible thus far.

^eMeasurements were not made for the gaseous fuels and n-heptane at 405.0 nm.

^fMeasurements were not made for the gaseous fuels at 800 nm.

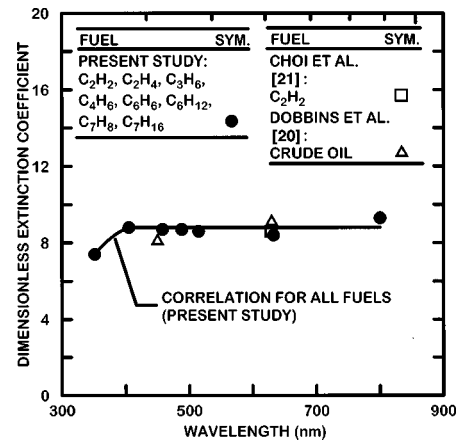


Fig. 2 Measured dimensionless extinction coefficients of soot in the visible as a function of wavelength. References cited in figure are Refs. [20] and [21].

due. Taken together, these results suggest remarkably little variation of K_e for wavelengths of 400–800 nm. In contrast, the earlier measurements of Wu et al. [17] for soot emitted from acetylene, propylene, ethylene, and propane-fueled flames in the long residence time regime yielded a smaller value of $K_e=5.1$ with a standard deviation of 0.5, although their observations of small effects of fuel type and wavelength were similar to the present study. Repeated testing could not confirm the findings of Wu et al. [17] during the present study, however, and their observations will not be considered any further in the following.

It is interesting that K_e is relatively independent of wavelength in the visible in spite of the strong variation of absorption and scattering cross sections for the RDG scattering approximation. For example, $Q_a^p \sim 1/\lambda$ and $Q_s^p \sim Q_{vv}^p \sim 1/\lambda^4$ for primary particles under the RDG scattering approximation. Scattering from aggregates of primary particles under RDG-PFA theory exhibits a reduced sensitivity to changes of wavelength; nevertheless, the general trend toward decreasing optical cross sections with increasing wavelength when refractive indices remain constant is similar. Thus, the relatively small variation of K_e with wavelength for the present test range requires compensating variations of the refractive index functions, $E(m)$ and $F(m)$. Results to be considered subsequently will show that this is the case.

Scattering Patterns. The RDG-PFA scattering theory was evaluated for soot resulting from combustion of each fuel at each wavelength in order to justify the present approach to find soot refractive index properties nonintrusively. Typical examples of this evaluation can be seen from the scattering patterns illustrated in Fig. 3. The results shown in this illustration represent the limiting scattering conditions for the present experiments: toluene at a wavelength of 351.2 nm which represents the largest value of x_p and thus potentially most questionable condition for the use of the evaluation; and ethylene at a wavelength of 632.8 nm which represents the smallest value of x_p and thus potentially the least questionable conditions for the use of the RDG scattering approximation but still a concern because soot refractive indices tend to increase with increasing wavelength which could lead to failure of the RDG scattering approximation ([17]). The agreement between measurements and predictions is seen to be excellent at both limits, justifying the use of RDG scattering theory to find refractive index properties for present conditions. Furthermore, plots of vv cross sections as functions of the modulus of the scattering vector (see Wu et al. [17] for typical examples) and the invariance of fractal dimensions with wavelength discussed earlier, all show that present scattering measurements properly reached the large-angle (power-law) regime required to use Eqs. (3) and (5) in order to find refractive index properties.

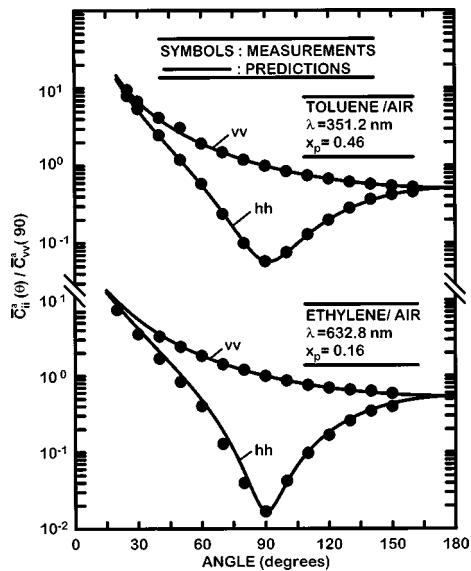


Fig. 3 Typical measured and predicted scattering patterns of soot in the visible

The refractive index function $E(m)$ was found from Eq. (4) based on present measurements of volumetric extinction and total scattering cross sections, and the gravimetric measurements of soot volume fraction. The resulting values of $E(m)$ are plotted as a function of fuel type (fuel molecular weight) and wavelength in Fig. 4. Mean values of $E(m)$, averaged over all the fuels, are shown on the plots for each wavelength; these average values of $E(m)$ are also summarized in Table 3. Effects of fuel type for $E(m)$ are qualitatively similar to those for the related property K_e with values for acetylene and n-heptane departing from the mean values to a somewhat larger degree than the rest (joined by ethylene for $E(m)$ to a greater degree than for K_e). Nevertheless, effects of fuel type on these plots are within experimental uncertainties and it is concluded that $E(m)$ is independent of fuel type over the present test range.

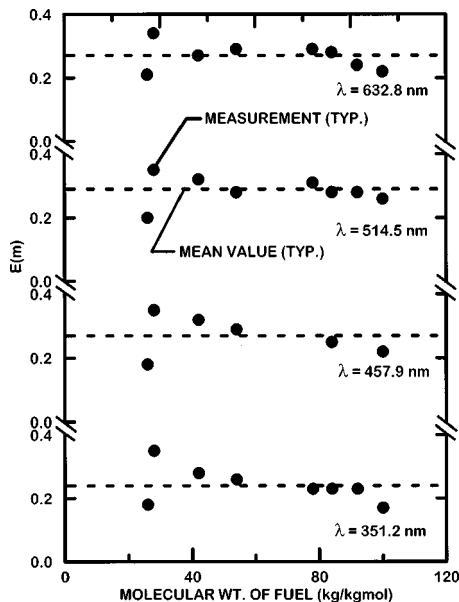


Fig. 4 Measured values of the refractive index function, $E(m)$, of soot in the visible as a function of fuel molecular weight and wavelength

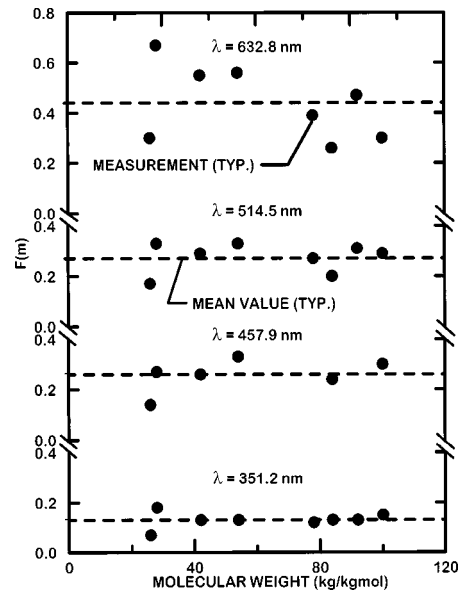


Fig. 5 Measured values of the refractive index function $F(m)$ of soot in the visible as a function of fuel molecular weight and wavelength

The refractive index function, $F(m)$, was found from Eq. (5), based on present measurements of absolute vv cross sections in the large-angle regime, present gravimetric measurements of soot volume fraction, TEM measurements of primary particle diameter, present measurements of the fractal dimensions, and values of the fractal prefactor from Köylü et al. [26]. The resulting values of $F(m)$ are plotted as a function of fuel type (fuel molecular weight) and wavelength in Fig. 5. Mean values, averaged over all the fuels, are also shown on the plots for each wavelength; these average values of $F(m)$ are also summarized in Table 3. In this case, values for acetylene continued to be smaller than the rest which may be attributable to the tarry residue observed for this soot, discussed in connection with the dimensionless extinction coefficient measurements. Scatter of the measurements of $F(m)$ also progressively increases with increasing wavelength due to progressively increasing difficulties in maintaining adequate signal-to-noise ratios for the Rayleigh scattering measurements from propane gas used to provide an absolute calibration of the soot scattering measurements. Thus, effects of fuel type on these plots do not exhibit any consistent trends and are comparable to experimental uncertainties and it is concluded that $F(m)$ is independent of fuel type over the test range, similar to $E(m)$.

Present mean values of $E(m)$ and $F(m)$, averaged over all fuel types, are plotted as a function of wavelength in the visible in Fig. 6. Present results were used in conjunction with the earlier laser extinction measurements of Köylü and Faeth [16] in order to obtain another nonintrusive estimate of $E(m)$ and $F(m)$. This was done by matching the values of $E(m)$ for the two data sets at 514.5 nm and then using present measurements of ρ_{sa} to compute values of $E(m)$ from the extinction measurements of Köylü and Faeth [16] in the visible. Then values of $F(m)$ were obtained from these estimates of $E(m)$ using a general correlation for the ratio $F(m)/E(m)$ developed from present measurements which is summarized in Table 4. These calculations were completed for acetylene, propylene, and ethylene soot which were the only fuels considered during both studies; notably, Köylü and Faeth [16] did not observe significant effects of fuel type during their investigation. The agreement between values of $E(m)$ and $F(m)$ from the present investigation and those extended from Köylü and Faeth [16] is excellent for wavelengths greater than 400 nm but present results are somewhat smaller than the extended results as the near uv is approached. The present values of $E(m)$ and $F(m)$ progres-

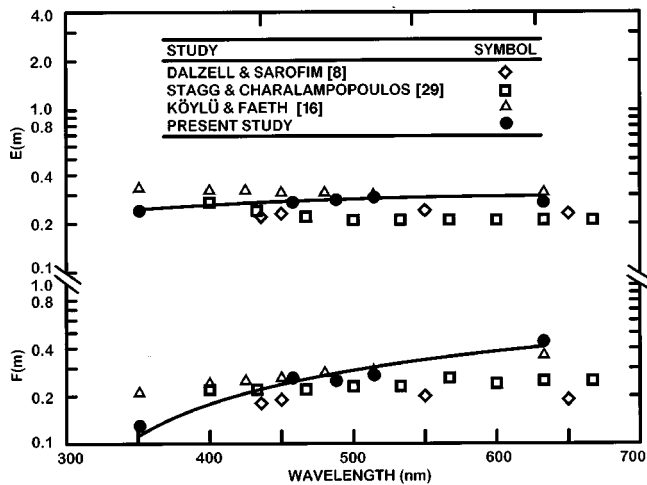


Fig. 6 Measured mean values of the refractive index functions, $E(m)$ and $F(m)$, of soot in the visible as a function of wavelength. References cited in figure are Refs. [8], [16], and [29].

sively increase with increasing wavelength in the near *uv* similar to the observations of Vaglieco et al. [12], and do not suggest an approach to a resonance condition for soot which would cause $E(m)$ and $F(m)$ to peak in this region, similar to the behavior of graphite (see [10,11]). Increasing $E(m)$ and $F(m)$ with increasing wavelength over the present test range is not unexpected, however, because this behavior is needed to explain why K_e is relatively independent of wavelength in the visible for soot aggregates that satisfy RDG-PFA scattering behavior.

Several earlier measurements of $E(m)$ and $F(m)$ are illustrated in Fig. 6. These measurements include the classical ex situ reflectometry measurements for soot in the fuel-lean region of acetylene and propane/air diffusion flames (taken as the average for the two fuels) due to Dalzell and Sarofim [8] and the more recent ex situ reflectometry measurements for soot in premixed propane/air flames due to Stagg and Charalampopoulos [29]. Other ex situ reflectometry measurements for soot in the fuel-lean regions of acetylene and propane/air diffusion flames due to Batten [7] have been omitted from the plot because they yield values of $E(m)$ and $F(m)$ roughly half the values of the rest and these results have not been subsequently duplicated. Finally, earlier well-known in situ measurements of soot refractive index properties in the visible due to Lee and Tien [11], Chang and Charalampopoulos [10], and Vaglieco et al. [12] have not been included on the plots due to the difficulties with these measurements mentioned earlier; e.g., they all involve questionable models for the optical properties of soot, some involve questionable soot transport properties in cases where dynamic scattering measurements were used to estimate soot aggregate properties, and some involve questionable approximations associated with either graphitic-based dispersion models or Kramers-Kronig causality relationships used to close the procedure to find soot refractive indices.

Present measurements of $E(m)$ illustrated in Fig. 6 generally fall within the span of the other measurements, agreeing within experimental uncertainties with the other measurements for wavelengths greater than 400 nm. The only measurements of $E(m)$ at shorter wavelengths are the extended results of Köylü and Faeth

[16] that are significantly larger than the present results at 351.2 nm, as discussed earlier. In this region, however, present results are thought to be more reliable because they do not involve the approximations used to extend the results of Köylü and Faeth [16], they consider many more fuels, and given the behavior of the results of Köylü and Faeth [16] at this wavelength, it would be very difficult to rationalize the behavior of K_e observed in Fig. 2 near this wavelength.

Present measurements of $F(m)$ in Fig. 6 agree with the results extended from Köylü and Faeth [16] for wavelengths greater than 400 nm but only agree with the ex situ studies for the wavelength range 400–500 nm. Overall, present measurements increase more rapidly with increasing wavelengths than the ex situ measurements illustrated in Fig. 6. Present results are consistent with the qualitative trends of $F(m)$ observed by Wu et al. [17] not plotted in Fig. 6, although the magnitudes of $F(m)$ differ from present results due to the problems discussed in connection with the measurements of K_e . In addition, the rapid increase of $F(m)$ with wavelength in the visible is also consistent with values of K_e relatively independent of wavelength in the visible as discussed earlier. Finally, somewhat reduced values of $E(m)$ and $F(m)$ for the ex situ measurements compared to the present in situ measurements, as seen in Fig. 6, is consistent with problems of correcting the ex situ measurements for effects of surface voidage of the compressed soot samples used for reflectometry measurements in the visible—a criticism of the ex situ measurements of soot refractive index properties that has been raised by Felske et al. [9].

Refractive Indices. Given $E(m)$ and $F(m)$, the real and imaginary parts of the refractive indices of soot can be found as a function of wavelength. Similar to the other refractive index properties of soot, effects of fuel type on n and κ were comparable to experimental uncertainties. Thus, values of n and κ averaged over the present results for soot from all the fuels, are plotted as a function of wavelength in Fig. 7; these average values of n and κ are also summarized in Table 3. Several earlier measurements are also shown on the plots as discussed in connection with $E(m)$ and $F(m)$, e.g., the in situ results extended from Köylü and Faeth [16] and the ex situ results from the reflectometry measurements of Dalzell and Sarofim [8] and Stagg and Charalampopoulos [29]. Present values of n agree with the other measurements well within experimental uncertainties. On the other hand, present values of κ only agree with the other measurements within experimental uncertainties for wavelengths of 400–550 nm and generally increase with increasing wavelength more rapidly than the rest. An excep-

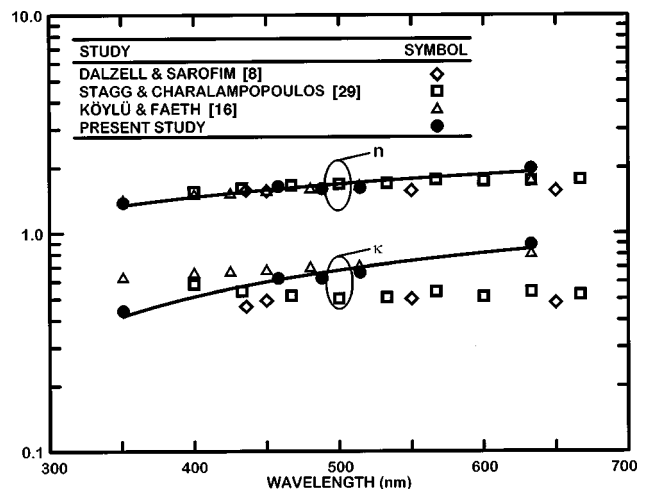


Fig. 7 Measured mean, real, and imaginary parts of the complex refractive index of soot in the visible as a function of wavelength. References cited in figure are Refs. [8], [16], and [29].

Table 4 Correlation of $F(m)/E(m)$ ^a

| Wavelength (nm) | 351 | 400 | 425 | 450 | 480 | 514 | 633 |
|-----------------|------|------|------|------|------|------|------|
| $F(m)/E(m)$ | 0.63 | 0.75 | 0.80 | 0.85 | 0.91 | 0.98 | 1.17 |

^aCorrelation developed using present measurements for all fuels.

tion not shown on the plot, however, is a recent theoretical estimate of $\kappa=0.8$ at 632.8 nm made by Mulholland and Mountain [30] based on the measurements of the specific extinction coefficients of acetylene and ethylene soot due to Mulholland and Choi [31], combined with a coupled dipole calculation, which is in excellent agreement with present measurements at this wavelength.

Conclusions

In situ observations of soot optical properties were undertaken for wavelengths of 351.2–800.0 nm considering soot emitted from buoyant turbulent diffusion flames in the long residence time regime where the properties of soot in the overfire region are independent of position and characteristic flame residence time. Soot was observed for a variety of gas and liquid hydrocarbon fuels (acetylene, ethylene, propylene, butadiene, benzene, cyclohexane, toluene, and n-heptane) burning in still air. Data analysis was based on RDG-PFA scattering theory for soot, which was evaluated successfully for primary particle size parameters as large as 0.46 at a wavelength of 351.2 nm and real and imaginary parts of the complex refractive index of soot that reached values of 1.99 and 0.89 at a wavelength of 632.8 nm. Major conclusions of the study are as follows:

1 Present dimensionless extinction coefficients were relatively independent of fuel type and wavelength (for wavelengths of 400–800 nm) yielding an average value of 8.4 and a standard deviation of 1.5. These results are in excellent agreement with earlier measurements of Dobbins et al. [13] and Choi et al. [21] for similar overfire soot populations, resolving discrepancies between these and earlier studies and the findings of Wu et al. [17].

2 Present values of the refractive index function for absorption, $E(m)$, were relatively independent of fuel type and agreed within experimental uncertainties with earlier *ex situ* reflectometry measurements of Dalzell and Sarofim [8] and Stagg and Charalampopoulos [29] for the wavelength range where they could be compared (400–630 nm).

3 Present values of the refractive index function for scattering, $F(m)$, were relatively independent of fuel type and agreed with the earlier *ex situ* reflectometry measurements of Dalzell and Sarofim [8] and Stagg and Charalampopoulos [29] for wavelengths of 400–500 nm; otherwise, present values of $F(m)$ increased more rapidly with increasing wavelength than observed before, although such behavior is consistent with dimensionless extinction coefficients being relatively independent of wavelength over the present test range.

4 Present values of the real and imaginary parts of the refractive indices of soot were relatively independent of fuel type. Present values of real part of the refractive index of soot agreed with the *ex situ* measurements of Dalzell and Sarofim [8] and Stagg and Charalampopoulos [29] within experimental uncertainties; on the other hand, similar agreement for the imaginary part of the refractive index of soot was only observed for wavelengths of 400–550 nm while otherwise increasing with increasing wavelength more rapidly than the rest. One exception to this was a recent theoretical estimate of κ at 632.8 nm due to Mulholland and Mountain [30] which agrees with present results within experimental uncertainties.

5 Present soot refractive indices did not exhibit an approach to a resonance condition in the near *uv* that is observed for graphite; instead, present refractive indices declined continuously with decreasing wavelength as the near *uv* was approached, similar to the findings of Vaglieco et al. [12] for amorphous carbon and soot.

Extending present observations of dimensionless extinction coefficients to other soot populations should be approached with caution; in particular, the present overfire soot involved large aggregates with significant effects of scattering and behavior might be very different for the small soot aggregates found in soot growth regions. On the other hand, relatively weak effects of fuel

type on soot refractive index properties in the visible offer substantial reductions of effort for estimating soot optical and radiative properties that definitely merits further study.

Acknowledgments

This research was supported by the Building and Fire Research laboratory of the Institute of Standards and Technology, Grant Nos. 60NANB4D1696 and 60NANB8D0084, with H. R. Baum serving as Scientific Officer.

Nomenclature

| | |
|-----------|--|
| C | = optical cross section |
| d | = burner diameter |
| d_p | = primary particle diameter |
| D_f | = mass fractal dimension |
| $E(m)$ | = refractive index function for absorption, $\text{Im}((m^2-1)/(m^2+2))$ |
| f_v | = soot volume fraction |
| $F(m)$ | = refractive index function for scattering, $ m^2-1 /(m^2+2)^2$ |
| i | = $(-1)^{1/2}$ |
| I | = light intensity |
| k | = wave number, $2\pi/\lambda$ |
| k_f | = fractal prefactor |
| K_e | = dimensionless extinction coefficient |
| L | = light path length |
| m | = soot refractive index, $n + i\kappa$ |
| M | = molecular weight |
| n | = real part of soot refractive index |
| N | = number of primary particles per aggregate |
| N_g | = geometric mean of the number of particles per aggregate |
| q | = modulus of scattering vector, $2k \sin(\theta/2)$ |
| Q | = volumetric optical cross section |
| \dot{Q} | = burner heat release rate |
| R_g | = radius of gyration of an aggregate |
| t_f | = characteristic flame residence time |
| x_p | = primary particle size parameter, $\pi d_p/\lambda$ |

Greek Symbols

| | |
|-------------|---|
| θ | = angle of scattering from forward direction |
| κ | = imaginary part of refractive index of soot |
| λ | = wavelength of radiation |
| ρ_{sa} | = ratio of total scattering to absorption cross sections |
| σ_D | = standard deviation of D_f |
| σ_g | = standard deviation of number of particles per aggregate from geometric mean |

Subscripts

| | |
|------|--|
| a | = absorption |
| av | = average value |
| e | = extinction |
| h | = horizontal polarization |
| ij | = incident (i) and scattered (j) polarization directions |
| s | = total scattering |
| v | = vertical polarization |
| o | = initial value |

Superscripts

| | |
|-----------------|---|
| a | = aggregate property |
| p | = primary particle property |
| $(\bar{\quad})$ | = mean value over a polydisperse aggregate population |

References

- [1] Faeth, G. M., and Köylü, Ü. Ö., 1995, "Soot Morphology and Optical Properties in Nonpremixed Turbulent Flame Environments," *Combust. Sci. Technol.*, **108**, pp. 207–229.
- [2] Charalampopoulos, T. T., 1992, "Morphology and Dynamics of Agglomerated

- Particulates in Combustion Systems Using Light Scattering Techniques," *Prog. Energy Combust. Sci.*, **18**, pp. 13–45.
- [3] Jullien, R., and Botet, R., 1987, *Aggregation and Fractal Aggregates*, World Scientific, Singapore, pp. 45–60.
- [4] Köylü, Ü. Ö., and Faeth, G. M., 1993, "Radiative Properties of Flame-Generated Soot," *ASME J. Heat Transfer*, **111**, pp. 409–417.
- [5] Tien, C. L., and Lee, S. C., 1982, "Flame Radiation," *Prog. Energy Combust. Sci.*, **8**, pp. 41–59.
- [6] Viskanta, R., and Mengüç, M. P., 1987, "Radiation Heat Transfer in Combustion Systems," *Prog. Energy Combust. Sci.*, **13**, pp. 97–160.
- [7] Batten, C. E., 1985, "Spectral Optical Constants of Soots From Polarized Angular Reflectance Measurements," *Appl. Opt.*, **24**, pp. 1193–1199.
- [8] Dalzell, W. H., and Sarofim, A. F., 1969, "Optical Constants of Soot and Their Application to Heat Flux Calculations," *ASME J. Heat Transfer*, **91**, pp. 100–104.
- [9] Felske, J. D., Charalampopoulos, T. T., and Hura, H., 1984, "Determination of the Refractive Indices of Soot Particles from the Reflectivities of Compressed Soot Pellets," *Combust. Sci. Technol.*, **37**, pp. 263–284.
- [10] Chang, H. Y., and Charalampopoulos, T. T., 1990, "Determination of the Wavelength Dependence of Refractive Indices of Flame Soot," *Proc. R. Soc. London, Ser. A*, **430**, pp. 577–591.
- [11] Lee, S. C., and Tien, C. L., 1980, "Optical Constants of Soot in Hydrocarbon Flames," *Eighteenth Symposium (International) on Combustion*, The Combustion Institute, Pittsburgh, PA, pp. 1159–1166.
- [12] Vaglieco, B. M., Beretta, F., and D'Alessio, A., 1990, "In Situ Evaluation of the Soot Refractive Index in the UV-Visible from the Measurements of Scattering and Extinction Coefficients in Rich Flames," *Combust. Flame*, **79**, pp. 259–271.
- [13] Dobbins, R. A., and Megaridis, C. M., 1991, "Absorption and Scattering of Light by Polydisperse Aggregates," *Appl. Opt.*, **30**, pp. 4747–4754.
- [14] Köylü, Ü. Ö., and Faeth, G. M., 1994, "Optical Properties of Overfire Soot in Buoyant Turbulent Diffusion Flames at Long Residence Times," *ASME J. Heat Transfer*, **116**, pp. 152–159.
- [15] Köylü, Ü. Ö., and Faeth, G. M., 1994, "Optical Properties of Soot in Buoyant Laminar Diffusion Flames," *ASME J. Heat Transfer*, **116**, pp. 971–979.
- [16] Köylü, Ü. Ö., and Faeth, G. M., 1996, "Spectral Extinction Coefficients of Soot Aggregates From Turbulent Diffusion Flames," *ASME J. Heat Transfer*, **118**, pp. 415–421.
- [17] Wu, J.-S., Krishnan, S. S., and Faeth, G. M., 1997, "Refractive Indices at Visible Wavelengths of Soot Emitted from Buoyant Turbulent Diffusion Flames," *ASME J. Heat Transfer*, **119**, pp. 230–237.
- [18] Sivathanu, Y. R., and Faeth, G. M., 1990, "Soot Volume Fractions in the Overfire Region of Turbulent Diffusion Flames," *Combust. Flame*, **81**, pp. 133–149.
- [19] Köylü, Ü. Ö., and Faeth, G. M., 1992, "Structure of Overfire Soot in Buoyant Turbulent Diffusion Flames at Long Residence Times," *Combust. Flame*, **89**, pp. 140–156.
- [20] Dobbins, R. A., Mulholland, G. W., and Bryner, N. P., 1993, "Comparison of a Fractal Smoke Optics Model With Light Extinction Measurements," *Atmos. Environ.*, **28**, pp. 889–897.
- [21] Choi, M. Y., Mulholland, G. W., Hamins, A., and Kashiwagi, T., 1995, "Comparisons of the Soot Volume Fraction Using Gravimetric and Light Extinction Techniques," *Combust. Flame*, **102**, pp. 161–169.
- [22] Rosner, D. E., Mackowski, D. W., and Garcia-Ybarra, P., 1991, "Size- and Structure-Insensitivity of the Thermophoretic Transport of Aggregated 'Soot' Particles in Gases," *Combust. Sci. Technol.*, **80**, pp. 87–101.
- [23] Manickavasagam, S., and Mengüç, M. P., 1993, "Effective Optical Properties of Coal/Char Particles Determined from FT-IR Spectroscopy Experiments," *Energy Fuels*, **7**, pp. 860–869.
- [24] Rudder, R. R., and Bach, D. R., 1968, "Rayleigh Scattering of Ruby-Laser Light by Neutral Gases," *J. Opt. Soc. Am.*, **58**, pp. 1260–1266.
- [25] Dyer, T. M., 1979, "Rayleigh Scattering Measurements of Time-Resolved Concentration in a Turbulent Propane Jet," *AIAA J.*, **17**, pp. 912–914.
- [26] Köylü, Ü. Ö., Faeth, G. M., Farias, T. L., and Carvalho, M. G., 1995, "Fractal and Projected Structure Properties of Soot Aggregates," *Combust. Flame*, **100**, pp. 621–633.
- [27] Köylü, Ü. Ö., 1992, "Structure of Overfire Soot in Buoyant Turbulent Diffusion Flames," Ph. D. thesis, The University of Michigan, Ann Arbor, MI.
- [28] Sivathanu, Y. R., Gore, J. P., Janssen, J. M., and Senser, D. W., 1993, "A Study of In Situ Specific Absorption Coefficients of Soot Particles in Laminar Flat Flames," *ASME J. Heat Transfer*, **115**, pp. 653–658.
- [29] Stagg, B. J., and Charalampopoulos, T. T., 1993, "Refractive Indices of Pyrolytic Graphite, Amorphous Carbon, and Flame Soot in the Temperature Range 25 to 600°C," *Combust. Flame*, **94**, pp. 381–396.
- [30] Mulholland, G. W., and Mountain, R. D., 1999, "Coupled Dipole Calculations of Extinction Coefficient and Polarization Ratio for Smoke Agglomerates," *Combust. Flame*, **119**, pp. 56–68.
- [31] Mulholland, G. W., and Choi, M. Y., 1998, "Measurement of the Mass Specific Extinction Coefficient for Acetylene and Ethane Using the Large Agglomerate Optics Facility," *Twenty-Seventh Symposium (International) on Combustion*, The Combustion Institute, Pittsburgh, PA, pp. 1515–1522.

An Experimental Investigation of the Transient Characteristics on a Flat-Plate Heat Pipe During Startup and Shutdown Operations

Y. Wang

K. Vafai

Professor, Fellow ASME

Department of Mechanical Engineering,
The Ohio State University,
Columbus, OH 43210-1107

This work presents an experimental investigation of the thermal performance of a flat-plate heat pipe during startup and shutdown operations. Using the analytical model developed in a previously study, analytical and experimental results on the effect of input power and cooling heat transfer coefficient on the thermal performance of the heat pipe are presented and discussed. The results indicate that the wick in the evaporator section provides the largest resistance to the heat transfer process followed by the wick in the condenser section. It is found that the heat transfer coefficient has an insignificant effect on the maximum temperature difference across the heat pipe where this difference refers to the maximum difference on the outside surfaces of the flat-plate heat pipe. However, as expected, the input heat flux has a substantial effect on the temperature rise where the temperature rise refers to the temperature increase on the outside surface of the heat pipe. It is found that the temperature difference across the heat pipe depends mainly on the input power. The heat transfer coefficient strongly affects the time it takes to reach steady state while input power has a substantially smaller effect. Empirical correlations for the maximum temperature rise, the maximum temperature difference and the time constants are obtained. The experimental results are compared with the analytical results and are found to be in very good agreement. [S0022-1481(00)01803-X]

Keywords: Experimental, Heat Pipes, Heat Transfer, Modeling, Transient.

1 Introduction

The flat-plate heat pipe finds numerous applications such as in electronics cooling and spacecraft radiator segments (Chi [1] and Peterson [2]). The flat-shaped heat pipe also finds applications for very localized heat dissipation where it is difficult to effectively utilize a conventional cylindrical heat pipe due to the limited heat source and sink areas. However, the research work on heat pipes has been mainly focused on the traditional cylindrical heat pipe for a wide variety of applications, and there is far less work conducted on the flat-plate heat pipe. In earlier studies by Vafai and his co-workers, both analytical and numerical investigations were conducted for the vapor and fluid flows as well as for the heat transfer characteristics for the startup process of a flat-plate heat pipe. Vafai and Wang [3] investigated the overall performance of an asymmetrical rectangular flat-plate heat pipe. They developed a pseudo-three-dimensional analytical model for steady incompressible vapor flow in the flat-plate heat pipe. Detailed physics of the transport processes within the heat pipe were analyzed and established. Zhu and Vafai [4] conducted a three-dimensional analytical and numerical study for the steady incompressible vapor and liquid flow in an asymmetrical flat-plate heat pipe. Their results demonstrated that the vapor velocity profile is nonsimilar and asymmetrical and that the transverse pressure variations are small. Later, Zhu and Vafai [5] developed an analytical model to predict the transient thermal behavior of asymmetrical flat-plate heat pipes during the startup process. The temperature distributions within the heat pipe walls and liquid-saturated wicks were obtained analytically. Wang and Vafai [6] developed an analytical model for predicting the thermal performance of flat-plate heat

pipes for startup and shutdown operations. The effects of input power and heat transfer coefficient on the performance of the flat-plate heat pipe were investigated.

There is a very limited number of experimental investigations available on flat-plate heat pipes. Furthermore, these few investigations reported system-specific applications and testing data for the flat-plate heat pipes. In addition, the heat pipes utilized in these experiments were based on a simpler structure than those proposed and analyzed by Vafai et al. Among the very few experimental investigations in this area, the works of Kikuchi et al. [7], Basiulis et al. [8], and Thomson et al. [9] can be cited. Kikuchi et al. [7] had carried out experiments on an electrohydrodynamic flat-plate heat pipe. The heat pipe was 100 cm in length and 10 cm in width, and employed three electrodes. The orientation of the heat pipe was horizontal in their study and Freon 11 and 113 were separately used as working fluids. It was found that Freon 11 was superior to Freon 113 from the point of view of thermal transport. Heat transport capabilities up to 150W were recorded. Basiulis et al. [8] conducted experiments to test the performance of flat-plate heat pipes for cooling printed wiring boards. A maximum power input up to 100 W and heat fluxes up to 2 W/cm² were reported for the tested heat pipes. Thomson et al. [9] performed experiments to investigate the application of flat-plate heat pipes in cooling of high-power amplifiers (HPA) for communication satellites. The surface temperatures of the heat pipe were measured for three different input powers. In the above studies, no vertical wicks were reported and the condensate return path was not specified. Additional works dealing with some restricted aspects of flat-plate heat pipes can be found in Refs. [10–16]. Once again, it should be noted that the heat pipes utilized in these works were substantially simpler in form than that analyzed by Vafai et al. [4,6,17]. A more recent investigation of the thermal performance of a flat plate heat pipe is given in Wang and Vafai [18].

In this work, an experimental and analytical investigation is

Contributed by the Heat Transfer Division for publication in the JOURNAL OF HEAT TRANSFER. Manuscript received by the Heat Transfer Division, July 3, 1999; revision received, Feb. 23, 2000. Associate Technical Editor: D. Poulikakos.

conducted to characterize the thermal performance of a flat-plate heat pipe. The effects of input heat flux and heat transfer coefficient on the thermal performance of a flat-plate heat pipe are investigated experimentally. The temperature and heat flux distributions as well as empirical correlations for the maximum temperature rise, the maximum temperature difference within the heat pipe, and time constants are presented. The experimental results are compared with the analytical results by Wang and Vafai [6].

2 Analytical Modeling

The analytical model for startup and shutdown operations developed in Wang and Vafai [6] was utilized to predict the performance of the experimental heat pipe. A summary description of the essential parts of the analytical modeling is given below.

The main assumptions for the analysis for the flat plate heat pipe are (1) the heat transfer in the wick is by conduction, (2) the temperature in the vapor phase is uniform at any given time, (3) the thermal properties of the heat pipe wall and the wick are taken to be constant, and (4) heat transfer along the top heat pipe wall and wick in the longitudinal direction is small and is neglected.

For a startup operation, the heat transfer process in the heat pipe is divided into five regimes. The first regime starts when power is turned on and ends when the thermal front reaches the wall-wick interface of the evaporator section. Following this period is the second regime, which starts when the thermal front resumes from the wall-wick interface and ends when the thermal front reaches the wick-vapor interface of evaporator section. In the third regime, the thermal front resumes from the wick-vapor interface and reaches the wick-wall interface of the condenser section. The fourth regime starts when the thermal front progresses from the wick-wall interface and ends when the thermal front reaches the outside wall surface of condenser section. In the fifth and final regime, the outside wall surface of the condenser section begins to increase. For the shutdown operation, the input power is zero and there is only one regime. During this regime, the heat pipe temperatures in all heat pipe walls and wicks decrease with time.

For each period, the temperature distributions in the heat pipe walls and wicks along the normal direction are presented using second-order formulations, which are functions of time. Based on separate energy balance for heat pipe walls and wicks and interface energy and temperature balance at the wall-wick and wick-vapor interfaces, detailed analytical models are developed for each regime in the startup operation. For a shutdown operation, similar procedure was utilized and a separate model is obtained. The derived models consist of close systems of equations, which can be solved numerically.

In the simulation, the temperature distribution within the heat pipe at the end of the startup operation is taken as the initial temperature distribution for the shutdown operation. In this work, the steady-state conditions are assumed to have been reached if the relative deviation between the input and output power is less than 0.2 percent. Similarly, during the shutdown operation, it is assumed that the heat pipe reaches its original temperature if the temperature rise at the outside wall surface of the evaporator section is less than 0.3°C ([6]).

3 Experimental Setup and Procedure

Figure 1 is a schematic of the flat-plate heat pipe. The heat pipe was 190.50 mm in length, 139.70 mm in width, and 34.93 mm in height. The working fluid for the heat pipe was water. The heat pipe walls were made of copper plate, 3.175 mm thick. Attached to the inner surfaces of the heat pipe wall are porous wicks, as shown in Fig. 1. In addition, vertical wicks are used to provide a secondary return mechanism for the condensate. The vapor region is composed of four identical channels. The wicks were composed of sintered copper powder with a thickness of 1.651 mm. The pore radius of the wicks was 3.1×10^{-5} m and their porosity was 50 percent. The permeability of the wicks was 7×10^{-12} m². A flexible heater (139.7 mm in length and 50.8 mm in width), specially

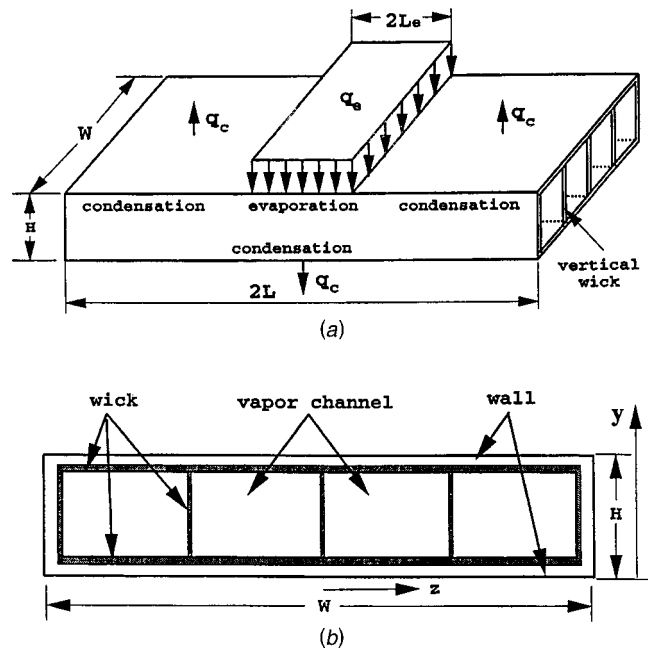


Fig. 1 Schematic of the flat-plate heat pipe: (a) geometry of the heat pipe, (b) cross-sectional view of the heat pipe

designed for this experiment (Watlow Company, Inc.), was attached along the centerline of the top surface of the heat pipe. The exposed side of the heater was insulated. The heat pipe can be divided into four sections, i.e., one evaporator section on the top center, two smaller identical condenser sections on the top, located on either side of the evaporator section, and a larger condenser section on the bottom (Fig. 1).

Figure 2 is a schematic of the experimental setup. The heat pipe was oriented horizontally in the experiment. A Lexan frame, 34.93 mm in thickness, was constructed to house the heat pipe. The function of the Lexan frame was threefold: (1) to support the heat pipe, (2) to reduce the heat loss through the four edges of the heat pipe, and (3) to insure uniformity of gap thickness around the heat pipe. Taking into account thermal expansion, the inner dimensions of the frame are made larger than the outside dimension of the heat pipe, and a flexible insulation material 2 mm in thickness was installed between the Lexan frame and the heat pipe. The flexible insulation material allows the heat pipe to expand at elevated temperatures. The flexible insulation material also reduces the heat loss through the four edges of the heat pipe.

A channel was designed to house the frame. The cross section of the channel was rectangular (Fig. 2b) and its inner dimensions were 217 mm in width, and 45 mm in height. The length of the channel was 540 mm. The frame enclosing the heat pipe was securely mounted within the chamber.

The center part of the top wall of the channel was detachable. The thermocouple wires and the power cord were fed through the detachable top wall; therefore the thermocouple wires and the power cord caused a minimal disturbance on the fluid flow through the channel. In order to seal the top detachable plate, another Lexan plate as well as a gasket were used as shown in Fig. 2(b). To insure uniform channel height for each of the three channels, identical spacers were constructed for each section as shown in Fig. 2. This design produces three channels for the water flow as shown in Fig. 2(b).

Cooling water enters the water tank through the water supply as shown in Fig. 2(a). The water pressure and flow rate were stabilized by the water tank. The cooling water enters the test section, which houses the heat pipe frame and the heat pipe. The flow rate was measured with two float flow meters with different flow rate

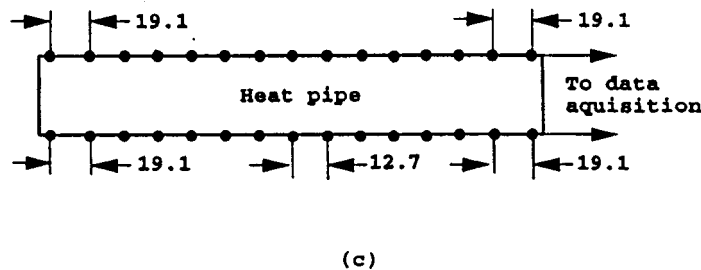
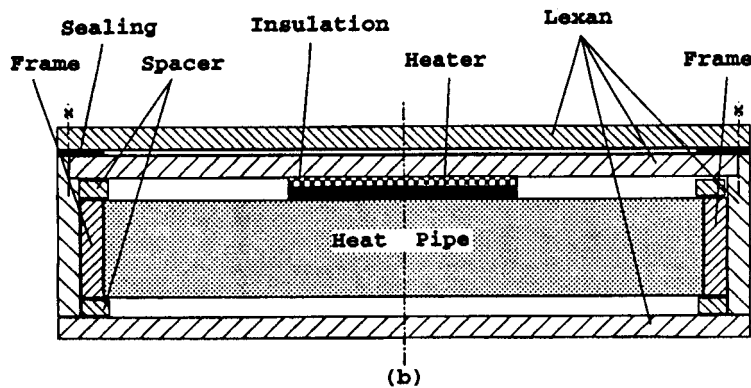
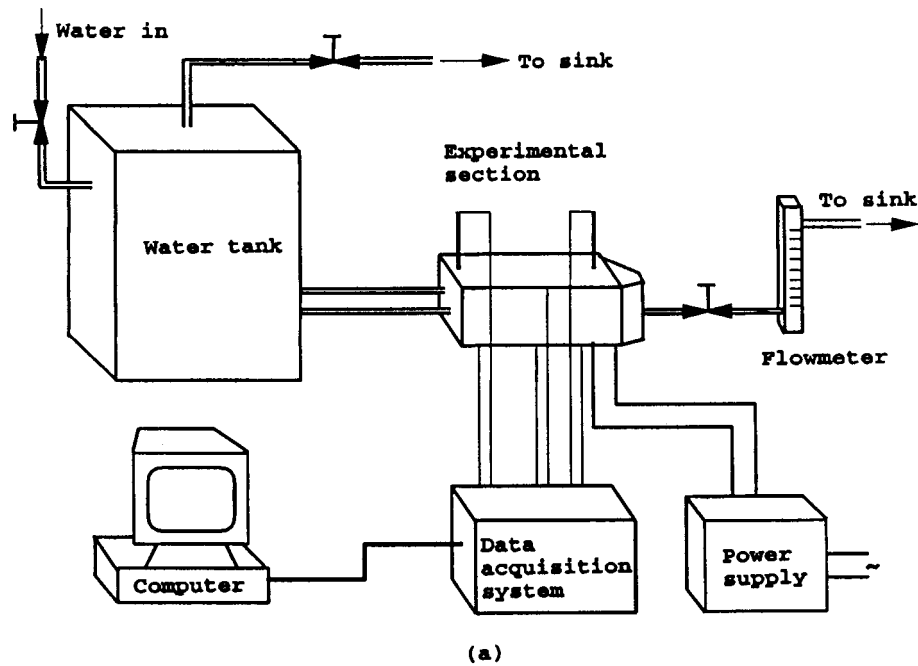


Fig. 2 Experimental setup: (a) experimental system, (b) cross-sectional view of the channel, (c) location of thermocouples on the heat pipe surfaces

ranges. The measured parameters include temperatures on the heat pipe surface, the temperature of the cooling water at inlet and outlet, the flow rate, and the input power. In each experimental run, the average heat transfer coefficient was maintained constant.

Thirty E-type thermocouples were utilized to measure the top and bottom surface temperatures at the centerline of the heat pipe with fifteen on each surface of the heat pipe. In order to reduce the disturbance, a 6-mm by 0.3-mm groove was machined in the heat pipe walls and a high conductivity cement was used to imbed the thermocouples within the heat pipe wall. The spacing between

adjacent thermocouples was 12.7 mm, except for the thermocouples at the end, which were separated 19.1 mm from each other, as shown in Fig. 2(c).

In order to monitor the heat loss through the insulated surfaces, thermocouples were also installed on both the inner and outer surfaces of the Lexan frame. In addition, two thermocouples were incorporated to monitor the cooling water temperature at the inlet and outlet, and three thermocouples were mounted on the inner surface of the bottom channel wall directly beneath the heat pipe. The room temperature was also measured with two thermo-

couples. The temperature data was collected through a data acquisition system. The temperatures were sampled every second. All data were collected through the data acquisition system.

For a typical experimental run, the flow rate was adjusted to a desired level. After reaching a steady flow rate, a desired heater power was applied. The power supply was turned off when steady-state conditions were achieved. The steady-state conditions were assumed to have been reached when the changes of the maximum temperature reading was less than 0.2°C within at least 90 seconds. Experiments were conducted to investigate the thermal behavior of the heat pipe during startup and shutdown processes. In addition, to analyze the cyclical operation of the heat pipe during startup and shutdown processes, the power was turned back on when initial conditions were achieved after the shutdown process and the procedure described above was repeated.

4 Data Reduction and Uncertainty Analysis

The heat fluxes on the outside surface of the heat pipe were calculated by

$$q_e = \frac{Q}{A_e} \quad (1)$$

where Q is the power supply and A_e the heat transfer area of the evaporator section. The heat transfer coefficient was obtained by

$$h_{\text{conv}} = \frac{Q}{A_c(T_{wa,oc} - T_\infty)} \quad (2)$$

where $T_{wa,oc}$ is the average temperature on the outside condenser surfaces at steady state and T_∞ is the temperature of cooling water, A_c is the heat transfer area of the condenser section, and

$$q_c = h_{\text{conv}}(T_{wa,oc}(t) - T_\infty(t)) \quad (3)$$

where q_c is the heat flux over the entire condenser section. The temperature at the heat pipe wall-wick interface of the evaporator section can be found from

$$T_{ww,e}(t) = T_{wa,oe}(t) - \frac{q_e h_{wa}}{k_{wa}} \quad (4)$$

where $T_{ww,e}(t)$ is the temperature at the wall-wick interface, $T_{wa,oe}(t)$ is the outside wall temperature of the evaporator section and h_{wa} and k_{wa} are the thickness and conductivity of the heat pipe wall. The temperature at the heat pipe wall-wick interface of the condenser section is similarly obtained from

$$T_{ww,c}(t) = T_{wa,oc}(t) + \frac{q_c(t) h_{wa}}{k_{wa}} \quad (5)$$

It should be noted that Eqs. (4) and (5) provide a linear extrapolation of instantaneous experimental data based on the measured surface temperatures. As such they approximate the thermal storage, which is implicitly built in the measured surface temperature values. It should be noted that the storage terms for all different layers of the flat-plate heat pipe are fully accounted for in the analytical solution. Since the thermal conductivity of the solid wall is relatively high, the following approximation is invoked at the heat pipe wall-wick interface in the evaporator section for extrapolating the data

$$T_{wa,oe}(t) \cong T_{ww,e}(t) \quad (6)$$

Similarly, the following approximation is made at the heat pipe wall-wick interface in the condenser section for extrapolating data:

$$T_{wa,oc}(t) \cong T_{ww,c}(t) \quad (7)$$

An energy balance between the evaporator section and the condenser section yields

$$q_{wv,e}(t) A_e = q_{wv,c}(t) A_c \quad (8)$$

Table 1 Uncertainty in heat transfer coefficient measurements

| h_{conv} , W/(m ² °C) | 285 | 500 | 800 | 1000 | 1260 |
|--|-------|-------|--------|--------|--------|
| $\epsilon_{h_{\text{conv}}}$ | ±5.8% | ±7.6% | ±10.1% | ±11.8% | ±13.9% |

where $q_{wv,e}$ and $q_{wv,c}$ are the heat fluxes at the wick vapor interfaces of the evaporator and condenser section, respectively. Assuming a linear temperature distribution, these heat fluxes can be represented as

$$q_{wv,e}(t) = k_w \frac{T_{wv,e}(t) - T_v(t)}{h_w} \quad (9)$$

$$q_{wv,c}(t) = k_w \frac{T_v(t) - T_{wv,c}(t)}{h_w} \quad (10)$$

where $T_v(t)$ is vapor temperature, and h_w and k_w are the thickness and conductivity of the wick. The conductivity of the wick can be determined by ([1])

$$k_w = k_{\text{eff}} = k_l \left[\frac{k_l + k_s - (1 - \epsilon)(k_l - k_s)}{k_l + k_s + (1 - \epsilon)(k_l - k_s)} \right] \quad (11)$$

Substituting Eqs. (8) and (9) into (7) yields

$$T_v(t) = \frac{A_e T_{wa,oe}(t) + A_c T_{wa,oc}(t)}{A_e + A_c} \quad (12)$$

The maximum uncertainty in temperature and power supply readings was ± 0.1°C and ± 3.4 percent, respectively. The uncertainty in the measurement of the thickness of the walls and wicks was ± 0.001 mm while the uncertainty in the measurement of the length, width, and height was about ± 0.01 mm. Using the method of Kline and McClintock [19], the uncertainties in the heat transfer coefficient measurement were determined and are displayed in Table 1. The overall energy balance was also checked and was found to be satisfied well within less than four percent.

5 Results and Discussion

Figure 3 shows the temporal temperature rise for the outside surface of the heat pipe for different input heat fluxes. As expected, the maximum top wall surface temperature increases with an increase in input heat flux. However, an increase in the input heat flux has less of an effect on the bottom surface temperature of the heat pipe since the heat flux at the condenser section is smaller than that of the evaporator section. The time that it takes for the startup operation to reach steady state is almost the same for these four cases, which indicates that input power has an insignificant effect on the startup time over the range considered in this work. The input heat flux-time histories are plotted in Fig. 4 for the four cases shown in Fig. 3. As expected, the heat flux in the condenser section increases with an increase in the input heat flux.

Figure 5 shows the transient temperature rise on the outside wall surface of the heat pipe for different heat transfer coefficients. As shown in Fig. 5, increasing the heat transfer coefficient reduces the wall surface temperatures on both the evaporator and condenser sections. As can be seen in Fig. 5, increasing the heat transfer coefficient reduces the time it takes to reach steady state. The heat flux-time histories for various heat transfer coefficients are plotted in Fig. 6. As can be seen in Fig. 6, for a fixed input power increasing the heat transfer coefficient reduces the time it takes to reach steady-state conditions. For all these figures, the maximum deviation for the relative temperature errors between analytical and experimental results is from 2.4 percent to 7.9 percent.

Figures 3 to 6 show excellent agreement between the measured and the analytical heat flux and temporal temperature distribu-

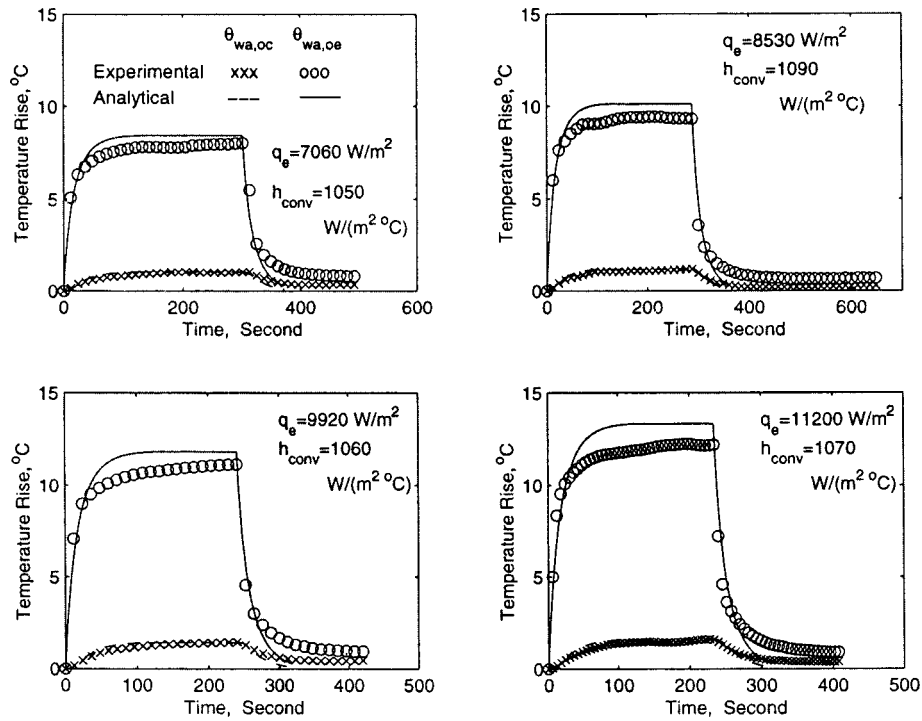


Fig. 3 Temporal temperature rise for the outside surfaces of the heat pipe for different input heat fluxes

tions. As can be seen in Figs. 3 and 5, the measured temperature distributions are a little lower than the analytical temperature distributions under steady-state conditions. This can be attributed to the secondary heat conduction path, i.e., the longitudinal conduction across the top heat pipe wall, which was not considered in the analytical model.

Figures 7 and 8 show the outside surface temperature distributions in the z direction for two typical cases. Strictly speaking, the heat transfer along the top wall is two-dimensional, normal as well as along the wall. The heat is predominantly transferred in the normal direction from the evaporator section to the condenser section through the evaporation of working fluid and condensation

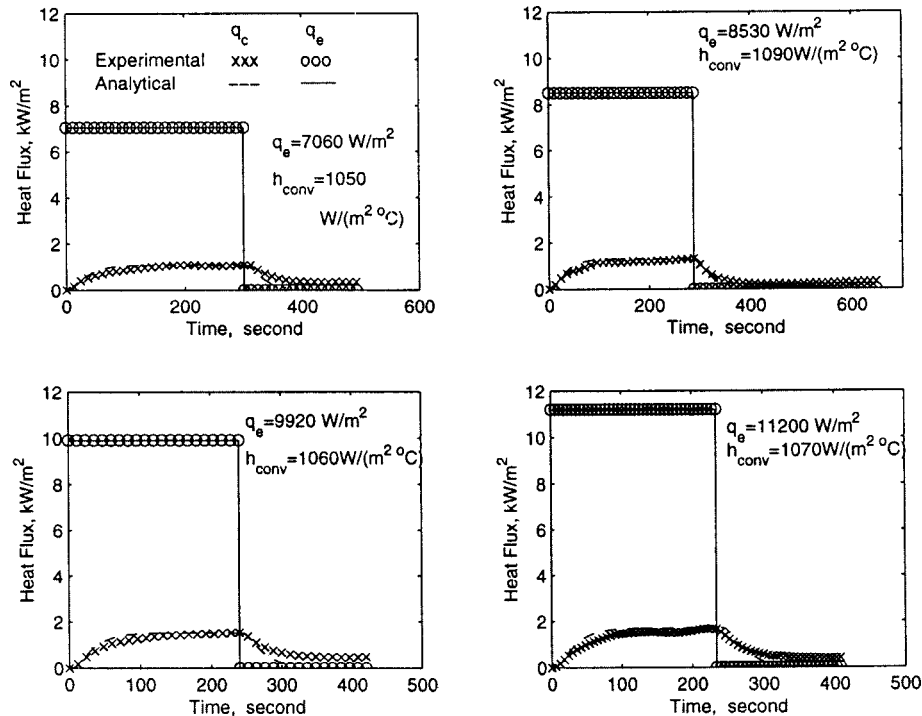


Fig. 4 Heat flux variations for different power inputs

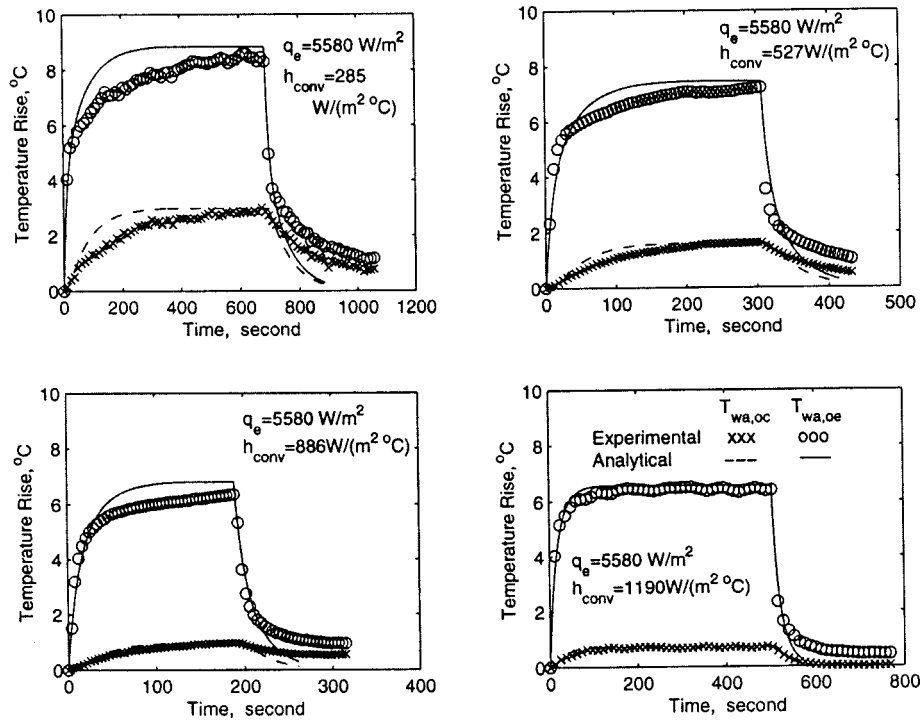


Fig. 5 Temporal temperature rise for the outside wall of the heat pipe for various heat transfer coefficients

of the vapor. The top wall also provides a secondary conduction path for the heat flow in the longitudinal direction. However, this is a relatively minor pathway as evidenced from the good agreement between earlier cited model by Wang and Vafai [6] and the experimental results. Heat transfer through the secondary path can

enhance the heat pipe performance by reducing its maximum temperature rise and the maximum temperature difference within the heat pipe.

The transient temperature distributions in the normal direction are plotted in Figs. 9 and 10 for two different input heat fluxes. As

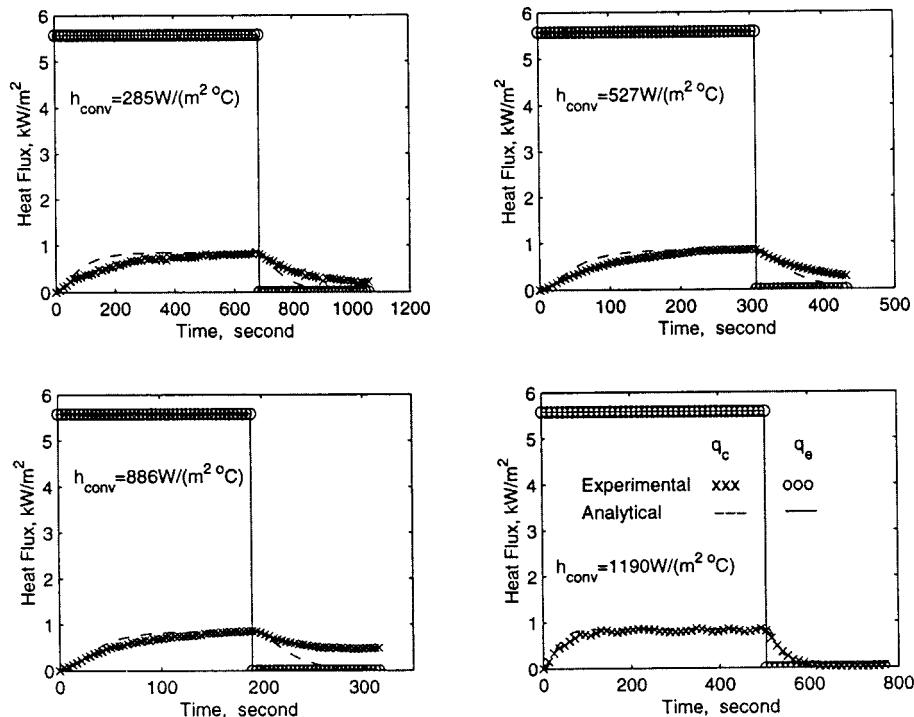


Fig. 6 Effect of heat transfer coefficient variations on the heat flux distribution

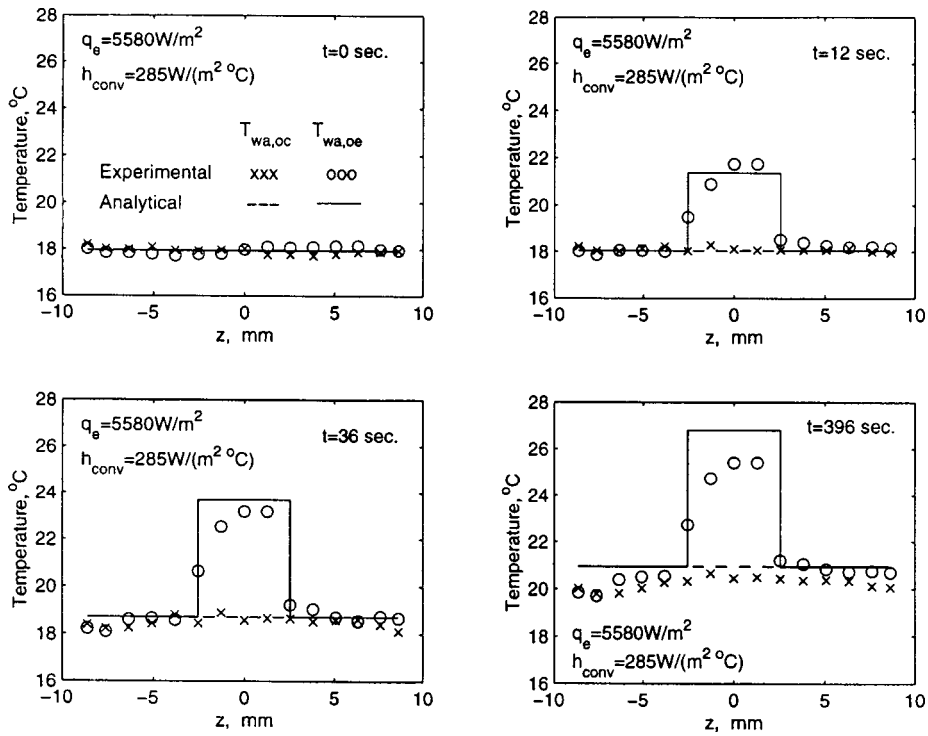


Fig. 7 Temperature distribution along the z-direction at different times: $q_e = 5580 \text{ W/m}^2$, $h_{\text{conv}} = 285 \text{ W/(m}^2 \text{ C)}$

can be seen in Figs. 9 and 10, the wick in the evaporator section contributes the largest resistance to the total heat transfer. The wick in the condenser section also offers a significant resistance to the total heat transfer resistance. After the power is turned off, the heat pipe tends to have a more uniform temperature distribution as

compared to the startup operation.

Figure 11 shows that a decrease in the heat transfer coefficient or an increase in input heat flux results in an increase in the maximum temperature rise. However, the maximum temperature difference within the heat pipe is not sensitive to the changes in

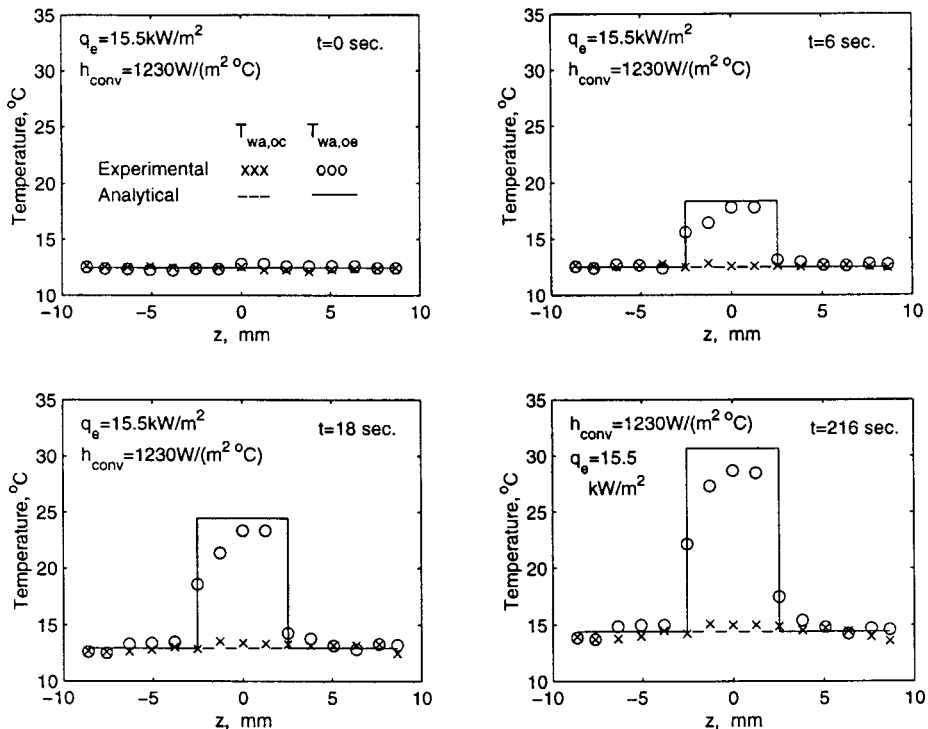


Fig. 8 Temperature distribution along the z-direction at different times: $q_e = 15500 \text{ W/m}^2$, $h_{\text{conv}} = 1230 \text{ W/(m}^2 \text{ C)}$

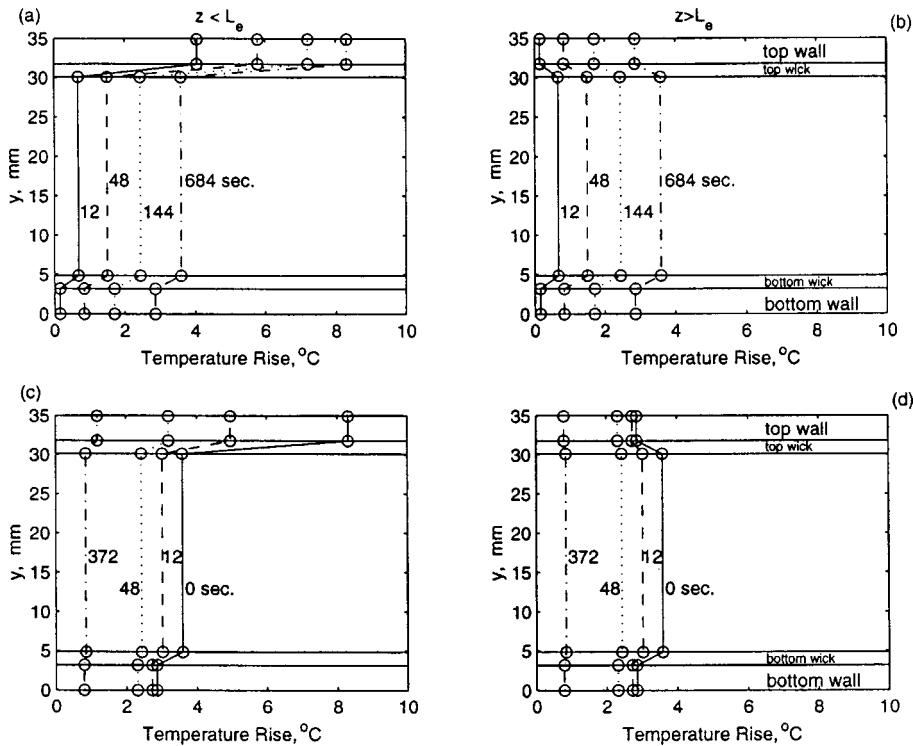


Fig. 9 Transient temperature distribution along the normal direction: $q_e=5580 \text{ W/m}^2$, $h_{\text{conv}}=285 \text{ W/(m}^2\text{°C)}$

the heat transfer coefficient. The maximum temperature rise refers to the largest temperature increase on the outside surface of the heat pipe. As can be seen in Fig. 11, variations in the heat transfer coefficient have less of an effect beyond $h_{\text{conv}} > 1000 \text{ W/m}^2$. It can be seen in Fig. 11 that the deviation between the experimental and

the analytical results is quite small. However, the deviation increases with an increase in the input power. This may be attributed to larger contributions of the secondary conduction path for higher input heat fluxes.

Variations of maximum temperature rise in terms of the heat

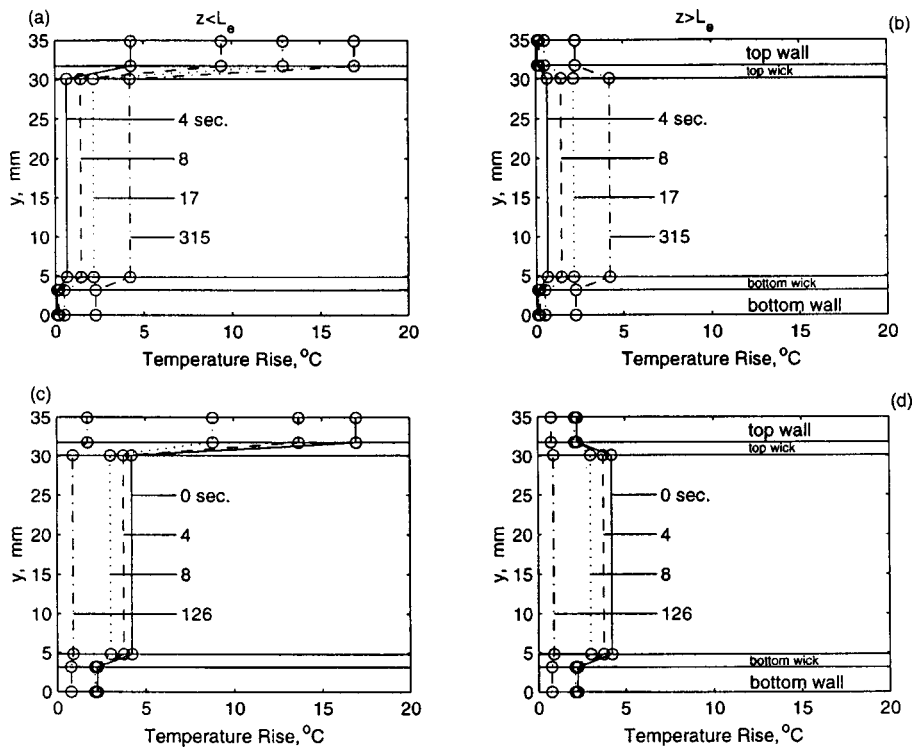


Fig. 10 Transient temperature distribution along the normal direction: $q_e=15500 \text{ W/m}^2$, $h_{\text{conv}}=1060 \text{ W/(m}^2\text{°C)}$

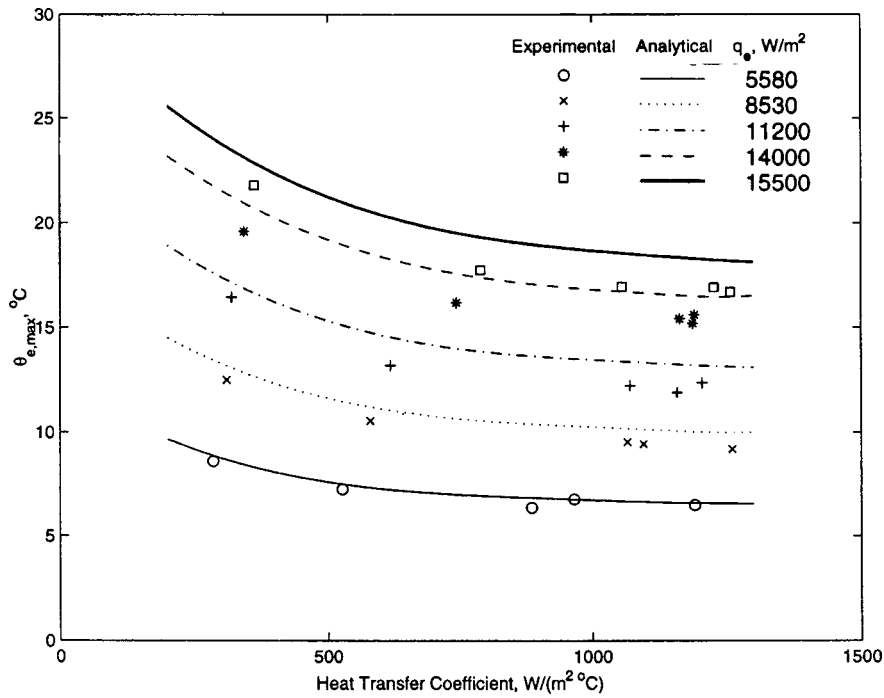


Fig. 11 Effect of variations in heat transfer coefficient and input power on the maximum temperature rise

transfer coefficient and input heat flux can be represented as shown in Fig. 12. This leads to an empirical correlation given below:

$$\theta_{\max} = \left(9.66 + \frac{1.57}{h_{\text{conv}}} \right) q_e \times 10^{-4} \quad (13)$$

where

$$5580 \text{ W/m}^2 \leq q_e \leq 15,500 \text{ W/m}^2$$

$$285 \text{ W/(m}^2\text{C)} \leq h_{\text{conv}} \leq 1260 \text{ W/(m}^2\text{C)}.$$

In the above equations, q_e is the input heat flux in W/m^2 and h_{conv} is the heat transfer coefficient in $\text{W/(m}^2\text{C)}$. The empirical correlation predicts the data with an average error of 1.6 percent. As expected, as in many empirical relationships, Eq. (13) includes system dependent parameters within it. Due to various parameters that are involved in the flat plate heat pipe, more general relationships can be obtained through the use of analytical results presented in Wang and Vafai [6] which have been shown in the present work to be in very good agreement with the experimental results.

Figure 13 displays the maximum temperature difference within the heat pipe as a function of the input heat flux, where this difference refers to the maximum temperature difference on the outside surfaces of the flat plate heat pipe. As shown in Fig. 13, the heat transfer coefficient has an insignificant effect on the maximum temperature difference. The heat input is the main factor, which determines the maximum temperature difference. Figure 13 indicates that the analytical maximum temperature difference is slightly larger than the measured one, which could be attributed to the secondary heat transfer path as discussed previously. Based on Fig. 13, the following correlation can be obtained:

$$\Delta T_{\max} = -0.301 + q_e \times 10^{-3}, \quad 5580 \text{ W/m}^2 < q_e < 15,500 \text{ W/m}^2 \quad (14)$$

where, q_e is the input heat flux in W/m^2 .

Figure 14 shows the time constants for both analytical and experimental results. These time constants are defined as the time it

takes for the temperature rise to reach 63.2 percent of its maximum value for a startup operation, and likewise as the time it takes for the temperature rise to drop 63.2 percent for a shutdown operation. As can be seen, there is a very good agreement between the analytical and experimental results. Based on the results given in Fig. 14, the following empirical correlations for the heat pipe time constants for the startup and shutdown operations are obtained:

$$t_{c,\text{up}} = 35.2 - 0.0341h_{\text{conv}} + 1.50 \times 10^{-5}h_{\text{conv}}^2$$

$$285 \text{ W/(m}^2\text{C)} < h_{\text{conv}} < 1260 \text{ W/(m}^2\text{C)} \quad (15)$$

$$t_{c,\text{down}} = 31.7 - 0.0321h_{\text{conv}} + 1.44 \times 10^{-5}h_{\text{conv}}^2$$

$$285 \text{ W/(m}^2\text{C)} < h_{\text{conv}} < 1260 \text{ W/(m}^2\text{C)} \quad (16)$$

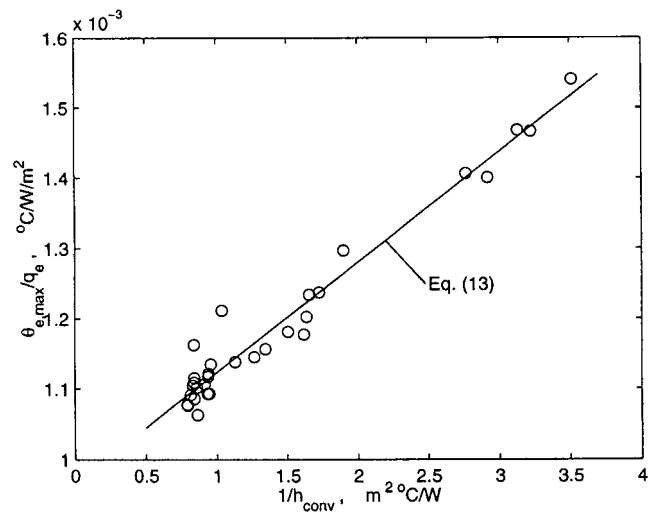


Fig. 12 Compact representation of the maximum temperature rise in terms of the heat transfer coefficient and input heat flux

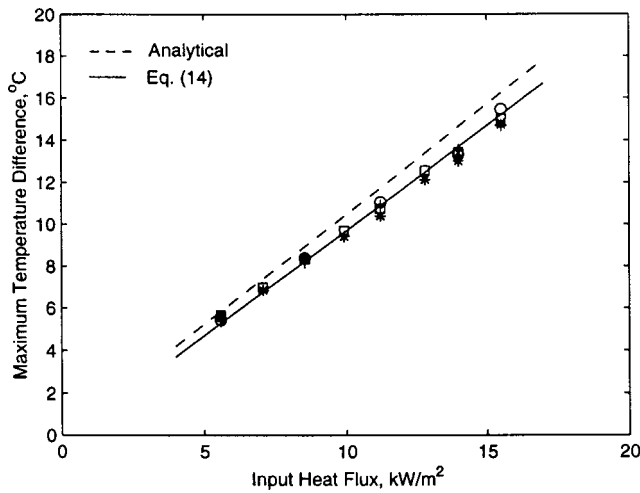


Fig. 13 Effect of input heat flux on the maximum temperature difference

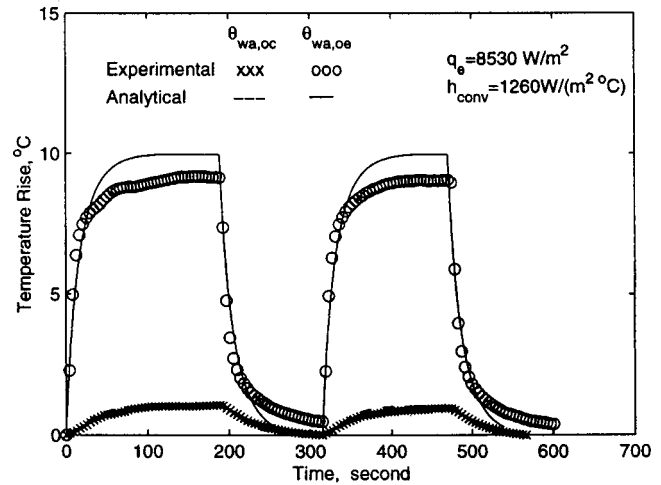


Fig. 16 Temporal temperature distribution for a cyclical operation: $q_e = 14,000 \text{ W/m}^2$, $h_{\text{conv}} = 1210 \text{ W/(m}^2\text{°C)}$

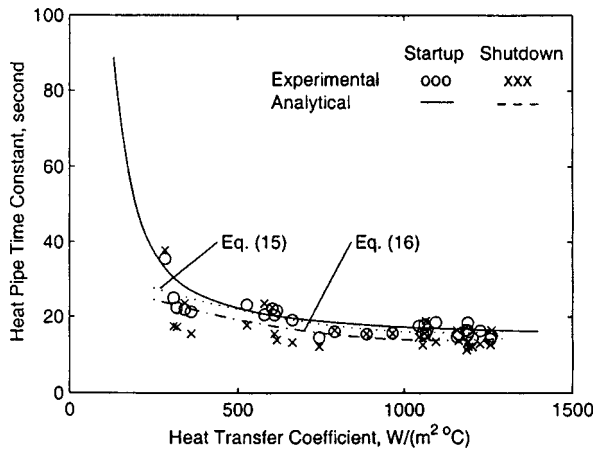


Fig. 14 Time constants for different input heat fluxes for startup and shutdown operations

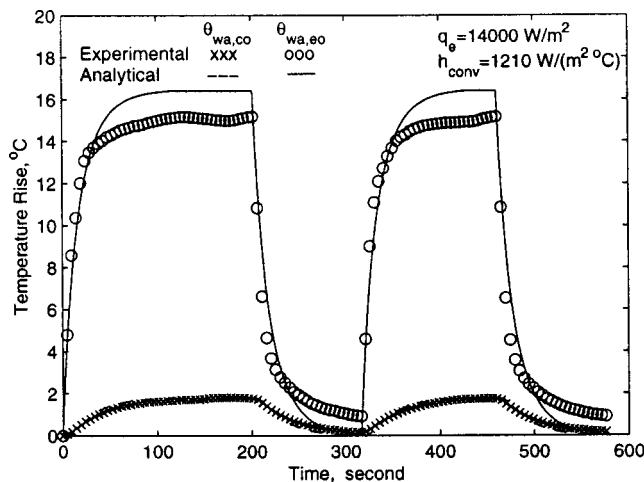


Fig. 15 Temporal temperature distribution for a cyclical operation: $q_e = 8830 \text{ W/m}^2$, $h_{\text{conv}} = 1260 \text{ W/(m}^2\text{°C)}$

where h_{conv} is the heat transfer coefficient in $\text{W/(m}^2\text{°C)}$. Equation (15) predicts the experimental results with an average deviation of 8.4 percent for the startup operation, while Eq. (16) predicts the experimental results with an average deviation of 14.7 percent for the shutdown operation. It should be noted that the four vertical wicks and four edges also affect the time constants.

Figures 15 and 16 show the temporal temperature distributions on the outside surfaces of the heat pipe for a cyclical operation. For the second and the consequent operation cycles, the initial temperature was taken as zero in the analysis, while that was not the case on the experimental side. As shown in Figs. 15 and 16, the initial temperature for the consequent startup operation does not affect the overall performance significantly. Therefore, Eqs. (13)–(16) can be utilized for the startup and shutdown processes during any of the operational cycles.

6 Conclusions

This work presents an analytical and experimental investigation of the thermal performance of a flat-plate heat pipe during startup and shutdown operations. The effects of input power and the heat transfer coefficient on the thermal performance of the heat pipe are investigated. The results show that the wick in the evaporator section provides the largest part of the total thermal resistance, and the wick in the condenser section also contributes a significant part of the total resistance. It is found that the maximum temperature rise increases linearly with input heat flux. For smaller values of the convective heat transfer coefficient (below $500 \text{ W/(m}^2\text{°C)}$), increasing h_{conv} results in a decrease in the maximum temperature rise, while for larger heat transfer coefficients (above $700 \text{ W/(m}^2\text{°C)}$), increasing h_{conv} would have a relatively insignificant effect on the maximum temperature rise.

It was also found that the maximum temperature difference within the heat pipe mainly depends on the input power while variations in the heat transfer coefficient did not have a significant effect. The heat transfer coefficient strongly affects the time it takes to reach steady state while input power has only a slight effect. Empirical correlations for the maximum temperature rise as a function of input heat flux and heat transfer coefficient, and the maximum temperature difference as a function of input heat flux were determined. Correlations were also given for the time constants in terms of heat transfer coefficients. The experimental results for the maximum outside surface temperature rise, maximum temperature difference, heat flux, and time constants were compared with the analytical results and were found to be in very good agreement.

Acknowledgment

The grant (DE-F602-93ER61612) by the Department of Energy is acknowledged and greatly appreciated.

Nomenclature

| | | |
|--------------------------|---|--|
| A | = | heat input area, m^2 |
| h | = | thickness, m |
| h_{conv} | = | heat transfer coefficient, $W/(m^2\text{ }^\circ\text{C})$ |
| H | = | height of the heat pipe, m |
| k | = | thermal conductivity, $W/(m\text{ }^\circ\text{C})$ |
| q | = | heat flux, W/m^2 |
| Q | = | power input rate, W |
| t | = | time, seconds |
| t_c | = | time constant, seconds |
| T | = | temperature, $^\circ\text{C}$ |
| y | = | normal coordinate |
| z | = | normal coordinate |
| ΔT | = | temperature difference, $^\circ\text{C}$ |
| ε | = | porosity |
| $\varepsilon_{h_{conv}}$ | = | uncertainty in heat transfer coefficient |
| θ | = | temperature rise, $^\circ\text{C}$ |

Subscript

| | | |
|----------|---|---------------------------------------|
| c | = | condenser |
| down | = | shutdown operation |
| e | = | evaporator |
| eff | = | effective |
| l | = | liquid |
| max | = | maximum |
| oc | = | outside surface of condenser section |
| oe | = | outside surface of evaporator section |
| s | = | solid |
| up | = | startup operation |
| v | = | vapor |
| w | = | wick |
| wa | = | wall |
| wv | = | wick and vapor interface |
| ww | = | wall and wick interface |
| ∞ | = | environment |

References

- [1] Chi, S. W., 1976, *Heat Pipe Theory and Practice*, Hemisphere, Washington, DC.
- [2] Peterson, G. P., 1990, "Thermal Control of Electronic Equipment and Devices," *Advances in Heat Transfer*, Vol. 20, Hartnett, J. P., and Irvine, T. F., Jr., eds., Academic Press, San Diego, CA, pp. 181–314.
- [3] Vafai, K., and Wang, W., 1992, "Analysis of Flow and Heat Transfer Characteristics of an Asymmetrical Flat Plate Heat Pipe," *Int. J. Heat Mass Transf.*, **35**, pp. 2087–2099.
- [4] Zhu, N., and Vafai, K., 1998, "Vapor and Liquid Flow in an Asymmetrical Flat Plate Heat Pipe: A Three-Dimensional Analytical and Numerical Investigation," *Int. J. Heat Mass Transf.*, **41**, pp. 159–174.
- [5] Zhu, N., and Vafai, K., 1998, "Analytical Modeling of the Startup Characteristics of Asymmetrical Flat Plate and Disk-Shaped Heat Pipes," *Int. J. Heat Mass Transf.*, **41**, No. 17, pp. 2619–2637.
- [6] Wang, Y., and Vafai, K., 1999, "Transient Characterization of Flat Plate Heat Pipes During Startup and Shutdown Processes," *Int. J. Heat Mass Transf.*, **43**, No. 15, pp. 2641–2655.
- [7] Reay, D. A., ed., *Proc. IV Int. Heat Pipe Conference*, Pergamon Press, Oxford, UK.
- [8] Basiulis, A., Tanzer, H., and McCabe, S., 1986, "Thermal Management of High Power PWB'S Through the Use of Heat Pipe Substrates," *Proc. 6th Annual International Electronic Packaging Conference*, Int. Electron. Packaging Soc., pp. 501–515.
- [9] Thomson, M., Ruel, C., and Donato, M., 1989, "Characterization of a Flat Plate Heat Pipe for Electronic Cooling in a Space Environment," *Heat Transfer in Electronics*, ASME, New York, pp. 59–65.
- [10] Bong, T. Y., Ng, K. C., and Bao, H., 1993, "Thermal Performance of a Flat-Plate Heat-Pipe Collector Array," *Sol. Energy*, **50**, pp. 491–498.
- [11] Chen, K. S., Tsai, S. T., and Yang, Y. W., 1994, "Heat Performance of a Double-Loop Separate-Type Hat Pipe: Measurement Results," *Energy Convers. Manage.*, **35**, pp. 1131–1141.
- [12] Khrustalev, D., and Faghri, A., 1995, "Thermal Characteristics of Conventional and Flat Miniature Axially Grooved Heat Pipes," *ASME J. Heat Transfer*, **117**, pp. 1038–1054.
- [13] Huang, X. Y., and Liu, C. Y., 1996, "The Pressure and Velocity Fields in the Wick Structure of a Localized Heated Flat Plate Heat Pipe," *Int. J. Heat Mass Transf.*, **39**, pp. 1325–1330.
- [14] Khrustalev, D., and Faghri, A., 1996, "Estimation of the Maximum Heat Flux in the Inverted Meniscus Type Evaporator of a Flat Miniature Heat Pipe," *Int. J. Heat Mass Transf.*, **39**, pp. 1899–1909.
- [15] Wei, J., Hijikara, K., Takayoshi, I., 1997, "Fin Efficiency Enhancements Using a Gravity-Assisted Heat Pipe," *Int. J. Heat Mass Transf.*, **40**, pp. 1045–1051.
- [16] Faghri, A., 1995, *Heat Pipe Science and Technology*, Taylor and Francis, Bristol, PA.
- [17] Vafai, K., Zhu, N., and Wang, W., 1995, "Analysis of Asymmetrical Disk-Shaped and Flat Plate Heat Pipes," *ASME J. Heat Transfer*, **117**, pp. 209–218.
- [18] Wang, Y., and Vafai, K., 2000, "An Experimental Investigation of the Thermal Performance of an Asymmetrical Flat Plate Heat Pipe," *Int. J. Heat Mass Transf.*, **43**, No. 15, pp. 2657–2668.
- [19] Kline, S. J., and McClintock, F. A., 1953, "Describing Uncertainties in Single Sample Experiment," *Mech. Eng. (Am. Soc. Mech. Eng.)*, **75**, No. 1, pp. 3–8.

J. R. Lukes

Graduate Student Researcher,
e-mail: jennifer@newton.me.berkeley.edu

D. Y. Li

Graduate Student Researcher,
e-mail: deyuli@newton.me.berkeley.edu

Department of Mechanical Engineering,
University of California,
Berkeley, CA 94720-1740

X.-G. Liang

Professor,
Department of Engineering Mechanics,
Tsinghua University,
Beijing 100084, China
e-mail: liangxg@tsinghua.edu.cn

C.-L. Tien

Hon. Mem. ASME
University Professor and NEC Distinguished
Professor of Engineering,
University of California,
Berkeley, CA 94720-1740
e-mail: nancie@uclink4.berkeley.edu

Molecular Dynamics Study of Solid Thin-Film Thermal Conductivity

This study uses the molecular dynamics computational technique to investigate the thermal conductivity of solid thin films in the direction perpendicular to the film plane. In order to establish a benchmark reference, the computations are based on the widely used Lennard-Jones argon model due to its agreement with experimental liquid-phase data, its physically meaningful parameters, and its simple two-body form. Thermal conductivity increases with film thickness, as expected from thin-film experimental data and theoretical predictions. The calculated values are roughly 30 percent higher than anticipated. Varying the boundary conditions, heat flux, and lateral dimensions of the films causes no observable change in the thermal conductivity values. The present study also delineates the conditions necessary for meaningful thermal conductivity calculations and offers recommendations for efficient simulations. This work shows that molecular dynamics, applied under the correct conditions, is a viable tool for calculating the thermal conductivity of solid thin films. More generally, it demonstrates the potential of molecular dynamics for ascertaining microscale thermophysical properties in complex structures.

[S0022-1481(00)02303-3]

Keywords: Conduction, Heat Transfer, Molecular Dynamics, Nanoscale, Thin Films

Introduction

Novel materials such as buckyballs and buckytubes, highly porous and ultrathin films, and quantum wires and dots are forming the building blocks of an exciting new world of submicron devices. For instance, solid thin films with characteristic dimensions from tens to hundreds of nanometers are key components in integrated-circuit transistors and quantum-well lasers. Device performance in these applications is very sensitive to operating temperature. Overheating in semiconductor lasers, for example, is a major obstacle to increased output power and integration ([1]). For the best design of micro and nanodevices and thin-film materials, knowledge of thermophysical properties such as thermal conductivity is of paramount importance.

It is well known from measurements on thin films that such materials display markedly lower thermal conductivities than their bulk counterparts. Several approaches exist to predict the thin-film thermal conductivity for materials where heat conduction by quantized lattice vibrations, or phonons, is dominant. These approaches include kinetic theory, the Boltzmann transport equation, and the Monte Carlo computational technique. Such methods, however, can have difficulty handling the nonuniformly distributed impurities, voids, cracks, dislocations, and complex geometries present in real films. Numerous studies, for example, that of Inoue et al. [2] show that the molecular dynamics technique is well suited for the study of nanoscale phenomena in solid-phase materials. Molecular dynamics is a computational method that simulates the real behavior of materials and calculates physical properties of these materials by simultaneously solving the equations of motion for a system of atoms interacting with a given potential. This method provides a needed supplement to experimental measurements, which can be extremely difficult at such length scales.

Despite the technological importance of solid thin films in thermally sensitive applications, no molecular dynamics calculation of the thermal conductivity of solid thin films as a function of thickness has been reported before. Related studies, however, have been made. Mountain and MacDonald ([3]) calculated the temperature dependence of thermal conductivity for two and three-dimensional 1000-particle solid films. Kaburaki and Machida [4] found that increasing the number of particles in a one-dimensional chain increases thermal conductivity. Kotake and Wakuri [5] showed for a two-dimensional solid system subjected to a constant flux that the resultant temperature gradients sharply increase as the system width is decreased. Recent work by Volz and Chen [6] indicates that solid nanowires exhibit a strong reduction in thermal conductivity as compared to the bulk.

Model of Argon-Type Solid Thin Films

Using the molecular dynamics technique in a three-dimensional computational domain, the current paper calculates thermal conductivity in a solid argon-type model system as the thickness in one dimension is varied. Although argon is not a real thin-film material, it is the best choice for an initial thin-film thermal conductivity molecular dynamics study. One important reason for this is the availability of a good intermolecular potential for argon. The widely accepted Lennard-Jones 12-6 (LJ) potential matches experimental data for bulk fluid argon reasonably well, employs meaningful physical constants as parameters, and possesses a simple, two-body form which requires much less computation time than more complex potentials involving three-body and higher terms ([7]). A rigorous quantum-mechanical approach is at present not feasible for systems of more than a few atoms because such a method is too numerically intensive. The efforts of many workers, for example, Car [8], are currently directed toward this problem.

Additional reasons for using the LJ potential to study solid thin films are that the results can be benchmarked against the large

Contributed by the Heat Transfer Division for publication in the JOURNAL OF HEAT TRANSFER. Manuscript received by the Heat Transfer Division, Feb. 28, 1999; revision received, Mar. 1, 2000. Associate Technical Editor: D. Poulikakos.

body of existing work on argon-type systems and that the argon model, as noted by Kristensen et al. [9], should reveal fundamental phenomena not only for argon but for a wide variety of materials. Also, the argon model, unlike models of more technologically relevant materials, should span from the microscale regime to the bulk regime in a reasonable computational domain size due to its short phonon mean free path.

After establishing a firm foundation for pure thin films, the argon model can then be extended to thin-film systems with impurities, pores, defects, and other types of complicated structures. To get the most quantitatively accurate results for a given material, a potential specific to that material should be used, but to predict qualitative trends, which is the aim of this paper, the argon model is a sensible choice.

Computational Procedure

Several molecular dynamics approaches can be used to calculate thermal conductivity [10]. The nonhomogeneous nonequilibrium approach was chosen for the present work because it provides a direct physical representation of heat flow in a thin film. A new nonhomogeneous nonequilibrium program, based on the equilibrium classical molecular dynamics subroutines of Allen and Tildesley [7], was written and used for all simulations.

The general approach of the program is to apply a constant heat flux to an argon-type solid system, calculate the resulting temperature gradient, and determine the thermal conductivity by a simple ratio of flux to temperature gradient. The reverse method, in which the system boundaries are kept at constant temperatures and the resultant flux is calculated, was initially tried. This was abandoned in favor of the current scheme due to the slow convergence of the heat flux value. The execution of the program proceeds as follows. First, the simulation cell is constructed of face-centered cubic unit cells. Each unit cell contains four atoms and corresponds to two atomic planes of atoms. Each atom is assigned a type according to its spatial position: "hot," "cold," "regular," or "fixed." The configuration of the simulation cell depends upon whether bulk (Fig. 1(a)) or perpendicular (Fig. 1(b)) conductivity is to be calculated. Bulk materials are simulated by using periodic boundary conditions, in which the actual simulation cell of a small number of atoms is essentially repeated infinitely in all three coordinate directions. A drawback of this method is that it suppresses phonons in solids with wavelengths larger than the simulation cell size ([7]).

For thin films, periodic boundary conditions are used in two coordinate directions. Fixed atoms, which remain at their lattice positions for the entire simulation, are usually used in the third, "thin" direction to enforce an adiabatic boundary condition. In some simulations, a free boundary condition was used in the thin direction. For these cases, the flux and initial temperature values had to be lowered to prevent evaporation of the surface atoms, and much longer simulations had to be run to reach steady state. Following the example of Kotake and Wakuri [5], four planes of fixed atoms are deemed sufficient to simulate an infinite wall due to the short range of the interatomic forces. All nonfixed atoms are given an initial temperature by choosing their velocities according to the Maxwell distribution at that temperature. After this, the program advances the difference equations of motion for a short equilibration period to allow a realistic thermodynamic state to be established.

The difference equations come from the widely used "velocity Verlet" algorithm ([11]). In this algorithm, new atomic positions are calculated based on old positions, velocities, and forces. Velocities are calculated using a two-step scheme, in which old forces are used to advance old velocities to "half-step" velocities, new forces are calculated from the LJ potential using the new positions, and new velocities are found using the half-step velocities and new forces. The LJ potential is

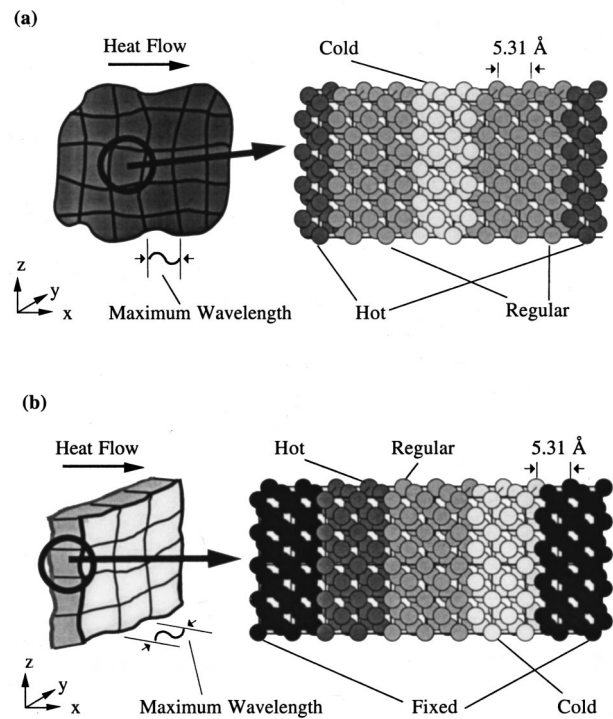


Fig. 1 Simulation cell schematic drawings: (a) bulk thermal conductivity, (b) perpendicular thermal conductivity

$$\phi_{LJ}(r_{ij}) = 4\epsilon_{LJ} \left\{ \left(\frac{\sigma_{LJ}}{r_{ij}} \right)^{12} - \left(\frac{\sigma_{LJ}}{r_{ij}} \right)^6 \right\}. \quad (1)$$

Only the neighbors of an atom within a certain cutoff radius, $2.6\sigma_{LJ}$, are included in the force calculations because faraway atoms have a negligible contribution to the total force on a given atom. This molecular dynamics convention keeps computation time manageable.

After equilibration, a heat flux is imposed on the system by adding a fixed amount of energy to hot atoms and removing the same amount of energy from cold atoms at every time step. This induces heat flow in the x -direction from the hot region to the cold region across the regular atoms. The algorithm of Ikeshoji and Hafskjold [12], which is used to apply the flux, alters kinetic energy in the hot region by scaling each hot atom's velocity by the same factor R and by subtracting the same small velocity v_{sub} from this scaled velocity. The values of R and v_{sub} , which change at each time step, are chosen to conserve momentum and to add the desired amount of energy. A similar procedure is followed for the cold atoms, except kinetic energy is subtracted rather than added.

Instantaneous temperatures in each atomic x -plane are calculated using the formula

$$T_l = m \sum_{i=1}^{N_l} v_i^2 / 3N_l k_B \quad (2)$$

where the squares of the magnitudes of the atomic velocities in a particular plane are summed in accordance with the equipartition principle. The time-averaged temperature, standard deviation of temperature, and standard error of temperature are then calculated for each plane. The standard error of the planar temperature [13,7]

$$\sigma_{\langle T_l \rangle} = \sigma_{T_l} \sqrt{2\tau_{corr} / \tau_{run}} \quad (3)$$

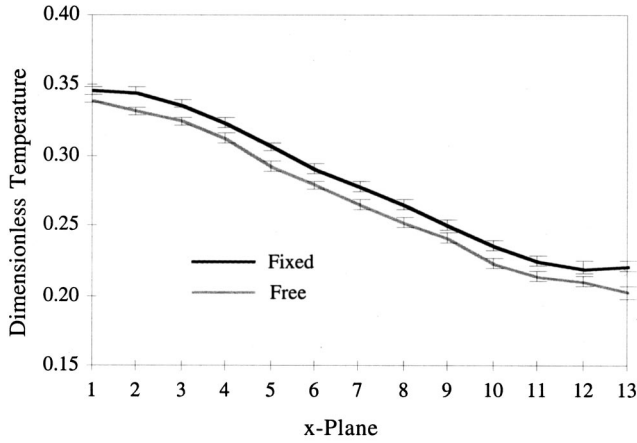


Fig. 2 Temperature in each x -plane of a five regular plane simulation for fixed and free boundaries

depends on the simulation run time at steady state and on the characteristic time over which the instantaneous planar temperatures are self-correlated. For simplicity, it is assumed that

$$\tau_{\text{corr}} \approx \text{MFP}/v_s, \quad (4)$$

$$\sigma_b = \sqrt{\left(\sum_{l=1}^p \frac{1}{\sigma_{\langle T_l \rangle}^2} \right) / \left[\left(\sum_{l=1}^p \frac{1}{\sigma_{\langle T_l \rangle}^2} \right) \left(\sum_{l=1}^p \frac{l^2}{\sigma_{\langle T_l \rangle}^2} \right) - \left(\sum_{l=1}^p \frac{l}{\sigma_{\langle T_l \rangle}^2} \right)^2 \right]} \quad (6)$$

are found using a weighted least-squares method ([18]).

Finally, thermal conductivity is found from

$$k = -a q_{\text{eff}} / 2b \quad (7)$$

where the factor $a/2$ accounts for the fact that the plane spacing is one-half the lattice parameter. Note that q_{eff} is not exactly the same as the ideal imposed heat flux due to small nonzero fluxes that occur in the y and z -directions. The actual heat flux through each regular plane is calculated from particle positions and velocities at regular intervals throughout the simulation using the equations of Irving and Kirkwood [19], and the time averages of these planar calculated fluxes are then spatially averaged over the regular planes

$$q_{\text{eff}} = \left(\sum_{l=1}^p \frac{\langle q_l \rangle}{\sigma_{\langle q_l \rangle}^2} \right) / \left(\sum_{l=1}^p \frac{1}{\sigma_{\langle q_l \rangle}^2} \right) \quad (8)$$

to yield effective flux. The standard error of planar flux is calculated as above for temperature in Eq. (3), and its squared reciprocal is used as the weighting factor in Eq. (8). For each simulation, the expression for error propagation in Press et al. [18] is used to calculate the probable error of effective flux

$$\sigma_{q_{\text{eff}}} = \sqrt{\sum_{l=1}^p \sigma_{\langle q_l \rangle}^2 \left(\frac{\partial q_{\text{eff}}}{\partial \langle q_l \rangle} \right)^2} \quad (9)$$

and is also used to find the probable error of thermal conductivity

$$\sigma_k = \sqrt{\sigma_{q_{\text{eff}}}^2 \left(\frac{\partial k}{\partial q_{\text{eff}}} \right)^2 + \sigma_b^2 \left(\frac{\partial k}{\partial b} \right)^2} \quad (10)$$

where the mean free path (MFP) in argon at the given planar temperature ([14,15]) and highest tabulated speed of sound for fluid argon from the CRC Handbook [16] are used. The fluid argon value was used because solid argon values were not available. The assumption of Eq. (4) is supported by the work of Volz et al. [17], who found good agreement between the autocorrelation time and the kinetic theory mean free time for molecular dynamics simulations on solid argon.

Figure 2 shows a pair of example temperature profiles; the magnitude of the standard error is indicated by the error bars. In this figure, the five regular atom x -planes in the center display a linear profile and the source (hot) and sink (cold) atoms on either side show the expected parabolic curvature. The slope of the best line fitted to the temperature profile of the regular atoms

$$b = \frac{\left(\sum_{l=1}^p \frac{1}{\sigma_{\langle T_l \rangle}^2} \right) \left(\sum_{l=1}^p \frac{l \langle T_l \rangle}{\sigma_{\langle T_l \rangle}^2} \right) - \left(\sum_{l=1}^p \frac{l}{\sigma_{\langle T_l \rangle}^2} \right) \left(\sum_{l=1}^p \frac{\langle T_l \rangle}{\sigma_{\langle T_l \rangle}^2} \right)}{\left(\sum_{l=1}^p \frac{1}{\sigma_{\langle T_l \rangle}^2} \right) \left(\sum_{l=1}^p \frac{l^2}{\sigma_{\langle T_l \rangle}^2} \right) - \left(\sum_{l=1}^p \frac{l}{\sigma_{\langle T_l \rangle}^2} \right)^2} \quad (5)$$

and the probable error of this slope

Results and Discussion

General Comments About Simulation. The simulations were run on DEC 3000 workstations, an AlphaServer 2000, and a Dell Optiplex GX1p PC running the Linux operating system. The numerical differences in results across the different platforms were negligible. Computation time varied from a few hours to several days, depending on the sizes of the systems considered. The total simulated time varied from tens of picoseconds to nanoseconds and was chosen to be proportional to the characteristic thermal diffusion time estimated for each system. Two types of thermal conductivity simulations were run: bulk and perpendicular. Critical input parameters for the simulations are listed in Table 1; other input parameters and detailed results for each simulation are listed elsewhere [20]. Standard LJ nondimensionalizations for temperature and thermal conductivity are used in the simulations:

Table 1 Simulation parameters

| Parameter | Value |
|--|----------------------------|
| LJ well depth parameter | 1.67×10^{-21} J |
| LJ equilibrium separation parameter | 3.4 Å |
| Argon atomic mass | 66.3×10^{-27} kg |
| Boltzmann's constant | 1.38×10^{-23} J/K |
| Lattice constant | 5.31 Å |
| Time step | 1 fs |
| Imposed dimensionless heat flux* | 1.0 |
| Cross-sectional unit cells* | 4 |
| Unit cells in each hot or cold region* | 2 |
| Unit cells in each fixed region | 2 |

*Parameters for specific simulations have been varied as noted in text.

$$T^* = \frac{k_B T}{\varepsilon_{LJ}} \quad k^* = k \frac{\sigma_{LJ}^2}{k_B} \sqrt{\frac{m}{\varepsilon_{LJ}}} \quad (11)$$

Since all parameters are dimensionless, the superscript will henceforth be dropped.

Two important criteria for the simulations are that q_{eff} is nearly the same as the imposed flux, and that the temperature profiles are reasonably close to linear. The profiles should not be expected to be completely linear, since thermal conductivity displays some temperature dependence. If the two criteria above are not satisfied, the thermal conductivity calculation, which is based on the Fourier law, is not valid. It was found that the typical reason that the criteria are not met is a too-short simulation time, although in very preliminary simulations lack of energy conservation due to a too-large time step and explosion of the lattice due to a too-small initial lattice spacing also occurred. It was observed that simulations not run long enough to attain a steady state yielded values of q_{eff} lower than the imposed fluxes and showed distinctly nonlinear temperature profiles. This is reasonable, since a finite time is required for the film to reach steady state after imposition of the heat flux at the boundaries. The flux discrepancies disappeared and the temperature profiles became more linear as the number of time steps in the simulation increased. Due to the difficulty in choosing a simulation time long enough to satisfy the criteria yet short enough to avoid undue computational burden, a trial-and-error process had to be followed to find values for τ_{run} . Values roughly 20 times the characteristic diffusion time were found sufficient to satisfy the criteria. For the thermal conductivity simulations reported here, the q_{eff} values were all within four percent of the ideal imposed flux and the temperature profiles were reasonably linear.

Momentum conservation, as expected, was found to hold exactly for the present 96 and 252-atom bulk simulations. In bulk simulations with more atoms, and in all thin-film simulations, however, the algorithm of Ikeshoji and Hafskjold [12] did not strictly conserve instantaneous total system momentum. Instead, the instantaneous momentum fluctuated rapidly about zero, the time-averaged system momentum value. The reason for this is not known, but is thought to be the result of small accumulated numerical errors due to roundoff and truncation of the potential at the cutoff radius. The standard deviation of the momentum fluctuations for the bulk and free-boundary thin-film simulations was several orders of magnitude smaller than that for fixed-boundary thin-film simulations, indicating that there may be some wall effect that works against momentum conservation. Considering that the wall atoms influence the motion of the regular, hot, and cold atoms without themselves being affected, in a manner analogous to a wall of infinite mass imparting impulses to impinging billiard balls, it is reasonable that momentum is not strictly conserved. Despite the lack of exact momentum conservation, no significant difference was found between the thermal conductivities for fixed and free-boundary simulations for both a 3 and a 5-regular plane case at a mean lattice temperature $T=0.27$ (Table 2). Thus, the observed small deviations from zero total momentum are not important for the purposes of this paper.

Table 2 Effect of boundary conditions on thermal conductivity

| Configuration | Thermal Conductivity | Error |
|----------------------|----------------------|-------|
| Free boundary | 0.391 | 0.075 |
| three regular planes | | |
| Fixed boundary | 0.402 | 0.075 |
| three regular planes | | |
| Free boundary | 0.474 | 0.051 |
| five regular planes | | |
| Fixed boundary | 0.444 | 0.044 |
| five regular planes | | |

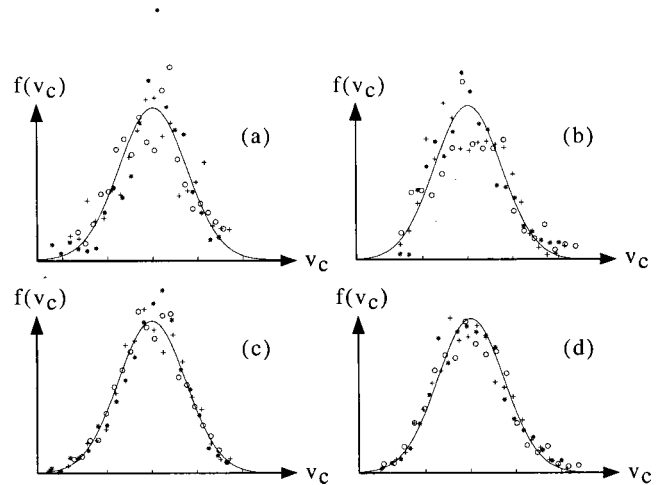


Fig. 3 Velocity distributions at $T=0.5$ for various cross sections and sampled time steps: (a) 4×4 , 10,000; (b) 6×6 , 10,000; (c) 4×4 , 30,000; (d) 6×6 , 30,000

Use of Eq. (2) to calculate planar temperature throughout the simulation assumes that a local thermodynamic equilibrium is established in each atomic plane. Tenenbaum et al. [21] and Hafskjold and Ratkje [22] assert that local thermodynamic equilibrium is established in molecular dynamics simulations of nonequilibrium fluids provided that the control volume thickness is roughly equal to the mean interatomic distance. If true for fluids, it is even more likely to be true for atomic planes in solids because the increased density causes increased interatomic interaction that aids interplanar energy transport. To test whether local thermodynamic equilibrium was established in the present case, the velocity of a single central atom in each regular, hot, and cold plane was monitored for the last 10,000 and 30,000 fs of a $T=0.5$ simulation of a thin film with seven regular planes. Two different values of cross section, or number of y unit cells by the unit of z unit cells, were used: 4×4 (32 atoms/plane) and 6×6 (72 atoms/plane). Figure 3 shows a histogram of the $x(o)$, $y(+)$, and $z(*)$ velocity components of the central atom for a representative regular plane along with the Maxwell distribution at the time-averaged planar temperature. The figure clearly shows that while there are some discrepancies between the Maxwell distribution and the calculated velocity distribution for the 10,000 cases, the 30,000 cases show much better agreement for both 4×4 and 6×6 cross sections. Since τ_{run} for all simulations is longer than 30,000 fs, it is reasonable to assume that the real calculated velocity distribution is even closer to a perfect Maxwellian. Increasing the cross section from 4×4 to 6×6 causes a much less dramatic improvement of the velocity distribution for both 10,000 and 30,000 at this temperature. This result suggests that longer simulations may be more effective than increased cross sections in attaining local thermodynamic equilibrium. The Maxwellian nature of the velocity distributions and the linear temperature profiles in the calculations indicate that the local thermodynamic equilibrium assumption is justified.

Bulk Thermal Conductivity. Bulk thermal conductivity was calculated for simulation cells of various sizes at dimensionless mean lattice temperatures of 0.3 and 0.5 to check the agreement of the model with experimental data for bulk solid argon. Mean lattice temperatures were found by spatially averaging the steady-state time-averaged temperatures of the regular atoms. Each data point in the $T=0.5$ case has a different cross section, increasing with the number of atoms from 2×2 to 8×8 . The conductivities at each temperature, normalized by the dimensionless experimental value corresponding to that temperature ([23]), are illustrated

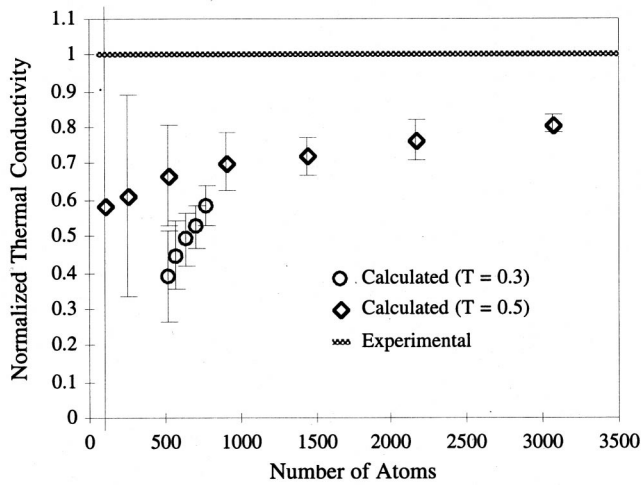


Fig. 4 Calculated and experimental bulk thermal conductivities at $T=0.3$ and 0.5 versus number of atoms

in Fig. 4. The error bars represent the normalized standard error of thermal conductivity (Eq. (10)) for each simulation.

For both temperatures, the calculated bulk thermal conductivity is observed to increase as the number of atoms is increased. The dependence of calculated macroscopic properties on the number of particles in a molecular dynamics simulation is a well-known artifact [24]. A recent example of the particle number dependence of bulk thermal conductivity can be found in Kaburaki et al.'s [25] calculation of solid bulk argon thermal conductivity for 256 and 500-atom systems, which shows a similar number dependence to that found in the present paper at comparable temperatures. The key to getting accurate bulk results from the molecular dynamics technique is to choose conditions that allow the finite simulation cell to represent, as closely as is feasible, an infinite bulk domain. True bulk-like behavior is indicated by minimal size dependence of the calculated values. Ideally, this could be accomplished by simulating a very large number of atoms, but in practice this is computationally quite burdensome.

It can be seen in Fig. 4 that the results at $T=0.3$, as compared to those at $T=0.5$, display a steeper number dependence and constitute a smaller portion of their corresponding bulk experimental value. This shows that for the same number of atoms, simulations run at higher temperatures better capture bulk behavior. A simple explanation for the more bulk-like behavior at higher temperatures is that the phonon mean free path is shorter, so the ratio of the mean free path to characteristic simulation cell dimension is smaller. In the bulk limit, this ratio is much less than 1.

Another interpretation is offered by the concept of phonon radiation ([26]). This concept, strictly valid in the ballistic limit of heat conduction in which the local thermodynamic equilibrium is not reached, can nevertheless offer some value in understanding the current results. Figure 5 thus uses the Planck formula ([27])

$$e(\lambda) = 2\pi C_1 / \lambda^5 (e^{C_2/\lambda T} - 1) \quad (12)$$

to estimate the spectral distribution for phonon "emissive power" under various conditions of temperature and computational domain size. Here the constants

$$C_1 = hv_s^2 \quad C_2 = hv_s/k_B \quad (13)$$

are defined using the speed of sound rather than the speed of light. Figures 5(a) and 5(b) show that for a given maximum allowed phonon wavelength, which is equal to the characteristic dimension of the simulation cell, raising the temperature increases the allowed phonon fraction due to the decreased peak phonon wavelength.

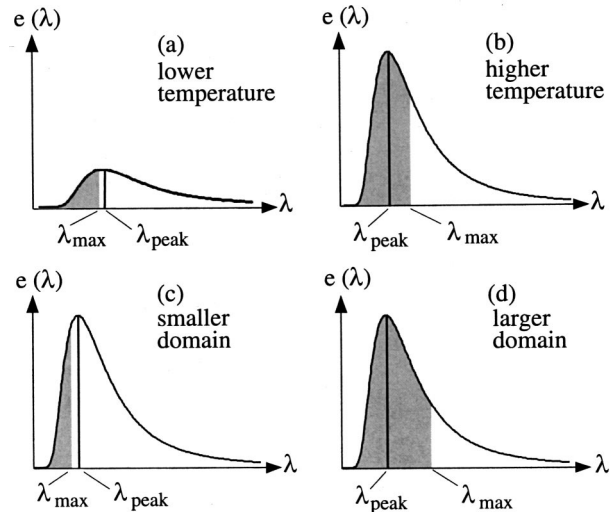


Fig. 5 Planck spectral distribution. Shaded areas indicate the fraction of total phonon emissive power allowed by the molecular dynamics simulation. (a) and (b) illustrate the effect of temperature, and (c) and (d) illustrate the effect of domain size.

The figures also suggest a guideline: $L/\lambda_{\text{peak}}(T)$ should be as much larger than 1 as possible. This will make the phonon fraction approach 1, ensuring that molecular dynamics simulations yield bulk-like results. A Wien's law formulation for phonons can be used to estimate $L/\lambda_{\text{peak}}(T)$. Taking the derivative of Eq. (12), iterating for C_2 , and substituting yields

$$\lambda_{\text{peak}} T \approx 0.2 \quad L/\lambda_{\text{peak}} \approx 5LT. \quad (14)$$

Increasing the computational domain size at a given temperature, as is shown going from Fig. 5(c) to Fig. 5(d), also increases the fraction allowed by the simulation. In the limit of infinite domain size the fraction becomes 1, but as discussed above, using higher temperatures is the most computationally economical choice.

A simulation cell size of 512 atoms, which corresponds to a system with eight regular x -planes of 4×4 cross section, yields thermal conductivity values at $T=0.5$ not much smaller than those with a significantly larger number of atoms. For computational efficiency it was thus assumed that four unit cells were adequate to represent infinite length in a particular direction. In

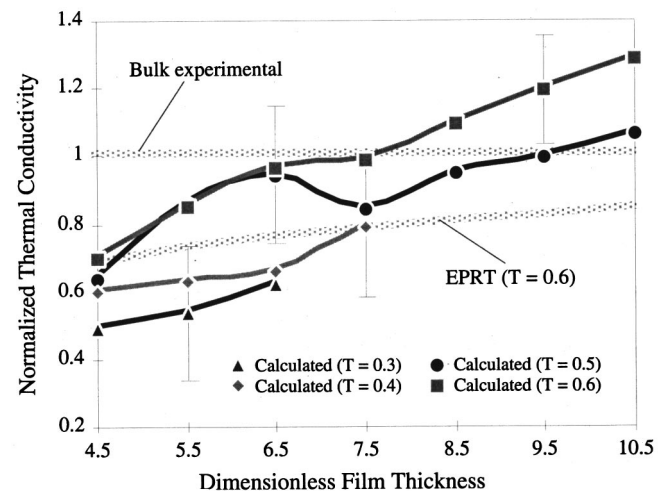


Fig. 6 Calculated, bulk experimental, and equation of photon radiative transfer (EPRT) thermal conductivities versus film thickness at various temperatures

the perpendicular thermal conductivity simulations of the following section, then, 4×4 cross sections were used to represent “infinite” length in the y and z -directions.

Perpendicular Thermal Conductivity. Figure 6 displays the calculation results for normalized perpendicular thermal conductivity versus dimensionless film thickness at several mean lattice temperatures. A thin film thermal conductivity estimate based on Majumdar’s equation of phonon radiative transfer ([28]) is shown for comparison. As in the bulk case, the results at each temperature are normalized by the experimental conductivity value at that temperature. For clarity, film thickness is nondimensionalized by a rather than by the typically used σ_{LJ} and only one error bar is shown for each set of temperature data. The error bar magnitude corresponds not to the actual calculated error at the corresponding thickness, but to the largest error of the set, which occurs at the dimensionless thickness 4.5 for all sets. A heat flux value of 1.5 was used in the $T=0.6$ case because the higher fluxes cause steady state to be reached sooner. Film thickness, which was varied by adding/subtracting atomic x -planes to/from the computational cell, corresponds to the thickness of the regular atoms plus the thickness of the three hot x -planes and the three cold x -planes nearest the regular atoms.

It is critically important to note that unlike the bulk simulations discussed above, which in the ideal case display little size/number dependence, thin film simulations *should* reveal thickness-dependent properties due to the effect of the boundaries. As the film thickness increases, the boundary effect should be less pronounced and the calculated results should approach the bulk thermal conductivity value. As anticipated, Fig. 6 shows that thermal conductivity at all temperatures increases with film thickness. The unexpected undulation of the $T=0.5$ curve is fully contained within the envelope of its error bars.

Four observations should be made from the calculated data. The first is that the conductivities of lower-temperature films constitute a smaller fraction of their corresponding bulk values than identically sized higher-temperature films. This is in agreement with the temperature trends displayed by the bulk results, and shows that thin-film size effects are more pronounced at lower temperatures. The second is that the molecular dynamics values for thermal conductivity at $T=0.6$, while showing the same trend as the equation of photon radiative transfer results at the same temperature, are higher in magnitude. This can be explained by the fact that the mean free path and v_s values used in Eq. (4) above were inserted into the equation of photon radiative transfer model. The mean free path, as estimated above, is only a ballpark figure, and v_s is undoubtedly on the low side since it is for high-density fluid argon.

The third observation is that while the expected behavior is an asymptotic increase of the thin film results toward the bulk value, the thicker films for the $T=0.5$ and 0.6 cases appear to have thermal conductivities that exceed their corresponding experimental bulk values. This discrepancy is about 30 percent for the $T=0.6$ case. Using a similar nonhomogeneous nonequilibrium method on a fluid argon system of comparable size to these thicker films, Ciccotti and Tenenbaum [29] calculated a bulk thermal conductivity 20 percent above the experimental value. A reason for these discrepancies could be the fact that experimental samples always contain impurities and imperfections that reduce thermal conductivity below its ideal maximum value. The “sample” in the simulation, in contrast, is a perfectly pure single crystal. As its thickness increases it is reasonable that the conductivity may at some point exceed the experimental value while still being lower than the ideal maximum value. Also, there is no obvious reduction in the rate of conductivity increase for the thicker films, whose maximum thickness 10.5 corresponds to about five times the mean free path. An explanation may be that the results affirm the validity of the criterion of Flik et al. [30], which holds that perpendicular thin film thermal conductivity size effects are important when the film thickness is smaller than seven times the

mean free path. Thicker films may need to be simulated in order to see unmistakable asymptotic behavior. On the other hand, it is possible that asymptotic behavior *is* occurring, and that it is simply obscured within the envelope of the error bars.

The fourth observation is that within error, the bulk thermal conductivities in Fig. 4 are the same as the $T=0.3$ and 0.5 thin-film conductivities for comparable x -direction thickness. This result was puzzling at first, because it contradicted the expectation that the calculated bulk values would always exceed calculated thin-film values even for comparable domain sizes. Phonon mode counting in solid state physics, however, indicates that periodic boundary conditions (bulk) and fixed end boundary conditions (thin film) yield the same number of phonon modes for the same number of atoms ([31]). This means that the abovementioned phonon fraction for similarly sized bulk and thin film configurations is similar, so the thermal conductivity will also be similar. There is nothing intrinsic about periodic boundary conditions that changes its value to differ from the thin film value. Support for this argument can also be found in Table 2, which illustrates the effect of free versus fixed boundary conditions on thin film thermal conductivity. The results imply that the thermal conductivity calculated in a molecular dynamics simulation is affected by the physical dimension of the film but not by the boundary conditions.

Effect of Varying Computational Parameters. To investigate the effect of the chosen parameters on the thin film molecular dynamics results, several simulations with differing values of these parameters were run. As discussed above, changing the boundary configuration has no effect on the calculated thermal conductivity. It does, however, influence the magnitude of the temperature profile. The fixed boundary profile is higher than the free boundary profile for both the 3 and 5-regular plane cases listed in Table 2. The profile for the 5-plane case is plotted in Fig. 2. The discrepancy in the temperature profiles is probably caused by the two percent expansion exhibited by the free-boundary film. Expansion causes an increase in the LJ potential energy, resulting in a decreased kinetic energy and thus a decreased temperature. Also, it can be seen from Fig. 2 that the adiabatic walls present in the fixed boundary case appear to have some moderating effect on the temperatures of the outermost hot and cold planes. Since the boundary condition simulations use a lower flux, it was also necessary to explore the influence of this parameter. Table 3 shows that varying the flux for a film with three regular planes at $T=0.5$ does not cause any significant change in thermal conductivity. The use of a different flux for the boundary condition simulations is thus unlikely to be the cause of any unusual effects.

Another parameter investigated in the simulations was the number of unit cells in each hot/cold region. The thickness of these “bath” regions was reduced to 1 unit cell from the usual value of 2 unit cells to see the effect on thermal conductivity. Figure 7 illustrates that bath regions do contribute to thermal conductivity, because decreasing their thickness decreases the conductivity value. This suggests that the thickness of the film should be defined not just in terms of the thickness of the regular atomic planes, but should also include the thickness of the bath atoms. Including the entire thickness of the bath regions in the length would effectively shift the two unit cells/bath curve (henceforth called “A”) two thickness units to the right relative to the one unit cell/bath curve (“B”). This, however, would cause a different discrepancy: the conductivity for B would be higher than that

Table 3 Effect of imposed flux on thermal conductivity

| Flux | Thermal Conductivity | Error |
|------|----------------------|-------|
| 0.6 | 0.699 | 0.144 |
| 1.0 | 0.731 | 0.149 |
| 1.4 | 0.683 | 0.095 |

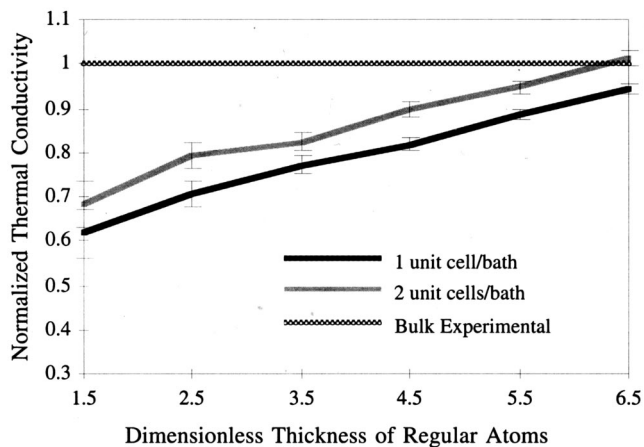


Fig. 7 Effect of number of unit cells per bath on thermal conductivity

for A. If only the first three hot and cold bath planes (1.5 unit cells) nearest the regular layers are included in the definition of film thickness rather than all four bath planes (2 unit cells) on each side, A shifts one thickness unit to the right and falls *directly* on top of B. This is the desired result, because the same thickness of atoms at the same temperature should necessarily produce the same calculated value of thermal conductivity. The fact that only three of the bath planes on either side appear to influence thermal conductivity is reasonable, since the cutoff radius $2.6\sigma_{LJ}$ corresponds to a thickness of 1.7 unit cells. The fourth plane is two unit cells away from the regular atoms and thus is too distant to interact with them. This also indicates that three planes of fixed atoms rather than four could be used to represent the fixed wall boundary condition.

The final parameter investigated was the cross section. Figure 8 shows thermal conductivity versus film thickness at $T=0.5$ for 4×4 and 6×6 cross sections. The error bars for the 4×4 case were made heavier than the 6×6 error bars for clarity. Within the error bars, the 6×6 case shows no discernible increase in thermal conductivity over the 4×4 case. Since large lateral dimensions were not necessary to obtain good thermal conductivity values, this result implies that the 4×4 case is large enough to capture the essential physics. Also, the unusual curvature discussed above for the 4×4 case disappears and the error bars shrink considerably. These two effects cannot be attributed to the increased cross section alone, however, because the steady-state simulation times

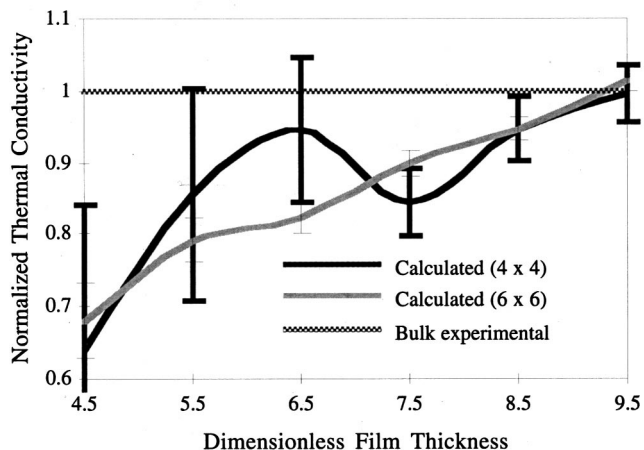


Fig. 8 Effect of cross section on thermal conductivity

Table 4 Effect of simulation time on thermal conductivity

| $4 \times 4 \tau_{run}, 6 \times 6 \tau_{run}$, Configuration | τ_{run} Ratio | σ_k Ratio | Percentage due to τ_{run} Difference |
|---|--------------------|------------------|---|
| 32.9 ps, 260.0 ps 3 regular planes | 7.90 | 3.92 | 50% |
| 45.9 ps, 360.0 ps 5 regular planes | 7.84 | 4.87 | 62% |
| 61.1 ps, 400.0 ps 7 regular planes | 6.55 | 4.62 | 71% |
| 128.4 ps, 440.0 ps 9 regular planes | 3.43 | 2.63 | 77% |
| 147.9 ps, 440.0 ps 11 regular planes | 2.97 | 2.70 | 91% |
| 169.6 ps, 440.0 ps 13 regular planes | 2.59 | 2.43 | 94% |

used for the 6×6 runs were always longer than those for the 4×4 runs. Since σ_{T_i} in Eq. (3) is roughly inversely proportional to the square root of τ_{run} , it can be seen that the thermal conductivity error is approximately inversely proportional to τ_{run} . This can be used to estimate the effect of simulation time on error and to try to isolate the effect of cross section. The steady-state time ratio in Table 4 is found by dividing τ_{run} for the 6×6 case by that for the 4×4 case, and the thermal conductivity error ratio is found by dividing the error of the 4×4 case by that of the 6×6 case for the various film thicknesses at their corresponding steady-state simulation times. The percentage column divides the error ratio by the time ratio, and is an estimate of the percentage of the difference in error between the 4×4 and 6×6 cases that is due to differences in simulation time. Table 4 indicates that for large τ_{run} , most of the difference in error between 4×4 and 6×6 thermal conductivity results is attributable to the simulation time difference, while at small τ_{run} , the cross section difference appears to make some contribution to the difference in error. Increasing the cross section, increasing the number of time steps, or increasing both yields more precise thermal conductivity results. Longer simulation times are more desirable, however, since they are less computationally demanding than larger cross sections. As in the discussion of local thermodynamic equilibrium above, it is concluded that longer simulation times are the best way to obtain good thermal conductivity values from molecular dynamics simulations.

Concluding Remarks

This paper explores the thermal conductivity of solid systems in both bulk and thin-film configurations using the molecular dynamics computational technique. As expected, the argon model yields results close to experimental data for bulk materials and predicts increased thermal conductivity observed for thin-film materials as film thickness is increased. Modest overprediction of thermal conductivity observed for the thicker films is probably caused by the perfect purity of the idealized argon model used in the simulations. Normalized thermal conductivity is substantially reduced in the colder films, indicating that thin film effects are more pronounced at low temperatures. Bulk systems with larger characteristic lengths and higher temperatures show better agreement with experimental data than those with smaller values; mean free path and maximum phonon wavelength arguments are presented to explain this behavior. Changing the boundary conditions and the imposed fluxes in the thin film simulations produces no significant change in thermal conductivity.

Two important criteria for valid molecular dynamics simulations are that the calculated effective flux be nearly the same as the imposed flux and that the temperature profiles be reasonably close to linear. The following recommendations are suggested as computationally efficient ways to satisfy these criteria. First, the smallest cross section possible that yields reasonable conductivity

values should be used. Second, a good initial choice for τ_{run} is 20 times the characteristic thermal diffusion time. Third, to reduce the error for a particular simulation, simulation time should be increased rather than cross section. Fourth, if the exact value of temperature is not critical, simulations should be run at as high a temperature as is feasible. High fluxes are also desired because they too cause quicker attainment of steady state and better averaging. Finally, fixed boundary simulations should be used for thin films because they allow the stable simulation of a wide range of conditions.

This work has shown that molecular dynamics can be a powerful tool for predicting the thermal behavior of solid thin films. Future work should be done to apply this versatile, conceptually simple technique to microscale problems where other experimental and analytical approaches are difficult. The molecular dynamics technique is especially suited to study the thermophysical properties of disordered materials such as doped and nanoporous thin films and materials with voids, cracks, dislocations, or other complex geometries.

Acknowledgments

The authors gratefully acknowledge the financial support of the National Science Foundation.

Nomenclature

| | |
|-----------------------|--|
| a | = lattice constant |
| b | = slope of line fitted to temperature profile of regular atoms |
| C_1, C_2 | = constants in Planck formula |
| e | = phonon spectral "emissive power" |
| f | = distribution of x , y , or z -velocity component |
| h | = Planck's constant |
| k | = thermal conductivity |
| k_B | = Boltzmann's constant |
| L | = shortest characteristic simulation cell dimension |
| l | = particular regular atomic plane |
| MFP | = mean free path |
| m | = atomic mass |
| N_l | = number of atoms in plane l |
| p | = total number of regular atomic planes |
| q_{eff} | = effective heat flux in x -direction |
| $\langle q_l \rangle$ | = time-averaged actual heat flux in x -direction through plane l |
| R | = rescaling factor |
| r_{ij} | = distance between atoms i and j |
| T | = temperature |
| T_l | = temperature of plane l |
| $\langle T_l \rangle$ | = time-averaged temperature of plane l |
| v_c | = x , y , or z -velocity component |
| v_i | = velocity of atom i |
| v_s | = speed of sound |
| v_{sub} | = velocity subtracted from rescaled velocity |

Greek Symbols

| | |
|--------------------------------|--|
| ϵ_{LJ} | = Lennard-Jones well depth parameter |
| λ | = phonon wavelength |
| λ_{max} | = maximum phonon wavelength allowed by simulation domain |
| λ_{peak} | = peak phonon wavelength at a given temperature |
| σ_b | = probable error of slope |
| σ_k | = probable error of thermal conductivity |
| σ_{LJ} | = Lennard-Jones equilibrium separation parameter |
| $\sigma_{q_{\text{eff}}}$ | = probable error of effective flux |
| $\sigma_{\langle q_l \rangle}$ | = standard error of the time-averaged flux through plane l |
| σ_{T_l} | = standard deviation of the temperature of plane l |
| $\sigma_{\langle T_l \rangle}$ | = standard error of the time-averaged temperature of plane l |

| | |
|----------------------|---------------------------------------|
| τ_{corr} | = correlation time |
| τ_{run} | = steady state simulation run time |
| ϕ_{LJ} | = Lennard-Jones interatomic potential |

Superscript

* = dimensionless

References

- [1] Osinski, M., 1991, "Vertical-Cavity Surface-Emitting Semiconductor Lasers: Present Status and Future Prospects," *Proc. SPIE*, **1418**, pp. 2–24.
- [2] Inoue, R., Tanaka, H., and Nakanishi, K., 1996, "Molecular Dynamics Simulation Study of the Anomalous Thermal Conductivity of Clathrate Hydrates," *J. Chem. Phys.*, **104**, pp. 9569–9577.
- [3] Mountain, R. D., and MacDonald, R. A., 1983, "Thermal Conductivity of Crystals: A Molecular-Dynamics Study of Heat Flow in a Two-Dimensional Crystal," *Phys. Rev. B*, **28**, pp. 3022–3025.
- [4] Kaburaki, H., and Machida, M., 1993, "Thermal Conductivity in One-Dimensional Lattices of Fermi-Pasta-Ulam Type," *Phys. Lett. A*, **181**, pp. 85–90.
- [5] Kotake, S., and Wakuri, S., 1994, "Molecular Dynamics Study of Heat Conduction in Solid Materials," *J. Ser. B*, **37**, pp. 103–108.
- [6] Volz, S., and Chen, G., 1999, "Molecular Dynamics Simulation of Thermal Conductivity of Silicon Nanowires," *Appl. Phys. Lett.*, **75**, pp. 2056–2058.
- [7] Allen, M. P., and Tildesley, D. J., 1987, *Computer Simulation of Liquids*, Clarendon Press, Oxford, UK.
- [8] Car, R., 1996, "Modeling Materials by Ab-Initio Molecular Dynamics," *Quantum Theory of Real Materials*, Chelikowsky, J. R., and Louie, S. G., eds., Kluwer Academic, Dordrecht, The Netherlands, pp. 23–37.
- [9] Kristensen, W. D., Jensen, E. J., and Cotterill, R. M. J., 1974, "Thermodynamics of Small Clusters of Atoms: A Molecular Dynamics Simulation," *J. Chem. Phys.*, **60**, pp. 4161–4169.
- [10] Chou, F. C., Lukes, J. R., Liang, X. G., Takahashi, K., and Tien, C. L., 1999, "Molecular Dynamics in Microscale Thermophysical Engineering," *Ann. Rev. Heat Transf.*, **10**, pp. 141–176.
- [11] Swope, W. C., Andersen, H. C., Berens, P. H., and Wilson, K. R., 1982, "A Computer Simulation Method for the Calculation of Equilibrium Constants for the Formation of Physical Clusters of Molecules: Application to Small Water Clusters," *J. Chem. Phys.*, **76**, pp. 637–649.
- [12] Ikeshoji, T., and Hafskjold, B., 1994, "Non-equilibrium Molecular Dynamics Calculation of Heat Conduction in Liquid and through Liquid-Gas Interface," *Mol. Phys.*, **81**, pp. 251–261.
- [13] Jacucci, G., and Rahman, A., 1984, "Comparing the Efficiency of Metropolis Monte Carlo and Molecular Dynamics Methods for Configuration Space Sampling," *Nuovo Cimento*, **D4**, pp. 341–356.
- [14] Dobbs, E. R., and Jones, G. O., 1957, "Theory and Properties of Solid Argon," *Rep. Prog. Phys.*, **20**, pp. 516–564.
- [15] Dugdale, J. S., and MacDonald, D. K. C., 1955, "Lattice Thermal Conductivity," *Phys. Rev.*, **98**, pp. 1751–1752.
- [16] *CRC Handbook of Chemistry and Physics*, 1996, CRC Press, Boca Raton, FL.
- [17] Volz, S., Saulnier, J.-B., Lallemand, M., Perrin, B., Depondt, P., and Marschal, M., 1996, "Transient Fourier-law Deviation by Molecular Dynamics in Solid Argon," *Phys. Rev. B*, **54**, pp. 340–347.
- [18] Press, W. H., Teukolsky, S. A., Vetterling, W. T., and Flannery, B. P., 1992, *Numerical Recipes in FORTRAN: The Art of Scientific Computing*, 2nd Ed., Cambridge University Press, Cambridge, UK.
- [19] Irving, J. H., and Kirkwood, J. G., 1950, "The Statistical Mechanical Theory of Transport Processes. IV. The Equations of Hydrodynamics," *J. Chem. Phys.*, **18**, pp. 817–829.
- [20] Lukes, J. R., 2000, "Molecular Dynamics Simulation of Thermal Conduction in Thin Films and Nanoporous Materials," Ph.D. thesis, University of California, Berkeley, CA, in progress.
- [21] Tenenbaum, A., Ciccotti, G., and Gallico, R., 1982, "Stationary Nonequilibrium States by Molecular Dynamics," *Phys. Rev. A*, **25**, pp. 2778–2787.
- [22] Hafskjold, B., and Ratkje, S. K., 1995, "Criteria for Local Equilibrium in a System with Transport of Heat and Mass," *J. Stat. Phys.*, **78**, pp. 463–494.
- [23] Touloukian, Y. S., Liley, P. E., and Saxena, S. C., eds., 1970, *Thermal Conductivity: Nonmetallic Liquids and Gases*, IFI/Plenum, New York.
- [24] Haile, J. M., 1992, *Molecular Dynamics Simulation: Elementary Methods*, Wiley, New York.
- [25] Kaburaki, H., Li, J., and Yip, S., 1999, "Thermal Conductivity of Solid Argon by Classical Molecular Dynamics," *Mater. Res. Soc. Symp. Proc.*, **538**, pp. 503–508.
- [26] Casimir, H. B. G., 1938, "Note on the Conduction of Heat in Crystals," *Physica*, **5**, pp. 495–500.
- [27] Siegel, R., and Howell, J. R., 1981, *Thermal Radiation Heat Transfer*, 2nd Ed., Hemisphere, Washington, DC.
- [28] Majumdar, A., 1993, "Microscale Heat Conduction in Dielectric Thin Films," *ASME J. Heat Transfer*, **115**, pp. 7–16.
- [29] Ciccotti, G., and Tenenbaum, A., 1980, "Canonical Ensemble and Nonequilibrium States by Molecular Dynamics," *J. Stat. Phys.*, **23**, pp. 767–772.
- [30] Flik, M. I., Choi, B. I., and Goodson, K. E., 1992, "Heat Transfer Regimes in Microstructures," *ASME J. Heat Transfer*, **114**, pp. 666–674.
- [31] Kittel, C., 1996, *Introduction to Solid State Physics*, 7th Ed., Wiley, New York.

An Experimental Study of Molten Microdroplet Surface Deposition and Solidification: Transient Behavior and Wetting Angle Dynamics

D. Attinger

Z. Zhao

D. Poulikakos

Laboratory of Thermodynamics
in Emerging Technologies,
Institute of Energy Technology,
Swiss Federal Institute of
Technology (ETH),
8092 Zurich, Switzerland

The basic problem of the impact and solidification of molten droplets on a substrate is of central importance to a host of processes. An important and novel such process in the area of micromanufacturing is solder jetting where microscopic solder droplets are dispensed for the attachment of microelectronic components. Despite the recent appearance of a few numerical studies focusing on the complex transient aspects of this process, no analogous experimental results have been reported to date to the best of our knowledge. Such a study is reported in this paper. Eutectic solder (63Sn37Pb) was melted to a preset superheat and used in a specially designed droplet generator to produce droplets with diameters in the range 50–100 μm . In a first series of experiments, the size, temperature, and impacting speed of the molten droplets were maintained constant. The primary variable was the temperature of the substrate that was controlled in the range from 48°C to 135°C. The dynamics of molten solder microdroplet impact and solidification on the substrate was investigated using a flash microscopy technique. The time for the completion of solidification from the moment of a solder droplet impact on the substrate varies between 150 μs and 350 μs . The dynamic interaction between the oscillation in the liquid region and the rapid advance of the solidification front was visualized, quantified, and presented in this paper. In a second series of experiments, the evolution of the wetting angle between the spreading drop and the substrate was recorded and analyzed. No quantitative agreement with Hoffman's correlation for wetting was found. It was established that the wetting angle dynamics is strongly coupled with the evolution of the droplet free surface. Two successive regimes were distinguished during the spreading. The influence of the initial impact velocity and substrate temperature on the dynamics of the measured wetting angle was described in both regimes. To the best of our knowledge, this study presents the first published experimental results on the transient fluid dynamics and solidification of molten microdroplets impacting on a substrate at the above-mentioned time and length scales that are directly relevant to the novel solder jetting technology. [S0022-1481(00)01403-1]

Keywords: Droplet, Heat Transfer, Manufacturing, Microscale, Visualization

1 Introduction

Scientific research interest on droplet-surface interactions has recently increased, driven by a need for an in-depth understanding of new aspects of droplet impact phenomena that are important to emerging technologies such as spray deposition ([1,2]) and picoliter size solder droplet dispensing. Picoliter size droplet dispensing (the application to which the present work is directly relevant) is used for advanced surface mount technologies (SMT) in the packaging of electronic microchips. In this technology, monodispersed arrays of molten metal microdroplets (25–100 μm in diameter) are printed on a substrate, each microdroplet (or bump) forming an electrical connection. Important advantages of picoliter size droplet dispensing over other bumping technologies are the flexibility and low cost, because neither masks nor screens are required ([3,4]).

Many physical phenomena related to the prediction of bump shape and metallic properties are not well understood. There is still a lack of basic understanding and modeling capabilities for

phenomena, such as the dynamic behavior of the wetting angle between the substrate and the droplet ([5]), the thermal contact resistance between splat and substrate as well as the rapid solidification phenomenon ([6]), including heterogeneous nucleation and recalescence, as well as the possible remelting of the substrate ([7]). These are typical mesoscopic phenomena, whose physics is often related to microscopic phenomena and cannot be understood using the classical continuum approach. A common way to handle these mesoscopic phenomena is to match experiments with numerical or analytical models in order to estimate the needed model parameters. Using this approach, several temperature measurements under relatively large (mm size) solidifying droplets have been performed and matched with numerical simulations in order to estimate the values of the thermal contact resistance between the splat and the substrate ([8–10]) or to estimate the nucleation temperature ([8]).

The evolution of the wetting angle during droplet spreading also contains largely unresolved physics. The wetting angle behavior at the molecular level is governed by intermolecular forces ([11]). The relation, if any, between the molecular angle and the macroscopic angle (visible with a low-power microscope, and measured in the present study) is also not well established ([12]).

Contributed by the Heat Transfer Division for publication in the JOURNAL OF HEAT TRANSFER. Manuscript received by the Heat Transfer Division, Oct. 25, 1999; revision received, Apr. 11, 2000. Associate Technical Editor: T. Avedisian.

Empirical correlations, such as Hoffman's law ([13]), express the dynamic evolution of the macroscopic wetting angle α as a function of the capillary number Ca and of the equilibrium wetting angle α_{eq} , for steady flows under conditions of negligible Weber number ([12]). In the impact of a droplet on a flat surface, the fluid dynamics is unsteady and the Weber number based on the contact line velocity is not negligible. Therefore, the motion of the droplet free surface near the contact line and the dynamics of the bulk fluid may influence the value of the wetting angle. Furthermore, in a molten droplet impact, there is the additional contribution of heat transfer, which can drastically change flow properties by glassification, or can even arrest the motion of the contact line by solidification. Fukai et al. [14] and Pasandideh-Fard et al. [9] used experimentally measured advancing and receding wetting angles in their numerical models to study the effects of surface wetting on the spreading and recoiling motion of a droplet after impingement on a dry surface. However, since these angles and substrate temperatures have been measured for rather larger systems, with respect to both time and space scales, the question arises if the conclusions can be applied to smaller scales of the kind found in picoliter size solder droplet dispensing and spray casting.

A promising approach to obtain direct insight in the thermophysics of picoliter-size molten droplet impact is the high-speed visualization of such a process. If it were possible to observe, with enough time and space resolution, the spreading and solidification dynamics of picoliter solder droplet impact, in addition to the direct information that the experiments would provide, a comparison with numerical studies of the same problem, such as those by Waldvogel and Poulidakos [15] and by Xiong et al. [16], would be feasible. Such experiments are reported in the present paper. A key finding of the above two papers is that a strong coupling occurs between heat transfer, fluid dynamics, and phase change, leading to a wavy surface of the solder bumps. Although this wavy surface appears in both numerical and experimental studies (the latter yielding only the shape of the completely solidified microbump), there is still a significant discrepancy between numerical results and final shape micrographs ([16]). A visualization of the microdroplet in motion accompanied by relevant quantitative measurements contributes significantly to the understanding of this phenomenon.

A variety of visualization techniques have been applied in the experimental investigations of droplet impact dynamics, including high-speed camera techniques ([17–21]), flash photography ([22–24]), and flash videography ([25–26]). There is one basic distinction between high-speed camera and flash techniques: the former records the highest number of frames from a single event, while the latter reconstructs the event by patching together several frames taken at different instants from several reproducible events. In our case, the expected short duration of the phenomenon (of the order of 100 microseconds) prevented the use of most high-speed cameras. For example, even a very fast CCD camera such as the Kodak EKTAPRO (40, 500 partial frames per second and available in our laboratory) could only give a rough qualitative recording of the phenomenon. Intensified CCD cameras have a time delay between two frames smaller than 50 ns and could have solved the time resolution problem. However, this expensive technology only allows recording a limited number of frames (8 to 30) of a single event ([27]) so that the reconstruction problematic of one event from several reproducible events would have arisen in this case as well. The high-speed 16-mm camera technique has not been considered because of its complex machinery, high costs, and difficulty of implementation ([28]).

In contrast with the methods discussed above, the flash photography and flash videography techniques are stroboscopic methods whereby a variable number of short-pulse illuminations (1 to 10 pulses) are produced at specific instants during each event and recorded by a 35-mm camera or a CCD camera, respectively. By generating a sequence of identical drops and practically identical

impact events per drop, one can capture different stages of the process in each event and piece together from images of droplets taken at progressive stages the entire impact, spreading, and solidification process. Key parameters describing the droplet spreading process, i.e., splat/substrate contact area, splat diameter, and thickness as well as the wetting angle ([9]), can be subsequently measured from the recorded pictures of spreading droplets. The flash techniques rely therefore on the generation of droplets in a highly repeatable manner ([22,25,24,26]) since the impact process is reconstructed from images of several impact events.

Good quality images of a droplet spreading process have been reported in the literature using short-duration flash photography ([22,9]) for millimeter-size droplets, and flash videography ([26]) for droplet diameters of the order of 60 μm to about 1 mm. To exemplify, the study of Pasandideh-Fard et al. [9] reports a visualization of impact and solidification of relatively large (approx. 2 mm) liquid metal tin drops on a cold substrate. Hence, the resulting Weber number value of $We=71$ does not correspond to the relatively low Weber domain ($4 < We < 10$) encountered in picoliter size solder droplet dispensing that is the focus of the present research. In the present study a flash videography technique, coupled with a digital grabbing of the images for the ease of postprocessing, is developed and implemented.

2 Experimental Setup

2.1 Molten Solder Microdroplet Deposition System. To investigate the dynamic process of impact and solidification of picoliter size molten metal droplet on the surface of a semiconductor device, a molten solder microdroplet jetting device was set up at ETH Zurich with technical assistance from MicroFab Technologies Inc. (Dallas, TX). The method used for the generation of monodispersed picoliter-size droplets of solder at demand with the potential of use in the manufacturing of electronic components was described in ([3]) and ([29]), and is summarized as follows.

By applying an electric pulse to a piezoelectric material not in direct contact with the fluid, picoliter volumes of molten metal are ejected from an orifice at demand in accordance with the electric pulse frequency. After oscillating, the ejected tiny amount of metal assumes a spherical shape due to minimization of surface tension energy. The process is termed solder jetting at demand. The jetting apparatus used in the present study is shown schematically in Fig. 1.

Solder is melted in an enclosed reservoir by resistance heating. The molten solder reservoir is pressurized with nitrogen to insulate the melt with a chemically inert environment and provide back pressure for jetting. A nitrogen flowing as a curtain around the path of the droplet toward the substrate limits the interaction with the surrounding air and prevents, at least to a good extent,

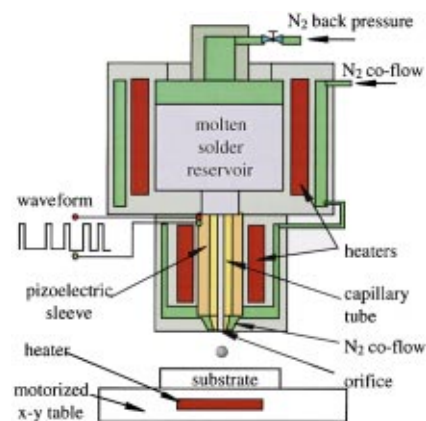


Fig. 1 Schematic of the picoliter size solder droplet deposition apparatus

droplet oxidation. Molten solder temperatures in the reservoir and the capillary tube are both monitored by thermocouples and controlled through the heaters. The waveform of the drive pulse for solder jetting is electronically generated and digitally controlled. By varying the waveform, the diameter and the velocity of ejected solder droplets can be altered in the ranges of 50–100 μm and 1–2.5 m/s, respectively. The alloy used in this study is a eutectic tin lead solder (63 percent Sn-37 percent Pb) with 99.99 percent purity, specially developed for solder jetting by Witmetaal B. V., Holland. Delay time between droplet ejection can be changed by varying the waveform driver frequency for droplet generation. However, the repeatability of droplet diameter and ejection velocity is greatly improved when the frequency of droplet ejection is maintained constant during the experiment. In the present study, a droplet generation frequency of 12 Hz was used.

After ejection from the orifice, a solder droplet travels approximately 1 mm and impacts the substrate mounted horizontally on a motorized x - y precision stage (Photon Control PTS 1000, England). The substrate in the present study is a semiconductor wafer (EM Marin, Switzerland) cut to a die size of approximately 10×50 mm. The wafer consists of the following layers from top to bottom: 0.1- μm -thick Au, 0.3- μm Ti90W alloy, 1- μm silicon nitride (conductivity $\lambda = 2.33 (+ - 0.11) \text{ Wm}^{-1}\text{K}^{-1}$, heat capacity $\rho c_p = 2.62 (+ - 0.22) * 10^{-6} \text{ Jm}^{-3} \text{ K}^{-1}$) ([30]) and 675- μm P-silicon. The substrate wafer slide is mounted on a heated copper plate with a thin layer of thermal interface paste (HTC Electro-lube, England) between the wafer and the copper plate, with $\lambda = 0.84 \text{ Wm}^{-1} \text{ K}^{-1}$. The wafer top ($T_{2,0}$) and bottom ($T_{3,0}$) surface initial temperatures are measured with two K-type thermocouples (Omega 304 SS9), the former being epoxied on the wafer with a 1-mm-size island of conductive epoxy (AV138M/HV998 Novartis, Switzerland) with $\lambda = 0.6 \text{ Wm}^{-1} \text{ K}^{-1}$. The bead diameter of the thermocouples is 250 μm . The copper plate temperature was PID-controlled to vary $T_{2,0}$ between 48°C and 135°C. Since the wafer slides used in printing have to be frequently replaced, the temperature measurements are carried out on another wafer slide, permanently deposited on the copper plate, and moved under the printhead at the same conditions as the wafer slide where droplets impact. Both radiation from the metallic parts of the printing device and convection from the co-flow increased significantly the wafer temperatures. The x - y stage motion (2 mm/s) is so slow that the thermocouples reach a steady-state value before passing under the jet orifice and maintain it after passing by the jet orifice. Therefore the transient temperature effect is considered to be negligible.

2.2 Visualization of Solder Droplet Deposition Using Flash Videography. As described in the Introduction, the technique used for the visualization of droplet impact and solidification is a flash videography technique ([26]) where only one image is taken at one instant during the impact and solidification process for each drop studied. The imaging system used to record the droplet deposition process is shown schematically in Fig. 2.

Backlighting for the first series of experiments is provided by a Xenon flash light unit (Hamamatsu L4634). The flash energy is 0.15 J/flash and the duration of each burst of flash is 1 μs with less than 200 ns jittering. The time resolution of the sequence recording is set to 5 μs . A Fresnel lens is used to provide uniform and intensified (focused) backlighting field for the microscope. The droplet images are magnified using a microscope objective (Microtech Zoom 70, USA) with $29\times$ optical magnification on the CCD matrix plane, which provides a space resolution of 1.2 μm in the object plane. The conditions for the wetting angle measurement are slightly different from the first experiments in this paper. The optical magnification is increased up to 36 times. In order to capture the fast kinematics during the beginning of the spreading (with contact line velocities of the order of 2 to 4 m/s), a faster Xenon flash light unit (FX-HSPS, Wedel, Germany) is employed. It provides a shorter flash duration of 150 ns with less than 60 ns

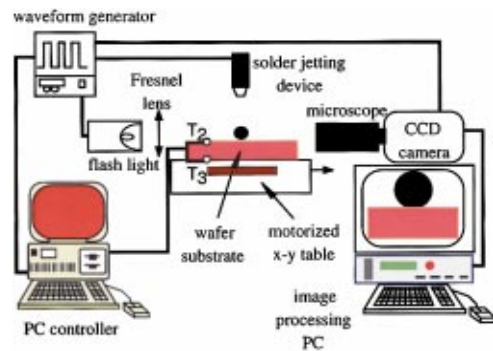


Fig. 2 Flash videography technique used for recording the solder droplet deposition process

jittering, with a flash energy of 0.1 J/burst. The time resolution of the sequence recording is also increased up to 300 nanoseconds during the first stage of the spreading.

Images of the droplets are acquired with a Jai M10 progressive scan CCD camera (Denmark) in triggered mode and are digitized and stored in the image processing PC. An example of the picture quality of a droplet in motion is given in Fig. 3(b). As a result of high power optical magnification, the ambient light introduces little optical noise on droplet images, and the flash light acts therefore as a shutter. The waveform generator that activates the solder

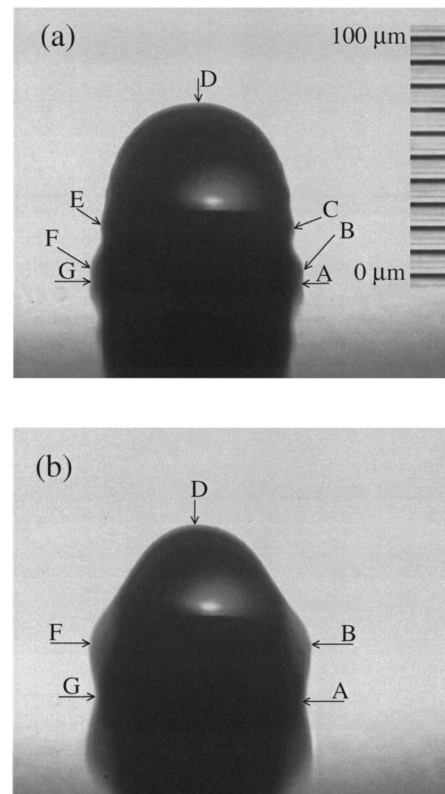


Fig. 3 Measured points on the droplet surface. Points A and G determine the droplet wetting area diameter. D is the highest visible point of the surface, when viewing from the side, not always at the axis of symmetry. The distance from D to segment AG determines the visible droplet height H above the surface (identified by the segment AG). The shadow below the surface and the light spot inside the droplet are optical effects. The accuracy in determining the vertical and horizontal position of A and G decreases for wetting angle values near 90 deg, and larger than 110 deg, respectively.

jetting device sends a signal with a preset delay to trigger the flash light when a solder droplet hits the substrate. To record the progressive stages of solder droplet spreading and solidification, the delay time between droplet ejection and a burst of back lighting is increased between successive images.

In order to provide a free impact surface for each impinging droplet, the motorized x - y stage is maintained at a constant linear speed of 2 mm/s in the focal plane of the microscope during experimental runs. This translation velocity of 2 mm/s is about three orders of magnitude smaller than the impact velocity of 1.5 m/s. In a reference frame attached to the translation stage, this motion corresponds to a deviation from the vertical direction of the impact smaller than 0.1 degrees, thus negligible.

2.3 Image Analysis and Discussion of the Experimental Uncertainties. Image analysis is carried out using an image processing software (Optimas 6.2, Media Cybernetics, USA) that allows the measurement of droplet area and the motion analysis of selected points for a sequence of images. Figure 3 shows a measurement example of droplet wetting area diameter (distance between A and G) and droplet height (distance from point D to segment AG). It should be emphasized that such measurements involve uncertainties, due to the human identification of the measured points. In the case of clearly defined points such as in Fig. 3(b), 20 measurements of the points on the same image yield a standard deviation (in percentage of the initial droplet diameter) of 0.06, 0.54, 0.91, 0.44 and 0.16 percent for the vertical position of D, the distance between D and segment AG, and the position of the single points A and G, as well as the wetting area diameter, respectively. It is worth noting that a wetting angle α larger than 110 deg can cause significant optical blurring (as in Fig. 4, 30 μ s), and therefore increase the error for the wetting area diameter.

The choice of a flash videography technique that consists of building an impact sequence from a series of single pictures, each of them taken from a different droplet requires a highly reproducible process. There are several factors that can influence the reproducibility of droplet release and solidification. We examined, with the setup used for the first series of experiments, two possible perturbation sources, i.e., the stability in the drop position and velocity as well as the importance of the wafer heating due to the heat released by solidification of the previous drop.

The positions of the top, bottom, left, and right extreme points of 99 solder droplets in the same conditions as in the experiment have been measured with a constant delay between ejection and flash. The standard deviation in the horizontal position of the extreme right and left position is, respectively, 1.32 percent and 1.46 percent of the diameter (80 μ m), and the standard deviation in the vertical position for the top and bottom points is 2.2 percent (± 1.76 μ m) and 1.72 percent, respectively. The maximum standard deviation in the vertical position corresponds to a jitter in the droplet ejection of ± 1.17 μ s. Since this error is markedly larger than the error due to the human identification of the measured points, the major cause of uncertainties in the measurements is due to the needed repeatability of the visualization technique.

The magnitude of wafer slide heating due to the heat released by solidification of the previous drop has been evaluated in two ways. First, we estimated the final increase in the wafer temperature after the impact of a series of droplets that corresponds to our experimental conditions. Then, we estimated if the transient local heat release of a previous drop would affect the initial conditions for the actual drop. The final temperature increase was estimated as follows. Assuming that the heat released by the drops increases the wafer temperature uniformly, we express the temperature increase ΔT of a typical wafer slide (10 mm by 50 mm surface):

$$\Delta T = \frac{nE_Q}{\sum_i \rho_i V_i c_{pi}} \quad (1)$$

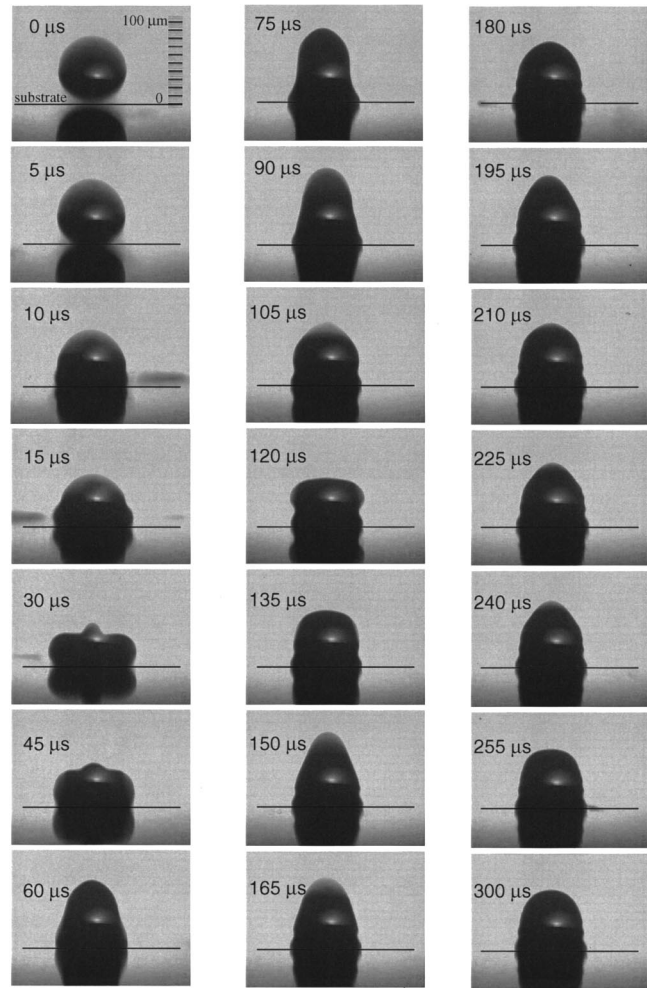


Fig. 4 Spreading, oscillations, and freezing of a solder droplet on a flat substrate. Initial conditions: $v_0=1.54$ m/s, $d_0=80$ μ m, $T_{1,0}=210^\circ$ C, $T_{2,0}=48^\circ$ C.

where n , E_Q , ρ , V , and c_p are the number of droplets, the heat released by droplet solidification and subcooling, the density, volume, and heat capacity of each layer i of the wafer. In the case where 300 droplets (i.e., 3 sequences of 100 drops) at 210°C impact a wafer slide of the same composition as the one used in the experiments, we maintain that the wafer temperature increase ΔT is less than 0.1K, and is thus negligible. The transient effect of the previous droplet impact on the actual drop can be calculated accurately numerically, but we obtained an acceptable estimate by assuming that the entire E_Q is released at time $t=0$ in a half-sphere of an infinite radius. In other words, we consider that each droplet acts as an instantaneous heat source on the surface. In this case, an analytical relation exists for the temporal and local evolution of the temperature ([31]). Considering a pitch distance between droplets of 166 micrometers (corresponding to a printing frequency of 12 Hz), the maximum transient temperature variation due to heat released by the previously impacting droplet for a distance of 166 micrometers from the heating source, was found to be 0.03 K in a gold hemisphere and 0.13 K in a silicon hemisphere, and is thus negligible.

A further difference between the experiments and the ideal case of a spherical droplet impinging on a substrate is that there are still small residual shape oscillations from the ejection process at the instant of impact. Hence, the droplet shape at the time of impact is not absolutely spherical. This error can be estimated by observing the maximum error in nonsphericity on the pictures

right before impact: At the distance used for printing, the diameter oscillation amplitude was ± 5 percent of the droplet diameter. A series of measurements showed that the phase lag between the oscillations of the horizontal diameter and the vertical diameter equals π , thus this oscillation should not influence the measurement of droplet size, based on the visible area. Accordingly, the measurement of droplet velocity before impact was based on the motion of the two points at the extreme left and right of the droplet. Their height is a bit more difficult to determine than, for example, the height of the bottom point of the droplet, but it does not oscillate in the vertical direction.

3 Results

3.1 Experimental Conditions. Two series of experiments were performed. The first series was focused on the transient behavior of the spreading and solidification process. The second series was focused on the wetting angle dynamics. In the first series, sequences of molten solder microdroplet impingement on a colder wafer, such as those shown in Figs. 4 and 5, have been recorded for different initial temperatures of the top surface of the wafer ($T_{2,0}=48, 62, 81, 98, 118, \text{ and } 135^\circ\text{C}$). The temperature $T_{3,0}$ of the bottom surface of the wafer was measured to be in each case 5 to 6 K lower than $T_{2,0}$. Each sequence was reconstructed from about 100 frames, the delay between drop release and flash being increased in steps of $5 \mu\text{s}$ between each frame. In each

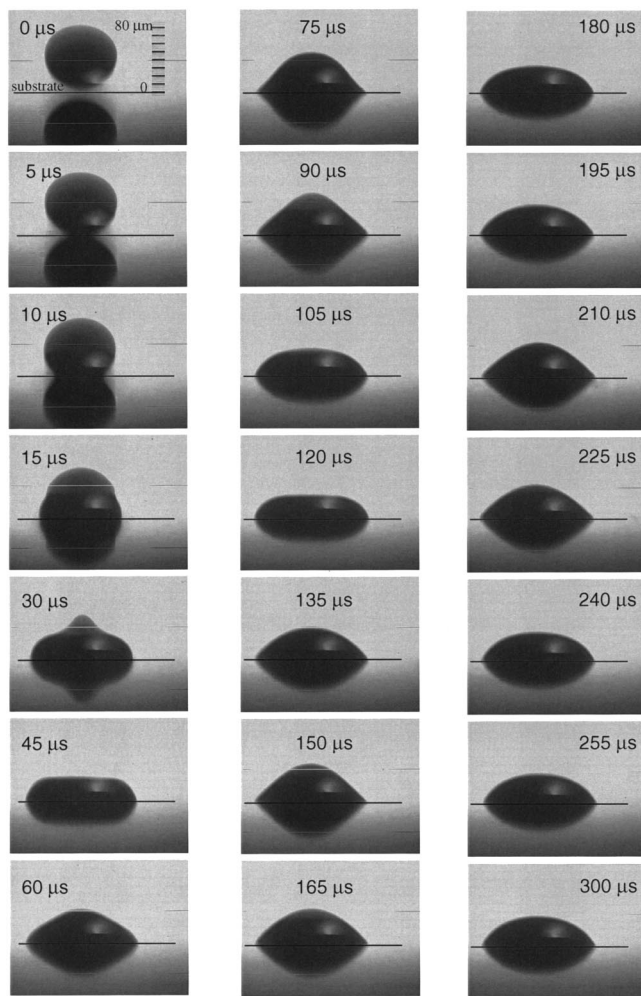


Fig. 5 Spreading, oscillations, and freezing of a solder droplet on a flat substrate. Initial conditions: $v_0=1.49 \text{ m/s}$, $d_0=84 \mu\text{m}$, $T_{1,0}=210^\circ\text{C}$, $T_{2,0}=135^\circ\text{C}$.

Table 1 Initial conditions for the first series of experiments pertaining to the overview of the spreading and solidification process

| | | | | | | |
|---------------------------|------|------|------|-----------------|------|------|
| $v_0(\text{m/s})$ | | | | 1.52 ± 0.06 | | |
| $T_{2,0}(^\circ\text{C})$ | 48 | 62 | 81 | 98 | 118 | 135 |
| Re | | | | 381 | | |
| We | | | | 4.4 | | |
| Ste | 0.77 | 0.69 | 0.58 | 0.48 | 0.37 | 0.27 |
| Oh | | | | 0.0055 | | |
| Pt | | | | 0.025 | | |

sequence, the time $t=0$ corresponds to the last picture before impact. The maximum corresponding error in determining the time $t=0$ when the droplet contacts the substrate is therefore $5 \mu\text{s}$. The produced drops had a mean diameter d_0 in the range of 79.7 to $83.9 \mu\text{m}$ and a velocity v_0 in the range of 1.49 to 1.58 m/s , with average values of $81.4 \mu\text{m}$ and 1.52 m/s , respectively. The characteristic numbers, defined in the Nomenclature, are shown in Table 1. They are based on the following values for the thermo-physical properties: $\sigma=0.345 \text{ Jm}^{-2}$, $\mu=0.00262 \text{ Pa s}$, $L=42,000 \text{ J/kg}$, $c_{pl}=238 \text{ J kg}^{-1} \text{ K}^{-1}$, $\lambda_1=25 \text{ Wm}^{-1} \text{ K}^{-1}$, and $T_m=183^\circ\text{C}$, and on the average measured values of velocities and diameter.

The second series of experiments, focusing on the evolution of the wetting angle, was performed with a more precise lighting, an increased optical magnification, and time resolution, as described above. Four sequences of data were collected, where the surface temperatures and the initial impact velocities were varied as shown in Table 2. The mean value of the initial diameter d_0 was slightly smaller than in the first series of experiments ($74.1 \pm 2 \mu\text{m}$), and has been used for the calculation of the Reynolds and Weber numbers. The remaining experimental conditions were the same as in the first series of experiments.

3.2 Qualitative Investigation of the Spreading and Solidification Process. Figure 4 shows a reconstructed sequence corresponding to an initial wafer temperature $T_{2,0}$ of 48°C . A qualitative inspection of Fig. 4 reveals that the spreading time (defined as the time taken by the droplet to spread to its maximum contact area) is approximately $30 \mu\text{s}$.

The subsequent contour shapes caused by the upward motion of the droplet fluid indicate that the fraction of solidified mass is small within the first cycle of the droplet oscillation. The large variation of droplet height during the subsequent oscillation also suggests that the damping effect of viscous force is less important than the effect of surface tension force.

In the case of impact on a substrate with $We > 1$, the radial pressure gradient induced by the impact drives the process of droplet spreading ([6,32,5,33]). Surface tension forces, liquid viscous forces, and solidification work together to arrest the droplet spreading. According to Bennett and Poulikakos [32], surface tension effects dominate the termination of droplet spreading over viscous effect when

$$We \leq 2.8 Re^{0.457} \quad (2)$$

For the droplet impingement conditions in Fig. 4, the right-hand side of the above equation has a value of 42.3. Comparison with

Table 2 Initial conditions for the second series of experiments focusing on the evolution of the wetting angle

| | | | | |
|---------------------------|--------|--------|--------|--------|
| $v_0(\text{m/s})$ | 2.35 | 2.31 | 1.49 | 1.51 |
| $T_{2,0}(^\circ\text{C})$ | 145 | 59 | 65 | 119 |
| Re | 546 | 537 | 348 | 350 |
| We | 9.7 | 9.4 | 3.9 | 4.0 |
| Ste | 0.22 | 0.70 | 0.67 | 0.36 |
| Oh | 0.0057 | 0.0057 | 0.0057 | 0.0057 |
| Pr | 0.025 | 0.025 | 0.025 | 0.025 |

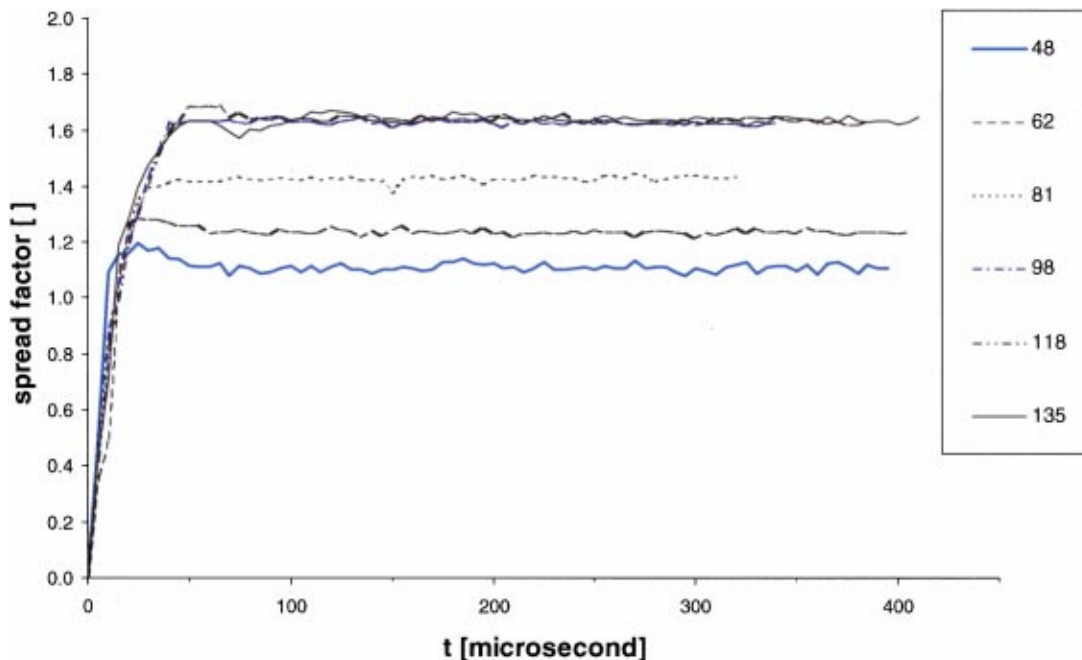


Fig. 6 Time evolution of the spread factor β , with the substrate temperature $T_{2,0}$ as a parameter. The error is estimated in Section 2.3.

the Weber number, about ten times smaller, indicates that the condition for the droplet deposition shown in Fig. 4 is well into the surface tension domain concerning the relative influence of viscous dissipation and surface tension.

Solidification effects can influence droplet motion ([33]). Neglecting the presence of contact thermal resistance between the substrate and the droplet bottom, the ratio of spreading time, t_{spr} , to the solidification time, t_s , can be estimated from ([33])

$$t_{spr}/t_s = \text{OhSte}/\text{Pr}. \quad (3)$$

The ratio calculated from the above equation is 0.17, indicating that the droplet spreading time is smaller than the solidification time. It is expected that the above ratio will be further reduced in the presence of interface thermal contact resistance. According to Fig. 4, the spreading time is approximately $30 \mu\text{s}$ before the recoiling motion in the liquid region. No changes of the droplet shape are visible for the points located at the top of the droplet contour after $255 \mu\text{s}$. Assuming that the arrest of droplet oscillatory motion is caused by solidification and not by viscous damping (which is reasonable since four visible ripples on the drop surface indicate that solidification arrested most of the drop motion), the ratio of the measured droplet spreading time to solidification time is 0.12. This agrees relatively well with the prediction of Eq. (3).

While droplet solidification is significantly slower than droplet spreading as shown above, it is also obvious that the subsequent oscillatory motion of the droplet is strongly affected by solidification. First, it can be shown by counting the number of frames for each oscillatory cycle that the oscillation frequency is increased with the upward propagation of the droplet solidification front, which reduces the total liquid mass of the droplet. Numerical simulations suggested that the oscillation frequency of an impacting droplet is closely related to the droplet natural frequency ([34])

$$f \propto (\sigma/\rho_l V_l)^{1/2} \quad (4)$$

where V_l is the liquid volume. As the solidification front propagates into the molten region, the remaining liquid mass of the droplet decreases, which results in an increase of the oscillation frequency. Second, Fig. 4 confirms that the ripples visible on the

drop surface are due to a strong coupling between solidification and oscillations, which was suggested by numerical results pertaining to a comparable parameter range ([15,16]).

Solidification can influence the spreading. This occurs by freezing at the wetting line ([35]), or by destruction of kinetic energy by solidification ([9]). The parameter measuring the spreading is the spread factor, β , defined as the ratio of the diameter d of the wetted substrate area over the initial droplet diameter d_0 . A comparison between Figs. 4 and 5 shows a significant increase of the maximum spread factor β_{max} when the substrate temperature is increased to 135°C . Assuming heat transfer between the substrate and the droplet only affects the spreading by delaying the solidification start ([6,33]), the increase of β_{max} with increasing substrate temperature shows that solidification influences the spreading.

Other effects caused by an increase in the substrate temperature are visible in comparing Figs. 4 and 5. The final height decreases and ripples are no longer visible: the droplet assumes a lens shape. These and other phenomena are discussed in the next section, which considers measurements from pictures of droplet spreading for increasing initial substrate temperatures.

3.3 Quantitative Investigation of the Spreading and Solidification Process. The time evolution of the spread factor β , measured as in Fig. 3, is shown in Fig. 6 with the substrate initial temperature $T_{2,0}$ as a parameter. The time resolution is $5 \mu\text{s}$. In the first $15 \mu\text{s}$ after impact, β increases from 0 to about 1 in a similar way for all values of $T_{2,0}$ examined. However, the attained final values β_∞ depend markedly on $T_{2,0}$. These final values increase with substrate temperature for $T_{2,0}$ between 48 and 98°C , and are almost constant for higher temperatures. The dynamic nondimensional parameters of impact, including We , Re , and Oh numbers, are approximately the same in every case. The difference is the thermodynamic parameter for phase change, the Stefan number, calculated in Table 1. The similar behavior of $\beta(t)$ for $T_{2,0}$ in the range 98 to 135°C indicates that above 98°C (i.e., below $Ste = 0.48$), there is no dependency of β on the Stefan number. This implies that solidification does not influence the spreading for $T_{2,0}$ over 98°C . Therefore, the assumption that the droplet spreads first and solidifies subsequently appears to be valid in this range of

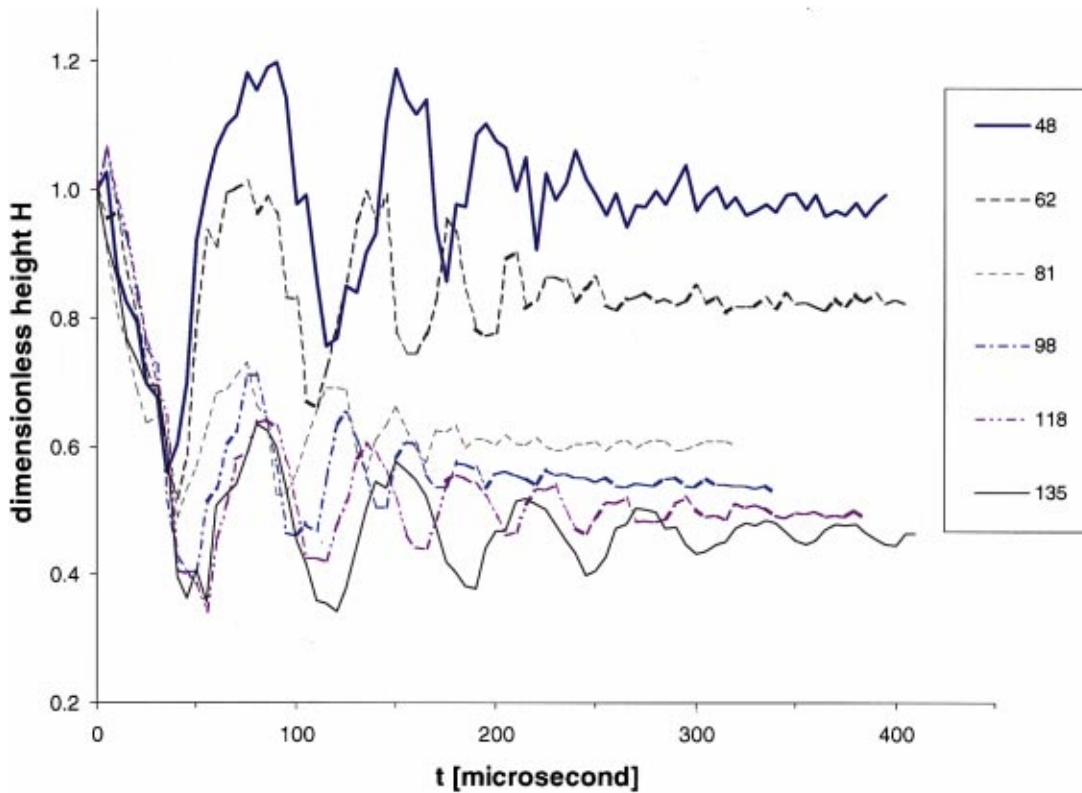


Fig. 7 Time evolution of the dimensionless visible droplet height over the substrate H , with the substrate temperature $T_{2,0}$ as a parameter. The error is estimated in Section 2.3.

$T_{2,0}$. This is indicated by the good agreement between the final spread factor we measured for $T_{2,0}$ above 98°C ($\beta \approx 1.6$) and results from an analytical relation of Pasandideh-Fard et al. [36]. This relation estimates the maximum spread factor in the absence of solidification to be 1.65 with our mean values of Re , We , and with an advancing wetting angle value of 135° in the early stages of spreading. It is worth noting that the above analytical relation is based on the assumption of a reasonably high Reynolds number, so as to produce a thin boundary layer in the liquid as it spreads, which is only partially valid in our case ($Re=381$). We found it interesting that this relation predicts within five percent the spreading ratio of our measurements in the absence of solidification (i.e., when the substrate initial temperature is high). This is why we have tested the extension of this relation [9] that considers solidification effects by assuming that the influence of solidification is manifested by kinetic energy destruction. In this case, the model results do not agree well with our experimental results. The calculated maximum spread factors lie between 1.52 and 1.57, and our experimental values are between 1.20 and 1.69. One possible reason for this discrepancy could be that solidification influences the spreading by arresting the wetting line via freezing rather than by destroying kinetic energy. In a published numerical study pertaining to the same parameter range as this experimental study, Waldvogel and Poulikakos [15] have shown that freezing at the wetting line controls wetting line arrest. This has also been observed experimentally by Schiaffino and Sonin [35] for low Weber numbers. However, the history of the spread factor β for the lowest substrate temperature $T_{2,0}=48^\circ\text{C}$ (Fig. 6) shows a maximum value of β significantly bigger (eight percent) than the final value of β . This measurement, concerning the highest Stefan number (0.77) of our measurement range, would contradict the hypothesis that freezing at the wetting line controls the maximum spreading. This apparent contradiction is probably a consequence of the significant blurring at the contact between

splat and substrate in Fig. 4 ($30 \mu\text{s}$), which makes the accurate measurement of the maximum spread factor difficult.

Figure 7 shows the time evolution of the dimensionless visible droplet height H over the substrate (defined in Fig. 3 as the maximum height when viewing from the side at any time instance), with $T_{2,0}$ as a parameter. It should be emphasized that the visible droplet height does not always correspond to the height of the intersection of the axis of symmetry with the free surface. For example, simulations by Waldvogel and Poulikakos [15] have shown that, in the early stages of the spreading, the height of the intersection of the axis of symmetry with the free surface is smaller than the droplet height visible from the side. The motion of the droplet height shown in Fig. 7 can be termed as a damped oscillation. Figure 8 shows the final, maximum and minimum values of the visible droplet height, each corresponding to a fixed

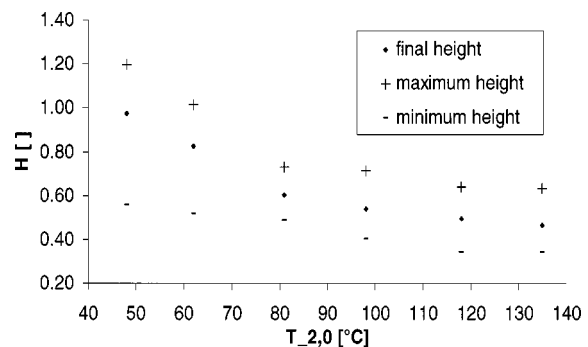


Fig. 8 Final, maximum and minimum droplet nondimensional visible height H as a function of $T_{2,0}$. The error is estimated in Section 2.3.

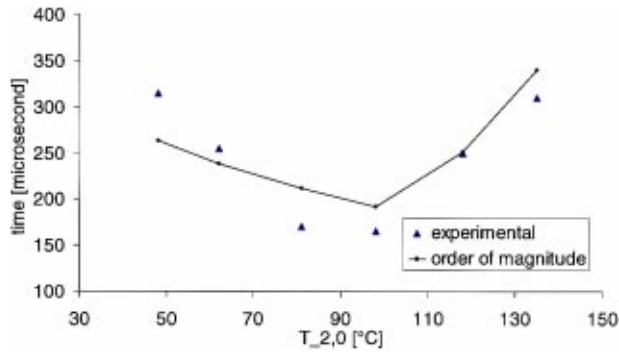


Fig. 9 Solidification time t_s as a function of $T_{2,0}$. The experimental values refer to the apparent solidification time, and the order of magnitude values refer to Eqs. (5) to (8).

substrate temperature. The maximum visible height is measured from the beginning of first recoiling, and the final visible height is measured by averaging the height of the ten last frames of each visualization series. The final maximum and minimum values of the visible droplet height decrease monotonically with $T_{2,0}$. At temperatures below 98°C, the monotonical decrease of final height with substrate temperature can be correlated with the increase of β_{\max} with substrate temperature (Fig. 6).

Quantitative information about the solidification time has been extracted from Fig. 7 as follows. We assume that the droplet is frozen when the droplet height remains constant (within ± 2 percent of the initial diameter) for a time length more than half a period of its oscillations (corresponding to a series of ten successive frames). The apparent solidification time is then defined arbitrarily as the time of the first frame of the above mentioned series. The apparent solidification time is represented in Fig. 9. It depends nonmonotonically on $T_{2,0}$, with a minimum of about 165 μs at $T_{2,0}=98^\circ\text{C}$. This nonmonotonic dependence of the apparent solidification time on $T_{2,0}$ indicates a nonmonotonic dependence of the effective solidification time on $T_{2,0}$, as calculated in previous numerical simulations ([15,16]). An order of magnitude explanation of this nonmonotonic dependence of the solidification time on $T_{2,0}$ is presented hereafter. If we neglect the effect of superheat and subcooling, we can consider that the energy E_s released by the solidification of the droplet is constant with respect to $T_{2,0}$:

$$E_s = \rho VL. \quad (5)$$

The solidification time t_s is expressed as follows:

$$t_s = \frac{E_s}{\dot{q}}. \quad (6)$$

We also assume that the heat flux \dot{q} can be expressed by

$$\dot{q} = h_e S (T_m - T_{2,0}) \quad (7)$$

where h_e is an effective heat transfer coefficient and

$$S = \frac{\pi}{4} d_0^2 \beta_\infty^2 \quad (8)$$

is the contact surface between splat and droplet (the final spread factor β_∞ is measured from Fig. 6). The variation of the solidification time t_s therefore only depends on \dot{q} , i.e., on the product of S (increasing with $T_{2,0}$) and the temperature difference (decreasing with increasing $T_{2,0}$). The coupling of these two opposite trends leads to a minimum in the solidification time. Values of the solidification time calculated by this order of magnitude model described above are plotted in Fig. 9. The value of the effective heat transfer coefficient used in Eq. (7) ($h_e = 4.3 \cdot 10^5 \text{ (Wm}^{-2} \text{K}^{-1})$) has been determined by minimizing the differences between the model and the experiments results, in a least square sense. It is

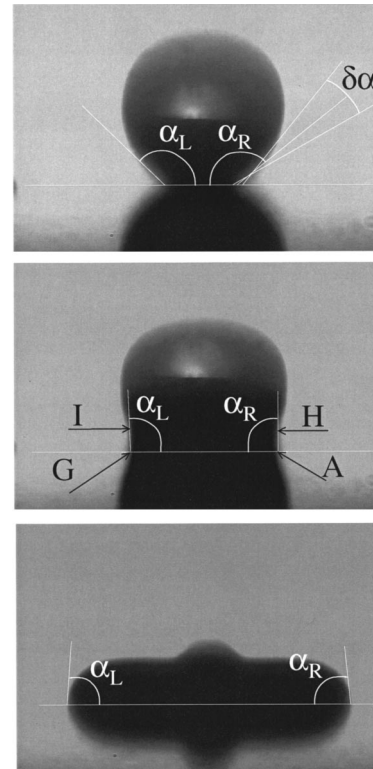


Fig. 10 Determination of the apparent dynamic wetting angles. Angle α_L is determined by points (I,G,A), and angle α_R by (H,A,G). The measurement incertitude $\delta\alpha_R$ comes primarily from the positioning of A and H, its value is estimated ± 12 deg.

worth noting that h_e expresses both the effects of convection in the liquid part of the splat and conductive heat transfer at the splat/substrate interface. These two heat transfer modes have been respectively examined by ([37]) and ([10]) matching experiments with numerical or analytical models. Although the goal of our analytical model is to give a physical explanation of the observed non-monotonic dependence of the solidification time on $T_{2,0}$ and not to provide quantitative results, the estimated value of h_e agrees in an order of magnitude sense with the results of ([10]). The effect of thermal contact resistance on the spreading dynamics cannot be accurately pursued with the present approximate model. A thorough study of this effect has been performed by Xiong et al. [16], who matched the shapes of solidified droplets with the shapes obtained by numerical simulations at different Biot numbers.

3.4 Investigation of the Wetting Dynamics. The visualization method presented here allows the measurement of the evolution of the apparent wetting angle α . This angle is always measured at the contact line between the droplet and the wafer substrate, as shown in Fig. 10, which is a representative frame for our wetting measurements. Each frame allows a double measurement of α , on the left and on the right of the droplet. A graphical estimate in Fig. 10 yields an angular precision of ± 12 deg. It is worth noting that α can only be considered to be a *wetting* angle as long as no solidification has occurred at the contact line. Indicators of the fact that solidification has not occurred are for example the temporal evolution of the spread factor and the temporal variation of the apparent wetting angle. The experimental conditions for the experiments on wetting dynamics are slightly different from the first series of experiments performed in this study, as described above. The time resolution of 300 ns used is well below the jitter due to instabilities in droplet ejection, so we

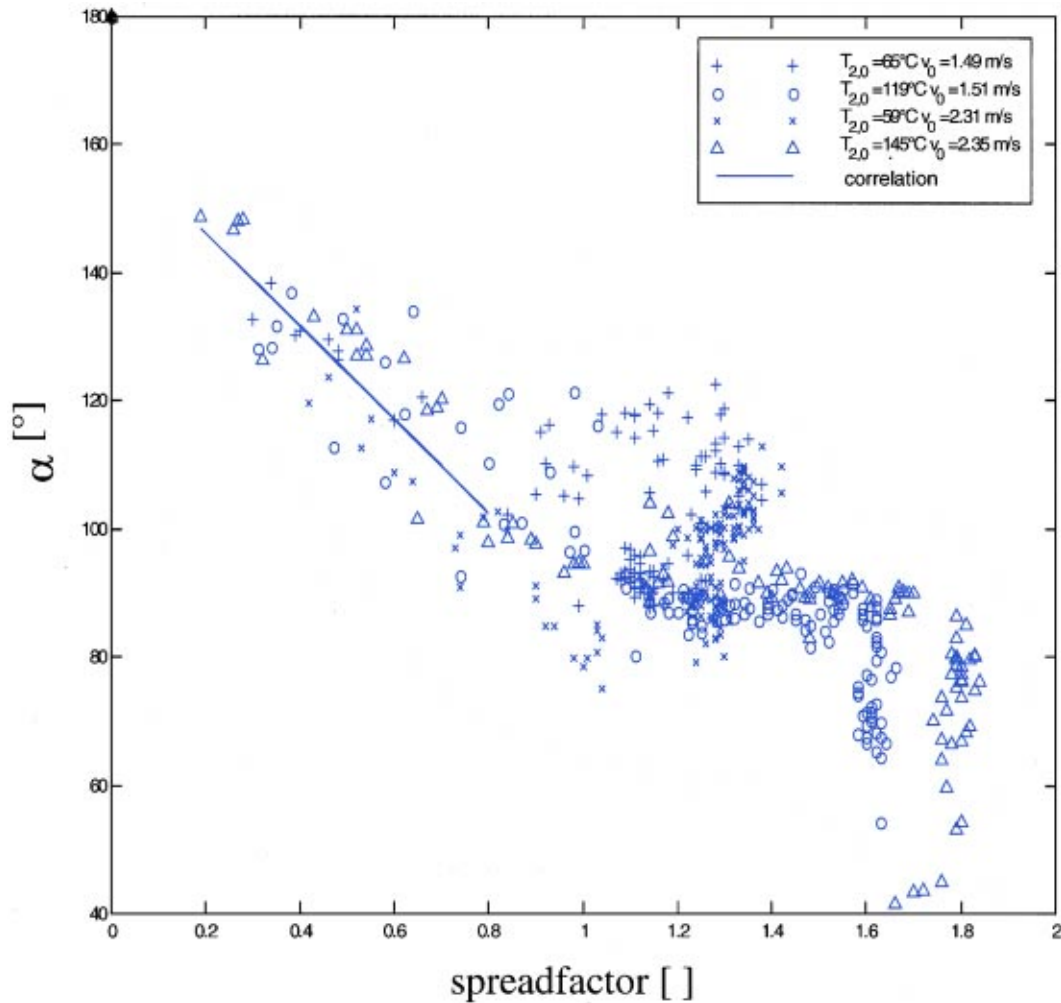


Fig. 11 Evolution of the wetting angle α as a function of the spread factor β for the specified initial substrate temperatures $T_{2,0}$ and impact velocities v_0 . The angular error is estimated in Fig. 10.

have selected to base our interpretation of the results on plots of the wetting angle as a function of the spread factor β (Fig. 11) instead of as a function of time (Fig. 12).

Figure 11 shows the evolution of the apparent wetting angle α as a function of the spread factor β for the four cases described in Table 2. These cases differ by the impact velocity v_0 and the initial substrate temperature $T_{2,0}$. At least two regimes can be distinguished in Fig. 11: a first regime where α decreases linearly ($\beta < 0.8$), and where the behavior is comparable in the four measurement sequences, and a second regime ($\beta > 0.8$), where no consistent behavior for all cases can be observed. In the first regime, measurements and a general optical inspection of the frames do not reveal significant angle and shape differences between the four examined cases, defined by their respective initial impact velocities v_0 and surface temperature $T_{2,0}$: (2.35, 145), (2.31, 59), (1.51, 119) and (1.49 m/s, 65°C). A linear curve fit in this first regime yields the following correlation, plotted in Fig. 11:

$$\alpha(\beta) = 160 \text{ deg} - 71\beta, \beta < 0.8. \quad (9)$$

The second regime can be either a horizontal plateau ($\alpha \sim 90$ deg) terminated by a region where the value of α oscillates at the maximum value of β as in the case (1.51, 119), or a regime of increase and subsequent decrease of α as in the cases (2.31, 59) and (1.49, 65), where α first increases to a local maximum and then decreases to a final value of about 90 deg (the interpretation of the results in Fig. 11 is aided by plots such as Fig. 12, where time is a coordinate). The last case (2.35, 145) can be viewed as a

combination of a plateau and a small zone of increase and subsequent decrease of α for $\beta \in [1.1, 1.3]$. It is worth stressing that, although not explicitly extractable from Fig. 11 because time is not a coordinate, oscillations of the value of α at the maximum values of β (for example $\beta = 1.6$ and $\beta = 1.8$) were observed. Witness to this fact are the frames between 45 and 150 μs in Fig. 5.

The results for α in the first regime can be interpreted as follows. The decrease of the apparent wetting angle value with the spread factor corresponds qualitatively to the predictions of Hoffman's experimental correlation ([12,13]), which expresses that the wetting angle decreases with decreasing capillary numbers (this is the case in the early part of the impact, because the spherical droplet shape induces a contact line velocity that decreases with time):

$$\alpha = f_{\text{Hoff}}(\text{Ca} + f_{\text{Hoff}}^{-1}(\alpha_{eq})) \quad (10)$$

$$f_{\text{Hoff}}(\text{Ca}) = 4.54\text{Ca}^{0.353}, \quad \text{Ca} < O(0.1). \quad (11)$$

The second term in the parenthesis of Eq. (10) is a correction factor for the influence of the equilibrium wetting angle α_{eq} . Theoretical verification of Hoffman's correlation has been obtained for the case of perfect wetting ($\alpha_{eq} = 0$) via hydrodynamic analyses by Voinov and Tanner [38,39]. Equation (11) expresses this correlation for the range of capillary number that pertains to our study [40].

Hoffman suggested analytically that flow inertia could influence α for $\text{We} > 0.015$ ([13]). The analyses of Tanner and Voinov

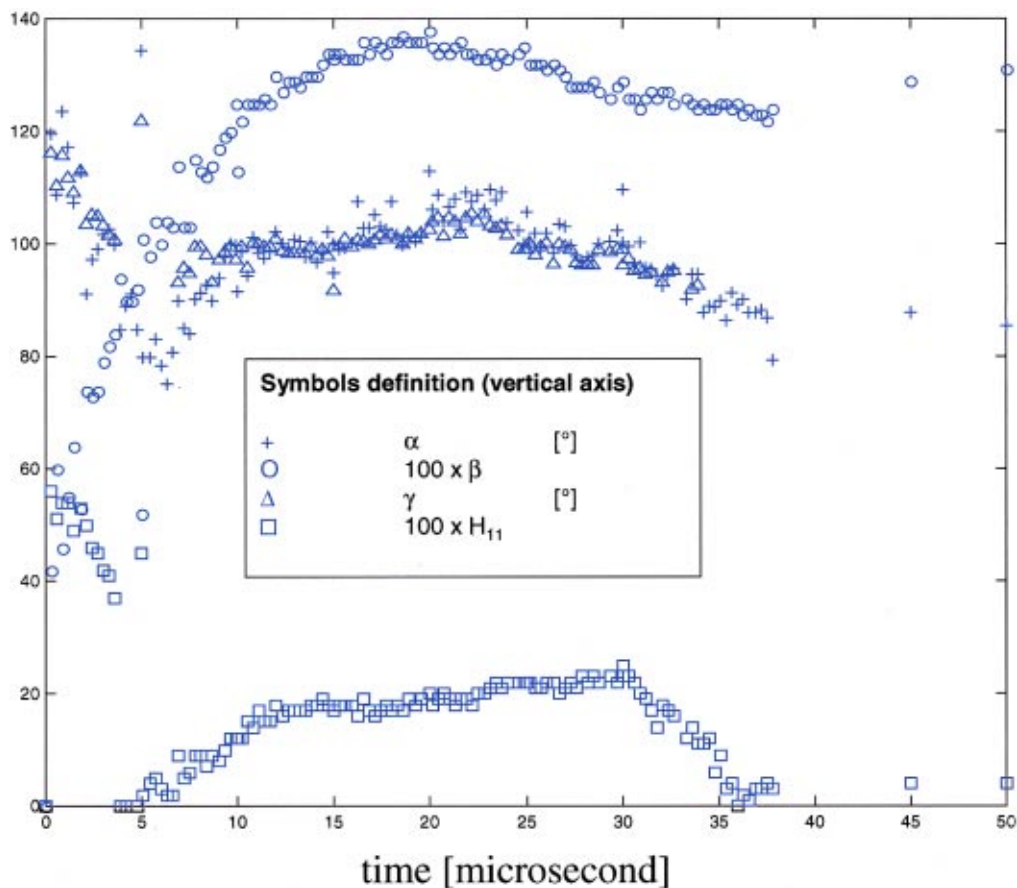


Fig. 12 Time evolution of the spread factor β , the contact angle α , the first ripple angle γ , and the first ripple nondimensional height H_{11} in the case ($v_0=2.31$ m/s, $T_{2,0}=59^\circ\text{C}$). The error is estimated in Section 2.3 and in Fig. 10.

focused on the slow viscous flow regime, neglecting flow inertia in the Navier-Stokes equations. Publications can be found stating that inertia effects on the wetting angle can be ignored for $Ca \leq O(0.1)$, without commenting on the influence of the Weber number ([40]). However, most of these wetting studies are performed with high viscosity oils. In the first regime of the droplet spreading observed in this study, the measured contact line velocities of 2–4 m/s correspond to Ca of the order of $1.5 \cdot 10^{-2}$ – $3.2 \cdot 10^{-2}$, and simultaneously to We of the order of 7 to 28. These moderate Weber number clearly implies that the fluid inertia is not negligible in comparison with capillary forces. This indicates the existence of situations where inertia is not negligible even at low Ca , for example in the case of low viscosity materials such as liquid metals.

A second limitation of Hoffman's correlation and of its hydrodynamic justifications is that they are expressed for steady flows only. Therefore, the application of Hoffman's correlation to an unsteady droplet impact is questionable. However, since Hoffman's correlation is the only widely known available general wetting correlation, it is worth comparing it with our measurements.

Quantitatively, it is difficult to compare the evolution of α with the evolution of the capillary number in this first regime since the equilibrium wetting angle is a priori unknown, and since we only measured an average velocity at the contact line, meaning an average Ca . Assuming an equilibrium wetting angle near zero, these values of Ca of $1.5 \cdot 10^{-2}$ and $3.2 \cdot 10^{-2}$ correspond via Eqs. (10)–(11) to wetting angles of, respectively, 59 deg and 77 deg. The assumption of a small equilibrium wetting angle value has been confirmed to some extent in this study experimentally. To this end, we placed on a microheater a wafer slide supporting a

solidified solder droplet (80 μm diameter) and heated the slide at 180°C during two minutes. Frames (a) and (b) in Fig. 13 are top views of the droplet respectively before (at solid state) and at the end of the heating. The drastic increase of diameter of the drop during melting indicates that the melting drop wets the substrate very well creating a film-like structure, corresponding to a small equilibrium wetting angle. We used atomic force microscopy (AFM) in order to quantify the wetting angle value as follows. The slide was removed from the heater right after heating and cooled on a steel surface at ambient temperature in order to freeze the equilibrium wetting angle. It is worth noting that AFM measurements of a liquid surface, in particular of a contact line region at relatively high temperatures are not very reliable and difficult to perform since AFM has been developed for solid surfaces. Implementation in liquid and molten interfaces measurements is at best at its infancy ([41]). The measured values of the frozen contact angle, from the border of the contact line up to nine microns from that line, were smaller than 30 deg (Fig. 13). Even if the equilibrium angle were 40 deg, the dynamic angles values calculated with Hoffman's correlation would only slightly increase (respectively from 59 deg to 65 deg and from 77 deg to 81 deg as discussed earlier), which still does not agree with the measured values that all lie between 90 deg and 140 deg. The fact that a single correlation Eq. (9) could be extracted from impacts with different velocities (Fig. 11) also suggests that Hoffman's correlation is not valid in the first part of the curve describing our measurements. Since Hoffman's correlation does not account for the bulk fluid inertia and the influence of the free surface shape in

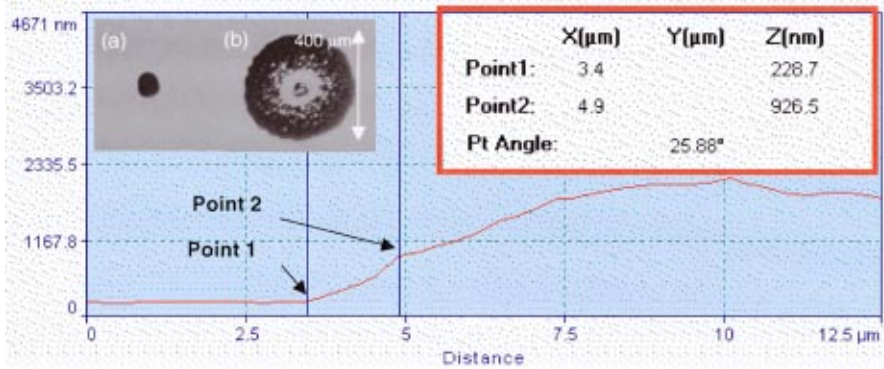


Fig. 13 Contact angle measurement with atomic force microscopy. The two vertical lines determine the position of the angle measurement on the splat profile. Frames (a) and (b) show the top view of the same (previously solidified) drop before (a) and after two minutes heating (b) above its melting temperature (180°C).

the vicinity of the contact line, further measurements had to be performed in order to consider the influence of these phenomena on droplet spreading.

The influence of the free surface motion near the wetting angle on this same angle can be examined by tracking the position of the first free surface ripple relative to the contact line. A characteristic free surface point describing the location of the first ripple is the lowest point above the substrate where the horizontal cross section of the droplet reaches a local maximum, represented by point *B* (or *F*) in Fig. 3 (this point can fall on the contact line, e.g., when the drop has a meniscus shape). An indicator of the influence of the first ripple position on the contact angle α is the angle γ , defined as the angle BAG (or AGF) in Fig. 3. It is worth noting that γ cannot be defined when points B and A (or F and G) coincide. This “first ripple angle” γ , when defined, is plotted in Fig. 12 as a function of time for the case (2.31 m/s, 59°C). A clear relation between α and γ during this first part of the spreading is obvious, and is also visible in the three other wetting angle measurement sequences (not plotted in Fig. 12 for clarity), as well as in the frames 2 and 3 of Fig. 5. The nondimensional height of the first ripple above the substrate H_{11} is also plotted in Fig. 12 in order to determine unequivocally the position of the first ripple.

The second regime of the spreading ($\beta > 0.8$) allows a better insight into the relation between γ and α . In Fig. 12 these two angles values exhibit a coordinated increase and subsequent decrease for $t \in [15, 30 \mu\text{s}]$. This indicates that the apparent wetting angle and the bending of the free surface over it represented by γ are dependent. This makes sense physically, for example, when one considers the limit case where the contact line freezes suddenly and the first ripple continues to advance because of the bulk fluid flow, as in cases (1.49 m/s, 65°C) and (2.31, 59) in Fig. 11: Here the apparent α will increase only because of the combination between bulk fluid dynamics and heat transfer, and not because of wetting phenomena. Frames 3–5 in Fig. 4 show a similar increase and subsequent decrease of the value of alpha, as in the measurement (1.49, 65). It is worth noting that the apparent receding observed in both low-temperature cases (Fig. 6, Fig. 11, and Fig. 12) is not consistent with the fact that solidification arrests the spreading at low temperature. The exact reasons are not clear to us at the present time.

Another increase and subsequent decrease of the value of α , smaller than in both low-temperature cases, is also observed in Fig. 11 in one high temperature case (2.35, 145). This can also be correlated with a bending of the free surface above the substrate and a corresponding increase of γ . Contrary to both low-temperature cases, this bending is probably caused by the bulk fluid motion instead of solidification, since the latter only affects the motion of the contact line at a later stage. In the other high-temperature case (1.51, 119) the wetting angle remains approxi-

mately constant at 90 deg for $\beta > 1$, while the characteristic point describing the location of the first ripple falls on the contact line. This absence of bending of the free surface near the substrate could be explained by an impact velocity lower than in the case (2.35, 145).

We also attempted to test Hoffman’s correlation in the second regime for both our high substrate temperature cases. Contact line velocities were estimated to be 1.44 m/s and 0.84 m/s for the cases (2.35 m/s, 145°C) and (1.51, 119), respectively, in the ranges of $\beta \in (1.4, 1.8)$ and $(1.2, 1.6)$. These velocities correspond to Ca of $1.1 \cdot 10^{-2}$ and $6.3 \cdot 10^{-3}$. The resulting wetting angle values obtained from Hoffman’s correlation, assuming again an equilibrium wetting angle of zero, are 53 and 43 deg, respectively. These values differ greatly from the measured values of about 90 deg. It should be noted that this finding is not sensitive to the assumed value of the equilibrium wetting angle: even if the measured equilibrium angle were 40 deg, the wetting angle predicted by Hoffman’s correlation would be increased by less than 11 deg, which is far from sufficient to yield agreement with our measurements.

4 Conclusion

To the best of our knowledge, this study presents the first experimental results on the transient fluid dynamics, wetting, and solidification of molten microdroplets impacting on a substrate, which are directly relevant to the novel solder jetting technology in manufacturing of microelectronics. It was shown that the ripples on the solidified drop surface are due to a strong coupling between flow oscillations and solidification, as was suggested by earlier numerical results pertaining to a comparable parameter range ([15,16]). The value of the substrate temperature was varied in order to study its influence on the spreading and solidification process. Transient measurements of the droplet height above the substrate have been carried out, showing a damped oscillation. Our results suggest that the solidification time depends nonmonotonically on the substrate temperature. This finding, although appearing counterintuitive, is supported by a simple order of magnitude analysis. Transient measurements of the spread factor showed that the substrate temperature significantly affects the spreading for substrate temperatures ranging from 48°C to 98°C ($Ste = 0.77$ to 0.48). This indicates that spreading is arrested by solidification at the wetting line. At higher temperatures, the spread factor was practically independent of the substrate temperature. Measurements of the wetting angle for different conditions of impact velocities and substrate temperature have also been carried out. It was established that the wetting angle dynamics is strongly coupled to the evolution of the droplet free surface and no quantitative agreement with Hoffman’s correlation was found. Two successive regimes during the spreading have been

distinguished. The influence of the initial conditions on the evolution of the apparent wetting angle was analyzed in both regimes.

Acknowledgments

This work has been partially supported by the Swiss National Science Foundation (Grant No. 21-49183.96). The authors would like to acknowledge Stefan Haferl whose experience with atomic force microscopy and valuable advice were a great help for realizing the measurement in Fig. 13.

Nomenclature

| | |
|-----------|---|
| Ca | = capillary number ($\mu\nu_c\sigma^{-1}$) |
| c_p | = specific heat ($\text{J kg}^{-1} \text{K}^{-1}$) |
| d | = diameter (m) |
| E | = energy (J) |
| f | = frequency (s^{-1}) |
| h | = heat transfer coefficient ($\text{W m}^{-2} \text{K}^{-1}$) |
| H | = nondimensional height ((visible height)/ d_0) |
| L | = latent heat (J kg^{-1}) |
| Oh | = Ohnesorge number ($(\text{We})^{1/2}/\text{Re}$) |
| Pr | = Prandtl number ($\mu c_p/\lambda_l^{-1}$) |
| \dot{q} | = heat transfer rate (W) |
| Re | = Reynolds number ($\rho\nu_0 d_0 \mu^{-1}$) |
| S | = surface (m^2) |
| Ste | = Stefan number ($c_{pl}(T_m - T_{2,0})L^{-1}$) |
| t | = time(s) |
| T | = temperature (K) |
| V | = volume (m^3) |
| v | = velocity (m s^{-1}) |
| We | = Weber number ($\rho v_0^2 d_0 \sigma^{-1}$) |

Greek Symbols

| | |
|-----------|--|
| α | = apparent wetting angle |
| β | = spread factor |
| γ | = first ripple angle |
| Δ | = difference |
| λ | = thermal conductivity ($\text{W m}^{-1} \text{K}^{-1}$) |
| μ | = dynamic viscosity (Pa s) |
| ρ | = density (kg m^{-3}) |
| σ | = surface energy (J m^{-2}) |

Subscripts

| | |
|----------|----------------------------|
| 0 | = initial |
| 1 | = droplet |
| 2 | = substrate top surface |
| 3 | = substrate bottom surface |
| 11 | = first ripple |
| c | = contact line |
| e | = effective |
| eq | = equilibrium |
| l | = liquid |
| m | = melting point |
| max | = maximum |
| s | = solid, solidification |
| spr | = spreading |
| ∞ | = final, arrested |

References

- [1] Orme, M., 1993, "A Novel Technique of Rapid Solidification Net-Form Materials Synthesis," *J. Mater. Eng. Perform.*, **2**, No. 3, pp. 399–405.
- [2] Orme, M., Huang, C., and Courter, J., 1996, "Deposition Strategies for Control of Microstructures Microporosity and Surface Roughness in Droplet-Based Solid Freeform Fabrication of Structural Materials," *Melt Spinning, Strip Casting and Slab Casting*, Matthys, E. F., and Truckner, W. G., eds., The Minerals, Metals and Materials Society, Warrendale, PA, pp. 125–143.
- [3] Hayes, D. J., and Wallace, D. B., 1998, "Solder Jet Printing: Wafer Bumping and CSP Applications," *Chip Scale Rev.*, **2**, No. 4, pp. 75–80.
- [4] Waldvogel, J. M., Diversiev, G., Poulikakos, D., Megaridis, C. M., Attinger, D., Xiong, B., and Wallace, D. B., 1998, "Impact and Solidification of

Molten-Metal Droplets on Electronic Substrates," *ASME J. Heat Transfer*, **120**, p. 539.

- [5] Haferl, S., Zhao, Z., Giannakouros, J., Attinger, D., and Poulikakos, D., 2000, "Transport Phenomena in the Impact of a Molten Droplet on a Surface: Macroscopic Phenomenology and Microscopic Considerations, Part I: Fluid Dynamics," *Annu. Rev. Heat Transfer*, C. L. Tien, ed.
- [6] Attinger, D., Haferl, S., Zhao, Z., and Poulikakos, D., 2000, "Transport Phenomena in the Impact of a Molten Droplet on a Surface: Macroscopic Phenomenology and Microscopic Considerations, Part II—Heat Transfer and Solidification," *Annu. Rev. Heat Transfer*, C. L. Tien, ed., in press.
- [7] Amon, C. H., Schmaltz, K. C., Merz, R., and Prinz, F. B., 1996, "Numerical and Experimental Investigation of Interface Bonding via Substrate Remelting of an Impinging Molten Metal Droplet," *ASME J. Heat Transfer*, **118**, pp. 164–172.
- [8] Bennett, T., and Poulikakos, D., 1994, "Heat Transfer Aspects of Splat-Quench Solidification: Modeling and Experiment," *J. Mater. Sci.*, **29**, pp. 2025–2039.
- [9] Pasandideh-Fard, M., Bohla, R., Chandra, S., and Mostaghimi, J., 1998, "Deposition of Tin Droplets on a Steel Plate: Simulations and Experiments," *Int. J. Heat Mass Transf.*, **41**, No. 19, pp. 2929–2945.
- [10] Wang, G. X., and Matthys, E. F., 1996, "Experimental Investigation of Interfacial Thermal Conductance for Molten Metal Solidification on a Substrate," *ASME J. Heat Transfer*, **118**, pp. 157–163.
- [11] Blake, T. D., and Haynes, J. M., 1969, "Kinetics of Liquid/Liquid Displacement," *J. Colloid Interface Sci.*, **30**, pp. 421–423.
- [12] Dussan, E. B., 1979, "On the Spreading of Liquids on Solid Surfaces: Static and Dynamic Contact Lines," *Annu. Rev. Fluid Mech.*, **11**, pp. 371–400.
- [13] Hoffman, R. L., 1975, "A Study of the Advancing Interface, I—Interface Shape in Liquid-Gas Systems," *J. Colloid Interface Sci.*, **50**, pp. 228–241.
- [14] Fukai, J., Shiba, Y., Yamamoto, T., Miyatake, O., Poulikakos, D., Megaridis, C. M., and Zhao, Z., 1995, "Wetting Effects on the Spreading of a Liquid Droplet Colliding With a Flat Surface: Experimental and Modeling," *Phys. Fluids*, **7**, No. 2, pp. 236–247.
- [15] Waldvogel, J. M., and Poulikakos, D., 1997, "Solidification Phenomena in Picoliter Size Solder Droplet Deposition on a Composite Substrate," *Int. J. Heat Mass Transf.*, **40**, No. 2, pp. 295–309.
- [16] Xiong, B., Magaridis, C. M., Poulikakos, D., and Hoang, H., 1998, "An Investigation of Key Factors Affecting Solder Microdroplet Deposition," *ASME J. Heat Transfer*, **120**, pp. 259–270.
- [17] Inada, S., Miyasaka, Y., Mishida, K., and Chandratilleke, G. R., 1983, "Transient Temperature Variation of a Hot Wall due to an Impinging Water Drop: Effect of Subcooling of the Water Drop," *Proceedings of the Joint ASME/JSME Thermal Engineering Conference*, Vol. 1, ASME, New York, pp. 173–182.
- [18] Pederson, C. O., 1970, "An Experimental Study of the Dynamic Behavior and Heat Transfer Characteristics of Water Droplets Impinging Upon a Heated Surface," *Int. J. Heat Mass Transf.*, **13**, pp. 369–381.
- [19] Savic, P., and Boulton, G. T., 1955, "The Fluid Flow Associated With the Impact of Liquid Drops With Solid Surfaces," Report No. MT-26, Nat. Res. Council Canada.
- [20] Toda, S., 1974, "A Study of Mist Cooling" (2nd Report: Theory of Mist Cooling and Its Fundamental Experiments), *Heat Transfer Japan. Res.*, **3**, No. 1, pp. 1–44.
- [21] Ueda, T., Enomoto, T., and Kanetsuki, M., 1979, "Heat Transfer Characteristics and Dynamic Behavior of Saturated Droplets Impinging on a Heated Vertical Surface," *Bull. JSME*, **22**, No. 167, pp. 724–732.
- [22] Chandra, S., and Avedisian, C. T., 1991, "On the Collision of a Droplet With a Solid Surface," *Proc. R. Soc. London, Ser. A*, **432**, pp. 13–41.
- [23] Stow, C. D., and Hadfield, M. G., 1981, "An Experimental Investigation of Fluid Flow Resulting From the Impact of a Water Drop With an Unyielding Dry Surface," *Proc. R. Soc. London, Ser. A*, **373**, pp. 419–441.
- [24] Wachters, L. H., and Westerling, N. A. J., 1966, "The Heat Transfer From a Hot Wall to Impinging Water Drop in the Spherical State," *Chem. Eng. Sci.*, **21**, pp. 1047–1056.
- [25] Mundo, C., Sommerfeld, M., and Tropea, C., 1995, "Droplet-Wall Collisions: Experimental Studies of the Deformation and Breakup Process," *Int. J. Multiphase Flow*, **21**, pp. 151–173.
- [26] Yarin, A. L., and Weiss, D. A., 1995, "Impact of Drops on Solid Surfaces: Self-Similar Capillary Waves and Splashing as a New Type of Kinematic Discontinuity," *J. Fluid Mech.*, **283**, pp. 141–173.
- [27] Ohl, C. D., Philipp, A., and Lauterborn, W., 1995, "Cavitation Bubble Collapse Studies at 20 Million Frames Per Second," *Ann. Phys. (Leipzig)*, **4**, No. 1, pp. 26–34.
- [28] Levin, Z., and Hobbs, P. V., 1971, "Splashing of Water Drops on Solid and Wetted Surfaces: Hydrodynamics and Charge Separations," *Philos. Trans. R. Soc. London, Ser. A*, **269**, pp. 555–585.
- [29] Hayes, D. J., Wallace, D. B., and Boldman, M. T., 1992, "Picoliter Solder Droplet Dispersion," *ISHM Symposium 92 Proceedings*, pp. 316–321.
- [30] Arx, M. v., 1998, "Thermal Properties of CMOS Thin Films," Ph.D. thesis, ETH Zurich.
- [31] Poulikakos, D., 1994, *Conduction Heat Transfer*, Prentice-Hall, Englewood Cliffs, NJ.
- [32] Bennett, T., and Poulikakos, D., 1993, "Splat-Quench Solidification: Estimating the Maximum Spreading of a Droplet Impacting a Solid Surface," *J. Mater. Sci.*, **28**, pp. 963–970.
- [33] Schiaffino, S., and Sonin, A. A., 1997, "Molten Droplet Deposition and Solidification at Low Weber Numbers," *Phys. Fluids*, **9**, pp. 3172–3187.

- [34] Fukai, J., Zhao, Z., Poulidakos, D., Megaridis, C. M., and Miyatake, O., 1993, "Modeling of the Deformation of a Liquid Droplet Impinging Upon a Flat Surface," *Phys. Fluids A*, **5**, pp. 2588–2599.
- [35] Schiaffino, S., and Sonin, A. A., 1997, "Motion and Arrest of a Molten Contact Line on a Cold Surface: An Experimental Study," *Phys. Fluids*, **9**, pp. 2217–2226.
- [36] Pasandideh-Fard, M., Qiao, Y. M., Chandra, S., and Mostaghimi, J., 1996, "Capillary Effects During Droplet Impact on a Solid Surface," *Phys. Fluids*, **8**, pp. S650–S659.
- [37] Zarzalejo, L. J., Schmalz, K. S., and Amon, C. H., 1999, "Molten Droplet Solidification and Substrate Remelting in Microcasting, Part I—Numerical Modeling and Experimental Verification," *Heat Mass Transfer*, **34**, pp. 477–485.
- [38] Tanner, L. H., 1979, "The Spreading of Silicon Oil Drops on Horizontal Surfaces," *J. Phys. D: Appl. Phys.*, **12**, pp. 1473–1484.
- [39] Voinov, O. V., 1976, "Hydrodynamics of Wetting," *Fluid Dyn.*, **11**, pp. 714–721.
- [40] Kistler, S. F., 1993, "Hydrodynamics of Wetting," *Wettability*, Berg, J. C., ed., Marcel Dekker, New York.
- [41] Haferl, S., Poulidakos, D., and Zhao, Z., 1999, "Employing Scanning Force Microscopy to Investigate the Dynamic Wetting Behavior of Liquid Microdroplets on Smooth Surfaces: Gathered Experiences," Poster Presentation, European Research Conferences (EURESCO) Solid/Fluid Interfaces: Complex Fluid Interfaces, Castelvecchio Pascoli, Italy.
- [42] Waldvogel, J. M., Poulidakos, D., Wallace, D. B., and Marusak, R., 1996, "Transport Phenomena in Picoliter Size Solder Droplet Dispersion," *ASME J. Heat Transfer*, **118**, pp. 148–156.

Forced Convection in High Porosity Metal Foams

V. V. Calmidi¹

R. L. Mahajan

CAMPmode,
Department of Mechanical Engineering,
University of Colorado at Boulder,
Boulder, CO 80309-0427

This paper reports an experimental and numerical study of forced convection in high porosity ($\epsilon \sim 0.89\text{--}0.97$) metal foams. Experiments have been conducted with aluminum metal foams in a variety of porosities and pore densities using air as the fluid medium. Nusselt number data has been obtained as a function of the pore Reynolds number. In the numerical study, a semi-empirical volume-averaged form of the governing equations is used. The velocity profile is obtained by adapting an exact solution to the momentum equation. The energy transport is modeled without invoking the assumption of local thermal equilibrium. Models for the thermal dispersion conductivity, k_d , and the interstitial heat transfer coefficient, h_{sf} , are postulated based on physical arguments. The empirical constants in these models are determined by matching the numerical results with the experimental data obtained in this study as well as those in the open literature. Excellent agreement is achieved in the entire range of the parameters studied, indicating that the proposed treatment is sufficient to model forced convection in metal foams for most practical applications. [S0022-1481(00)01903-4]

Keywords: Convection, Experimental, Heat Transfer, Porous Media, Thermal

Introduction

Forced and buoyancy-induced convection in porous media have been studied extensively for over 50 years (see Kaviany [1] for a good review on the subject). However, most studies in this category have been restricted to packed beds and granular materials, since they have direct application to naturally occurring porous media, with porosities in the range 0.4–0.6. As discussed below, there are relatively few investigations of transport phenomena in very high porosity media ($\epsilon > 0.9$) such as metal foams.

Only during the last ten years, transport phenomena in metal foams have started to receive attention ([2–6]). Hunt and Tien [2] studied forced convection in metal foams with water as the fluid phase. Using the technique of volume averaging, and under the simplifying assumption of local thermal equilibrium, they showed that a single energy equation could adequately describe forced convection in metal foams. Sathe et al. [3] studied combustion in metal foams as applied to porous radiant burners. Lee et al. [4] studied the application of metal foams as high-performance air-cooled heat sinks in electronics packaging. In their experimental study, they demonstrated that a 1 cm² chip dissipating 100 W could be cooled using an aluminum foam heat sink, and a low-power muffin fan. Recently, Calmidi and Mahajan [5] addressed heat conduction in aluminum metal foams. They obtained experimental data and developed an analytical model for the thermal conductivity, taking into account the open-celled structure of metal foams. Bhattacharya et al. [6] extended that work to cover a wider range of solid to fluid conductivity ratios. Further, the analytical model was refined to address issues of isotropicity.

Our review suggests that there are no thermal transport studies in the literature (pertaining to high porosity metal foams) that (a) employ experimentally validated thermal conductivity data, (b) consider local thermal nonequilibrium among phases, and (c) accurately consider metal foam microstructure. The focus of this paper is to take these factors into account.

Metal foams (Fig. 1) can be broadly classified as porous media

in which the medium has a distinct but continuous and rigid solid phase, and a fluid phase. They are typically available in high porosities ($\epsilon > 0.9$). They also have a unique open-celled structure. As a result, most of the past studies on packed beds, and granular porous media are not applicable to metal foams. There is thus a need to develop a fundamental understanding of the transport phenomena in these foams. As shown later in this paper, both numerical and experimental studies are currently needed to generate heat transfer information for practical applications.

Energy transport in porous media has generally been studied with the assumption of local thermal equilibrium among the two phases. That is, a single homogeneous equation is used to describe transport with the assumption that the solid and fluid phases have the same temperature field. Following such an assumption, the effective stagnant thermal conductivity, k_e , of a porous medium is used to account for the solid and fluid phase conductivities. The stagnant conductivity k_e , is sometimes augmented by the dispersion conductivity, k_d . Dispersion is a hydrodynamic phenomenon which becomes prominent at high Reynolds numbers, especially if k_e is small in magnitude. Several empirical and analytical studies have attempted to quantify dispersion in porous and fibrous media ([2,7–9]). The general conclusion is that at high Peclet numbers, k_d is linearly proportional to the local flow velocity.

Under certain situations, however, the assumption of local thermal equilibrium has to be relaxed. Such a condition might arise when there is internal heat generation ([3]) or when the difference in the stagnant conductivities of the solid and the fluid phases is significant. The latter situation is encountered when metal foams are used with low-conductivity fluids like air or water. With local thermal nonequilibrium, the solid and fluid temperature fields have to be obtained separately. In addition, appropriate coupling is necessary between the solid and fluid phase energy equations to account for the interfacial heat transfer.

The focus of this study is forced convection in metal foams. First, the experimental method used to obtain Nusselt number data for a number of aluminum metal foam samples with air as the fluid medium is described. Following a discussion of the appropriate form of the governing equations of momentum and energy in metal foams, the details on the numerical method used to solve them are provided. Finally, the numerical results are compared with the experimental data to obtain values of empirical constants

¹To whom correspondence should be addressed. Currently at the Advanced Thermal Engineering Laboratory, IBM Microelectronics, 1701 North Street, Endicott, NY 13760.

Contributed by the Heat Transfer Division for publication in the JOURNAL OF HEAT TRANSFER. Manuscript received by the Heat Transfer Division, May 17, 1999; revision received, Feb. 14, 2000. Associate Technical Editor: R. Douglass.

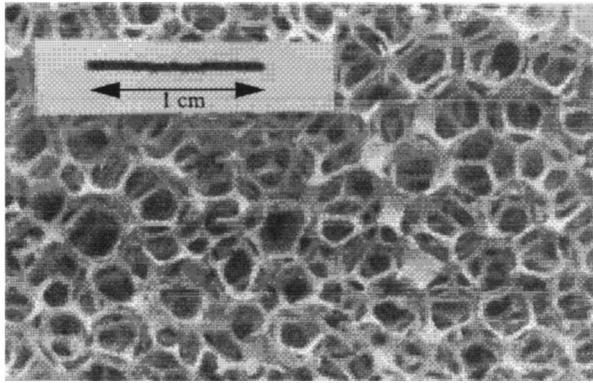


Fig. 1 Picture of a typical metal foam sample

in the thermal dispersion and the interfacial heat transfer coefficient models.

Experiment

A schematic of the experimental setup is shown in Fig. 2. Aluminum metal (alloy T-6201) foam samples of size 63 mm×45 mm×196 mm were used in the experiments. Table 1 lists the characteristics of the samples that were used in the experiment. The porosity is the void volume fraction and the pore density is the number of pores per unit length of the material (PPI, pores per inch) and, d_f and d_p are the average fiber diameter and pore diameter, respectively. The porosity of each sample was estimated using the weight of a given volume of the sample and the density of aluminum alloy T-6201. The fiber diameter, d_f , was measured using a microscope, and the pore diameter, d_p , was estimated by counting the number of pores in a given length of material. Both d_f and d_p are average values. The pore density (PPI) is a nominal value supplied by the manufacturer.

For each experimental run, a metal foam sample was placed in a plexiglass tube. Air flow was achieved by connecting the plexi-

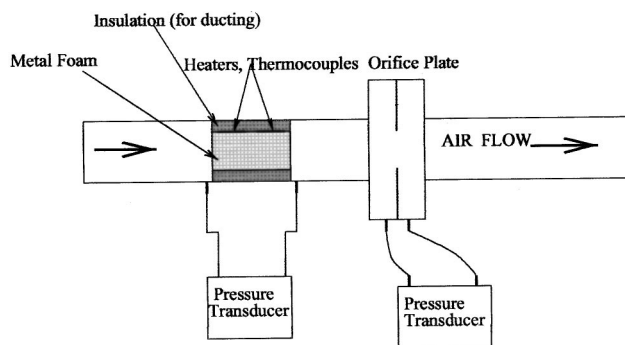


Fig. 2 Schematic of the experimental setup used for the forced convection experiments

glass tube to a fan/motor assembly (not shown in figure) downstream of the test sample. The direction of air flow is from left to right as shown in Fig. 2. Very low conductivity styrofoam was used to block the space around the sample to fully prevent flow bypass. A pressure transducer was used to measure the pressure drop across the metal foam sample. An orifice plate was used to measure the flow rate through the metal foam sample.

The metal foam samples were brazed to 9.5-mm thick aluminum skins on two sides. On one of the skins, grooves were cut to isolate a section of the metal foam. Patch heaters were fixed to this isolated portion of the skin between the grooves (Fig. 3). The resulting physical dimensions of the heated section of the metal foam are 63 mm×45 mm×114 mm. The grooves in the skin were loosely filled with insulating material to prevent conduction losses from the heated to the unheated sections. Then, two thin (2-mm) grooves were cut in the metal foam below the grooves on the skin (Fig. 3). This was done to prevent back-conduction of heat from the heated to the unheated sections. This isolating scheme ensures that fully developed flow enters the heated section of the metal foam (Calmidi [10]). Six 36-gage T-type thermocouples (axial thermocouples) were fixed along axial locations in the skin as shown in Fig. 3. For some samples, two thermocouples were fixed at off-center locations (25 mm from the center). Two additional thermocouples were used to monitor the ambient temperature and the temperature of the air at the midplane before it entered the heated section. The total flow rate was estimated according to ASME/ISO-5167-1:1991 using the pressure drop across the orifice plate as well as the temperature and pressure of the air entering the orifice plate. The average velocity (superficial) of air flowing through the metal foam, u_o , is then the average flow rate divided by the area of cross section.

During a typical experiment run, the speed of the motor was adjusted such that the flow velocity was set at a desired value. The power input to the patch heaters was set between 15–35 W. The temperature readings indicated by the thermocouples were monitored until they reached steady state. This took approximately 5–10 minutes depending on the flow velocity. It typically took longer at lower flow velocities. The temperatures were monitored for an additional interval of five minutes to ensure that steady state had indeed been reached. Steady state was assumed if the temperature did not vary more than 0.1°C during a five-minute interval. The temperature readings of all the thermocouples with respect to the ambient temperature were noted. The temperature variation along the axis (x -direction) was within 15 percent of the average value, while the temperature variation perpendicular to the axis (z -direction) was less than 0.1°C in all the experimental runs. The air temperature before it entered the heated section (T_{in}) was also measured. It was slightly higher than the ambient temperature (T_{amb}), but always less than two percent of the maximum wall temperature, indicating that back-conduction effects were negligible. Figure 4 shows the data (wall temperature variation) collected from a typical experiment for Sample 2 (Table 1). The data collected for all the samples is documented in Calmidi [10].

Using the measured wall temperature data, the heat flux is con-

Table 1 Characteristics of metal foam samples used in experimental study

| # | Porosity | PPI | d_f (m) Fiber Dia. | d_p (m) Pore Dia. | f | K (*10 ⁷ m ²) | k_{se} (W/m-K) | k_{fe} (W/m-K) |
|---|----------|-----|-------------------------|------------------------|-------|---|---------------------|---------------------|
| 1 | 0.9726 | 5 | 0.00050 | 0.00402 | 0.097 | 2.7 | 2.48 | 0.0256 |
| 2 | 0.9118 | 5 | 0.00055 | 0.00380 | 0.085 | 1.8 | 6.46 | 0.0237 |
| 3 | 0.9486 | 10 | 0.00040 | 0.00313 | 0.097 | 1.2 | 4.10 | 0.0248 |
| 4 | 0.9546 | 20 | 0.00030 | 0.00270 | 0.093 | 1.3 | 3.71 | 0.0250 |
| 5 | 0.9005 | 20 | 0.00035 | 0.00258 | 0.088 | 0.9 | 7.19 | 0.0233 |
| 6 | 0.9272 | 40 | 0.00025 | 0.00202 | 0.089 | 0.61 | 5.48 | 0.0242 |
| 7 | 0.9132 | 40 | 0.00025 | 0.00180 | 0.084 | 0.53 | 6.37 | 0.0237 |

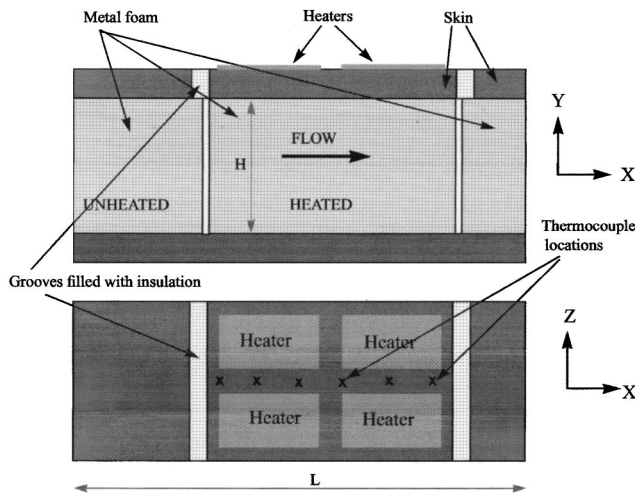


Fig. 3 Schematic of side and top views of metal foam samples used in the experiments

verted into an average Nusselt number. The average temperature ΔT_{avg} is defined as the average of the six values of the temperature measured. That is,

$$\Delta T_{avg} = \left(\sum_{i=1}^n T_{wi} \right) / n - T_{in} \quad (1)$$

where n is the number of points where the wall temperature was measured. It is noted that, although this value is not the actual average wall temperature, it does represent an appropriate scale to represent the temperature difference. Next an average heat transfer coefficient is defined as

$$\bar{h} = q / (A \Delta T_{avg}) \quad (2)$$

where q is the power input to the heaters and A is the area of cross section of the metal foam. From this, an average Nusselt number is calculated using

$$Nu = \bar{h} L / k_e \quad (3)$$

where L is the length of the heated section of the metal foam, and k_e is the effective thermal conductivity ($k_{fe} + k_{se}$) as given in Table 1.

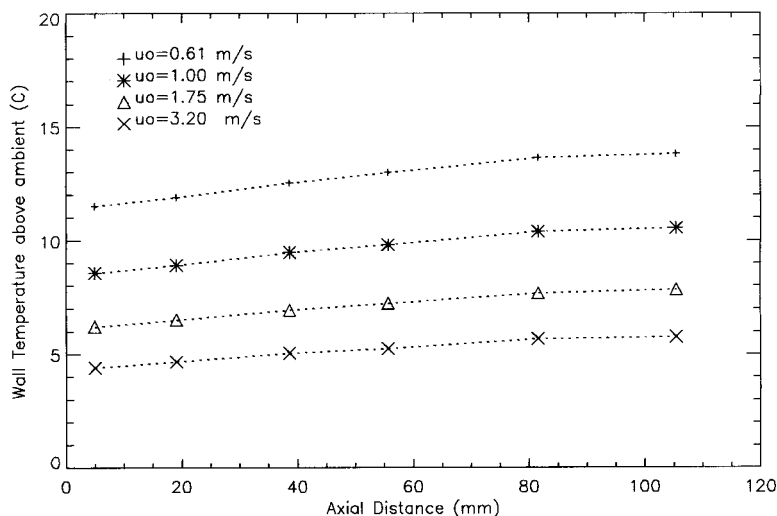


Fig. 4 Variation in wall temperature with average flow velocity (Sample 2, Table 1)

The effect of varying the power input to the heaters was also investigated to verify that nonlinear effects like buoyancy, radiation, and property variation were negligible. In all cases studied, the Nusselt number was found to be nearly independent of the input power.

The experimental error estimate can be made based on the accuracies in the measurement of the individual quantities. The error (thermocouple calibration and resolution of the data acquisition device) in the estimation of ΔT_{avg} is 0.3°C. Based on the published accuracies of the voltmeter and ammeter, the error in the estimate of q is two percent. The errors in the estimate of the length and area are neglected because they are extremely low (<0.3 percent of the measured quantity). Based on these values, the error in the estimate of the Nusselt numbers is 4.3 percent. This estimate is based on a representative value of ΔT_{avg} of 8°C. Based on the accuracy of the pressure transducers, the error in the estimate of the velocity is 4.1 percent.

Analysis

The steady volume-averaged momentum equation that governs fluid flow in porous media is given by

$$\frac{\rho}{\varepsilon^2} \nabla \cdot \mathbf{u} \mathbf{u} = -\nabla p + \frac{\mu}{\varepsilon} \nabla^2 \mathbf{u} - \frac{\mu}{K} \mathbf{u} - \frac{\rho f}{\sqrt{K}} \|\mathbf{u}\| \mathbf{u}. \quad (4)$$

In Eq. (4), the drag due to the fibers is represented by the familiar non-Darcy formulation. The third term on the R.H.S. of Eq. (4) is the traditional Darcy term which is used to account for the pressure drop due to viscous friction at the walls of the fibers, and the fourth term is the nonlinear correction and represents the pressure drop due to the form drag and the flow separation that takes place at higher Reynolds numbers. A linear superposition of the two terms as shown here is semi-empirical, but has been known to match experimental data in many situations ([2,8,11–13]). A modified form of Eq. (4) was used by Calmidi [10], Chapter 3, to determine the permeability, K , and the inertia coefficient, f , of the metal foam samples. These are listed in Table 1.

The energy equations for the solid and the fluid phases based on thermal nonequilibrium are

$$0 = \frac{\partial}{\partial x} \left(k_{se} \frac{\partial T_s}{\partial x} \right) + \frac{\partial}{\partial y} \left(k_{se} \frac{\partial T_s}{\partial y} \right) - h_{sf} a_{sf} (T_s - T_f) \quad (5)$$

$$(\rho c_p)_{fu} \frac{\partial T_f}{\partial x} = \frac{\partial}{\partial x} \left((k_{fe} + k_d) \frac{\partial T_f}{\partial x} \right) + \frac{\partial}{\partial y} \left((k_{fe} + k_d) \frac{\partial T_f}{\partial y} \right) + h_{sf} a_{sf} (T_s - T_f). \quad (6)$$

The coupling between the two equations is achieved using the interfacial term which represents the heat transfer between the two phases via a heat transfer coefficient, h_{sf} , and the specific surface area, a_{sf} . It is important to note that Eqs. (5), and (6) are semi-empirical and are not the full volume-averaged forms of the energy equations ([14,15]). The full volume-averaged treatment is considerably complex, and has been solved exactly only for a one-dimensional system of parallel capillary tubes ([16]). However, it is noted that the semi-empirical treatment employed here has been successfully used in the past to model transport in beds of spheres ([17,18]).

An analytical model for obtaining the effective conductivity of metal foams has been derived in ([5]). Their experimentally validated model was based on the structure of metal foams. It is reproduced as

$$k_e = \left(\left(\frac{2}{\sqrt{3}} \right) \left(\frac{r \left(\frac{b}{L} \right)}{k_f + \left(1 + \frac{b}{L} \right) \frac{(k_s - k_f)}{3}} + \frac{(1-r) \left(\frac{b}{L} \right)}{k_f + \frac{2}{3} \left(\frac{b}{L} \right) (k_s - k_f)} \right) + \frac{\frac{\sqrt{3}}{2} \frac{b}{L}}{k_f + \frac{4r}{3\sqrt{3}} \left(\frac{b}{L} \right) (k_s - k_f)} \right)^{-1} \quad (7)$$

where $r = 0.09$, and the ratio b/L is given by

$$\frac{b}{L} = \frac{-r + \sqrt{r^2 + 4(1-\varepsilon) \frac{\sqrt{3}}{2} \left(\left(2 - r \left(1 + \frac{4}{\sqrt{3}} \right) \right) / 3 \right)}}{\frac{2}{3} \left(2 - r \left(1 + \frac{4}{\sqrt{3}} \right) \right)}. \quad (8)$$

The solid-phase conductivity, k_{se} , is obtained by setting $k_f = 0$, in Eq. (7). By doing so

$$k_{se} = \left(\left(\frac{2}{\sqrt{3}} \right) \left(\frac{r \left(\frac{b}{L} \right)}{\left(1 + \frac{b}{L} \right) \frac{k_s}{3}} + \frac{(1-r) \left(\frac{b}{L} \right)}{\frac{2}{3} \left(\frac{b}{L} \right) k_s} + \frac{\frac{\sqrt{3}}{2} \frac{b}{L}}{\frac{4r}{3\sqrt{3}} \left(\frac{b}{L} \right) k_s} \right) \right)^{-1}. \quad (9)$$

Similarly, k_{fe} is obtained by setting $k_s = 0$ in Eq. (7),

$$k_{fe} = \left(\left(\frac{2}{\sqrt{3}} \right) \left(\frac{r \left(\frac{b}{L} \right)}{k_f + \left(1 + \frac{b}{L} \right) \frac{(-k_f)}{3}} + \frac{(1-r) \left(\frac{b}{L} \right)}{k_f + \frac{2}{3} \left(\frac{b}{L} \right) (-k_f)} \right) + \frac{\frac{\sqrt{3}}{2} \frac{b}{L}}{k_f + \frac{4r}{3\sqrt{3}} \left(\frac{b}{L} \right) (-k_f)} \right)^{-1}. \quad (10)$$

Values of k_{se} and k_{fe} obtained using Eqs. (9) and (10) are listed in Table 1.

In Eqs. (5) and (6), the dispersion conductivity is assumed to be isotropic. That is

$$k_{dx} = k_{dy} = k_d. \quad (11)$$

Based on earlier work ([2,7]), the following model is proposed for the dispersion conductivity:

$$\frac{k_d}{k_e} = C_D (\text{Re}_K \text{Pr}_e) \frac{u}{u_o}. \quad (12)$$

In Eq. (12), the coefficient of thermal dispersion, C_D , remains to be determined. As a simplification, this model for k_d does not account for wall effects ([19,20]) except through the change in the velocity profile near the wall.

One of the most comprehensive models for the interfacial heat transfer coefficient, h_{sf} , for packed beds is by Wakao et al. ([17]). For foamed materials, however, no such general model exists. However, the radial temperature gradients within the fibers are expected to be small and it is reasonable to use the Nusselt number correlation for external flow over a body of an appropriate cross section. Based on a correlation developed by Zukauskas [21] for cylinders in crossflow in the range of Reynolds numbers (40–1000), a model for the interfacial heat transfer is proposed as follows:

$$\text{Nu}_{sf} = \frac{h_{sf} d_f}{k_f} = C_T \text{Re}^{0.5} \text{Pr}^{0.37}. \quad (13)$$

In Eq. (13), an empiricism has been introduced in the form of the undetermined coefficient C_T . The Reynolds number is based on the cylinder diameter and Pr is the fluid Prandtl number. In applying this correlation, the noncircular cross section of fibers has to be considered. However, upon examination of the Nusselt number correlations for external flow over bodies of varying cross sections ([22]), it appears that the exponent of the Reynolds number has a weak dependence on the cross section. The multiplicative constant in Eq. (13), however, varies considerably. Based on these observations, Zukauskas' correlation has been modified as shown in Eq. (13). Further, it is noted that, in Eq. (13), the Reynolds number is based on the fluid velocity near the fiber. Hence, due to the presence of the solid matrix, its point value is $\text{Re} = (u d_f / \varepsilon \nu)$. The solid-fluid interfacial surface area for arrays of parallel cylinders intersecting in the three mutually perpendicular directions is

$$a_{sf} = \frac{3 \pi d_f}{d_p^2}. \quad (14)$$

For metal foams, this expression is modified by taking the structure into account (i.e., open cells shaped like dodecahedra, and noncircular fiber cross-section). By doing so, the values of d_p and d_f , as given in Table 1, are multiplied by 0.59, and $1 - e^{-((1-\varepsilon)/0.04)}$, respectively (see [10], Chapter 1) before being used in Eq. (14).

The transport equations (Eqs. (4)–(6)) are nondimensionalized using $-X = x/H$, $Y = y/H$, $U = u/u_o$, $\theta = (T - T_{in}) / \Delta T_{\text{avg}}$ where u_o is the average velocity entering the channel, H is the height of the channel, ΔT_{avg} is the average wall temperature, and T_{in} in the inlet fluid temperature. The resulting equations are

$$\frac{d^2 U}{dY^2} = \frac{\varepsilon}{\sqrt{\text{Da}}} (U - 1) + \frac{\text{Re}_K}{\text{Da}} f \sqrt{\varepsilon} (U^2 - 1) \quad (15)$$

$$0 = \frac{1}{\text{Bi}_s} \left(\frac{d^2 \theta_s}{dX^2} + \frac{d^2 \theta_s}{dY^2} \right) - (\theta_s - \theta_f) \quad (16)$$

$$U \frac{\partial \theta_f}{\partial X} = \frac{\partial}{\partial X} \left(\left(\frac{\text{Da}}{\text{Re}_K \text{Pr}_{fe}} + C_D U \right) \frac{\partial \theta_f}{\partial X} \right) + \frac{\partial}{\partial Y} \left(\left(\frac{\text{Da}}{\text{Re}_K \text{Pr}_{fe}} + C_D U \right) \frac{\partial \theta_f}{\partial Y} \right) + \frac{\text{Bi}_f}{\text{Re}_K \text{Pr}_{fe}} (\theta_s - \theta_f) \quad (17)$$

where

$$\text{Re}_K = \frac{u_o \sqrt{K}}{\nu} \quad \text{Da} = \frac{\sqrt{K}}{H} \quad \text{Bi}_s = \frac{h_{sf} a_{sf} H^2}{k_{se}} \quad \text{Bi}_f = \frac{h_{sf} a_{sf} H \sqrt{K}}{k_{fe}} \quad (18)$$

Note that Bi_s and Bi_f are not constants but vary along the y -direction, since h_{sf} (Eq. (13)) depends on the velocity. In Eqs. (15)–(18), all quantities except C_D and C_T are known.

The heat dissipation from the heated wall occurs both through the fluid phase and the solid phase. Hence, the total heat transferred can be written as

$$q = \bar{h} L \Delta T_{\text{avg}} = - \int_0^L \left(k_{se} \frac{\partial T_s}{\partial y} + k_{fe} \frac{\partial T_f}{\partial y} \right) dx \quad (19)$$

Writing Eq. (19) in nondimensional form, an average Nusselt number for the heated surface is

$$\text{Nu} = \frac{\bar{h} L}{k_e} = - \int_0^{L/H} \left(\frac{k_{se}}{k_e} \frac{\partial \theta_s}{\partial Y} + \frac{k_{fe}}{k_e} \frac{\partial \theta_f}{\partial Y} \right) dX \quad (20)$$

Equation (20) has been formulated to directly compare experimental results with model predictions.

Numerical Procedure

A schematic of the numerical domain is shown in Fig. 5 along with the orientation of the coordinate axes. Numerical boundary conditions are also shown in Fig. 5. For the heated wall, the experimentally determined wall temperature profile is specified. The temperature gradients for both the solid phase and the fluid phase are zero on the insulated wall. At the inlet, the fluid is assumed to enter at the inlet temperature T_{in} . At the exit, a zero diffusion condition is assumed for the fluid phase. This assumption is reasonable, since advection is expected to be the dominant mode of transport in the streamwise (x) direction. The solid phase is assumed to be insulated at both the inlet and the exit.

A fully developed velocity profile is prescribed at the inlet. This velocity profile (function of Y alone) is calculated using the exact solution for the second-order nonlinear ODE, Eq. (15). Following Vafai and Kim [23], the exact solution due to flow through a channel is given by expressing the pressure drop in terms of the center-line velocity. It is reproduced below:

$$U = U_c \left[1 - \left(\frac{A+B}{A} \right) (\cosh(D(1-2Y+C)))^2 \right] \quad (21)$$

$$A = \varepsilon f \text{Re}/6\text{Da}^2 \quad B = \varepsilon/(4\text{Da}^2) + 2A$$

$$C = -\frac{1}{D} \text{acosh} \left(\sqrt{\frac{A+B}{A}} \right) - 1 \quad D = \sqrt{\frac{A+B}{2}}$$

Since the average velocity u_o , and not the center-line velocity is known, the center-line velocity had to be guessed and iterated until mass balance was achieved. That is, the integral of the non-dimensional velocity over the height of the channel is unity within

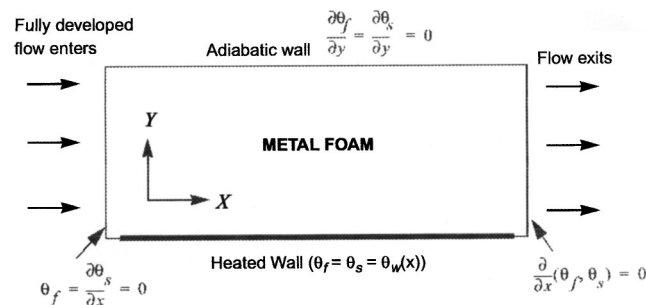


Fig. 5 Schematic of numerical domain with boundary conditions

a specified error of 10^{-5} . This method of calculating the velocity profile was checked by solving the full two-dimensional momentum equation, Eq. (4) in a rectangular domain with an aspect ratio (length to height) of two using the ADI Method of Peaceman and Rachford (see [24]). The fully developed velocity profile obtained from this simulation was identical to the exact solution given by Eq. (21). Since computational time could be saved considerably by using the exact solution, it was employed for all further computations.

The energy equations were solved using the ADI finite difference scheme of Peaceman and Rachford ([24]). The convective term in the fluid-phase equation was discretized using first-order upwind differencing for increased stability. The diffusion terms in the solid-phase and fluid-phase equations were discretized using three-point stencils in each direction. To avoid energy balance problems, the numerical domain was extended by five percent at the inlet and the exit. Extensions of 10 percent and 15 percent had no effect on the temperature field or the Nusselt number in the heated section. The equations were marched to asymptotic steady state. The convergence criterion for steady state was that the change in the solid-phase and fluid-phase temperatures was less than 10^{-4} between successive iterations. At steady state, a heat balance within one percent was obtained. A time-step of size 0.03 was found to be an efficient value. While reducing the time-step below this value did not have any effect on the final solution, the convergence rate slowed down.

Grid Dependency and Code Validation

A constant grid spacing was used in the X -direction and a variable grid spacing was used in the Y -direction. The variable grid was laid out in three layers. In Layers I and III, adjacent to the heated and insulated walls, respectively, a constant grid spacing ΔY was used. In Layer II, sandwiched between Layers I and III, a variable grid was used. Table 2 summarizes the results obtained during the grid dependency tests for one of the test samples (see [10], Chapter 4) with $\text{Re}_K=84.1$.

The first column in Table 2 refers to the constant grid spacing ΔY in Layers I and III in the Y -direction. The second and third columns refer to the number of grid points in Layer II and the total number of grid points in the Y -direction, respectively. The fourth column is the number of grid points in the heated section along the X -direction. Based on the grid dependence study, the grid parameters listed in the second row were used for all computations.

In order to validate the code, numerical results were compared to those of Yokoyama and Mahajan [25] as summarized in Table 3. The numerical results ([25]) are indicated within parentheses. Pe^* in Table 3 is defined according to ([25]).

Table 2 Results from grid dependency simulations

| ΔY | nY2 | nY | n×heat | Nu |
|----------------------|-----|-----|--------|-------|
| 5×10^{-4} | 51 | 63 | 80 | 10.97 |
| 2.5×10^{-4} | 51 | 73 | 80 | 11.02 |
| 2.5×10^{-4} | 101 | 123 | 80 | 11.02 |
| 2.5×10^{-4} | 51 | 73 | 120 | 11.02 |

Table 3 Comparison of numerical results with those in Yokoyama and Mahajan [25]

| Pe^* | $C_D=0$ | $C_D=0.025$ |
|---------------|-------------|---------------|
| 5000 | 64.9 (64.5) | 80.1 (79.4) |
| 7000 | 75.5 (75.0) | 98.5 (97.9) |
| 10000 | 88.8 (88.1) | 123.6 (124.9) |

Results and Discussion

Using the numerical code, computations were performed for the conditions of the experiments to verify if the results could be matched in a reasonable manner, and to determine appropriate values for C_D and C_T . The experimental data was collected in the range of nondimensional parameters, $Re_K \sim 11-135$, $Da \sim 5 \times 10^{-3} - 1 \times 10^{-2}$, and $Pr_e \sim 2.6 \times 10^{-3} - 7.5 \times 10^{-3}$. Note that the effective Prandtl number values are extremely small compared to the fluid Prandtl number (0.707) due to the high thermal conductivity of the metal foam.

First, the condition of zero dispersion (i.e., $C_D = 0$) was studied. Figure 6 shows a plot of the Nusselt number as a function of $Re_K Pr_e$ for different values of C_T with $C_D = 0$. The results are for Sample 2, and the experimental points are shown by the solid symbols. As expected, the Nusselt number increases with increase in C_T since the efficiency of heat transfer between the two phases improves. However, note that there is practically no difference in the computed results for $C_T > 0.52$ indicating that the phases are close to the thermal equilibrium condition. Figure 7 shows the variation of the temperature profile along the transverse direction at the midplane for three different Reynolds numbers. Note that the adiabatic wall temperature (i.e., the wall temperature at $Y = 1$) for the solid and fluid phases is not the same as the ambient temperature for all three values of Re_K . However, as Re_K increases, the adiabatic wall temperature approaches the ambient temperature. The indication is that the thermal boundary layer at the heated wall decreases with increase in Re_K .

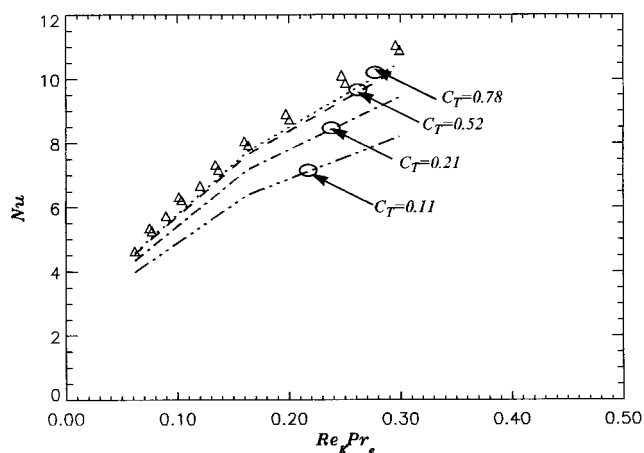


Fig. 6 Nu as a function of $Re_K Pr_e$ for different values of C_T . Data are for Sample 2.

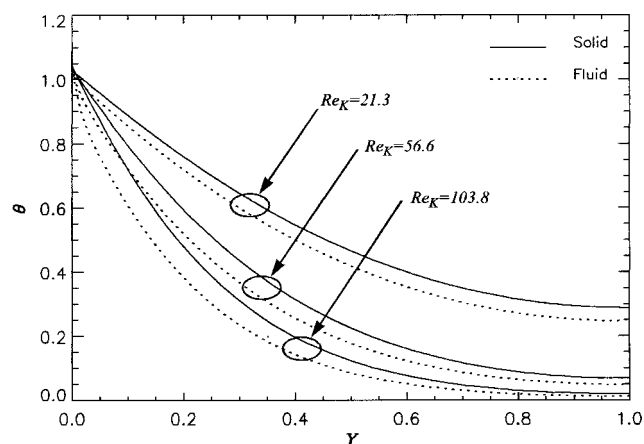


Fig. 7 Nondimensional temperature along the transverse direction. $C_T = 0.52$, Sample 2.

To understand the relative magnitudes of the various transport phenomena, it is useful to examine the solid and fluid-phase heat transfer rates at the heated wall. In Fig. 8, the local variations of the nondimensional heat transfer rates (the two components of Eq. (20)) are plotted. Clearly, the fluid-phase component accounts for a negligibly small portion of the total heat rate. Further, its local value decreases rapidly along the streamwise direction. This can be explained as follows. The predominant mode of transport from the heated surface to the fluid is by conduction through the solid phase and interfacial heat transfer from the solid to the fluid phase. Due to the efficient interfacial heat transfer, the fluid temperature is close to the solid temperature. This has an effect of decreasing the fluid temperature gradient at the wall (by thickening the boundary layer), and consequently the local heat transfer rate. Further, since the fluid conductivity is much smaller than the solid conductivity, the net heat transferred from the wall to the fluid is low.

In the numerical results presented so far, thermal dispersion has not been taken into account. It can be seen from the plot in Fig. 8 that the heat transferred directly to the fluid from the heated wall is negligible compared to the heat transferred interfacially from the solid to the fluid. Hence, the dispersion phenomenon that primarily enhances the wall heat transfer, is expected to be low. Figure 9 shows a plot of the total Nusselt number as a function of $Re_K Pr_e$ for Sample 2. The plots are for two different values of C_T as shown in the figure. For each C_T value, two lines are shown. They are the results of numerical simulations with and without the inclusion of dispersion effects. For the simulations for which dis-

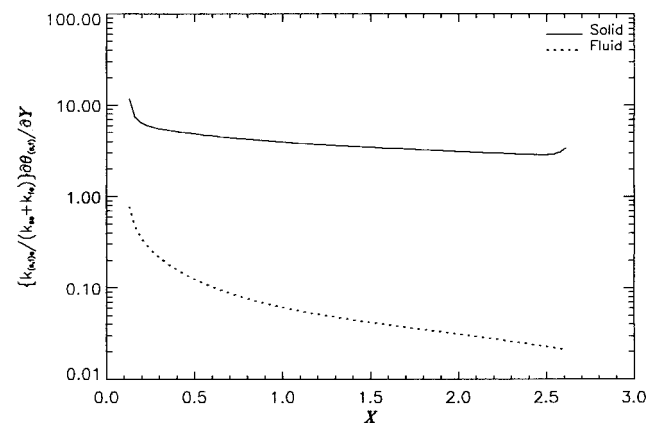


Fig. 8 Solid and fluid phase local heat transfer rate. Sample 2, $Re_K = 103.8$.

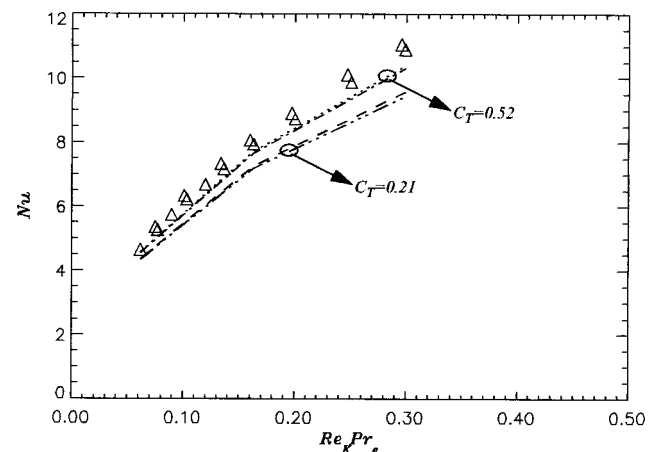


Fig. 9 Nu as a $Re_K Pr_e$ with dispersion effect included ($C_D = 0.1$). Data is for Sample 2.

Table 4 Characteristics of foam samples used in Hunt and Tien [2]

| No. | Material | ε | d_p (cm) | $K \cdot 10^7$ (m ²) | f | k_{se} (W/m-K) | k_{fe} (W/m-K) |
|-----|----------|---------------|------------|-------------------------------------|-------|---------------------|---------------------|
| H1 | C | 0.97 | 0.2 | 4.1 | 0.11 | 0.073 | 0.58 |
| H2 | C | 0.97 | 0.1 | 0.92 | 0.077 | 0.073 | 0.58 |
| H3 | Ni | 0.97 | 0.1 | 0.96 | 0.089 | 0.854 | 0.579 |
| H4 | Al | 0.97 | 0.2 | 4.8 | 0.17 | 2.19 | 0.579 |
| H5 | Al | 0.94 | 0.25 | 17.0 | 0.30 | 3.84 | 0.558 |

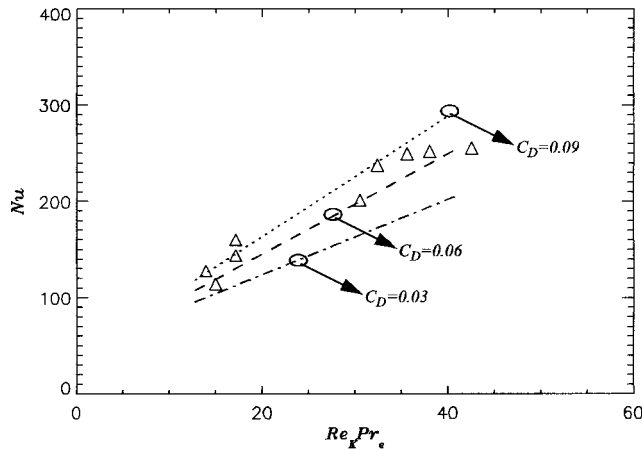


Fig. 10 Nusselt number as a function of $Re_k Pr_e$ for different values of C_D (Sample H3)

persion effects were included, a value $C_D=0.1$ was used. As it is evident from the figure, dispersion has no significant effect on the total transport. This is immediately clear by re-examining the thermal dispersion model postulated earlier,

$$\frac{k_d}{k_e} = C_D(Re_k Pr_e). \quad (22)$$

For k_d to have any significant effect on the overall transport, it must be at least of the same order of magnitude as k_e . For a typical value of $Re_k Pr_e=0.3$, and $C_D=0.1$, k_d is merely three percent of the total stagnant thermal conductivity. Although its value is still *seven* times higher than the fluid conductivity, the

effect on the overall transport is negligible because, as mentioned before, the dominant mode of transport is by conduction through the solid phase and interfacial convection, which is largely unaffected by dispersion. The value, $C_D=0.1$, used for illustrating this is not entirely arbitrary. It is based on order of magnitude estimates in ([7]). In any case, it is clear that it is difficult to accurately quantify dispersion effects when the solid-phase conductivity is much larger than its fluid-phase counterpart, as is the case here.

Although an accurate estimate of C_D cannot be made by using the metal foam-air experiments, an estimate of C_T is possible. From Fig. 9, it is seen that a good match of the data with the numerical results is obtained with $C_T=0.52$. This value is representative of heat transfer from cylinders in crossflow ([21]). Further, as will be seen later, this value of C_T is sufficient to model forced convection transport in metal foams with water as the fluid phase. We note here that a two-equation model for energy may not be necessary for all combinations of experimental data. However, a detailed study that establishes bounds for nondimensional parameters for which two-equation analyses are necessary may be useful for application to practical situations (see, for example, [26]).

The only other experimental and theoretical work that addresses forced convection in metal foams is that of Hunt and Tien [2]. Their study used foams made of aluminum, nickel, carbon, with water as the fluid phase. Hence, the fluid conductivity is not a negligible fraction of the effective conductivity. Consequently, dispersion effects are expected to be much higher. Although an error was found in the numerical calculations (which eventually led to the conclusion that $C_D=0.025$), the experiments seemed to be in order. Of the seven samples used in their experiment, five representative samples were chosen for analysis here (see Table 4). The conductivities in the last two columns of Table 4 were evaluated using the expressions developed in this study (Eqs. (9),(10)). Since water was used as the fluid phase, interfacial heat transfer was efficient and all samples satisfied local thermal equilibrium conditions as expected. ($C_T=0.52$ was used for the computations, based on the aluminum-air study described earlier.)

To study the dispersion effect numerically, Sample H3 was chosen for investigation. The average heat transfer coefficients were extracted from their experimental Nusselt numbers and used here for comparison. The computed Nusselt numbers for different values of the dispersion coefficient, C_D , are shown in Fig. 10 along with the experimental data. A reasonable fit is obtained for $C_D=0.06$. As expected, and unlike in the aluminum foam-air

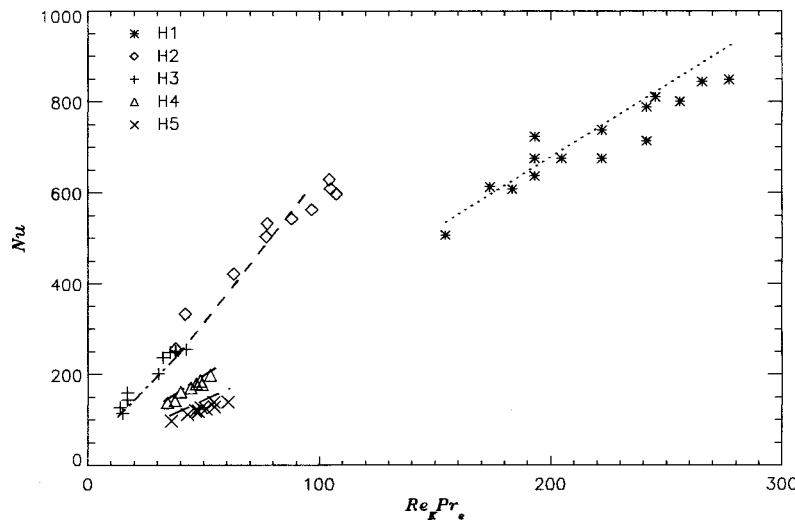


Fig. 11 Comparison of numerical simulations (this study) with the experimental results in Hunt and Tien [2] for samples in Table 4

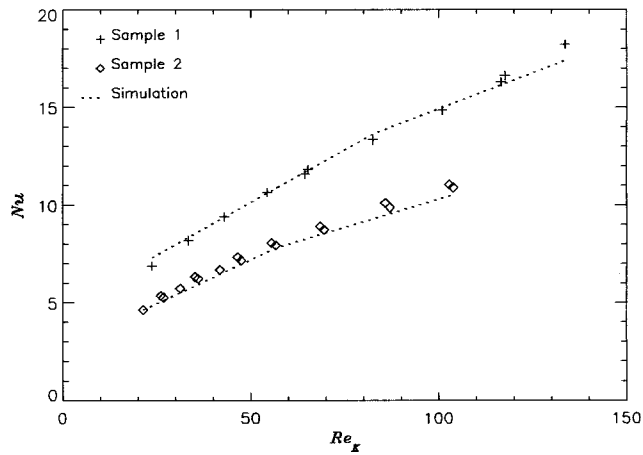


Fig. 12 Nusselt number as a function of Re_K for the five PPI samples (Table 1)

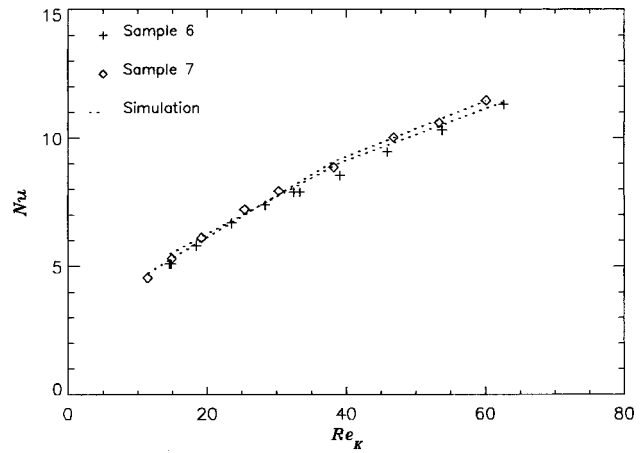


Fig. 15 Nusselt number as a function of Re_K for the 40 PPI samples (Table 1)

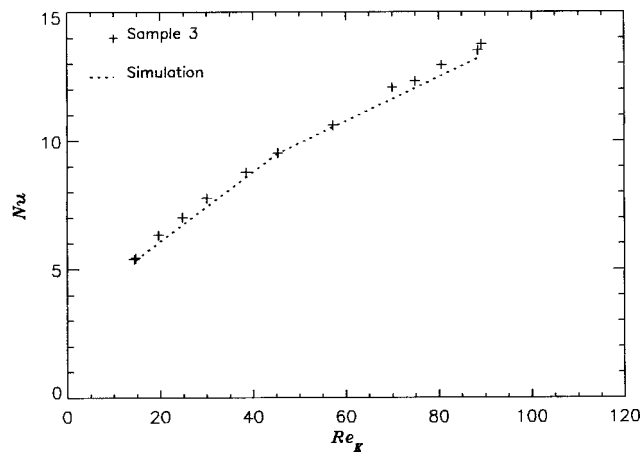


Fig. 13 Nusselt number as a function of Re_K for the ten PPI samples (Table 1)

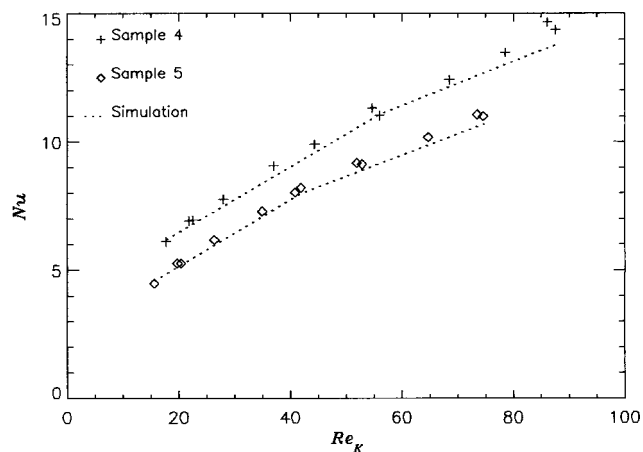


Fig. 14 Nusselt number as a function of Re_K for the 20 PPI samples (Table 1)

combination used in this study, the dispersion effect is considerable here. In this particular case, heat transfer enhancement due to dispersion is almost 80 percent. Using Eq. (22), and a representative value of $Re_K Pr_e = 30$, the dispersion conductivity is calculated to be 175 percent of the stagnant conductivity. This is a significant

enhancement compared to the low value of three percent obtained earlier for the aluminum-air combination. The experimental results in ([2]) are plotted in Fig. 11 for a thermal dispersion coefficient value of 0.06. A good fit is obtained for all samples, suggesting that $C_D = 0.06$ is appropriate.

By analyzing the data collected in this study for foam-air combinations, and that published in Hunt and Tien [2] for foam-water combinations, the coefficients C_T and C_D values of 0.52, and 0.06 seem reasonable. As a last check, numerical simulations were performed for the same experimental conditions of all samples (Table 1) used in the present study. The results of these simulations are plotted in Figs. 12–15 as a function of the Reynolds number, along with the experimental data. Once again, a very good fit with the experimental data is obtained confirming the values of C_D and C_T to be good. However, the following point is noted. There appears to be a systematic deviation between the experimental and computed results for high Reynolds number. In particular, the numerical results appear to underpredict the experimental Nusselt number for $Re_K > 80$. The indication is that some other transport enhancing effect (e.g., turbulence) may be taking effect. No such systematic deviation is observed in the experimental results of Hunt and Tien [2]. However, the maximum Reynolds number in that study was around 60.

Summary

A detailed study of forced convection in metal foams has been performed. The goal of the study was to quantify thermal dispersion and thermal nonequilibrium effects in metal foams. To this end, both experimental and numerical methods were employed. Experiments were performed with a wide variety of aluminum metal foams. Results indicate that for foam-air combinations, the transport enhancing effect of thermal dispersion is extremely low due to the relatively high conductivity of the solid matrix. However, for foam-water combinations, ours and past available results indicate that thermal dispersion can be very high and accounts for bulk of the transport.

A thermal nonequilibrium model was used in all cases. The values $C_T = 0.52$, and $C_D = 0.06$ were found to be appropriate. Currently, forced convection transport in foamed materials is being studied using foams of other materials (carbon, copper) along with various fluids (air, water, FC-72) in order to reconfirm the results of the present study. Those findings will appear in a future publication.

Acknowledgments

This work was funded by CAMPmode at the University of Colorado. The authors wish to thank Dr. Yoichi Yokoyama for

helpful discussions and Mr. Bryan Leyda of ERG, Inc. for providing the experiment samples and for discussions at various stages of this work.

Nomenclature

- a_{sf} = specific solid-fluid interfacial surface area (m^{-1})
 $Bi_f = h_{sf} a_{sf} H \sqrt{K} / k_{fe}$, fluid-phase effective Biot number
 $Bi_s = h_{sf} a_{sf} H^2 / k_{se}$, solid-phase effective Biot number
 C_D = coefficient of thermal dispersion
 C_T = coefficient in Eq. (13)
 $Da = \sqrt{K} / H$, Darcy number
 f = inertia coefficient
 h_{sf} = interfacial heat transfer coefficient (W/m^2-K)
 K = permeability (m^2)
 $Pr_e = \mu c_p / k_e$, Prandtl number based on effective conductivity
 q = heat input to patch heaters (W)
 $Re_K = u_o \sqrt{K} / \nu$, Reynolds number based on permeability
 T_{in} = measured fluid temperature (before entering heated section) ($^{\circ}C$)
 T_{amb} = measured fluid temperature (before entering unheated section) ($^{\circ}C$)
 T_{wi} = measured wall temperatures ($^{\circ}C$)
 ΔT_{avg} = average wall temperature with respect to fluid inlet temperature, T_{in}
 u_o = measured average flow velocity entering foam sample (m/s)

Greek Symbols

$$\theta = (T - T_{in}) / (\Delta T_{avg})$$

Subscripts

- d = dispersive
 e = effective

References

- [1] Kaviany, M., 1991, *Principles of Heat Transfer in Porous Media*, Springer-Verlag, New York.
- [2] Hunt, M. L., and Tien, C. L., 1988, "Effects of Thermal Dispersion on Forced Convection in Fibrous Media," *Int. J. Heat Mass Transf.*, **31**, pp. 301–309.
- [3] Sathe, S. B., Peck, R. E., and Tong, T. W., 1990, "A Numerical Analysis of Heat Transfer and Combustion in Porous Radiant Burners," *Int. J. Heat Mass Transf.*, **33**, No. 6, pp. 1331–1338.
- [4] Lee, Y. C., Zhang, W., Xie, H., and Mahajan, R. L., 1993, "Cooling of a FCHIP Package With 100 W, 1 cm² Chip," *Proceedings of the 1993 ASME Int. Elec. Packaging Conf.*, Vol. 1, ASME, New York, pp. 419–423.
- [5] Calmidi, V. V., and Mahajan, R. L., 1999, "The Effective Thermal Conductivity of High Porosity Fibrous Metal Foams," *ASME J. Heat Transfer*, **121**, pp. 466–471.
- [6] Bhattacharya, A., Calmidi, V. V., and Mahajan, R. L., 1999, "An Analytical-Experimental Study for the Determination of the Effective Thermal Conductivity of High-Porosity Fibrous Foams," *ASME IMECE '99*, ASME, New York, pp. 13–20.
- [7] Koch, D. L., and Brady, J. F., 1986, "The Effective Diffusivity of Fibrous Media," *AIChE J.*, **32**, pp. 575–591.
- [8] Hsu, C. T., and Cheng, P., 1990, "Thermal Dispersion in Porous Media," *Int. J. Heat Mass Transf.*, **33**, No. 8, pp. 1587–1597.
- [9] Adnani, P., Catton, I., and Abdou, M. A., 1995, "Non-Darcian Forced Convection in Porous Media With Anisotropic Dispersion," *ASME J. Heat Transfer*, **117**, pp. 447–451.
- [10] Calmidi, V. V., 1998, "Transport Phenomena in High Porosity Metal Foams," Ph.D. thesis, University of Colorado, Boulder, CO.
- [11] Beavers, G. S., and Sparrow, E. M., 1969, "Non-Darcy Flow Through Fibrous Porous Media," *ASME J. Appl. Mech.*, **36**, pp. 711–714.
- [12] Vafai, K., and Tien, C. L., 1981, "Boundary and Inertial Effects on Flow and Heat Transfer in Porous Media," *Int. J. Heat Mass Transf.*, **24**, pp. 195–203.
- [13] DuPlessis, P., Montillet, A., Comiti, J., and Legrand, J., 1994, "Pressure Drop Prediction for Flow Through High Porosity Metallic Foams," *Chem. Eng. Sci.*, **49**, pp. 3545–3553.
- [14] Carbonell, R. G., and Whitaker, S., 1984, "Heat and Mass Transfer in Porous Media," *Fundamentals of Transport Phenomena in Porous Media*, Bear and Corapcioglu, eds., Martinus Nijhoff, Dordrecht, The Netherlands, pp. 121–198.
- [15] Kaviany, M., 1994, *Convective Heat Transfer*, Springer-Verlag, New York.
- [16] Zanotti, F., and Carbonell, R. G., 1984, "Development of Transport Equations for Multiphase System-III," *Chem. Eng. Sci.*, **39**, pp. 299–311.
- [17] Wakao, N., Kaguei, S., and Funazkri, T., 1979, "Effect of Fluid Dispersion Coefficients on Particle-to-Fluid Heat Transfer Co-efficients in Packed Beds," *Chem. Eng. Sci.*, **34**, pp. 325–336.
- [18] Hwang, G. J., and Chao, C. H., 1994, "Heat Transfer Measurements and Analysis for Sintered Porous Channels," *ASME J. Heat Transfer*, **117**, pp. 725–732.
- [19] Cheng, P., and Vortmeyer, D., 1988, "Transverse Thermal Dispersion and Wall Channelling in a Packed Bed With Forced Convective Flow," *Int. J. Heat Mass Transf.*, **43**, No. 9, pp. 2523–2532.
- [20] Koch, D. L., 1996, "Hydrodynamic Diffusion Near Solid Boundaries With Applications to Heat and Mass Transport Into Sheared Suspensions and Fixed-Fibre Beds," *J. Fluid Mech.*, **318**, pp. 31–47.
- [21] Zukauskas, A. A., 1987, "Convective Heat Transfer in Cross-Flow," *Handbook of Single-Phase Heat Transfer*, Kakac, S., et al., eds. Wiley, New York.
- [22] Incropera, F. P., and DeWitt, D., 1997, *Fundamentals of Heat and Mass Transfer*, Wiley, New York.
- [23] Vafai, K., and Kim, S. J., 1989, "Forced Convection in a Channel Filled with a Porous Medium: An Exact Solution," *ASME J. Heat Transfer*, **111**, pp. 1103–1106.
- [24] Roache, P. J., 1982, *Computational Fluid Dynamics*, Hermosa, Albuquerque, NM.
- [25] Yokoyama, Y., and Mahajan, R. L., 1995, "Non-Darcian Convective Heat Transfer in a Horizontal Duct," *Proceedings of the National Heat Transfer Conference*, Vol. 7, ASME, New York, pp. 83–92.
- [26] Amiri, A., and Vafai, K., 1994, "Analysis of Dispersion Effects and Local Thermal Non-Equilibrium, Non-Darcian, Variable Porosity Incompressible Flow Through Porous Media," *Int. J. Heat Mass Transf.*, **37**, pp. 939–954.

Estimating Number of Shells in Shell and Tube Heat Exchangers: A New Approach Based on Temperature Cross

B. B. Gulyani¹

Research Associate,
Department of Chemical Engineering,
University of Roorkee,
Roorkee 247667, India
e-mail: bbgulyani@yahoo.com

Multipass heat exchangers are often designed by using the rule of thumb $F_T \geq 0.75$, which is rather arbitrary. F_T falls sharply with the increase in temperature cross. Hence, only a limited temperature cross can be allowed. The ability to accommodate temperature cross increases rapidly as the number of shell passes is increased. Though many investigators have emphasized the importance of temperature cross in exchanger design, it has as yet not been explicitly accounted for in the design. This paper introduces a new approach for estimating the number shells in a shell and tube exchanger which directly accounts for temperature cross, rather than routing this effect through F_T or X_p (Ahmad et al.'s parameter, which is again a correction factor not directly related to temperature cross). The approach is compatible with the established design procedures and bypasses the F_T . It generates better designs by defining maximum permissible temperature cross, than the traditional designs based on specifying minimum permissible F_T . Expressions have also been provided which correlate the present formulation with that of Ahmad et al. [S0022-1481(00)00803-3]

Keywords: Analytical, Heat Exchangers, Heat Transfer

1 Introduction

Shell and tube heat exchangers have long been established as industry standard because of several advantages including higher heat transfer coefficients and compactness, ease of construction and maintenance. In case of the simplest shell and tube exchanger, the 1–2 type, the liquid in one tube pass flows in counter flow while in the other pass flows in parallel relative to shell fluid (Fig. 1). The method of calculation of log mean temperature difference, LMTD for counter flow as well as parallel flow, is well established ([1]). For a case, like that of 1–2 shell and tube exchanger where both types of flow co-exist, an analytical expression for estimating effective temperature difference has been developed by Underwood [2] and later modified by Bowman et al. [3]. In this design practice, a correction factor F_T is introduced into the basic heat exchanger design equation, Eq. (1) to take into account the above phenomena,

$$Q = UA(LMTD)F_T \quad \text{where} \quad 0 < F_T < 1. \quad (1)$$

The F_T factor can be represented as the ratio of actual mean temperature difference in a 1–2 exchanger to counter flow LMTD for the same terminal temperatures. The physical significance of F_T is given by many authors ([4–6]).

The difference between the outlet temperature of hot fluid, T_2 , and that of the cold fluid, t_2 is thermally significant, and is called *temperature cross* if negative, and *temperature approach* if positive. When there is a large temperature cross in a 1–2 exchanger, local reversal of heat flow may be encountered, requiring excessive exchanger area or even making the design infeasible. This fact manifests itself into low values of F_T . Since the ability to accommodate temperature cross increases with increasing shell

passes, low F_T values force the designer to go for higher shell pass arrangements. Hence, F_T is used as a criterion to screen alternative designs.

When multishell arrangements are found necessary, it becomes pertinent to estimate number of shells required. This is done using either a trial and error approach or the explicit formulation given by Ahmad et al. [7].

This paper describes a new approach for estimating the number shells in a shell and tube exchanger which directly accounts for temperature cross. The approach is compatible with the established design procedures and bypasses the F_T . Its main advantages are as follows:

- 1 The number of shells are calculated explicitly.

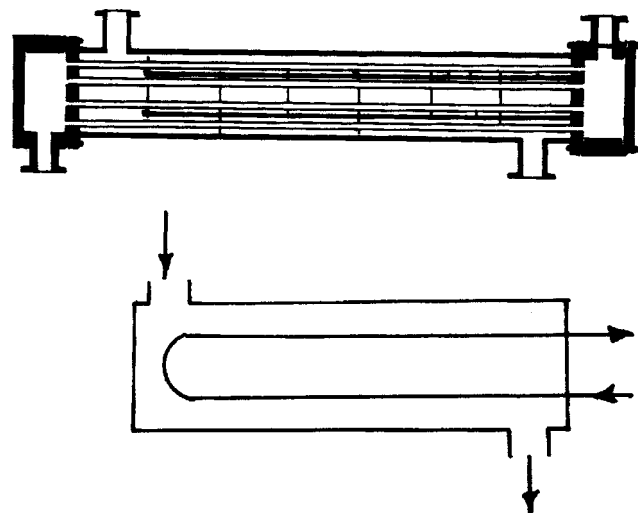


Fig. 1 Schematic of a 1–2 exchanger

¹Address for correspondence: 71/3, Govind Puri, University of Roorkee, Roorkee 247667, India.

Contributed by the Heat Transfer Division for publication in the JOURNAL OF HEAT TRANSFER. Manuscript received by the Heat Transfer Division, Dec. 1, 1998; revision received, Feb. 14, 2000. Associate Technical Editor: D. Kaminski.

2 It generates better designs by defining maximum permissible temperature cross, than the traditional designs based on rules of thumb for specifying minimum permissible F_T .

3 The procedure is conceptually better as it directly accounts for the effect of temperature cross, rather than routing this effect through F_T or X_P (Ahmad's parameter, which is again a correction factor not directly related to temperature cross).

Expressions have also been provided which correlate the present formulation with that of Ahmad et al. [7].

2 The F_T Correction Factors

F_T has been correlated as a function of dimensionless ratios R and S , where

$$\text{heat capacity ratio, } R = \frac{T_1 - T_2}{t_2 - t_1} \quad (2)$$

and

$$\text{thermal effectiveness, } S = \frac{t_2 - t_1}{T_1 - t_1}. \quad (3)$$

Since F_T is used to screen alternative designs, before resorting to detailed design calculation, designs with unacceptably low F_T values are discarded. A commonly used rule of thumb requires $F_T > 0.75$ for the design to be considered practical. However, the use of this ad hoc criterion for 1–2 exchanger is arbitrary, and can lead to poor designs if not used with caution ([7,8]). Frank [9] recommends that the 1–2 exchangers should not be designed where F_T factors approach a vertical slope, as small departure from the design point can result in precipitous decline of correction factor. Thus, the advice to the designer to refrain from designing with $F_T < 0.75$ comes mainly because of steep slopes of the F_T curves in that region, which prohibits the designer to estimate F_T correctly. Secondly, the performance becomes sensitive to small departure from given temperatures. Therefore, small fluctuations in terminal temperatures (consequently, in S) will lead to considerable variation in the value of F_T , leading to poor operability.

3 The X_P Design Method

Ahmad et al. [7] have given an alternative approach based on the fact that for any value of R there exists a maximum asymptotic value of S , defined as S_{\max} and can be expressed as

$$S_{\max} = \frac{2}{R + 1 + \sqrt{R^2 + 1}}. \quad (4)$$

A 1–2 exchanger designed for $S = S_{\max}$ will not be feasible, since it corresponds to $F_T = -\infty$. Ahmad et al. defined an acceptable design having the value of S as a fraction, X_P , of S_{\max} . Accordingly,

$$S = S_{\max} X_P \quad \text{where } 0 < X_P < 1. \quad (5)$$

However, they don't provide a sound criterion to select the design value of X_P . Also, X_P does not reflect the effect of temperature cross.

4 Design for Multipass Exchangers

Designers often encounter situations where either the F_T is too low or the slope of F_T versus S curve is too large. If this happens, the designer might be forced to consider multipass exchangers.

Traditionally, the designer would approach a problem requiring multiple shells by trial and error. By assuming a number of shells, usually one in the first instance, the F_T is evaluated. If the F_T is not acceptable then the number of shells in series is progressively increased until a satisfactory value of F_T is obtained for each shell.

Ahmad et al. [7] have given an analytical expression for calculating number of shells directly,

$$N = \frac{\ln \frac{(1 - RS)}{(1 - S)}}{\ln W}, \quad (6)$$

where N is real (noninteger) number of shells, and

$$W = \frac{R + 1 + \sqrt{R^2 + 1} - 2RX_P}{R + 1 + \sqrt{R^2 + 1} - 2X_P}. \quad (7)$$

Equation (6) gives a value of N that satisfies precisely the chosen value of X_P . The problem now is, what should be the design value of X_P ? And how it will affect temperature cross and, consequently, F_T ? Though Ahmad et al. emphasized the importance of temperature cross in exchanger design, they did not explain how X_P accounts for temperature cross. Their choice of value of $X_P = 0.9$ is based on $F_T = 0.75$ at $R = 1$, which is again arbitrary. What if a designer wants to use a lower value of X_P ? How much improvement in temperature cross and F_T shall be achieved by this?

5 Accounting for Temperature Cross

Since a 1–2 exchanger is a combination of counterflow and parallel-flow passes, it may be expected that the outlet temperature of one process stream cannot approach the inlet temperature of the other very closely ([1]). In fact, the difference between the outlet temperature of hot fluid, T_2 , and that of the cold fluid, t_2 has particular thermal significance and introduces the terminology of temperature approach, temperature "meet," and temperature cross, as

when $t_2 < T_2$, there is temperature approach.

when $t_2 = T_2$, there is temperature meet.

when $t_2 > T_2$, there is temperature cross.

For a 1–2 exchanger, F_T falls sharply with increase in the value of temperature cross, ($t_2 - T_2$). At large temperature cross, local reversal of heat flow leads to waste of heat transfer area. Hence, only a limited temperature cross can be allowed. The ability to accommodate a temperature cross increases rapidly as the number of shell passes is increased.

A dimensionless group, G , proposed by Wales [10] and Gulyani and Mohanty [11] accounts for the extent of temperature approach or cross. G is defined as

$$G = \frac{T_2 - t_2}{T_1 - t_1}. \quad (8)$$

F_T decreases moderately with decreasing positive G values, but falls sharply both where the temperature meet ($G = 0$) and where the G values are negative (temperature cross). This fact is revealed in Fig. 2, which shows the effect of G on F_T for 1–2 exchanger. From this figure, it is also evident that the higher the R , the sharper is the fall in F_T .

The parameter G is related to parameter R and S , by the equation

$$G = 1 - S(1 + R). \quad (9)$$

For any value of R there exists a minimum asymptotic value of G (corresponding to $F_T = -\infty$), say G_{\min} , which represents the maximum temperature cross theoretically feasible in 1–2 exchanger. The expression for G_{\min} is (relevant derivations are provided in Appendix)

$$G_{\min} = \frac{\sqrt{R^2 + 1} - (R + 1)}{\sqrt{R^2 + 1} + (R + 1)}. \quad (10)$$

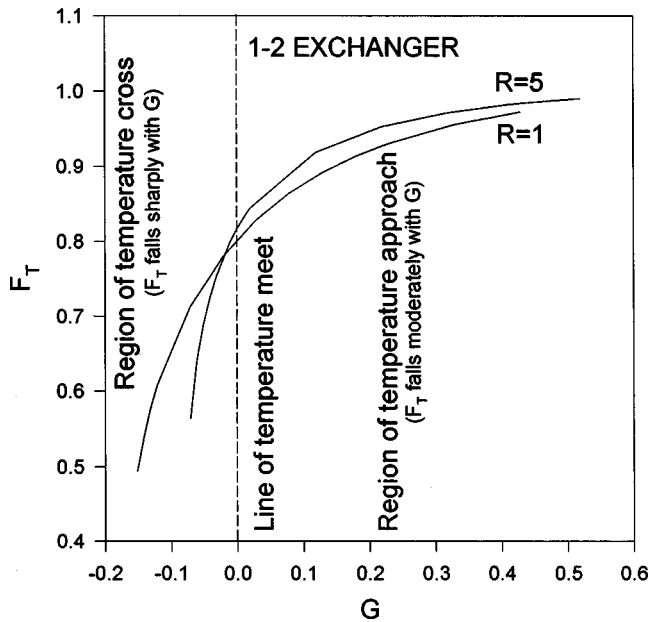


Fig. 2 Effect on G on F_T

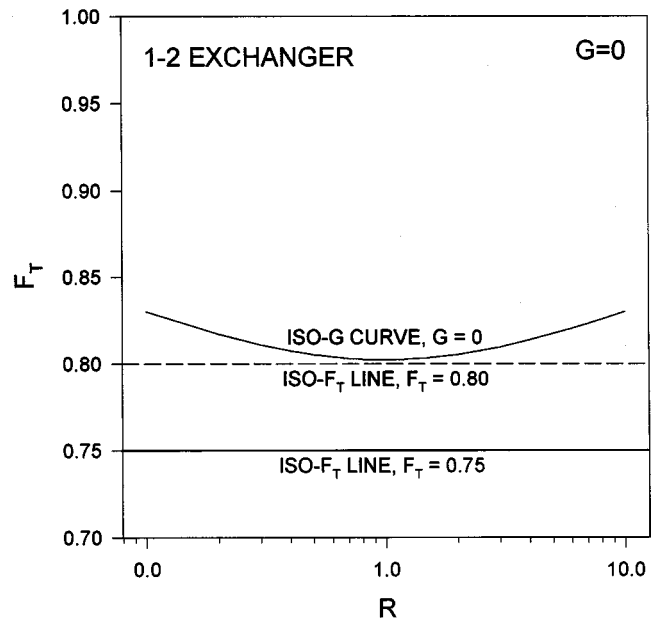


Fig. 3 Variation of F_T with R for $G=0$

A 1–2 exchanger designed for $G=G_{\min}$ will not be feasible. Any increment in G from G_{\min} will make the exchanger feasible, and improve exchanger effectiveness and F_T . Let the desired increment be Y . Then

$$G = G_{\min} + Y \quad (11)$$

where Y is a constant set by the designer. Now, the expression for estimating the number of shells can be written as

$$N = \frac{\ln \frac{(1 - RG_N)}{(R + G_N)}}{\ln W} \quad (12)$$

where G_N is G for multipass exchanger, and

$$W = \frac{\sqrt{R^2 + 1}(R + 1 - RY) - (R + 1)(R - 1 - RY)}{\sqrt{R^2 + 1}(R + 1 - Y) - (R + 1)(R - 1 - Y)} \quad (13)$$

Y can be correlated with X_P as (see Appendix for derivation)

$$Y = \frac{2(R + 1)(1 - X_P)}{\sqrt{R^2 + 1} + (R + 1)} \quad (14)$$

Alternatively,

$$X_P = \frac{(R + 1)(2 - Y) - Y\sqrt{R^2 + 1}}{2(R + 1)} \quad (15)$$

6 The Significance of Y

It must be noted that unlike F_T and X_P , Y is not a correction factor. Y is a measure of the extent the temperature cross is away from the limiting value (G_{\min}). In that sense, it is similar to G . As it is directly related to the terminal temperatures of the exchanger, it may be seen as a “primary” parameter (like R , S , and G), as against the secondary parameters (F_T and X_P). Hence, Y clearly reflects the designer’s attempt to reduce the temperature cross.

7 The Criteria for Selecting Y

While the design value of F_T is chosen so as to avoid the regions of steep fall, and that of the X_P is chosen on a similar basis, the criterion for selecting a design value of Y is simple,

intuitive, and straightforward. Y is chosen by the designer’s decision on how much temperature cross he is going to allow in the design. Here, two cases may be considered:

1 Do Not Allow any Temperature Cross. This criteria pertains to $G=0$; or $Y = -G_{\min}$. Figure 3 shows the variation of F_T with R for $G=0$. Figure 4 shows variation of F_T with S for $G=0$. Both figures reveal that for $G=0$, $F_T > 0.8$. Also, F_T is minimum at $R=1$, and increases when R is either increased or decreased. Hence, if no temperature cross is allowed, it means that F_T is always greater than 0.8 (which is indeed the value of F_T recommended by some investigators). This serves as a convenient criterion for calculating the number of shells. Substituting $G=0$ in Eq. (A17) of the Appendix, we get

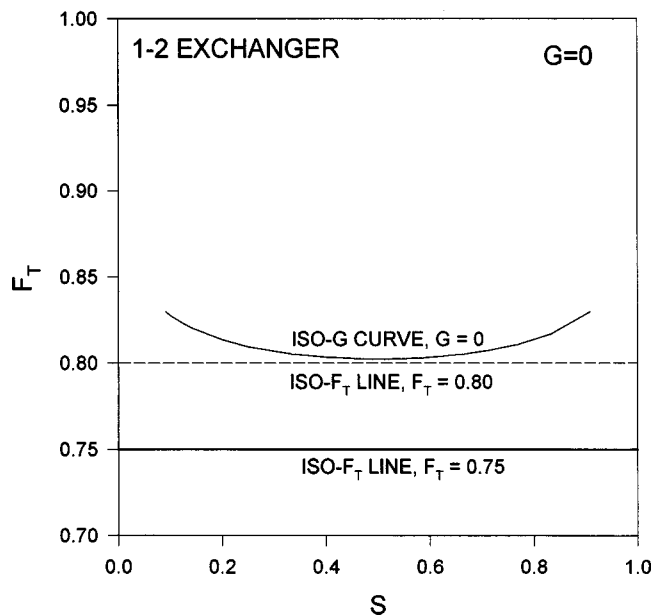


Fig. 4 Variation of F_T with S for $G=0$

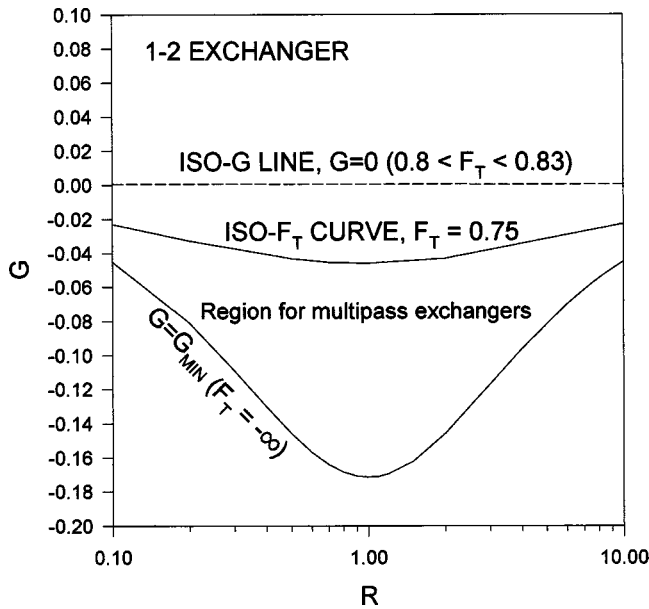


Fig. 5 Comparison of $G=0$ criteria with $F_T=0.75$ criteria

$$N = \frac{\ln\left(\frac{R + G_N}{1 + R G_N}\right)}{\ln(R)} \quad (16)$$

Figure 5 compares this criteria with $F_T=0.75$ criteria. The region below the iso- G line (or iso- F_T curve) is the region of multipass exchangers. From this figure, it can be readily known whether designer has to opt for a multipass exchanger, using either of the two criteria ($G=0$ or $F_T=0.75$).

2 Allow Some Temperature Cross. Based on the chosen Y and using Eq. (13) and (12) the number of shells can be estimated. Figure 6 shows the effect of Y on F_T for $0.1 \leq R \leq 1.0$ (it actually amounts to range of R : $0.1 \leq R \leq 10$; since F_T is the same for R and $1/R$). There are three regions in Fig. 6 marked as A, B, and C. In region A, $Y \leq 0.022$, F_T is less than 0.75 for all values of R . This region is *always infeasible*. In region C, $Y \geq 0.1255$, F_T is

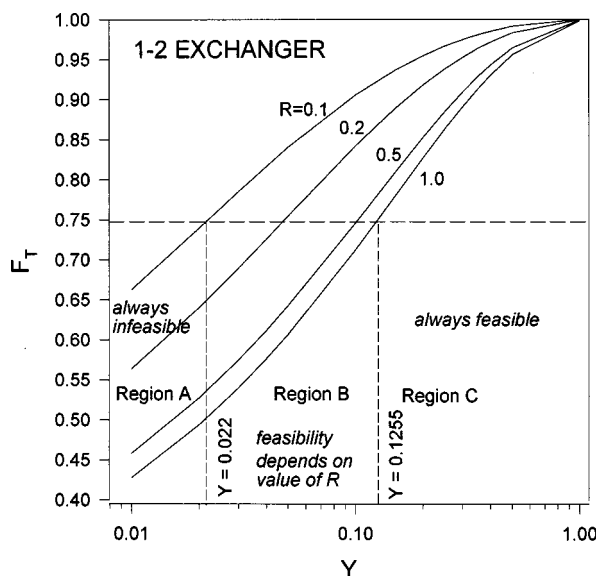


Fig. 6 Effect of Y on F_T

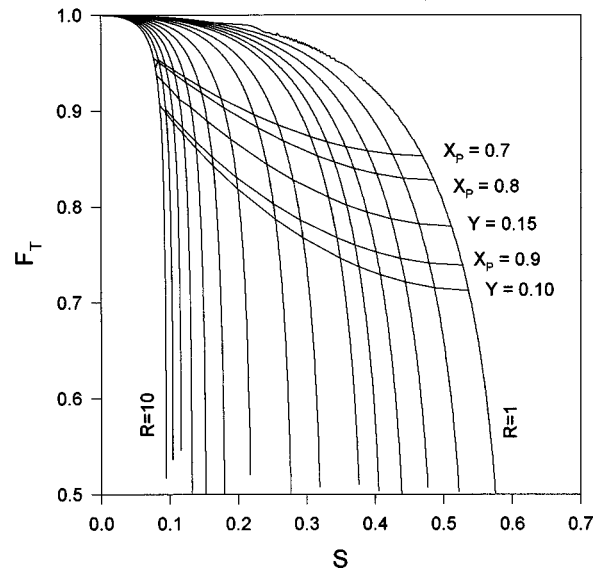


Fig. 7 Comparison of X_p and Y parameters

always greater than 0.75. This region is always feasible. In region B, $0.022 < Y < 0.1255$, feasibility of $F_T \geq 0.75$ criteria is R -dependent.

The designer is usually too colloquial to the F_T concept. He would like to know the value of F_T at the assumed Y (or X_p). The value of F_T can be readily obtained from G by using linear equations provided by Gulyani and Mohanty [11].

It is worthwhile here to compare all the three approaches (the F_T approach, the X_p approach, and the Y approach). In Fig. 7, iso- Y and iso- X_p lines are shown on standard F_T plot for 1-2 exchanger.

This figure serves two purposes. It gives the value of F_T (and X_p) at the selected value of Y . Secondly, it gives the estimate of Y (thus temperature cross) for the chosen value of F_T (or X_p).

Figure 7 also reveals that, to be compatible with the existing design practices ($F_T > 0.75$; or $X_p = 0.9$), a value of Y in the range 0.1 to 0.15 may be selected.

8 Effect of Y on Number of Shells, N

Figure 8 shows the effect of Y on N for $R=0.2$ and for different G_N values. Figure 9 shows the effect of Y on N for $R=1.0$ and for different G_N values. These figures reveal that both Y and G_N contribute to increase the number of shells. At higher temperature cross, the effect of Y on N is more pronounced. Figures 8 and 9 may also be used to estimate the number of shells for given R and G and chosen Y .

9 The Effect of Rounding Off N

It must be mentioned here that the number of shells computed using Ahmad et al.'s expression (Eq. (6)) as well as the expression developed in this paper (Eq. (12)), is in fact the real (non-integer) number of shells. However, in actual practice, the design can have only an integer number of shells. Hence, the number of shells obtained from Eq. (12) is rounded off to next integer. This results in improvement in Y .

Now, the designer would like to know that if N is rounded off to integer M , how much is Y improved? This can be calculated from following expression:

$$Y' = \frac{R-1}{R-W} \frac{\sqrt{R^2+1}(W-1) + (R+1)(W+1)}{\sqrt{R^2+1} + R + 1} \quad (17)$$

where Y' is improved Y , and

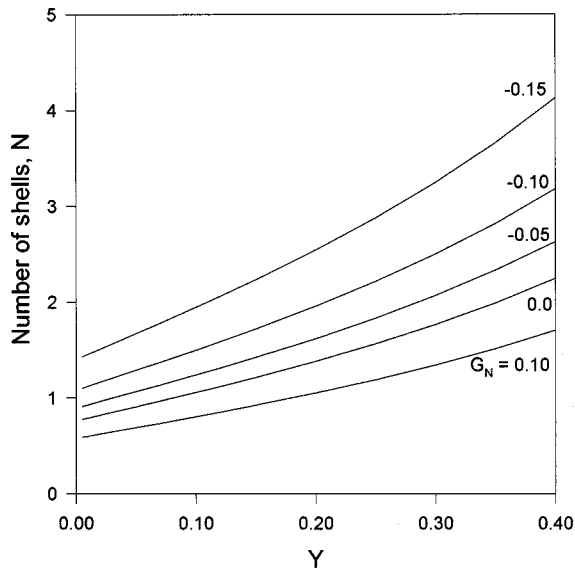


Fig. 8 Effect of Y on number of shells, N for $R=0.2$

$$W = \left(\frac{1+RG}{R+G} \right)^{1/M} \quad (18)$$

Equation (17), used in conjunction with Eq. (18), gives improved Y (i.e., Y') for integer number of shells $M (> N)$. In fact, Y should be calculated at both $(M-1)$ and M shells; in some cases, the designer may find Y at $(M-1)$ shells acceptable. This might essentially be the case while targeting for shells in heat exchanger networks, where rounding, say, 3.1 shells to 4 shells, may escalate the total cost target. The designer may want to optimize between “three shells with a bit lower Y ” and “four shells with higher Y ” on the basis of total cost targets.

Nomenclature

- F_T = LMTD correction factor, dimensionless
- G = $(T_2 - t_2)/(T_1 - t_1)$, dimensionless
- G_{\min} = minimum value of G , defined by Eq. (10)
- G_N = value of G for N -pass exchanger
- LMTD = log mean temperature difference, K

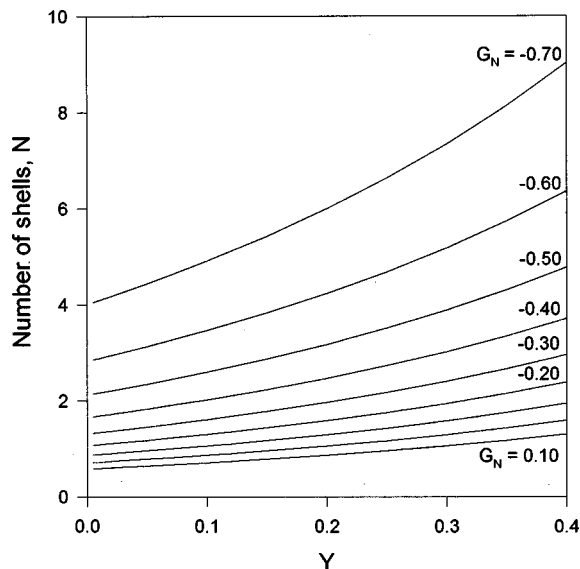


Fig. 9 Effect of Y on number of shells, N for $R=1.0$

- M = number of shells (integer)
- N = real (noninteger) number of shells
- R = heat capacity ratio, $(T_1 - T_2)/(t_2 - t_1)$ dimensionless
- S = temperature efficiency, $(t_2 - t_1)/(T_1 - t_1)$ dimensionless
- S_{\max} = maximum value of S , defined by Eq. (4)
- T_1 = hot fluid inlet temperature, K
- T_2 = hot fluid outlet temperature, K
- t_1 = cold fluid inlet temperature, K
- t_2 = cold fluid outlet temperature, K
- ΔT = actual mean temperature difference, K
- X_p = parameter defined by Ahmad et al., defined by Eq. (5), dimensionless
- Y = parameter defined by Eq. (11), dimensionless

Appendix

Derivation of Expressions for Computing Number of Shells Based on Temperature Cross. Here, the expressions for computing number of shells based on temperature cross in an exchanger are developed and described.

Start With the Following Definitions and Relationships.

$$G = 1 - S(1+R) \quad (A1)$$

where

$$R \equiv \frac{T_1 - T_2}{t_2 - t_1} \quad \text{and} \quad S \equiv \frac{t_2 - t_1}{T_1 - t_1}$$

$$S_{\max} = \frac{2}{R + 1 + \sqrt{R^2 + 1}} \quad (A2)$$

$$S = S_{\max} X_p \quad (A3)$$

$$G = G_{\min} + Y \quad (A4)$$

Estimating G_{\min} .

$$G_{\min} = 1 - S_{\max}(1+R) \quad (A5)$$

$$G_{\min} = 1 - \frac{2(1+R)}{\sqrt{R^2+1} + R + 1} = \frac{\sqrt{R^2+1} - R + 1}{\sqrt{R^2+1} + R + 1}$$

Estimating G at a Given Y . Assume a value of Y . For feasible design, $G = G_{\min} + Y$.

Substituting Eq. (A5) in Eq. (A4),

$$G = \frac{\sqrt{R^2+1} - R + 1 + Y[\sqrt{R^2+1} + R + 1]}{\sqrt{R^2+1} + R + 1} \quad (A6)$$

$$G = \frac{\sqrt{R^2+1}(1+Y) - (R+1)(1-Y)}{\sqrt{R^2+1} + R + 1}$$

Estimating S at a Given Y . From Eqs. (A1) and (A4),

$$G = 1 - S(1+R) = G_{\min} + Y$$

$$S = \frac{1 - G_{\min} - Y}{R + 1} = \frac{2(R+1) - Y[\sqrt{R^2+1} + R + 1]}{(R+1)[\sqrt{R^2+1} + R + 1]} \quad (A7)$$

$$S = \frac{2}{\sqrt{R^2+1} + R + 1} - \frac{Y}{R+1} = S_{\max} - \frac{Y}{R+1}$$

Estimating G at Given X_p . From Eqs. (A1) and (A4),

$$G = 1 - S_{\max} X_p(1+R) = 1 - \frac{2X_p(1+R)}{\sqrt{R^2+1} + R + 1} \quad (A8)$$

$$G = \frac{\sqrt{R^2+1} - (R+1)(2X_P-1)}{\sqrt{R^2+1} + R + 1}$$

Relating X_P to G . From Eqs. (A1) and (A3),

$$S = S_{\max} X_P = \frac{1-G}{1+R} \quad (A9)$$

$$X_P = \frac{1-G}{1+R} \frac{\sqrt{R^2+1} + R + 1}{2} = \frac{\sqrt{R^2+1} + R + 1}{2(1+R)} (1-G)$$

Relating Y to X_P . From Eqs. (A1), (A3), and (A4),

$$G = 1 - S(R+1) = 1 - S_{\max} X_P(R+1) = G_{\min} + Y$$

$$Y = 1 - G_{\min} - S_{\max} X_P(R+1) = 1 - \frac{\sqrt{R^2+1} - (R+1)}{\sqrt{R^2+1} + (R+1)} - \frac{2X_P(R+1)}{\sqrt{R^2+1} + (R+1)} \quad (A10)$$

$$Y = \frac{2(R+1)}{\sqrt{R^2+1} + (R+1)} (1 - X_P)$$

and

$$Y = S_{\max}(R+1)(1 - X_P) \quad (A11)$$

Relating X_P to Y . From Eqs. (A1), (A3), and (A4),

$$X_P = \frac{1 - G_{\min} - Y}{S_{\max}(R+1)} = \frac{(R+1)(2-Y) - Y\sqrt{R^2+1}}{2(R+1)} \quad (A12)$$

$$X_P = 1 - \frac{\sqrt{R^2+1} + R + 1}{2(R+1)} Y = 1 - \frac{Y}{S_{\max}(R+1)} \quad (A13)$$

Relating N (Number of Shells) to Y .

$$S_N = \frac{1 - \left(\frac{1-RS}{1-S}\right)^N}{R - \left(\frac{1-RS}{1-S}\right)^N} \quad (A14)$$

where S is value of S for one shell and S_N is value of S for the N -shell exchanger.

Inverting Eq. (A14),

$$N = \frac{\ln\left(\frac{1-RS_N}{1-S_N}\right)}{\ln\left(\frac{1-RS}{1-S}\right)}, \quad (A15)$$

since

$$\left(\frac{1-RS}{1-S}\right) = \frac{1+RG}{R+G}$$

Hence,

$$N = \frac{\ln\left(\frac{1+RG_N}{R+G_N}\right)}{\ln W} \quad (A16)$$

where

$$W = \frac{1-RS}{1-S} = \frac{1+RG}{R+G} \quad (A17)$$

$$W = \frac{1+R(G_{\min}+Y)}{R+G_{\min}+Y}$$

$$W = \frac{\sqrt{R^2+1}(R+1+RY) - (R+1)(R-1-RY)}{\sqrt{R^2+1}(R+1+Y) + (R+1)(R-1-Y)} \quad (A18)$$

If N is Rounded Off to Next Integer M ($M > N$), How Much Y is Improved?

$$M = \frac{\ln\left(\frac{1+RG_N}{R+G_N}\right)}{\ln W}$$

$$\ln W = \frac{1}{M} \ln\left(\frac{1+RG_N}{R+G_N}\right) \quad (A19)$$

$$W = \left(\frac{1+RG_N}{R+G_N}\right)^{1/M}$$

From Eq. (A17), $G_1 = RW - 1/R - W = G_{\min} + Y'$ where Y' is improved Y .

$$Y' = \frac{RW-1}{R-W} - G_{\min} = \frac{RW-1}{R-W} - \frac{\sqrt{R^2+1} - R + 1}{\sqrt{R^2+1} + R + 1} \quad (A20)$$

$$Y' = \frac{R-1}{R-W} \frac{\sqrt{R^2+1}(W-1) + (R+1)(W+1)}{\sqrt{R^2+1} + R + 1}$$

Eq. (A20), used in conjunction with Eq. (A19) gives improved Y (i.e., Y') for the integer number of shells M ($> N$).

References

- [1] Kern, D. Q., 1965, *Process Heat Transfer*, McGraw-Hill, New York.
- [2] Underwood, A. J. V., 1934, "The Calculation of the Mean Temperature Difference in Multipass Heat Exchangers," *J. Inst. Pet. Tech.*, **20**, pp. 145-158.
- [3] Bowman, R. A., Mueller, A. C., and Nagle, W. M., 1940, "Mean Temperature Difference in Design," *Trans. ASME*, **62**, pp. 283-293.
- [4] Walker, G., 1982, *Industrial Heat Exchangers: A Basic Guide*, Hemisphere, Washington, D.C.
- [5] Saunders, E. A. D., 1988, *Heat Exchangers: Selection, Design and Construction*, John Wiley and Sons, New York.
- [6] Gulyani, B. B., and Mohanty, B., 1995, "A Novel F_T Plot for Shell and Tube Heat Exchangers," *Res. Ind.*, **40**, pp. 189-192.
- [7] Ahmad, S., Linnhoff, B., and Smith, R., 1988, "Design of Multipass Heat Exchangers: An Alternative Approach," *Trans. ASME*, **110**, pp. 304-309.
- [8] Bell, K. J., 1983, *Heat Exchanger Design Handbook*, Vol. 3, Hemisphere, Washington, D.C.
- [9] Frank, O., 1978, *Practical Aspects of Heat Transfer*, AIChE, New York.
- [10] Wales, R. E., 1981, "Mean Temperature Difference in Heat Exchangers," *Chem. Eng.*, **88**, pp. 77-81.
- [11] Gulyani, B. B., and Mohanty, B., 1996, "Estimating Log Mean Temperature Difference in Multipass Exchangers," *Chem. Eng.*, **103**, No. 11, pp. 127-130.

Flow and Heat Transfer Correlations for Porous Fin in a Plate-Fin Heat Exchanger

S. Y. Kim¹

e-mail: seoykim@kist.re.kr
Assoc. Mem. ASME

J. W. Paek

B. H. Kang

Thermal/Flow Control Research Center,
Korea Institute of Science and Technology,
Seoul 130-650, Korea

The present experimental study investigates the impact of porous fins on the pressure drop and heat transfer characteristics in plate-fin heat exchangers. Systematic experiments have been carried out in a simplified model of a plate-porous fin heat exchanger at a controlled test environment. The porous fins are made of 6101 aluminum-alloy foam materials with different permeabilities and porosities. Comparison of performance between the porous fins and the conventional louvered fins has been made. The experimental results indicate that friction and heat transfer rate are significantly affected by permeability as well as porosity of the porous fin. The porous fins used in the present study show similar thermal performance to the conventional louvered fin. However, the louvered fin shows a little better performance in terms of pressure drop. For compactness of the heat exchanger, the porous fins with high pore density and low porosity are preferable. Useful correlations for the friction factor and the modified j -factor are also given for the design of a plate-porous fin heat exchanger. [S0022-1481(00)01103-8]

Keywords: Experimental, Finned Surfaces, Heat Exchangers, Heat Transfer, Porous Media

Introduction

Heat exchange processes are indispensable to modern thermal engineering applications. On this account, tremendous studies on heat exchangers have been performed to enhance thermal transport between fluids during past several decades ([1]). Recent studies have concentrated on the development of high-performance compact heat exchangers to reduce energy consumption as well as material cost.

Various types of compact heat exchangers have been developed for specific applications. To exchange thermal energy between gas and liquid especially, compact heat exchangers with extended surfaces in the gas-side, such as wavy fin, offset strip fin, and louvered fin, are often utilized. Such fins substantially reduce the gas-side thermal resistance, which always acts as the major factor of degrading the performance of plate-fin heat exchangers.

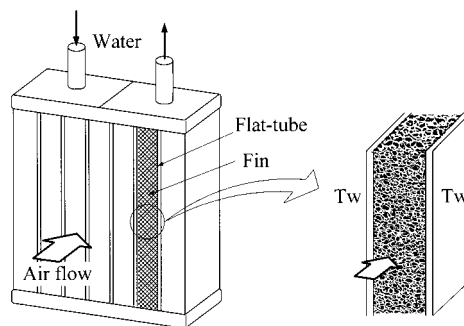
To date, the louvered fin is known to be the most efficient and effective surface geometry in view of enhanced heat transfer rate and it is being widely used in automotive and aircraft air-cooled heat exchangers ([2,3]). However, the manufacturing process of a louvered fin is rather complicated in that it requests a heavy financial investment for maintenance. Furthermore, the louvered fin has another potential disadvantage in structural strength since it is made of a very thin aluminum sheet. Consequently, there has been a demand for a new compact heat exchanger with fins that have a high heat transfer rate, and structural strength as well as a simple manufacturing process.

In an attempt to respond to the demand, we have focused on the utilization of a porous metal fin in place of the conventional louvered fin. The impetus is a high-surface-area-to-volume ratio as well as enhanced flow mixing due to the tortuous path of the porous fin. In addition, it has excellent characteristics in the structural strength as well as the simple manufacturing process of

metal foaming ([4]). Therefore, it is expected that the overall performance of plate-fin heat exchangers can be improved by using the porous fin.

The literature surveyed reveals that much research on the porous materials can be found, mainly in energy-related problems, which include the utilization of geothermal energy, the control of pollutant spread in ground water, high performance insulation, etc. ([5]). Recently several papers have emphasized substantial heat transfer enhancement by using porous inserts in a flow passage ([6–11]). However, efforts to get flow and heat transfer data of the porous fin for the design of compact heat exchanger are not being accomplished.

In the present study, a simplified model of a plate-fin heat exchanger, as shown in Fig. 1, is selected to investigate the impact of the porous fin on a plate-fin heat exchanger in detail. The simplified model emulates one flow passage of a conventional plate-fin heat exchanger. A porous fin is placed inside a channel, in which two channel walls are maintained at a constant temperature. The correlations of friction factor f and the j -factor for the porous fin will be sought to provide a design parameter for heat exchangers. Further, we scrutinize the performance of the porous fin in a plate-fin heat exchanger, compared with that of the louvered fin.



(a) Plate-fin heat exchanger (b) Simplified model

Fig. 1 Schematic configuration of the problem

¹To whom correspondence should be addressed. Thermal/Flow Control Research Center, Korea Institute of Science and Technology, P.O. Box 131, Cheongryang, Seoul 130-650, Korea.

Contributed by the Heat Transfer Division for publication in the JOURNAL OF HEAT TRANSFER. Manuscript received by the Heat Transfer Division, June 24, 1999; revision received, March 10, 2000. Associate Technical Editor: M. Hunt.

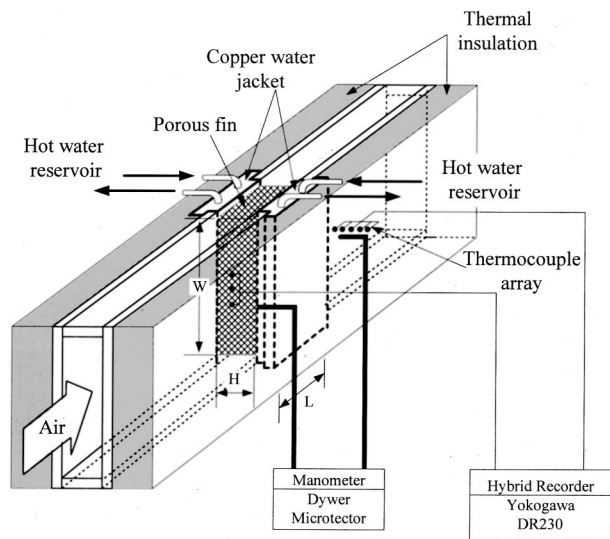


Fig. 2 Experimental apparatus

Experimental Apparatus and Test Procedure

A schematic diagram of the experimental apparatus is shown in Fig. 2. The experiments were conducted in a channel fabricated of Plexiglas of height $H=9.0$ mm and width $W=90.0$ mm. Test specimens of aluminum-alloy porous fins were made of height $H=9.0$ mm, $W=90.0$ mm, and length $L=30.0$ mm as depicted in Fig. 2. Pressure taps were installed at 5 mm upstream and downstream of the test section. The outlet of the channel was open to the atmosphere while the inlet was connected to a calming chamber in which the compressed air at 4 atm was induced through a rotameter. The rotameter was carefully calibrated by a bubble flow meter. Frontal air velocities U_i tested in the present experiments ranged from 0.48 m/s to 3.64 m/s, and the corresponding Reynolds number based on the fin height H was $Re_H=270-2050$. To measure the pressure drop through the test specimen, the precision manometer (Dwyer Microtector 1430) with a resolution of 1/100 mm in water height was used.

Two hot-water jackets made of copper were mounted on both side walls of the channel to provide a constant wall temperature condition. The water circulation loop supplied hot water to the jackets, as seen in Fig. 2. The temperature difference between the wall surface and the inlet air was set at 35°C during the experiments. The inlet air temperature was about 20°C. Three clamps were used to reduce thermal contact resistance between the jacket wall and the test specimen. As the compression loading of clamps was increased, the outlet air temperature approached an asymptotic value that was considered as a condition for minimal contact resistance. Three copper-constantan thermocouples (Omega AWG36) were also inserted between the jacket wall and the surface of the test specimen to verify the uniformity of the

wall surface temperature. At steady state, the temperature deviation along the hot walls was less than 0.2°C. All the channel walls were thermally insulated.

To measure the inlet air temperature, three copper-constantan thermocouples (Omega AWG36) were used at 5 mm upstream of the test section. Five copper-constantan thermocouples (Omega AWG36) were also horizontally distributed at 5 mm downstream of the test section to measure the air temperature at the outlet. The downstream air temperatures measured at the core region in the channel were slightly lower than those at the wall region. For a high flow rate, the maximum deviation between the thermocouples was about 6.2 percent. By averaging the temperatures measured upstream and downstream of the test section, the overall temperature rise of air was evaluated. The overall temperature rise of air was varied from 20.4°C to 33.8°C according to the flow rate and the specimen.

Experiments were started by inducing air flow to the channel and by maintaining the water jackets at constant temperature after installing the test specimen to the channel. The temperatures were monitored during the heat-up time by a data acquisition system (Yokogawa DR230). After reaching a thermal steady state, the temperature data were recorded on the storage device for data analysis.

Test Specimen and Data Reduction

The test specimens used in the present study are porous fins made of aluminum-alloy 6101 foam. The porous fins have three distinct pore densities, i.e., 10, 20, and 40 PPI (pores per inch) at the same porosity of $\epsilon=0.92$, and four different porosities, i.e., $\epsilon=0.89, 0.92, 0.94$, and 0.96 at the same pore density of 20 PPI, as described in Table 1. The surface-area-to-volume ratio β of the porous fin increases as the pore density (PPI) increases or the porosity decreases. The permeability K of the porous fin gradually decreases with an increase in the pore density due to the increased bulk friction. It is noted that permeability of the porous fin with 20 PPI is proportional to $(1-\epsilon)^2$, which shows a peak at $\epsilon=0.94$. It may be attributed to the change of microscopic pore shape according to the porosity of the porous fins ([12]). The permeabilities of the porous fins were determined by using the Forchheimer-extended Darcy model after measuring the pressure drop through the porous fin. The effective thermal conductivity of the present porous fin is little affected by the change of pore density while it is linearly increased by the decrease of porosity [13].

The friction factor f and the modified j -factor j^* are defined to assess the pressure drop and the heat transfer rate of the fins:

$$f = \frac{A_c}{A_o} \frac{2\rho\Delta P}{G_c^2} \quad (1)$$

$$j^* = \frac{\eta_s h}{G_c C_p} Pr^{2/3} = \eta_s j \quad (2)$$

In Eq. (1), the entrance and the exit loss coefficients are neglected ([14]). A_c indicates the minimum free flow area, $A_c = \epsilon A$, where A

Table 1 Test specimens of porous fins

| Porous Fin | Pore Density (PPI) | Porosity ϵ | Surface-area to-Volume Ratio $\beta=A_o/V$ (m^2/m^3) | Permeability K (m^2) | Darcy Number $Da=K/H^2$ | Effective Thermal Conductivity k_e (W/mK) [13] |
|------------|--------------------|---------------------|--|----------------------------|-------------------------|--|
| 1 | 10 | 0.92 | 790 | 2.36×10^{-7} | 2.85×10^{-3} | 5.33 |
| 2 | 20 | 0.92 | 1720 | 1.07×10^{-7} | 1.30×10^{-3} | 5.56 |
| 3 | 40 | 0.92 | 2740 | 7.15×10^{-8} | 8.63×10^{-4} | 6.01 |
| 4 | 20 | 0.89 | 2020 | 8.96×10^{-8} | 1.08×10^{-3} | 6.77 |
| 5 | 20 | 0.94 | 1510 | 1.30×10^{-7} | 1.57×10^{-3} | 4.27 |
| 6 | 20 | 0.96 | 1240 | 1.16×10^{-7} | 1.41×10^{-3} | 2.82 |

is the frontal area of the porous fin, $A = WH$. A_o is the total heat transfer area of porous fins, i.e., $A_o = A_f + A_b$, where A_f and A_b are the fin area and the base area, respectively. ρ is the density and ΔP the pressure drop through the fins. G_c is the mass velocity, $G_c = \rho U_i$, where U_i is the frontal velocity.

In Eq. (2), the modified j -factor includes the surface efficiency η_s of the fin to compare the thermal performance of the porous fin with that of the conventional louvered fin. Since it is difficult to evaluate the surface efficiency of the porous fin, we have multiplied the known value of the surface efficiency for the conventional louvered fin to its j -factor correlation ([15]). The surface efficiency η_s of the louvered fin is obtained from

$$\eta_s = 1 - \frac{A_f}{A_o} (1 - \eta_f). \quad (3)$$

The fin efficiency η_f is calculated from ([16])

$$\eta_f = \frac{\tanh(ml)}{ml}, \quad (4)$$

where

$$m = \sqrt{\frac{2h}{kt}}. \quad (5)$$

Here, the fin length l is the half of the channel height defined by $l = H/2 - t$. The t is the fin thickness and k the thermal conductivity of fin. The calculated surface efficiency of the louvered fin used in the present study was in the range of 0.93–0.98.

The h denotes the convective heat transfer coefficient for the air side that is determined from the overall energy balance without considering contact thermal resistance:

$$\eta_s h = U = \frac{G_c C_p A \Delta T}{A_o \Delta T_m}. \quad (6)$$

In the present model of the porous fin, therefore, $\eta_s h$ equals the overall heat transfer coefficient U . Then, the modified j -factor from Eq. (2) is expressed as

$$j^* = \frac{A}{A_o} \frac{\Delta T}{\Delta T_m} \text{Pr}^{2/3}. \quad (7)$$

In Eq. (7), the temperature difference of air between the inlet and the outlet ΔT and the logarithmic mean temperature difference (LMTD) ΔT_m are

$$\Delta T = T_o - T_i, \quad (8)$$

$$\Delta T_m = \frac{\Delta T}{\ln[(T_w - T_i)/(T_w - T_o)]}, \quad (9)$$

where T_i , T_o , and T_w denote, respectively, the air inlet, the air outlet, and the wall temperatures.

The uncertainties in the present experimental results were estimated by the single-sample experiment analysis described by Kline and McClintock ([17]). The uncertainties for the friction factor and the modified j -factor were mainly attributed to the variation of temperature, velocity, pressure, and the thermophysical properties of fluid while the effect of geometric uncertainty of the test section was meager. Therefore, the uncertainty of the friction factor can be expressed by

$$\frac{\delta f}{f} = \sqrt{\left(\frac{\delta \varepsilon}{\varepsilon}\right)^2 + \left(\frac{\delta \rho}{\rho}\right)^2 + \left(\frac{\delta \Delta P}{\Delta P}\right)^2 + \left(\frac{\delta A_o}{A_o}\right)^2 + \left(2 \frac{\delta G_c}{G_c}\right)^2}. \quad (10)$$

In Eq. (10), the uncertainties of the porosity ε and the total surface area A_o were 1.1 percent. The density variation was generally less than 1.5 percent because the friction factor was evaluated from the results of the cold-flow experiment. The uncertainties in the pres-

sure drop and the mass velocity were, respectively, 2.8 percent and 1.5 percent at 95 percent confidence. Then, the uncertainty in the friction factor was about 4.6 percent.

The uncertainty of the modified j -factor that can be derived from Eq. (7) is

$$\frac{\delta j^*}{j^*} = \sqrt{\left(\frac{\delta \Delta T}{\Delta T}\right)^2 + \left(\frac{\delta \Delta T_m}{\Delta T_m}\right)^2 + \left(\frac{\delta A_o}{A_o}\right)^2 + \left(\frac{2}{3} \frac{\delta \text{Pr}}{\text{Pr}}\right)^2}. \quad (11)$$

At $\text{Re} = 1530$, for example, the inlet, the outlet, and the wall temperatures were varied within ± 0.08 , 0.16 , and 0.22°C at 95 percent confidence, respectively. Therefore, the uncertainties in ΔT and ΔT_m were, respectively, 0.6 percent and 2.0 percent in 95 percent confidence level. The uncertainty in the Prandtl number ($\delta \text{Pr}/\text{Pr}$) was 0.7 percent. Consequently, the uncertainty in the modified j -factor was estimated by 2.4 percent.

Results and Discussion

Before presenting the results for the porous fins, it is necessary to confirm the appropriateness of the experimental test model. Thus, the benchmark test by using a conventional louvered fin has been performed, and the friction and j -factor values experimentally obtained were compared with the previous friction and j -factor correlations for the louvered fins in Fig. 3 ([18,3,15]). The louvered fin used in the present benchmark test has a dimension of louver pitch $L_p = 1.0$ mm, louver length $L_i = 8.0$ mm, fin height $H = 9.0$ mm, fin pitch $F_p = 1.88$ mm, flow depth $F_d = 26$ mm, and fin thickness $t = 0.1$ mm. Surface-area-to-volume ratio β of the louvered fin is $1320 \text{ m}^2/\text{m}^3$.

In Fig. 3, the friction factors of the present louvered-fin model are estimated to be comparable to the Achaichia and Cowell's correlation ([18]) for $\text{Re}_{L_p} > 200$. The correlation presented by Chang et al. [3] yields slightly lower values than the present louvered fin data. It may be attributed that the fin height of the louvered fins used in Chang et al. [3] is about two times larger than the present louvered fin. However, the trend of the friction factors according to the Reynolds number based on the louver pitch is very similar. The j -factors of the present louvered fin show a good agreement with the correlation by Chang and Wang [15]. Consequently, it is believed that the present experimental model for fins is satisfactory to estimate the fin performance of a plate-fin heat exchanger with reasonable accuracy.

Figure 4 shows the friction factor f for the porous fins as a function of the Reynolds number. The Reynolds number is based on the fin height H and the porosity ε is 0.92. For comparison, the friction factor of the louvered fin tested in the present study is also

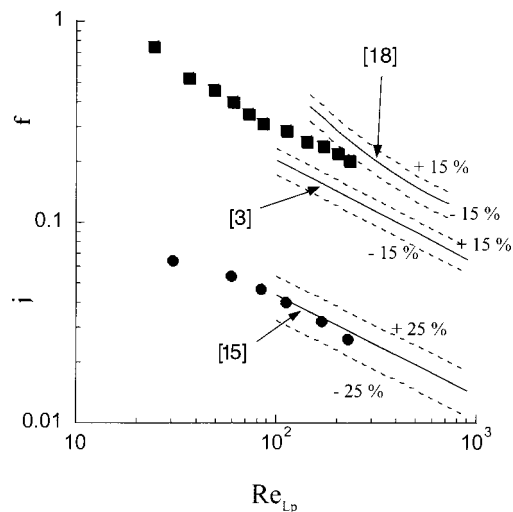


Fig. 3 Comparison of the friction and j -factors for the present louvered fin with the previous correlations

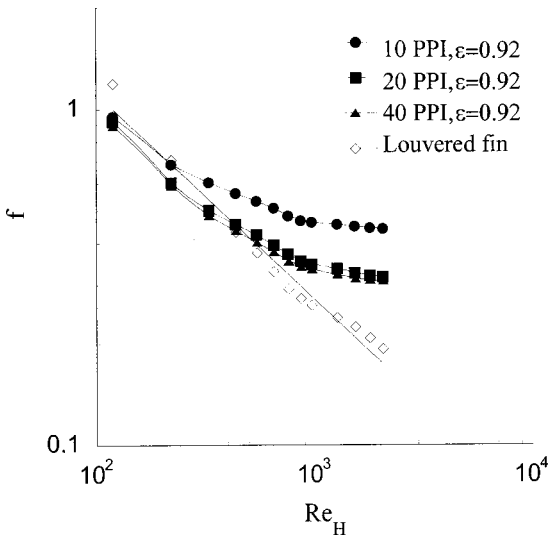


Fig. 4 Effect of pore density on the friction factors of the porous fin at $\varepsilon=0.92$

plotted in the figure. The friction factor f decreases gradually as Re increases. The friction factor f of the high permeable porous fin of 10 PPI is much higher than that of the lower permeable porous fins. This is attributed to the relatively small surface area of the high permeable porous fin. It is also noted that the friction factor of the louvered fin is slightly higher than that of the porous fins at low Reynolds numbers. As Re_H increases, however, the porous fins are shown to have higher friction factors compared to the louvered fin.

The effect of porosity variation of the porous fin on the friction factor is also displayed in Fig. 5. The pore density is fixed at 20 PPI. The porous fin of high porosity $\varepsilon=0.96$ shows a higher friction factor. Although the dimensional pressure drop decreases with the increase of the porosity $\varepsilon \geq 0.92$ ([11]), the friction factor defined in Eq. (1) increases due to the relatively rapid decrease in the surface area. It is also noted that the porous fins of porosity $\varepsilon < 0.96$ have similar friction factors without displaying any monotonic decrease. It is caused by nonlinear behavior of the pressure drop (permeability) according to the variation of porosity, as mentioned in Table 1.

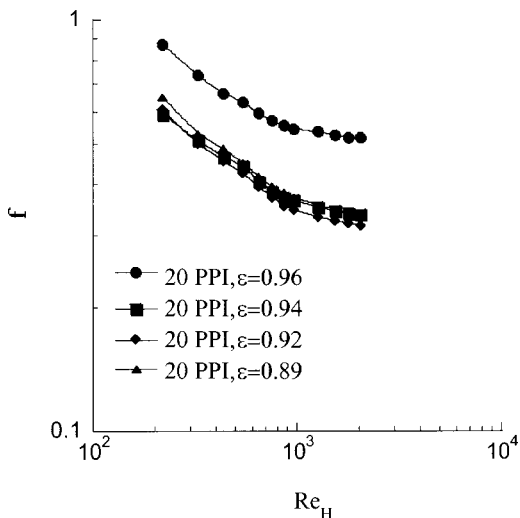


Fig. 5 Effect of porosity on the friction factors of the porous fin at 20 PPI

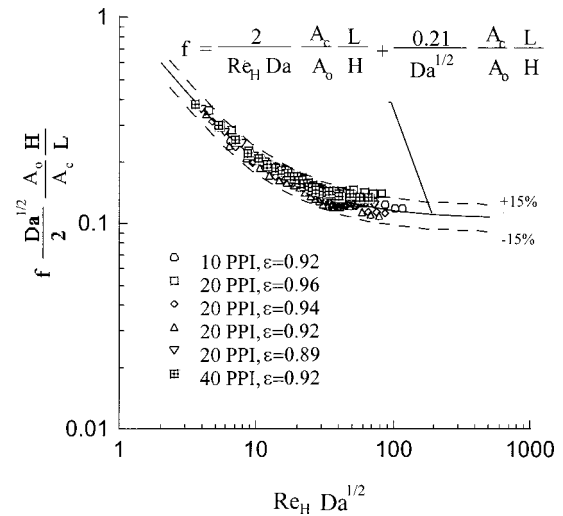


Fig. 6 Friction factor correlation of the porous fins

To derive a correlation of friction factors for the porous fins, the f data in Figs. 4 and 5 are converted by using the nondimensional parameters such as $Da^{1/2}$, A_c/A_o and L/H , as demonstrated in Fig. 6. Then, it is found that the friction factors f for the porous fins tested in the present study generally merge to a single curve with maximum 15 percent deviation:

$$f = \frac{2}{Re_H \cdot Da} \frac{A_c L}{A_o H} + \frac{0.21}{Da^{1/2}} \frac{A_c L}{A_o H} \quad (12)$$

Here, Da denotes the Darcy number K/H^2 . If the porous fin is considered as a local volume averaged continuous medium, the above definition of the friction factor can be expressed in terms of the pressure drop in a smooth porous channel without fins. Rearranging the above equation yields

$$\frac{(\Delta P/L)H}{\rho U_i^2} = \frac{1}{Re \cdot Da} + \frac{0.105}{Da^{1/2}} \quad (13)$$

It is interesting to note that Eq. (13) is exactly the same as the Forchheimer-extended Darcy model for porous media with an inertia coefficient of $C_E=0.105$ ([5]). In Eq. (13), the inertia coefficients C_E of the present porous fins are slightly varied from 0.095 to 0.115 according to the pore density and the porosity of the fin.

Now we shall deal with the modified j -factor to show the heat transfer characteristics of the porous fins. Figure 7 displays the effect of pore density on the modified j -factor j^* of the porous fins as a function of Reynolds number. The porosity is 0.92. As Re_H increases, the modified j -factors are decreased and the corresponding convective heat transfer rates h are increased. This is in accordance with the previous results by Huang and Vafai [7], Amiri and Vafai [19], and Kim et al. [11]. The modified j -factors are substantially pronounced as the pore density of the porous fin becomes small. It is also observed that the modified j -factor of the louvered fin used in the present study shows a similar value to that of the porous fin with 10 PPI.

The effect of porosity of the porous fin on the modified j -factor j^* is also exhibited in Fig. 8. The pore density is fixed at 20 PPI. The modified j -factor values of the porous fin with $\varepsilon=0.96$ are higher than those with lower porosity. For the fins of low porosity $\varepsilon \leq 0.94$, the modified j -factors show similar values. This may be caused by the combined effect of the surface area and the effective thermal conductivity according to the change of the porosity (see Table 1).

In an attempt to get a modified j -factor correlation of the porous fins, the nondimensional parameter, the Darcy number Da , is em-

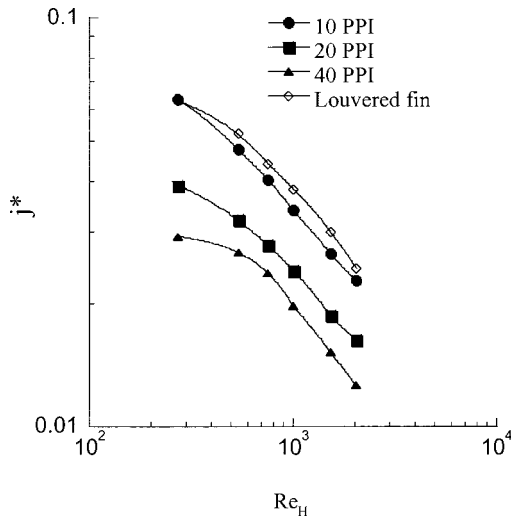


Fig. 7 Effect of pore density on the modified j -factors of the porous fins at $\varepsilon=0.92$

ployed again. When the modified j -factor data in Figs. 7 and 8 are converted using this nondimensional parameter, the data merge to a single line in the log-log plot exhibited in Fig. 9. Then, it gives a simple modified j -factor correlation with maximum 17 percent deviation for $270 < Re_H < 2050$:

$$j^* = 13.73(Re_H^{-0.489} Da^{0.451}). \quad (14)$$

The above equation implies that thermal performance of Al-alloy porous fins can be easily predicted from measuring permeability K at a known flow rate. It should be noted here that the above modified j -factor correlation has similar functional relationship to that for conventional heat exchangers ([3]):

$$j^* = C(Re^m \lambda^n), \quad (15)$$

where C denotes a constant and λ is the finning factor that reflects the flow geometry effects of the fin. Thus, it is obvious that the Darcy number Da in Eq. (14) implicates the equivalent finning factor of the porous fin in heat exchangers.

Compactness of a heat exchanger is another important design parameter. Therefore, the volume goodness factor will be considered here. The air-side performance of the porous fin for a unit

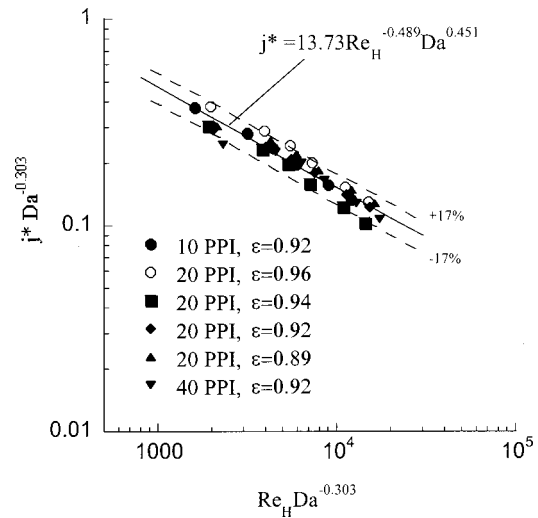


Fig. 9 Modified j -factor correlation of the porous fins

volume is expressed by $\eta_s h \beta$. Here we should distinguish the air-side performance from the aforementioned modified j -factor. While the modified j -factor shows the heat transfer from a unit heat transfer surface, the air-side performance represents the total heat transfer that can be obtained in a unit heat-exchanging volume. Therefore, the porous fin with low j -factors can show a high air-side performance when it has a high-surface-area-to-volume ratio. Also, the friction power consumption per a unit volume can be evaluated by ([14])

$$E\beta = \frac{U_i A_c \Delta P}{A_o} \frac{A_o}{V}. \quad (16)$$

Figure 10 delineates the air-side performance $\eta_s h \beta$ and friction power $E\beta$ characteristics for the porous fins at $\varepsilon=0.92$. The air-side performance $\eta_s h \beta$ of the porous fin increases with an increase in the friction power $E\beta$. As the pore density PPI increases, the $\eta_s h \beta$ at the same friction power is pronounced. At a low friction power range, the $\eta_s h \beta$ of the louvered fin is higher than that of the porous fins. When the friction power exceeds $E\beta > 10^3$, however, the $\eta_s h \beta$ of the porous fin with 40 PPI is

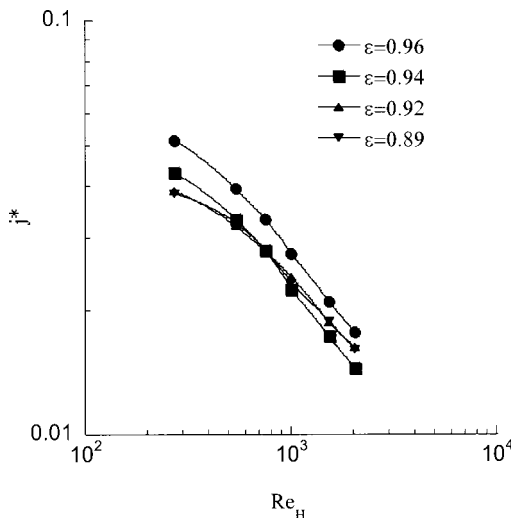


Fig. 8 Effect of porosity on the modified j -factors of the porous fins at 20 PPI

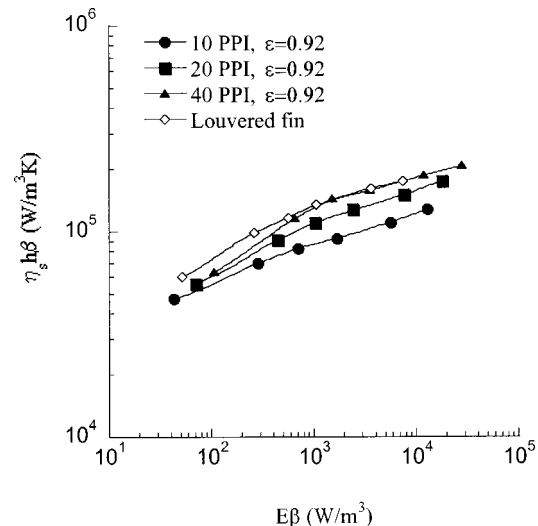


Fig. 10 Effect of pore density on the air-side performance $\eta_s h \beta$ of the porous fins at $\varepsilon=0.92$

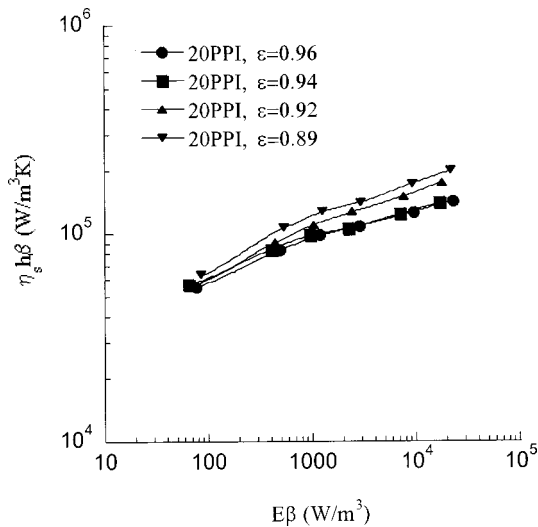


Fig. 11 Effect of porosity on the air-side performance $\eta_s h \beta$ of the porous fins at 20 PPI

comparable to that of the louvered fin. Therefore, it may be more beneficial to use the low permeable porous fin at the high-volume flow range.

Influence of porosity of the porous fin on the air-side performance $\eta_s h \beta$ and the friction power consumption $E \beta$ is also depicted in Fig. 11. As the porosity decreases for a fixed pore density of 20 PPI, the $\eta_s h \beta$ of the porous fin increases. Therefore, it may be concluded that the porous fins with low permeability and low porosity are preferable in terms of the compactness of heat exchangers.

Conclusion

An experimental investigation on the effect of porous fin in a simplified model of plate-fin heat exchanger has been performed. Six aluminum-alloy porous fins of various permeabilities and porosities were selected to scrutinize the performance of porous fins for the application to plate-fin heat exchangers. Comparison of heat transfer and friction characteristics between the porous fins and the conventional louvered fin was made.

Experimental results indicate that the friction factor is much lower for low permeable porous fins due to relatively larger surface area. The louvered fin exhibits slightly higher friction factor values than that of the porous fins at low Reynolds numbers. When the Reynolds number is high, however, the porous fins show much higher friction factors compared to the louvered fin. The modified j -factors of the porous fins decrease as the pore density increases or as the porosity decreases. It is noted that the present porous fins have a similar thermal performance compared to the conventional louvered fin; however, the louvered fin shows a little better performance in terms of pressure drop. The friction and heat transfer correlations for the porous fins have been obtained by employing the Darcy number, Da , and the geometrical parameters such as A_c/A_o and L/H . It is also found that the porous fins with low permeability and low porosity are preferable to compactness of plate-porous fin heat exchangers.

Acknowledgment

This work was supported by a grant from the Critical Technology 21 Project of the Ministry of Science and Technology, Korea and Jang-Han Engineering, Inc. The support of test specimen from ERG, Inc. is deeply acknowledged by the authors.

Nomenclature

- A = frontal area of test specimen (m^2), $A = WH$
- A_b = heat transfer area at the base of porous fin (m^2), $A_b = WL$
- A_c = minimum free-flow area (m^2), $A_c = \varepsilon A$
- A_f = fin surface area of porous fin (m^2)
- A_o = total heat transfer surface area of porous fin (m^2), $A_o = A_f + A_b$
- C_p = specific heat at constant pressure (J/kgK)
- Da = Darcy number, K/H^2
- D_h = hydraulic diameter (m), $2H$
- E = friction power, Eq. (16)
- f = friction factor, Eq. (1)
- h = length-averaged heat transfer coefficient, Eq. (3) (W/m^2K)
- H = height of channel (m)
- j = Colburn j -factor, $j = (h/G_c C_p) Pr^{2/3}$
- j^* = modified j -factor, Eq. (2)
- k = thermal conductivity of fin
- K = permeability of porous fin (m^2)
- L = length of porous fin (m)
- L_p = louver pitch of louvered fin (m)
- PPI = pores per inch
- Pr = Prandtl number, ν/α
- Re_H = Reynolds number based on the fin height H , $U_i H/\nu$
- Re_{L_p} = Reynolds number based on the louver pitch of louvered fin, $U_i L_p/\nu$
- T_i = inlet air temperature (K)
- T_o = outlet air temperature (K)
- T_w = wall temperature (K)
- U_i = frontal air velocity (m/s)
- W = width of channel (m)

Greek Symbols

- β = heat transfer surface area to volume ratio (m^2/m^3), A_o/V
- ΔP = pressure drop of air flow (Pa)
- ΔT = temperature difference of air between the inlet and the outlet (K), Eq. (4)
- ΔT_m = log mean temperature difference (K), Eq. (5)
- ε = porosity
- ρ = density of air (kg/m^3)
- ν = kinematic viscosity (m^2/s)
- η_f = fin efficiency
- η_s = surface efficiency

References

- [1] Webb, R. L., 1994, *Principles of Enhanced Heat Transfer*, John Wiley and Sons, New York.
- [2] Sahnoun, A., and Webb, R. L., 1992, "Prediction of Heat Transfer and Friction for the Louver Fin Geometry," *ASME J. Heat Transfer*, **114**, pp. 893–900.
- [3] Chang, Y.-J., Wang, C.-C., and Chang, W. J., 1994, "Heat Transfer and Flow Characteristics of Automotive Brazed Aluminum Heat Exchangers," *ASHRAE Trans.*, **100**, No. 2, pp. 643–652.
- [4] Gibson, L. J., and Ashby, M. F., 1997, *Cellular Solids*, Cambridge University Press, Cambridge, UK.
- [5] Kaviany, M., 1991, *Principles of Heat Transfer in Porous Media*, Springer-Verlag, New York.
- [6] Hunt, M. L., and Tien, C. L., 1988, "Effects of Thermal Dispersion on Forced Convection in Fibrous Media," *Int. J. Heat Mass Transf.*, **31**, pp. 301–309.
- [7] Huang, P. C., and Vafai, K., 1993, "Flow and Heat Transfer Control Using a Porous Block Array Arrangement," *Int. J. Heat Mass Transf.*, **36**, pp. 4019–4032.
- [8] Huang, P. C., and Vafai, K., 1994, "Analysis of Forced Convection Enhancement in a Channel Using Porous Blocks," *J. Thermophys. Heat Transfer*, **8**, pp. 563–573.
- [9] Hadim, A., 1994, "Forced Convection in a Porous Channel With Localized Heat Sources," *ASME J. Heat Transfer*, **116**, pp. 465–472.
- [10] Sung, H. J., Kim, S. Y., and Hyun, J. M., 1995, "Forced Convection From an Isolated Heat Source in a Channel With Porous Medium," *Int. J. Heat Fluid Flow*, **16**, pp. 527–535.
- [11] Kim, S. Y., Kim, J.-H., and Kang, B. H., 1998, "Effect of Porous Fin in a

- Plate-Fin Heat Exchanger," *Proceedings of the ASME Heat Transfer Division*, **3**, ASME, New York, pp. 477–482.
- [12] ERG Duocel Aluminum Foam Catalog, 1995, Energy Research and Generation, Inc. Oakland, CA.
- [13] Paek, J. W., Kang, B. H., Kim, S. Y., and Hyun, J. M., 2000, "Effective Thermal Conductivity and Permeability of Aluminum Foam Materials," *Int. J. Thermophys.*, **21**, pp. 453–464.
- [14] Kays, W. M., and London, A. L., 1984, *Compact Heat Exchangers*, McGraw-Hill, New York.
- [15] Chang, Y.-J., and Wang, C.-C., 1997, "A Generalized Heat Transfer Correlation for Louver Fin Geometry," *Int. J. Heat Mass Transf.*, **40**, pp. 533–534.
- [16] McQuiston, F. C., and Parker, J. D., 1994, *Heating, Ventilating, and Air-Conditioning Analysis and Design*, John Wiley and Sons, New York.
- [17] Figliola, R. S., and Beasley, D. E., 1995, *Theory and Design for Mechanical Measurements*, Wiley, New York.
- [18] Achaichia, A., and Cowell, T. A., 1988, "Heat Transfer and Pressure Drop Characteristics of Flat Tube and Louvered Plate Fin Surfaces," *Exp. Therm. Fluid Sci.*, **1**, pp. 147–157.
- [19] Amiri, A., and Vafai, K., 1994, "Analysis of Dispersion Effects and Non-Thermal Equilibrium Non-Darcian, Variable Porosity Incompressible Flow Through Porous Medium," *Int. J. Heat Mass Transf.*, **37**, pp. 939–954.

Optimization of Matrix Heat Exchanger Geometry

K. Pavan Kumar
G. Venkatarathnam¹
e-mail: gvenkat@acer.iitm.ernet.in

Refrigeration and Airconditioning Laboratory,
Department of Mechanical Engineering,
Indian Institute of Technology, Madras,
Chennai 600 036, India

Matrix heat exchangers are used in a number of applications such as helium liquefiers, sorption refrigerators, and in Kleemenko cryocoolers. In this paper the methods for the optimum sizing of balanced flow and unbalanced flow matrix heat exchangers of rectangular and circular shapes are presented. Using the methods developed, the relative size of matrix heat exchangers of rectangular and circular shapes are compared.
[S0022-1481(00)01503-6]

Keywords: Cryogenics, Heat Exchangers, Heat Transfer, Optimization

1 Introduction

Perforated plate matrix heat exchangers (Fig. 1) were invented in 1949 by McMahon et al. [1] and are finding increasing use in the recently introduced Kleemenko (mixed refrigerant cascade) cryocoolers, as well as in very low temperature systems such as sorption refrigerators and Helium II systems. A detailed description of the chronological developments, the fabrication techniques, and the heat transfer phenomenon in matrix heat exchanger has been presented by Venkatarathnam and Sarangi [2].

A matrix heat exchanger essentially consists of a stack of copper perforated plates alternating with stainless steel or plastic spacers. When bonded together they form a monolithic block with leak free passages for two or more streams exchanging heat with one another. The main purpose of the spacers is to decrease the longitudinal (axial) heat conduction through the wall. The spacers also serve to increase the convective heat transfer coefficients by interrupting the flow. Matrix heat exchangers can be made of many shapes. The most common are (a) rectangular shape with two passages shown in Fig. 1, (b) circular shape with two or more passages shown in Fig. 2, and (c) rectangular shape with multiple passages, originally used by Fleming [3] as shown in Fig. 3.

1.1 Heat Transfer Phenomenon. The heat transfer between the streams is essentially controlled by the following resistances:

- convective heat transfer resistance in the flow channels (perforated plates)
- conduction resistance offered by the perforated plates in either flow channel
- lateral conduction resistance offered by the plates
- longitudinal conduction resistance of all the walls of the matrix heat exchanger

The convective heat transfer coefficients depend on a number of geometrical parameters such as the plate porosity, ratio of the plate thickness to perforation diameter, ratio of the plate thickness to spacer thickness, alignment of perforations in adjacent plates, and the type of perforations used (circular holes, rectangular slits, etc.). General convective heat transfer correlations that take into account all these effects are not yet available. Some authors have presented convective heat transfer correlations applicable for some range of parameters, and for very specific cases (see [2]).

A number of methods have been developed during the last 50 years to analyze the performance of matrix heat exchangers. In most of the initial studies, the matrix heat exchanger was treated as a conventional heat exchanger, but with the wall having different thermal conductance in the lateral and longitudinal directions

¹To whom correspondence should be addressed.

Contributed by the Heat Transfer Division for publication in the JOURNAL OF HEAT TRANSFER. Manuscript received by the Heat Transfer Division, June 24, 1999; revision received, April 17, 2000. Associate Technical Editor: B. Chung.

to account for the the presence of low thermal conductivity spacers in between the copper or aluminum plates. The perforated plates were treated as fins to account for the thermal resistance of the plate. Sarangi and Barclay [4] first showed that the attainable effectiveness is a strong function of the number of plate-spacer pairs in the heat exchanger. Their study clearly showed that the matrix heat exchanger can be treated as a conventional heat exchanger only when the number of plate-spacer pairs is very large. They, however, neglected the effect of lateral thermal resistance in the wall as well as the thermal resistance of perforated plates, which are both non-negligible in all practical matrix heat exchangers. Most of the later workers have adopted the approach of Sarangi and Barclay [4] and have taken into account the effect of a finite number of plate-spacer pairs while analyzing the steady state as well as the transient response of matrix heat exchangers.

Venkatarathnam [5] presented an analytical expression for the effectiveness of a matrix heat exchanger in terms of the different thermal resistances including the thermal resistance of the perforated plates and the effect of finite plate-spacer pairs as follows:

$$\epsilon = \frac{NTU_{\text{eff}}}{NTU_{\text{eff}} + 1} \quad (\nu = 1) \quad (1)$$

$$\epsilon = \frac{1 - e^{-NTU_{\text{eff}}(1-\nu)}}{1 - \nu e^{-NTU_{\text{eff}}(1-\nu)}} \quad (\nu < 1) \quad (2)$$

where ν is the heat capacity rate ratio and NTU_{eff} is the effective number of heat transfer units and is defined for the balanced flow ($\nu = 1$) and unbalanced flow ($\nu < 1$) cases as follows:

$$NTU_{\text{eff}} = \frac{n(1-\alpha_1)(1-\alpha_2)}{n\lambda(1-\alpha_1)(1-\alpha_2) + 1 - \alpha_1\alpha_2 + (1-\alpha_1)(1-\alpha_2)/ntu_{p,o}} \quad (\nu = 1) \quad (3)$$

$$NTU_{\text{eff}} = \frac{n \ln(\varphi)}{n\lambda \ln(\varphi) + \nu - 1} \quad (\nu < 1) \quad (4)$$

where φ is an intermediate variable, n is the number of plate spacer pairs, ntu_f is the number of heat transfer units per side, λ is the axial conduction parameter of the walls, and $ntu_{p,o}$ is the dimensionless conductance of the entire perforated plate forming the two flow channels and the wall and are defined as follows:

$$\varphi = \frac{\kappa + \alpha_1 + \frac{1-\alpha_1}{ntu_{p,o}}}{1 + \kappa\alpha_2 + \frac{1-\alpha_1}{ntu_{p,o}}}; \quad \kappa = \frac{1-\alpha_1}{1-\alpha_2} \nu; \quad (5)$$

$$\alpha_i = \exp(-ntu_{f,i}); \quad ntu_{f,i} = \left(\frac{hA}{\dot{m}c_p} \right)_i$$

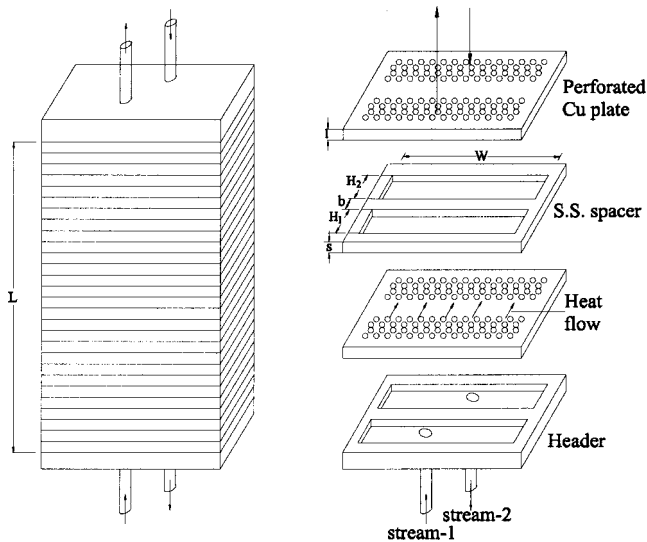


Fig. 1 Schematic of a matrix heat exchanger of rectangular geometry with two passages

$$\lambda = \frac{k_s A_w / s}{n(\dot{m} c_p)_1}; \quad \frac{1}{ntu_{p,o}} = \frac{1}{F ntu_{p,1}} + \frac{1}{\lambda_p} + \frac{\nu}{F ntu_{p,2}} \quad (6)$$

In the above expression F is a factor dependent on the geometry of the perforated plates. The expressions for the geometry factor F and $ntu_{p,i}$, the dimensionless conductance of the perforated plate in the i th channel, and λ_p , the lateral dimensionless conductance of the separating wall for rectangular, circular, and annular geometries are given in Tables 1 and 2.

Though a number of workers analyzed the performance of matrix heat exchangers, very few studies are available on the design (sizing) of matrix heat exchangers. Recently, Venkatarathnam [6] presented a method for the optimum sizing of a two-channel matrix heat exchanger of rectangular geometry with balanced flow condition ($\nu = 1$). The study was based on the assumption that the lateral thermal resistance ($1/\lambda_p$) of the wall is negligible compared to that of the perforated plate in either channel ($1/ntu_{p,i}$). Also the longitudinal heat conduction through the wall separating the two streams was only taken account in the analysis. Longitudinal conduction through the walls separating the fluid from the environment was not considered in that analysis. With the above assumptions, Venkatarathnam [6] showed that for an optimum design, the overall longitudinal (axial) heat conduction parameter

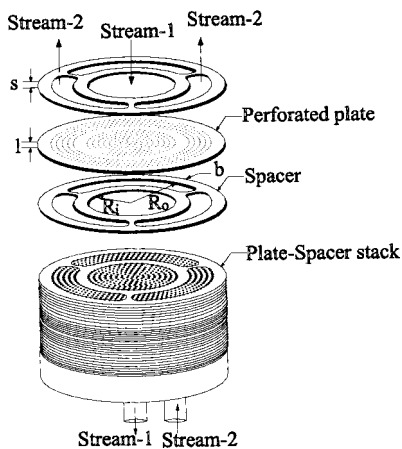


Fig. 2 Schematic of a matrix heat exchanger of circular geometry

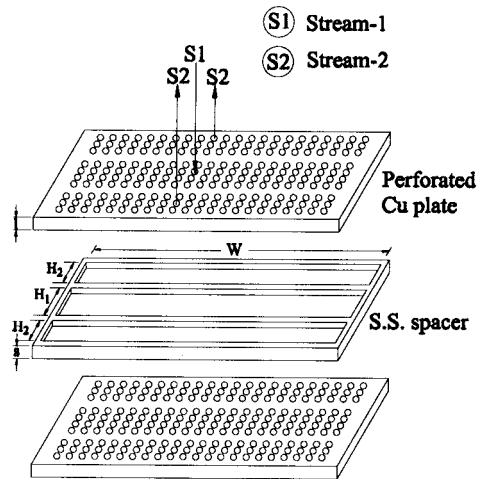


Fig. 3 Schematic of a matrix heat exchanger of rectangular geometry with multiple passages

(λ), the number of plate-spacer pairs (n), and the overall dimensionless thermal conductance ($ntu_{p,o}$) of the perforated plate are related as follows:

$$n\lambda = \frac{2}{ntu_{p,o}} \quad (\nu = 1, \lambda_p \rightarrow \infty) \quad (7)$$

Balanced flow conditions ($\nu = 1$) will exist in matrix heat exchangers used in cryorefrigerators operating with helium only when the operating temperature lies between 300K and 80K and when the flow rates of the two streams are equal. At lower temperatures, however, the flow will be unbalanced even when the flow rates of the two streams are equal because of the variation of specific heat of helium with pressure. The flow will also be unbalanced in many matrix heat exchangers used in Kleemenko cryocoolers operating with a mixture of gases. There is a need for design methods for balanced and unbalanced cases as well as for matrix heat exchangers of circular shape, and to account the different resistances neglected in reference [6], which are non-negligible in most practical matrix heat exchangers.

The main aim of this paper is to derive comprehensive methods for the optimum sizing of matrix heat exchangers of rectangular and circular shapes taking into account all the thermal resistances and to compare the sizes of matrix heat exchanger of circular and

Table 1 Expressions for the dimensionless plate conductance (ntu_p) and geometry factor F .

| Shape | ntu_p | F |
|-------------|-------------------------|--|
| Rectangular | $(Wlk)/(H\dot{m}c_p)$ | 3 |
| Circular | $(\pi lk)/(\dot{m}c_p)$ | 8 |
| Annular | $(\pi lk)/(\dot{m}c_p)$ | $((R_o^2 - R_i^2)^2) / \left(\frac{R_o^2 R_i^2}{2} - \frac{3}{8} R_o^4 - \frac{1}{8} R_i^4 + \frac{R_o^4}{2} \ln \frac{R_o}{R_i} \right)$ |

Table 2 Expressions for λ and λ_p

| Parameter | λ | λ_p |
|---------------------------|---|--|
| Rectangular (two channel) | $\frac{k_s b(3W + 2H_1 + 2H_2 + 6b)}{sn(\dot{m}c_p)_1}$ | $\frac{k_p l W}{b(\dot{m}c_p)_1}$ |
| Circular | $\frac{2k_s \pi b(R_j + R_o)}{sn(\dot{m}c_p)_1}$ | $\frac{2k_p l \pi}{(\dot{m}c_p)_1 \ln \left(\frac{R_i + b}{R_i} \right)}$ |

rectangular shape for meeting required heat transfer and pressure drop constraints. In the case of matrix heat exchanger of circular geometry, it is not clearly known whether the inner (circular) or outer (annular) channel needs to be chosen for the low pressure stream so that the overall volume is minimized. Authors from the former Soviet Union have shown a preference for the circular shape, whereas those in other parts of the world have predominantly preferred the rectangular shape. A comparison of volumes of matrix heat exchangers of rectangular shape with two and three channels and a matrix heat exchanger of circular shape is not available in the open literature. This problem is also addressed in this paper.

2 Optimum Sizing of Matrix Heat Exchangers

The design of a perforated plate matrix heat exchanger essentially consists of choosing the following:

- a heat transfer surface (type of perforation, porosity (p), plate thickness (l) and spacer thickness (s)).
- overall dimensions such as the heat exchanger width (W), the height of the plate in each channel (H_1, H_2) in the case of rectangular plates, and the diameter or radius of the different channels (R_o, R_i) in the case of circular plates, as well as the number of plate-spacer pairs (n) to be used. These dimensions are illustrated in Figs. 1 and 2.

In this work the methods for the selection of overall dimensions, width, height in the case of a matrix heat exchanger of rectangular shape, or outer and inner radius in the case of a matrix heat exchanger of circular shape are derived for a given surface. Also, the criteria for the choice of a particular geometry is discussed.

The volume (mass) of a matrix heat exchanger affects the performance of a heat exchanger in three different ways:

- 1 A large volume will result in an increased heat leak from the ambient and hence result in a lower effectiveness.
- 2 A large volume (mass) also increases the cool-down time considerably.
- 3 A large volume will also necessitate a larger refrigerant charge in the system, particularly in the case of Kleemenko cryocoolers in which the fluids undergo a phase change in the heat exchanger.

It is therefore necessary to design cryogenic heat exchangers for minimum volume. In optimization studies the function that is minimized or maximized is normally termed as the objective function. In the case of the matrix heat exchanger, the design should also meet the requirements of heat load (effectiveness) as well as pressure drop requirements. These are normally termed as constraints. The optimization problem can be expressed mathematically as follows:

Objective Function

$$\text{Minimize (Volume) or } \min[n(W+2b)(H_1+H_2+3b)] \quad (\text{rectangular}) \quad (8)$$

$$\text{or } \min[n(R_o+b)^2] \quad (\text{circular}) \quad (9)$$

The dimensions W, H_1, H_2, b , and R_o are shown in Figs. 1 and 2.

Constraints

$$\epsilon = \epsilon(\text{specified}) \quad (10)$$

$$\Delta P \leq \Delta P(\text{allowable}) \quad (11)$$

Normally the pressure drop of the low-pressure stream is more critical than that on the high-pressure stream in most cryogenic heat exchangers including the matrix heat exchanger. The pressure drop is a function of the number of plates (n) and can be determined using the following expression ([2]):

$$\Delta P = n\xi \frac{G_d^2}{\rho} \quad (12)$$

where ξ is the drag coefficient which has been found to be generally independent of Re for $Re > 160$ and weakly dependent on Re for $Re < 160$ ([7,8]). In the above expression, G_d is the mass flux through any perforation and ρ is the density of the fluid.

2.1 Assumptions. The optimization problem is based on the following assumptions:

- 1 The number of plates in the exchanger is large and can be treated as a continuous variable.
- 2 The heat exchanger will be designed such that the allowable pressure drop on the low-pressure side is utilized fully.
- 3 The thermophysical properties do not vary along the length of the heat exchanger.

3 Optimization Procedure

It is customary to use dimensional variables such as length, width, or height of the heat exchanger in all optimization studies. On the other hand, most analytical and experimental results are presented in terms of dimensionless variables or groups. In order to use the information generated in analytical studies, it is beneficial to convert the dimensional variables of the optimization study into dimensionless variables. Following Venkatarathnam [6], dimensionless variables $ntu_{f,1}$, $ntu_{f,2}$, and $ntu_{p,1}$ are used in the place of width and height of the plate in each of the fluid flow channels in the case of a rectangular shape matrix heat exchanger. In the case of a matrix heat exchanger of circular shape, $ntu_{f,1}$, $ntu_{f,2}$ are used as the variables of the optimization study. There are several advantages in using dimensionless groups as design variables instead of dimensional variables such as width, height, etc.

- It may be possible to derive closed-form analytical relationships between different dimensionless groups.
- Realistic starting points can be used in optimization studies, based on prior analytical and experimental studies.
- Certain limits can be imposed for the dimensionless variables based on earlier studies, or to satisfy mathematical or physical limits. For example, the fin efficiency η will vary between 0 and 1, $ntu_{f,i}$ between 0 and 2 ([5]), etc. It is difficult to impose similar limits on dimensional variables such as length, height, or width. This approach is particularly helpful when a new type of heat exchanger design is being optimized or the designer is somewhat inexperienced and lacks a feel for the physical size of the heat exchanger that may be required to meet a given heat duty.

The procedure followed for the optimization of matrix heat exchangers consists of the following broad steps:

- 1 expression of the design variables in terms of relevant dimensionless variables/groups.
- 2 expression of the objective function (volume) and constraints (pressure drop, and effectiveness required) in terms of dimensionless groups.
- 3 formulation of the Lagrangian equations and solution of the equations to derive algebraic relationships between the different parameters.

3.1 Optimization of a Matrix Heat Exchanger of Rectangular Geometry. The dimensionless plate conductance parameter $ntu_{p,i}$ and the number of heat transfer units per plate $ntu_{f,i}$ are dependent on the plate width (W) and the plate height in each channel (H_i) as follows:

$$ntu_{p,i} = \left(\frac{k_p W l}{H \dot{m} c_p} \right)_i \quad ntu_{f,i} = \left(\frac{h A'' W H l}{\dot{m} c_p} \right)_i \quad (13)$$

In the above expression the heat transfer coefficient (h) is determined using the expression

$$Nu = C Re^\gamma \quad (C \text{ and } \gamma \text{ function of surface geometry}). \quad (14)$$

Using the above definitions of $ntu_{p,i}$ and $ntu_{f,i}$, the dimensional design variables H_i and W can be expressed as follows:

$$W = (\omega_i \psi_i)^{0.5} ntu_{p,i}^{0.5} ntu_{f,i}^{0.5\beta_i} \quad (i = 1, 2) \quad (15)$$

$$H_1 = \left(\frac{\omega_1}{\psi_1} \right)^{0.5} ntu_{p,1}^{-0.5} ntu_{f,1}^{0.5\beta_1} \quad H_2 = \frac{\omega_2}{(\omega_1 \psi_1)^{0.5}} ntu_{p,1}^{-0.5} \frac{ntu_{f,2}^{\beta_2}}{ntu_{f,1}^{0.5\beta_1}} \quad (16)$$

where β_i , ω_i , and ψ_i are dimensionless constants made up of surface characteristics and thermophysical constants and mass flow rate as follows:

$$\beta_i = \left(\frac{1}{1 - \gamma_i} \right) \quad \omega_i = \left[\left(\frac{\dot{m} c_p d}{A''' k_f C} \right) \left(\frac{p \mu}{\dot{m} d} \right)^\gamma \right]^{\beta_i} \quad \psi_i = \left(\frac{\dot{m} c_p}{k_p l} \right)_i \quad (17)$$

The pressure drop in matrix heat exchangers is a strong function of the number of plate-spacer pairs. Assuming that the allowable pressure drop on the low-pressure side is fully utilized, the number of plate-spacer pairs can be expressed in terms of the design variable $ntu_{f,1}$ using Eqs. (12), (15), and (16) as follows:

$$n = \frac{\Delta P \rho}{\xi G_d^2} = K ntu_{f,1}^{2\beta_1} \quad \left(K = \frac{\Delta P \rho_1 p^2 \omega_1^2}{\xi \dot{m}^2} \right). \quad (18)$$

K is independent of Reynolds number (Re) or the design variable ntu_f in the turbulent flow regime but is function of ntu_f in the case of laminar flow since ξ is a function of the Reynolds number Re . The exact definition of K in laminar flow regime will depend on the particular ξ correlation used.

The objective function, namely, volume (Eq. (8)) as well as other parameters such as $ntu_{p,o}$, λ , λ_p can all be expressed in terms of the dimensionless design variables using Eqs. (15) and (16).

3.2 Optimization of a Matrix Heat Exchanger of Circular Geometry. The major dimensions of a matrix heat exchanger of circular shape are the outer radius (R_o) of the heat exchanger and the radius of the annular channel (R_i). In the case of circular geometry, the number of heat transfer units per side ($ntu_{f,i}$) and the dimensionless plate conductance parameter ($ntu_{p,i}$) are defined as follows:

$$ntu_{p,i} = \frac{\pi l k_p}{\dot{m} c_p}; \quad ntu_{f,1} = \frac{h A''' \pi R_i^2 l}{(\dot{m} c_p)_1};$$

$$ntu_{f,2} = \frac{h A''' \pi (R_o^2 - (R_i + b)^2) l}{(\dot{m} c_p)_2}. \quad (19)$$

Using the above definitions of $ntu_{f,1}$ and $ntu_{f,2}$, the dimensional design variables R_i and R_o can be expressed in terms of dimensionless design variables as follows:

$$R_i = \Omega_1^{0.5} ntu_{f,1}^{0.5\beta_1} \quad (20)$$

$$R_o^2 = \Omega_1 ntu_{f,1}^{\beta_1} + \Omega_2 ntu_{f,2}^{\beta_2} + 2b \sqrt{\Omega_1 ntu_{f,1}^{\beta_1} + b^2} \quad (21)$$

where Ω_1 and Ω_2 are dimensionless constants made up of thermophysical constants, surface characteristics, and mass flow rates as follows:

$$\Omega_i = \left[\left(\frac{\dot{m} c_p d}{\pi A''' l k_f C_i} \right) \left(\frac{\pi p \mu}{\dot{m} d} \right)^{\gamma_i} \right]^{\beta_i} \quad (i = 1, 2). \quad (22)$$

As in the case of rectangular geometry, the number of plates (n) can be expressed in terms of the pressure drop constraint as follows:

$$n = K ntu_{f,1}^{2\beta_1} \quad \text{with} \quad K = \frac{\Delta P \rho \pi^2 p^2 \Omega_1^2}{\xi \dot{m}^2}. \quad (23)$$

As in the case of a matrix heat exchanger of rectangular shape, the objective function (volume) as well as other parameters such as $ntu_{p,o}$, λ , λ_p can all be expressed in terms of the dimensionless design variables $ntu_{f,1}$ and $ntu_{f,2}$ using the Eqs. (20), (21), and (23).

4 Solution Procedure

The design problem can now be fully expressed in terms of dimensionless parameters namely $ntu_{f,1}$, $ntu_{f,2}$, and $ntu_{p,1}$ in the case of rectangular geometry and $ntu_{f,1}$, $ntu_{f,2}$ in the case of circular geometry. The constrained optimization problem can be converted to an unconstrained one by the Lagrangian multiplier technique and a new objective function (L) can be defined as follows:

$$L = V + Z(\epsilon - \epsilon_{\text{specified}}). \quad (24)$$

In the above expression Z is a constant, and $\epsilon_{\text{specified}}$ is the effectiveness required and is specified to the designer. The necessary conditions for optimum to exist for rectangular and circular geometries are as follows:

$$\frac{\partial L}{\partial ntu_{f,1}} = 0 \quad \frac{\partial L}{\partial ntu_{f,2}} = 0 \quad \frac{\partial L}{\partial ntu_{p,1}} = 0 \quad \frac{\partial L}{\partial Z} = 0 \quad (\text{rectangular}) \quad (25)$$

$$\frac{\partial L}{\partial ntu_{f,1}} = 0 \quad \frac{\partial L}{\partial ntu_{f,2}} = 0 \quad \frac{\partial L}{\partial Z} = 0 \quad (\text{circular}). \quad (26)$$

4.1 Solution of the Optimization Problem for a Matrix Heat Exchanger of Rectangular Geometry. The optimization problem can be solved only by a numerical solution of all the equations that result from expressions in Eqs. (25) and (26). However, some analytical solutions can be obtained relating the different parameters from one of the conditions.

4.1.1 Balanced Flow ($\nu = 1$). One of the conditions for the optimum to exist, ($\partial L / \partial ntu_{p,1} = 0$) (Eq. (25)), essentially reduces to the following expression in the case of a balanced flow ($\nu = 1$) condition:

$$\frac{\partial}{\partial ntu_{p,1}} \left(n\lambda + \frac{1}{ntu_{p,o}} \right) = 0. \quad (27)$$

Substitution of expressions for λ and $ntu_{p,o}$ (based on total foot print area of the spacer, see Table 2) into the above equation yields the following:

$$n\lambda_{\text{opt}} = \frac{2}{ntu_{p,o}} - \frac{1}{\lambda_p} + \frac{k_s b}{sn(\dot{m} c_p)_1} \left[2 \sum_{i=1}^2 \left(\frac{\omega_i}{\psi_i} \right)^{0.5} ntu_{p,i}^{-0.5} ntu_{f,i}^{0.5\beta_i} \right]. \quad (28)$$

When the width of the heat exchanger is much larger than the plate height ($H_i \ll W$), Eq. (28) reduces to the following expression:

$$n\lambda_{\text{opt}} = \frac{2}{ntu_{p,o}} - \frac{1}{\lambda_p} \quad (W \gg H_i). \quad (29)$$

If the lateral thermal conductance of the wall is assumed to be infinity ($\lambda_p \rightarrow \infty$) as in Ref. [6], then Eq. (28) will reduce to that derived in Ref. [6]:

$$n\lambda_{\text{opt}} = \frac{2}{ntu_{p,o}} \quad (W \gg H_i, \lambda_p \rightarrow \infty). \quad (30)$$

4.1.2 Unbalanced Flow ($\nu < 1$). Solution of the equation ($\partial L / \partial ntu_{p,1} = 0$) will yield the following expression in the case of unbalanced flow heat exchangers:

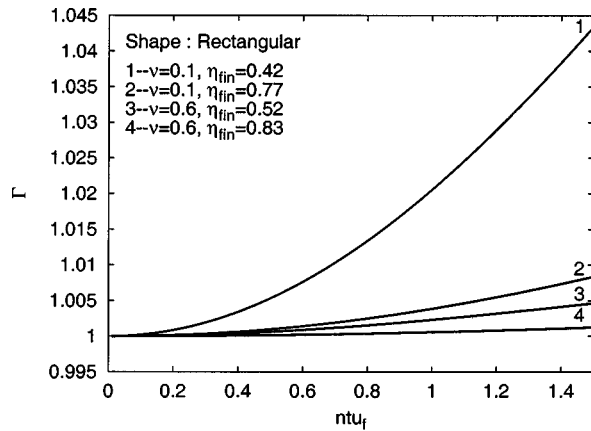


Fig. 4 Variation of Γ with $ntu_{f,i}$

$$n\lambda_{opt} = \left(\frac{2}{ntu_{p,o}} - \frac{1}{\lambda_p} \right) \Gamma \quad (W \gg H_i) \quad (31)$$

where Γ is a function of the heat capacity rate ratio (ν) and other design variables as follows:

$$\Gamma = \frac{1}{\varphi} \left[\frac{1-\varphi}{\ln \varphi} \right]^2 \quad (32)$$

Figure 4 shows the variation of Γ with ntu_f , η_{fin} and ν . In order to simplify the analysis it was assumed that $ntu_{f,1} = ntu_{f,2} = ntu_f$ and $ntu_{p,1} = ntu_{p,2} = ntu_p$ (equal thermal resistance in two channels). The equivalent fin efficiency was evaluated using the expression derived by Fleming [3],

$$\eta_{fin} = \frac{1}{1 + \frac{ntu_f}{3ntu_p}} \quad (33)$$

It can be seen from Fig. 4 that the maximum Γ will be close to 1 even under extreme design conditions. Therefore, for all practical purposes, Eq. (28) can be used even for unbalanced flow ($\nu < 1$) conditions. Substitution of Eq. (28) into Eqs. (3) and (4) will result in expressions for the effectiveness of optimum rectangular configurations.

It can be easily shown using the L'Hospital rule that Eq. (31) will reduce to Eq. (29) when ($\nu = 1$). For any given plate cross section ($A = W * H$), an increase in width will result in an increase in longitudinal heat conduction, but a decrease in plate conduction resistance (due to decrease in plate height). Equations (29) and (31) express the ratio of longitudinal and lateral resistances of the wall that must be maintained for achieving highest effectiveness (for a given area) or lowest plate area (volume) for a required effectiveness. In the case of circular geometry, the lateral heat transfer path between the streams is fixed by the diameter (area) of the plate used, and these two cannot be varied independently as in rectangular geometry. Closed-form solutions have become possible in the case of rectangular geometry only because of the dimensionless approach adopted for the optimum study.

In most practical heat exchangers the aspect ratio is quite high, and the longitudinal heat conduction through the outer walls in the lateral heat transfer path (area = $2b(h_1 + h_2)$) is much smaller compared to that through the walls that separate the streams and those parallel to it (area = $3Wb$). Equations (29) and (31) can therefore be used without much loss of accuracy for most matrix heat exchangers.

As with any nonlinear equation set, multiple solutions can exist for the given problem. The correct solution of $ntu_{f,1}$ and $ntu_{f,2}$ is that which will result in the least volume. In general, three sets of $ntu_{f,1}$, $ntu_{f,2}$, and $ntu_{p,1}$ satisfy Eqs. (25). Of the two positive

Table 3 Heat transfer and friction factor correlations for a perforated plate matrix heat exchanger

| | |
|-------------------------------------|-------------------|
| $StPr^{1/3} = C Re^n$ | $300 < Re < 3000$ |
| $C = 0.00036((1-p)p - 0.2)^{-2.07}$ | $0.3 < p < 0.6$ |
| $n = -4.36 * 10^{-2} * p^{-2.34}$ | Ref. [8] |
| $\xi = 16.34 Re^{-0.55} \xi_{sim}$ | $Re < 160$ |
| $\xi = \xi_{sim}$ | $Re > 160$ |
| $\xi_{sim} = (1.707 - p)^2 / 2$ | Ref. [8] |

solutions, one corresponds to a very high value of $ntu_{f,1}$ and $ntu_{f,2}$ and another to $ntu_{f,1}$ and $ntu_{f,2}$ between 0 and 2. Since the volume is directly proportional to $ntu_{f,1}$ and $ntu_{f,2}$, the later solution set should be adopted. Also, analytical and numerical studies of Venkatarathnam [5] and Venkatarathnam and Sarangi [9] confirm that the maximum value of ntu_f will be less than 2 for most cases of rectangular geometry. Analytical and numerical studies undertaken by us show that the maximum value of ntu_f would be less than 4.5 in the case of a matrix heat exchanger of circular geometry. Using this information the search space for ntu_f and ntu_p can be reduced to a very narrow margin of 0 to 5. With this procedure there is no need to check for the other solution set.

We have used the Newton-Raphson method to successfully arrive at the solution for a large variety of problems with starting values of $ntu_{f,1} = ntu_{f,2} = ntu_{p,1} = 1$. In the case of a matrix heat exchanger of circular geometry, the starting values used are $ntu_{f,1} = ntu_{f,2} = 1$.

The main strength of the procedure presented above lies in the expression of the volume V and the effectiveness ϵ in terms of the dimensionless design variables $ntu_{f,1}$, $ntu_{f,2}$ and $ntu_{p,1}$ analytically.

Equations (25) and (26) turn out to be long and complex. However, using a modern mathematical program such as Maple, Mathematica, or Mathcad, one can obtain the final solutions directly, without expanding Eqs. (25) and (26). The whole procedure can be programmed in Maple or Mathematica in about 20 to 40 lines.

The method for sizing of a matrix heat exchanger can now be summarized as follows:

Rectangular Geometry

- Express W and H_i in terms of $ntu_{f,i}$ and $ntu_{p,i}$ using Eqs. (15) and (16).
- Replace W and H_i in all other expressions ($\lambda, \lambda_p, ntu_{p,o}$) with expressions given in Eqs. (15) and (16).
- Solve Eqs. (25) simultaneously by Newton-Raphson technique with starting points $ntu_{f,1} = ntu_{f,2} = ntu_{p,1} = 1$.

Circular Geometry

- Express R_i and R_o in terms of $ntu_{f,1}$ and $ntu_{f,2}$ using Eqs. (20) and (21).
- Replace R_i and R_o in all other expressions ($\lambda, \lambda_p, ntu_{p,o}$) with expressions given in Eqs. (20) and (21).
- Solve Eqs. (26) simultaneously by the Newton-Raphson technique with starting points $ntu_{f,1} = ntu_{f,2} = 1$.

5 Results and Discussion

The optimum size of a matrix heat exchanger of rectangular and circular geometry was determined for different operating conditions (ν , NTU_{eff} , and ΔP) encountered in a typical helium liquefier, using the methods discussed above. The design constants, heat transfer, and flow friction correlations used in our study are given in Tables 3 and 4. All the results presented in this section have been obtained by using the methods presented in this paper and are optimum values. The computations were performed using the Newton-Raphson method with a convergence criteria of $1.0e-5$ for different dimensionless parameters which are normally in the range of 0 and 5.

Table 4 Design constants adopted

| Variable | Value |
|---|------------------------|
| Perforation diameter | 0.5 mm |
| Thickness of perforated plate | 1 mm |
| Thickness of separator | 1 mm |
| Plate porosity | 0.3 |
| Density of helium in cold channel | 0.48 kg/m ³ |
| Density of helium in hot channel | 4.72 kg/m ³ |
| Thermal conductivity of plate material | 200 W/(mK) |
| Thermal conductivity of spacer material | 12 W/(mK) |
| Effective thermal conductivity of He | 118.5 mW/(mK) |
| Specific heat of helium | 5.26 kJ/(kg K) |
| Viscosity of He | 15 μPas |

The effectiveness of a high effectiveness heat exchanger such as a matrix heat exchanger will be less than that predicted using commonly used ϵ -NTU relationships because of irreversibilities such as longitudinal heat conduction, effect of finite number of plate-spacer pairs, etc. An effective NTU (NTU_{eff}) can be defined taking into account all the irreversibilities (Eqs. (1)–(4)).

The effective NTU is thus the equivalent number of heat transfer units of a conventional heat exchanger without any irreversibilities which has the same effectiveness as that of a matrix heat exchanger with different irreversibilities under consideration. The NTU_{eff} helps in the comparison of heat exchangers subjected to different irreversibilities as well as those not subjected to different irreversibilities on a common denominator basis.

The volumes of a matrix heat exchanger of rectangular (two-channel) and circular geometries for the same heat duty are compared in Fig. 5. It can be seen that the volume of a matrix heat exchanger of circular shape is also dependent on the channel used for the low-pressure stream as shown in Fig. 5. It is evident that the use of inner (circular) channel is preferable to the use of annular channel for the low-pressure stream. The least volume is required when the rectangular two-channel matrix heat exchanger is adopted at all effectiveness (NTU_{eff}) conditions. The difference between volumes of a matrix heat exchanger of rectangular and circular shapes, however, is small for NTU_{eff} , less than 20 (or effectiveness less than about 95 percent).

Figure 6 shows the volumes of an optimum matrix heat exchanger of rectangular shape with two and three channels (Figs. 1 and 3). The size of the three-channel heat exchanger can be determined by assuming it to be two two-channel heat exchangers in parallel, but with the advantage of having one outer wall less (because of symmetry) compared to a normal two-channel heat exchanger. It can be seen from Fig. 6 that the volume of multi-

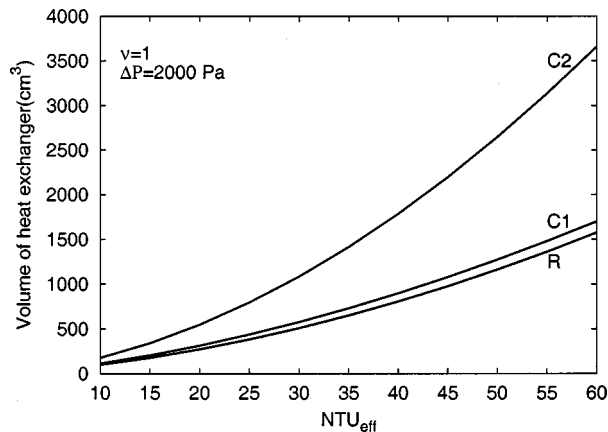


Fig. 5 Effect of the matrix heat exchanger geometry on the heat exchanger volume. (R: rectangular, C1: circular geometry with low-pressure stream in the inner channel, C2: circular geometry with low-pressure stream in the annular channel.)

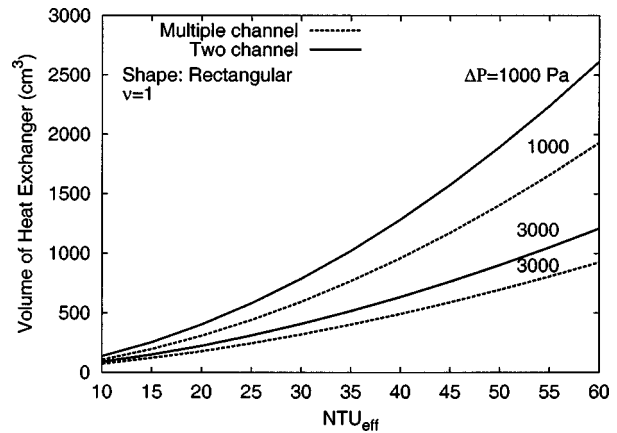


Fig. 6 Variation of heat exchanger volume with NTU_{eff} for rectangular (two-channel and multiple-channel) shape matrix heat exchanger with balanced flow conditions

channel heat exchanger is much lower than a corresponding two-channel heat exchanger, particularly at low allowable pressure drops. When the allowable pressure drop is high (>2000 Pa), and the effectiveness is less than about 95 percent, the volume of a matrix heat exchanger in the two cases is nearly the same. The major advantage in using multiple channels, however, lies in the overall aspect ratio (width to breadth) of the heat exchanger. It can be seen from Fig. 7 that the aspect ratio for a multichannel heat exchanger has a ball park value of 4, compared to about 14 for two-channel rectangular matrix heat exchangers.

Figure 8 shows the effect of height of separating wall (b). It can be seen that the volume of a matrix heat exchanger nearly doubles by increasing the spacer width from 1 mm to 2 mm, at all values of NTU_{eff} . Any increase in the width of the separating wall b (see Fig. 1) will result in an increase in lateral thermal resistance between the streams as well as a decrease in the longitudinal thermal resistance and will require therefore higher volume (area). In most matrix heat exchangers, the effect of increase in longitudinal heat conduction is more predominant than a decrease in lateral thermal conductance. The value of b adopted, in general, depends on effectiveness of the bonding between the spacers and the perforated plates and the bonding strength. Figure 8 is thus an indirect indicator of the relationship between the effectiveness of the bonding and the overall volume of the matrix heat exchanger.

Figure 9 shows the variation of radii of the two channels of a matrix heat exchanger of circular geometry for two cases (C1 and C2). In case C1 a much smaller flow cross section is provided for

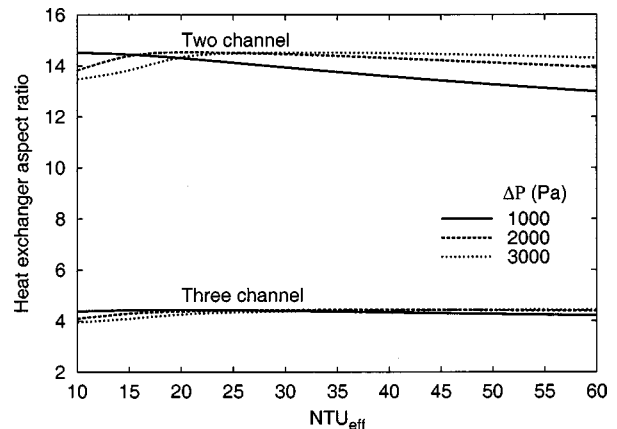


Fig. 7 Variation of an aspect ratio with NTU_{eff} for a rectangular shape matrix heat exchanger with balanced flow conditions

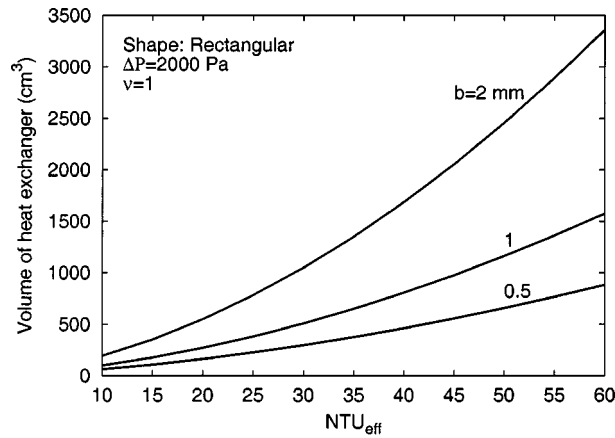


Fig. 8 Variation of volume (V) with NTU_{eff} for a rectangular matrix heat exchanger at different values of separator thickness (b)

the high-pressure stream compared to the low-pressure stream. When the low-pressure stream is passed through the annular channel (case C2), the flow cross section and also convective heat transfer area available for the high-pressure stream is much higher than that for case C1. The lateral heat transfer path, however, is also longer in case C2 compared to case C1. Consequently, the conduction resistance in case C2 will be much larger than case C1. The increase in conduction resistance will be much larger than increase in convective heat transfer area in case C2 compared to case C1, necessitating use of larger heat exchanger volume.

Figure 10 shows the variation of Reynolds numbers of high and low-pressure streams in a two-channel rectangular shape matrix heat exchanger. It can be seen that the Reynolds numbers are higher than 160 (corresponding to a turbulent regime ([8])) at all values of NTU_{eff} and ΔP in the case of high-pressure stream and much less than Re of 160 for the low-pressure stream. A similar observation can also be made in the case of matrix heat exchangers of circular geometry. While the results show that laminar flow regime will exist in the low-pressure channel of optimized matrix heat exchangers, very little data are available on the variation of Nusselt number (Nu) at such low Reynolds numbers. Shevykova and Orlov [8] presented a correlation for the friction factor for laminar flow regime, but not for heat transfer. Even in our case, we have extended the correlation of Shevykova and Orlov [8] to low Reynolds number, even though they are valid only at $Re > 300$.

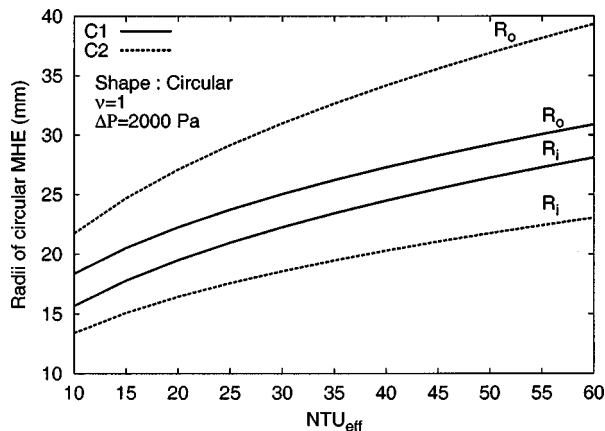


Fig. 9 Effect of channel used for the low-pressure stream on the channel radii. (C1: low-pressure stream in the inside channel and C2: low-pressure stream in the annular channel.)

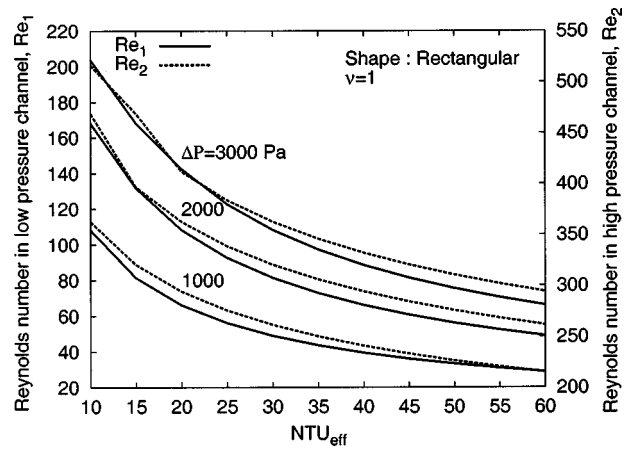


Fig. 10 Variation of Reynolds number in a low-pressure channel and high-pressure channel with NTU_{eff} for a rectangular shape matrix heat exchanger with balanced flow conditions

6 Conclusions

- The volume of a matrix heat exchanger of rectangular (two channel) and circular geometry are quite close at NTU_{eff} less than 15. At higher values of NTU_{eff} the volume of a matrix heat exchanger of rectangular (multi channel) geometry will be much lower than all other configurations.
- It is preferable to use the inner channel for the low pressure stream and the annular channel for the high-pressure stream, in the case of a matrix heat exchanger of circular geometry.
- The low-pressure stream is more likely to operate in a laminar flow regime, particularly at high effectiveness in an all optimum matrix heat exchanger, and in a turbulent flow regime in the case of a high-pressure stream.

Nomenclature

- A = heat transfer area (m)
- A''' = heat transfer area per unit volume of plate (m^2/m^3)
- A_w = foot print area of the spacer (m^2)
- b = height of the separator (m)
- C = constant in Nusselt number correlation (Eq. (14))
- d = perforation diameter (m)
- F = geometric factor (Eq. (6))
- G_d = mass flux through any perforation (kg/m^2s)
- H = Plate height in any channel (m)
- h = heat transfer coefficient ($W/(m^2K)$)
- K = intermediate constant
- k = effective thermal conductivity ($W/(mK)$)
- l = plate thickness (m)
- \dot{m} = mass flow rate (kg/s)
- Nu = Nusselt number
- n = number of plate-spacer pairs
- ntu_f = number of convective heat transfer units per stream ($= hA/\dot{m}c_p$)
- ntu_p = dimensionless plate conductance (Eq. (6))
- $ntu_{p,o}$ = overall dimensionless plate conductance (Eq. (6))
- p = plate porosity
- R_i = inner radius of the circular shape matrix heat exchanger (m)
- R_o = outer radius of the circular shape matrix heat exchanger (m)
- Re = Reynolds number
- s = spacer thickness (m)
- V = volume of the heat exchanger (m^3)
- W = plate width (m)
- Z = constant

Greek Letters

- α = intermediate parameter ($\alpha = \exp(-ntu_f)$)
 β = intermediate parameter ($\beta = 1/(1 - \gamma)$)
 Γ = intermediate factor (Eq. (32))
 γ = exponent in Nusselt number correlation (Eq. (14))
 ΔP = pressure drop in the low-pressure channel (Pa)
 ϵ = heat exchanger effectiveness
 η_{fin} = fin efficiency (Eq. (33))
 κ = intermediate parameter (Eq. (5))
 λ = overall axial conduction parameter
($= k_s A_w / sn(\dot{m}c_p)_1$)
 λ_p = dimensionless lateral conductance of the separating wall (see Table 2)
 μ = viscosity of the fluid (Pa.s)
 ν = heat capacity rate ratio [$(\dot{m}c_p)_1 / (\dot{m}c_p)_2$]
 ξ = drag coefficient (Eq. (12))
 ρ = density of the fluid (kg/m^3)
 φ = intermediate parameter (Eq. (5))
 ψ = intermediate parameter (Eq. (17))
 Ω = intermediate parameter (Eq. (22))
 ω = intermediate parameter (Eq. (17))

Subscripts

- 1 = cold fluid
2 = hot fluid
eff = effective

- f = fluid
 i = 1,2 channel numbers
 p = plate
 o = overall
 s = spacer
 w = separating wall

References

- [1] McMahan, H. O., Bowen, R. J., and Bleyle, G. A., 1950, "A Perforated Plate Heat Exchanger," *Trans. ASME*, **72**, pp. 623–632.
- [2] Venkatarathnam, G., and Sarangi, S., 1990, "Matrix Heat Exchangers and Their Application in Cryogenic Systems," *Cryogenics*, **30**, pp. 907–918.
- [3] Fleming, R. B., 1969, "A Compact Perforated Plate Heat Exchanger," *Adv. Cryog. Eng.*, **14**, pp. 197–204.
- [4] Sarangi, S., and Barclay, J. A., 1984, "An Analysis of Compact Heat Exchanger Performance," *Cryogenic Processes and Equipment—1984*, P. J. Kerney et al., eds., ASME, New York, pp. 37–44.
- [5] Venkatarathnam, G., 1996, "Effectiveness N_{tu} relationship in perforated plate matrix Heat Exchangers," *Cryogenics*, **36**, pp. 235–241.
- [6] Venkatarathnam, G., 1998, "A Straight Forward Method for the Sizing of Perforated Matrix Heat Exchangers," *Proc. of Cryogenic Eng. Conf.*, July 28–Aug. 2, Portland, OR, pp. 1643–1650.
- [7] Mikulin, E. I., Shevich, Yu. A., Potapov, V. N., Solntsev, M. Ya., and Yusova, G. M., 1980, "Study of Matrix Type Heat Exchangers Made of Perforated Plates," *Trans. Chem. Pet. Eng.*, pp. 514–519.
- [8] Shevyakova, S. A., and Orlov, V. K., 1983, "Study of Hydraulic Resistance and Heat Transfer in Perforated Plate Heat Exchangers," *Trans. J. Eng. Phys.*, pp. 734–737.
- [9] Venkatarathnam, G., and Sarangi, S., 1991, "Analysis of Matrix Heat Exchanger Performance," *ASME J. Heat Transfer*, **113**, pp. 830–837.

Influence of Crossflow-Induced Swirl and Impingement on Heat Transfer in an Internal Coolant Passage of a Turbine Airfoil

S. V. Ekkad¹

Assistant Professor,
Assoc. Mem. ASME
e-mail: ekkad@me.lsu.edu

G. Pamula

Graduate Student,
Mem. ASME

S. Acharya

L. R. Daniel Professor,
Fellow ASME

Mechanical Engineering Department,
Louisiana State University,
Baton Rouge, LA 70803

Detailed heat transfer distributions are presented inside a two-pass coolant channel with crossflow-induced swirl and impingement. The impingement and passage crossflow are generated from one coolant passage to the adjoining coolant passage through a series of straight or angled holes along the dividing wall. The holes provide for the flow turning from one passage to another typically achieved in a conventional design by a 180-deg U-bend. The holes direct the flow laterally from one passage to another and generate different secondary flow patterns in the second pass. These secondary flows produce impingement and swirl and lead to higher heat transfer enhancement. Three different lateral hole configurations are tested for three Reynolds numbers ($Re=10,000, 25,000, 50,000$). The configurations were varied by angle of delivery and location on the divider wall. A transient liquid crystal technique is used to measure the detailed heat transfer coefficient distributions inside the passages. Results with the new crossflow feed system are compared with the results from the traditional 180-deg turn passage. Results show that the crossflow feed configurations produce significantly higher Nusselt numbers on the second pass walls without affecting the first pass heat transfer levels. The heat transfer enhancement is as high as seven to eight times greater than obtained in the second pass for a channel with a 180-deg turn. The increased measured pressure drop (rise in friction factor) caused by flow through the crossflow holes are compensated by the significant heat transfer enhancement obtained by the new configuration. [S0022-1481(00)03103-0]

Keywords: Forced Convection, Heat Transfer, Impingement, Swirling, Turbines

Introduction

Heat transfer augmentation inside airfoil internal channels is an important issue for the gas turbine industry. As turbine inlet temperatures are increased, there is a greater need for more efficient cooling. Several strategies are being examined by various investigators where combinations of turbulated serpentine passage cooling, impingement cooling, double-wall cooling, and film cooling are considered. The focus of this study is to investigate an alternative internal cooling strategy where additional secondary flows and heat transfer enhancement are generated without radical alteration to the existing internal designs of cooling passages. This strategy consists of replacing the conventional U-bend between the two passages (Fig. 1(a)) with a series of cylindrical holes along the dividing wall connecting the two passages (Fig. 1(b)). The cylindrical holes permit lateral injection from the first passage to the second passage; this leads to a combination of impingement and crossflow-induced swirl in the second passage. This combination of impingement and swirl is expected to provide a higher and more uniform heat transfer in the second passage. If significant enhancement in the second passage is obtained, this strategy may also be useful for leading edge cooling (with coolant injected in the lateral rather than longitudinal direction) where the heat transfer loads are most significant.

There have been several studies on two-pass channels reported in the literature. Boyle [1] provided centerline heat transfer coefficient information inside serpentine passages. Metzger and Sahn [2] presented Nusselt numbers near sharp 180-deg turns in smooth

channels of rectangular cross section, and they provided regional averaged heat transfer on the top, bottom, and outer walls around the turn. Abuaf et al. [3] provided pressure drop and heat transfer measurements inside serpentine channels. Fan and Metzger [4] studied heat transfer in two-pass smooth channels connected by a 180-deg turn. They compared the effect of channel aspect ratio on the heat transfer inside the channels. Chyu [5] provided detailed mass (heat) transfer distributions inside two-pass and three-pass smooth channels connected by a series of 180-deg turns. Ekkad and Han [6] focused on the 180-deg turn region and presented detailed heat transfer distributions around the turn region. They indicated the strong three dimensionality of the flows due to the centrifugal forces and their effects on heat transfer. Flow through the 180-deg turn causes enhancement and nonuniform heat transfer distributions in the second pass immediately downstream of the turn. A more recent study by Hibbs et al. [7] indicates that bend-induced secondary flows and heat transfer nonuniformities are also present under conditions of rotation.

Several other researchers ([8–11]) have all focused on enhancing heat transfer in both the first pass and second pass using rib turbulators. The maximum enhancement reported in the second pass of a serpentine channel with a combination of the turn and discrete rib turbulators is around six to seven times higher than the fully developed flow Nusselt number (Dittus-Boelter Equation).

Recently, it has been observed that swirl induction in the flow aids in heat transfer enhancement. This has been investigated by Glezer et al. [12], Ligrani et al. [13], and Moon et al. [14]. They create swirl by injecting air into the tube through tangential jets along the wall. Hedlund et al. [15] presented measurements inside a tubular swirl chamber for simulating turbine blade internal cooling. Swirl cooling appears to be a promising alternative to using discrete turbulators for achieving higher heat transfer enhance-

¹To whom correspondence should be addressed.

Contributed by the Heat Transfer Division for publication in the JOURNAL OF HEAT TRANSFER. Manuscript received by the Heat Transfer Division, Aug. 4, 1999; revision received, Apr. 12, 2000. Associate Technical Editor: J. Han.

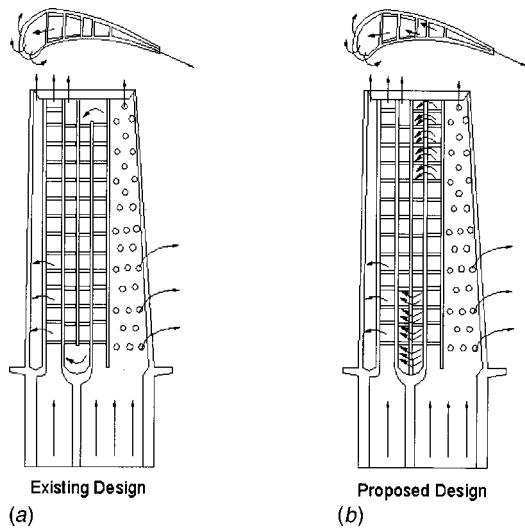


Fig. 1 Illustration of channels with (a) 180 deg turn (b) holes

ment. All the above studies are, however, in circular one-pass tubular channels and are not similar to the system proposed in the present study.

The present study, as indicated earlier, focuses on investigating an alternative approach for heat transfer enhancement without significantly altering the internal cooling design existent in the present cooled blades. The aim is to deliver the coolant from first passage to second passage through lateral slots along the dividing wall. Lateral injection leads to a combination of impingement and crossflow-induced swirl and is expected to produce significant heat transfer enhancement in the second pass. In this study, the

lateral injection holes are drilled through the divider wall between the two channels and the turn is eliminated. The holes are angled at $\beta=0$ deg and 45 deg towards one sidewall to produce different swirl flow conditions in the second pass. The location of the hole on the divider wall is also a parameter in the configuration. For each case, three flow channel Reynolds numbers of 10,000, 25,000, and 50,000 are tested. It is expected that the heat transfer distributions on the two sidewalls will be different for all cases due to strong impingement on one wall. Results are presented for both sidewalls of the two passes, which represent the pressure side and suction side surfaces of the airfoil. For comparison, results are also presented for a two-pass channel connected by a 180-deg turn.

Experimental Setup

Figure 2 presents a schematic of the experimental setup. The experimental setup consists of an image processing system (RGB Color CCD Camera, Color Frame Grabber Card, PC and Imaging Software), temperature measurement system, flow loop, and the test section. The RGB camera is focused on the test section and the color FG card is programmed through the software to analyze real-time images for color signals during a transient heat transfer test.

The flow circuit consists of an air supply from a 300-psi compressor. The air is regulated and metered through a standard orifice meter to measure the flow rate through the test section. The air is then routed through an in-line air heater (3 KW) controlled by a temperature controller system. The air from the heater is then diverted away from the test section with a three-way ball diverter valve. The heated air temperature is monitored by the temperature control unit by measuring the heated air temperature immediately downstream of the heater. When the valve is flipped, the air is

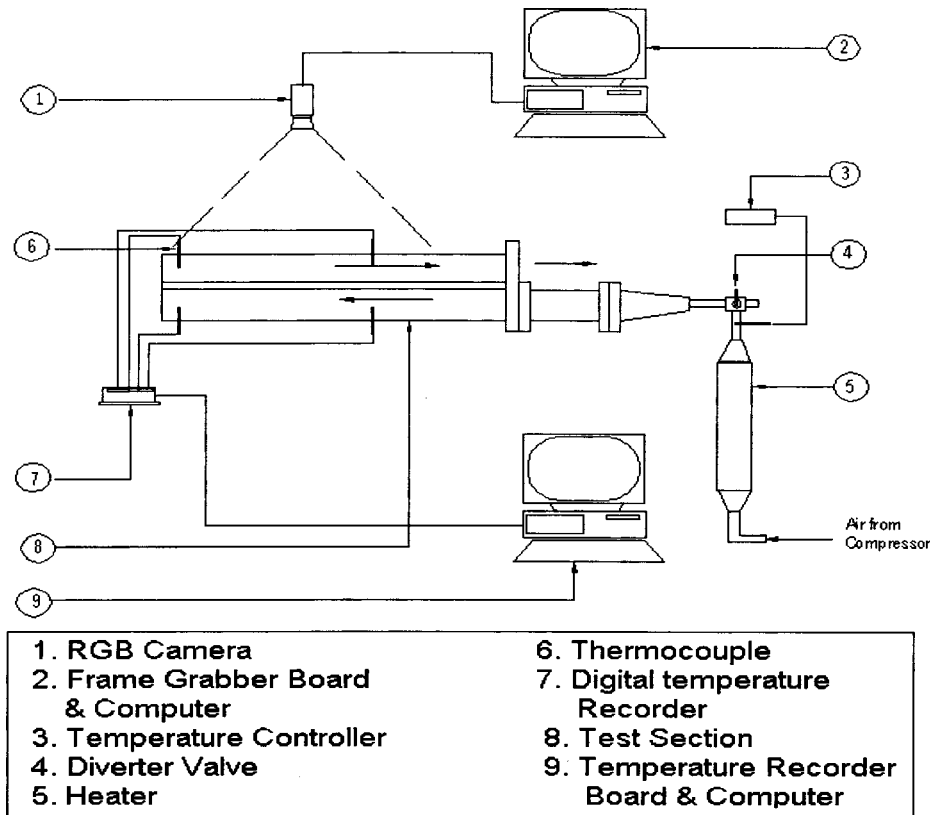
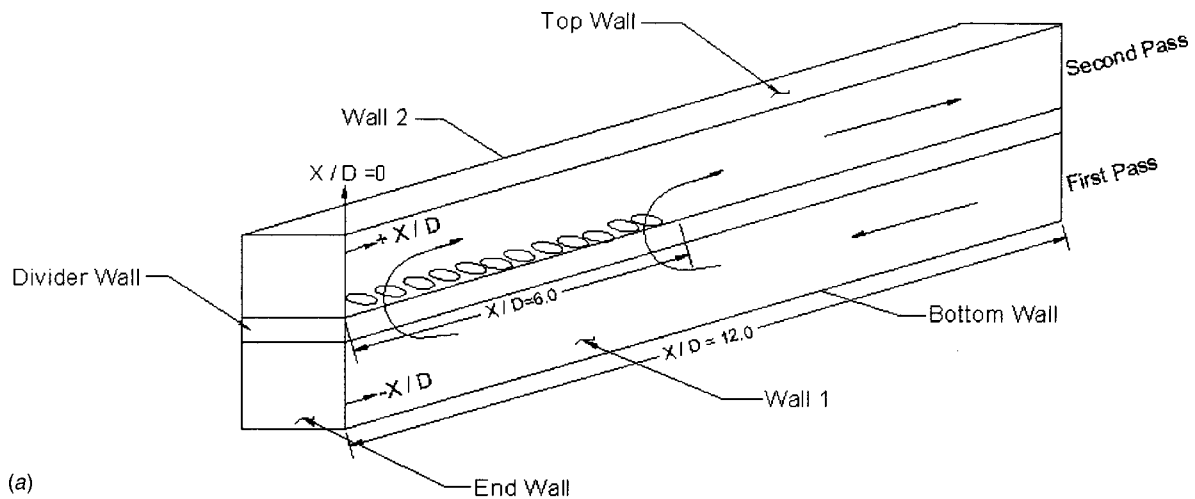
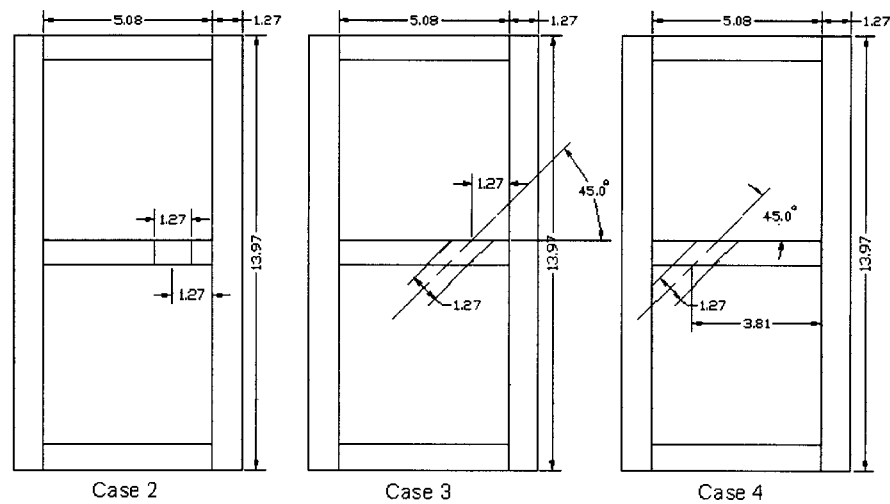


Fig. 2 Experimental test setup



(a)



(b)

Fig. 3 Three test channel configurations; (a) Case 2, (b) Case 3, (c) Case 4

routed through the test section. A series of honeycomb strips and a mesh help produce a uniform flow at the entrance into the test section.

Figure 3(a) shows a schematic of the test section. The test channel is a 5.08-cm square cross section through the 60.96-cm length. The channel length to hydraulic diameter ratio (L/D) is 12. There is no 180-deg turn for the channels connected by the holes. All of the flow passes through the holes. There are no holes along the divider wall for the first 30.48 cm of the channel length from entrance ($L/D = 6$). The 12 holes are then evenly distributed over the next 30.48 cm of the channel length. There are 12 holes of 1.27-cm diameter each. The holes are spaced two-hole diameters (centerline to centerline) apart from each other. The lateral hole locations on the divider wall were designed to produce different swirling flow conditions in the channel. The ratio of the total area of all the holes to the turn region area in the 180-deg turn case was 0.6. The thickness of all the walls in the test section was 1.27 cm. The primary walls are designated Wall 1 and Wall 2. These walls are the channel walls that are exposed to the pressure and suction surfaces of the airfoil. The top and bottom walls are only exposed to only the coolant flow (in the actual turbine blade). These are considered secondary walls for convection cooling in actual turbine blades. The endwall is the wall that is exposed to the blade tip (blades) or the plenum region for the vane.

Figure 3(b) shows the three hole configurations viewed from the side of the test section. The two-pass with the 180-deg turn is

denoted as Case 1. In Case 2 the divider wall consists of normal angled holes ($\beta = 0$ deg) and the lateral jets are expected to impinge on the opposite secondary wall (top wall). The holes are placed such that the hole centerline is 1.27 cm from Wall 1. In Case 3, the holes are angled at $\beta = 45$ deg. The holes are positioned such that the flow is directed towards Wall 1, and the exit location of the hole centerlines entering the second pass are 1.27 cm from Wall 1. In Case 4, the holes are also angled at $\beta = 45$ deg, but with the exit hole centerlines located 3.81 cm from Wall 1. This case is different than Case 3, in that, the lateral angle is directed away from the nearest wall to the hole location.

The heat transfer measurements are made only on Wall 1 and Wall 2 of the Plexiglas test section. The surfaces are coated on the inside with a thin layer of liquid crystals (Hallcrest: R35C1W). A thin black paint coating is sprayed behind the liquid crystal coating to ensure visibility of the liquid crystal color changes when viewed from the outside. Once the test section is coated with both the liquid crystal and black paint layers, the insides of the channel are opaque. Thermocouples are placed at inlet and outlets of each passage (a total of four) to measure the local bulk temperature of the heated air as a function of time. The transient thermocouple outputs are digitized during the test using an eight-channel A/D system. Since the air temperature from a sudden switching of the valve does not produce a step change, it is important to measure the transient response of the air temperature.

Procedure and Data Reduction

The air mass flow rate is set for the required channel Reynolds number condition, and then heated through the in-line air heater. The temperature at the exit of the heater is set based on some qualification tests to produce acceptable liquid crystal color change times during the transient test. The heated air is initially routed away from the test section. The temperature measurement system and the image processing system are set to trigger for initiating data measurement at the same instant. When the air is heated to the steady required temperature, the diverter valve is flipped to let the hot air into the test section. The thermochromic liquid crystal coating is heated by the hot air and changes color when it reaches its display color range. Liquid crystal color temperatures are pre-set and are calibrated under lab lighting conditions. The liquid crystal used in this study has a narrow band (1°C) with the initial red color appearing at 35.1°C, then green color appearance at 35.4°C, and finally blue color at 35.9°C. The image processing system maps the test section into 500×200 pixel locations and monitors each location individually for color changes. The reference point in this study is set as the appearance of green color during the transient. Thresholding was used to determine the actual color appearance during the transient test. Thus the image processing system will provide time of color changes at every pixel when it reaches 35.4°C. The test duration is typically a maximum of 150 seconds. The air temperature is set such that the times of color changes for all pixels are between 10–150 seconds. During the time period, the test section does not violate the semi-infinite solid assumption.

The test section is made of Plexiglas[®] so that a semi-infinite solid assumption can be applied on the test section wall. The local air bulk temperature for each axial pixel location is interpolated

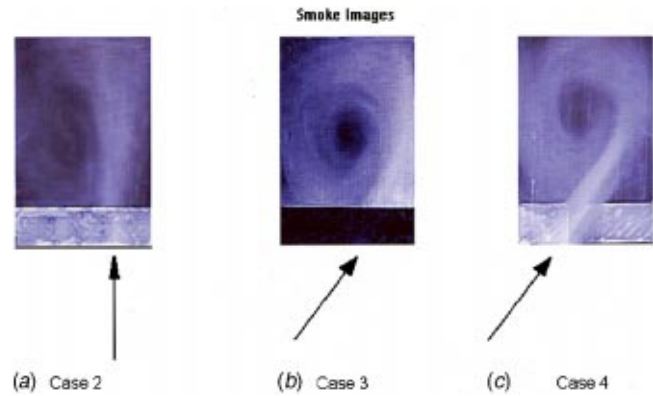


Fig. 4 Smoke flow visualization results for (a) Case 2, (b) Case 3, (c) Case 4

from the measured thermocouple locations. The time-step changes are then included into the equation to obtain a function of the form given below. Since the air temperature is not a step-change function but time-dependent, Metzger and Larson [16] proposed to use the Duhamel's superposition integral to include the time-dependent heated air response into the above equation. Assuming negligible axial conduction, the surface temperature response (T_w) of the exposed semi-infinite wall with a convective boundary condition can be written as ([10])

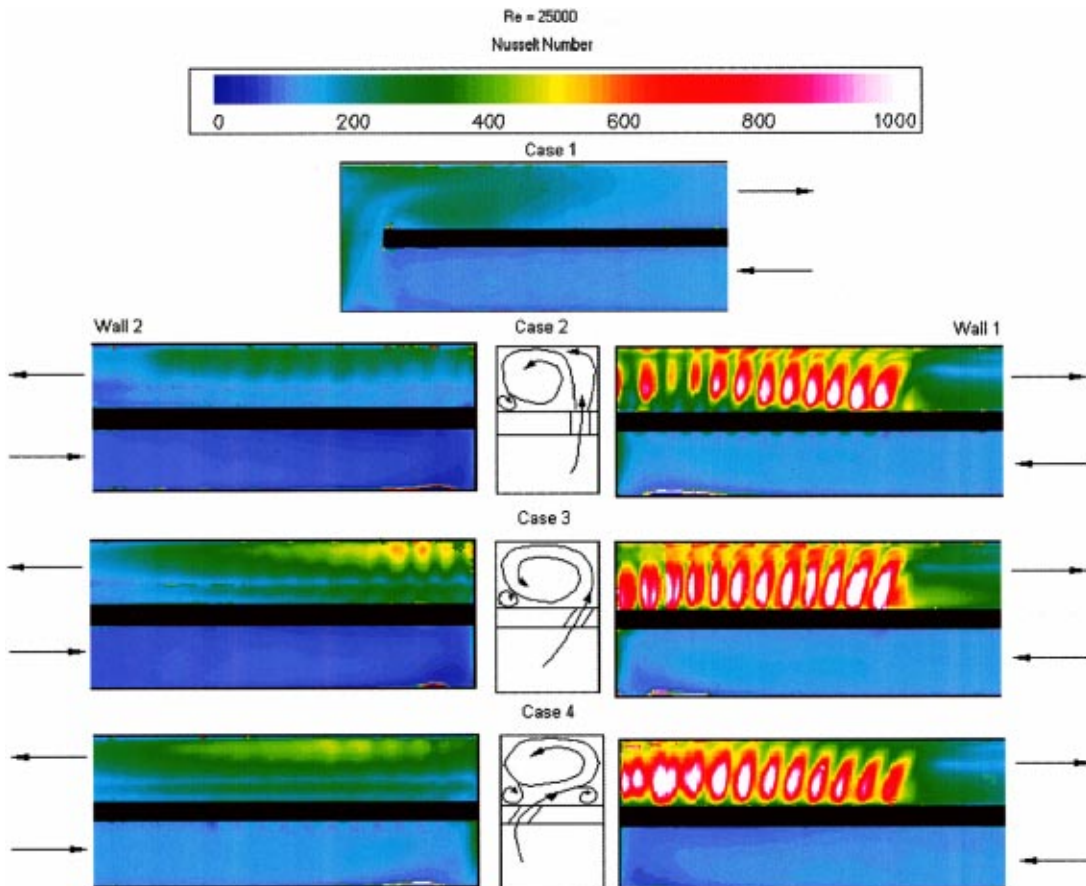


Fig. 5 Detailed heat transfer distributions for all channels at Re=25,000

$$T_w - T_i = \sum_{j=1}^N \left\{ 1 - \exp\left[\frac{h^2 \alpha (t - \tau_j)}{k^2}\right] \operatorname{erfc}\left[\frac{h \sqrt{\alpha (t - \tau_j)}}{k}\right] \right\} \times [\Delta T_{m,(j,j-1)}] \quad (1)$$

where $\Delta T_{m,(j,j-1)}$ and τ_j are the temperature and time-step changes interpolated from the digitized temperature outputs. T_m , and T_i are the heated air and test section initial temperatures, respectively. Plexiglass properties, thermal diffusivity (α) and thermal conductivity (k), are known. The time, t , of color change to green is measured by the image processing system. This equation is applicable at each pixel location on the test surface. The equation is solved at every pixel location to obtain the local heat transfer coefficient, h . Ekkad and Han [6,10] used a similar approach.

The overall friction factor for any configuration is determined by measuring the pressure drop across the test section (ΔP). The friction factor is defined as $f = 2\Delta P(D/L)/(\rho \bar{V}^2)$. The overall measured friction factor is normalized with a calculated friction factor for the same length of a straight smooth channel given by $f_0 = 0.046 \operatorname{Re}^{-0.2}$.

The average experimental uncertainty based on the methodology of Kline and McClinton [17] is on the order of ± 7.4 percent.

The individual uncertainties in the measurement are listed below as: time of color change, $t \pm 3$ percent; thermal properties of wall (α, k) ± 5 percent; mainstream temperature, $T_m \pm 3$ percent; color change temperature, $T_w \pm 2$ percent; initial temperature, $T_i \pm 3$ percent. The maximum uncertainty is incurred at the areas of shortest or longest color changes. The shortest color changes (if time of color change is lower than five seconds) produce uncertainty levels as high as ± 14.5 percent. The uncertainty in friction factor measurement is on the order of ± 8.0 percent based on the uncertainty in pressure differential measurement and mass flow measurements.

Results and Discussion

Flow Visualization. Flow visualization was performed using smoke flow injection. The image processing system was triggered to capture continuous frames from the initiation of the smoke flow. The sequential grabbing of frames was curtailed when the test section was completely filled with smoke. The saved images were then animated to determine the flow behavior inside the channels. The smoke flow visualization was performed at a low flow rate condition (low Reynolds number). Although the flow conditions in the actual heat transfer tests are different, these vi-

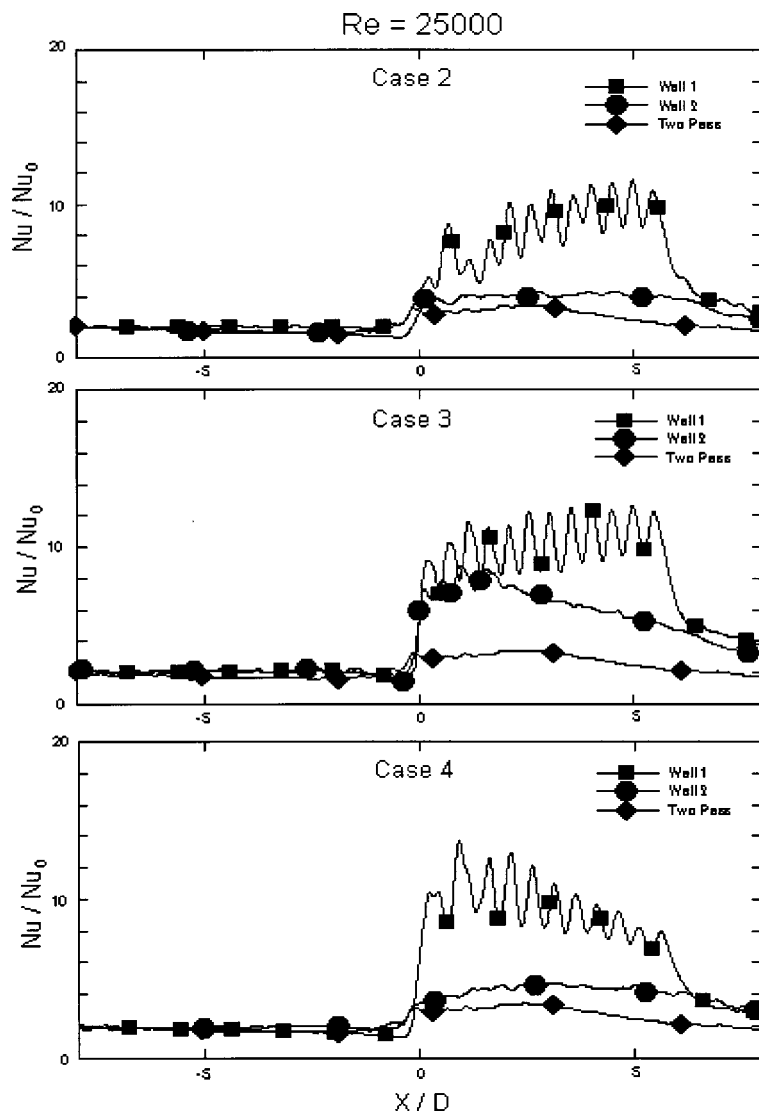


Fig. 6 Spanwise averaged Nusselt number distributions on both walls compared to a two-pass with turn for $\operatorname{Re}=25,000$

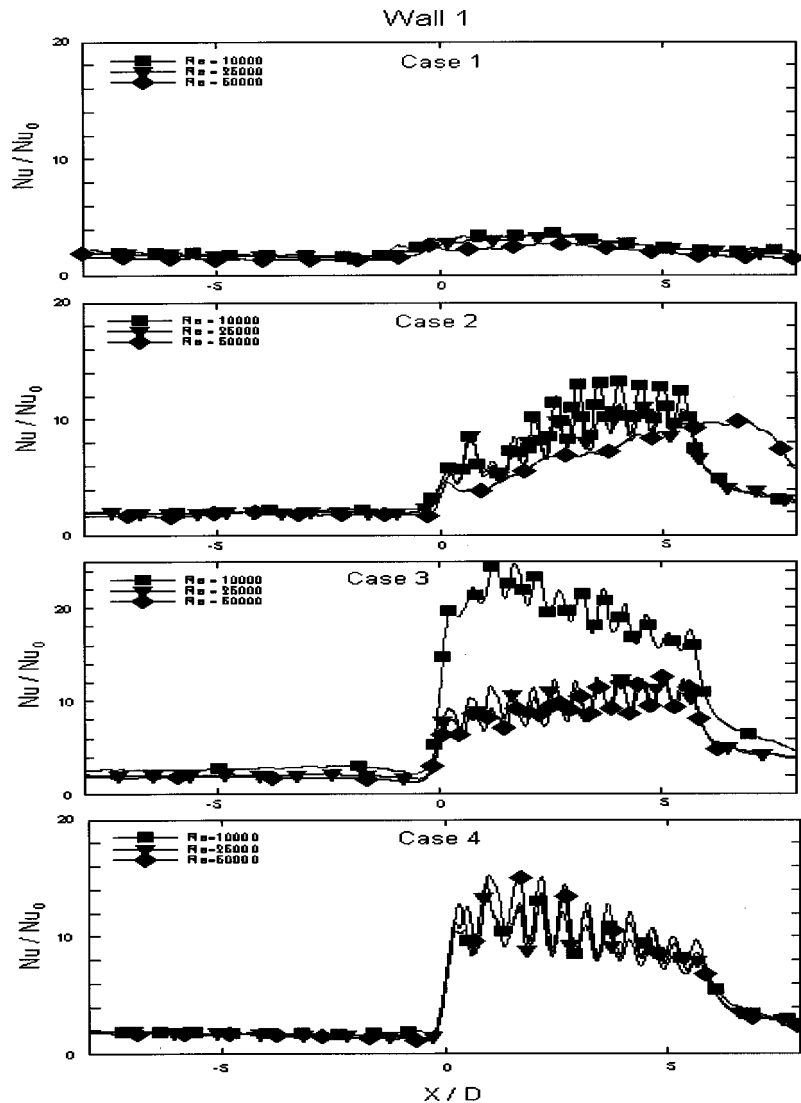


Fig. 7 Effect of flow Reynolds number for each case on Wall 1

sualization experiments were used to provide better understanding of the complex heat transfer distributions inside the channel. The visualizations were performed only for the channels with lateral holes. The 180-deg turn channel has been widely investigated previously so it is not presented.

Figure 4 shows the smoke flow patterns in the second pass. The camera was placed to view the inside of the channel from the endwall side so the captured images truly reflect the flow patterns at the farthest location of the channel from the inlet/exit location. For each case with holes, only one of the sequential frames are presented. For Case 2, the flow appears to exit the hole into the second pass as a jet. The jet seems to impinge on the top wall and ricochets back towards the divider wall. The jet breaks up into two structures. The first structure almost immediately re-impinges on Wall 1 and is pushed downward by the crossflow. A small recirculation region is formed at the right-hand bottom corner of the second pass. For Case 3, the jets strongly impinge on Wall 1. The distance from the exit of the hole to the wall is very short thus producing a strong impingement. The jet is deflected towards the top wall where it is redeflected toward Wall 2. The flow appears to roll into a vortex with the core flow being the slowest. The slower flow is then pushed downstream by the crossflow. For Case 4, the jets appear to impinge strongly on Wall 1. The impingement location along the wall is at higher location than for

Case 3. The jet exits are farther from Wall 1 in this case which causes the higher impingement location. After impingement on Wall 1, the flow behavior appears to be similar to that for Case 3. The strong vortical structure from the smoke flow visualizations provide qualitative proof on the presence of the swirl induced due to impingement on the walls of the channel for Cases 3 and 4. It is, however, not very clear for Case 2.

Heat Transfer Measurements. Detailed heat transfer distributions are presented for all four cases at three channel Reynolds numbers of 10,000, 25,000, and 50,000. In presenting these results, the primary goal is to compare the heat transfer performance for Cases 2, 3, and 4 with that of the baseline Case 1.

The detailed Nusselt number contours are presented for $Re = 25,000$ in Fig. 5. The top figure shows the distributions for Case 1 (180-deg turn). The results for both Wall 1 and Wall 2 are the same so data for only one wall is presented for Case 1. However, results for both walls are presented for the other three cases. The sidewall on which impingement occurs first is called Wall 1 and the opposite facing wall is called Wall 2. The lower passage in Fig. 5 is the inlet passage (first pass) and the upper passage is the exit passage (second pass). Based on the surface heat transfer distributions and the pressure measurements, a conceptual schematic of the flow pattern is shown for each case.

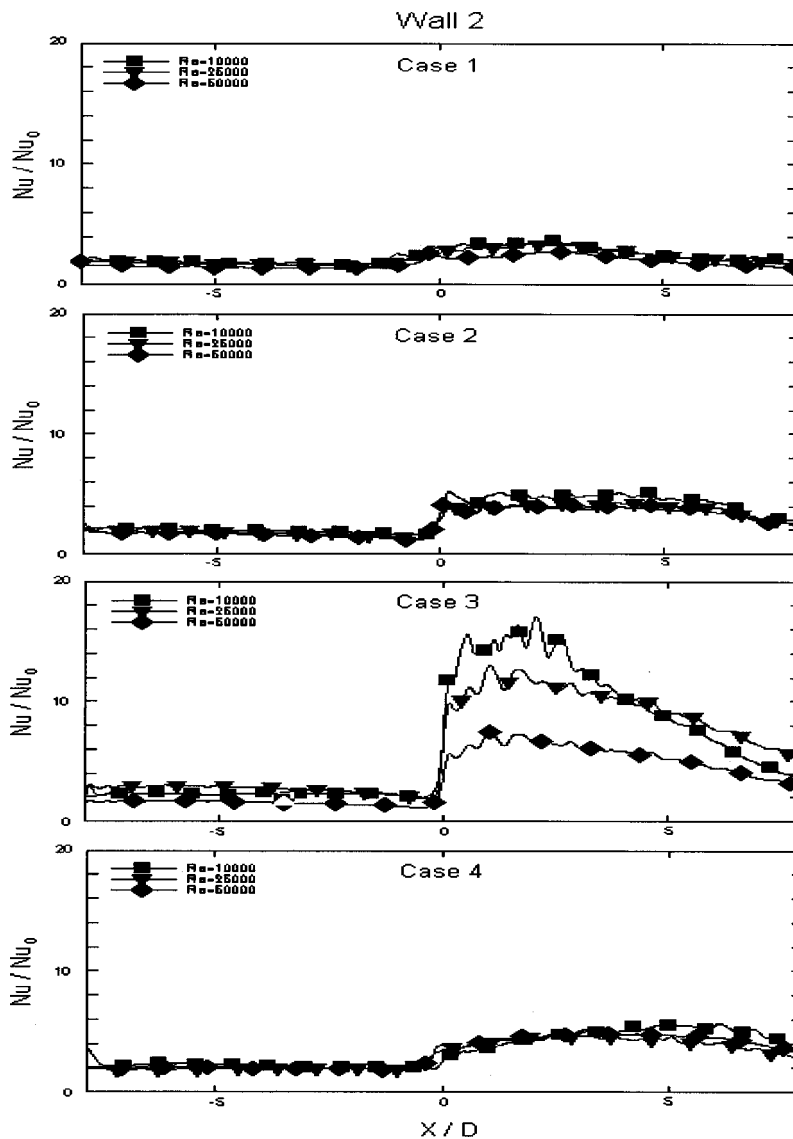


Fig. 8 Effect of flow Reynolds number for each case on Wall 2

The first pass or inlet passage is minimally affected by the changes in configuration (Cases 1–4) as seen from the color contours. This observation is encouraging since enhancements in the second pass are not associated with heat transfer reductions in the first pass. The second pass, expectedly, has different Nusselt number distributions depending upon the configuration. For Case 1, where the air turns into the second pass through a 180-deg turn, flow separation and reattachment are clearly observed past the bend. The first-pass airflow impinges directly on the endwall and turns 180 deg towards the second pass. The flow is then pulled away from the divider wall due to the centrifugal forces generated by the turn and thus heat transfer is enhanced near the outer wall as the flow impinges on to it. The secondary flow is then pushed back into the middle of the duct and mixes with the main flow structures and enhances heat transfer over the entire span immediately after the turn. Further downstream of the turn, the flow appears to become more spanwise uniform and tends to approach fully developed flow conditions. The heat transfer is unevenly enhanced only for a distance of two hydraulic diameters downstream of the turn. Due to this reason, there is a necessity to provide turbulators to enhance the heat transfer in serpentine

channels connected by 180-deg turns. The present results are consistent with the results for smooth channels presented by Ekkad and Han [6,10].

For Case 2, the air enters axially in one direction into the first pass and is routed into the second pass through the series of straight laterally directed holes. The heat transfer coefficient is strongly enhanced on Wall 1, which is closer to the hole row. The laterally injected flow undergoes a sudden expansion through the hole and impinges along Wall 1 causing localized high heat transfer regions for each jet location. The lower heat transfer below the impingement region is due to recirculation of slower separated flow. The flow after impingement on Wall 1 is redirected by the top wall towards Wall 2. The other side of the jet expansion (towards the channel center) directly impinges on the top wall and is also deflected towards Wall 2. The jet impingement location on Wall 1 is at a higher location from the divider wall for the jets near the endwall. The impingement location is shifted downward towards the exit, due to the increasing strength of the passage flow as it moves towards the exit. The passage flow near the endwall is minimal and increases as the number of jets increases from the endwall to the exit of the second pass.

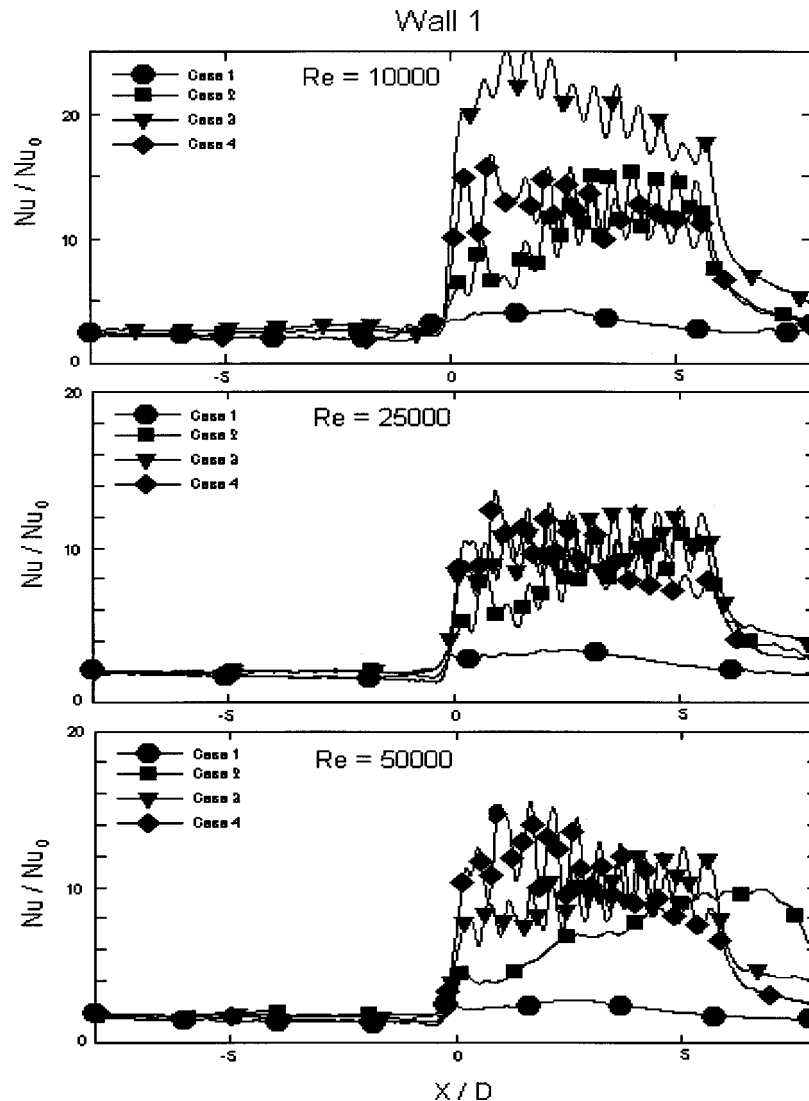


Fig. 9 Effect of flow configuration (case) on Wall 1 for each Reynolds number

For Case 3, the air is routed from the first pass into the second pass through a series of angled holes directed at Wall 1. The direct impingement causes extremely high Nusselt numbers on Wall 1. Also, the effect of passage crossflow is reduced as the impingement is strong and jets travel a very short distance before impingement. For all 12 jets, the location of impingement on the wall is at nearly the same spanwise location relative to the jet. The strong impingement on Wall 1 also produces a fairly high Nusselt numbers on the upper side of Wall 2. This effect is most noticeable on Wall 2 close to the endwall of the passage where the signatures of individual jets can be seen. As the flow moves downstream and the crossflow gets stronger, the discrete effects of the individual jets can no longer be observed.

For Case 4, the jets are located closer to Wall 2, but are oriented in the same direction as in Case 3, and impinge on Wall 1. The impingement is strongest for the middle jets. The heat transfer enhancement is significant on the impingement wall (Wall 1) with the heat transfer enhanced only on the top half of Wall 2. The schematic flow pattern shown (Fig. 4) identifies the reasons for the higher enhancement in the top corners of Wall 1 and Wall 2; a small recirculation zone in the bottom right corner, and slower fluid at the left bottom corner of the channel.

Figure 6 presents the spanwise-averaged results comparing the heat transfer enhancement (\bar{Nu}/Nu_0) versus the streamwise loca-

tion (X/D) on both walls for each crossflow injection case with the baseline 180-deg turn case at $Re=25,000$. Due to high resolution of the measurement technique, only some of the data points are marked with symbols to avoid confusion. There are around 1000 data points in each curve. The Nusselt number for fully developed flow (Nu_0) in a channel (Dittus-Boelter Equation) was used for normalizing the experimental results. All the four cases show small variation in the first pass (inlet passage) ($X/D \leq 0$) Nusselt number distributions. Also, both the walls for each case show similar heat transfer ratio (Nu/Nu_0) values. In the second pass, the primary impingement wall (Wall 1) for Cases 2, 3, and 4 always shows the highest enhancement with values as high as 10. The Nusselt numbers exhibit wavy patterns reflective of jet impingement. However, the wavy oscillations are small (about 30 percent) relative to the baseline. All three injection Cases (2, 3, 4) show significant enhancement over Case 1 with Case 3 showing the most uniform enhancement levels through the channel length. On Wall 2, all three cases again show enhancements over Case 1. For Case 3, the Wall 2 data is nearly three times higher than the Case 1 (180-deg bend) data. For Cases 2 and 4, the Wall 2 data also shows enhancement although they are more modest.

Figure 7 compares the effect of Reynolds number on spanwise-averaged Nusselt number enhancement for each case on Wall 1. This is the impingement wall for Cases 2, 3, and 4. For Case 1, the

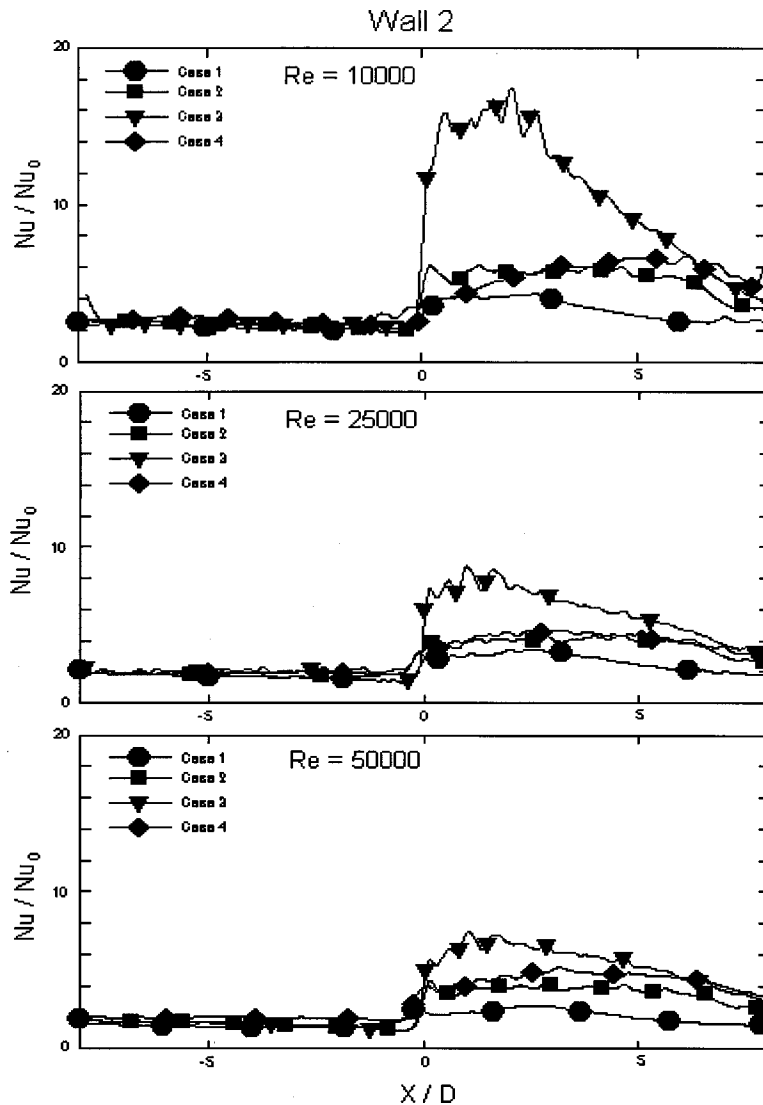


Fig. 10 Effect of flow configuration (case) on Wall 2 for each Reynolds number

Nusselt number ratio is similar at all Reynolds numbers throughout the duct. The highest enhancement after the turn region obtained for this configuration is about three times the fully developed value for channel flow. For Case 2, Nusselt number enhancement is at similar levels in the first pass at all Reynolds numbers. In the second pass, the Nusselt number ratios indicate impingement like distributions with peaks and valleys for $Re = 10,000$ and $25,000$ with slightly lower values at higher Reynolds number of $25,000$. However, at $Re = 50,000$, the Nusselt number distribution is different than for the other two Reynolds numbers and the wavy impingement induced behavior is no longer seen. It appears that at such high Reynolds numbers, the configuration produces significant streamwise crossflow effects reducing the effect of local impingement. However, the Nusselt number ratios are comparable to that at lower Reynolds numbers and still considerably higher than the baseline case. This indicates that the crossflow jets impart a strong degree of swirl to the crossflow, and lead to enhancements in heat transfer. Nusselt number ratios are highest closer to the exit than at individual upstream ($X/D > 0$) impingement locations. For Case 3, the impingement effect is the strongest. First-pass results show very small effect of Reynolds number. For the second pass, at a low Reynolds number of $10,000$, the impingement effect causes Nusselt number ratios to

exceed 20. Further increase in Reynolds number produces lower Nusselt number ratios around 8–9 due to increased crossflow effects. The crossflow velocity versus local jet velocity is the primary reason for the Reynolds number effect for this case. At lower Reynolds number, the generated crossflow velocity in the second pass due to accumulation of coolant is much smaller than the local jet velocity through each hole. For Case 4, the Reynolds number effect is negligible. The Nusselt number ratios are similar through the duct for all Reynolds numbers.

Figure 8 compares the effect of Reynolds number on spanwise-averaged Nusselt number enhancement for each case on Wall 2. Reynolds number effect is very small for Cases 1, 2, and 4. It appears that the channel flow effect is predominant for all these cases and hence the Nusselt number can be normalized with the fully developed flow Nusselt number for that particular Reynolds number and the data collapses on to a single curve. However, for Case 3, this is not evident. The Nusselt number enhancement ratio decreases with increasing Reynolds number. This may be due to the increasing crossflow effect for higher Reynolds number cases. Also, for this case, the first impingement of the jets on Wall 1 is stronger, creating a ricocheting flow toward the opposite wall that produces a fairly strong impingement on Wall 2 leading to the high Nusselt numbers observed.

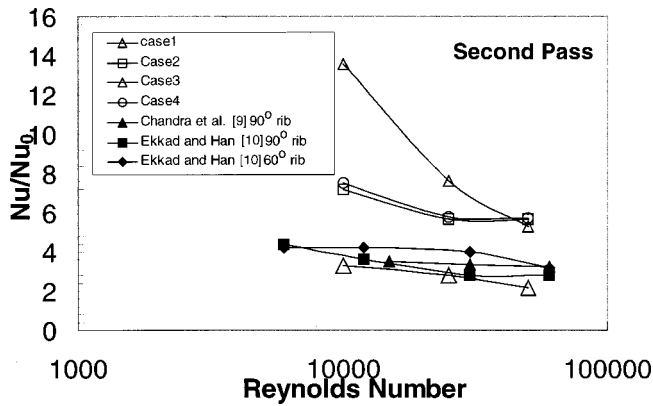


Fig. 11 Comparison of present data to published Nusselt number ratios for the overall averaged rib turbulated second pass

Figure 9 compares the effect of different configurations (cases) for each Reynolds number for Wall 1. At $Re=10,000$, all cases produce similar heat transfer levels in the first pass. In the second pass, Case 3 produces the highest enhancement due to stronger impingement on Wall 1. Case 1 produces lowest heat transfer enhancement in the region near $X/D=1$ and increases towards the exit. Case 4 produces the opposite effect with higher heat transfer around $X/D=1$ and decreasing toward the exit. At $Re=25,000$, Cases 2, 3, and 4 produce similar levels of enhancement in the impingement region (See Fig. 6). Case 1 produces significantly lower heat transfer enhancement than the other three cases. At $Re=50,000$, Case 4 produces the highest heat transfer enhancement close to the endwall and decreases with increasing streamwise crossflow distance. Case 3 produces opposite effect with lower heat transfer near the endwall and higher heat transfer toward the exit. This may be attributed to longer impingement distance from hole exit and stronger crossflows pushing the jets away from the walls. Case 2 does not show impingement like enhancement distributions as seen for the other cases. This implies that the laterally directed jets do not impinge on Wall 1 at this high Reynolds number, and instead contribute to increasing the swirl and thus the heat transfer.

Figure 10 compares the effect of different configurations (cases) for each Reynolds number for Wall 2. All four cases produce similar heat transfer enhancement levels in the first pass. Case 3 produces the highest enhancement at all three Reynolds numbers in the second pass. Cases 2 and 4 produce similar levels and Case 1 produces the lowest enhancement as expected.

Figure 11 compares the overall averaged Nusselt number ratios (\bar{Nu}/Nu_0) for the second pass for Cases 1–4 to averaged Nusselt number ratios for rib turbulated second pass of a two-pass channel with 180-deg turn from Chandra et al. [9], and Ekkad and Han [10]. Both Chandra et al. [9] and Ekkad and Han [10] did not provide any results for pressure drop to compare overall performance results. Ekkad and Han [10] has only one sidewall ribbed whereas Chandra et al. [9] has both sidewalls ribbed in their study. It is clear that all the three geometries introduced in this present study outperform the 90-deg and 60-deg rib effect in the second pass. These comparisons clearly show the effectiveness of these new cooling geometry channels compared to conventional designs.

Overall Pressure Drop and Heat Transfer Distributions.

Overall pressure drops through each of the channels are measured at all three Reynolds numbers using static pressure taps that were placed along the top and bottom secondary walls to measure the overall pressure differential across the entire row of holes or the turn. The pressure differential was measured in inches of water

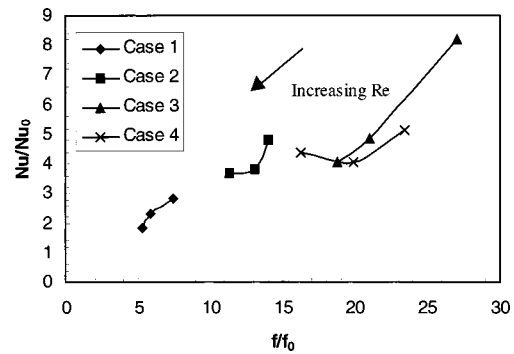


Fig. 12 Overall averaged Nusselt number ratio versus friction factor ratio for all four cases

using a precision manometer. The Darcy friction factor (\bar{f}) is computed using the known pressure drop (ΔP) across the entire two-pass channel and the mass flux ($\rho \bar{V} = G$) through the channel. The Darcy friction factor is normalized by the Darcy friction factor of a smooth channel given as $f_0 = 0.046 Re^{-0.2}$. The friction factor ratio (f/f_0) is computed for each channel at a particular Reynolds number. The overall averaged Nusselt number ratio (\bar{Nu}/Nu_0) is obtained by averaging the detailed Nusselt number distributions of both walls for both passes so as to obtain a single Nusselt number enhancement value for the entire channel irrespective of the channel configuration. The \bar{Nu}/Nu_0 value is plotted against the corresponding f/f_0 for the channel in Fig. 12. At low Reynolds numbers of around 10,000, Case 3 provides significantly higher heat transfer enhancement than all other channels but also provides higher friction factor ratio. At $Re=25,000$ and 50,000, it appears that all three cases with crossflow injection appear to produce similar heat transfer enhancement levels. However, among the three cases, Case 2 produces the lowest friction factor ratio. The heat transfer enhancement is around 10–12 times higher than the smooth channel friction factor.

The thermal performance of the channel is computed using the formulation suggested by Gee and Webb [18] for ribbed channels. The thermal performance parameter is given as $(\bar{Nu}/Nu_0)/(\bar{f}/f_0)^{1/3}$. The thermal performance parameter for each case is plotted against Reynolds number in Fig. 13. Case 3 provides the highest thermal performance parameter value at a Reynolds number of 10,000. At higher Reynolds numbers, Cases 2, 3, and 4 produce similar thermal performance values. Based on Figs. 11–13, it can be concluded that channels connected by orifices instead of a 180-deg turn provide higher heat transfer enhancement. However, the pressure drop penalty is also higher for such channels

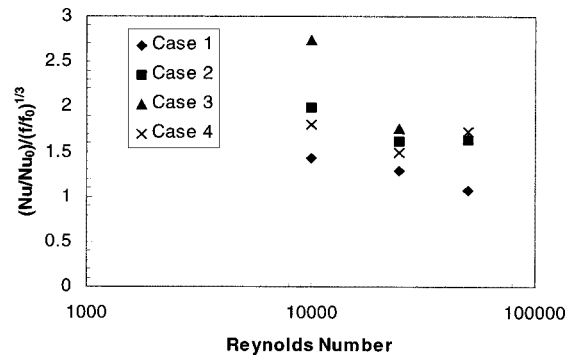


Fig. 13 Overall thermal performance parameter compared to Reynolds number for each case

compared to a smooth channel with 180-deg turn. Since there is no data available on thermal performance parameter for two-pass channels in published literature, comparisons are not provided.

Conclusions

This paper presents detailed heat transfer measurements inside two-pass channels connected by a series of holes on the divider wall. Three lateral hole-injection configurations are tested and compared to the common 180-deg U-turn channel. For each case, results are presented for three channel Reynolds numbers of 10,000, 25,000, and 50,000. Detailed heat transfer distributions show that the heat transfer in the second pass is significantly enhanced due to a combination of impingement and swirl induced by the lateral injection. Heat transfer enhancements higher than 10 are obtained on the impingement wall and around 4–6 on the opposite wall. The heat transfer distributions on the first pass wall are not affected significantly due to the change from a 180-deg turn to a series of holes. This method of coolant supply from one channel to another inside the blade therefore appears more promising than the conventional U-bend serpentine channel design. Importantly, the need for rib turbulators on the second pass may be eliminated due to the significantly higher heat transfer enhancement obtained using the lateral hole-injection configuration. There is a pressure drop penalty associated with the new geometry that is about 200–300 percent higher than that for a two-pass channel with a 180-deg turn. However, rib turbulators on channel walls also provide additional pressure drop (100–150 percent higher) as compared to the smooth channel with a 180-deg turn.

Nomenclature

b = divider wall thickness
 d = hole diameter
 D = square channel width or height, also hydraulic diameter
 f = Darcy friction factor, $2\Delta P(D_h/(2L))/(\rho\bar{v}^2)$
 f_0 = Darcy friction factor in all-smooth wall channel, $0.046 \text{Re}^{-0.2}$
 h = convective heat transfer coefficient
 k = thermal conductivity of test surface material
 k_a = thermal conductivity of air
 L = length of each pass
 \dot{m} = mass flow rate
 Nu = Nusselt number, hD/k_a
 Nu_0 = fully developed flow Nusselt number, $0.023 \text{Re}^{0.8}\text{Pr}^{0.4}$
 p = hole pitch
 P = pressure
 Pr = Prandtl number
 Re = channel Reynolds number, $\rho\bar{v}D/\mu$
 t = time of color change
 T = temperature
 \bar{v} = average flow velocity
 X = axial distance from middle of turn

Greek Symbols

α = thermal diffusivity of test surface material
 β = angle of inclination of the divider wall holes

μ = dynamic viscosity of air
 ρ = density
 τ = time step used in integration

Subscripts

0 = correlation based
 i = initial condition
 j = time step based
 m = bulk flow or mainstream
 w = wall

References

- [1] Boyle, R. J., 1984, "Heat Transfer in Serpentine Passages with Turbulence Promoters," ASME Paper No. 84-HT-24.
- [2] Metzger, D. E., and Sahn, M. K., 1986, "Heat Transfer Around Sharp 180° Turns in Smooth Rectangular Channels," ASME J. Heat Transfer, **108**, pp. 500–506.
- [3] Abuaf, N., Gibbs, R., and Baum, R., 1986, "Pressure Drop and Heat Transfer Coefficient Distributions in Serpentine Passages With and Without Turbulence Promoters," *Proceedings 8th International Heat Transfer Conference*, ASME, New York, pp. 2837–2845.
- [4] Fan, C. S., and Metzger, D. E., 1987, "Effect of Channel Aspect Ratio on Heat Transfer in Rectangular Passage Sharp 180-deg Turns," ASME Paper 87-GT-113.
- [5] Chyu, M. K., 1991, "Regional Heat Transfer in Two-Pass and Three-Pass Passages with 180-deg Sharp Turns," ASME J. Heat Transfer, **113**, pp. 63–70.
- [6] Ekkad, S. V., and Han, J. C., 1995, "Local Heat Transfer Distributions Near a Sharp 180 deg Turn of a Two-Pass Square Channel Using a Transient Liquid Crystal Image Technique," J. Flow Visual. Image Process., **2**, No. 3, pp. 287–298.
- [7] Hibbs, R., Acharya, S., Chen, Y., and Nikitopoulos, D., 1996, "Heat/Mass Transfer in a Two-Pass Rotating Smooth and Ribbed Channel," ASME National Heat Transfer Conference, Houston, Aug.
- [8] Han, J. C., Chandra, P. R., and Lau, S. C., 1988, "Local Heat/Mass Transfer Distributions Around Sharp 180 deg Turns in Two-Pass Smooth and Rib-Roughened Channels," ASME J. Heat Transfer, **110**, pp. 91–98.
- [9] Chandra, P. R., Han, J. C., and Lau, S. C., 1988, "Effect of Rib Angle on Local Heat/Mass Transfer Distribution in a Two-Pass Rib-Roughened Channel," ASME J. Turbomach., **110**, pp. 70–79.
- [10] Ekkad, S. V., and Han, J. C., 1997, "Detailed Heat Transfer Distributions in Two-Pass Square Channels With Rib Turbulators," Int. J. Heat Mass Transf., **40**, No. 11, pp. 2525–2537.
- [11] Hibbs, R., Acharya, S., Chen, Y., Nikitopoulos, D., and Myrum, T., 1998, "Heat Transfer in a Two-Pass Internally Ribbed Turbine Blade Coolant Channel With Cylindrical Vortex Generators," ASME J. Turbomach., **120**, No. 4, pp. 724–734.
- [12] Glezer, B., Moon, H. K., and O'Connell, T., 1996, "A Novel Technique for the Internal Blade Cooling," ASME Paper 96-GT-181.
- [13] Ligrani, P. M., Hedlund, C. R., Thambu, R., Babinchak, B. T., Moon, H. K., and Glezer, B., 1997, "Flow Phenomena in Swirl Chambers," ASME Paper 97-GT-530.
- [14] Moon, H. K., O'Connell, T., and Glezer, B., 1998, "Heat Transfer Enhancement in a Circular Channel Using Lengthwise Continuous Tangential Injection," International Heat Transfer Conference, Seoul, South Korea.
- [15] Hedlund, C. R., Ligrani, P. M., Moon, H. K., and Glezer, B., 1998, "Heat Transfer and Flow Phenomena in a Swirl Chamber Simulating Turbine Blade Internal Cooling," ASME Paper 98-GT-466.
- [16] Metzger, D. E., and Larson, D. E., 1986, "Use of Melting Point Surface Coatings for Local Convection Heat Transfer Measurements in Rectangular Channel Flows With 90-deg Turns," ASME J. Heat Transfer, **108**, pp. 48–54.
- [17] Kline, S. J., and McClintock, F. A., 1953, "Describing Uncertainties in Single Sample Experiments," Mech. Eng. (Am. Soc. Mech. Eng.), **75**, No. 1, pp. 3–8.
- [18] Gee, D. L., and Webb, R. L., 1980, "Forced Convection Heat Transfer in Helically Rib-Roughened Tubes," Int. J. Heat Mass Transf., **23**, pp. 1127–1136.

This section contains shorter technical papers. These shorter papers will be subjected to the same review process as that for full papers.

Transient Double Diffusive Convection in a Vertical Enclosure With Asymmetrical Boundary Conditions

S. Mergui¹

e-mail: mergui@fast.u-psud.fr

D. Gobin

FAST-UMR CNRS 7608 (Universities Paris VI and Paris XI), Campus Universitaire, Bâtiment 502, 91405 Orsay Cedex, France

This study deals with the numerical analysis of transient heat and species transfer by natural convection in a binary fluid vertical layer. The cavity is differentially heated and a solutal buoyancy force is created by imposing a concentration step at one vertical wall. This refers to the experimental situation where the composition gradient inducing the solutal buoyancy force is created by melting of pure ice in a salty solution. The constitution of the flow structure and the time evolution of the heat and mass transfer characteristics are studied for opposing body forces over a range of thermal and solutal Rayleigh numbers. The numerical results allow to provide a better insight into the mechanisms driving the heat and species transfer at high Lewis number thermohaline convection. [S0022-1481(00)00303-0]

Keywords: Computational Double Diffusion, Heat Transfer, Modeling, Natural Convection

1 Introduction

Thermosolutal convective flows in multicomponent fluids are met in a large range of natural phenomena or industrial processes. The competition between thermal and solutal buoyancy forces leads to complex flow structures and the understanding of their interaction with heat and mass transport is relevant in many fields, such as vulcanology, oceanography, materials processing, separation or solidification processes.

Actual situations are relatively difficult to simulate in laboratory experiments under controlled conditions, due to the limitations in specifying composition boundary conditions. Among the many possible configurations in double diffusive convection ([1,2]), we will focus our attention on situations usually designated as "lateral heating," where temperature (or heat flux) con-

ditions are imposed at the vertical boundaries of a rectangular cell containing a binary fluid. The present paper refers to the experimental studies reported in the bibliography on melting of ice in an aqueous solution. This has been experimented by Huppert and Turner [3] or Bénard et al. [4] among others, but there have been very few attempts to propose a complete numerical simulation ([5,6]).

It has been shown elsewhere (see [4]) that a purely convective model could retain the main double diffusive mechanisms and simulate the dominating transport phenomena present in the problem: A binary fluid at an initial concentration C_0 is initially at rest in a rectangular cavity at a uniform temperature T_0 ; at time $t^* = 0$, the temperature of the left wall is raised to a temperature $T_1 > T_0$, and a uniform concentration $C_1 = 0$ is specified at the right wall, while its temperature is maintained at T_0 . Only the process of cell formation has already been studied and the purpose of the present paper is to analyze the time evolution of heat and species transfer in relation with the flow structure.

2 Governing Equations

The coupled thermal and solutal convective flow created in the enclosure is essentially a transient process and the time-dependent equations have to be considered. The dimensionless temperature θ and concentration ϕ are defined using T_0 and C_0 , the initial temperature and concentration of the solution, as the reference values. The dimensionless length and time are defined using H and H^2/ν as the reference quantities.

Equations. The flow is assumed to be laminar, incompressible, and the fluid satisfies the Boussinesq approximation. In terms of the variables defined above, the governing dimensionless equations in the binary liquid are the following:

$$\nabla \cdot \mathbf{V} = 0, \quad (1)$$

$$\frac{\partial \theta}{\partial t} + \mathbf{V} \cdot \nabla \theta = \frac{1}{\text{Pr}} \Delta \theta, \quad (2)$$

$$\frac{\partial \phi}{\partial t} + \mathbf{V} \cdot \nabla \phi = \frac{1}{\text{LePr}} \Delta \phi, \quad (3)$$

$$\frac{\partial \mathbf{V}}{\partial t} + (\mathbf{V} \cdot \nabla) \mathbf{V} = \nabla^2 \mathbf{V} - \nabla P + (\text{Gr}_T \theta + \text{Gr}_S \phi) \mathbf{k}. \quad (4)$$

The classical dimensionless parameters appearing in the equations are the thermal and solutal Grashof numbers, built on the height H of the enclosure, $\text{Gr}_T = g \beta_T (T_1 - T_0) H^3 / \nu^2$ and $\text{Gr}_S = g \beta_S (C_0 - C_1) H^3 / \nu^2$. We will also use the ratio of the buoyancy forces ($N = \text{Gr}_S / \text{Gr}_T$). The fluid properties are combined in the Prandtl and Lewis numbers.

The initial conditions are zero temperature and concentration. All the walls are assumed to be rigid, impermeable except the cold wall. The horizontal walls are adiabatic. The boundary conditions are $\theta(x=0, z, t) = 1$ at the hot wall, $\theta(1/A, z, t) = 0$ and $\phi(1/A, z, t) = -1$ at the cold wall.

¹To whom correspondence should be addressed.

Contributed by the Heat Transfer Division for publication in the JOURNAL OF HEAT TRANSFER. Manuscript received by the Heat Transfer Division, Aug. 6 1999; revision received, Apr. 11, 2000. Associate Technical Editor: C. Beckermann.

Numerical Resolution. The set of coupled equations governing the problem and the associated initial and boundary conditions is solved using a finite volume technique directly derived from the SIMPLER method proposed by Patankar [7]. Time integration uses a first-order implicit scheme and the centered scheme is retained for spatial discretization of the convective terms. An ADI procedure using a vectorized version of the TDMA algorithm solves the linear systems of discretized equations, and convergence at each time step is checked using the L^2 norm of the residues of the continuity equation.

The computational grid used in the foregoing calculations is usually defined as follows:

1 In the vertical direction a regular grid is used, since multicellular patterns with size changing cells are expected: For the $A = 3$ aspect ratio studied hereafter, 281 regularly spaced nodes are usually required in order to describe the flow structures.

2 The grid used in the horizontal direction is irregular, since higher gradients are located close to the walls. The major constraint is due to the solutal boundary layer thickness, whose order of magnitude may be estimated from the usual scaling laws [8] based on the solutal Rayleigh number ($Ra_S = N Le Ra_T$): $\delta_S \approx H Ra_S^{-1/4}$. The number of nodes of the irregular grid must be such that at least five or six nodes are present in the solutal boundary layer. On the other hand the irregular node distribution must be smooth enough to describe the thicker thermal boundary layer. This is the reason why a sinusoidal distribution has been preferred to a geometrical progression: Most simulations have been performed using a 93 node horizontal grid.

3 The accuracy of the calculations has been assessed by comparison with a reference solution obtained by an independent pseudo-spectral Chebyshev algorithm described in LeQuéré [9]. For a typical case of double diffusive convection ($A = 3$, $Pr = 11$, $Le = 192$, $Ra_T = 10^6$, $N = -22$), the reference solution [10] has been compared to our finite volume calculations, using either a centered or a hybrid discretization scheme, with two different time-steps $\delta t = 5 \times 10^{-5}$ and $\delta t = 1.5 \times 10^{-5}$. The Nusselt number for the centered scheme solution differs by less than two percent from the reference solution for both time-steps while the hybrid scheme underpredicts the Nusselt number by about nine percent. The relative differences on the Sherwood numbers are of the order of one percent for both schemes and time-steps. As a consequence, the results presented hereafter have been obtained from computations using a centered scheme and a time-step $\delta t = 5 \times 10^{-5}$.

3 Results

The discussion of the results deals essentially with the heat and mass transfer evolution, but we first recall a few aspects of the flow structure.

Building Up of the Flow Structure. A typical time evolution of the different fields is displayed in Fig. 1 for $A = 3$, $Pr = 10$, $Le = 210$, $Ra_T = 9 \times 10^5$, $N = -22$. At early times of the process, an ascending thermal natural convective flow develops along the hot wall. The hot fluid horizontally crosses the top of the cavity and competes with the upward solutal boundary layer developing along the cold wall. During an initial transient stage, the core gets filled with the heated fluid by horizontal layering and a thermal recirculation cell is created, in the same way as in pure thermal natural convection. The thermal cell remains uniformly at the initial concentration while the temperature field gets vertically stratified. The ascending fluid along the cold wall has a lower concentration than the core and accumulates in the upper part of the cavity building up a very low velocity zone, called the "stagnant zone." This zone is fed by the cold side only and is not penetrated by the fluid from the hot boundary layer. Heat transfer in the top of this zone is clearly diffusive while the concentration field is vertically stratified. Depending on the range of parameters, ther-

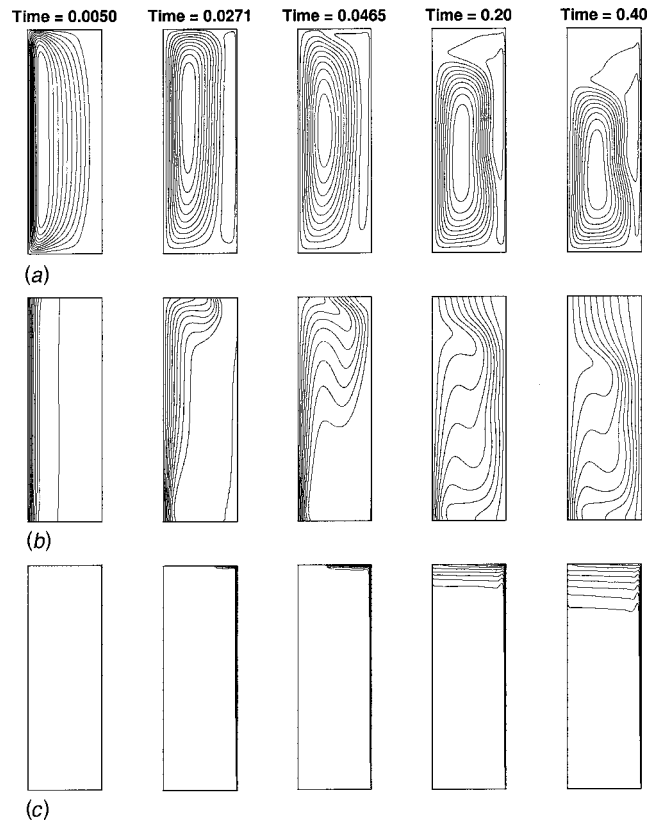


Fig. 1 Time evolution of the streamlines (a), isotherms (b), and isopleths (c) ($A = 3$, $Pr = 10$, $Le = 210$, $Ra_T = 9 \times 10^5$, $N = -22$)

mosolutal cells can develop in the bottom part of the stagnant zone, in a region where the vertical density gradient is weaker.

The set of numerical simulations presented in the following sections has been performed in order to study the influence of the dimensionless parameters on the average heat and mass transfer at the vertical walls and on the behavior of the thermal cell. The parametric study is limited to the influence of the thermal Rayleigh number Ra_T and of the buoyancy ratio N . The other parameters are kept unchanged: $Pr = 10$ and $Le = 210$ are typical of aqueous solutions and the aspect ratio, $A = 3$. Moreover, the solutal Rayleigh numbers have been chosen in such a way that the stagnant zone remains stable (no thermosolutal cell). Hence, the range of parameters under study is $-8 \leq N \leq -75$, $2.7 \times 10^5 \leq Ra_T \leq 1.5 \times 10^7$ and $1.5 \times 10^9 \leq Ra_S \leq 2.5 \times 10^{10}$.

Heat Transfer. The dimensionless heat flux in a vertical cross section of the enclosure, the average Nusselt number, is defined as

$$Nu = \int_0^1 \varphi(z) dz = \int_0^1 \left[\frac{\partial \theta}{\partial x} - Pr(u\theta) \right] dz. \quad (5)$$

A characteristic time evolution of the average Nusselt number at the hot wall ($Nu_h(t)$) and at the cold wall ($Nu_c(t)$) is depicted in Fig. 2 for a set of values of the buoyancy ratio at a given thermal Rayleigh number. A transient evolution corresponding to the development of the thermal boundary layer and to the building up of the temperature stratification in the thermal cell can be observed. This stage is also illustrated by the evolution of the temperature field depicted in Fig. 1 for $N = -22$. At early times of the process, the decrease in the hot wall Nusselt number is not monotonic: This feature is also present in the pure thermal convection simulation ($N = 0$) displayed in the figure, proving that it is due to the evolution of the temperature field. After a transient stage,

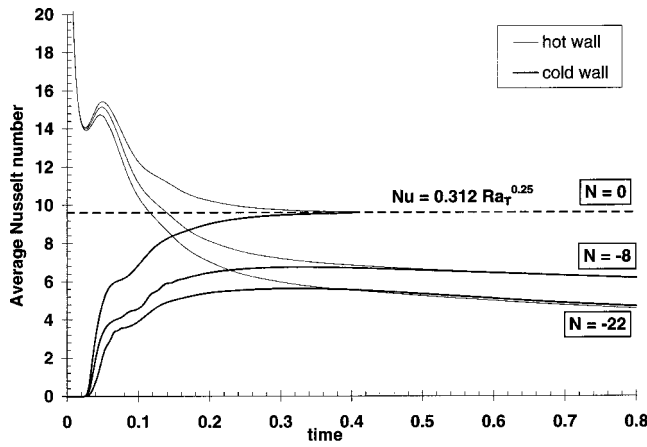


Fig. 2 Time evolution of the average heat transfer at the cold and hot walls ($A=3$, $Pr=10$, $Le=210$, $Ra_T=9 \times 10^5$)

$Nu_h(t) = Nu_c(t)$ (let us note $t = t_{QS}$ the corresponding time) and then both the cold and hot average Nusselt number slightly decreases.

Also visible in Fig. 2 is the influence of the solutal buoyancy force attenuating the average heat transfer. For a given value of Ra_T , the Nusselt number indeed decreases with increasing $|N|$. It is expected that the average heat transfer increases with increasing Ra_T , N or Ra_S being held constant. To correlate the influence of each dimensionless parameter on the Nusselt number, we search a classical power-law dependence of Nu on N and Ra_T as $Nu = \mathcal{A}|N|^a Ra_T^b$. As the process under study does not reach a steady state, the Nusselt number value used to establish such a correlation is the value at $t = t_{QS}$. It can be checked that choosing the values of Nu at a time corresponding to the same height of the stagnant zone for all cases leads to the same correlation. The identification of the exponents from our set of results (one decade for N and two decades for Ra_T) leads to the following correlation, illustrated in Fig. 3:

$$Nu_{QS} = 0.322(1 + |N|)^{-0.17} Ra_T^{0.25} \quad (6)$$

It should be noted that the 0.25 exponent for Ra_T arising from the identification is not particularly expected, since the boundary layer approximations used for the derivation of the classical scaling laws in natural convection (see [8]) do not necessarily apply in this range of parameters. The correlation has been derived, however, in terms of $(1 + |N|)$ in order to recover a relevant correla-

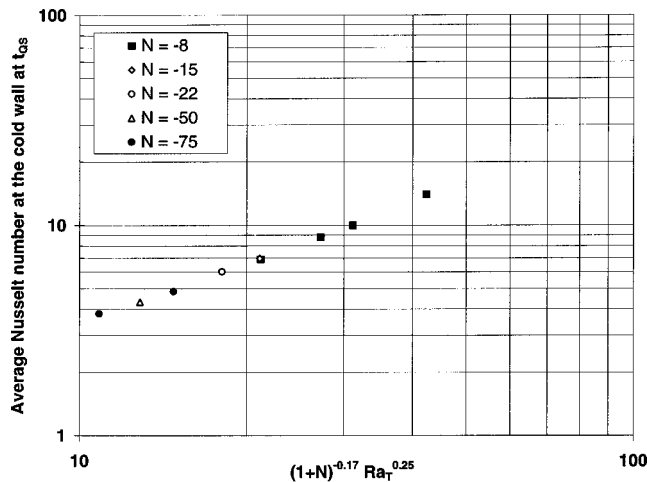


Fig. 3 Correlation $Nu = f(N, Ra_T)$

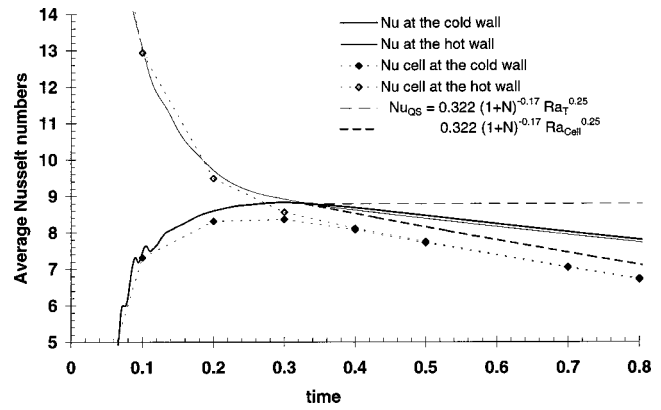


Fig. 4 Time evolution of the average heat transfer at the cold and hot walls ($A=3$, $Pr=10$, $Le=210$, $Ra_T=2.5 \times 10^6$, $N=-8$)

tion in the pure thermal convection limit ($N=0$). If we refer to laminar thermal convection in fixed enclosures, for a given Prandtl number, it is well known that the Nusselt number may be expressed as $\mathcal{B}Ra_T^{0.25}$. The simulation in the pure thermal case at $Pr=10$, yields a value $\mathcal{B}=0.312$, which is reasonably close to the coefficient identified in (6). This value is also in good agreement with the 0.32 value reported in previous reference studies (see [11]).

Let us now examine the further time evolution of the heat transfer after t_{QS} . As previously said, there is a slow decrease in the average Nusselt number, Nu , as defined by Eq. (5) corresponding to the dimensionless average heat flux on the whole height of the enclosure. As previously observed, the flow is structured in two domains: a stagnant zone where the heat transfer is mainly diffusive and a thermal convection cell of decreasing height, z_{TH} . In order to study the contribution of each zone to the heat flow, we will define a "cell" Nusselt number, Nu_{cell} , corresponding to the dimensionless heat flux on the height of the thermal cell:

$$Nu_{cell} = \int_0^{z_{TH}} \varphi(z) dz.$$

Figure 4 depicts the time evolution of those quantities for $N = -8$, $Ra_T = 2.5 \times 10^6$. We can observe that $Nu_{cell} < Nu$, the difference corresponding to the contribution of the stagnant zone to the global heat transfer. This diffusive contribution is not negligible and increases with time, from six percent at $t = t_{QS}$ ($z_{TH} = 0.835$) to 14 percent at $t = 0.8$ ($z_{TH} = 0.640$). Also plotted in the figure are the previous Nusselt number correlation (6) assessed at $t = t_{QS}$ and the same correlation as a function of a time-dependent thermal Rayleigh number based on z_{TH} :

$$Ra_{cell} = \frac{g \beta_T (T_1 - T_0) z_{TH}^3}{\nu \alpha}.$$

It can be seen that the Nu_{cell} decrease is identical to this latter correlation, involving that the heat transfer evolution in the thermal cell is directly related to the decrease in its height, $Nu_{cell} \sim z_{TH}^{3/4}$. Moreover, since the Nusselt number is identical at both walls, the heat balance between the stagnant zone and the thermal cell is zero. This clearly denotes that the thermal cell behaves like a differentially heated cavity of height z_{TH} with adiabatic conditions at the bottom and top boundaries, despite the presence of the stagnant zone and the shear between the ascending solutal flow and the downward thermal boundary layer along the cold wall.

Let us now consider the time evolution of the local Nusselt number distribution on the cold wall along the normalized height of the thermal cell (z/z_{TH}), displayed in Fig. 5. The figure shows a significant increase in the local heat transfer at early times ($t = 0.05$ and 0.1) during the development of the stratification in the

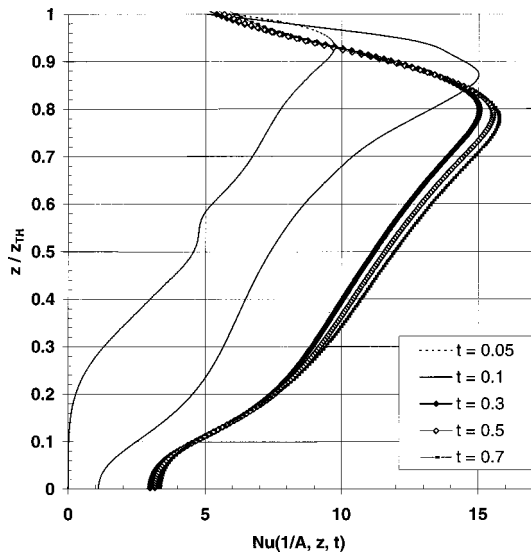


Fig. 5 Local Nusselt number distribution at the cold wall along the thermal cell at different times ($A=3$, $Pr=10$, $Le=210$, $Ra_T=9 \times 10^5$, $N=-8$)

thermal cell. For the next three times, a striking feature of this representation is the similarity of the distribution especially in the 20 percent top and bottom parts of the wall. Elsewhere, the local heat transfer at a given height increases. Defining the average of the local Nusselt number on the thermal cell as

$$\frac{1}{z_{TH}} \int_0^{z_{TH}} \varphi(z) dz = \frac{1}{z_{TH}} Nu_{cell},$$

it can be shown that this quantity slightly increases as the thermal cell height reduces and varies as $z_{TH}^{-1/4}$. This feature confirms that the thermal cell surprisingly behaves like a differentially heated cavity of height z_{TH} .

Mass Transfer. The dimensionless mass flux in a vertical cross section of the enclosure, the average Sherwood number, is defined as

$$Sh = \int_0^1 \left[\frac{\partial \phi}{\partial x} - Sc(u\phi) \right] dz. \quad (7)$$

A characteristic time evolution of the average Sherwood number at the cold wall is depicted in Fig. 6, for a set of simulations obtained at a given solutal Rayleigh number and various values of

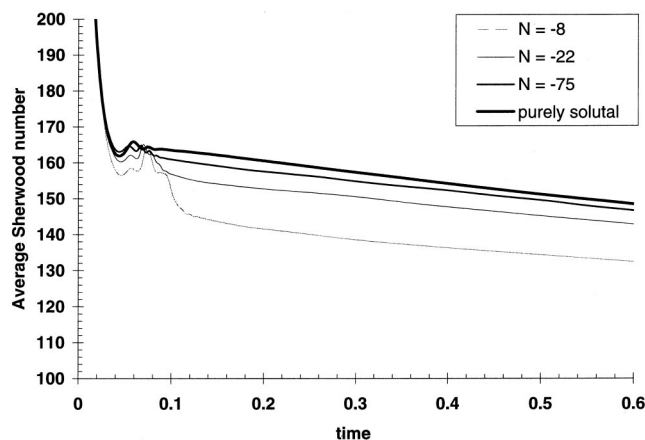


Fig. 6 Time evolution of the average mass transfer at the cold wall ($A=3$, $Pr=10$, $Le=210$, $Ra_S=4.2 \times 10^9$)

the buoyancy ratio. After a transient stage corresponding to the development of the solutal boundary layer and the building up of the stagnant zone, the Sherwood number slightly decreases. Figure 6 points out an increase in the mass transfer with $|N|$, for a given value of Ra_S . As expected, it can be shown that the Sherwood number increases with increasing Ra_S , N , or Ra_T being given. One might expect a negligible separate influence of $|N|$ on the mass transfer and a $Sh \sim Ra_S^{0.25}$ correlation, since the usual boundary layer correlations apply for solutally dominated double diffusive convection. This could not be quantitatively assessed from our calculations, since the Ra_S range of our results is too limited.

In addition, the time evolution of the average Sherwood number for the purely solutal case is plotted in the figure. This situation, representing the $N \rightarrow \infty$ limit ($Ra_T=0$), is the analog of the ‘‘filling box’’ configuration studied by Worster and Leitch [12]. The general trend of the Sherwood number evolution is similar for the different values of N represented in the figure, and the highest value of $N(N=-75)$ used in the simulation is seen to be very close to the limit where the thermal effect has no impact on mass transfer. The horizontal concentration profile for the purely solutal case is little affected even by the strong thermal effect at $N=-8$ for which the relative difference on the average Sherwood number is about 12 percent. This feature is also confirmed by the local mass transfer distribution along the cold wall (not shown). Along the thermal cell, the local mass transfer for $N=-8$ is lower than for pure solutal convection, while it is much closer in the stagnant zone. Moreover, it can be shown that the local mass transfer at a given height remains remarkably constant in time in the decreasing thermal cell. Thus, the overall decrease in the average Sherwood number is due to the variation in the stagnant zone.

4 Conclusion

The numerical simulation of transient thermosolutal convection of a binary fluid in a differentially heated enclosure with asymmetric concentration conditions is studied to approach the problem of melting of a pure solid in a binary mixture. The present analysis concerns the average heat and species transfer in the system, before destabilization of the stagnant zone.

The study, limited to a given range of parameters (Pr and Le numbers of aqueous solutions, opposing buoyancy forces, dominating solutal effect) at relatively high thermal Rayleigh numbers, confirms the heat transfer characteristics observed in the experiments by Mergui et al. [13]. However, the numerical simulations are not in quantitative agreement with the measurements, and the predicted time evolution of the building up process is still significantly slower than in the experiments. This might be due to the fact that the model assumptions concerning the boundary conditions at the cold wall do not account for phase change. A space and time variation of the interface temperature and composition may arise from dissolution at the ice-liquid front in the areas where the melting rate is low (the stagnant zone). The model is currently developed to solve the fully coupled interaction between double diffusive convection and phase change in order to describe the real boundary conditions at the interface.

Acknowledgments

The computations were made on the Cray C94 at IDRIS (CNRS–France) under Grant No. 98-0336. The authors acknowledge the support of the SPI Department of CNRS. The authors wish to thank Patrick Le Quéré for his contribution to the numerical tests.

References

- [1] Turner, J., 1979, *Buoyancy Effects in Fluids*, Cambridge University Press, Cambridge, UK.
- [2] Ostrach, S., 1980, ‘‘Natural Convection With Combined Driving Forces,’’ *Phys.-Chem. Hydrodyn.*, **1**, No. 1, pp. 233–247.

- [3] Huppert, H. E., and Turner, J. S., 1989, "Ice Block Melting Into a Salinity Gradient," *J. Fluid Mech.*, **100**, pp. 367–384.
- [4] Bénard, C., Bénard, R., Bennacer, R., and Gobin, D., 1996, "Melting Driven Thermosolutal Convection," *Phys. Fluids*, **8**, No. 1, pp. 112–130.
- [5] Beckermann, C., and Viskanta, R., 1988, "Double Diffusive Convection Due to Melting," *Int. J. Heat Mass Transf.*, **31**, pp. 2077–2089.
- [6] Schütz, W., and Beer, H., 1991, "Heat Transfer in Melting of Ice Influenced by Laminar, Double Diffusive Convection With Density Inversion of Water," in *7th Int. Conf. Num. Methods Thermal Problems*, Vol. 7, Stanford, CA, Pineridge Press, Swansea, UK, p. 144.
- [7] Patankar, S., 1980 *Numerical Heat Transfer and Fluid Flow*, Hemisphere, Washington, DC.
- [8] Bejan, A., 1995, *Convection Heat Transfer*, Wiley, New York.
- [9] LeQuéré, P., 1991, "Accurate Solutions to the Square Thermally Driven Cavity at High Rayleigh Number," *Comput. Fluids*, **20**, No. 1, pp. 29–41.
- [10] LeQuéré, P., 1998, personal communication.
- [11] Henkes, R., 1990, "Natural Convection Boundary Layers," Ph.D. thesis, TU Delft–NL.
- [12] Worster, M. G., and Leitch, A. M., 1985, "Laminar Free Convection in Confined Regions," *J. Fluid Mech.*, **156**, pp. 301–319.
- [13] Mergui, S., Joly, D., Feroual, B., Bénard, C., and Gobin, D., 1998 "Experiments on Phase-Change Processes Controlled by Convective Heat and Mass Transfer," in *Modelling, Casting, Welding and Advanced Solidification Processes VIII*, TMS Publishers, San Diego, CA, pp. 721–728.

Natural Convection in Low Prandtl Number Fluids With a Vertical Magnetic Field

S. Saravanan

Junior Research Fellow

P. Kandaswamy

Professor

Department of Mathematics, Bharathiar University,
Coimbatore 641046, Tamil Nadu, India
e-mail: pkgk@bharathi.ernet.in

Keywords: Cavities, Finite Difference, Heat Transfer, Liquid Metals, Natural Convection

1 Introduction

Proper selection of coolant is crucial in many thermodynamical systems. For example, in the case of nuclear reactors an enormous amount of heat energy is released. Nowadays liquid metals/alkali metals and their alloys (like NaK alloy) are used in slender tubes surrounding the nuclear core to absorb and remove the heat [1]. There are some special features connected with the heat transfer in these metals. These have high thermal conductivity and hence low Prandtl number ranging from 0.005 to 0.03. Especially the liquid alkali metals have low density, low viscosity and high thermal conductivity which make them suitable for heat transfer media (coolant) in exothermic reactions. Moreover the low melting and high boiling points of these metals enable to handle them in the liquid state with high temperature more efficiently.

The pioneering works in convection in tubes and enclosures are those of Lighthill [2] and Wilkes and Churchill [3], respectively. Earlier studies on natural convection in enclosures include experimental studies of Eckert and Carlson [4], Elder [5], and numerical studies, for example, by Polezhaev [6], Catton et al. [7], and Mallinson and de Vahl Davis [8]. In relation to direct numerical simulation of convection in low Prandtl number fluids, we refer to Jones [9] and Hadid and Roux [10]. Hall et al. [11] and Nicolette

et al. [12] addressed transient heating of a square cavity through either one or two vertical walls. Jones and Briggs [13] and Kazmierczak and Chinoda [14] studied the effect of different boundary conditions in the same geometry. Recent advances include those of Kwak and Hyun [15], Bergman and Hyun [16], and Aydin et al. [17]. Magnetoconvection plays an important role in various industrial fields. Examples include magnetic control of molten iron flow in the steel industry, liquid metal cooling in nuclear reactors and magnetic suppression of molten semiconducting materials. Studies of magnetic field on low Prandtl number fluids include those of Fumizawa [18], Okada and Ozoe [19], and Tagawa and Ozoe [20]. Recently Mobner and Muller [21] have made a complete investigation of three-dimensional magnetoconvection in rectangular cavities. Bejan [22], Gebhart [23], Alchaar [24], and Eckert et al. [25] provide a good review of literature on convection in enclosures.

The dependence of thermal conductivity of a few liquid metals/alkali metals ($Pr \ll 1$) on temperature are shown in Fig. 1(a) ([26]). From this we infer that thermal conductivity is nearly linear against temperature. Most published works that use low Prandtl number fluids with large-scale temperature variation (for example, [27] and [28]) neglect the dependence of thermal conductivity on temperature. Also the turbulent eddy diffusivity is much less than molecular diffusivity. Hence in the present analysis we shall concentrate on the effect of variable thermal conductivity of the fluid on the laminar heat transfer characteristics.

2 The Equations

Consider a two-dimensional square cavity of height H and length L (Fig. 1(b)) filled with the fluid. The cartesian coordinates (x, y) with the corresponding velocity components (u, v) are as indicated in the figure. The vertical walls located at $y=0$ and $y=L$ are isothermal but maintained at different temperatures θ_h and θ_c ($\theta_c < \theta_h$), respectively. The bottom and top of the cavity are assumed to be thermally insulated. The gravity g and magnetic field B_o act normal to the y -direction. To analyze the natural convection of liquid metal in the presence of a magnetic field, it is assumed that the induced magnetic field and viscous heating are negligible and the liquid metal is not magnetized. The thermal conductivity k of the fluid is assumed to vary linearly with temperature as

$$k(\theta) = k_c [1 - a(\theta - \theta_c)] \quad (1)$$

where a is the temperature coefficient of thermal conductivity and the subscript c refers to the reference state at the cold wall.

The nondimensional equations governing the laminar two-dimensional incompressible flow of the fluid under consideration with constant physical properties except density in the external force and thermal conductivity are

$$T_\tau + UT_X + VT_Y = (1/Pr_c) \{ T_{XX} + T_{YY} - \eta [TT_{XX} + TT_{YY} + T_X^2 + T_Y^2] \} \quad (2)$$

$$\zeta_\tau + U\zeta_X + V\zeta_Y = Gr T_Y + \zeta_{XX} + \zeta_{YY} - Ha^2 V_X \quad (3)$$

$$\Psi_{XX} + \Psi_{YY} = -\zeta \quad (4)$$

$$U = \psi_Y, \quad V = -\psi_X, \quad \text{where } \zeta = V_X - U_Y, \quad (5)$$

with the initial and boundary conditions

$$\begin{aligned} \tau = 0: \quad & U = V = \Psi = T = 0; \quad 0 \leq X, \quad Y \leq 1 \\ \tau > 0: \quad & \Psi = \Psi_X = \Psi_Y = 0, \quad T = 1 \quad Y = 0 \\ & \Psi = \Psi_X = \Psi_Y = 0, \quad T = 0; \quad Y = 1 \\ & \Psi = \Psi_X = \Psi_Y = 0, \quad T_X = 0; \quad X = 0 \quad \text{and} \quad 1. \end{aligned} \quad (6)$$

The diffusion scales are $X = x/L$, $Y = y/L$, $U = uL/\nu$, $V = vL/\nu$, $\tau = t\nu/L^2$, $\Psi = \varphi/\nu$, $\zeta = \omega L^2/\nu$, $T = (\theta - \theta_c)/(\theta_h - \theta_c)$. The vorticity at the walls is calculated using $\zeta_{\text{wall}} = -\Psi_{nn}$ where n is the

Contributed by the Heat Transfer Division for publication in the JOURNAL OF HEAT TRANSFER. Manuscript received by the Heat Transfer Division, Oct. 1, 1999; revision received, Apr. 4, 2000. Associate Technical Editor: P. Ayyaswamy.

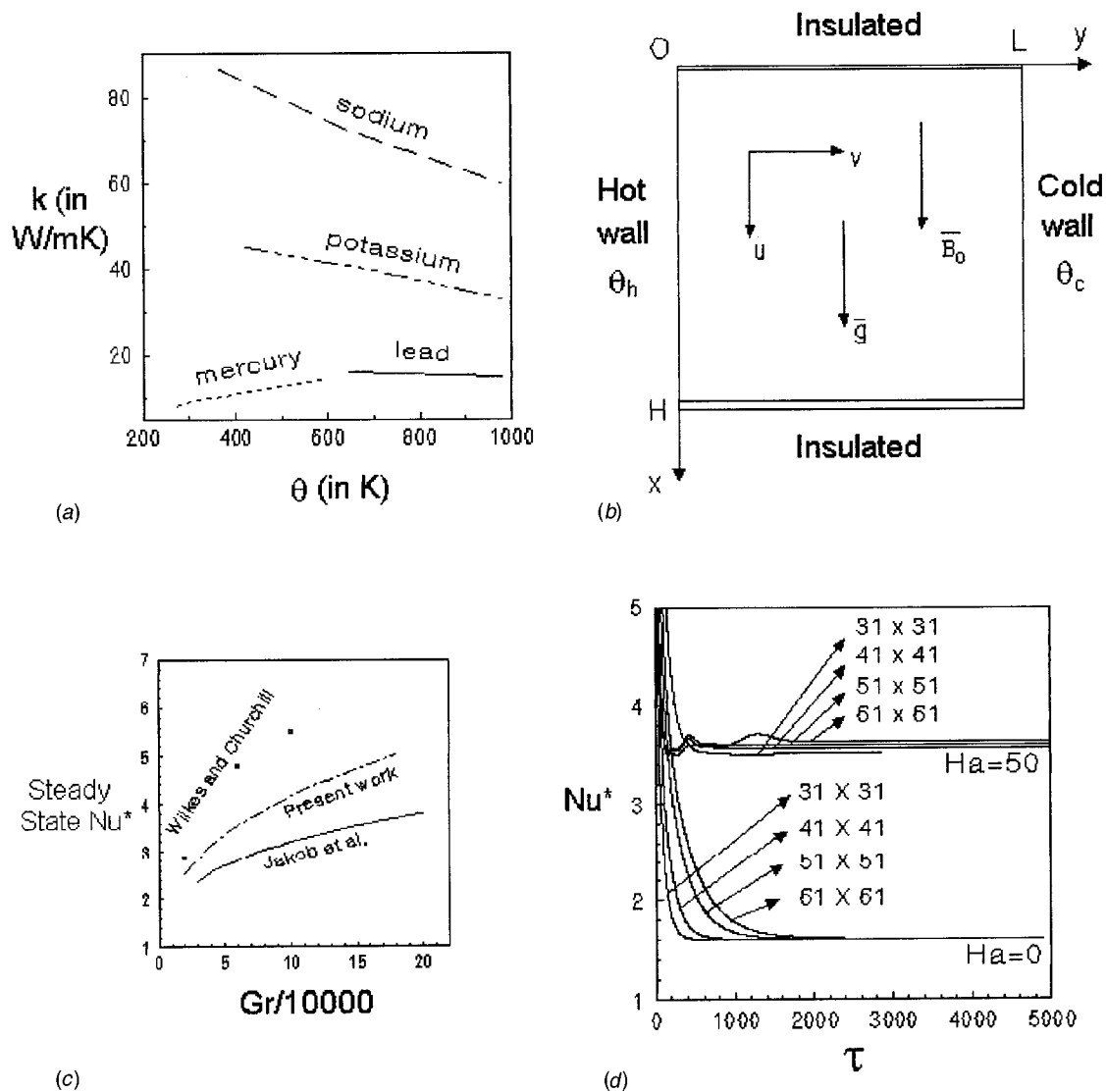


Fig. 1 (a) The dependence of k on θ ; (b) physical configuration; (c) correlation of present numerical results with others; (d) transient responses of Nu^* for various mesh sizes

outward drawn normal to the surface. The nondimensional parameters are the Grashof number $Gr = g\beta(\theta_h - \theta_c)L^3/\nu^2$, the Prandtl number $Pr_c = \nu/\alpha_c$, the Hartmann number $Ha = B_o L(\sigma/\mu)^{1/2}$, the aspect ratio $A = H/L = 1$ and $\eta = (\theta_h - \theta_c)$. The local Nusselt number is $Nu = T_\gamma$ at the hot wall. The average Nusselt number is expressed as

$$Nu^* = \frac{1}{A} \int_0^A Nu dX.$$

3 Numerical Solution

The Eqs. (2)–(6) are solved numerically by finite difference technique with a uniform mesh. The numerical procedure followed is similar to that of Jones and Cai [29] except for the advective terms. We use forward difference and central difference approximations for time and space derivatives, respectively, in the advective terms. The Alternating Direction Implicit scheme ([30]) and Successive Over Relaxation method are used in each time step. This is repeated for each of the next time levels until the steady-state solution is obtained satisfying the convergent criteria used by Rudraiah et al. [28]. For verifying the code, we used the results of Wilkes and Churchill [3], Rudraiah et al. [28], and the

Table 1 Effect of η on steady-state Nu^* : ($Pr_c = 0.054$, $A = 1$)

| Gr | Ha | η | Steady-State Nu^* | Max Ψ | |
|-----------------|----|--------|--------------------------|------------|------|
| 2×10^4 | 0 | 0 | 1.1972 (1.11444 [28]) | 27 | |
| | | 0.5 | 1.8633 | 25 | |
| | | 0.9 | 4.4665 | 21 | |
| | 50 | 0 | 0 | 1.0013 | 1.05 |
| | | | 0.5 | 1.4757 | 1.1 |
| | | | 0.9 | 3.7905 | 1.02 |
| | | 100 | 0 | 1.0002 | 0.27 |
| | | | 0.5 | 1.4734 | 0.32 |
| | | | 0.9 | 3.7861 | 0.3 |
| 2×10^5 | 0 | 0 | 2.2296 (1.91219 [28]) | 102 | |
| | | 0.5 | 3.5737 | 87 | |
| | | 0.9 | 7.1139 | 74 | |
| | 50 | 0 | 0 | 1.0578 | 10.3 |
| | | | 0.5 | 1.6046 | 10.8 |
| | | | 0.9 | 4.0047 | 9.6 |
| | | 100 | 0 | 1.0059 | 2.76 |
| | | | 0.5 | 1.4869 | 3.2 |
| | | | 0.9 | 3.8070 | 3.1 |

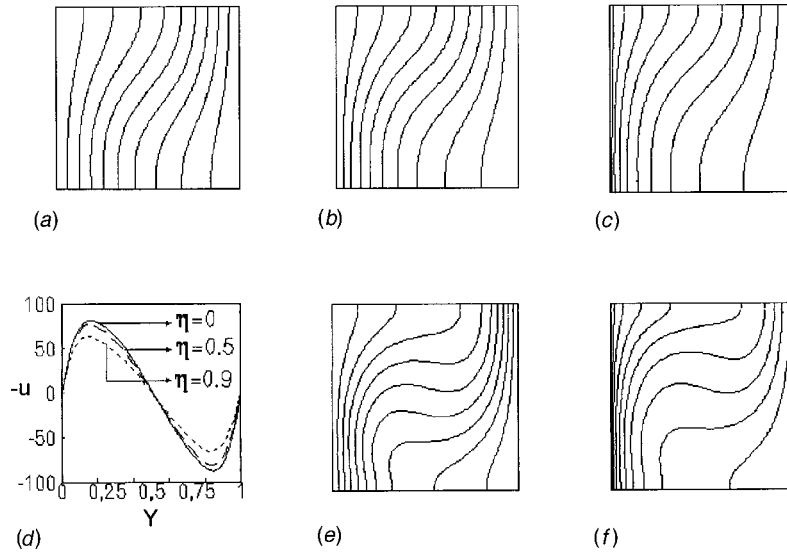


Fig. 2 (a), (b), and (c) Steady-state isotherms for $Gr=2 \times 10^4$, $\eta=0, 0.5$ and 0.9 ; (d) velocity profiles at midheight ($X=0.5$) for $Gr=2 \times 10^4$, different η ; (e) and (f) steady-state isotherms for $Gr=2 \times 10^5$, $\eta=0$ and 0.9

experimental correlation of Jakob [31]. All these papers provide steady-state Nu^* for natural convection with Boussinesq approximation. By setting $\eta=0$, we found our results match well (Fig. 1(c) and Table 1). It is well known that the finite difference computation suffers the numerical errors, especially the truncation error. Thus the computations were carried out with 31×31 , 41×41 , 51×51 and 61×61 grids. Figure 1(d) shows the effect of grid size on the average Nusselt number for $Gr=2 \times 10^5$, $\eta=0.5$, $Ha=0$, and $Ha=50$. We observe that these similar curves attain almost the same steady-state value. The slight increase in the values of steady-state Nu^* is due to the increase in the number of grid points at the hot wall. Hence it is assumed that the computational results from the present code are independent of the grid size. The detailed results in the remainder of the paper are all from a 41×41 grid.

4 Results and Discussion

The effect of temperature-dependent thermal conductivity on buoyancy induced convection in the presence of a uniform magnetic field is investigated numerically. The computations are carried out by fixing Gr as 2×10^4 and 2×10^5 , Pr_c as 0.054 corresponding to liquid metals and varying η . η is a measure for the variation of the thermal conductivity. Increase in the value of η denotes a decrease in $k(\theta)$. For example, in the case of liquid Sodium ($Pr=0.011$), $a=0.00051$ and hence η ranges from 0.1 to 0.31 for a temperature difference of 200 K to 600 K by fixing the cavity length as 0.01 m. The value of a are still higher for some liquid alloys whose deviation in $k(\theta)$ against θ is more. The range for η is $0 \leq \eta < 1$. $\eta=1$ is excluded as it corresponds to $k_h=0$.

Figures 2(a) to 2(d) show the effect of thermal conductivity variation on buoyancy driven convection in the absence of magnetic field $Ha=0$ for $Gr=2 \times 10^4$. Figure 2(a) corresponds to $\eta=0$ (constant $k(\theta)$, i.e., $k(\theta)=k_c$) and 2(b) and (c) correspond to $\eta=0.5, 0.9$ (varying $k(\theta)$, i.e., $k(\theta) < k_c$), respectively. Streamlines are not displayed here as they depict a simple clockwise rotating unicellular flow pattern. We notice that as η increases the lower part of the isotherms near the hot wall begins to crowd and starts forming a thermal boundary layer. This is clearly seen in Fig. 2(c) showing only a meagre quantity of heat is propagated from the hot wall to cold wall across the cavity. We also observe from Fig. 2(d) and Table 1 that an increase in η reduces the convective flow. Table 1 shows the heat transfer rate for $\eta=0.5$

comes to a steady state with $Nu^*=1.8633$. This together with the decrease in stream function values shows conductive mode of heat transfer is reduced. Thus the heat transfer from the hot wall to the adjoining fluid begins to drop. Further increase in η confirms the above fact. Thus in general the heat transfer at the hot wall does not get transported well to the cold wall because of the reduction in the conduction and convection modes. For higher Gr values a typical flow behavior is seen with increased speed of circulation (see Table 1). Figures 2(e) and (f) depict the same behavior for $\eta=0, 0.9$ at $Gr=2 \times 10^5$ with a stratified core corresponding to higher Gr as reported by Bejan [22].

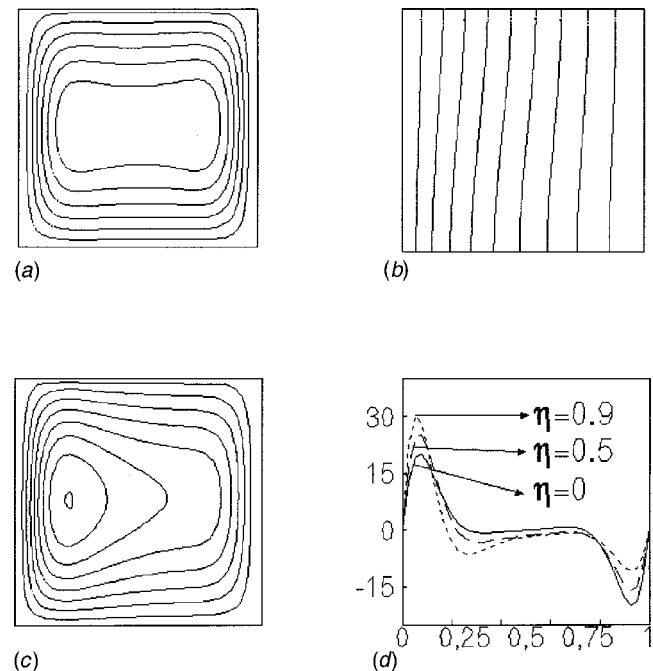


Fig. 3 (a) Steady-state streamlines for $Gr=2 \times 10^5$, $Ha=100$, $\eta=0$; (b) and (c) steady-state isotherms and streamlines for $Gr=2 \times 10^5$, $Ha=100$ and $\eta=0.5$; (d) velocity profiles at mid-height for $Gr=2 \times 10^5$, $Ha=100$ and different η

When an external magnetic field of value $Ha=100$ is applied parallel to gravity, a horizontal body force is induced. So the streamlines are stretched horizontally and isotherms become nearly parallel and equidistant, i.e., the magnetic field retards the vertical velocity of the fluid particles except near the hot and cold walls where the forces due to local density variations dominate. This is also observed from the nearly vanishing vertical velocity at the midheight in the middle of the cavity. Figure 3(a) shows the corresponding streamlines. But no attraction of streamlines towards the hot wall is observed. This attraction is an expected one because of the Lorentz force. Figures 3(b) and (c) show the flow pattern when $Gr=2 \times 10^5$, $Ha=100$, and $\eta=0.5$. Now the streamlines are attracted towards the hot wall as anticipated and hence the convection across the cavity is highly damped. This shows the drawback of taking k to be a temperature-independent quantity. Figure 3(d) shows the increase in the vertical velocity near the hot wall due to attraction. Also the isotherms are attracted to the hot wall, with an increase in steady-state Nu^* . This implies that the heat energy from the hot wall remain only in the neighborhood of the hot wall because of the reduced conductive and highly reduced convective modes.

5 Conclusion

The effect of temperature-dependent thermal conductivity on the buoyancy induced convection in low Prandtl number fluids contained in a square cavity is studied. It is found that an increase in η reduces both conductive and convective modes of heat transfer in the absence of a magnetic field. In the presence of a vertical magnetic field, this increase in η produces a highly damped convection (because of the attraction of convective cell towards the hot wall) and conduction. This is expected in laminar convection since all heat transfer from the wall must be through molecular conduction. We can conclude that it is advantageous to use low Prandtl number liquid metals or alloys as coolants in fast reactors whose thermal conductivity does not depend much on temperature.

Acknowledgment

One of the authors (S.S.) thanks CSIR, India, for its financial support through the Junior Research Fellowship (NET).

Nomenclature

| | |
|----------|--|
| a | = temperature coefficient of thermal conductivity (1/K) |
| A | = aspect ratio= $H/L=1$ |
| B_o | = magnetic flux density (Wb/m ²) |
| g | = acceleration due to gravity (m/s ²) |
| Gr | = Grashof number= $g\beta(\theta_h - \theta_c)L^3/\nu^2$ |
| H | = height of the cavity (m) |
| Ha | = Hartmann number= $B_oL(\sigma/\mu)^{1/2}$ |
| k | = thermal conductivity of fluid (W/mK) |
| L | = length of the cavity (m) |
| Nu | = local Nusselt number= $(T_Y) _{Y=0}$ |
| Nu^* | = average Nusselt number= $(1/A)\int_0^A Nu dX$ |
| p | = pressure (Pa) |
| Pr | = Prandtl number (ν/α) |
| t | = time (s) |
| T | = dimensionless temperature |
| u | = vertical velocity (m/s) |
| U | = dimensionless vertical velocity |
| v | = horizontal velocity (m/s) |
| V | = dimensionless horizontal velocity |
| x | = vertical coordinate (m) |
| X | = dimensionless vertical coordinate |
| y | = horizontal coordinate (m) |
| Y | = dimensionless horizontal coordinate |
| α | = thermal diffusivity of fluid (m ² /s) |
| β | = volumetric coefficient of expansion of fluid (1/K) |
| θ | = temperature of fluid (K) |

| | |
|------------|--|
| θ_c | = cold wall temperature (K) |
| θ_h | = hot wall temperature (K) |
| η | = dimensionless temperature coefficient of thermal conductivity ($a(\theta_h - \theta_c)$) |
| φ | = stream function (m ² /s) |
| μ | = dynamic viscosity of fluid (Pa.s) |
| ν | = kinematic viscosity of fluid= μ/ρ (m ² /s) |
| ρ | = density of fluid (kg/m ³) |
| σ | = electrical conductivity of fluid (1/(Ω .m)) |
| τ | = dimensionless time |
| ω | = vorticity (1/s) |
| ψ | = dimensionless stream function |
| ζ | = dimensionless vorticity |

Subscript

| | |
|-----|------------------------------------|
| c | = reference state at the cold wall |
| h | = reference state at the hot wall |

References

- [1] Etherington, H., 1958, *Nuclear Engineering Handbook*, McGraw-Hill, New York.
- [2] Lighthill, M. J., 1953, "Theoretical Considerations on Free Convection in Tubes," *Q. J. Mech. Appl. Math.*, **6**, Part 5, pp. 398-439.
- [3] Wilkes, J. O., and Churchill, S. W., 1966, "The Finite Difference Computation of Natural Convection in a Rectangular Enclosure," *AIChE J.*, **12**, No. 1, pp. 161-166.
- [4] Eckert, E. R. G., and Carlson, W. O., 1961, "Natural Convection in an Air Layer Enclosed Between Two Vertical Plates With Different Temperatures," *Int. J. Heat Mass Transf.*, **2**, pp. 106-120.
- [5] Elder, W. J., 1965, "Laminar Free Convection in a Vertical Slot," *J. Fluid Mech.*, **23**, pp. 77-98.
- [6] Polezhaev V. I., 1967, "Numerical Solution of a System of Two Dimensional Unsteady Navier-Stokes Equations for a Compressible Gas in a Closed Region," *Fluid Dyn.*, **2**, pp. 70-74.
- [7] Catton, I., Ayyaswamy, P. S., and Clever, R. M., 1974, "Natural Convection Flow in a Finite, Rectangular Slot Arbitrarily Oriented With Respect to the Gravity Vector," *Int. J. Heat Mass Transf.*, **17**, pp. 173-184.
- [8] Mallinson, G. D., and de Vahl Davis, G., 1977, "Three Dimensional Natural Convection in a Box: A Numerical Study," *J. Fluid Mech.*, **83**, 1-31.
- [9] Jones, I. P., 1982, "Low Prandtl Number Free Convection in a Vertical Slot," AERE Harewell Report R-10416.
- [10] Hadid, H. B., and Roux, B., 1987, "Oscillatory Buoyancy Driven Flow in a Horizontal Liquid Metal Layer," *ESA-SP-256*, pp. 477-485.
- [11] Hall, J. D., Bejan, A., and Chaddock, J. B., 1988, "Transient Natural Convection in a Rectangular Enclosure With One Heated Side Wall," *Int. J. Heat Mass Transf.*, **9**, pp. 396-404.
- [12] Nicolette, V. F., Yang, K. T., and Lloyd, J. R., 1985, "Transient Cooling by Natural Convection in Two-dimensional Square Enclosure," *Int. J. Heat Mass Transf.*, **28**, pp. 1721-1732.
- [13] Jones, D. N., and Briggs, D. G., 1989, "Periodic Two-Dimensional Cavity Flow: Effect of Linear Horizontal Thermal Boundary Condition," *ASME J. Heat Transfer*, **111**, pp. 86-91.
- [14] Kazmierczak, M., and Chinoda, Z., 1992, "Buoyancy Driven Flow in an Enclosure With Time Periodic Boundary Conditions," *Int. J. Heat Mass Transf.*, **35**, No. 6, pp. 1507-1518.
- [15] Kwak, H. S., and Hyun, J. M., 1996, "Natural Convection in an Enclosure Having a Vertical Side Wall With Time Varying Temperature," *J. Fluid Mech.*, **329**, pp. 65-88.
- [16] Bergman, T. L., and Hyun, M. T., 1996, "Simulation of Two-Dimensional Thermosolutal Convection in Liquid Metals Induced by Horizontal Temperature and Species Gradients," *Int. J. Heat Mass Transf.*, **39**, No. 12, pp. 2883-2894.
- [17] Aydin, O., Unal, A., and Ayhan, T., 1999, "Natural Convection in Rectangular Enclosures Heated From One Side and Cooled From the Ceiling," *Int. J. Heat Mass Transf.*, **42**, pp. 2345-2355.
- [18] Fumizawa, M., 1980, "Natural Convection Experiment With Liquid NaK Under Transverse Magnetic Field," *J. Nucl. Sci. Technol.*, **17**, No. 2, pp. 98-105.
- [19] Okada, K., and Ozoe, H., 1992, "Experimental Heat Transfer Rates of Natural Convection of Molten Gallium Suppressed Under an External Magnetic Field in Either x , y or z -direction," *ASME J. Heat Transfer*, **114**, pp. 107-114.
- [20] Tagawa, T., and Ozoe, H., 1997, "Enhancement of Heat Transfer Rate by Application of a Static Magnetic Field During Natural Convection of Liquid Metal in Cube," *ASME J. Heat Transfer*, **119**, pp. 265-271.
- [21] Mobner, R., and Muller, U., 1999, "A Numerical Investigation of Three-Dimensional Magnetoconvection in Rectangular Cavities," *Int. J. Heat Mass Transf.*, **42**, pp. 1111-1121.
- [22] Bejan, A., 1984, *Convection Heat Transfer*, Wiley, New York.
- [23] Gebhart, B., Jaluria, Y., Mahajan, R. L., and Sammakia, B., 1988, *Buoyancy Induced Flows and Transports*, Hemisphere, Washington, DC.
- [24] Alchaar, S., Vasseur, P., and Bilgen, E., 1995, "Natural Convection Heat

Transfer in a Rectangular Enclosure With a Transverse Magnetic Field," ASME J. Heat Transfer, **117**, pp. 668–673.

- [25] Eckert, E. R. G., Goldstein, R. J., Ibele, W. E., Patankar, S. V., Simon, T. W., Strykowski, P. J., Tamma, K. K., Kuehn, T. H., Bar-Cohen, A., Heberlein, J. V. R., Davidson, J. H., Bischof, J., Kulacki, F., and Kortshagen, U., 1999, "Heat Transfer—A Review of 1995 Literature," Int. J. Heat Mass Transf., **42**, pp. 2717–2797.
- [26] Lide, D. R., 1993, *Handbook of Chemistry and Physics*, CRC Press, Boca Raton, FL.
- [27] Hadid, H. B., and Roux, B., 1992, "Buoyancy and Thermocapillary Driven Flows in Differentially Heated Cavities for Low Prandtl Number Fluids," J. Fluid Mech., **235**, pp. 1–36.
- [28] Rudraiah, N., Venkatachalappa, M., and Subbaraya, C. K., 1995, "Combined Surface Tension and Buoyancy Driven Convection in a Rectangular Open Cavity in the Presence of a Magnetic Field," Int. J. Non-Linear Mech., **35**, pp. 759–770.
- [29] Jones, G. F., and Cai, J., 1993, "Analysis of a Transient Asymmetrically Heated/Cooled Open Thermosyphon," ASME J. Heat Transfer, **115**, p. 621.
- [30] Jaluria, M., and Torrance, K. E., 1986, *Computational Heat Transfer*, Hemisphere, pp. 178–183.
- [31] Jakob, M., 1949, *Heat Transfer*, Vol. 1, John Wiley and Sons, New York.

Approximate Solution of a Class of Radiative Heat Transfer Problems

H. Qiao

Research Assistant Professor, Department of Manufacturing Engineering and Engineering Management, City University of Hong Kong, Tat Chee Avenue, Kowloon, Hong Kong
e-mail: mehong@cityu.edu.hk

Y. Ren

Research Fellow, Fujitsu Parallel Computing Research Centre, Imperial College, 180 Queen's Gage, London SW7 2BZ, UK
e-mail: yr@ic.ac.uk

B. Zhang¹

Senior Lecturer, School of Mathematical and Information Sciences, Coventry University, Coventry CV1 5FB, UK
e-mail: b.zhang@coventry.ac.uk

An approximate solution is presented for a class of radiative heat transfer problems within enclosures having black or diffuse-gray surfaces based on a modified Taylor series expansion method; such radiative transfer problems are generally represented by integral equations. The approach avoids use of any boundary/initial conditions associated with the original Taylor series expansion method and leads to an approximate solution in a simple closed form to the radiant integral equations, which can be computed straightforwardly on a modern personal computer using symbolic computing codes such as Maple. The method can be effectively and efficiently applied to deal with enclosures involving more than one or two surfaces, for which direct numerical integration may be subject to instability, or require an excessive amount of computation. The computed numerical results for representative thermal problems are in excellent agreement with those obtained by other numerical approaches. [S0022-1481(00)00203-6]

Keywords: Computational Heat Transfer, Numerical Methods

¹To whom correspondence should be addressed.

Contributed by the Heat Transfer Division for publication in the JOURNAL OF HEAT TRANSFER. Manuscript received by the Heat Transfer Division, June 24, 1999; revision received, March 30, 2000. Associate Technical Editor: P. Menguc.

Introduction

Radiative heat transfer within enclosures having black or diffuse-gray surfaces, where heat transfer is only by radiation, is generally formulated by single or simultaneous linear Fredholm integral equations of the second kind for the unknown surface temperature or heat flux distributions ([1,2]). Integral equations also arise when radiation exchange is considered within a radiating medium such as a gas. These integral equations involve configuration factors that, for most geometries, are not of simple forms. There is usually little chance that exact solutions in closed form can be found, so numerical solutions are used. Numerical solutions for general linear Fredholm integral equations of this second kind have been studied by many authors using Galerkin, collocation, and quadrature (or Nyström) methods (see, e.g., [3] and the references quoted there). The use of some of these methods for radiation integral equations can be found in, e.g., the books of Siegel and Howell [1] and Sparrow and Cess [2] and the references quoted there. These numerical methods transform the integral equation to a set of algebraic equations that can be solved in principle by direct or iterative methods. In practice, however, instability, slow convergence, and excessive computation may limit either method. Hence, despite the continued advance in computers and numerical methods, approximate methods remain of interest and utility in this field.

Approximate solution procedures have been proposed for solving the Fredholm integral equations of the second kind arising in radiative heat transfer (see, e.g., Siegel and Howell [1], Chapter 7) and Sparrow and Cess [2], Chapter 3), which transform the integral equation to a linear ordinary differential equation that can be solved analytically or numerically if the boundary conditions can be specified. One such an approach is the Taylor series expansion method which was proposed by Krishnan and Sundaram [4] and Perlmutter and Siegel [5] for solving an integral equation of radiative heat transfer within a gray circular tube. The physical idea that motivates this method is that the geometric configuration factor can often decrease quite rapidly as the distance is increased between the two elements exchanging radiation. This means that the radiative heat balance at a given location may be significantly influenced only by the radiative fluxes leaving surface elements in the immediate vicinity, so that a Taylor series expansion can be made for the unknown radiative heat flux distribution in order to obtain a good approximation to the integral in the radiative integral equation. This transforms the integral equation to a linear ordinary differential equation with variable coefficients and requires the manufacture of an appropriate number of boundary conditions ([4,5,1,2]). Though the boundary conditions may be derived, as illustrated in the paper of Perlmutter and Siegel [5], from the physical constraints in the system, such as symmetry or an overall heat balance, it is in general very difficult to determine them. The method is thus difficult to be extended to deal with enclosures involving more than one or two surfaces. To avoid use of boundary conditions a collocation method utilizing the first term of the Taylor series expansion was proposed by Choi and Churchill [6] to build a higher-order approximation and applied to radiative exchange integral equations between two parallel plates and within a cylinder cavity. It should be remarked that as pointed out by Choi and Churchill [6] the accuracy of their collocation method depends on the location of the collocation points.

In this note we present a numerical study of a class of radiative heat transfer problems, which are formulated as Fredholm integral equations of the second kind, by making use of a novel modification of the Taylor series expansion method. The approach is simple yet effective and avoids use of any boundary conditions associated with the original Taylor series expansion method. In fact, our approach leads to an approximate solution in a simple, closed form which can be easily and efficiently computed on a modern personal computer using symbolic computing codes such as Maple. So the approach can be easily applied to deal with enclosures involving more than one or two surfaces, e.g., radiative

exchange in a catalytic monolith with square or circular channels where a system of radiative integral equations was used to model the radiative exchange (see, e.g., [7]). Note that, since the system of integral equations is often coupled with a complex system of differential and algebraic equations that models channel interaction and other processes in the catalytic combustor, the conventional numerical methods for the integral equations often makes the problem intractable (see [7]). To illustrate the efficiency and accuracy of the method in the present note we study an example of radiant heat transfer problems in detail.

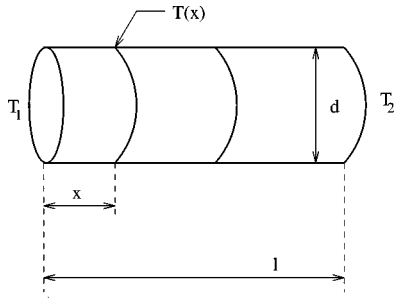


Fig. 1 Model for radiative transfer between a gray cylindrical tube

Radiant Flux Within a Cylindrical Tube

As an example we consider a circular, cylindrical tube of diameter d and length l (see Fig. 1).

The temperature distribution along the cylindrical wall is a known function of $X=x/d$. The ends of the cylinder at $X=0$ and at $X=l/d=L$ may be considered to be black surfaces at T_1 and T_2 , respectively, or open to blackbody surroundings at these temperatures. Suppose that the emissivity ϵ is the same for all surfaces. Then the governing equation for the dimensionless radiosity is given by

$$\beta(X) = \epsilon \theta^4(X) + (1 - \epsilon) \left[F(X) + \theta_1^4 F(L - X) + \int_0^L \beta(\xi) K(|X - \xi|) d\xi \right], \quad (1)$$

where $\beta(X) = B(x)/\sigma T_1^4$ is the dimensionless radiosity on the surface of the cylinder, $\theta(X) = T(X)/T_1$ is the specified dimensionless temperature distribution with $T(X)$ being the absolute temperature along the cylindrical wall, and $\theta_1 = T_2/T_1$ is the dimensionless temperature of the end of the cylinder at $X=L$ (see, e.g., [6,1,2]). The function $F(X)$ is the configuration factor from the end of the cylinder at $X=0$ to a differential ring at X on the cylindrical wall and is given as follows (see Eq. (34)) in Appendix C of Siegel and Howell [1]):

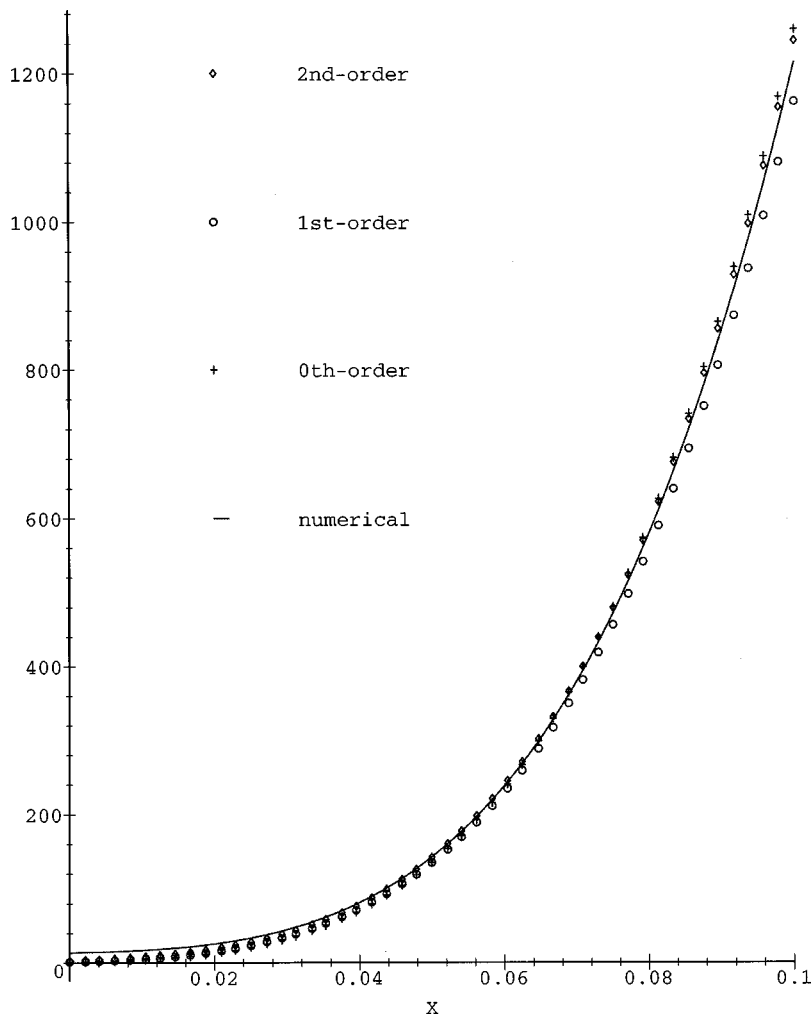


Fig. 2 Comparison of approximations and numerical solution for dimensionless radiosity on inside surface of a cylinder with $\epsilon=L=0.1$

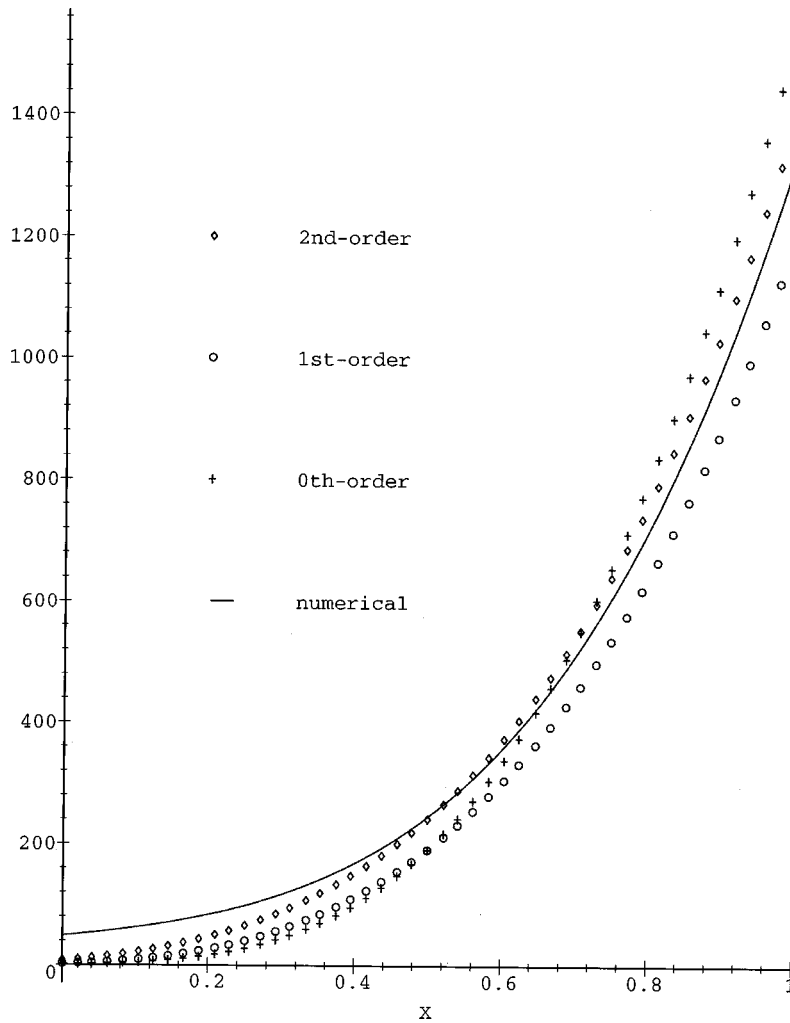


Fig. 3 Comparison of approximations and numerical solution for dimensionless radiosity on inside surface of a cylinder with $\epsilon=0.5$ and $L=1$

$$F(X) = \frac{X^2 + 0.5}{(X^2 + 1)^{1/2}} - X, \quad (2)$$

and $F(L-X)$ is the configuration factor from the end of the cylinder at $X=L$ to a differential ring at X on the cylindrical wall and can be obtained from (2) by substituting $L-X$ for X . The function $K(|X-\xi|)$ is the configuration factor between two differential-rings at X and ξ on the cylindrical wall (see Eq. (33) in Appendix C of Siegel and Howell [1]) given by

$$K(|X-\xi|) = 1 - \frac{|X-\xi|[(X-\xi)^2 + 1.5]}{[(X-\xi)^2 + 1]^{3/2}}. \quad (3)$$

Defining $f(X) = \epsilon\theta^4(X) + (1-\epsilon)[F(X) + \theta_1^4 F(L-X)]$, we can write Eq. (1) as

$$\beta(X) = f(X) + (1-\epsilon) \int_0^L \beta(\xi) K(|X-\xi|) d\xi. \quad (4)$$

This is a Fredholm integral equation of the second kind with the kernel $K(|X-\xi|)$ being continuous but having discontinuous derivatives at $X=\xi$.

Equation (4) was first solved by using the product Nyström method and an N -point equal-interval quadrature rule with arbitrary weight suggested by Press et al. ([8], pp. 791-794). The mesh size N was taken very large ($N=20L$ for (4)) so as to provide accurate numerical solutions for evaluation of the accuracy of the approximations developed below.

Zeroth-Order Approximation. Taking the first term of the Taylor series expansion at $\xi=X$ of $\beta(\xi)$, namely $\beta(X)$, in the integral of (4) gives

$$\beta(X) \approx f(X) + (1-\epsilon)\beta(X) \int_0^L K(|X-\xi|) d\xi.$$

This leads to the zeroth-order approximation to the solution $\beta(X)$:

$$\beta_0(X) = \frac{f(X)}{1 - (1-\epsilon)I_L(X)}, \quad (5)$$

where

$$I_L(X) = \int_0^L K(|X-\xi|) d\xi = 1 - F(X) - F(L-X)$$

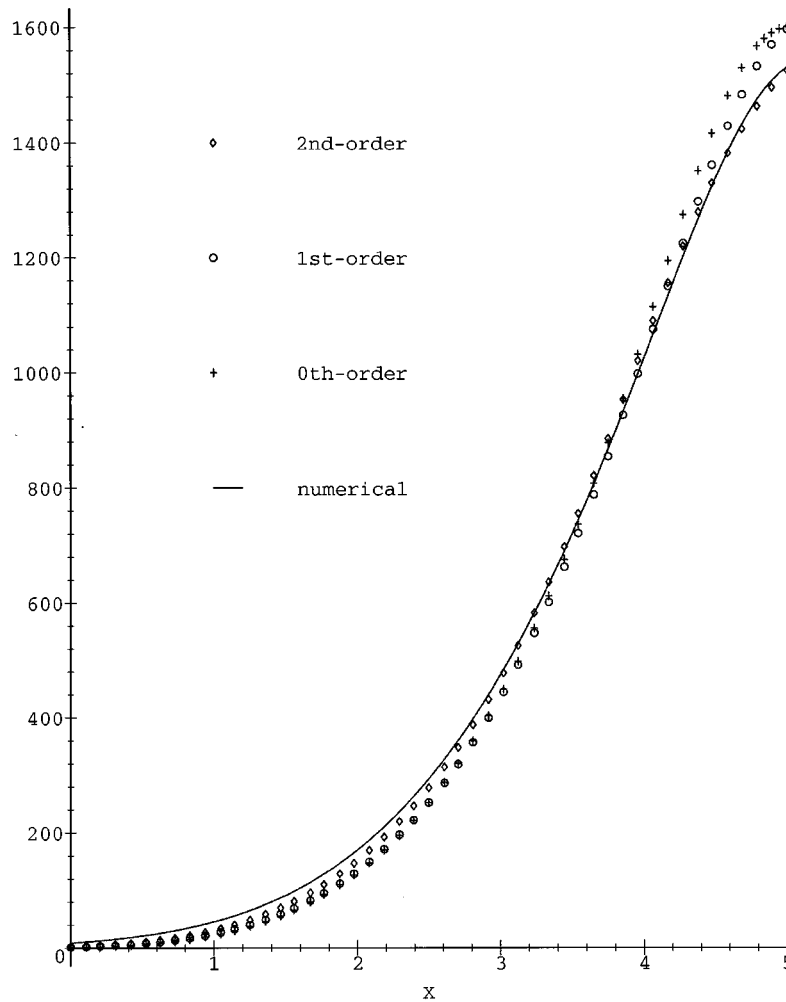


Fig. 4 Comparison of approximations and numerical solution for dimensionless radiosity on inside surface of a cylinder with $\epsilon=0.5$ and $L=5$

and F is given by (2). As is seen in the first model problem, this approximation is only of qualitative value in most cases. Higher-order approximations can be derived similarly as before but a modification is needed since the kernel $K(|X-\xi|)$ has discontinuous derivatives at $X=\xi$.

Higher-Order Approximations. Improved approximations can be obtained as before by taking more terms of the Taylor series expansion at $\xi=X$ of $\beta(\xi)$ in the integral of (4). Thus, if

$$\beta(\xi) \approx \beta(X) + \beta'(X)(\xi - X) + \dots + \frac{1}{n!} \beta^{(n)}(X)(\xi - X)^n, \quad (6)$$

it follows that

$$\begin{aligned} \beta(X) \approx & f(X) + (1 - \epsilon)\beta(X) \int_0^L K(|X - \xi|) d\xi \\ & + (1 - \epsilon)\beta'(X) \int_0^L K(|X - \xi|)(\xi - X) d\xi + \dots \\ & + \frac{1 - \epsilon}{n!} \beta^{(n)}(X) \int_0^L K(|X - \xi|)(\xi - X)^n d\xi. \end{aligned} \quad (7)$$

Integrals in the above equation can be evaluated analytically or numerically so, if $\beta^{(m)}(X)$ can be determined, the n th-order approximation $\beta_n(X)$ to $\beta(X)$ will follow from (7).

First-Order Approximation. Note that the integral in (4) can be split into the sum of two integrals:

$$\int_0^X K(X - \xi)\beta(\xi) d\xi + \int_X^L K(\xi - X)\beta(\xi) d\xi.$$

Thus differentiating both sides of (4) gives

$$\begin{aligned} \beta'(X) = & f'(X) + (1 - \epsilon) \left[\int_0^X K'(X - \xi)\beta(\xi) d\xi \right. \\ & \left. - \int_X^L K'(\xi - X)\beta(\xi) d\xi \right]. \end{aligned}$$

Taking $\beta(\xi) = \beta(X)$ in the above integrals and rearranging lead to the result

$$\beta'(X) \approx f'(X) + (1 - \epsilon)[K(X) - K(L - X)]\beta(X). \quad (8)$$

Substituting this into (7) with $n=1$ implies the first-order approximation $\beta_1(X)$ to $\beta(X)$:

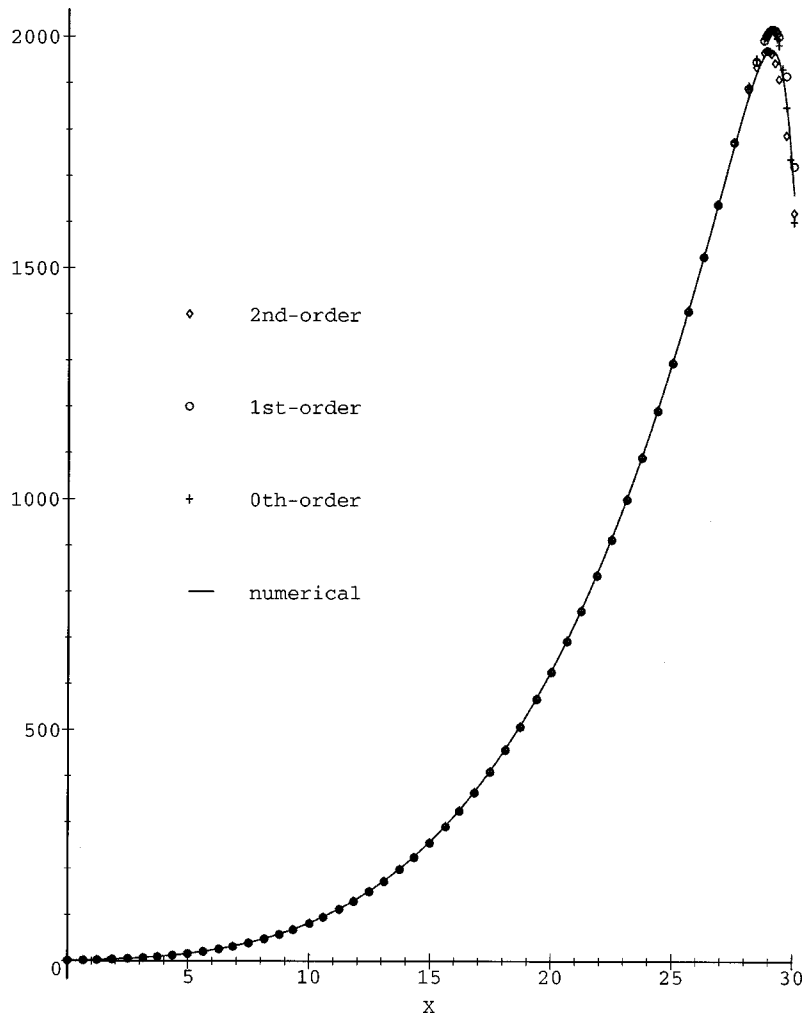


Fig. 5 Comparison of approximations and numerical solution for dimensionless radiosity on inside surface of a cylinder with $\epsilon=0.5$ and $L=30$

$$\beta_1(X) = \frac{f(X) + (1-\epsilon)I_{1L}(X)f'(X)}{1 - (1-\epsilon)I_L(X) - (1-\epsilon)^2 I_{1L}(X)[K(X) - K(L-X)]}, \quad (9)$$

where

$$I_{1L}(X) = \int_0^L K(|X-\xi|)(\xi-X)d\xi$$

can be evaluated analytically or numerically.

Second-Order Approximation. To derive the second-order approximation we differentiate both sides of (8) to obtain

$$\beta''(X) \approx f''(X) + (1-\epsilon)[K'(X) + K'(L-X)]\beta(X) + (1-\epsilon)[K(X) - K(L-X)]\beta'(X). \quad (10)$$

This, together with (8) and (7) with $n=2$, gives the second-order approximation $\beta_2(X)$ to $\beta(X)$:

$$\beta_2(X) = \frac{R(X)}{A(X)} \quad (11)$$

where

$$R(X) = f(X) + (1-\epsilon)I_{1L}(X)f'(X) + (1-\epsilon)I_{2L}(X) \times \{f''(X) + (1-\epsilon)[K(X) - K(L-X)]f'(X)\}$$

$$A(X) = 1 - (1-\epsilon)I_L(X) - (1-\epsilon)^2 I_{1L}(X)[K(X) - K(L-X)] - (1-\epsilon)^2 I_{2L}(X)\{K'(X) + K'(L-X)\} + (1-\epsilon)[K(X) - K(L-X)]^2$$

with

$$I_{2L}(X) = \frac{1}{2} \int_0^L K(|X-\xi|)(\xi-X)^2 d\xi.$$

Higher-order approximations may be derived similarly, but their expressions are very complicated and not given here.

Illustrative Calculations. The zeroth, first, and second-order approximations were compared with the accurate numerical solutions for $\epsilon=0.1, 0.3, 0.5, 0.7, 0.9$ and $L=0.1, 0.5, 1, 5, 10, 20, 30, 60$ in the case when $\theta_1=1$ and the wall-temperature distribution is linear:

$$\theta(X) = 1 + 6X/L.$$

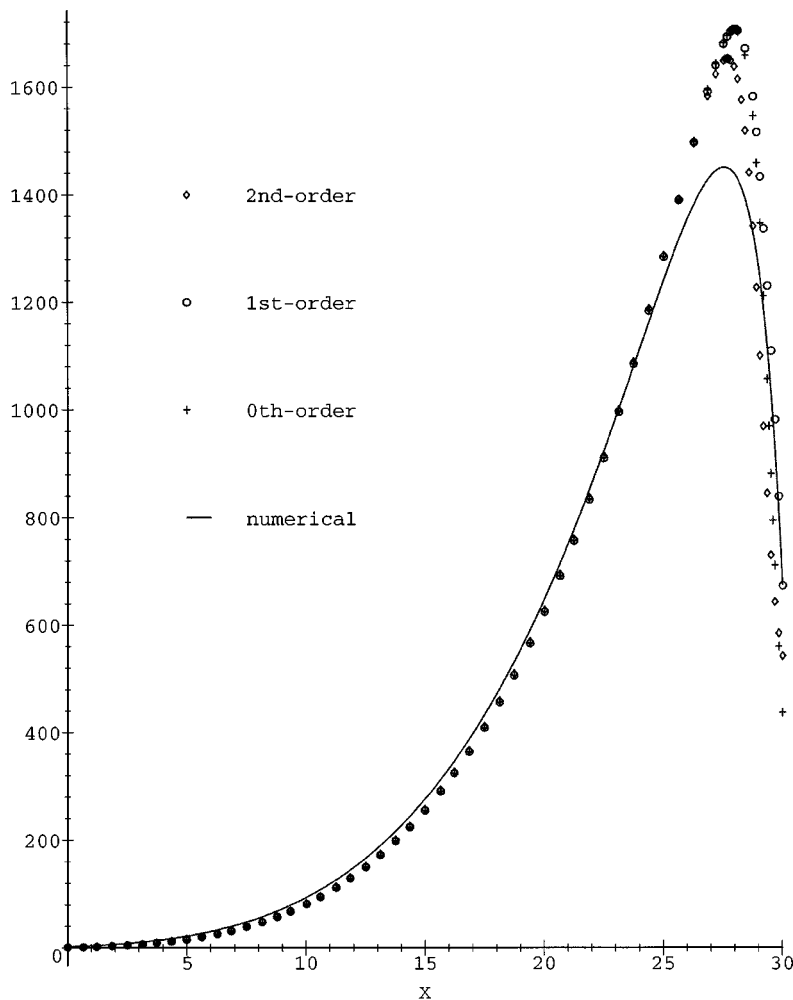


Fig. 6 Comparison of approximation and numerical solution for dimensionless radiosity on inside surface of a cylinder with $\epsilon=0.1$ and $L=30$

However, only some of these (e.g., in the case when $\epsilon=0.1, 0.5$ and $L=0.1, 1, 5, 30$) are shown here because of the length limits.

All computations were carried out using Maple V Release 4 on an IBM Pentium Personal Computer, and it took only several minutes to get all the computed results.

It is seen from the computed results that for large values of ϵ (e.g., $\epsilon \geq 0.5$) the second-order approximations are in good agreement with the numerical solutions for all values of L (see, e.g., Fig. 2–5), and in particular, all the zeroth, first, and second-order approximations are in an excellent agreement in the case when $\epsilon=0.9$ for all L . When $\epsilon=0.3$ (not shown), the second-order approximations are in reasonable overall agreement with the numerical solutions for all L except for $L=1$ in which case the approximation is slightly less accurate near the end at $X=0$ of the cylinder. For large L (e.g., $L \geq 10$) all the zeroth, first, and second-order approximations give excellent approximation except near the peak in the radiosity close to the end at $X=L$ of the cylinder and, with L getting larger, the accuracy of the approximations is increasing for all X , while, for small L (e.g., $L \leq 0.5$) all the zeroth, first, and second-order approximations are good approximation and, with L getting smaller, they are getting more accurate for all X . In the case when $\epsilon=0.1$, all the zeroth, first, and second-order approximations are in an excellent agreement with the numerical solutions for large L ($L \geq 20$) except near the peak in the radiosity close to the end at $X=L$ of the cylinder where the approximations are not very accurate even for very large L (e.g., $L=60$), as shown

in Fig. 6. Also, all the zeroth, first, and second-order approximations are very accurate overall for $L=0.1$ (Fig. 7) and slightly less accurate for $L=0.5$. However, for $0.5 < L < 20$ all the approximations give highly inaccurate results for $\epsilon=0.1$.

Conclusions

This paper presents a simple yet effective method based on the Taylor series expansion to solve a class of radiative heat transfer problems between gray surfaces represented here by a class of second kind Fredholm integral equations. The approach leads to an approximate solution of the problem which can be expressed explicitly in a simple, closed form (Eqs. (5)–(11)) and which can be effectively computed on any modern Personal Computer using symbolic computing codes such as Maple. So the approach can be easily applied to deal with enclosures involving more than one or two surfaces, e.g., radiative exchange in a catalytic monolith with square or circular channels where a system of radiative integral equations was used to model the radiative exchange (see, e.g., [7]).

To illustrate the efficiency and accuracy of the method in the present paper we presented a detailed study for an example of radiant heat transfer problems represented here by the integral Eq. (1). For large values of ϵ (e.g., $\epsilon \geq 0.5$) the second-order approximations give good approximation for all values of L , the ratio of the length of the cylinder to its diameter. When $\epsilon=0.3$, the

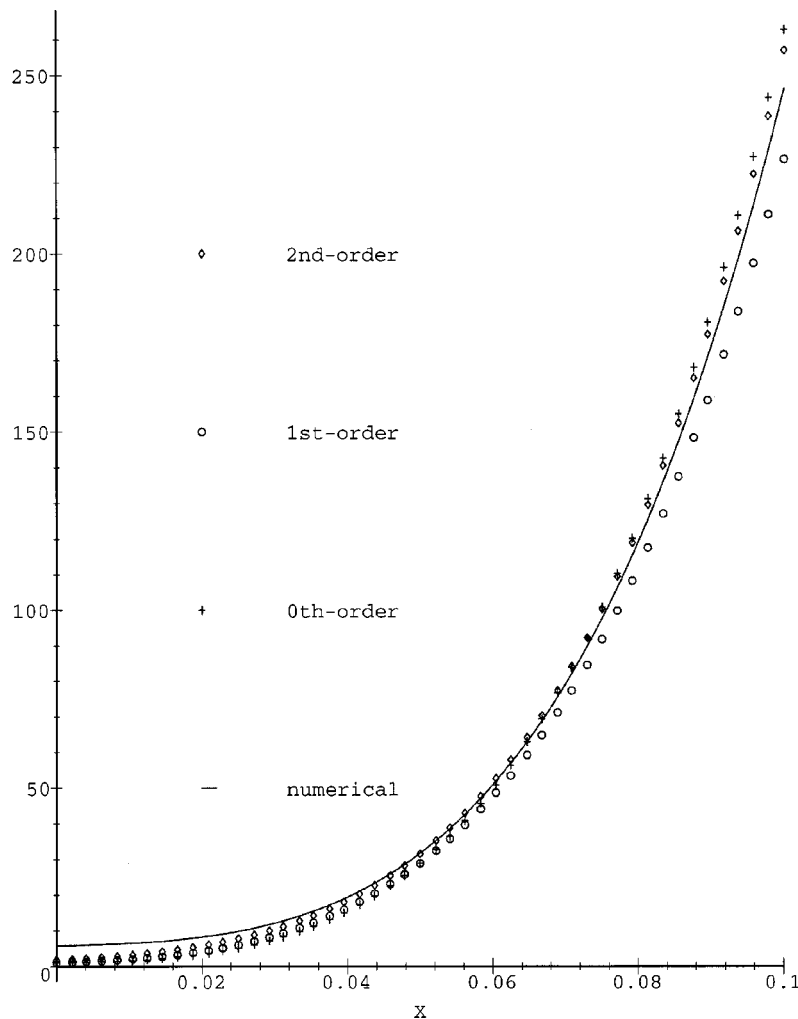


Fig. 7 Comparison of approximations and numerical solution for dimensionless radiosity on inside surface of a cylinder with $\epsilon=0.1$ and $L=0.1$

second-order approximations are still of sufficient accuracy overall for all L . For small ϵ ($\epsilon < 0.3$) the second-order approximations are accurate overall for small L (e.g., $L < 0.5$, and the accuracy is increasing with L getting smaller) and for large L (e.g., $L \geq 20$) except near the peak in the radiosity close to the end at $X=L$ of the cylinder where the approximations are not very accurate even for very large L (e.g., $L = 60$). However, for $0.5 < L < 20$ all the approximations give highly inaccurate results in the case of small ϵ ($\epsilon < 0.3$).

References

- [1] Siegel, R., and Howell, J. R., 1992, *Thermal Radiation Heat Transfer*, 3rd Ed., Hemisphere, Washington, DC.
- [2] Sparrow, E. I., and Cess, R. D., 1970, *Radiation Heat Transfer Rev. Ed.*, Wadsworth, Belmont, CA.
- [3] Atkinson, K. E., 1997, *The Numerical Solution of Integral Equations of the Second Kind*, Cambridge University Press, Cambridge, UK.
- [4] Krishnan, K. S., and Sundaram, R., 1960, "The Distribution of Temperature Along Electrically Heated Tubes and Coils, I. Theoretical," *Proc. R. Soc. London, Ser. A*, **257**, pp. 302–315.
- [5] Perlmutter, M., and Siegel, R., 1963, "Effect of Specularly Reflecting Gray Surface on Thermal Radiation Through a Tube and From Its Heated Wall," *ASME J. Heat Transfer*, **85**, No. 1, pp. 55–62.
- [6] Choi, B. C., and Churchill, S. W., 1985, "A Technique for Obtaining Approximate Solutions for a Class of Integral Equations Arising in Radiative Heat Transfer," *Int. J. Heat Fluid Flow*, **6**, No. 1, pp. 42–48.
- [7] Worth, D. J., Spence, A., Crumpton, P. I., and Kolaczowski, S. T., 1996, "Radiative Exchange Between Square Parallel Channels in a Concentric Monolith Structure," *Int. J. Heat Mass Transf.*, **39**, No. 7, pp. 1463–1474.
- [8] Press, W. H., Teukolsky, S. A., Vetterling, W. T., and Flannery, B. P., 1994, *Numerical Recipes in FORTRAN*, 2nd Ed., Cambridge University Press, Cambridge, UK.

An Analytical Model to Predict Condensation of R-410A in a Horizontal Rectangular Channel

Z. Guo¹

Graduate Research Assistant

N. K. Anand²

Professor

Department of Mechanical Engineering, Texas A&M University, College Station, TX 77843-3123

An analytical model to predict condensation heat transfer coefficient in a horizontal rectangular channel was developed. The total local condensation heat transfer coefficient was represented as the weighted average of heat transfer coefficients for each wall. The analytical predictions compared well with the experimental data on the condensation of R-410A in a rectangular channel. The mean deviation was 6.75 percent. [S0022-1481(00)00503-X]

Keywords: Channel Flow, Condensation, Heat Transfer, Phase Change

Introduction

There are numerous investigations on condensation of refrigerants inside circular tubes. A summary of these investigations is presented in Table 1. However, a limited number of investigators have studied condensation and two-phase flow in rectangular channels. Troniewski and Ulbrich [1] and Wambsganss et al. [2,3] studied two-phase air-water flow in vertical and/or horizontal rectangular channels. They developed their own flow regime maps and proposed methods for calculating pressure drop in such two-phase mixture flows. Guo and Anand [4] measured regionally averaged heat transfer coefficients for condensation of R-410A in a rectangular (0.5 in. × 1.0 in.) horizontal channel. The longer side of the channel cross section was parallel to the gravitational vector. Their experiments were conducted over a mass flux range of 30–2200 kg/s.m², refrigerant saturation temperature range of 7.8–36.7°C, and saturation pressure range of 1.02–2.23 MPa. The model presented in this work is a combination of numerical and analytical procedures. R-410A is an azeotropic mixture of HFC-32 and HFC-125 each 50 percent by weight. R-410A condenses and boils with a temperature glide of less than 0.5°C, thus behaves as a single component refrigerant. The database for condensation heat transfer and models to predict condensation heat transfer coefficient in rectangular channels is crucial to the design of plate-fin heat exchangers. Small rectangular channels are representative of plain-fin geometries in plate-fin heat exchangers. Plate-fin heat exchangers have certain unique characteristics such as large ratio of heat transfer surface to volume and ability to achieve true counterflow conditions. They also promote good mixing. These plate-fin heat exchangers are considered for application in vapor-compression cycles. The azeotropic mixture R-410A is considered as a chlorine-free replacement for HCFC-22. The main objective of this study is to develop an analytical model to predict local condensation heat transfer coefficient in

rectangular channels and validate the model against the experimental data obtained by authors [4,5] for condensation of R-410A in rectangular channels.

Analytical Model

Based on the experimental results discussed by Guo [5] and Guo and Anand [4], the condensing flow in a rectangular channel in the current study was in stratified wavy flow regime (Fig. 1(a)). The flow of liquid phase within such a flow regime tends to be activated by both the vapor shear force in the direction of the main flow and the gravitational force. This is particularly the case when the longer edges of the rectangular channel are in the vertical direction. The physical mechanism on the vertical walls of the channel is that the gravitational force that tends to pull the condensate down the channel wall is much stronger than the vapor shear force that tends to pull the condensate in the direction of the main flow. Thus, a condensate film forms on the inner top wall of the channel and grows in thickness as it flows down along the side walls. The bottom portion of the tube is filled with a liquid pool that transports the condensed liquid through the channel in the direction of the main flow.

The heat transfer mechanism in stratified wavy flow regime is considered to be dominated by the conduction across the film at the top and side walls of the channel. However, wavy surface effects on the flow along the bottom wall are not considered in this model. In the current model, separate analyses are conducted to calculate the heat transfer through the top, the vertical, and the bottom walls as shown in Fig. 1(b). For the heat transfer through the condensate layer of the top wall of the channel, the von Karman analogy between heat transfer and momentum transfer is used. For the heat transfer through the vertical walls, the mechanism is very similar to that in external falling film condensation. The external film condensation on a vertical plate (as shown in Fig. 1(c)) was first studied by Nusselt [6]. For this reason, heat transfer analyses for gravity-driven internal film condensation rely heavily on the extensive theoretical development for external condensation. The heat transfer through the bottom wall of the rectangular channel will be calculated by finding the depth of the liquid pool flowing through the channel. The total local heat transfer is calculated by weighted averaging of the heat transfer coefficients for the top, the vertical, and the bottom walls of the channel at each cross section.

$$\bar{h} = \frac{h_{\text{top}}A_{\text{top}} + h_{\text{vertical}}A_{\text{vertical}} + h_{\text{bottom}}A_{\text{bottom}}}{A_{\text{top}} + A_{\text{vertical}} + A_{\text{bottom}}} \quad (1)$$

In Eq. (1), A is the inner surface area of unit length of the rectangular channel. A_{top} , A_{vertical} , and A_{bottom} are the surface areas of the top, the side, and the bottom of the channel, respectively. The analytical model developed in this paper is validated by the experimental data obtained by Guo and Anand [4] and Guo [5]. The current model differs significantly from the ones reported in the literature for condensation in horizontal circular tubes (Table 1) and the differences are detailed in Guo [5].

Heat Transfer Through the Top Wall. To predict heat transfer coefficient across the top wall (h_{top}) of the channel, the von Karman analogy between heat transfer and momentum transfer was used. The details can be found elsewhere ([5]). Here a brief summary is presented. Variation of temperature and velocity in the y -direction was neglected. Accordingly, the variation of heat transfer coefficient with y -direction was also neglected. Because the film is thin compared to the downstream length, the usual boundary layer approximations have been adopted. The pressure gradient term in the momentum equation was neglected as it is very small compared to viscous and turbulent shear stress terms. The energy equation was integrated across the condensate film with von Karman's Universal Velocity Profile. The integration was performed over the laminar sublayer and buffer layer. The shear in the buffer layer was assumed to be approximately

¹Presently with Polyscience, Niles, IL.

²To whom correspondence should be addressed.

Contributed by the Heat Transfer Division for publication in the JOURNAL OF HEAT TRANSFER. Manuscript received by the Heat Transfer Division, Nov. 14, 1998; revision received, Feb. 21, 2000. Associate Technical Editor: P. Ayyaswamy.

Table 1 Correlations and analytical models for stratified flow in horizontal channels

| Investigators | Model equations | Comments |
|-----------------------|--|---|
| Nusselt [6] | $\overline{Nu}(x) = 0.943 \left[\frac{\rho_l(\rho_l - \rho_v)gh_{lv}x^3}{k_l\mu_l\Delta T} \right]^{1/4}$ | <ul style="list-style-type: none"> external condensation on a vertical wall analytical |
| Chato [10] | $Nu = 0.555 \left[\frac{\rho_l(\rho_l - \rho_v)gh_{lv}D_h^3}{k_l\mu_l\Delta T} \right]^{1/4}$ | <ul style="list-style-type: none"> internal condensation—circular tube analytical Heat transfer through top only |
| Jaster and Kosky [11] | $Nu = 0.728\alpha^{3/4} \left[\frac{\rho_l(\rho_l - \rho_v)gh_{lv}D_h^3}{k_l\mu_l\Delta T} \right]^{1/4}$ | <ul style="list-style-type: none"> internal condensation—circular tube experimental correlation heat transfer through top only |
| Rosson and Myers [9] | $Nu_{top} = 0.31 Re_v^{0.12} \left[\frac{\rho_l(\rho_l - \rho_v)gh_{lv}D_h^3}{k_l\mu_l\Delta T} \right]^{1/4}$ $Nu_{bottom} = \frac{\phi_{l,li} \sqrt{8} Re_l}{5 \left[1 + \frac{\ln(1 + 5 Pr_l)}{Pr_l} \right]}$ | <ul style="list-style-type: none"> internal condensation—circular tube experimental correlation for Nu_{top} von Karman analogy for Nu_{bottom} laminar flow assumed at the bottom |
| Dobson [8] | $Nu_{top} = \frac{0.23 Re_v^{0.12}}{1 + 1.11 X_{tt}^{0.58}} \left[\frac{\rho_l(\rho_l - \rho_v)gh_{lv}D_h^3}{k_l\mu_l\Delta T} \right]^{1/4}$ | <ul style="list-style-type: none"> internal condensation—circular tube experimental correlation for Nu_{top} |
| Guo [5] | Nu_{bottom} —Traviss [12] experimental correlation for annular flow Nu_{top} —von Karman analogy $Nu_{vertical}$ —Nusselt's approach Nu_{bottom} —liquid pool depth accumulated from top and vertical walls | <ul style="list-style-type: none"> Nu_{bottom}—for both laminar and turbulent flow internal condensation—rectangular channel all analytical Nu_{bottom}—for both laminar and turbulent flow |

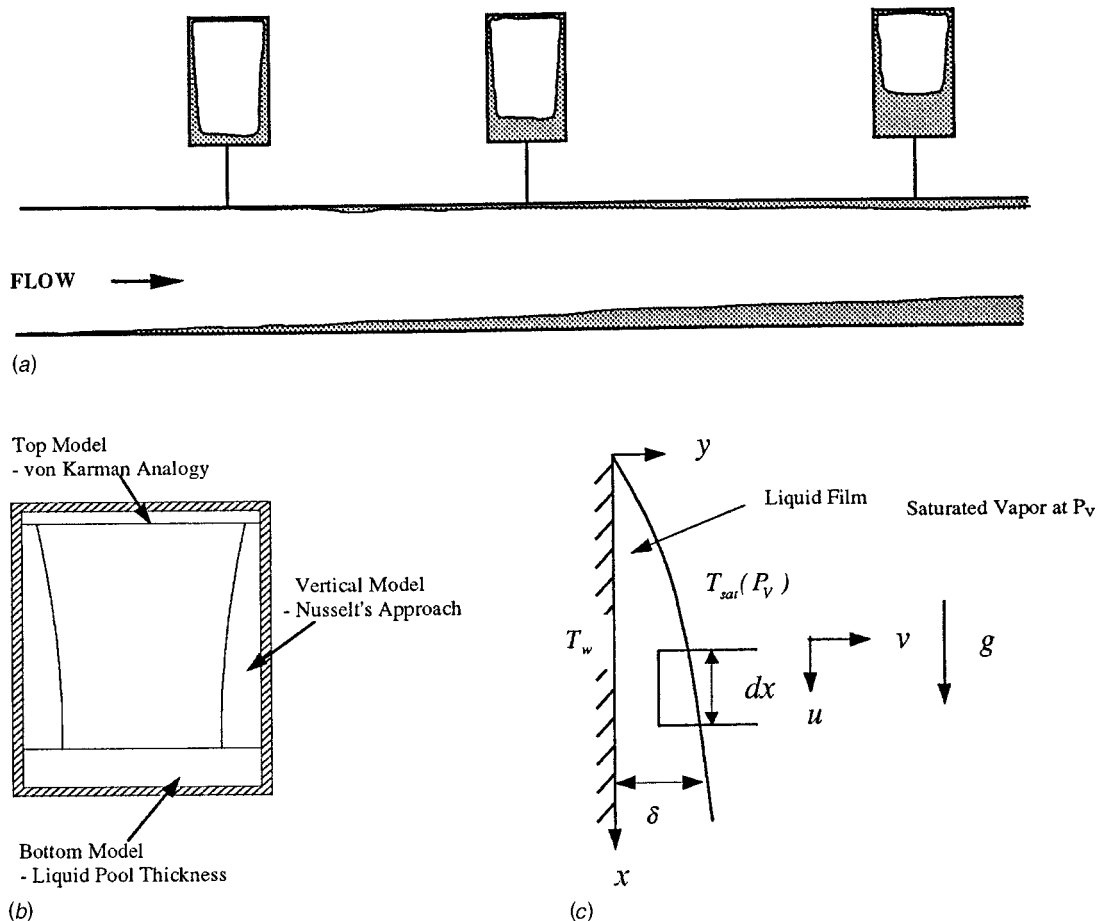


Fig. 1 Model. (a) Idealized schematic of the stratified wavy flow during condensation. (b) A model for calculating heat transfer through the top, the vertical, and the bottom walls. (c) Schematic of the external condensation on a vertical wall modeled by Nusselt [6].

equal to the shear at the wall ($\tau/\tau_w=1.0$), and the ratio of the eddy diffusivity of heat to that of momentum was assumed to be unity ($Pr_t=\epsilon_M/\epsilon_H=1.0$). Based on this simplifying assumption an expression for ΔT is obtained as

$$\Delta T = \frac{5 Pr_l}{c_{pl}} \frac{q}{\tau_w A} \sqrt{\frac{\tau_w}{\rho_l}} \times \left[1 + \frac{1}{Pr_l} \ln(5 Pr_l + 1) \right]. \quad (2)$$

The heat transfer coefficient h_{top} is defined so that

$$\frac{q}{A} = h_{top} \Delta T. \quad (3)$$

Then

$$h_{top} = \frac{\rho_l c_{pl}}{Pr_l} \sqrt{\frac{\tau_w}{\rho_l}} \left/ \left[5 + \frac{5}{Pr_l} \ln(5 Pr_l + 1) \right] \right. \quad (4)$$

or in terms of the Nusselt number $h_{top} D_h / k$

$$Nu_{top} = \frac{\rho_l D_h}{\mu_l} \sqrt{\frac{\tau_w}{\rho_l}} \left/ \left[5 + \frac{5}{Pr_l} \ln(5 Pr_l + 1) \right] \right. \quad (5)$$

A correlation to predict local shear stress in horizontal two-phase flow is not available. It may be reasonable to assume the local shear to be not drastically different from the average shear. This assumption does, in fact, lead to fairly good correlation of data with the Lockhart and Martinelli method [7] used to evaluate the shear stress at the wall. Accordingly, the expression for Nu_{top} can be expressed in terms superficial friction factor (f_{ls}) and liquid Reynolds number (Re_l) as

$$Nu_{top} = \frac{\phi_l Re_l \sqrt{f_{ls}/2}}{5 + \frac{5}{Pr_l} \ln(5 Pr_l + 1)}. \quad (6)$$

The details for obtaining ϕ_l and f_{ls} can be found in Guo [5].

Heat Transfer Through the Vertical Walls. To calculate the heat transfer through the vertical walls of the rectangular channel, the method of external film condensation on a vertical plate by Nusselt [6] will be adopted. There is at least one problem with applying Nusselt's approach to the internal condensation that has not been formally addressed. Nusselt's theory assumes that the condensate flow is entirely driven by the gravity in the downward direction. In an internal flow, however, a finite shear stress always exists in the mean flow direction. This is indicated schematically in Fig. 2(a). This shear stress will curve the streamlines of the condensate, so that they are not straight down as assumed. Thus, the Nusselt type solutions appear to be strictly applicable only for zero shear cases, or cases of stagnant vapor. The finite vapor velocity is in fact what ultimately creates the transition from stratified flow to annular flow.

The physical model in Fig. 2(a) illustrates the effect of a vapor flow (or a finite shear stress) on external condensation on a vertical surface. It is assumed throughout this analysis that the inertial forces are negligible in comparison with the viscosity, gravity, and pressure forces, and that the convective heat transfer is negligible in comparison to the conduction across the film. These are the classical Nusselt assumptions ([6]); hence much of the analysis follows his original integral analysis. Based on the literature review, these assumptions should be applicable to the present study where the Prandtl numbers are greater than unity and the Jakob numbers are much less than unity.

Starting with the Nusselt's pioneering analysis, we can derive our new equations with horizontal vapor friction imposed on the falling film. In the current study, the vapor flowing in the main direction of the channel did impose a strong drag force on the falling liquid film. However, this drag force imposed by the vapor in the z -direction should not affect the u -velocity profile of the liquid film in the y -direction due to the gravity. For this reason, at any fixed cross section in the z -direction (streamwise), the

u -velocity profile of the falling film should be the same as the one obtained by Nusselt. A schematic of the physical situation modeled by Nusselt is shown in Fig. 1(c), which is assumed to be at a location with fixed z as shown in Fig. 2(a). Starting with the governing two-dimensional boundary layer equations:

Continuity equation

$$\frac{\partial u}{\partial x} + \frac{\partial v}{\partial y} = 0. \quad (7)$$

Momentum equation in x -direction

$$u \frac{\partial u}{\partial x} + v \frac{\partial u}{\partial y} = \nu_l \frac{\partial^2 u}{\partial y^2} + \frac{(\rho_l - \rho_v)g}{\rho_l}. \quad (8)$$

Compared to the interfacial shear and the pressure gradient in the main flow direction, the pressure term in the x -direction (direction parallel to the vertical walls) is negligible. Knowing that the crossstream (y) component of velocity, $v=0$ everywhere, further simplification results in the conservation equation $\partial u/\partial x=0$ because of $v=0$. The momentum equation reduces to

$$0 = (\rho_l - \rho_v)g + \mu_l \frac{\partial^2 u}{\partial y^2} \quad (9)$$

with boundary conditions

$$u(y=0) = 0 \quad (10a)$$

and

$$\frac{\partial u}{\partial y}(y=\delta) = 0. \quad (10b)$$

Subject to the boundary layer assumptions, the y -momentum equation reduces to $\partial P/\partial y=0$. Thus the formulation for y -momentum is quasi two-dimensional.

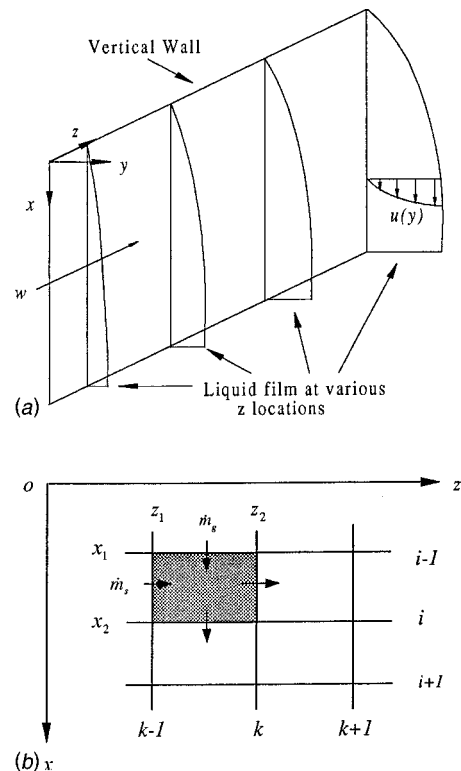


Fig. 2 Condensation along the vertical wall. (a) Schematic for condensation of a flowing vapor on a vertical wall. (b) A control volume and discretization grid on the vertical wall.

Integrating this equation twice and applying the boundary conditions, we obtain the following relation for the u -velocity profile of the liquid film at any fixed location in the z -direction as shown in Fig. 2(a):

$$u = \frac{(\rho_l - \rho_v)g}{\mu_l} \left(y\delta - \frac{y^2}{2} \right). \quad (11)$$

A small element with unit width is shown on Fig. 2(b). The mass flow rate per unit width in the z -direction due to this gravitational component of the flow is designated as \dot{m}_g :

$$\dot{m}_g = \rho_l \int_0^\delta u dy = \frac{\rho_l(\rho_l - \rho_v)g\delta^3}{3\mu_l}. \quad (12)$$

The derivative of the gravity driven mass flow rate with respect to δ is then given by

$$\frac{d\dot{m}_g}{d\delta} = \frac{\rho_l(\rho_l - \rho_v)g\delta^2}{\mu_l}. \quad (13)$$

Now let us consider the effect of vapor-liquid interfacial friction (τ_i) in the z -direction. Neglecting inertial terms and the pressure gradient (which is appropriate for the external case) in the z -momentum equation results in

$$0 = \mu_l \frac{\partial^2 w}{\partial y^2}, \quad (14)$$

subject to

$$w(y=0) = 0 \quad (15a)$$

$$\frac{\partial w}{\partial y}(y=\delta) = \frac{\tau_i}{\mu_l}. \quad (15b)$$

Integrating Eq. (14) twice and applying boundary conditions gives a linear relationship for the w -velocity component

$$w = \frac{\tau_i}{\mu_l} y. \quad (16)$$

The w -velocity profile can also be integrated across the film to determine the shear driven mass flow rate per unit width in the x -direction. The result is

$$\dot{m}_s = \rho_l \int_0^\delta w dy = \frac{\tau_i \delta^2}{2\nu_l}. \quad (17)$$

The derivative of the shear driven mass flow rate is then given by

$$\frac{d\dot{m}_s}{d\delta} = \frac{\tau_i \delta}{\nu_l}. \quad (18)$$

Conservation of mass over an element of thickness δ from x_1 to x_2 and z_1 to z_2 (shown in Fig. 2(b)) requires that the net flow into the element due to gravity, shear, and condensate formation be zero:

$$\dot{m}_g(x_1) - \dot{m}_g(x_2) + \dot{m}_s(z_1) - \dot{m}_s(z_2) + \dot{m}_c = 0. \quad (19)$$

Solving Eq. (19) for the condensed mass flow rate, expressing the other terms in integral form, and grouping the integrals in the x and z -directions, gives

$$\begin{aligned} \dot{m}_c = & \int_{z_1}^{z_2} [\dot{m}_g(\delta(x_2, z)) - \dot{m}_g(\delta(x_1, z))] dz \\ & + \int_{x_1}^{x_2} [\dot{m}_s(\delta(x, z_2)) - \dot{m}_s(\delta(x, z_1))] dx. \end{aligned} \quad (20)$$

If the derivatives of the gravity and shear driven mass flow rates, given by Eq. (13) and Eq. (18), exist and are integrable over the

element, Green's theorem can be used to express each of the bracketed terms in Eq. (20) as integrals. This, combined with the chain rule, results in the following equation:

$$\dot{m}_c = \int_{x_1}^{x_2} \int_{z_1}^{z_2} \left[\frac{d\dot{m}_g}{d\delta} \frac{\partial \delta}{\partial x} + \frac{d\dot{m}_s}{d\delta} \frac{\partial \delta}{\partial z} \right] dz dx. \quad (21)$$

Neglecting energy advection, a first law statement on an arbitrary element of the liquid film gives

$$\dot{Q} = \dot{m}_c h_{lv}. \quad (22)$$

Based on the assumption that the convective heat transfer is negligible in comparison to the conduction across the liquid film, the classical Nusselt approach leads to a linear temperature profile, which results in the heat transfer coefficient being given by

$$h = \frac{k_l}{\delta}. \quad (23)$$

The heat transfer rate can be expressed in terms of the heat transfer coefficient as

$$\dot{Q} = \int_{x_1}^{x_2} \int_{z_1}^{z_2} h(x, z) \Delta T dz dx. \quad (24)$$

Combining Eqs. (21)–(24), and realizing that the area of integration is arbitrary, on rearranging, the following partial differential equation for δ arises:

$$\frac{d\dot{m}_g}{d\delta} \frac{\partial \delta}{\partial x} + \frac{d\dot{m}_s}{d\delta} \frac{\partial \delta}{\partial z} = \frac{k_l \Delta T}{h_{lv} \delta}. \quad (25)$$

Substituting for the derivatives from Eq. (13) and Eq. (18) into Eq. (25) gives

$$\frac{g(\rho_l - \rho_v)\delta^2}{\nu_l} \frac{\partial \delta}{\partial x} + \left(\frac{\tau_i \delta}{\nu_l} \right) \frac{\partial \delta}{\partial z} = \frac{k_l \Delta T}{h_{lv} \delta}. \quad (26)$$

Equation (26) is a quasi-linear, first-order hyperbolic partial differential equation. Only initial conditions are needed to solve this hyperbolic equation:

$$x = 0, \quad \delta(0, z) = \delta_{\text{top}}(z); \quad (27)$$

$$z = 0, \quad \delta(x, 0) = 0. \quad (28)$$

In Eq. (27), $\delta_{\text{top}}(z)$ is the local condensate film thickness from the top wall of the channel, which can be estimated by

$$\delta_{\text{top}} = \frac{k_l}{h_{\text{top}}} = \frac{D_h}{\text{Nu}_{\text{top}}}. \quad (29)$$

Once the solution to Eq. (26) is found, the heat transfer coefficient can be determined as a function of both x and z using Eq. (23). The average local heat transfer coefficient at any cross section is then determined by

$$h_{\text{vertical}}(z) = \frac{k_l}{\frac{1}{B} \int_0^B \delta(x, z) dx}. \quad (30)$$

In Eq. (30), B is the height of the rectangular cross section.

The closed-form solution for Eq. (26) is complicated, the numerical method was chosen to directly solve this equation. The partial differential Eq. (26) can be simply discretized by using finite difference method with first order accuracy. The final accuracy of the numerical solution will mainly depend on the grid size used and the convergence criteria implemented.

Following the discretization index as shown in Fig. 2(b), Eq. (26) can be discretized as

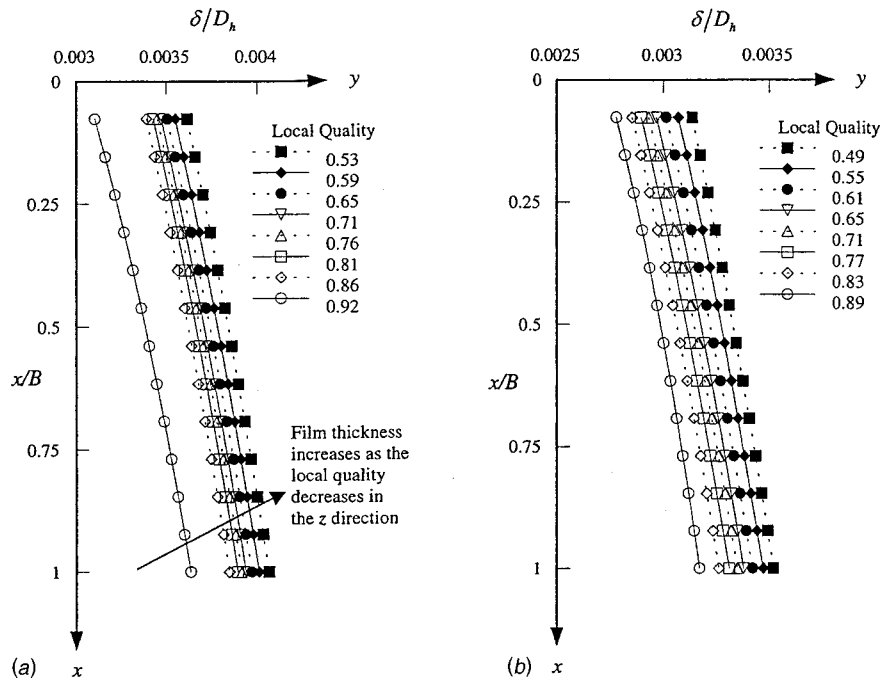


Fig. 3 Liquid refrigerant film thickness on the vertical wall due to condensation. (a) $G=143.8 \text{ kg/s m}^2$. (b) $G=178.1 \text{ kg/s m}^2$.

$$\frac{\rho_l(\rho_l - \rho_v)g(\delta_{i,k})^2}{\mu_l} \left(\frac{\delta_{i,k} - \delta_{i-1,k}}{\Delta x} \right) + \frac{\rho_l \tau_i \delta_{i,k}}{\mu_l} \left(\frac{\delta_{i,k} - \delta_{i,k-1}}{\Delta z} \right) = \frac{k_l \Delta T}{h_{lv} \delta_{i,k}} \quad (31)$$

By defining three coefficients

$$A = \frac{\rho_l(\rho_l - \rho_v)g(\delta_{i,k})^2}{\mu_l \Delta x}, \quad B = \frac{\rho_l \tau_i \delta_{i,k}}{\mu_l \Delta z}, \quad \text{and} \quad C = \frac{k_l \Delta T}{h_{lv} \delta_{i,k}} \quad (32)$$

the liquid film thickness is written in the form of

$$\delta_{i,k} = \frac{A \delta_{i-1,k} + B \delta_{i,k-1} + C}{A + B} \quad (33)$$

The initial conditions are

$$\delta_{1,k} = \delta_{\text{top},k} \quad \text{and} \quad \delta_{i,1} = 0 \quad (34)$$

The Gauss-Seidel method was used to iteratively solve the equation. The variable $\delta_{i,k}$ appearing in the three coefficients (i.e., nonlinearity) is the result from the previous iteration. To obtain grid-independent solution, the average of film thickness on the vertical wall is calculated:

$$\bar{\delta}_{\text{vertical}} = \frac{\sum_{k=1}^k \sum_{i=1}^{i \text{ max}} (\delta_{i,k} dx dz)}{A_{\text{vertical}}} \quad (35)$$

Increase of $i \text{ max}$ and $k \text{ max}$ results in a change of $\bar{\delta}_{\text{vertical}}$. The criterion for grid independence is that the relative change of $\bar{\delta}_{\text{vertical}}$ between two consecutive grid sizes is less than three percent. For most of the cases the grid size of $i \text{ max}=14$ and $k \text{ max}=11$ satisfied this criterion. Convergence criteria for the solution was set such that

$$\text{Max} \left| \frac{\delta_{i,k}^{N+1} - \delta_{i,k}^N}{\delta_{i,k}^N} \right| \leq 10^{-3} \quad (36)$$

where N and $N+1$ are iteration levels.

Figure 3 shows the calculated local film thickness on the vertical wall for two different mass flow rates. In these two plots, the vertical axis represents the location along the channel vertical wall from top to the bottom (dimensionless value from 0 to 1). The horizontal axis represents the film thickness normalized with respect to the hydraulic diameter of the rectangular channel. Each curve describes a film thickness profile at a z -location along the main flow direction of the channel with a local quality (x) of the two-phase flow. The curve with the highest local quality is the film thickness profile at the entrance region of the channel, and the curve with the lowest local quality describes the profile at the exit region of the channel.

The calculated film thickness curves on the vertical wall of the rectangular channel illustrate the condensation characteristics as expected. As the refrigerant condenses, the liquid layer grows as it flows downward from the top to the bottom on the vertical wall. The liquid film thickness at the top ($x/B \sim 0$) is the one calculated from the analytical model for the top wall of the channel. The liquid film from the top wall is combined with the condensate formed along the vertical walls from top to the bottom, then it is carried down to the bottom of the channel to accumulate in the liquid pool.

Comparing curves for different local qualities (x) reveals that the film thickness increases as the two-phase flow quality decreases along the main flow direction. This indicates that a larger amount of liquid refrigerant is accumulated on the vertical wall at lower qualities. It also explains that as vapor flow slows down, the interfacial shear acting on the liquid layer by the vapor flow decreases as the quality decreases.

Comparison of Fig. 3(a) and Fig. 3(b) reveals that as the refrigerant mass flux increases, the film thickness decreases. Smaller amount of liquid refrigerant is adhered on the vertical walls as the mass flux increases due to the higher vapor and liquid velocity in the main flow direction. These two figures also shows a common

characteristic which is that the thickness of the first liquid film curve with the highest local quality (x) is significantly less than the thickness of other curves that are at further downstream locations of the channel and with lower local qualities. This phenomenon is particularly significant in Figure 3(a). The film thickness increases at a higher rate in the entrance region, while in the further downstream section of the channel the film thickness growth rate is much smaller. At the channel entrance, there is no or little liquid film attached to the channel walls. The heat transfer coefficient at the entrance is high. As the liquid film grows along the channel in the main flow direction z , the liquid film acts as a barrier against the heat transfer between the condensing refrigerant and the cold wall. After a certain length, the growth of the liquid film slows down and finally approaches a stage where there is no more increase in liquid layer due to the heat transfer across the vertical wall. Dobson [8] drew the same conclusion by analyzing the characteristic solution of Eq. (26). In his discussion, Dobson implied that the film thickness δ grows within a certain range in the direction of z . After liquid film is fully developed, the thickness would be unaffected by the interfacial shear τ_i in the direction of z at any fixed value on x -axis.

Heat Transfer Through the Bottom Wall. As the liquid refrigerant accumulates to the bottom of the channel due to gravitational action, the heat transfer across the bottom wall of the rectangular channel would be lower compared to the heat transfer across the top and vertical walls of the channel. Still this portion of heat transfer can be considered as the heat transfer across the refrigerant liquid pool depth accumulated on the bottom of the channel. It is assumed that the liquid refrigerant accumulated in the bottom portion of the rectangular channel is mainly due to the condensation from the top and the vertical walls. Accordingly, the

depth of the refrigerant liquid pool increases as the liquid film thickness increases on the top and vertical walls along the streamwise distance z (mean flow direction). The increase of condensate along z due to the heat transfer through the bottom wall is neglected. Based on the above assumption, the liquid pool depth should be equal to the total condensate film thickness from the ends of both vertical walls.

$$\delta_{\text{bottom}} = 2 \delta_{i \text{ max},k} \quad (37)$$

It is known that δ_{bottom} is the depth of the liquid refrigerant flowing on the bottom of the channel, and $\delta_{i \text{ max},k}$ is the film thickness at the end of the vertical walls of the channel. The only heat transfer through the bottom of the channel is due to the temperature gradient across the liquid pool.

$$q'' = k \frac{(T_{\text{sat}} - T_{\text{wall}})}{\delta_{\text{bottom}}} = h_{\text{bottom}}(T_{\text{sat}} - T_{\text{wall}}) \quad (38)$$

From Eq. (38), the local heat transfer coefficient for the bottom of the channel along any location z is calculated from

$$h_{\text{bottom}}(z) = \frac{k_l}{\delta_{\text{bottom}}(z)} \quad (39)$$

Results and Discussion

In this section, the results from the analytical model described in the previous sections are compared with the experimental re-

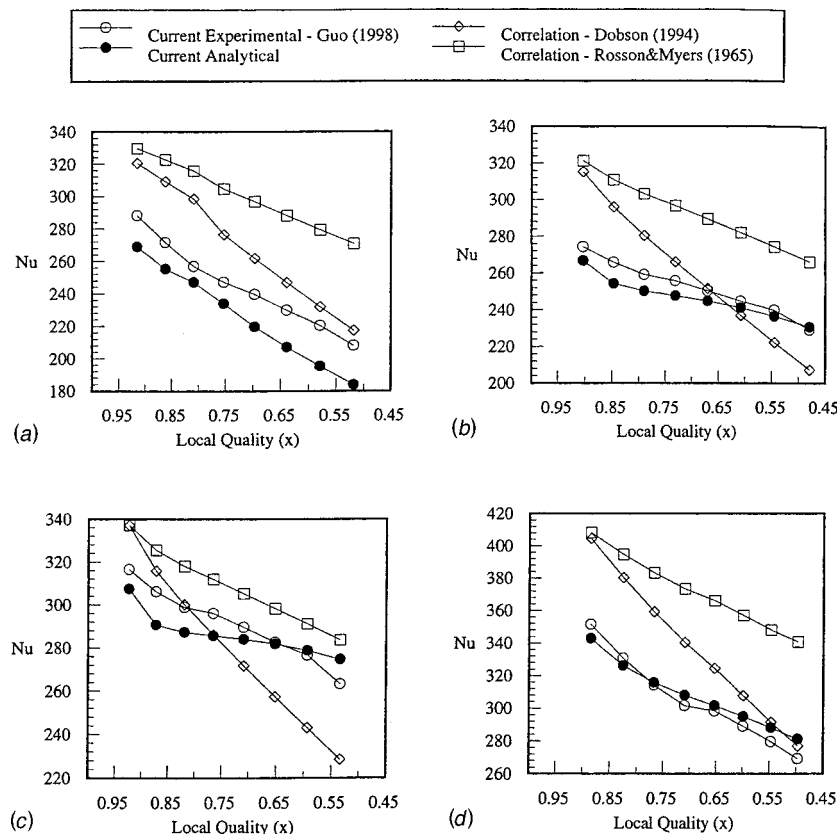


Fig. 4 Comparison of the analytically predicted local Nusselt number with the current experimental data for the rectangular channel and others for circular tubes. (a) $G=73.9 \text{ kg/s m}^2$. (b) $G=114.2 \text{ kg/s m}^2$. (c) $G=143.8 \text{ kg/s m}^2$. (d) $G=178.1 \text{ kg/s m}^2$.

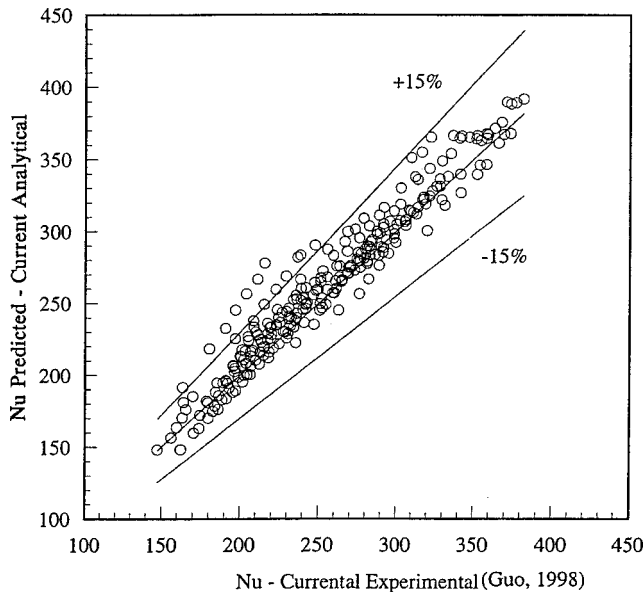


Fig. 5 Comparison of the experimental data of Guo [5] with the current analytical predictions

sults of Guo [5]. Also compared are the results from correlation equations developed by other investigators.

Among the correlations presented in Table 1, only the correlations by Rosson and Myers [9] and by Dobson [8] are used for comparison with the current results. The reason for this choice is discussed in Guo [5].

Figure 4 shows the graphs of both experimentally ([5]) and analytically obtained local heat transfer coefficient as a function of the quality. The four sets of test runs for different mass fluxes were chosen to represent the entire range of the experimental conditions investigated ([5]). As can be seen from the graphs in Fig. 4(a), at a mass flow rate of 73.9 kg/s m^2 , the correlations by Rosson and Myers [9] and by Dobson [8] overpredicted the experimental measurements of Guo [5]. The reason for the significant difference between analytical predictions and experimental data at low mass fluxes could be due to the fact that the condensation along the bottom wall is neglected in the present analytical model. At low mass fluxes greater amount of refrigerant gets condensed along the bottom resulting in greater resistance to heat transfer. While at higher mass flow rates, as shown in Fig. 4, the difference between the experimental data and the predicted values are getting smaller to an acceptable range (within ± 10 percent). The comparison also indicates that, at low mass flux ($G = 73.9 \text{ kg/s m}^2$), the current analytical model predicts the experimental results better than the correlations of the other investigators. Details of calculation of experimental uncertainty is given elsewhere ([5]). Any experimental data with an uncertainty greater than ten percent were discarded by Guo and Anand [4] and Guo [5].

The predictions of the current analytical model are compared with the current experimental data in Fig. 5. To compare the closeness of two sets of data, the definition of the mean deviation is introduced:

$$S = \sqrt{\frac{1}{N} \sum_{i=1}^N \left(\frac{h_{\text{analytical},i} - h_{\text{experimental},i}}{h_{\text{experimental},i}} \right)^2} \quad (40)$$

The agreement is very good. The mean deviation between the

predicted and experimental values is 6.75 percent, and the maximum deviation between these two is 34.3 percent, which is considerably better than the correlations from the literature.

Summary

An analytical model to predict local condensation heat transfer coefficient in a horizontal rectangular channel was developed. The local heat transfer coefficient for the top, the vertical, and the bottom walls were determined separately. The total local condensation heat transfer coefficient was represented as the weighted average of the heat transfer coefficients for each wall. The von Karman analogy was used to determine the condensation heat transfer coefficient along the top wall. The classic Nusselt analyses for condensation on a vertical wall was modified to obtain a first-order partial differential equation for the liquid film thickness along the inside of the vertical wall. The resulting partial differential equation was solved using a finite difference technique. The liquid film thickness, along the bottom wall, was determined by the mass balance of the liquid condensate, from the top and vertical walls, and the heat transfer coefficient was determined by the energy balance. The analytical predictions compared well with the experimental data on the condensation of R-410A in a rectangular channel obtained by Guo [5]. The mean deviation was 6.75 percent.

Acknowledgment

This work was performed under the auspices of a research contract (W08511-07) from the Electric Power Research Institute (EPRI). The authors are grateful to the EPRI for their financial support of the project. The authors wish to thank the Project Manager, Mr. Andrew Saleh, for his technical input.

Nomenclature

- A = area, m^2
- B = height of cross section of rectangular channel test tube, m
- c_p = specific heat, J/kg K
- D_h = hydraulic diameter of rectangular channel, m
- f = friction factor
- G = mass flux of condensing refrigerant, kg/s m^2
- g = acceleration due to gravity, m/s^2
- h = heat transfer coefficient, $\text{W/m}^2 \text{K}$
- h_{lv} = latent heat of refrigerant, J/kg
- \dot{m} = mass flow rate, kg/s
- k = thermal conductivity, W/m K
- N = number of data points
- Nu = Nusselt number, hD/k
- P = local pressure, N/m^2 (psi)
- Pr = Prandtl number of liquid refrigerant, $\mu_l c_{pl} / k_l$
- \dot{Q} = heat flow rate, W
- q'' = heat flux, W/m^2
- Re_l = Reynolds number of liquid refrigerant, $G(1-x)D_h / \mu_l$
- S = mean deviation
- T = temperature, K , ($^{\circ}\text{C}$, $^{\circ}\text{F}$)
- u, v, w = velocities in the x, y, z -directions, m/s
- X = Martinelli parameter
- x = local quality of condensing refrigerant
- x = coordinate direction along the vertical walls of the rectangular channel
- y = coordinate direction along the horizontal wall of the cross section
- z = coordinate direction of the rectangular channel along the flow direction

Greek Symbols

- α = void fraction
 δ = film thickness, m
 ε = eddy diffusivity
 μ = dynamic viscosity, kg/m s
 ν = kinematic viscosity, m²/s
 ρ = density of refrigerant, kg/m³
 τ = local shear stress, N/m²
 ϕ_l = two-phase pressure drop multiplier
 Δ = difference

Superscripts

- N = iteration number
- = averaged

Subscripts

- bottom = bottom wall
 c = condensation
 fr = friction
 g = gravity
 H = heat
 h = hydraulic diameter
 i = inlet or index in x -direction or vapor-liquid interface
 k = index in z -direction
 l, liq = liquid refrigerant
 ls = liquid superficial
 M = momentum
 s = shear
sat = saturation
top = top wall
 v = vapor refrigerant
vertical = side wall
 w = wall of the channel
 t = turbulent
 tt = turbulent vapor flow and turbulent liquid flow
 lt = laminar liquid flow and turbulent liquid flow

References

- [1] Troniewski, L., and Ulbrich, R., 1984, "Two-Phase Gas-Liquid Flow in Rectangular Channels," *Chem. Eng. Sci.*, **39**, No. 4, pp. 751–765.
- [2] Wambsganss, M. W., Jendrzeczyk, J. A., France, D. M., and Obot, N. T., 1990, Two-Phase Flow Patterns and Frictional Pressure Gradients in Small, Horizontal, Rectangular Channel," Argonne National Laboratory, Research Report ANL-90/19, University of Illinois, Chicago, IL.
- [3] Wambsganss, M. W., Jendrzeczyk, J. A., France, D. M., and Obot, N. T., 1990, Two-Phase Flow Patterns and Pressure Gradients in a Small Rectangular Channel: A Comparison Between Two Horizontal Orientations," Argonne National Laboratory, Research Report ANL-90/46, University of Illinois, Chicago, IL.
- [4] Guo, Z., and Anand, N. K., 1999, "Condensation of R-410A in a Rectangular Channel," *Int. J. HVAC&R Res.*, **5**, pp. 99–123.
- [5] Guo, Z., 1998, "Condensation of R-410A in Horizontal Rectangular Channel," Ph.D. dissertation, Texas A&M University, College Station, TX.
- [6] Nusselt, W., 1916, "Die Oberflächenkondensation des Wasserdampfes," *Z. Vereins Deutsch. Ing.*, **60**, pp. 541–557.
- [7] Lockhart, R. W., and Martinelli, R. C., 1949, "Proposed Correlation of Data for Isothermal Two-Phase, Two-Component Flow in Pipes," *Chem. Eng. Prog.*, **45**, No. 5, pp. 39–48.
- [8] Dobson, M. K., 1994, "Heat Transfer and Flow Regimes During Condensation in Horizontal Tubes," Ph.D. dissertation, University of Illinois at Urbana-Champaign, Champaign, IL.
- [9] Rosson, H. F., and Myers, J. A., 1965, "Point Values of Condensing Film Coefficients Inside a Horizontal Pipe," *Chem. Eng. Prog., Symp. Ser.*, **61**, No. 59, pp. 190–199.
- [10] Chato, J. C., 1962, "Laminar Condensation Inside Horizontal and Inclined Tubes," *ASHRAE J.*, **4**, pp. 52–60.
- [11] Jaster, H., and Kosky, P. G., 1976, "Condensation in a Mixed Flow Regime," *Int. J. Heat Mass Transf.*, **19**, pp. 95–99.
- [12] Traviss, D. P., Rohsenow, W. M., and Baron, A. B., 1973 "Forced Convection Condensation in Tubes: A Heat Transfer Correlation for Condenser Design," *ASHRAE Trans.*, **79**, No. 1, pp. 157–165.

Subcooled Flow Boiling in Circumferentially Nonuniform and Uniform Heated Vertical Channels With Downward Flow

Q. Peatiwala

71B Barakat Al-Haidry Memorial Market, Block 'E',
North Nazimabad, Karachi 74700, Pakistan
e-mail: qpeatiwala@hotmail.com

R. D. Boyd, Sr.

Fellow ASME, Honeywell Professor of Engineering and
Director of the Thermal Science Research Center
(TSRC), Department of Mechanical Engineering, Prairie
View A&M University, Prairie View, TX 77446
e-mail: ronald_boyd@pvamu.edu

Results are presented for new experimental data for subcooled flow boiling heat transfer in circumferentially nonuniform (single-side) and uniformly heated tubes. Although the Liu-Winterton correlation had better agreement at low power levels and axial locations, Shah's correlation had better agreement at higher power levels and at axial locations near the center of the heated length. Both correlations overpredicted the data near the exit. Therefore, additional correlational developmental work is needed for local (axial) flow boiling heat transfer in circumferentially nonuniform heated channels. [S0022-1481(00)00603-4]

Keywords: Boiling, Forced Convection, Multiphase Flows, Nonuniform Heat Flux

Introduction

Subcooled flow boiling can accommodate high levels of heat flux in a variety of diverse processes and applications such as advanced space thermal management systems, plasma-facing fusion components, electronic and computer components, and manufacturing and material processing.

Subcooled flow boiling heat transfer is a complicated phenomenon involving many factors, among which circumferential heat flux distribution on the channel wall is an important one. Beside the heat flux distribution, there are many different variables which influence the flow boiling heat transfer. These variables include pressure, mass flow rate, quality, thermophysical properties, wall material, surface characteristics, and channel geometry. A clear understanding of the influence of different variables on heat transfer during single-phase flow may be obtained through analytical equations and well established empirical correlations; but, flow boiling heat transfer with a circumferential nonuniform external heat flux distribution is more complex due to interactions between the two phases, fluid interaction with the channel wall in the presence of both convective and boiling modes of heat transfer, and the complex geometric boundary influences. However, by introducing reasonable physical abstraction, it is sometimes possible to greatly simplify the problem and obtain useful results.

In the past, one of the first simplifying assumptions made to advance the two-phase flow boiling theory was to study heat transfer in uniformly heated tubes. This simple geometry was used

Contributed by the Heat Transfer Division for publication in the JOURNAL OF HEAT TRANSFER. Manuscript received by the Heat Transfer Division, Mar. 26, 1999; revision received, Mar. 9, 2000. Associate Technical Editor: S. Sadhal.

usually to (1) decrease the experimental complexity, (2) directly use previous single-phase data as a basis to isolate the boiling contribution, and (3) to avoid the inclusion of the complexity of circumferential heat flux variations on the channel inner wall. From the literature, it is clear that there has been much work completed for flow boiling heat transfer correlations for a uniform heat flux distribution. Correlations presented by Chen [1], Shah [2], Kandlikar [3,4], Steiner et al. [5], Gunger and Winterton [6,7], and Boyd and Meng [8] cover different fluids, vast ranges of flow rates, the entire spectrum of quality, and low and high sub-cooling. Some of these correlations are recommended for both saturated and subcooled flow boiling. These correlations are valid for only smooth tubes, and one must avoid using them when orientation is important.

As stated above, several researchers have proposed correlations for the prediction of heat transfer coefficients in flow boiling systems. But to simplify the heat transfer modeling and reduce the experimental complexities, most of the research efforts have been limited to heat transfer correlation for uniformly heated channels. In addition, very little effort has been made to study heat transfer in complex and nonuniform heated channels.

In this paper, the results of flow boiling heat transfer in nonuniform or single-side heated tubes are presented, and the experimental heat transfer coefficients are compared with selected existing single-phase and two-phase flow boiling correlations. In order to establish a basis for the comparisons with data for the single-side heated channel, base line comparisons for uniformly heated channels are made with data from: (1) the literature, and (2) from the same flow loop used to produce the single-side heat flux data but with uniformly heated wall conditions. Among the two-phase correlations considered are heat transfer correlations for uniformly heated tubes developed by Shah [2] and Liu and Winterton [9]. Because they are frequently used by many designers and researchers in a variety of engineering fields, the selected single-phase correlations are (1) the Dittus-Boelter correlation, and (2) the Petukhov correlation. Using the results from the above comparisons, we will (1) assess these correlations and data for the uniform heat flux case, and (2) adapt the correlations to the single-side heat flux case.

Experimental Summary

A series of experiments were run to obtain the axial heat transfer coefficient distribution for both the uniform and single-side heated configurations. Results for two experimental test cases are presented. These cases involve both uniform and single-side heated configurations under identical flow conditions. The results are presented for Freon-11 flowing in a 25.4 mm inside diameter (i.d.) tube, with a mass velocity (G) of 210.0 kg/m²s, an inlet temperature of 22.6°C, and an exit pressure of 0.1843 MPa (absolute). The external heated surface area for the single-side heated case was 0.0512 m². The outside diameter of the heated channel was 28.4 mm. Peatiwala and Boyd [10] presented two-dimensional wall temperature measurements in the circumferential and axial directions for the above noted flow conditions. In addition, comparisons were made with similar data for horizontal flow ([11]). Further results were presented in terms of circumferentially and axially averaged heat transfer coefficients. The present work extends that study by presenting axial variations of the heat transfer coefficient and comparing these variations with selected correlations. The detailed description of the experimental flow boiling loop (see Fig. 1(a)), the test sections used, the experimental procedure, and error analysis are summarized below.

Flow Loop. The flow loop is shown in Fig. 1(a). The Freon-11 flows from the reservoir to the filter, where the contaminant is removed before the fluid enters the positive displacement pump. The positive displacement pump requires a net positive suction of at least 0.02 MPa. After leaving the pump, the fluid passes through the pulsation damper. The damper reduces the pressure and flow oscillations. The pressure fluctuations are also

minimized by using a pneumatically controlled metering valve. After exiting the control valve, the fluid flows to a heat exchanger, where its temperature is set to a desired value by adjusting the constant temperature bath. After exiting the heat exchanger, the fluid passes through the turbine flow meter and enters the unheated "flow developing" section or upstream part of the test section which has a length greater than 40 times the test section diameter. The fluid then enters the heated section of the test section. A downstream pneumatically controlled valve is used to control the test section exit pressure. The heated fluid then passes through another heat exchanger where the energy generated in the test section is removed partially by using tap water. Finally, the fluid flows back to the reservoir and the flow cycle is completed.

Test Section Description. The test sections are 2.235-m long copper tubes (see Fig. 1(b)), and consist of two parts: (1) an upstream unheated section to facilitate flow development, and (2) a downstream single-side heated section. For the present case, the inside diameter (D) was 25.4 mm and the outside diameter was 28.5 mm.

The 1.22-m long downstream portion of the test section is heated with heater tapes which vary in width based on tube diameter. Each tape has a power generation capacity of 2.66 kW. The entire test section is insulated to minimize the heat losses which are accounted for in the data reduction. In addition to the primary two parts of the main test section, each part has pressure-temperature measurement ports upstream and downstream of the test section.

The heated part of the test section is divided into seven 0.203 m axial intervals. At each of the axial locations, there are seven thermocouples installed circumferentially at the angles of 0, $\pi/4$, $3\pi/8$, $\pi/2$, $5\pi/8$, $3\pi/4$, and π radians, with 0 corresponding to the plane of symmetry at the heated side.

Data Reduction Analysis. Forty-nine local temperature measurements are made on the outside surface of the heated portion of the test section for each experiment. These outside temperatures are related to the inside wall temperature in order to determine the inside heat transfer coefficient. Figure 2 shows the model used for the data reduction. This model was used to compute a circumferentially averaged heat transfer coefficient from the circumferentially averaged wall temperature. The latter temperature was computed from the seven wall temperature measurements made on the outside of the test section at each of the seven axial locations.

Briefly, this approach involves estimating the inside channel wall temperature by using an equivalent uniformly heated tube whose diameter is equal to the ratio of four times the flow cross-sectional area to the heated perimeter. This is done by accounting for the temperature drop across the flow channel wall and the heat losses (convection and radiation) from the test section to the ambient. An iterative scheme was necessary to compute the inside wall temperature. After accounting for finite heat losses, the circumferentially averaged heat transfer coefficient is given by

$$h_m = A/B, \quad (1)$$

where

$$A = \left(\frac{k_A}{r_A}\right) B_1 \left[\ln\left(\frac{r_D}{r_C}\right) + \frac{k_C}{h_\infty r_D} \right] - \frac{k_C}{r_A} (T_m - T_\infty),$$

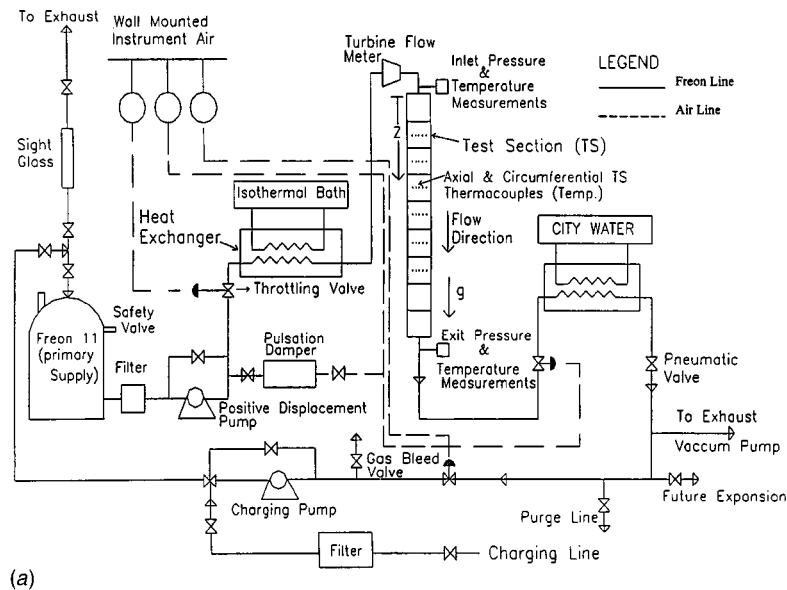
$$B = B_2 + B_3 + B_4,$$

$$B_1 = P_p r_C / A_s k_B,$$

$$B_2 = (T_m - T_\infty) \left[\ln\left(\frac{r_D}{r_C}\right) + \frac{k_C}{h_\infty r_D} + \frac{k_C}{k_B} \ln\left(\frac{r_C}{r_B}\right) \right],$$

$$B_3 = (T_m - T_\infty) \left[\frac{k_C}{k_A} \ln\left(\frac{r_B}{r_A}\right) \right] - \left[\ln\left(\frac{r_D}{r_C}\right) + \frac{k_C}{h_\infty r_D} \right] (T_f - T_\infty),$$

and



LOCATION OF MEASUREMENTS (m)

| Z1 | Z2 | Z3 | Z4 | Z5 | Z6 | Z7 |
|-----|--------|--------|--------|--------|-------|-------|
| 0.0 | 0.2032 | 0.4064 | 0.6096 | 0.8128 | 1.016 | 1.219 |

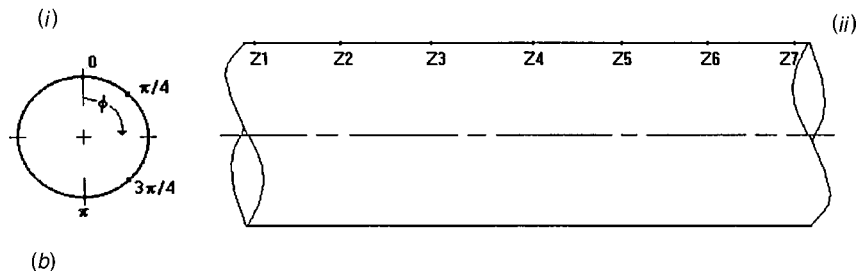


Fig. 1 (a) Schematic of the vertical downward flow boiling loop. (b) Wall temperature measurement locations: (i) cross section locations, (ii) axial locations along heated length.

$$B_4 = B_1 \left[\ln \left(\frac{r_C}{r_B} \right) + \frac{k_B}{k_A} \ln \left(\frac{r_B}{r_A} \right) \right].$$

In Eq. (1), T_f is the bulk fluid temperature and A_s is the outside surface area of the copper tube (domain A). At each axial location, the circumferentially averaged heat transfer coefficient was computed from the circumferentially averaged wall temperature (T_m). The circumferentially averaged temperature was computed from the seven wall temperature measurements made on the copper tube outside surface at each axial location by using the piecewise linear approach used by Reid et al. [12]. Using their approach, the circumferentially averaged outside wall temperature can be related to the seven circumferential measured temperatures (T_{m1} at 0 radians, T_{m2} at $\pi/4$, T_{m3} at $3\pi/8$, etc.) by the equation given below:

$$T_m = \frac{2T_{m1} + 3T_{m2} + 2T_{m3} + 2T_{m4} + 2T_{m5} + 3T_{m6} + 2T_{m7}}{16}. \quad (2)$$

The temperature T_m was used in Eq. (1) to account for the temperature drop across the channel wall, and convective and radiative

heat losses to the surroundings. Using this model, the mean heat transfer coefficient (h_m) at a given axial location was obtained.

Uncertainty Analysis. This study has resulted in the determination of circumferentially mean heat transfer coefficients from measurements of (1) the test section outside local wall temperature; (2) the flow conditions, which include flow rates, exit pressure, and inlet and exit bulk temperatures; and (3) the ambient temperature. The relationships between these quantities were summarized in Eqs. (1) and (2). Following the approach outlined by Moffat [13,14], the uncertainty in the heat transfer coefficient h_m is

$$\delta h_m = \left[\left(\frac{\partial h_m}{\partial X_i} \delta X_i \right)^2 + \left(\frac{\partial h_m}{\partial C_i} \delta C_i \right)^2 \right]^{1/2}, \quad (3)$$

where X_i represents all independent variables and C_i represents corrections used to account for calibration defects, system-sensor interactions, and system disturbance errors. The double indices in Eq. (3) imply summation over all independent or correction variables. The uncertainty in h_m can be approximated by

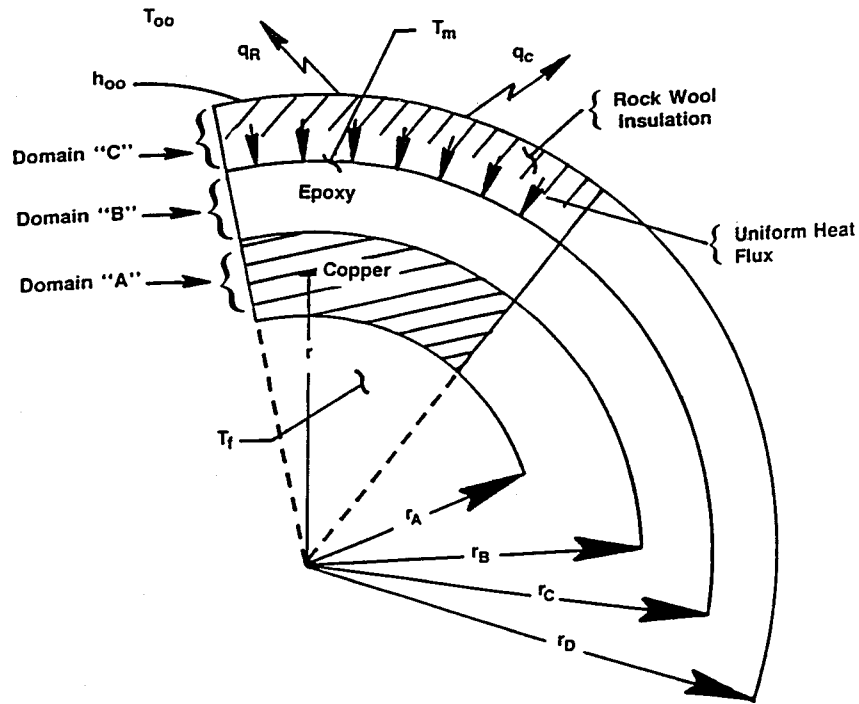


Fig. 2 Control volume for the heated hydraulic diameter model

$$\delta h_m \approx \left[\left(\frac{\partial h_m}{\partial A} \delta A \right)^2 + \left(\frac{\partial h_m}{\partial B} \delta B \right)^2 \right]^{1/2}, \quad (4)$$

$$\delta A = \left[\left(\frac{\partial A}{\partial P_p} \delta P_p \right)^2 + \left(\frac{\partial A}{\partial T_m} \delta T_m \right)^2 + \left(\frac{\partial A}{\partial T_\infty} \delta T_\infty \right)^2 \right]^{1/2};$$

where A and B are given in Eq. (1). Since A and B are not actually independent variables, their relationships with these variables are as follows:

$$\delta A = \text{Function}(T_m, P_p, T_\infty), \quad (5)$$

$$\delta B = \text{Function}(T_\infty, T_m, T_f, P_p), \quad (6)$$

so that

so that

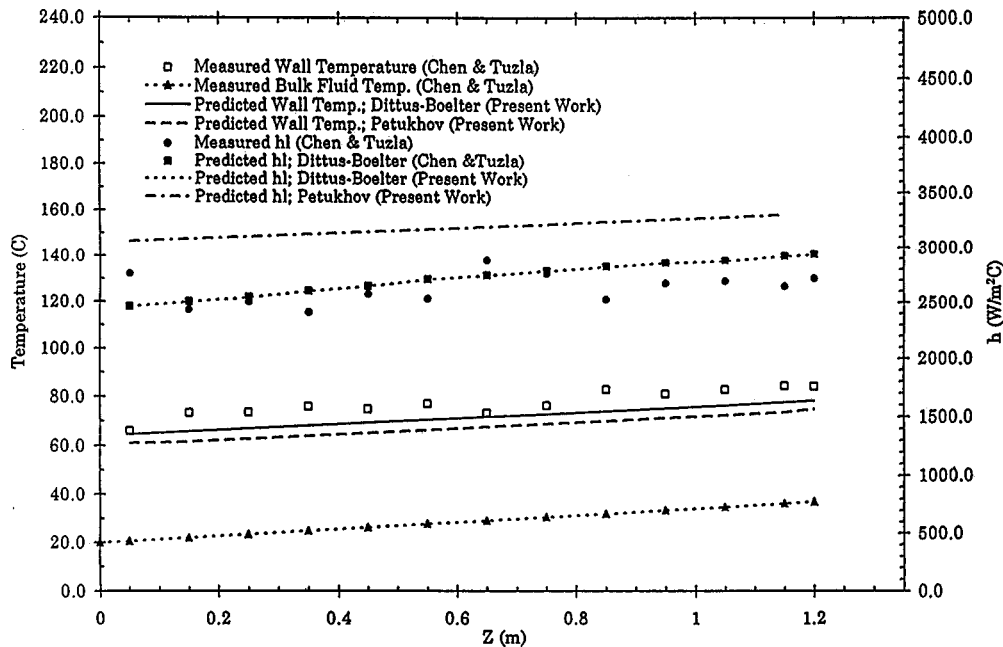


Fig. 3 Comparisons of low heat flux, single-phase heat transfer data with predictions. $Q = 125.0 \text{ kW/m}^2$; $g = 500.0 \text{ kg/m}^2$; $D = 15.7 \text{ mm}$; and $T_{\text{sat}} = 120^\circ\text{C}$ (Chen and Tuzla [15]).

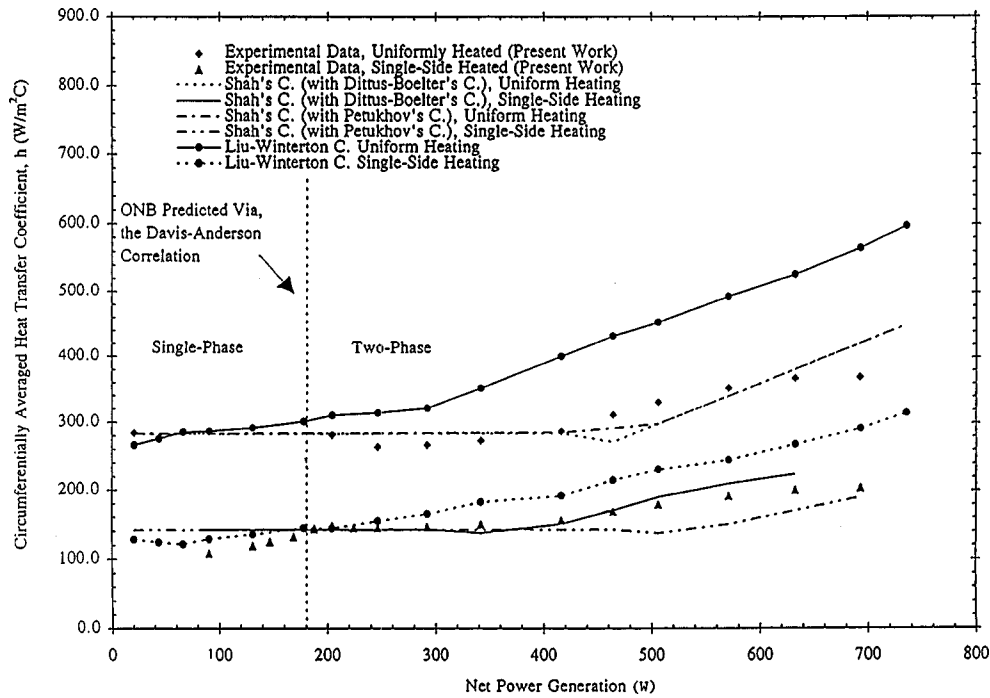


Fig. 4 Comparisons of correlations (C) with experimental Freon-11 data for single-phase and two-phase heat transfer coefficients for uniform and single-side heated vertical smooth channels with downward flow for the following flow conditions: $G=210.0 \text{ kg/m}^2\text{s}$, $D=25.4 \text{ mm}$; $Z=Z_4=0.6096 \text{ m}$, with an exit pressure of 0.1843 MPa (absolute)

$$\delta B = \left[\left(\frac{\partial B}{\partial P_p} \delta P_p \right)^2 + \left(\frac{\partial B}{\partial T_m} \delta T_m \right)^2 + \left(\frac{\partial B}{\partial T_\infty} \delta T_\infty \right)^2 + \left(\frac{\partial B}{\partial T_f} \delta T_f \right)^2 \right]^{1/2}$$

The uncertainties for each measurement in this experiment are as follows: (1) for geometric measurements, $\pm 0.1 \text{ mm}$; (2) for voltage, $\pm 0.05 \text{ mV}$; (3) for current, $\pm 0.005 \text{ mA}$; (4) for pressure,

$\pm 0.7 \text{ kPa}$; (5) for mass velocity, $8.4 \text{ kg/m}^2\text{s}$; and (6) for temperature, $\pm 0.2^\circ\text{C}$. This resulted in $\delta h_m \approx \pm 14.6 \text{ W/m}^2\text{C}$.

Results

Before the single-phase correlations were used for comparisons with our experimental data, they were compared with single-phase

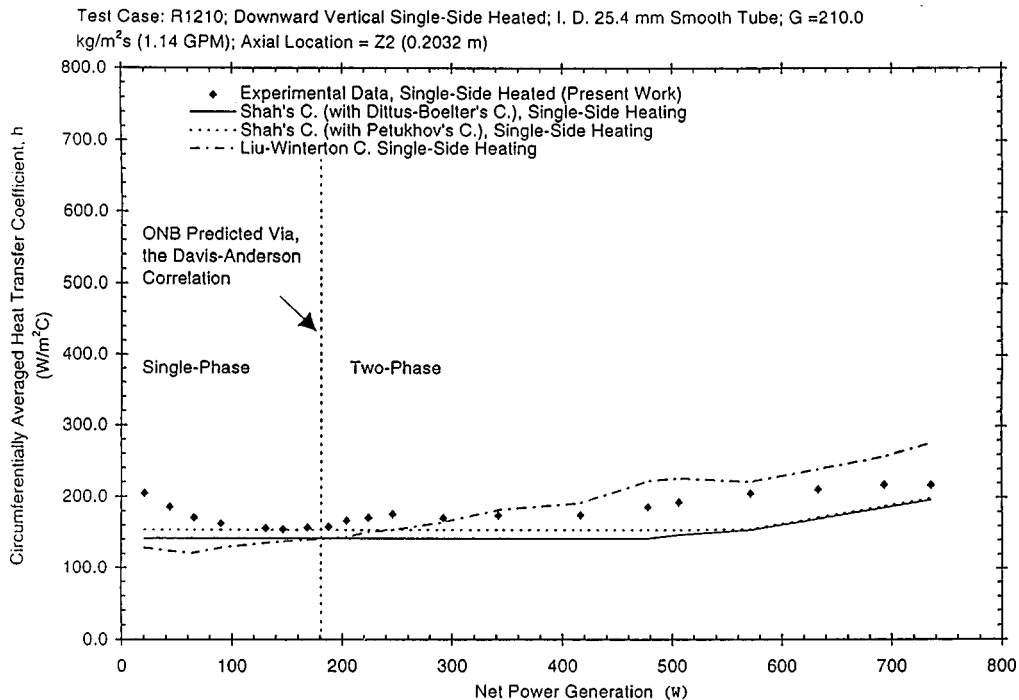


Fig. 5 Comparisons of correlations (C) with experimental Freon-11 data for single-phase and two-phase heat transfer coefficients for single-side heated vertical smooth channels with downward flow for the following flow conditions: $G=210.0 \text{ kg/m}^2\text{s}$, $D=25.4 \text{ mm}$; $Z=Z_2=0.2032 \text{ m}$, with an exit pressure of 0.1843 MPa (absolute)

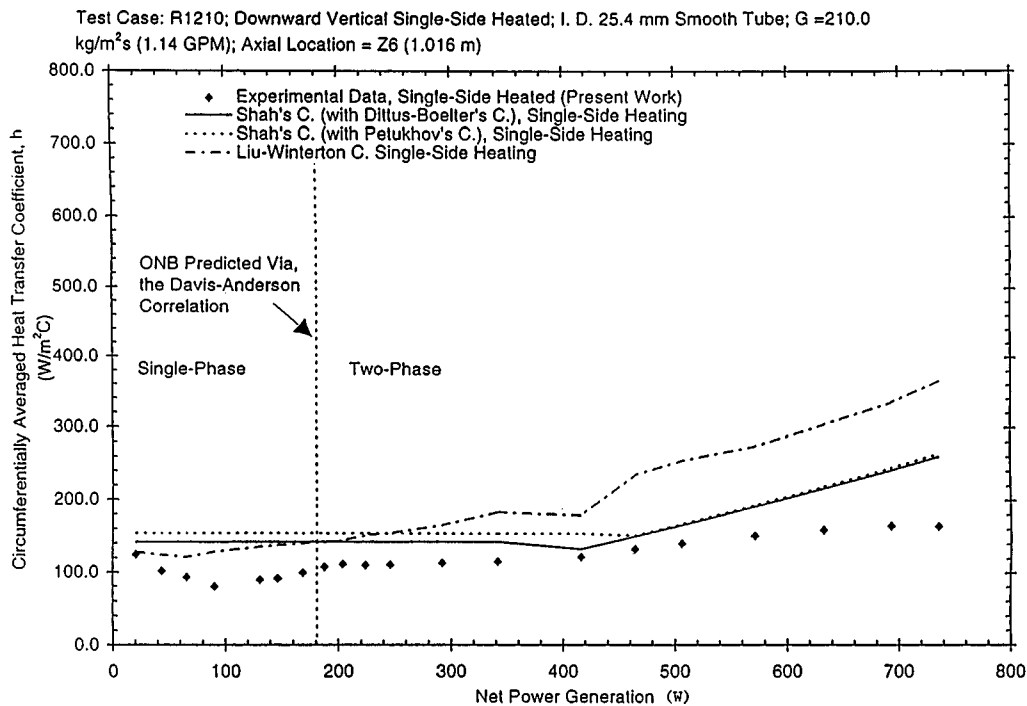


Fig. 6 Comparisons of correlations (C) with experimental Freon-11 data for single-phase and two-phase heat transfer coefficients for single-side heated vertical smooth channels with downward flow for the following flow conditions: $G = 210.0$ kg/m²s, $D = 25.4$ mm; $Z = Z_6 = 1.016$ m, with an exit pressure of 0.1843 MPa (absolute)

data produced by Chen and Tuzla [15] and Boyd [16]. It is important to note that the Chen and Tuzla water data was produced using a very low heat flux of 125.0 kW/m². For comparison at higher heat fluxes, Peatiwala and Boyd ([17], Fig. 3 in that publication) show that the Petukhov's correlation has better success than the Dittus-Boelter correlation. However, Fig. 3 in the present work shows that the Dittus-Boelter correlation fared better at lower heat fluxes. As Boyd and Meng [8] demonstrated, Shah's correlation has good predictability for high heat flux conditions in the partial nucleate boiling region when it is used along with Petukhov's correlation rather than the Dittus-Boelter correlation.

Figure 4 shows the comparison of the present experimental data obtained at an axial location near the middle of the test section with the above noted single-phase and two-phase correlations for both uniform and single-side heated boundary conditions. Since none of the correlations selected accounts for orientation, we anticipate only qualitative comparisons. Before the comparisons are discussed, it should be noted that the effects of single-side heating was accounted for by using a particular correlation as usual with the exception of using the thermal hydraulic diameter (D_t) as the characteristic length in place of the channel diameter (D). So that D_t is given by $4A_c/P_H$, where P_H is the heated perimeter and A_c is the flow channel cross-sectional area. With this definition of D_t , one readily observes the effect of the different reference lengths in Fig. 4 for both a uniformly heated channel and the single-side heated channel. As shown in the figure, there is qualitative agreement with the data in the single-phase region and good agreement with Shah's correlation in the two-phase region. For the single-side heated case and at further upstream axial locations, there is fairly good agreement between all single-phase correlations and the data for Z between 0.203 and 0.416 m. After the ONB, Fig. 5 shows that there is better agreement between the data and the Liu-Winterton correlation at upstream locations ($Z < 0.4$ m) and lower power levels. However, for increased values of Z between 0.4 m and 0.8 m or at higher levels of power, Fig. 4 and Peatiwala and Boyd ([17], Fig. 5 in that publication) show that Shah's correlation gave better predictions. At larger values of

Z , all correlations overpredicted the data (see Fig. 6). This overprediction at larger values of Z may be related to (1) the flow passing into a fully developed flow boiling regime, and (2) the inability of using D_t alone to account for the circumferentially nonuniform heat flux, orientation effects, as well as the three-dimensional two-phase effects—all of which would become more significant as Z increases. Very few if any existing correlations can address these effects simultaneously.

Conclusions

When used directly in the single-phase regime, the Liu-Winterton correlation compared well with the single-side heated Freon-11 data when D_t was chosen as the characteristic length. However, Shah's correlation characterized the data better in the two-phase region. Since all correlations overpredicted the data near the exit of the test section for the two-phase region, additional correlational development will be needed to completely characterize flow boiling heat transfer and nonuniform circumferential heating effects. Finally, good agreement was obtained between the correlations for uniformly heated channels and water data under the following conditions: (1) for low heat fluxes ($q \leq 125$ kW/m²), the Dittus-Boelter correlation is recommended for single-phase convection; (2) for high heat fluxes (125 kW/m² $< q \leq 30,000$ kW/m²), Petukhov's correlation is recommended for single-phase convection; and (3) for high heat fluxes, Shah's correlation is recommended for partial nucleate subcooled flow boiling.

Acknowledgments

This work was supported under NASA contract #NAG9-631 and under DOE contract DE-FG03-97ER54452.

Nomenclature

D = channel inside diameter (m)
 G = mass velocity (kg/m²s)

- h = heat transfer (H. T.) coefficient (W/m²C)
 h_m = axially distributed but circumferentially averaged heat transfer coefficient (W/m²C)
 h_∞ = Heat transfer coefficient due to natural convection (W/m²C)
 hl = Single-Phase heat transfer coefficient (W/m²C)
 k = thermal conductivity (W/mC)
 ONB = onset of nucleate boiling
 P_p = net power generation (W)
 q = heat flux (W/m²)
 q_c = heat flux due to natural convection from outside of test section (W/m²)
 q_R = heat flux due to radiation from the outside of the test section (W/m²)
 Q/Q_2 = ratio of the net power to the power required to cause saturated liquid condition to occur at the exit
 r = radial coordinate for the data reduction model (m)
 T = Temperature (Temp) (C)
 T_f = bulk temperature of the flowing fluid (K)
 $T_{mi}(\phi, Z)$ = local circumferential measured outside wall temperature of the test section (K)
 $T_w(\phi, Z)$ = outside wall temperature of the test section [$=T_{mi}(\phi, Z)$] (K)
 T_∞ = ambient temperature (K)
 Z = axial coordinate for the heated portion of the test section (m)

References

- [1] Chen, J. C., 1966, "A Correlation for Boiling Heat Transfer to Saturated Fluids in Convective Flows," *Ind. Eng. Chem. Process Des. Dev.*, **5**, No. 3, pp. 322–329.
- [2] Shah, M. M., 1977, "A General Correlation for Heat Transfer During Subcooled Boiling in Pipes and Annuli," *ASHRAE Trans.*, **83**, pp. 202–215.
- [3] Kandlikar, S. G., 1990, "A General Correlation of Saturated Two-Phase Flow Boiling Heat Transfer Inside Horizontal and Vertical Tubes," *ASME J. Heat Transfer*, **112**, pp. 219–228.
- [4] Kandlikar, S. G., 1991, "Development of Flow Boiling Map for Subcooled and Saturated Flow Boiling of Different Fluids Inside Circular Tubes," *ASME J. Heat Transfer*, **113**, pp. 190–200.
- [5] Steiner, D., and Taborek, J., 1992, "Flow Boiling Heat Transfer in Vertical Tubes Correlated by an Asymptotic Model," *Heat Transfer Eng.*, **13**, No. 2, pp. 43–66.
- [6] Gungor, K. E., and Winterton, R. H. S., 1986, "A General Correlation for Flow boiling in Tubes and Annuli," *Int. J. Heat Mass Transf.*, **29**, No. 3, pp. 351–358.
- [7] Gungor, K. E., and Winterton, R. H. S., 1987, "Simplified General Correlation for Saturated Flow Boiling and Comparison of Correlations with Data," *Chem. Eng. Res. Des.*, **65**, pp. 148–156.
- [8] Boyd, R. D., and Meng, X., 1995, "Boiling Curve Correlation for Subcooled Flow Boiling," *Int. J. Heat Mass Transf.*, **38**, pp. 758–760.
- [9] Liu, Z., and Winterton, R. H. S., 1991, "A General Correlation for Saturated and Subcooled Flow Boiling in Tubes and Annuli, Based on a Nucleate Pool Boiling Equation," *Int. J. Heat Mass Transf.*, **34**, No. 3, pp. 2759–2763.
- [10] Peatiwala, Q., and Boyd, R. D., 1995, "Forced Convection and Flow Boiling in a Single-Side Heated Vertical Smooth Channel with Downward Flow," *Proceedings of the ASME National Heat Transfer Conference*, Vol. 314, ASME, New York, pp. 133–143.
- [11] Boyd, R. D., Smith, A., and Turknett, J., 1995, "Two-Dimensional Wall Temperature Measurements and Heat Transfer Enhancement for Top-Heated Horizontal Channels With Flow Boiling," *Exp. Therm. Fluid Sci.*, **11**, pp. 372–386.
- [12] Reid, R. S., Pate, M. B., and Bergles, A. E., 1987, "Evaporation of Refrigerant 113 Flowing Inside Smooth Tubes," *ASME 87-HT-51*.
- [13] Moffat, R. J., 1988, "Describing the Uncertainties in Experimental Results," *Exp. Therm. Fluid Sci.*, **1**, pp. 3–17.
- [14] Moffat, R. J., 1990, "Estimating the Credibility of Experimental Work," Department of Mechanical Engineering, Stanford University, Stanford, CA.
- [15] Chen, J. C., and Tuzla, K., 1995, "Contribution of Convection and Boiling to Convective Flow Boiling," *Convective Flow Boiling International Conference Proceedings*, Engineering Foundation, paper No. IV-10, Banff, Alberta, Canada.
- [16] Boyd, R. D., 1989, "Subcooled Flow Boiling at 1.66 MPa Under Uniform High Heat Flux Conditions," *Fusion Technol.*, **16**, pp. 324–330.
- [17] Peatiwala, Q., and Boyd, R. D., 1996, "Subcooled Flow Boiling in Circumferentially Non-Uniform and Uniform Heated Vertical Channels with Downward Flow: Comparisons With Selected Two-Phase Correlations," *Process Enhanced and Multiphase Heat Transfer*, R. M. Manglik and A. D. Kraus, eds., Begell House, New York, pp. 183–189.

Fusion Zone Shapes in Electron-Beam Welding Dissimilar Metals

P. S. Wei

Professor, Mechanical Engineering Department, National Sun Yat-Sen University, Kaohsiung, Taiwan, ROC
 e-mail: pswei@mail.nsysu.edu.tw

Y. K. Kuo

Graduate Student, Mechanical Engineering Department, National Sun Yat-Sen University, Kaohsiung, Taiwan, ROC

J. S. Ku

Institute of Materials Science and Engineering, National Sun Yat-Sen University, Kaohsiung, Taiwan, ROC

Experiments on welding dissimilar metals, such as aluminum or copper to iron with an electron-beam welder, are conducted. It is found that the observed depth-to-width ratio of the fusion zone in aluminum can be greater than unity while that in iron is around unity. The former is attributed to the formation of a cavity resulting from a high vapor pressure. The difference in depths increases with beam power. The observed depth-to-width ratios of fusion zones in welding copper to iron can be greater than unity. A unique maximum depth is near the joint plane, as a result of strong convective mixing and high incident flux, even though the melting temperatures are different. Strong mixing is confirmed by measured concentration profiles across the fusion zones of dissimilar metals. To a first approximation fusion zone depths with depth-to-width ratios greater than or identical to unity are determined from scale analyses of heat conduction equations in welding the same metals with a high and low-power-density beam, respectively. The propositions are verified by experimental results. [S0022-1481(00)00103-1]

Keywords: Heat Transfer, Manufacturing, Phase Change, Scaling, Welding

Introduction

Weldments are often made from dissimilar metals in order to satisfy different requirements for performance. A successful weld between dissimilar metals is that it possesses sufficient tensile strength and ductility so that the joint will not fail. Such joints can be obtained in a variety of different metals and welding processes ([1,2]). The phenomena encountered in welding dissimilar metals are complicated. Tinkler et al. [3] observed that when samples with different penetration characteristics were welded together, the weld pool was displaced toward the material with the lower sulfur content. Because sulfur is a surface active element, an increase of sulfur content results in a decrease of surface tension ([4]). Hence, Mills and Keene [5] interpreted that the flow from high sulfur to low sulfur results in the transport of hot metal to the low sulfur side. The melt back will occur preferentially in the low sulfur steel, and an asymmetric weld will be produced.

Recently, Chung and Wei [6] and Wei and Chung [7] computed quasi-steady and unsteady velocity, temperature and concentration fields, and shapes of the molten regions in welding dissimilar metals. Imposing a Marangoni force on the flat free surface, as-

Contributed by the Heat Transfer Division for publication in the JOURNAL OF HEAT TRANSFER. Manuscript received by the Heat Transfer Division, July 7, 1998; revision received, January 14, 2000. Associate Technical Editor: D. Kaminski.

suming immiscible molten metals, and accounting for distinct properties between metals and phases, it was found that flow patterns depend on signs and magnitudes of surface-tension coefficients, the asymmetric temperature profile, and locations of the interface between dissimilar molten metals. In contrast to surface widths, the depths are relatively insensitive to Marangoni convection induced by negative surface tension coefficients of dissimilar molten metals.

In this study, the fusion zone shapes in welding dissimilar metals are measured and analyzed. In the case of Marangoni convection induced by negative surface tension coefficients, the prediction of fusion zone depths based on a pure heat conduction model is reliable. Scaling the heat conduction equation, the results determine the fusion zone depths in the joint of dissimilar metals. The proposition is verified by photographic measurements.

Experimental Procedure

A bead-on-plate weld was made for workpieces Al 1050, pure copper, and iron with an electron-beam welder having a maximum accelerating voltage of 60 kV and a welding current of 50 mA. The joint planes were finished by a grinding machine and a grinder polisher with a mixture of 1-mm alumina and water on branners. It was further cleaned with spirits in an ultrasonic wave cleaner to remove oxide layers and debris. The focal spot was adjusted on the workpiece surface because of its strong influence on the depth of penetration ([8]). After welding, the specimen was cut, mounted, and polished by 800–2000 grit emery papers. High-purity alumina of 1–0.05 mm were used for polishing. Chemical solutions to etch the specimen were also required. The chemical etchant for Al 1050 was 10 ml HF and 15 ml HCl, 90 ml H₂O, while that for Cu is 10 ml HNO₃, 90 ml H₂O and for Fe was 25 ml HNO₃, and 75 ml H₂O. The fusion zone was observed by a zoom microstereoscope with magnification of 3–10. The coefficient of determination for the depths will be shown in the corresponding figures. A scanning electron microstereoscope with EDS (Energy Dispersive Spectrometer) was used to examine microstructures and analyze concentrations after polishing by the grinder polisher with a mixture of 0.05-mm alumina and water on branners.

System Model and Analysis

A low-power-density beam produces a molten region or fusion zone with a depth-to-width ratio of around unity. On the other hand, a high-power-density beam can produce a cavity or keyhole. This results in a deep penetration with the depth-to-width ratio much greater than unity ([9]). In this work, predictions of the fusion zone depths are described as follows:

A Welding the Same Metals. The unsteady energy equation in the heat-affected zone around the molten pool is

$$\frac{\partial T_s}{\partial t} - U \frac{\partial T_s}{\partial x} = \alpha_s \nabla^2 T_s. \quad (1)$$

Provided that Eq. (1) is scaled as

$$\frac{1}{t_c} \ll \frac{U}{\delta_T} \sim \frac{\alpha_s}{\delta_T^2} \quad (2)$$

which indicates that as time scale $t_c > \alpha_s / U^2$ a quasi-steady state can be assumed. The global energy balance on the solid-liquid interface is scaled by

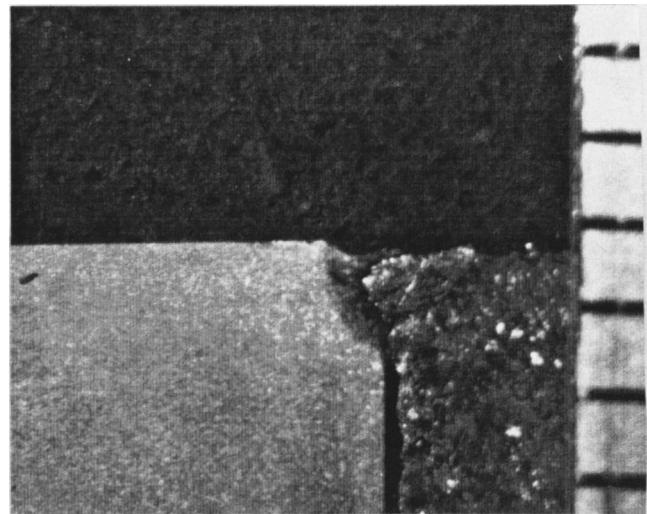
$$k_s \frac{T_m - T_\infty}{\delta_T} wh \sim Q. \quad (3)$$

In view of less than one-hundredth of beam power, latent heats for melting and solidification can be ignored. A substitution of Eq. (2) into Eq. (3) leads to

$$\frac{k_s(T_m - T_\infty)}{\alpha_s} wh \sim \frac{Q}{U} \quad \text{or} \quad Q^* = c_1 Pe_w. \quad (4)$$

Evidently, Eq. (4) is applicable for both low and high-power-density welding. Linear relationships can be seen for both moving line and point sources in the range of a high Peclet number ([10]). Swift-Hook and Gick [11] found $c_1 = 2.07$ in a high speed limit for analytical solutions in high-power-density welding. A gradual decrease in the slope of the dimensionless beam power as the Peclet number decreases is attributed to the welding speed gradually reducing its effect on heat transfer. High and low-power-density welds are further discussed as follows:

(a) *High-Power-Density Welding.* The surface width of the fusion zone can be scaled by the opening radius of the cavity or the energy distribution parameter of the beam in the range of a high Peclet number. This is because the surface width of the fusion zone decreases with increasing welding speed. The surface width, however, cannot be less than the cavity opening radius. Replacing the surface width by the energy distribution parameter, Eq. (4) becomes



(a)



(b)

Fig. 1 Photographs of fusion zones in Al-Fe welding with accelerating voltage 50 kV, welding speed 0.04 m/s, and welding currents of (a) 12 mA, and (b) 20 mA

$$Q^* = c_2 Pe_\sigma. \quad (5)$$

The use of the energy distribution parameter rather than the surface width of the fusion zone or cavity opening radius is due to the fact that the energy distribution function is an independent quantity that can be measured prior to welding. Furthermore, the energy distribution parameter is related to the energy density incident on the surface of the workpiece. As the Peclet number decreases a decrease in the welding speed increases the surface width of fusion zone ([11,10]). Hence, Eq. (5) is inaccurate.

(b) *Low-Power-Density Welding.* Scaling the surface width of the fusion zone in Eq. (4) cannot be simply obtained, because surface width is strongly affected by Marangoni convection. However, in most cases, low-power-density welding induces the molten region with depth-to-width ratio of the order of unity ([12]). To a first approximation, it is feasible to choose $w \approx h$. Equation (5) then yields

$$\frac{Uh}{\alpha_s} = c_3 \sqrt{n}. \quad (6)$$

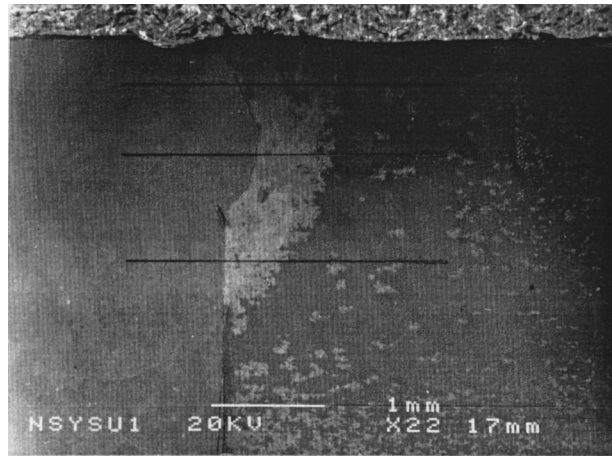
The empirical constant c_3 depends on Marangoni convection, the energy distribution parameter, and several unknown minor effects.

B Welding Dissimilar Metals. A scale analysis for studying the joint between dissimilar metals is difficult. To a first approximation, it is proposed that the fusion zones in dissimilar metals are, separately, identical to the fusion zones in welding the same metals. For example, the fusion zones on the sides of aluminum and iron in Al-Fe welding are determined by the fusion zones in Al-Al and Fe-Fe welding, respectively. As a conse-

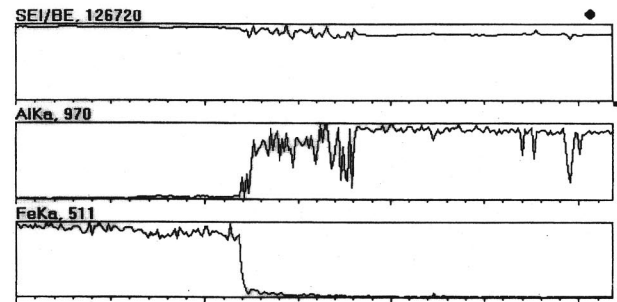
quence, the analyses in part A can be used effectively. The accuracy of this assumption is verified by experimental data, as will be seen later.

Results and Discussion

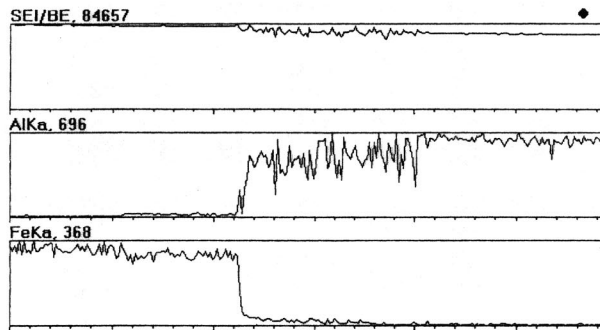
Experimental measurements of the fusion zone depths in welding aluminum or copper to iron were conducted. In contrast to the surface widths, the depths of the fusion zones are relatively insensitive to Marangoni convection induced by negative surface tension coefficients of dissimilar molten metals ([6,7]). This is because most energy is transferred to the edges of the molten region and the energy to the bottom is reduced. As a consequence, the prediction of fusion zone depth based on a pure heat conduction model is more reliable. The effects of beam power on fusion zone depths in welding aluminum to iron are shown in Fig. 1. The right and left-hand sides are iron and aluminum, respectively. A division in the ruler is a millimeter. Although fusion zone depths of aluminum and iron are different for a low power of 600 W, the depth-to-width ratios are of the order of unity, as shown in Fig. 1(a). The difference in depths of aluminum and iron increases by increasing beam power to 1000 W, as presented in Fig. 1(b). The depth-to-width ratio on the side of aluminum is around 3, which implies the existence of a cavity in the aluminum. In this study, the fusion zone in aluminum is proposed to be modeled from a high-power-density welding. On the other hand, a unity depth-to-width ratio in iron is simulated by a low-power-density welding. The formation of the cavity in aluminum results from a higher vapor pressure ([13]). Considering the free surface temperature to be 2000 K, vapor pressures of Fe and Al are, respectively, around 40 and 800 Pa. The sharp boundary between fusion zones of aluminum and iron is due to the same order of magnitude of Ma-



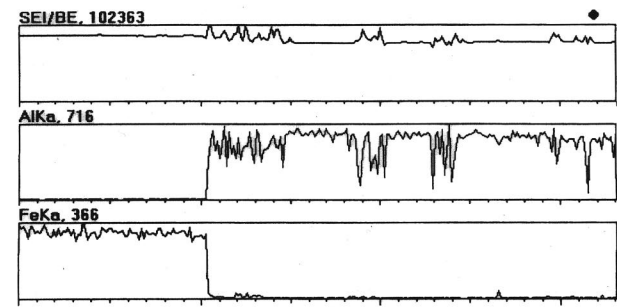
(a)



(c)

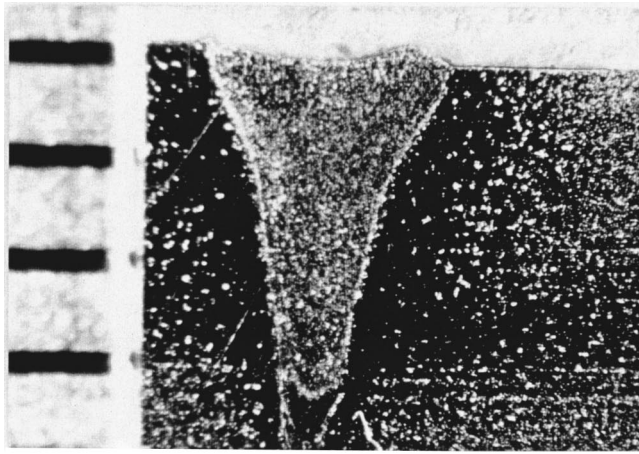


(b)

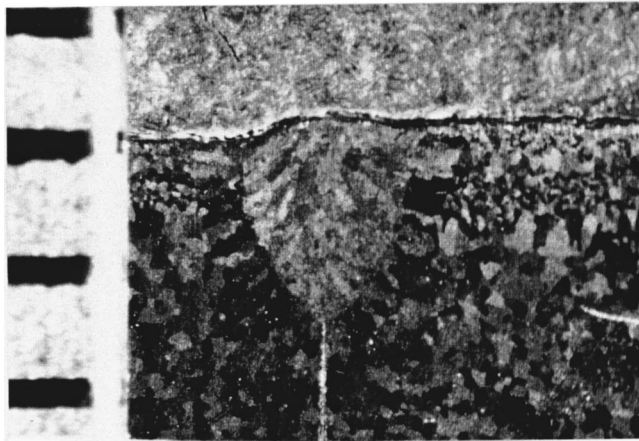


(d)

Fig. 2 (a) Fusion zone, and concentration profiles at (b) upper, (c) intermediate, and (d) lower locations in Al-Fe welding with beam power 1000 W and welding speed 0.045 m/s



(a)



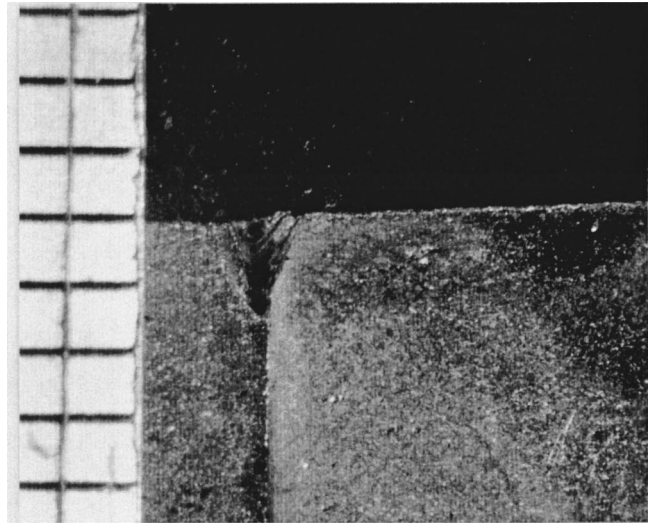
(b)

Fig. 3 Photographs of fusion zones in (a) Al-Al, and (b) Fe-Fe welding with accelerating voltage 50 kV, welding current 20 mA, and welding speed 0.04 m/s

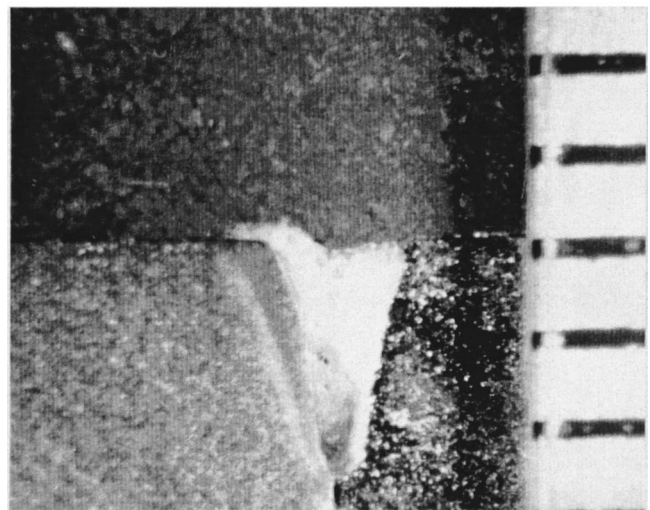
Marangoni numbers with negative surface tension coefficients for dissimilar molten metals. The molten pool is not well mixed, because fluid flow is upward near the interface between dissimilar molten metals and velocity component normal to the interface is small.

Figure 2 shows profiles of concentration on three horizontal planes across fusion zones of aluminum and iron. Metals on the left and right-hand sides of Fig. 2(a) are, respectively, iron and aluminum. Concentration profiles of aluminum and iron at an upper position are shown in Fig. 2(b). The upper figure represents roughness on the position measured. The total length for measuring is 2.941×10^{-3} m. The lower two figures, respectively, show concentration profiles of aluminum and iron. The ordinate denotes concentration from 0 to 100 percent while the abscissa is horizontal spatial location. It can be seen that a rather sharp boundary exists between the solidified aluminum and iron. Hence, molten metals of aluminum and iron are immiscible during melting and solidification processes ([6,7]). Since the sum of the concentrations for aluminum and iron is less than 100 percent (atom percentage), other minor elements such as Si, Mg, Zn, P, S, and Ti exist in the fusion zone. Similar results are shown in Figs. 2(c) and (d). Several sudden drops take place in the bulk phase of aluminum due to the existence of pores by referring to the figures for roughness.

An investigation of the difference in the fusion zones in welding dissimilar metals and the same metals is crucial. Referring to



(a)

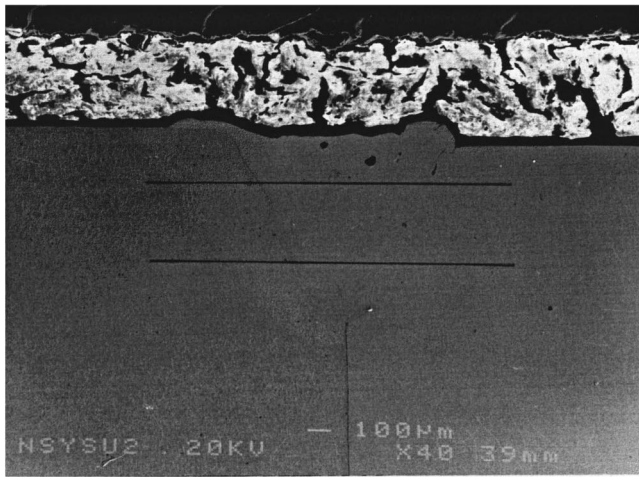


(b)

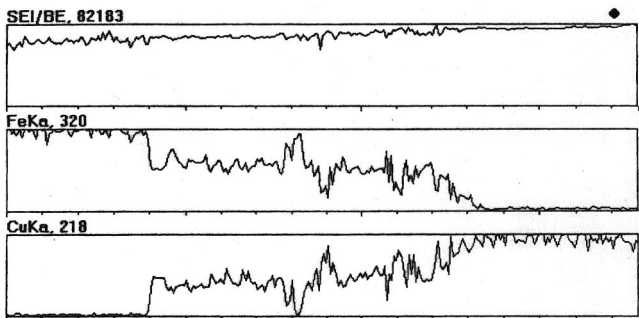
Fig. 4 Photographs of fusion zones in Fe-Cu welding with accelerating voltage 50 kV, welding speed 0.025 m/s, and welding current of (a) 20 mA, and (b) 30 mA

Fig. 1(b), it is found that the fusion zone depths of aluminum in the joints between the same metals and dissimilar metals are roughly the same as shown in Fig. 3(a), even though the fusion zone shapes are different. Depths of the fusion zone in iron are also similar in welding the same and dissimilar metals, as shown in Fig. 3(b). This leads to a proposition to determine the fusion zone depth of a dissimilar joint from an analysis of the same metals.

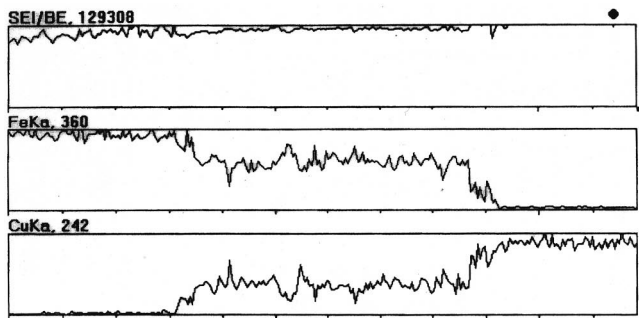
Figures 4(a) and (b) show the variations of the fusion zone with beam power in welding copper and iron. Evidently, an increase in beam power increases depths of fusion zones. Depths of copper and iron are nearly identical in contrast to the joint between aluminum and iron as shown previously. Although vapor pressures of molten iron and copper are, respectively, around 40 and 400 Pa, mixing due to strong Marangoni convection, as can be seen later, reduces the distinct depths of the fusion zone in iron and copper. In contrast to that in welding Al-Fe, strong Marangoni mixing is attributed to a significant difference in the product of the surface tension coefficient-to-dynamic viscosity ratio with temperature gradient (or Marangoni number) between dissimilar molten metals ([6,7]). Interestingly, even though the melting temperatures of



(a)



(b)



(c)

Fig. 5 (a) Fusion zone, and concentration profiles at (b) upper and (c) lower locations in Fe-Cu welding with beam power 1000 W and welding speed 0.04 m/s

copper and iron are, respectively, 1358 and 1810 K, the difference in depths of the fusion zone or the solid-to-liquid interface in copper and iron is negligible. This is attributed to a high temperature gradient near the cavity base. If the beam power is 1000 W, the energy distribution parameter is 1 mm while the liquid thermal conductivity is 100 W/m-K, and the temperature gradient at the cavity base is 3.2×10^6 K/m ([14]). A temperature difference of 452 K then occurs in a distance of 1.4×10^{-4} m, which is only five percent of the fusion zone depth. Figure 5 shows concentration profiles of iron and copper on two horizontal planes across the fusion zones. Metals on the left and right-hand sides of Fig. 5(a) are, respectively, iron and copper. Strong mixing is revealed by gradual variations in the concentrations of iron and copper in fusion zones, as shown in Figs. 5(b) and (c).

The dimensionless beam power versus Peclet number, with the energy distribution parameter as a length scale, in welding copper

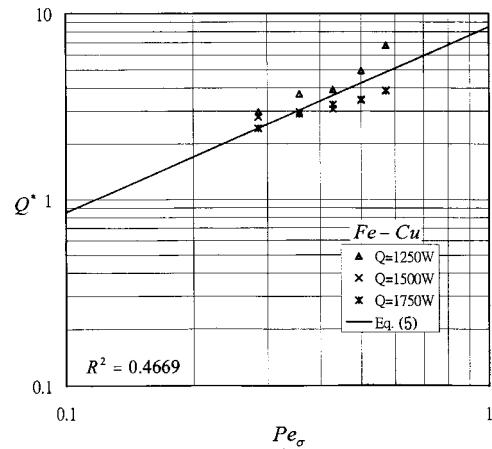


Fig. 6 Measured and predicted dimensionless beam power versus Peclet number for different beam powers in Fe-Cu welding

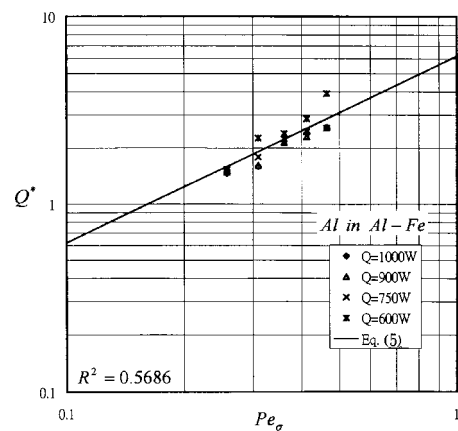


Fig. 7 Measured and predicted dimensionless beam power versus Peclet number for Al in Al-Fe welding with different beam powers

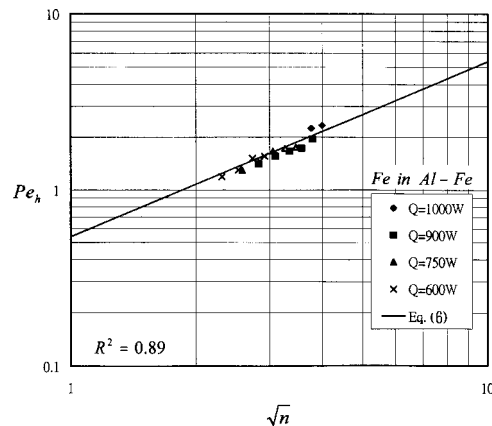


Fig. 8 Measured and predicted Peclet number versus square root of operating parameter for Fe in Al-Fe welding with different beam powers

to iron is shown in Fig. 6. Thermal properties are chosen to be the mean values evaluated at the temperature between the ambient and melting temperatures and dissimilar metals. The energy distribution parameter is estimated to be 0.5 mm. Equation (5) governing a deep penetration shows an agreement with experimental data for different beam powers and welding speeds. The deviations between the predictions and measurements can be due to

rough approximations for the relationship between the width and depth of the fusion zone and the energy distribution parameter, an incomplete absorption by the workpiece surface, and inherent uncertainties in thermal properties. The dimensionless beam power versus Peclet number for aluminum in welding aluminum to iron is shown in Fig. 7. It can be seen that experimental data are close to Eq. (5) for different beam powers and welding speeds. Figure 8 shows the measured Peclet number, with the depth of iron as a length scale, versus the square root of operating parameter in welding aluminum to iron. It is found to agree quite well with the prediction from Eq. (6) based on low-power-density welding.

Nomenclature

c_1, c_2, c_3 = empirical constant
 h = fusion zone depth
 k = thermal conductivity
 n = operating parameter $\equiv QU/[\alpha_s k_s (T_m - T_\infty)]$
 Pe = Peclet number, $Pe_w \equiv Uw/\alpha_s$, $Pe_\sigma \equiv U\sigma/\alpha_s$
 Q = beam power, $Q^* \equiv Q/[hk_s(T_m - T_\infty)]$
 T, T_m, T_∞ = temperature, melting, and ambient temperatures
 U = welding speed
 w = surface width
 x = Cartesian coordinate along welding line

Greek Letters

α = thermal diffusivity
 δ_T = heat-affected zone thickness
 σ = energy distribution parameter

Subscript

s = solid

References

- [1] Sun, Z., and Moio, T., 1994, "Effect of Processing Parameters on Laser Welded Dissimilar Steel Joints," *Weld. J. (Miami)*, **73**, pp. 63–70.
- [2] Cary, H. B., 1989, *Modern Welding Technology*, 2nd Ed., Prentice-Hall, Englewood Cliffs, NJ, pp. 555–559.
- [3] Tinkler, M. J., Grant, I., Mizuno, G., and Gluck, C., 1983, "The Effects of Residual Impurity and Microalloying Elements on Weldability and Weld Properties," Paper 29, The Welding Institute, Abington, UK.
- [4] Belton, G. R., 1976, "Langmuir Adsorption, the Gibbs Adsorption Isotherm, and Interfacial Kinetics in Liquid Metal Systems," *Metall. Trans. B*, **7B**, pp. 35–42.
- [5] Mills, K. C., and Keene, B. J., 1990, "Factors Affecting Variable Weld Penetration," *Int. Mater. Rev.*, **35**, pp. 185–216.
- [6] Chung, F. K., and Wei, P. S., 1999, "Mass, Momentum, and Energy Transport in Molten Pool When Welding Dissimilar Metals," *ASME J. Heat Transfer*, **121**, pp. 451–461.
- [7] Wei, P. S., and Chung, F. K., 2000, "Unsteady Marangoni Flow in Molten Pool When Welding Dissimilar Metals," *Metall. Mater. Trans.*, submitted for publication.
- [8] Wei, P. S., and Chow, Y. T., 1992, "Beam Focusing Characteristics and Alloying Element Effects on High-Intensity Electron Beam Welding," *Metall. Trans. B*, **23B**, pp. 81–90.
- [9] Tong, H., and Giedt, W. H., 1970, "A Dynamic Interpretation of Electron Beam Welding," *Weld. J. (Miami)*, **49**, pp. 259s–266s.
- [10] Elmer, J. W., Giedt, W. H., and Eagar, T. W., 1990, "The Transition from Shallow to Deep Penetration During Electron Beam Welding," *Weld. J. (Miami)*, **69**, pp. 167s–176s.
- [11] Swift-Hook, D. T., and Gick, A. E. F., 1973, "Penetration Welding With Lasers," *Weld. J. (Miami)*, **52**, pp. 492s–499s.
- [12] Christensen, N., Davies, V. de L., and Gjermundsen, K., 1965, "Distribution of Temperatures in Arc Welding," *Br. Weld. J.*, **12**, pp. 54–75.
- [13] Schauer, D. A., and Giedt, W. H., 1978, "Prediction of Electron Beam Welding Spiking Tendency," *Weld. J. (Miami)*, **57**, pp. 189s–195s.
- [14] Heiple, C. R., and Roper, J. R., 1982, "Mechanism for Minor Element Effect on GTA Fusion Zone Geometry," *Weld. J. (Miami)*, **61**, pp. 97s–102s.

Discussion: “Heat Transfer Measurement and Analysis for Sintered Porous Channels” (Hwang, G. J., and Chao, C. H., 1994, ASME J. Heat Transfer, 116, pp. 456–464)

S. J. Kim and D. Kim

Department of Mechanical Engineering, KAIST,
Taejon, Korea

Our purpose in this discussion is to demonstrate that some of the results stated in Hwang and Chao’s paper appear to be in error. We can show that a recalculation of Hwang and Chao’s

equations leads to different results that differ from those put forth in their paper. Specifically, some of the calculated values of $Nu_{f\infty}$ for $d_p = 1.59$ mm in Fig. 6 of their paper are incorrect. This can be proven by comparing their numerical results with the exact $Nu_{f\infty}$, which is obtained from analytical solutions for velocity and temperature distributions in the case of no dispersion. The momentum Eq. (9) in their paper can be analytically solved to yield the closed-form solution for the velocity distribution as follows ([1]):

$$U = \left(\frac{z+1}{z-1} \right)^2 \left(3U_\infty + \frac{3}{2F_s} \right) - 2U_\infty - \frac{3}{2F_s}, \quad (1)$$

where

$$F_s = \frac{Re_d}{d_p} F \sqrt{K}, \quad Da = \frac{K}{\varepsilon H^2}, \quad U_\infty = \frac{-1 + \sqrt{1 + 4F_s C}}{2F_s}$$

$$z(Y) = \begin{cases} \frac{\sqrt{2U_\infty + \frac{3}{2F_s}} + \sqrt{3U_\infty + \frac{3}{2F_s}}}{\sqrt{2U_\infty + \frac{3}{2F_s}} - \sqrt{3U_\infty + \frac{3}{2F_s}}} \exp \left[Y \sqrt{\frac{2F_s}{Da} U_\infty + \frac{1}{Da}} \right] & \text{for } 0 \leq Y \leq \frac{1}{2} \\ \frac{\sqrt{2U_\infty + \frac{3}{2F_s}} + \sqrt{3U_\infty + \frac{3}{2F_s}}}{\sqrt{2U_\infty + \frac{3}{2F_s}} - \sqrt{3U_\infty + \frac{3}{2F_s}}} \exp \left[(1-Y) \sqrt{\frac{2F_s}{Da} U_\infty + \frac{1}{Da}} \right] & \text{for } \frac{1}{2} \leq Y \leq 1. \end{cases}$$

In the case of no dispersion, energy Eqs. (10) and (11) in their paper can be reduced to

$$0 = Bi(\theta_f - \theta_s) + \frac{d^2 \theta_s}{dY^2} \quad (2)$$

$$U = \theta_s - \theta_f. \quad (3)$$

Equations (2) and (3) can be merged into Eq. (4).

$$\frac{d^2 \theta_s}{dY^2} = BiU \quad (4)$$

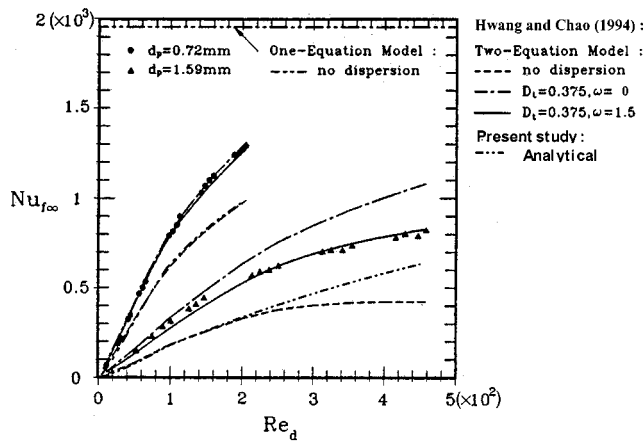
By integrating Eq. (4), the analytical solution for the solid temperature distribution can be obtained as follows:
for $0 \leq Y \leq 1/2$,

$$\theta_s = \frac{Bi}{B} \left[12 \left(U_\infty + \frac{1}{2F_s} \right) \left\{ \frac{2}{A \exp\left(\frac{1}{2}B\right) - 1} - \frac{1}{A-1} \right\} - U_\infty (\ln A + B) \right] Y + \frac{Bi}{B} \left[\frac{U_\infty}{2} \{ (\ln z)^2 - (\ln A)^2 \} - 12 \left(U_\infty + \frac{1}{2F_s} \right) \ln \frac{A(z-1)}{(A-1)z} \right], \quad (5a)$$

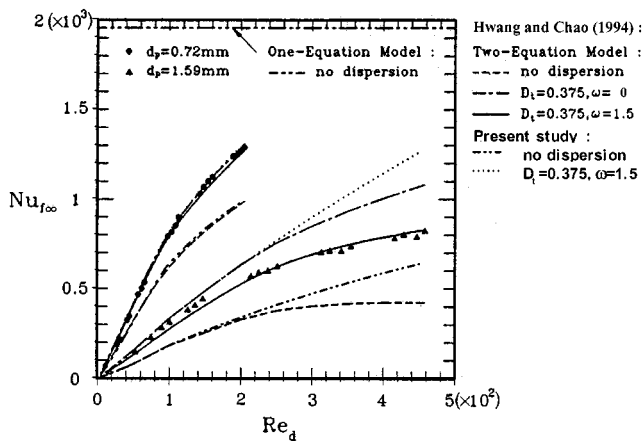
for $1/2 \leq Y \leq 1$,

$$\theta_s = \frac{Bi}{B} \left[U_\infty \ln A - 12 \left(U_\infty + \frac{1}{2F_s} \right) \frac{1}{A-1} \right] Y + \frac{Bi}{B} \left[\frac{U_\infty}{2} \{ (\ln z)^2 - (\ln A + B)^2 \} - 12 \left(U_\infty + \frac{1}{2F_s} \right) \ln \frac{A \exp(B)(z-1)}{(A \exp(B) - 1)z} \right], \quad (5b)$$

where



(a)



(b)

Fig. 1 Comparisons of the fully developed Nusselt number; (a) analytical result for no dispersion, (b) numerical results for limiting cases

$$A = \frac{\sqrt{2U_\infty + \frac{3}{2F_s}} + \sqrt{3U_\infty + \frac{3}{2F_s}}}{\sqrt{2U_\infty + \frac{3}{2F_s}} - \sqrt{3U_\infty + \frac{3}{2F_s}}}, \quad B = \sqrt{\frac{2F_s}{Da} U_\infty + \frac{1}{Da}}$$

Now the fluid temperature distribution can be obtained by rearranging Eq. (3) as

$$\theta_f = \theta_s - U. \quad (6)$$

From the definition of the overall Nusselt number, the analytical form of $Nu_{f\infty}$ can be obtained as

$$Nu_{f\infty} = -\frac{5k_s^*Bi}{3k_f\theta_{fb}}, \quad (7)$$

where $\theta_{fb} = \int_0^1 U\theta_f dY$.

Figure 1 shows the relation between $Nu_{f\infty}$ and Re_d . For the case of $w = \infty$ (no dispersion), the numerical results (broken line) of Hwang and Chao start deviating from the analytical results (double-dotted broken line) of Eq. (7) when $Re_d > 200$, as shown in Fig. 1(a). In contrast with the results of Hwang and Chao, results from our numerical simulation (double-dotted broken line in Fig. 1(b)) for the same problem are in excellent agreement with the exact $Nu_{f\infty}$ of Eq. (7) (double-dotted broken line in Fig. 1(a)). For another limiting case where $D_t = 0.375$, $w = 0$ (maximum dis-

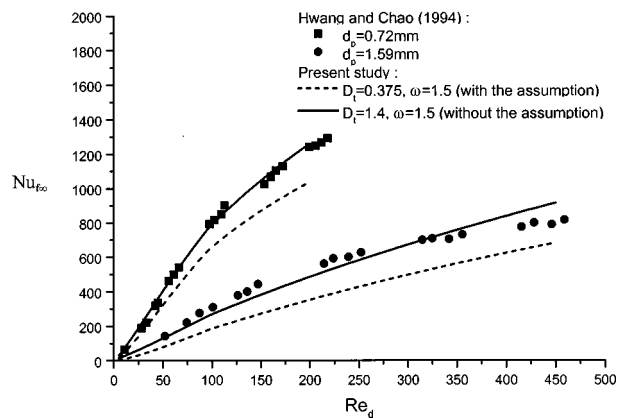


Fig. 2 Comparison of the fully developed Nusselt number

persion), similar deviations between our results (dotted line) and the results of Hwang and Chao (single-dotted broken line) exist for $Re_d > 200$, as shown in Fig. 1(b). Note that “ $w = \infty$ ” in Fig. 6 of their paper should be replaced by “ $w = 0$.”

In addition, it is worth mentioning that Hwang and Chao employ an inappropriate assumption in their paper. They assumed that the effective thermal conductivity of the fluid is negligible. However, the effective thermal conductivity of the fluid is not negligible in comparison with the thermal dispersion conductivity when Re_d is small, because the thermal dispersion conductivity decreases with Re_d . Re_d in their paper ranges from 0 to 500 which is not large enough to neglect the effective thermal conductivity. Hence in their case the neglect of the effective thermal conductivity of the fluid can result in more than a ten percent error.

Hwang and Chao proposed that $D_t = 0.375$ and $w = 1.5$ in order to match their numerical results to the experimental results by using the inappropriate assumption and their simulation code. Now we tried to obtain the more appropriate values of D_t and w for which our numerical results, without neglecting effective thermal conductivity, can match the experimental data of Hwang and Chao. From Eqs. (11) and (12) in their paper, it can be clearly seen that increasing D_t or decreasing w has the same effect on the thermal dispersion conductivity. Therefore, by adjusting either D_t or w , it is possible to match the numerical results to the experimental results. In our numerical simulation, D_t is selected as a variable for adjustment, since D_t is proportional to the thermal dispersion conductivity, as shown in Eq. (11) in their paper. On the other hand, w is fixed at 1.5 which has been consistently used in previous studies ([2,3]). From our numerical simulation for the condition that Hwang and Chao proposed, it can be shown that $D_t = 0.375$ and $w = 1.5$ are not appropriate, as denoted by broken lines in Fig. 2. Without using the assumption of Hwang and Chao, which neglects the effective thermal conductivity of the fluid, our numerical results are shown to be in good agreement with the experimental results of Hwang and Chao when $D_t = 1.4$ and $w = 1.5$, as denoted by solid lines in Fig. 2.

References

- [1] Kuznetsov, A. V., 1999, “Fluid Mechanics and Heat Transfer in the Interface Region Between a Porous Medium and a Fluid Layer: A Boundary Layer Solution,” *J. Porous Media*, **2**, pp. 309–321.
- [2] Cheng, P., and Hsu, C. T., 1986, “Applications of Van Driest’s Mixing Length Theory to Transverse Thermal Dispersion in Forced Convective Flow Through a Packed Bed,” *Int. Commun. Heat Mass Transfer*, **13**, pp. 613–625.
- [3] Hunt, M. L., and Tien, C. L., 1988, “Effects of Thermal Dispersion on Forced Convection in Fibrous Media,” *Int. J. Heat Mass Transf.*, **31**, pp. 301–309.

Note from the Editor: Professor G. J. Hwang passed away last year, and despite repeated attempts, the Editor was unable to locate or contact the second author, C. H. Chao. Any response from Dr. Chao will be published in a later issue.